ENGINEERING MECHANICS 2024

30th INTERNATIONAL CONFERENCE

MAY 14 – 16, 2024, MILOVY, CZECH REPUBLIC

BOOK OF FULL TEXTS

Editors: Vladimír Fuis
Petr Hájek

Institute of Solid Mechanics, Mechatronics and Biomechanics,
Faculty of Mechanical Engineering, Brno University of Technology

Institute of Thermomechanics
of the Czech Academy of Sciences – branch Brno

Institute of Theoretical and Applied Mechanics
of the Czech Academy of Sciences

ŽĎAS, a.s., Žďár nad Sázavou

IFToMM Member Committee of the Czech Republic

Czech Society for Mechanics

All papers were reviewed by members of the international Scientific Committee.

1st edition, 2024

Cover figure: ***Simulation of blood velocity at the artificial mechanical bileaflet aortic valve at an almost-closed position***

Z. Sant – Department of Mechanical Engineering, University of Malta, Msida

ISBN 978-80-214-6235-9

ISSN 1805-8248

Scientific Committee

Chairman:

Assoc. Prof. Vladimír Fuis, PhD.	**Brno University of Technology & IT AS CR, Brno, CZ**

Members:

Prof. Ivan Baláž, PhD.	**Slovak University of Technology in Bratislava, SK**
Prof. dr. Pavol Bauer	**Delft University of Technology, NL**
Prof. Ján Benčat, PhD.	**University of Žilina, SK**
Prof. Jiří Burša, PhD.	**Brno University of Technology, CZ**
Assoc. Prof. Vladimír Čech, PhD.	**OPROX, a.s., Brno, CZ**
Prof. Matej Daniel, PhD.	**Czech Technical University in Prague, CZ**
Prof. Ľudovít Fillo, PhD.	**Slovak University of Technology in Bratislava, SK**
Cyril Fischer, PhD.	**ITAM CAS, Prague, CZ**
Prof. Paola Forte	**University of Pisa, IT**
Prof. Ardeshir Guran, PhD.	**Institute of Structronics, Ottawa, CA**
Assoc. Prof. Lidia Ilieva-Mitutsova, PhD.	**Bulgarian Academy of Sciences, Sofia, BG**
Assoc. Prof. Zdeněk Jegla, PhD.	**Brno University of Technology, CZ**
Prof. Zbyněk Keršner, PhD.	**Brno University of Technology, CZ**
Prof. Michal Kotoul, DSc.	**Brno University of Technology, CZ**
Assoc. Prof. Daniel Kytýř, PhD.	**ITAM CAS, Prague, CZ**
Prof. Anne-Maria Laukkanen, PhD.	**University of Tampere, FI**
Prof. Arkadiusz Mężyk	**Silesian University of Technology, Gliwice, PL**
Prof. Dr. Damijan Miljavec	**University of Ljubljana, Ljubljana, SI**
Jiří Náprstek, DSc.	**ITAM CAS, Prague, CZ**
Assoc. Prof. Michail Pavlenko	**Moscow State Mining University, RU**
Prof. Dr. Paolo Pennacchi	**Politecnico di Milano, Milan, IT**
Prof. Kazimierz Peszynski, PhD.	**Univ. of Technol. and Life Science, Bydgoszcz, PL**
Prof. Jindřich Petruška, PhD.	**Brno University of Technology, CZ**
Prof. Stanislav Pospíšil, PhD.	**ITAM CAS, Prague, CZ**
Vojtěch Radolf, PhD.	**Institute of Thermomechanics CAS, Prague, CZ**
Prof. Dr. Eduard Rohan, DSc.	**University of West Bohemia in Pilsen, CZ**
Assoc. Prof. Zdenka Sant, PhD.	**University of Malta, MT**
Prof. Ing. Milan Sokol, PhD.	**Slovak University of Technology, Bratislava, SK**
Prof. Alexander Tesár, DSc.	**ICA, SAS, Bratislava, SK**
Prof. Tomasz Topoliński	**Univ. of Technol. and Life Science, Bydgoszcz, PL**
Assoc. Prof. Stanislav Věchet, PhD.	**Brno University of Technology, CZ**
Prof. Yuri Sergeevich Vorobiev	**NAS of Ukraine, Kharkov, UA**
Prof. Jaroslav Zapoměl, DSc.	**Institute of Thermomechanics CAS, Ostrava, CZ**

Honourary Committee

Pavel Cesnek, MSc., MBA — **Managing Director of the ŽĎAS Inc.**

Organizing Committee

Assoc. Prof. Vladimír Fuis, PhD.	**Brno University of Technology & IT AS CR, Brno, CZ**
Petr Hájek, PhD.	**Brno University of Technology, CZ**
Michael Formánek, MSc.	**ŽĎAS Inc., Žďár nad Sázavou, CZ**

List of sections

KEY **Keynote Lectures**

BIO **Biomechanics**

DYN **Dynamics**

FLU **Fluid Mechanics**

KIN **Kinematics**

MCT **Mechatronics**

REL **Reliability of Structures**

SOL **Mechanics of Solids**

TEC **Technological Processes**

TER **Thermomechanics**

Main Headings

Table of Contents

KEYNOTE LECTURES

PAPERS

Table of Contents (by Sections)

DYN Dynamics

FLU Fluid Mechanics

KIN Kinematics

MCT Mechatronics

REL Reliability

SOL Mechanics of Solids

TEC Technological Processes

TER Thermomechanics

KEYNOTE LECTURES

30th International Conference
ENGINEERING MECHANICS 2024
Milovy, Czech Republic, May 14 – 16, 2024

DYNAMICS OF ROTATING SYSTEMS FOCUSED ON INDUSTRIAL APPLICATIONS

Hajžman M.[*], **Bulín R.**[**], **Byrtus M.**[***], **Dyk Š.**[†], **Polach P.**[††], **Rendl J.**[†††], **Smolík L.**[‡]

Abstract: *This paper introduces the specific issues of dynamic behaviour and the possibilities of computational modelling in rotating systems. Initially, it revisits the basic properties of rotating systems supported by journal bearings. Subsequently, it explores the instabilities associated with various types of journal bearings. Three intriguing industrial applications are then presented. The first application explores the nonlinear dynamics of high-speed turbochargers, focusing on their specific floating ring bearings. Computational results are compared with experimentally obtained data for validation. Conversely, the second application concerns the dynamics of large turbine rotors used in power plants. Particular attention is given to addressing challenges related to stator and foundation considerations in computational models. Lastly, the third application aims to model a specific vertical rotor immersed in fluid and operating under extreme temperatures.*

Keywords: Rotordynamics, journal bearing, instability, turbocharger, turbine.

1. Introduction

Dynamics, a branch of mechanics, focuses on understanding the motion of mechanical systems in response to applied forces. When considering various types of motion, the inertia forces acting on specific bodies add complexity to dynamic analysis. Introducing rotation into the system reveals intriguing behaviours such as gyroscopic effects, spin softening, and centrifugal stiffening, e.g. Byrtus et al. (2010). Additionally, rotating components require support and coupling with non-rotating parts, achieved through various types of bearings. The main bearing groups consist of rolling element bearings and journal bearings. While journal bearings can feature a relatively simple design, they are versatile and can be effectively utilized in various applications, see Someya (1989). These journal bearings introduce additional complexities, including instabilities and qualitative changes in system properties summarized by Rendl (2021). In engineering and industry, the development of computational tools reflecting these dynamics is essential for properly and effectively designing rotating systems, see Friswell et al. (2010).

This paper focuses on selected interesting applications of rotor dynamics in industrial settings. Firstly, small-scale turbochargers, rotating at exceptionally high speeds and supported by specialized floating ring

[*] Assoc. Prof. Ing. Michal Hajžman, PhD.: Department of Mechanics, University of West Bohemia, Univerzitní 8; 306 00, Pilsen; CZ, mhajzman@kme.zcu.cz

[**] Ing. Radek Bulín, PhD.: NTIS – New Technologies for the Information Society, University of West Bohemia, Technická 8; 301 00, Pilsen; CZ, rbulin@ntis.zcu.cz

[***] Assoc. Prof. Ing. Michal Byrtus, PhD.: Department of Mechanics, University of West Bohemia, Univerzitní 8; 306 00, Pilsen; CZ, mbyrtus@kme.zcu.cz

[†] Ing. Štěpán Dyk, PhD.: NTIS – New Technologies for the Information Society, University of West Bohemia, Technická 8; 301 00, Pilsen; CZ, rbulin@ntis.zcu.cz

[††] Assoc. Prof. Dr. Ing. Pavel Polach: NTIS – New Technologies for the Information Society, University of West Bohemia, Technická 8; 301 00, Pilsen; CZ, ppolach@ntis.zcu.cz

[†††] Ing. Jan Rendl, PhD.: NTIS – New Technologies for the Information Society, University of West Bohemia, Technická 8; 301 00, Pilsen; CZ, rendlj@ntis.zcu.cz

[‡] Ing. Luboš Smolík, PhD.: NTIS – New Technologies for the Information Society, University of West Bohemia, Technická 8; 301 00, Pilsen; CZ, carlist@ntis.zcu.cz

doi: 10.21495/em2024-018

bearings that exhibit inherent instability, are introduced. Secondly, a contrasting application involving large turbine rotors utilized in power plants is examined. Lastly, a unique case study involving a vertical rotor submerged in a homogeneous mixture of Pb and Li at extreme temperatures is presented.

2. Stability analysis of a system with journal bearings

Journal bearings are well known for their low friction behaviour, low wear and mainly effective vibration-damping capabilities. Unfortunately, they can lead to fluid-induced instability resulting in undamped self-excited vibrations of a supported rotor commonly known as oil whirl, see Muszynska (2005). This behaviour has a dominant vibration frequency occurring at roughly 0.42X–0.49X of the rotor speed. Additionally, significant shaft flexibility can give rise to another phenomenon called oil whip developed from the oil whirl instability at the moment when the oil whirl frequency coincides and locks into the system's natural frequency. Rotor operation typically exhibits three phases: stable vibrations, fully developed instability and a transient state between the two. The speed at which the rotor becomes unstable is called the threshold speed. Interestingly, the threshold speeds identified during run-up and coast-down operations may vary.

A typical journal centre trajectory during the run-up with developed oil whirl is depicted in Fig. 1. The journal centre follows equilibrium locus until the threshold speed ω_t is surpassed. After surpassing this point, the rotor loses stability and oscillates with increasing lateral displacements. The hydrodynamic force stabilises this phenomenon until the second threshold speed ω_g. Here, the stabilising effect is lost and undamped orbital motion is significantly increased which leads to fully developed instability. Detailed behaviour during the oil whirl instability development is depicted in subfigures in Fig. 1.

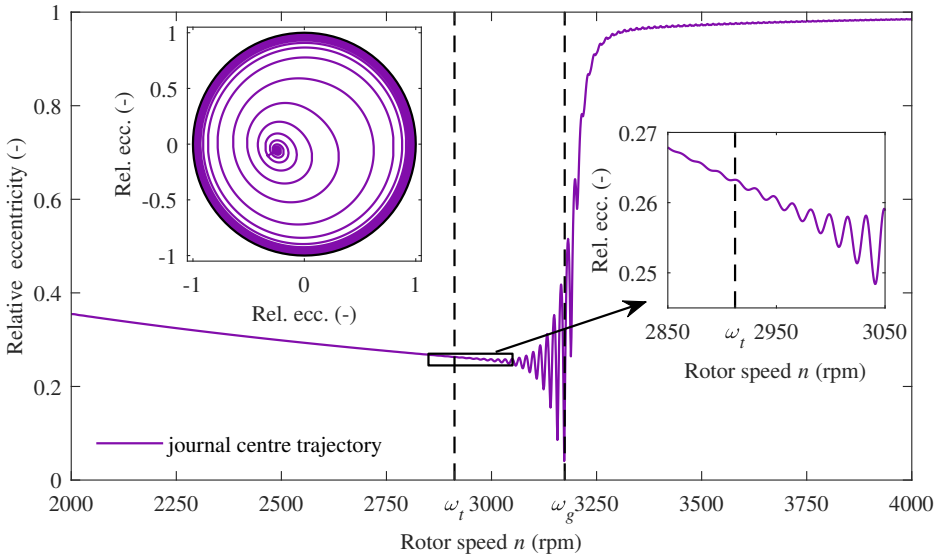

Fig. 1: Journal centre trajectory during the run-up with detected threshold speeds (adopted from Rendl (2021)).

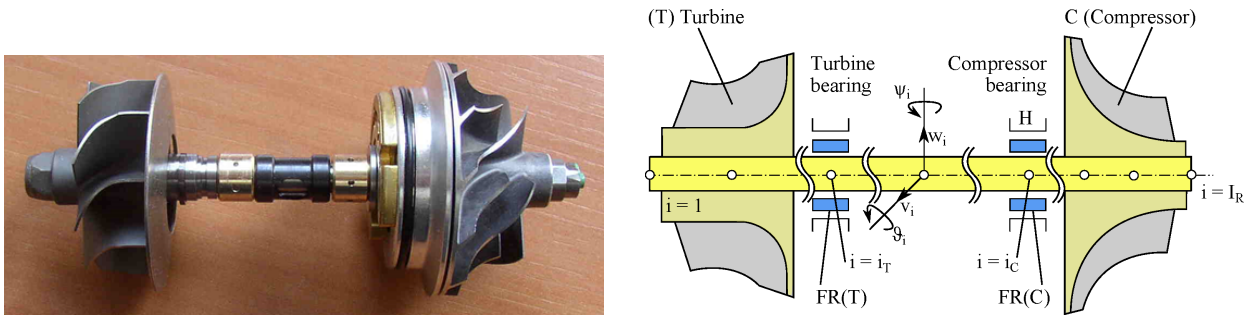

Fig. 2: Real turbocharger rotor (left) and its scheme (right).

3. Dynamics of turbochargers

Turbochargers are modern and highly dynamic systems integrated into various engines to boost their power output. Operating at speeds of hundreds of thousands of revolutions per minute, they are prone to fatigue and stability issues. Turbocharger rotors are usually supported by floating ring bearings (Fig. 2). Dyk et al. (2020) studied the possibilities of linearization of bearing forces in the turbocharges dynamic analysis. Used bearings feature two distinct bearing clearances: one between a journal and a floating ring, and another between the floating ring and its housing. These clearances vary based on temperature differences within the oil films and their effect was analyzed by Smolík et al. (2017). Modal analysis can conducted on a simplified linear model replacing each floating ring journal bearing with two linear springs, aiming to gain a deeper understanding of the system's dynamic properties (see Fig. 3).

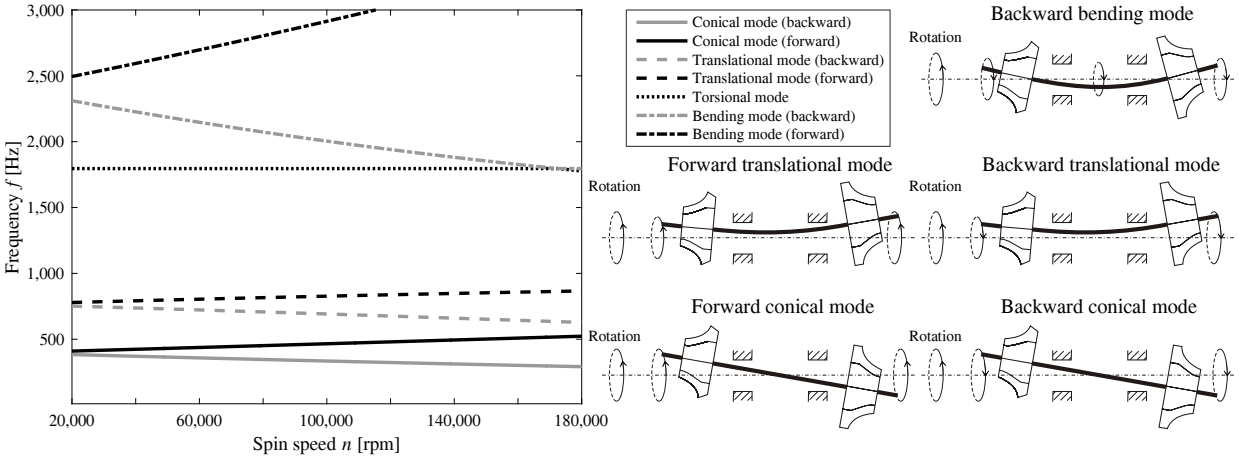

Fig. 3: Typical Campbell diagram of a turbocharger with dominant lateral mode shapes (adopted from Smolík et al. (2017)).

The turbocharger examined in this paper is modelled using flexible multibody dynamics methods. The behaviour of the bearings is characterized using the Reynolds equation, which is solved numerically in the time domain. Given the examination of the turbocharger across a speed range of 60 000 to 150 000 revolutions per minute (rpm), waterfall plots are employed to present the results visually (see Fig. 4 right). These plots illustrate the calculated response spectra as a function of the rotor's spin speed n. To validate the model, experimental measurements were performed and are shown in Fig. 4 on the left.

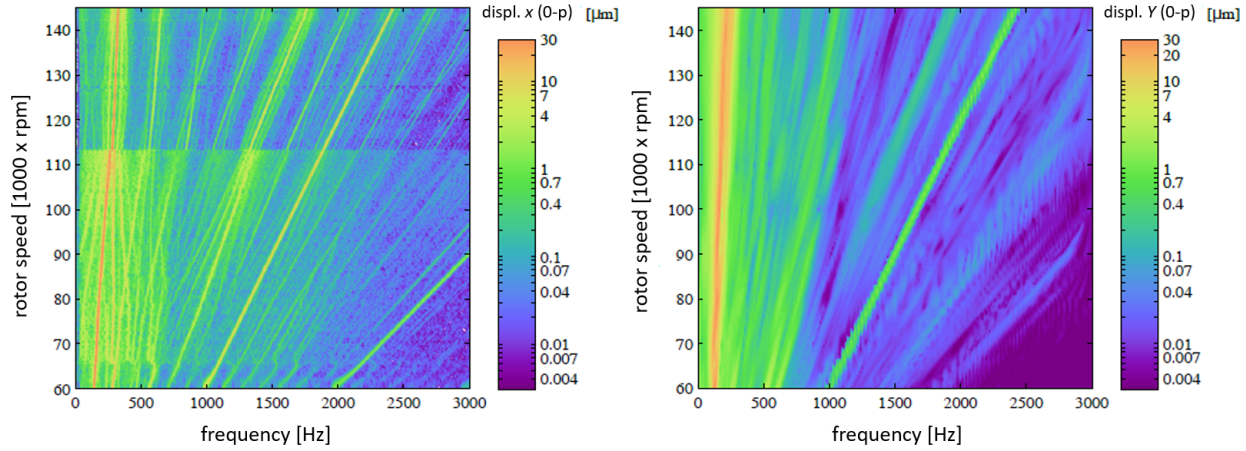

Fig. 4: Measured (left) and simulated (right) turbocharger dynamic response.

4. Large-scale rotor train dynamics

Turbines typically consist of two primary components and their connections (see Fig. 5). One major non-rotating component is the foundation, encompassing all stator parts of the turbogenerator. It can be fixed to the ground via viscous-elastic couplings, designed to provide appropriate stiffness and damping properties to enhance the overall dynamic behaviour of the turbine system. The second primary component is the

rotor train, which varies in size and complexity depending on the specific type of turbine. The rotor train is linked to the foundation via bearings, commonly fluid-film bearings of various designs. The dynamics of turbines can experience significant influence from the presence of a rotor foundation. Consequently, the development of suitable modelling approaches is necessary to acquire accurate analysis tools. The method assessing the dynamic compliance of the foundation concerning the rotor's angular velocity is compared with the approach utilizing modal synthesis of rotor and foundation models. The overall methodology was introduced by Hajžman et al. (2022). The in-house computational tools in MATLAB were developed for the purpose of presented analysis.

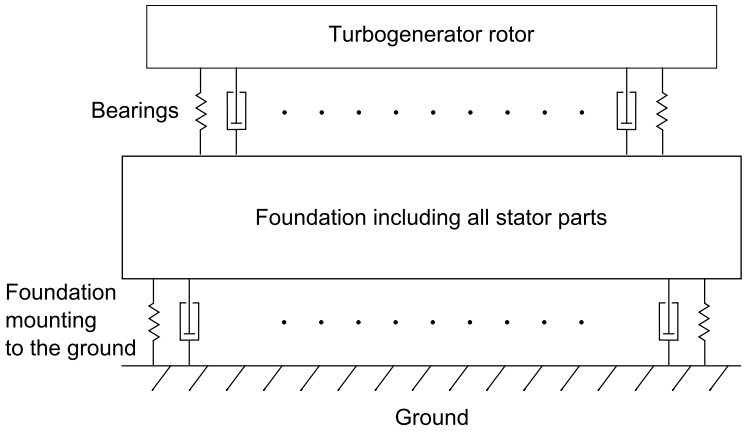

Fig. 5: General scheme of the turbogenerator rotor mounted to its foundation.

The rotor train (see Fig. 6 left), modelled using shaft finite elements with lumped rigid disks, consists of several parts: a high-pressure section (HP), an intermediate-pressure section (MP), two low-pressure sections (LP1 and LP2), a generator (G), and an exciter (E). The rotor support system comprises eleven oil-film bearings with frequency-dependent damping and stiffness properties. The relationship between particular eigenfrequencies of the rotor train with foundation effects (measured in revolutions per minute) and the rotor speed (also in revolutions per minute) is illustrated using the Campbell diagram (Fig. 6 right). Particular mode shapes are characterized by the dominant vibration of denoted rotors (HP to E).

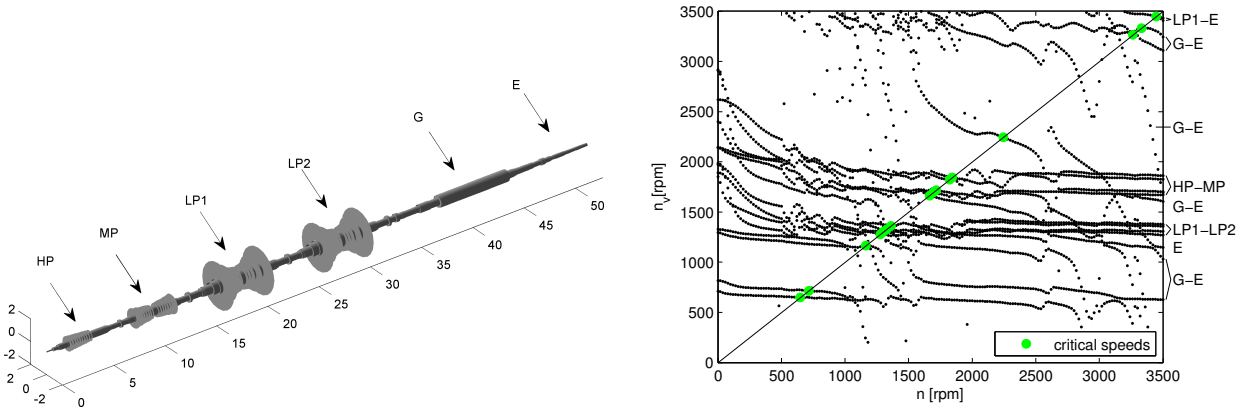

Fig. 6: Visualization of the turbogenerator (left) and a typical Campbell diagram (right), adopted from Hajžman et al. (2022).

5. Vertical rotor immersed in hot fluid

The device known as a saturator, utilized in fusion reactor research, can be designed as a vertical rotor featuring multiple thin discs. This apparatus is situated within a pressure vessel. The gap between the saturator and the vessel is filled with a lead-lithium mixture (PbLi), which undergoes mixing as it circulates through the vessel, facilitated by the rotation of the saturator. When the resulting mixture solidifies, it forms an *eutectic material*, a homogenous mixture of two solids produced under the laminar flow conditions.

Since the temperature of the PbLi mixture reaches 550 °C, the use of rolling element bearings or petroleum-based lubricants in journal bearings is impossible. The dynamic viscosity of the PbLi mixture is ca.

1.28 mPa s at 550 °C, and its density is ca. 9 300 kg m^{-3}. Therefore, it can be used as a lubricant in journal bearings but exerts significant forces on the rotor due to buoyancy and inertia effects. More concretely, a part of the fluid rotates together with the saturator, which causes a force that is proportional to the moving mass of the fluid and its acceleration and a force corresponding to the conservative gyroscopic force (Axisa and Antunes , 1992). In addition, the fluid can exert a viscous damping force and a conservative elastic force on the rotor (Axisa and Antunes , 1992).

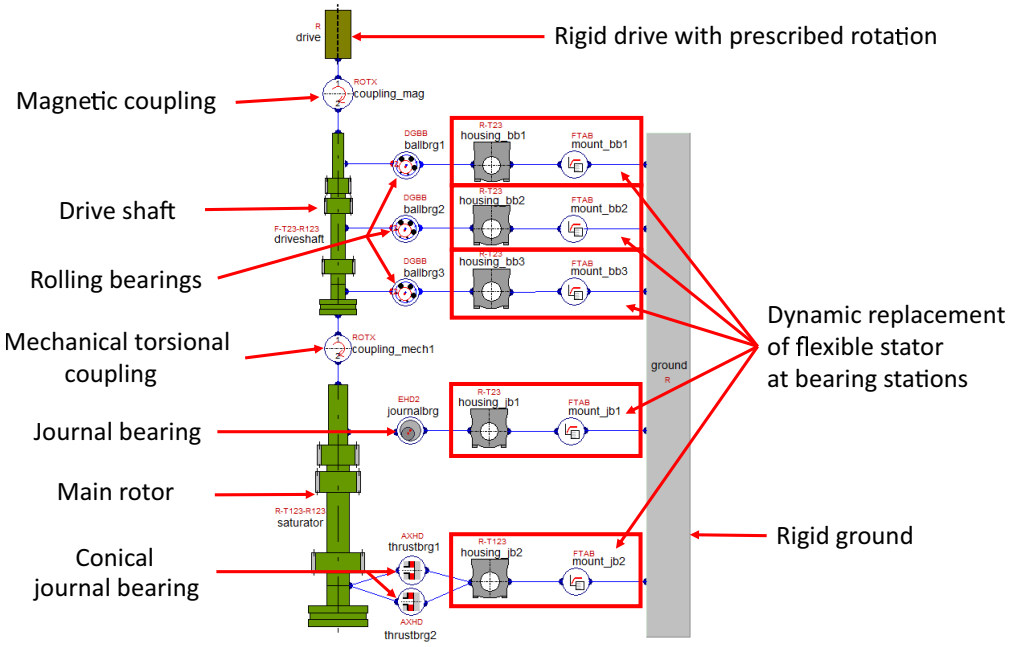

Fig. 7: Scheme of the model of a saturator assembly.

Fig. 7 depicts a saturator assembly comprising three flexible bodies (main rotor, drive shaft, and stator), a rigid drive, and couplings, including a radial journal bearing, a conical bearing supporting the main rotor both radially and axially, three deep groove ball bearings, and two torsional couplings. Due to the presence of multiple flexible bodies and nonlinear couplings in the assembly, its motion is described using the Newton-Euler equations for multi-body dynamics. The whole model was created in the AVL Excite software and numerically solved in order to verify the suitability of the bearing design with respect to instabilities, see Smolík et al. (2022).

Fig. 8 shows a simulated waterfall plot of absolute radial vibrations of the bearing housing that accommodates the upper bearing, see Fig. 7. Up to 600 rpm, the vibrations are caused by the rotating imbalance that causes a response synchronous to the rotor speed. However, as the speed exceeds 650 rpm, asynchronous vibration at ca. 45 Hz (2 700 rpm) becomes prominent. This frequency corresponds with the first stator eigenfrequency and the vibration can be linked with the lower conical bearing that supports both static thrust load and dynamic radial loads due to imbalance. At higher speeds, the conical bearing acts as a pump because of the low thrust load (remember that the thrust load is decreased by the buoyancy). This effect can be effectively mitigated by introducing an extra thrust load.

6. Conclusions

This paper presents some interesting applications of rotating systems related to various effects of rotation and employed bearings. Fluid-induced instability resulting in undamped self-excited vibrations (oil whirl) is introduced for a simple supported rigid rotor. Further, the paper shows how to deal with high-speed turbocharger modelling, with the analysis of large turbines in power plants and with design assessment of the vertical rotor immersed in the specific fluid. The development of appropriate computational approaches and the implementation of related software tools are necessary for the design and diagnostics of many rotating machines used in the industry. There are, naturally, many other topics and practical issues in rotor dynamics that haven't been covered in this paper. For instance, exploring the impact of rotor dynamics on tilting pad journal bearings and examining their detailed response presents an actual and interesting problem (Rendl et al. (2021)).

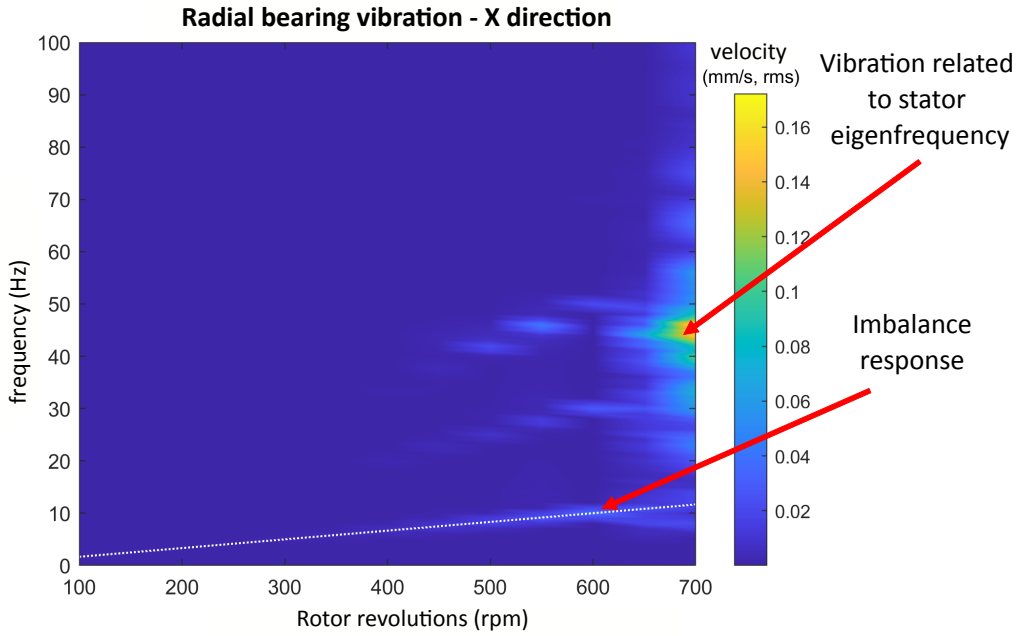

Fig. 8: Simulated waterfall plot of absolute stator vibrations at the upper journal bearing of the saturator.

Acknowledgment

This research work was supported by the Czech Science Foundation project 22-29874S. Chosen simulations were performed in the AVL Excite software which is available in the framework of the University Partnership Program of AVL List GmbH, and whose usage is greatly acknowledged.

References

Axisa, F. and Antunes, J. (1992) Flexural vibrations of rotors immersed in dense fluids, Part I: Theory. *Journal of Fluids and Structures*, 6, pp. 3–21.

Byrtus, M., Hajžman, M. and Zeman, V. (2010) Dynamics of rotating systems. University of West Bohemia, Pilsen.

Dyk, Š., Smolík, L. and Rendl, J. (2020) Predictive capability of various linearization approaches for floating-ring bearings in nonlinear dynamics of turbochargers. *Mechanism and Machine Theory*, 149, 103843.

Friswell, M. I., Penny, J. E. T., Garvey, S. D. and Lees, A. W. (2010) Dynamics of Rotating Machines. Cambridge University Press, Cambridge.

Hajžman, M., Balda, M., Polcar, P. and Polach, P. (2022) Turbine Rotor Dynamics Models Considering Foundation and Stator Effects. *Machines*, 10, 2, paper 77.

Muszynska, A. (2005) Rotordynamics. Taylor & Francis, Boca Raton.

Rendl, J. (2021) Nonlinear dynamics of rotating systems with journal bearings. PhD Thesis, University of West Bohemia, Pilsen.

Rendl, J., Dyk, Š. and Smolík, L. (2021) Nonlinear dynamic analysis of a tilting pad journal bearing subjected to pad fluttering. *Nonlinear Dynamics*, 105, pp. 2133–2156.

Smolík, L., Bulín, R., Hajžman, M., Byrtus, M. and Rendl, J. (2022) Vibration analysis of a vertical rotor immersed in fluid at extreme operating temperatures. In: *Proc. of Computational Mechanics 2022*, University of West Bohemia, Pilsen, pp. 141–144.

Smolík, L., Hajžman, M. and Byrtus, M. (2017) Investigation of bearing clearance effects in dynamics of turbochargers. *International Journal of Mechanical Sciences*, 127, pp. 62–72.

Smolík, L., Rendl, J., Omasta, M., Byrtus, M., Šperka, P., Polach, P., Hartl, M. and Hajžman, M. (2023) Comprehensive analysis of fluid-film instability in journal bearings with mechanically indented textures. *Journal of Sound and Vibration*, 546, paper 117454.

Someya, T. (1989) Journal-Bearing Databook. Springer-Verlag, Berlin.

30th International Conference
ENGINEERING MECHANICS 2024
Milovy, Czech Republic, May 14 – 16, 2024

QUO VADO BIOMECHANICS

Sant Z.*

Abstract: *To understand history, we need to look through a wide-angle lens. The knowledge of history is an irreplaceable component to an awareness of the circumstances in which we find ourselves. Evolution, the gradual process lasting over millions of years, which generated the first hominids from the earlier primates. They differed from other kinds of living organism by bipedal walk. Except for this they showed ingenuity, diligence, and organizational skills, that provide other distinctions from further living creatures. The earliest hominids lived in the world about 20 000 years ago in several complex societies in Africa and Mesopotamia where laid the foundations for civilization, acquired the knowledge of agriculture, art, production of weapons, social structure, and politics. Archaeologists say it is the earliest example of modern culture, based on an extraterrestrial collection of the oldest toolkits that match those used by living humans. The development of their knowledge and skills continued, and with it the necessary tools. Just like today's generation, there was a need to preserve health, so the first, thus oldest implants were tooth replacements. Nowadays, dental implants are very sophisticated, just like many other tools and devices that were created according to the needs of doctors.*

Keywords: Hominid, evolution, biomechanics, gait, implants.

1. Introduction

The oldest evidence of walking on two legs comes from fossils of the earliest humans known, which date back to around 6 million years ago. The most widely accepted theory suggests that the australopithecines, who lived around four million years ago, were the first hominids to walk bipedally. The Laetoli footprints, which date back to 3.5 million years ago, provide solid evidence for bipedalism. The earliest indisputable evidence that our distant ancestors had shifted from four legs to two comes from footprints found in volcanic ash that date back to 3.66 million years ago. Evolution continues, and from hominids became presently humans - Homo sapiens Evolution brought a lot of new things, but as it turned out later, everything new is not perfect. Thanks to evolution, we are humans with bipedal walk, upright posture to see higher and further, and differed from other living creatures. Our anatomy changed to keep upright posture, thus muscular and bony elements had to change size, shape, and with these changes even the transfer of the forces (Niemitz, 2010).

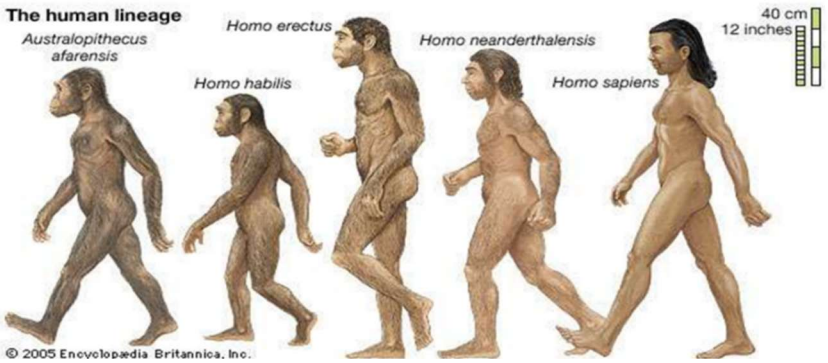

Fig. 1: Evolution of hominid to human in the lineage.

* Assoc. Prof. Zdenka Sant, PhD.: Mechanical Engineering Dept., University of Malta, Tal-Qroqq; MSD2080, Msida; MT, zdenka.sant@um.edu.mt

doi: 10.21495/em2024-024

What is the result of evolution? In 2020, low back pain (LBP) affected 619 million people globally and it is estimated that the number of cases will increase to 843 million cases by 2050, driven largely by population expansion and ageing, increasing of the weight, and decreasing of the muscle strength (WHO).

2. History of Science continues

Mayans, Egyptians, Mesopotamians, and Phoenicians were known for their developed knowledge in astrology and mathematics, but their understanding of nature events was combined with their myths. It was ancient Greeks, who left a record of human inquiry, concerning the relationship of nature and the world with respect to powers of perception at their era. The relative freedom of political and religious restrictions influenced the development of science between 6th to 4th century B.C. and made the first attempt to separate the myths from the knowledge together with building the foundation for scientific inquiry. The development of knowledge, together with awareness of the nature around and science, was classified by historians into seven historical epochs:

Antiquity (650 BC–200 AD),
Middle Ages (200 BC–1450),
Italian Renaissance (1450–1600),
Scientific Revolution (1600–1730),
Enlightenment (1730–1800),
Gait Century (1800–1900) and
20th Century (1900–2000),

where each was influenced by the prevailing reigning group. At each era you could find few famous personalities who enriched the world by art, science novelty, philosophy, and knowledge which, at the later stage of 20th century, become a foundation stone to a new branch of the science, later named Biomechanics.

2.1. Ancient Greeks

Greece flourished in the time of the Ancient Greeks era; scientists and philosophers taught and broadened the horizons of the younger generation. Socrates, the best philosopher at time, was known for spreading his philosophic idea that became famous; “first understand our own nature, to be able to understand the world around us”. Junior to Socrates, Plato began the philosophical inquiries leading to a concept of Western philosophy, psychology, and logic, as well as politics. His conceptualization of mathematics as the life force of science created the necessary womb for the birth and growth of mechanics. Aristotle, son of a physician, studied at Plato’s academy, was gifted for observation, great curiosity in anatomy, and the structure of living organisms. His first book presented observation of the movement of animals. Later he promoted qualitative, common-sense science, without mathematics, leading to deductive methods of modern science, and the fundamental scientific tools – deductive, and mathematical reasoning, which we inherited from the Greek era. These were the first steps towards the new science, that was later named “Biomechanics”.

2.2. Middle Ages

They are known as a “Dark age” that lasted over 1 000 years. This period starts at 476 yr. with the fall of the Western Roman Empire, and the rise of Islam at 610 yr. The creation of the new Holy Roman Empire in northern Europe at 800 years was followed by Medieval thinking. With the fall of Rome, much scientific knowledge was lost. The scientific inheritance from antiquity was saved thanks to translation of the work from Greek to Arabic. Until the rise of the Roman Empire, scientific development in general was discouraged. During the High Middle Ages (1000–1300) period, the population of Europe increased, and academic learning increased together with scholasticism, which developed into a philosophy of learning. Meanwhile, the Crusades and invasions between Christians and the Muslim continued. This period also saw significant growth of feudalism, and hierarchical system of rule. The Late Middle Ages were up-to the yr. 1492 at crisis. Warfare between the kingdoms, the Black Plague that killed a large part of the population, and at the same time, arts and culture progressed and gradually transitioned into a golden age of the Renaissance. At the Late Middle era, **Galen**, the anatomist, and physician left his monumental work, “On the Function of the Parts”, as the world’s standard medical text. His understanding of anatomy and medicine was affected by the then-current theory of humourism. What is the theory of humourism? The Four Humourism were bodily fluids (blood, yellow bile, black bile, and phlegm), that determined a person’s

temperament and his imbalance that led to certain sicknesses dependent upon the type of humors, and its excess or deficit. The humors were connected to celestial bodies, seasons, body parts, and stages of life. Galen's anatomical reports, based on dissection of monkeys and pigs, remained uncontested until 1543, when printed descriptions and illustrations of human dissections were published in the work *De humani corporis fabrica* by **Andreas Vesalius** where Galen's physiological theory was accommodated to new observations. Galen's theory of the physiology of the circulatory system endured until 1628, when **William Harvey** established that the blood circulates with the heart acting as a pump.

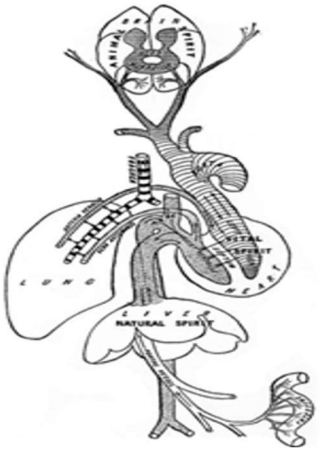

Fig. 2: An interpretation of Galen's human "physiological system".

2.3. Italian Renaissance

After the "Dark age", a new way of life was brought, that was characterized by freedom of thought, which revitalized scientific work, laid the foundations of modern anatomy and physiology, and introduced the first studies of human movement, with relation to muscle activity. The foundation of modern anatomy was based on autopsy observation, and dissection. **Leonardo da Vinci**, self-educated artist, observed the body of humans and horses during their movement, to understand the mechanics of their motion, and provide the mechanical analysis of human movement in relation to bones, muscles, joints, etc. He also contributed to engineering, mainly to mechanics, and several military and civil engineering projects. Already mentioned **Andreas Vesalius,** taught his anatomical theories, and acknowledged that human anatomy could only be learned from dissection and observation. He stimulated scientific debate about the relationship between the muscles and nerves. Leonardo Da Vinci, Andreas Vesalius, Bartolomeo Eustachio, and Costanzo Varolio furthered the study of neuroanatomy. **Nicolaus Copernicus** was Renaissance polymath, his most important contributions was in the field of astronomy, and the concept of a heliocentric solar system in 1514. The Revolutions of the Heavenly Spheres not only revolutionized astronomy, but revolutionized science by reintroducing mathematical reasoning, the antithesis of Aristotelian common-sense physics. It had direct implications for biomechanics, and the desire to explain the orbits of the heavenly spheres led directly to the development of mechanics.

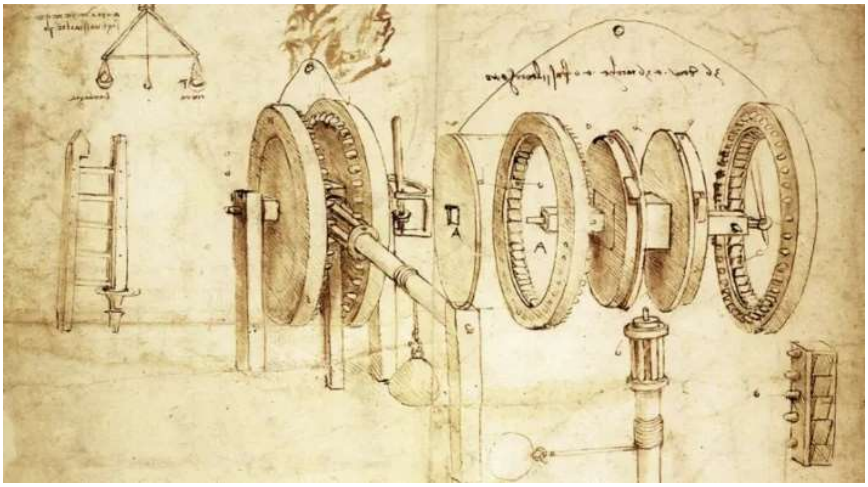

Fig. 3: Vintage Leonardo Da Vinci art work.

2.4. Scientific Revolution

17th century and beginning of the 18th century is associated with great names as **Galileo Galilei**, **Johannes Kepler**, **Rene Descartes**, and **Isaac Newton**. Intellectual freedom was highly respected, new scientific societies were emerging, and the exchange of new ideas was encouraged. Experimentation was the core of the new scientific methods. **Galileo Galileo's** work related to biomechanics of the human jump, and analysis of the gait of horses preceded the work by **Borelli**. **Santorio Santorio**, a physiologist, physician, and professor, that introduced the quantitative approach into life sciences, is therefore deemed the father of modern quantitative experimentation in medicine. **William Harvey** became the first "cardiac biomechanic", and his concept of blood circulation is considered to be a scientific classic. He applied mechanical theory of the heart, and its function as a pump. He identified the mechanical nature of the vascular system. **Rene Descartes** was philosopher who devised Cartesian coordinate system that facilitate the possibility of describing the movement in the space. **Giovanni Borelli** was physiologist, physicist, and mathematician. He was born in Naples in 1608, and his De Motu Animalium, was published in 1680. At this work he extended the rigorous analytical methods, developed by Galileo in the field of mechanics, to the biology. Borelli was credited with earliest descriptions of the distinct phases of the gait cycle and the muscle action during walking. (Al-Zahrani, 2008) He contributed to the modern principle of scientific investigation by continuing Galileo's practice of testing hypotheses opposed to observation. He is called the father of biomechanics. The new instruments such as the mechanical calculator, compound microscopes, barometer, revolutionized physiology, and the focus on movement and motion persisted from 17th to 18th century.

Fig. 4: Compound microscope by R. Hooke (1671-1700).

2.5. Enlightenment

After the scientific revolution, the new phase had a significant contribution to a development of natural science, and the association with three mathematicians. **L. Euler** was a Swiss mathematician, physicist, astronomer, geographer, logician, and engineer who founded the studies of graph theory and topology. He is also known for his work in mechanics, fluid dynamics, optics, astronomy, music theory, and developed mathematical theories describing the motion of vibrating bodies and buckling beams. **D'Alembert** stated "Newton's third law of motion holds not only for fixed bodies but also for those free to move" that directly applies to the principles of kinetics of motion. **J. L. Lagrange** focused his work on analytical mechanics that expressed second Newton's law in terms of kinetic and potential energy. The 18th century provided new approach to physiology that was based on the philosophy "forms follow function" advocated by **M. F. Bichat**. The discovery of electricity amplified the interest in muscle research and understanding of the nature of muscles. **Baglivi** differentiated between the structures and functions of smooth and striated muscle. **D. Bernoulli** developed a mechanical theory of muscular contraction, studied mechanics of breathing, and the mechanical work of the heart. Every field of science needed tools for

experiments or observation. Not everyone had possibility to use the microscope; that invention was dated to late 16th century, created by a modest Dutch eyeglass maker **Z. Janssen**. Janssen's microscope (Chodos, 2004) was nonetheless a seminal advance in scientific instrumentation. By the end of 18th century, the tools such as thermometer, refrigeration machine, weighing scale, compressor, lithography printing technique, and other sophisticated tools, modified for more holistic approach, thus more useful for studying human movements, and better understand the human body. **J. J. Rousseau** revived the idea of a complementary development of body and intellect. The invention of the steam engine by **J. Watt** started the industrial revolution, and the storming of the Bastille signaled the end of monopoly on sport and leisure by the upper class (Scaruffi, 2005).

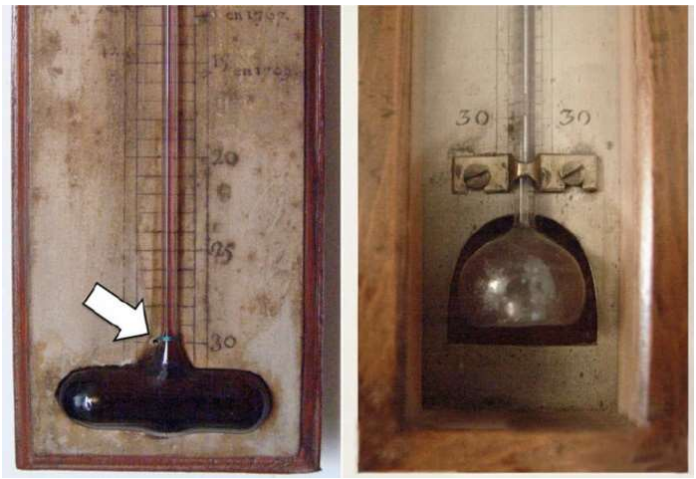

Fig. 5: Reaumur thermometer early version (left), improved version (right).

2.6. Gait Century

19th century continued with analysis of human gait. Science flourished with large number of educated scholars, interested to enrich the science by using they knowledge, and follow the research of human motion. The interest was supported by new equipment and tools that offer a new possibility to investigate the gait better than it was at 18th century, when their observation of the limb's motion could not be quantify due to lack of measuring tools, which resulted in many questions but very little answers. As a writer, **Honoré de Balzac** was interested in the analysis of gait. He also wrote a treatise called "Théorie de la demarche", in which he used his keen powers of observation to define the gait using a literary style. He observed that the gait is divided into phases and listed the factors that influence gait, such as personality, mood, height, weight, profession, and social class, and also provided a description of the correct way of walking. (Collado-Vázquez, 2015) At this time, scientists were oriented towards lower and upper limbs, and any visible and measurable parts. The first foundation stone, created from 17th to 19th century was laid for future science of the human motion. Except of the human motion, there was a desire to learn more about the movement, and how the motion is generated, and controlled by the muscles, and how the muscles work. The 19th century was full of inventions, and new theories. **L. Pasteur** stipulated that bacteria cause infection and disease, and the molecules of living organisms are asymmetric. English doctor **J. Lister** pioneers

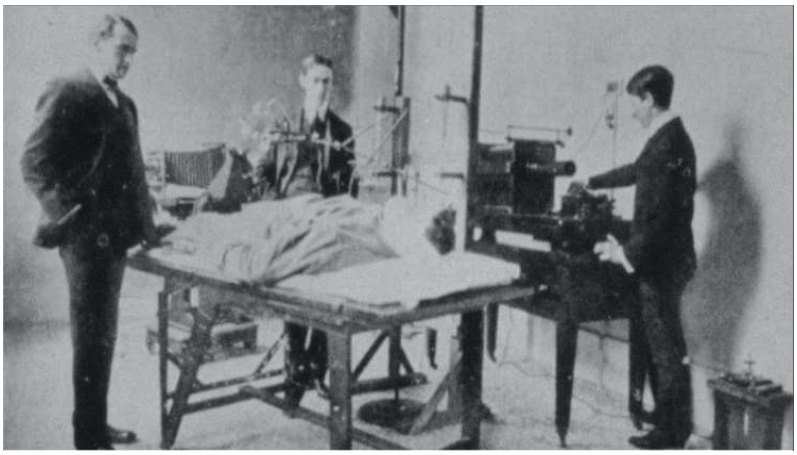

Fig. 6: Wilhelm Roentgen discovers the X-Ray.

the sterile surgery, that become common practice after 1890. The first fitted splints to treat orthopaedic injuries were made by the **DePuy** Manufacturing Company in 1895, as the world's first orthopaedics company. At the same time, it was **W. Roentgen** who discovered X-rays, that are invisible to the human eyes, and the X-ray machine was built within few weeks. **D. Mendeleyev** published his periodic table of elements, **T. Edison** invents the phonograph, **E.-J. Marey's** design a chronophotograph, **S. R. Cajal** proved that the neuron is the elementary unit of nervous system, that processing tasks in the brain, **Lumiere** brothers invented cinema. Another important contribution based on very simple measurements was attained by brothers **Willhelm** and **Eduard Weber**, working in Leipzig. Their work on wave theory was published in 1825, and a treatise on the mechanics of walking in 1833. Both **J. E. Marey** in France, and **E. Muybridge** in America, made significant advances in measurement technology, by making rapid sequences of photographs of motion, and further developed **O. Fischer** in collaboration with **W. Braune**. **Jules Amar** developed a three-component force plate with a mechanical system compressing rubber bulbs and pneumatic transmission of the signals to evaluate the reaction force of the gait. His work is notable, as he was a rehabilitation specialist, driven by a clinical need (Baker, 2007).

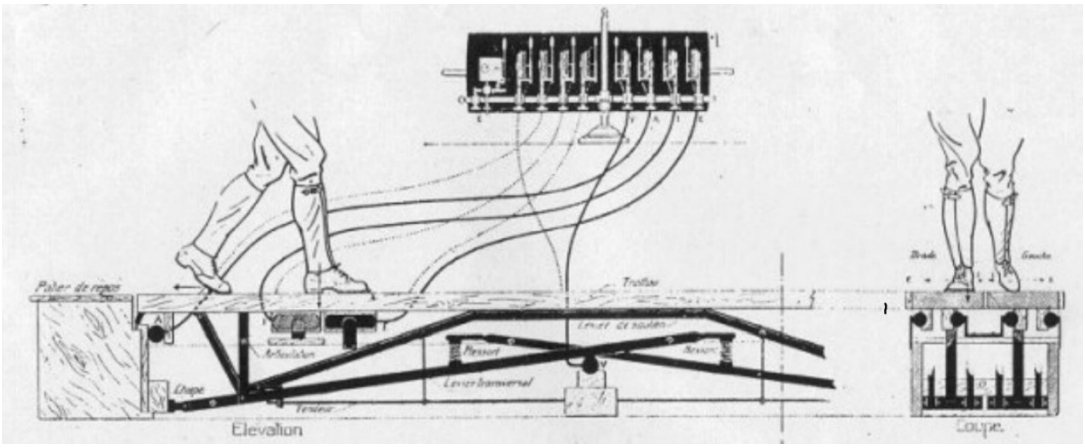

Fig. 7: Three-component force plate with a mechanical system and pneumatic transmission.

3. 20th Century or Electronic Century?

At the turn of the 19th to 20th century, major developments were made. Due to war at the start of the new century, there was a need to heal broken bones, and amputation of the legs, for which the surgeons needed blood, that forced the scientists and engineers to try to solve these problems. **DePuy** Johnson & Johnson came up with their invention to produce metallic splints to heal broken bones.

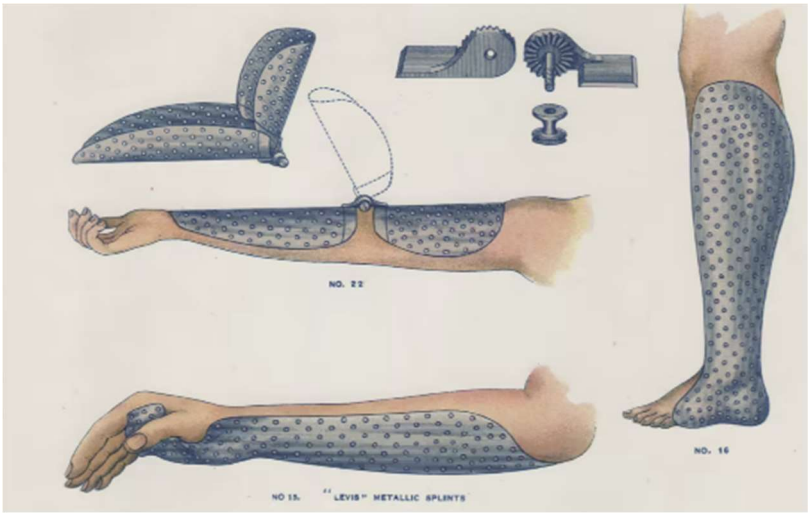

Fig. 8: Metallic splints to heal broken bones.

Australian scientist **Karl Landsteiner** discovered in 1901, four distinct blood types, due to unique antigen, present on the red blood cells' surface. In 1907, was done the first successful blood transfusion by doctor **R. Ottenberg**, but this invention was not suitable for situations when the blood is stored for some time

outside of the body. A team headed by **Verne Inman** and **Howard Eberhart** made major advances in America shortly after the Second War, by developing force plates and understanding of kinetics. **David Sutherland** and **Jacquelin Perry** pioneered clinical applications in America, and **Jurg Baumann** in Europe. At time of the war, there was a need to keep good sterility for surgery, that was provided by use of the seamless glows for surgery and invented an "irrigation system" **Carrel-Dakin**. The deadly epidemic at 1919 call for solution, thus face masks were created. The first electron microscope, that was invented by German physicist **E. Ruska** and engineer **M. Knoll** in 1931, opened a new "science area", and at 1938 was sold first updated type of microscope, named "transmission electron microscope."(Shampo, 1997).

Fig. 9: The first electron microscope.

DNA's structure was discovered in 1953 by **J. Watson** and **F. Crick**, which suggested a method of replicating genetic material. At year 1958 was founded a research study group in Switzerland **AO** (Arbeitsgemeinschaft fur Osteosynthesefragen), which aimed to further advance in the science of treating bone injuries, and later expanded their research to treatments for joint reconstruction, spinal orthopedic trauma, and craniomaxillofacial injuries. Further development was supported by new activities, and introductions by new graduate programs in medicine, biomechanics, and bioengineering at universities across the whole world. Human ingenuity, diligence, organizational skills, and new growing industrial technologies manifested themselves in many areas. Area that was previously unbeatable and become surmountable, are healthcare and medicine. Scientists working in the field of the medicine and physiotherapy, organized in 1971 a seminar at America, followed by the conference, at which they established a society for scientists and students from America, naming it "*International Society of Biomechanics"* (ISB), that was established in 1973. The European seminar (1974) followed the same path, and set "European Society of Biomechanics" (ESB) in 1976 at Brussels. The name "Biomechanics", was accepted after the long years of questioning, if the word *mechanics*, that in Greek language means "motion", is suitable. Thus, the name became the official one for a new science, which is conform to the research of human and animals' motion, their limbs, cells behaviour, and human fluids, including the blood. **Hay**'s definition of Biomechanics from 1973 is related more to an engineering mechanics, and the second-best definition from year 1974, formulated by **H. Hatze**, is a better version of the definition: *"Biomechanics is the study of the structure and function of biological systems by means of the methods of mechanics."* (Hatze, 1974) The second half of the 20th century brought changes not only at the level of knowledge but as well in the growing interest of the young generation to learn more about the body and provides new opportunities for the jobs. Within a few years, biomechanics, that was considered to be a science of gait, started to diversify into branches of specialized biomechanics areas.

3.1. Motion Analysis

This branch of biomechanics continues to analyze motion, using modern systems. The first modern motion laboratory was established at University of California, Berkeley. The first motion laboratory in Europe was the University of Giessen in 1607 as a Lutheran university. ETH Zurich founded their laboratory on 7th February 1854 by the Swiss Confederation, that was modernized on the turn of the century. Modern motion laboratory system records positions of all markers, attached to the skin of a tested subject, then are processed by a digital system to obtain trajectories. Presently, the basic capture system is normally settled from

Fig. 10: Subject with markers and attached sEMG device.

a minimum of six fast infrared cameras, reflective markers, the computer with VICON system code, and usually three force plates. Recorded data are provided in two forms, one is .CSV data suitable for Excel, and the other are in form .c3d, which is a special form used by biomechanics software Mokka and AnyBody. Another tool that can be synchronized with the basic system is an electromyography system (EMG), that has two forms. The clinical system of EMG records the muscle activity invasively via needle, while the laboratory system records the muscle signal from the surface (sEMG) via electrodes. These EMG's record a potential (eV) value, which is recompute to the muscle force in Newton's units. Improved motion capture

Fig. 11: Simulation with AnyBody and VICON data.

technology has enabled more accurate tracking, hence better analysis of human or animal movements, and aids in understanding gait patterns, improving athletic performance, injury prevention, and rehabilitation strategies, which has grown into the wide range of uses that knowledge can achieve. Another step forward can be done with software AnyBody. The motion trajectory is recorded via VICON system, and muscular forces are computed using the inverse dynamics of muscle system applied on recorded data .c3d. The general skeleton of the human subject can be used for simulation of different activities, including the motion of a subject at work with a bicycle or any elements.

3.2. Medical Implants and Prosthetics

From the beginning of mankind, humans used dental implants to replace missing teeth. The first dental, stone implant, was prepared and placed at the mandible in the early Honduran culture around 800 AD (Ring, 1985). The teeth problem was, is and will still be, thus even the implants will exist but more sophisticated due to the latest technology, and materials, same as the second implant in history line.

Orthopaedics is a medical specialty that focuses on diagnosis, and treatment of problems related to the musculoskeletal system. Their orthopaedic implants were the second in a line of the implant's history. Though the date at which an orthopaedic implant was first used cannot be ascertained with any certainty, the fixation of bone fracture using an iron wire was reported for the first time in a French manuscript in 1775 (Hernigou, 2016). The first techniques of operative fracture treatment were developed at the end of 18th and start of 19th century. Presently the surgeon can provide replacement of the big joint such as a hip, knee, fix a fracture, and many other supports that belong to the group of orthotics. Orthoses treat certain conditions of the body such as scoliosis, ankle instability, etc. The first evidence of the use of spinal orthoses in the form of a traction device, can be traced to Galen in 1889 (Moore). The prosthesis is a man-made substitute for a missing body part. A 3 000-year-old mummy was recently discovered sporting a prosthetic big toe. The toe is one of the oldest examples, but from pirates' peg legs to Tycho Brahe's

Fig. 12: Prosthesis of upper arm.

metal nose, replacement body parts have a long and inventive history (MacDonald, 2017). Since each person is an individual one, it is very difficult to precisely adjust the artificial prosthesis for a specific patient. Unfortunately, there are few specialists who can process prosthesis or prosthetics. Till now, we are talking about problems that mainly concern visible or tangible segments of the body. The turn of the 20th to 21th century is marked by a new cardiac implants. The heart is the most significant and vital organ, without it we could not live. In 1628 William Harvey proved that the heart works as a pump but full knowledge of its function was found at a later stage. It is one of the complicated organs that cannot be controlled by anyone nor the brain, as it is controlled by the SA node, which generates the electrical stimulus. If the heart is diseased, and the fibres of electrical conduction are damaged, then the heart beating becomes arrhythmia, and might lead in the stop of the heart. The solution of the mentioned pathological behaviour of the heart calls for implantation of the pacemaker device, containing a pulse generator with built a microcontroller, endocardial leads which have the dual capability of sensing and pacing, and a battery. Since 1812 the inventors were looking for solution how to create a totally artificial heart.

It was in 1982, when the first permanent artificial heart was transplanted. The artificial valves were used from 1952 with a first valve created from the caged with the ball inside, in 1969 new version of tilting-disc valve, and 10 year later bi-leaflet valve. The pacemaker's battery life is limited to 7–10 years for modern pacemakers; thus, the patient must undergo an operation to change the battery. Inventors came with a number of ideas, and one of it is harvest the energy from mechanical energy that will prolongs the life of the battery. A similar task came from the cardiac surgeon; to monitor the behaviour of the valve and observe if the valve doesn't have any unwanted elements or moss.

Fig. 13: Orthopaedic implants.

3.3. Sports Biomechanics

Investigations into sports performance have expanded, involving detailed biomechanical analyses to optimize techniques, prevent injuries, and enhance athletic performance across various sports disciplines. Sport biomechanics is only one part of sport medicine, that works with other disciplines such physiology, psychology, and pathology phenomena. Active athletes have a 50 % chance to sustain an injury, from common are sprain, strain, fractures, dislocations, that must be treated medically. Each sport can have a different injury; thus the sports are split into three types: *collision* sports (rugby, American football, ice hockey), *contact* (basketball, baseball, soccer, water polo, etc.), and *non-contact* (archery, badminton,

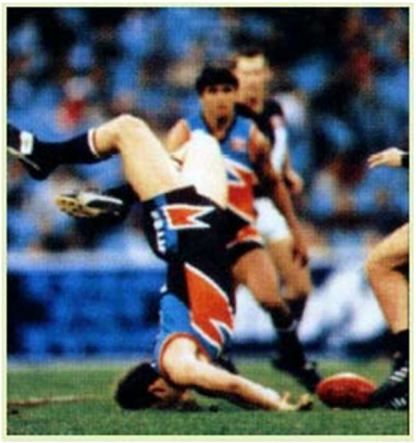

Fig. 14: Injuries in rugby.

bowling, fencing, skiing, etc.). It is important to reduce the risk of injury, so prevention starts at physical condition, good nutrition, and attention to the selection, and fitting of gear and equipment. The physical aspects, the psychological and emotional aspects play a game in the performance. It is a common practice that each sport club has its own team made of professionals in different therapeutic careers that work closely together. Biomechanics specialists provide quantifying tasks, such as an evaluation of the selected muscles, and providing the muscular forces to a physiotherapist, and discuss the strategy how to improve the performance. Even though ballet is not a sport, it is a similar position for the ballerina, with a small diversion

in term of questions and solutions. Ballerina must perform movements that create a smooth trajectory, and result of the analysis is qualitative evaluation.

Fig. 15: Precision of the trajectory.

3.4. Biomechanics in Ergonomics

Using biomechanics in combination with physiology is a good start to avoid occupational disease. Since many workers must repeat an uncomfortable movement for 8 hours throughout the work week and many months, they risk suffering from pain. Continuation of this situation can lead to physical, biological, and chemical hazard. After long time of suffering with pain, they can reach cumulative trauma disorder, and variety of muscular conditions due to incorrect posture, overexertion, or muscle fatigue. These problems must be solved from many reasons; financial problem for the company because the worker is very often out of work, regulatory agencies, reduce of the salary, and other issues. It is necessary to adjust the environment for the workers according to their age, physical ability according to the type of work, and health status of worker.

4. The scientific legacy

To review the history of science, is opening a new desire to learn even more, and widen your horizon. Uncovering the date when the European Society of Biomechanics was founded seems to be just a few years ago. Considering the existence of some discovery from the time BC feels impossible, because it took so long to establish new science Biomechanics. Through history you learn more about different inventions, and it feels that their appetite to bring some new, to understand why things move. Present centuries seem to be packed with novelties, and our days look too be short. There is no time to stop and think about how to improve our planet, our country. At Greek age, Biomechanics was just motion of humans and living creatures. Therefore, mathematics was the priority science, and as time went on, the medics privileged biology, anatomy, and physiology. Presently, even the doctors study mathematics, physics, cooperate with engineers, and bringing new ideas how to improve their devices that can provide a service for doctors, as well for the patient, so doctor can monitor internal organ, which is impossible to monitor by the medics.

5. Conclusions

Two requests from cardiology, found my desk with very challenging work. Two different medics with two ideas that have a different purpose but fit into the cooperation, and solution for final task.

Life is one big book of philosophy, but we often don’t have time to open it. Now we must open a book that will open a part of engineering philosophy. Closing this conclusion with a few quotes.

> “Science can amuse and fascinate us all, but it is engineering that changes the world.”
>
> *Isaac Asimov, American writer, professor of biochemistry*

"The aim of medicine is to prevent disease and prolong life; the ideal of medicine is to eliminate the need of a physician".

William J. Mayo, Founder of Mayo Clinic

"What we usually consider as impossible are simply engineering problems… there's no law of physics preventing them."

Michio Kaku, Theoretical Physicist

References

Al-Zahrani, K. S. and Bakheit, M. O. (2008) A historical review of gait analysis. *Neurosciences*, vol. 13 (2): pp. 105–108.

Baker, C. (2007) The history of gait analysis before the advent of modern computers. *Gait & Posture*, vol. 26, iss. 3, pp. 331–342.

Collado-Vazquez, S. (2015) Balzac and human gait analysis. *Neurología*. 30(4): pp. 240–246.

Chodos, A. and Ouellette, J. (2004) Lens Crafters Circa 1590: Invention of the Microscope. *APS News*, vol. 13, no. 3.

Hatze, H. (1974) The meaning of the term biomechanics. *Journal of Biomechanics*, 7(2):189–190.

Hernigou, P. and Pariat, J. (2016) History of internal fixation (part 1): early developments with wires and plates before World War II, *International Orthopaedics (SICOT)*.

MacDonald, J. (2017) A brief history of prosthetic limbs, *JSTOR*.

Moore, D. P., Tilley, E. and Sugg, P. Spinal Orthoses, https://musculoskeletalkey.com/spinal-orthoses.

Niemitz, C. (2010) The evolution of the upright posture and gait—a review and a new synthesis. *Naturwissenschaften*, 97:241–263.

Ring Malvin E. (1985) Dentistry: an illustrated history. 2nd ed. Abradale Press.

Shampo, M. A. and Kyle, R. A. (1997) Stamp Vignette on Medical Science. In: *Mayo Clin. Proc*. pp. 72:148.

https://www.britannica.com/science/human-evolution

https://en.wikipedia.org/wiki/The_Structure_of_Scientific_Revolutions#History

https://en.wikipedia.org/wiki/Leonhard_Euler

https://www.who.int/news-room/fact-sheets/detail/low-back-pain

https://www.scaruffi.com/science/19th.html

PAPERS

30th International Conference
ENGINEERING MECHANICS 2024
Milovy, Czech Republic, May 14 – 16, 2024

INFLUENCE OF THE ETCHING TIME OF TI6AL4V TITANIUM ALLOY WITH SELECTED ACID SOLUTIONS ON CHANGES IN PHYSICAL PARAMETERS OF THE ELEMENT

Abramczyk I.*, Ligaj B.**

Abstract: *Chemical surface treatment is one of the methods of finishing metals and their alloys. Chemical etching of surfaces is increasingly used for products manufactured using additive methods, also known as 3D printing. The article presents a method of finishing the surface of titanium alloy Ti_6Al_4V ELI elements produced traditionally using a bath in HF/HNO_3 solutions. The influence of etching solutions on the surface quality and material loss was presented. As the etching time increased, the penetration of solutions into the surface increased, which resulted in an increase in the depth of the lowest profile recess (Rv parameter) relative to the height of the highest profile elevation (Rp parameter). The etching process affected the surface of the tested material, causing its hardness to decrease. The highest parameters of hardness decrease were obtained in a 3-minute etching process for B and C solutions. Extending etching to 15 minutes for individual solutions resulted in a varied effect, and in extreme cases, an increase in the surface hardness of the tested material. The obtained results showed a mass loss that was strictly dependent on time.*

Keywords: **Ti_6Al_4V titanium alloy, etching process, HNO_3 acid solution, solution of HNO_3 + HF acid mixture.**

1. Introduction

Producing implants that replace skeletal defects, the medical industry requires high strength, plasticity and hardness of the material. An equally important aspect is the possibility of creating a porous implant structure, which constitutes a scaffold and allows for the reconstruction of natural tissue. The most popular material in this area is the titanium alloy Ti_6Al_4V, which is used due to its biocompatibility with human tissue, as well as its low weight and corrosion resistance (Dallago et al., 2018). The efficiency of tissue penetration into the biomaterial depends on the pore size. Produced biomaterials must perform their functions properly have macropores ranging from 50 to 500 μm (Jones et al., 2003). Surface modification methods are able to improve speed and quality osseointegration processes, which results in increased bone deposition and a shorter repair period (Rieger et al., 2015, Shokuhfar et al., 2014, Torres et al., 2015, Vasconsellos et al., 2017, Yavari et al., 2016 and Zuo et al., 2013). The main purpose of the treatments is to create a passive layer on the surface of the elements, constituting a protective layer against corrosion for the material. The passive layer includes: TiO, Ti_2O_3 and TiO_2 (Baszkiewicz et al., 2006). As a result of chemical etching, porous TiO_2 is formed on the surface of the titanium alloy. The pore size and thickness of the TiO_2 layer depend on the concentration of the solutions and the duration of the process (Oishi et al., 2022). Based on the polarization curves obtained in experimental studies (Sutter et al., 1990), solutions with different surface interaction characteristics were determined. Manipulating the amount of HF makes it possible to control the polishing speed and the degree of interference in the material geometry. Experimental studies have shown a significant loss of mass of the etching material as a function of time

* MSc Izabela Abramczyk PhD candidate: Department of Mechanical Engineering, Bydgoszcz University of Science and Technology, Kaliskiego 7 Street, 85-789 Bydgoszcz, PL, izawil002@pbs.edu.pl

** Prof. Bogdan Ligaj. PhD.: Faculty od Mechanical Engineering, Bydgoszcz University of Science and Technology, Kaliskiego 7 Street, 85-789 Bydgoszcz, PL, bogdan.ligaj@pbs.edu.pl

doi: 10.21495/em2024-038

for the solution proportions of 1.3 % HF and 9 % HNO_3 (Bijlmer et al., 1970). After achieving the maximum weight loss, surface passivation occurs.

The aim of this article is to present the results of preliminary research on the assessment of the influence of the etching process time and the type of etching solution on selected physical parameters of Ti_6Al_4V titanium alloy elements.

2. Methods

The tests used Ti6Al4V titanium alloy in the form of a drawn rod with a diameter of 12 mm in the annealed state, made in accordance with the AMS 4928 standard. The rod was cut and ground using intensive cooling on rollers approximately 3.5 mm high (base diameter 12 mm). Three samples were prepared for each test, and the shape of the samples is shown in Fig. 1.

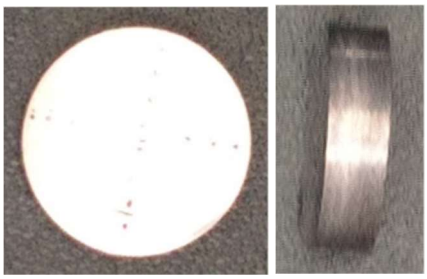

Fig. 1: Samples for the study of the influence of the etching process.

The samples were then heat treated in a vacuum oven in temperature t = 800 °C, maintained for an 1 hour.

The samples were chemically etched in acid solutions, the chemical composition of which was determined based on scientific publications (Bijlmer et al., 1970; Wysocki et al., 2016). To carry out the process, three chemical solutions with different amounts of components were prepared, as shown in Tab. 1.

Mark	Percentage of the substance in the etching solution			Total solution volume
	HF [%]	HNO_3 [%]	H_2O [%]	H_2O [ml]
A	2.0	20.0	78.0	500
B	1.3	9.0	90.0	500
C	1.0	5.0	95.0	500

Tab. 1: Percentage and volume fraction of a substance in the etching solution.

The sample etching process was carried out in three etching solutions for three adopted times, being multiples of the interval of 3 minutes: I - t = 3 minutes, II - t = 6 minutes, III - t = 15 minutes. The samples prepared in this way were tested before and after chemical polishing for: mass, surface roughness by profilometr MahrSurf XR20 and surface hardness by HV5 Vickers hardness tester.

3. Results

3.1. Mass measurement

Analysis of the test results for the mass of samples before and after the etching process indicates that the loss of material depends on the solution used and the duration of the process, as shown in Fig. 2.

The highest mass loss Dm was observed for etching solution B, while the lowest value was obtained for solution A. During the first three minutes of the etching process, the mass loss was:

- for solution A – Dm = 0.020 %,
- for solution B – Dm = 0.034 %,
- for solution C – Dm = 0.025 %.

Further mass loss (in the time interval 3 min < t ≥ 6 min) occurred:

- for solution A – Dm = 0.007 %,

- for solution B – Dm = 0.006 %,
- for solution C – Dm = 0.006 %.

Standard deviation results of 0.00043 g were obtained for the test performed. The presented results indicate that the intensity of interference of solution B was the highest compared to solutions A and C. The obtained results did not indicate the moment of stopping the mass loss in the etching process.

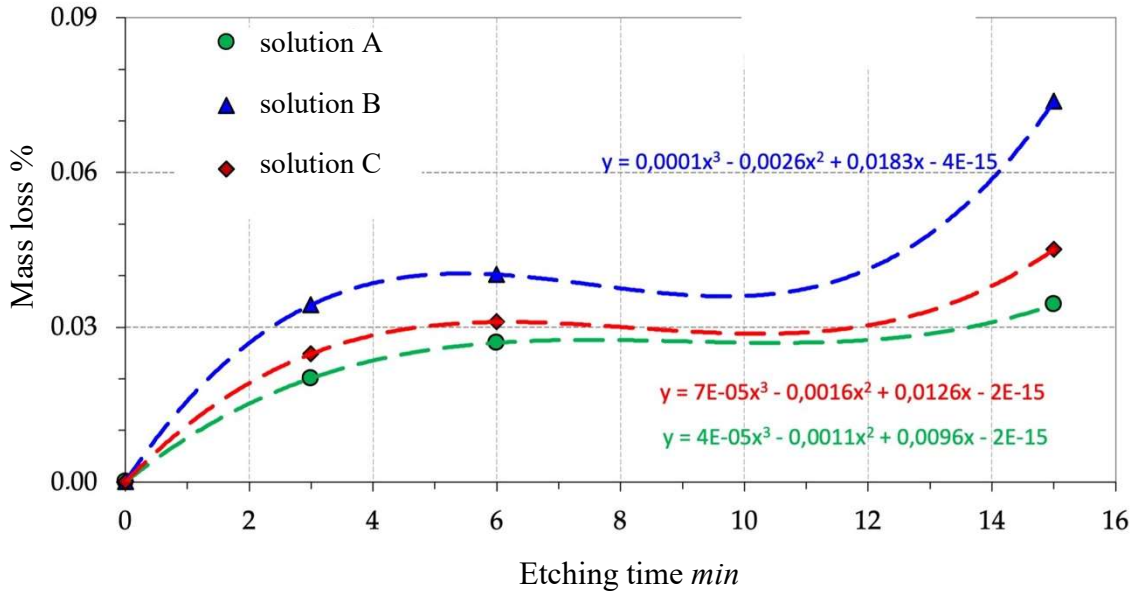

Fig. 2: Relationship Dm = f(t) for the accepted etching compounds.

3.2. Roughness measurement

The following parameters were considered when testing the surface roughness: average R_a, total R_z, smoothness R_p, recess R_v. Analysis of the results presented in Tab. 2 indicates that for most samples there was an increase in surface roughness after the chemical etching process. Only in the case of the Ra parameter for solution A and the etching time did it not give a linear change result. Therefore, the results obtained for this parameter were further examined.

Roughness parameter	Duration of the etching process t [min]	Relative difference d_R [%]		
		Solution A	Solution B	Solution C
R_a	3	20.2	5.4	4.2
	6	-10.3	5.2	17.8
	15	8.0	36.7	32.5

Tab. 2: Relative differences in the roughness values of the sample surface before and after the etching process.

For solutions B and C, the value of the Ra parameter increased with the increase of the etching time. In the case of solution A, the value of the Ra parameter was variable, initially it increased by 20.2 % after 3 minutes of etching, then decreased by 30.5 % after 6 minutes, to increase again by approximately 20 % after 15 minutes of etching process.

Changes in the value of the relative difference d_R of sample roughness were in the range:

- R_a – $-10.3\ \% \leq d_R \geq 36.7\ \%$,
- R_z – $93.9\ \% \leq d_R \geq 228.7\ \%$,
- R_p – $43.0\ \% \leq d_R \geq 221.9\ \%$,
- R_v – $209.3\ \% \leq d_R \geq 1\,056.8\ \%$.

3.3. Hardness measurement

The analysis of the results presented in Tab. 3 shows that for the duration t = 15 minutes, an increase was achieved for all solutions used. The highest relative difference value was obtained for solution C.

Etching time t = 6 minutes, a decrease in the hardness of the material was observed. The highest value was obtained for solution C.

In the case of t = 3 minutes, the relative difference values for solutions B and C have similar values indicating a decrease in the material hardness value after the etching process. Etching the material with solution A resulted in an increase in hardness.

The largest changes in material hardness as a function of the process duration were observed for solution C, while the smallest changes were observed for solution A. The etching process in solution B, after an initial drop in hardness, resulted in its return to oscillating initial values after 15 minutes of etching.

Duration of the etching process t [min]	Relative difference d_H [%]		
	Solution A	Solution B	Solution C
3	0.1 ± 0.1	-6.1 ± 0.4	-6.2 ± 0.3
6	-1.4 ± 0.2	-0.9 ± 0.2	-2.3 ± 0.4
15	0.3 ± 0.2	0.5 ± 0.2	2.2 ± 0.1

Tab. 3: Relative differences in the hardness of the sample surface before and after the etching process.

4. Conclusions

Tests of Ti6Al4V titanium alloy samples before and after the etching process according to the presented experimental plan showed that:

a) the largest material loss was obtained for solution B,
b) the intensity of material loss decreases with the process implementation time for solutions A and C,
c) selection of the roughness parameter used to describe the surface geometry, influences the assessment of process implementation,
d) the etching process increases the surface roughness for each solution used,
e) in the initial phase after 3 minutes of etching, the hardness of the material decreases and increases with its duration for solutions B and C.

The obtained results are the basis for continuing material tests of the etched material, also in the form of samples produced using the 3D additive method.

References

Baszkiewicz J., Kamiński M. (2006) *Korozja materiałów.* Oficyna Wydawnicza Politech. Warszawskiej (in Polish).

Bijlmer P. F. A. (1970) Pickling titanium in hydrofluoric-nitric acid, *J. Met. Finish.*, 68 (1970), pp. 64–72.

Dallago M., Fontanari V., Torresani E., Leoni M., Pederzolli C., Potrich C. and Benedetti M., (2018) Fatigue and biological properties of Ti-6Al-4V ELI cellular structures with variously arranged cubic cells made by selective laser melting, *Journal of the Mechanical Behavior of Biomedical Materials*, 78, 381–394.

Jones J. R. and Hench L. L. (2003) Effect of surfactant concentration and composition on the structure and properties of sol-gel-derived bioactive glass foam scaffolds for tissue engineering, *Journal of Materials Science*, vol. 38.

Oishi T., Matsubara. T. and Katagiri A. (2022) Formation of porous TiO2 by anodic oxidation and chemical etching of titanium*, Electrochemistry*, vol. 68, iss. 2, pp. 106–111.

Rieger N.E., Dupret-Bories E., Salou A., Metz-Boutigue L., Layrolle M. H., Debry P., Lavalle C. and Vrana P. (2015) Controlled implant/soft tissue interaction by nanoscale surface modifications of 3D porous titanium implants, *Nanoscale*.

Shokuhfar T., Hamlekhan A., Chang J.Y., Choi C.K., Sukotjo C. and Friedrich C. (2014) Biophysical evaluation of cells on nanotubular surfaces: the effects of atomic ordering and chemistry, *Int. J. Nanomedicine*, 9.

Sutter E. M. M. and Goetz-Grandmont G. J. (1990) The behaviour of titanium in nitric-hydrofluoric acid solutions, *Corros. Sci.*, 30.

Torres D. L., Pereira M. C., Silva J. W. J., Codaro E. N. and Acciari H. A. (2015) Effect of Phosphoric Acid Concentration and Anodizing Time on the Properties of Anodic Films on Titanium, 10.

Vasconcellos L. M. R. and Villaça-Carvalho M. F. L. (2017) A Study About Cell Activity on Anodized Ti-6Al-4V by Means of Pulsed Current, 12, pp. 1–13.

Wysocki B., Idaszek J., Szlązak K., Strzelczyk K., Brynk T., Kurzydłowski K. J. and Święszkowski W. (2016) Post processing and biological evaluation of the titanium scaffolds for bone tissue engineering, *Materials (Basel)*.

30th International Conference
ENGINEERING MECHANICS 2024
Milovy, Czech Republic, May 14 – 16, 2024

TURBULENCE ESTIMATION BY EDDY DISSIPATION RATE AT LOW-ALTITUDES USING UAV IN-SITU DATA

Balážová R.*, Ferrari S., Hlinka J.***, Santus A.†**

Abstract: *Deploying Unmanned Aerial Vehicles (UAVs) into routine operation requires accurate hyperlocal data. The requirements are set with a significant difference compared to the meteorological information and forecasts that have been sufficient until now. Several challenges need to be solved for the safe operation of UAVs. One of the most significant weaknesses of current meteorological information is turbulence and its detection. This article is focused on the low-altitudes turbulence detection using multicopters and their estimate processed by eddy dissipation rate. A low-cost low-weight method has been identified and will be tested on the field. Eventually, a first attempt to define a minimum safety distance from buildings for the UAVs, depending on building size and wind speed, is investigated via numerical simulations.*

Keywords: Turbulence, Eddy dissipation rate, UAV, sonic anemometer, low altitudes.

1. Introduction

Unmanned Aircraft System (UAS) operations in civilian airspace are growing rapidly, and many analyses and forecasts (Ahmed et al., 2022) predict that trend will continue rapidly over the next decade as regulations are adjusted to allow for greater access to airspace. It is essential that the system maintains a high level of safety and security during its growth so that the potential of UAS (performed by UAVs – Unmanned Aerial Vehicles, also named drones) can be fully realized (Alarcón et al., 2020, Shakhatreh et al., 2019). UAVs are quite sensitive to wind gusts and turbulence; hence, unexpected wind changes and turbulences are a major complication. The unique characteristics of UAS require current aviation meteorological information to be improved and provide drone users with the necessary real-time information to ensure a high safety level.

The review of meteorological information gap for unmanned (low-altitudes) operations in middle Europe was the first part of this dissertation research. In the first phase, a detailed summary of all previous research focused on hyperlocal meteorological information gap for low altitudes was conducted. Subsequently, extensive survey analysis (Voice of the Customer) was performed, that identified gaps between existing aviation information and data requirements from drone operators and their users. Both, results of the survey of existing research works and own Voice of the Customer survey (VOC), identified gaps in information services for future drone operations as critical to achieving safe drone operations in Very Low Level (VLL) airspace. This analysis outlined a potential topic for research, namely, how to fill this lack of information regarding low-altitude turbulence, which is addressed in the second phase of research in 2024. Most respondents of the VOC questionnaire observe frequent “unexpected” turbulence during flights around buildings/bridges/pillars. While conducting a survey of meteorological information and service providers,

* Ing. Renáta Balážová, MSc: Brno University of Technology, Faculty of Mechanical Engineering, Institute of Aerospace Engineering; Technická 2896/2; Brno 616 69; CZ, renata.balazova@vut.cz

** Assoc. Prof. Simone Ferrari, PhD.: University of Cagliari; Dept. of Civil, Environmental Engineering and Architecture; via Marengo 2; 09123, Cagliari; IT, ferraris@unica.it

*** Assoc. Prof. Jiří Hlinka, PhD.: Brno University of Technology, Faculty of Mechanical Engineering, Institute of Aerospace Engineering; Technická 2896/2; Brno 616 69; CZ, hlinka@fme.vutbr.cz

† Ing. Alessandro Santus, MSc: University of Cagliari; Dept. of Civil, Environmental Engineering and Architecture; via Marengo 2; 09123, Cagliari; IT, alessandro.santus@unica.it

doi: 10.21495/em2024-042

it was found that information about turbulence is a missing meteorological parameter that no one provides for hyperlocal conditions at low altitudes. The topic of turbulence detection at low altitudes using high-quality anemometers has been addressed by several previous studies (Shelekhov et al., 2022, Luce et al., 2019). This paper is focused on the detection of turbulence at low altitudes with low-cost sensor (the limit for this research is 150 m Above Ground Level).

In the aviation in general, information about the occurrence of turbulence is shared based on two sources. The first form of information is Pilot reports (PIREP), which are routine pilot observation reports. This type of reporting is highly imprecise due to time and positional inaccuracy, pilot subjectivity and aircraft dependency. Due to the inaccuracy of PIREP reports, the detection and prediction of turbulence for commercial aircraft is currently based on the use of In-Situ data, from which it is possible to estimate 3 turbulence indicators: Vertical acceleration, Derived Equivalent Vertical Gust Velocity (Derived Equivalent Vertical Gust - DEVG) and Eddy Dissipation Rate (EDR). The International Civil Aviation Organization (ICAO) has designated EDR as the preferred and standard metric for turbulence reporting (ICAO, 2001). However, the current version of the EDR algorithm created by National Center for Atmospheric Research (NCAR), is not applicable for multicopters. The list of required parameters contains parameters (e.g., Angle of attack) that cannot be measured on a multicopter. Consequently, the first aim of this article (and, in general, of the dissertation) is the operational identification of an EDR measurement system that is easily and feasibly applicable to multicopters. This must be a low-cost and light solution for turbulence detection, mountable on a wide range of multicopters to provide In-situ data. The inspiration is the current deployment of the NCAR algorithm across the world fleet of commercial aircraft and their mutual information sharing. It should be emphasized that the sought solution must be inexpensive. The second aim is a first attempt to define minimum safety limits from buildings depending on building size and wind speed; in fact, UAVs often fly in the Urban Boundary Layer (UBL), where the buildings strongly modify the wind patterns, causing recirculation zones and turbulent wakes which can be dangerous for the UAV flight.

In Chapt. 2., the authors describe 4 important information of the research: the first is the calculation formula; the second is the selection of the measurement sensor; the third is devoted to numerical simulations and their importance, especially in determining the minimum safety limits from buildings depending on the size of the building and wind speed; the last part describes the prepared demonstration mission, which will be carried out in the spring of 2024. The conclusion summarizes the findings so far and explains the next stages of research with a clearly defined goal.

2. Methods

2.1. EDR Calculation possibilities

The eddy dissipation rate (EDR) is the cube root of the dissipation rate of turbulent kinetic energy (TKE) ε, and hence has units of $m^{2/3}\ s^{-1}$. Summarizing, the most relevant velocity processing methods for ε evaluation (Guichao et al., 2022) are: Fluctuating velocity gradients; Smagorinsky closure method; Dimensional analysis; Structure function; Energy spectrum; and Forced balance of the TKE equation. After thorough analysis of previous research activities and taking into an account the specifics of the multicopter, the "Inertial Dissipation Method Using Structure Function" alternative (Kim et al., 2021) was selected as the EDR formula. The anemometers generate a sequence of wind velocities at a set position. To apply the mathematical turbulence models established in the spatial dimension, it becomes essential to utilize Taylor's frozen hypothesis, which links the connection between the physical variables in the spatial domain and those in the time domain. As per Kolmogorov's turbulence hypothesis (Kolmogorov, 1991), the EDR adheres to a particular spatial separation pattern within the Inertial Range (IR) for isotropic turbulence. Following Taylor's frozen hypothesis, EDR is then formulated in relation to temporal separation (τ) and structure function (SF), as:

$$EDR = \left(\frac{1}{U}\right)^{1/3} \left[\frac{\overline{D_U(\tau)\tau^{-2/3}}}{C_K}\right]^{1/2} \quad (1)$$

where the overbar notation is the arithmetic average within the IR, U is the mean velocity, and C_K is Kolmogorov constant (C_K = 0.52) and $D_U(\tau)$ is the SF.

In previous studies (using anemometer with sample rate of 10 Hz), the range of τ was set between 0.1 s and 2.0 s and time window around 120 s to calculate SF. Considering the limits of our low-cost concept (sample

rate of 1 Hz), the range of τ is set between 1.0 s & 2.0 s and the time window is extended.

2.2. Sensor selection

Summarizing all previous research activities (e.g. Palomaki et al., 2017 and Adkins, 2019), it seems that use of ultrasonic anemometer is an ideal solution for drone-based wind measurement. The main disadvantage of this measurement technique is price that has a range from 1 500 € to 20 000 €. This price range is associated with high-quality anemometers (sample rate of 10 Hz and more). Considering our primary goal, which is to provide a low-cost solution that can be implemented by a wide range of users, high-quality anemometers are not an alternative for use in this research.

A very important and key step was to summarize the specifications of the ultrasonic devices used and the accuracy that was achieved. This information was used as the basic specifications in the search for an ultrasonic anemometer within affordable sensors. One of the main selection criteria was the purchase price, which must not be higher than 300 €. Another parameter is the weight of the sensor, because with quadcopter platforms the user is limited by a maximum payload of 0.5 kg. And the third important factor is to find a sensor that does not need an external power-battery, data logger, etc. and everything will be integrated within the sensor. After a thorough analysis of the market, the model "Ultrasonic Portable Mini" from the manufacturer CALYPSO instruments was selected. This is a wireless, Bluetooth (BLE) and battery-powered, pocket-sized ultrasonic anemometer with sample rate of 1 Hz. Weight of the sensor is 78 g and the purchase price is within the set budget. Sonic anemometers will be integrated in the number of two pieces, one in the horizontal direction and the other in the vertical direction, in order to obtain a 3D wind characteristic.

2.3. Numerical simulations

In the first phase, two different numerical simulation models are processed. One is the AdMaS campus, where a demonstration mission will take place in the spring of 2024 (see Sect. 2.4.) and the results of the numerical simulation will be compared with directly measured In-Situ data using a multicopter (Fig. 1). All numerical simulations were processed using ENVI-met software (license provided by the University of Cagliari).

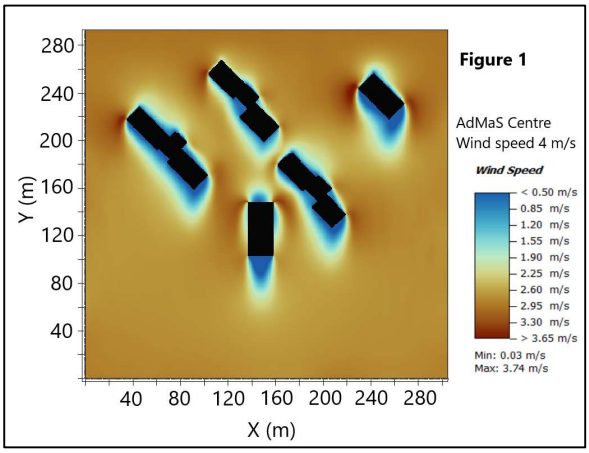

Fig. 1: Numerical simulation "AdMaS Campus".

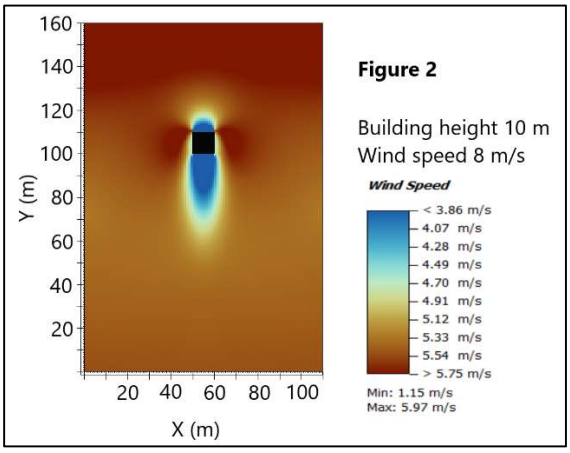

Fig. 2: Numerical simulation "Single building".

Second set of processed numerical simulations are simple scenarios with stand-alone buildings with different heights and under different meteorological conditions. In this set of simulations, the focus is on eddies around buildings and especially on their size. The result of this analysis will be the dependence between 3 key factors, which are the size of the building, the speed of the prevailing wind and the size of the turbulent eddy around the building. Fig. 2 shows an example output of a numerical simulation with a "cube" building size of 10 x 10 x 10 m and a wind speed of 6 m/s. The numerical simulations consist of multiple scenarios with different building heights up to 30 m and wind speeds up to 10 m/s.

2.4. Demonstration Mission

Key test flights, which are considered the most important phase of this research, are planned for spring 2024, (i.e. April – May). This demonstration mission will be performed in Brno, in the AdMaS area (near

building H). The unmanned aerial vehicle will be a multicopter, specifically a quadcopter (probably a DJI Phantom 3 Advanced) with an integrated two Calypso sonic anemometers. Test days will be chosen based on weather forecasts. The most important meteorological parameter is wind speed, and the ideal conditions for detecting turbulent eddies are at least 5 m/s and higher.

3. Conclusions

As part of the research, all the weaknesses that need to be overcome to ensure safe UAV operation from the meteorological point of view have been summarized in previous work. Among all the challenges, the main problem was selected with focus on turbulence estimation. The solution is inspired by classic manned aviation, ICAO standard and NCAR algorithm. Since UAVs have significant differences in the concept of the vehicle, maximum payload, different sensor equipment and measured in-situ data, a major modification of EDR algorithm for UAV use is required. The main criterion and goal of this research is not to have the most accurate data possible using a sophisticated sensor, but applicability in a wide spectrum. As part of the research, all possibilities of the EDR formula for estimating turbulence were summarized and the final selection is presented in Sect. 2.1. For the given calculation, it is necessary to have real-time data, which unfortunately the basic DJI platform does not contain, and that is why the integration of an additional sensor is essential. Based on a detailed and comprehensive survey of the market, the final selection was processed with regard to maximum payload, purchase price, power supply and data storage. Selected product is model "Ultrasonic Portable Mini" manufactured by Calypso with a sample rate of 1 Hz. Two pieces of the given sensor will be integrated to ensure 3D wind characteristics. The demonstration mission will be carried out in the spring of 2024 in the premises of the AdMaS center. For this demonstration mission, numerical simulations have been processed using the ENVI-met software, and the results will be compared with directly measured UAV data. Another set of numerical simulations is a domain with single building, where it is monitored the dependence between the height of the building (up to 30 m high), the wind speed (up to 10 m/s) and the size of the vortex behind the building. Based on the dependence between these 3 parameters, minimum safety limits from buildings will be determined. The results of numerical simulations as well as test flights will be published in the summer of 2024.

Acknowledgement
This work has been supported by the project No. FSI-S-23-8163 funded by the Ministry of Education, Youth and Sport (MEYS, MŠMT in Czech) institutional support.

References

Adkins, K. A. (2019) Urban flow and small unmanned aerial system operations in the built environment. *International Journal of Aviation, Aeronautics, and Aerospace*, 6.

Ahmed, F., Mohanta, J. C., Keshari, A. and Yadav, P. S. (2022) Recent Advances in Unmanned Aerial Vehicles: A Review. *Arab J Sci Eng* 47, 7963–7984.

Alarcón, V., García, M., Alarcón, F., Viguria, A., Martínez, Á., Janisch, D., Acevedo, J. J., Maza, I. and Ollero, A. (2020) Procedures for the Integration of Drones into the Airspace Based on U-Space Services. *Aerospace*, 7, 128.

Guichao W., Fan Y., Ke W., Yongfeng M., Cheng P., Tianshu L. and Lian-Ping W. (2021) Estimation of the dissipation rate of turbulent kinetic energy: A review. *Chemical Engineering Science*, vol. 229, 116133.

Kim, J., Kim, J. -H. and Sharman, R. D. (2021) Characteristics of Energy Dissipation Rate Observed from the High-Frequency Sonic Anemometer at Boseong, South Korea. *Atmosphere*, 12, 837.

Kolmogorov A. N. (1991) The local structure of turbulence in incompressible viscous fluid for very large Reynolds numbers. *Proc. R. Soc. Lond.*, A4349–13.

Luce, H., Kantha, L., Hashiguchi, H. and Lawrence, D. (2019) Estimation of Turbulence Parameters in the Lower Troposphere from ShUREX (2016–2017) UAV Data. *Atmosphere*, 10, 384.

Palomaki, R. T., N. T. Rose, M. van den Bossche, T. J. Sherman, and S. F. J. De Wekker, 2017: Wind Estimation in the Lower Atmosphere Using Multirotor Aircraft. *J. Atmos. Oceanic Technol.*, 34, 1183–1191.

Shakhatreh, H., Sawalmeh, A. H., Al-Fuqaha, A., Dou, Z., Almaita, E., Khalil, I., Othman, N. S., Khreishah, A. and Guizani, M. (2019) Unmanned Aerial Vehicles (UAVs): A Survey on Civil Applications and Key Research Challenges. IEEE Access, 7, 48572-48634. Article 8682048.

Shelekhov, A., Afanasiev, A., Shelekhova, E., Kobzev, A., Tel'minov, A., Molchunov, A. and Poplevina, O. (2022) Low-Altitude Sensing of Urban Atmospheric Turbulence with UAV. *Drones*, 6, 61.

30th International Conference
ENGINEERING MECHANICS 2024
Milovy, Czech Republic, May 14 – 16, 2024

APPLYING A TWO DEGREE OF FREEDOM MODEL FOR DRIVE-BY IDENTIFICATION

Bayer J.*

Abstract: *A new concept of drive-by identification is examined applying the analogy with a Two Degree Of Freedom (DOF) system where the bridge is considered the ground-supported spring-mass and the moving spring-mass the second DOF. The response of the moving spring-mass is simulated on a bridge model using different road profiles and compared to parameters of the corresponding two DOF system. The focus is the spectral shift that can be observed on the moving spring-mass during its passage along the bridge and could possibly be applied for drive-by identification. The accuracy mainly depends on the relation of the moving spring-mass to the bridge mass and the relation between the natural frequency of the spring-mass and those of the bridge. The simulations showed that road profile can significantly reduce the accuracy of identified results, which imposes limits on practical applications.*

Keywords: Drive-by identification, structural health monitoring, finite element analysis, road roughness, two DOF system.

1. Introduction

Drive-by Identification has been studied since the closed-form solution for a sprung mass on a beam was published (Yang, 2004). A recent review of the achievements in the field of Vehicle Scanning Method (VSM), formerly called "drive-by identification", can be read in (Wang et al., 2022). However, the theory formulated by (Yang, 2004 and 2021) only applies when the vehicle mass is negligible compared to the bridge mass. In this case the effect on the spring-mass will also hardly have any measurable effects on the bridge vibrations. When the moving spring-mass is insignificant it is reduced to a kind of moving transducer that measures vibrations induced by other phenomena, which may not always provide credible results because the loading can change over time.

This article considers the case where the moving vehicle mass with a spring-mass is significant. It should be noted here that an ideal moving spring-mass is nearly impossible to achieve under practical circumstances; a sprung mass cannot roll directly on a roadway or rail because it has to be pulled by another vehicle or have its own drive. Therefore, the effect of the moving mass has to be considered along with the effect of the moving spring-mass. The moving mass continuously changes the natural frequencies of the mechanical system (bridge + moving body) as a function of its position. Moreover, the moving spring-mass also causes a spectral shift of the natural frequencies—similar to the one that occurs when two single DOF systems are coupled together, as in the case of a tuned spring damper (Ormondroyd, 1928). The main advantage of this approach is that the moving spring-mass parameters are known, thus "only" the 2nd DOF—a bridge DOF parameters—need be identified from the response.

To estimate the chances that the above-mentioned spectral shift could be used for bridge frequency estimation on a vehicle driving along the bridge, a simulation case study was performed. The response of a moving vehicle consisting of a mass and spring-mass when driving across a bridge model was analyzed using different road profiles (RP). The shifted spectral peaks of the spring-mass were extracted from the response and compared to theoretical values of the corresponding two DOF system. Because the vehicle

* Ing. Jan Bayer, CSc.: Institute of Theoretical and Applied Mechanics of the CAS, Prosecká 809/76; 190 00, Prague 9; CZ, bayer@itam.cas.cz

doi: 10.21495/em2024-046

mass causes a continuous change in bridge parameters, only the response from driving over a middle section of the bridge model was used in order to keep the parameter changes as small as possible.

2. Assumptions & objectives

Free vibrations of a bridge can be described using modal decomposition. The modes of the bridge (or beam in this article, see Fig. 1) are continuously altered by a passing spring mass with dashpot due to dynamic coupling effect. Within short sequences, the frequencies of the system "bridge & spring mass" can be averaged and considered constant. The inaccuracy caused by averaging is known and can be considered as a system uncertainty. Statement: mostly influenced is the bridge mode closest to the natural frequency of the passing spring mass. The article examines if the frequency of this mode and the spring mass frequency could be measured on the passing spring mass and applied for the identification of bridge natural frequencies using the analogy with a two-DOF system.

3. Simulations

Simulations were computed for a laboratory bridge model consisting of a 4 m long simply supported beam made from Jäckel steel U-210x50x4 with a first natural frequency of 7 Hz and the mass of 33.3 kg (see Fig. 1). The simulations of the passage of a spring mass across the beam were carried out using the method described in (Bayer, 2023). The four parameter sets given in Tab. 1 were considered here with the vehicle speed limited to 0.1 m/s for clarity of presented results.

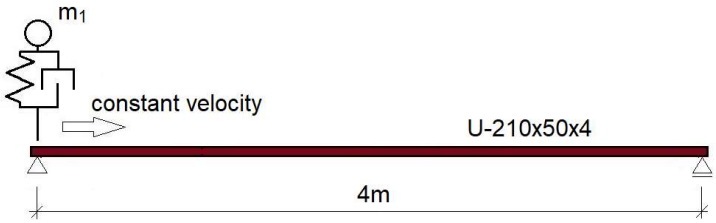

Fig. 1: Considered mechanical system.

m_1 [kg]	f_n(SM) [Hz]	f_n(B) [Hz]	m_1/m_2 [%]	f_n'(SM) [Hz]	f_n'(B) [Hz]	Δ(SM) [%]	Δ(B) [%]
0.245	6.72	6.77	1.48	6.36	7.15	-5.38	5.68
0.620	6.72	6.77	3.76	6.14	7.40	-8.59	9.40
0.245	9.50	6.77	1.48	9.63	6.68	1.37	-1.35
0.620	9.50	6.77	3.76	9.81	6.55	3.30	-3.20

Tab. 1: Decisive parameters of a two DOF system applied in the simulations (m_1 moving spring mass (SM), m_2 bridge(B) modal mass, f_n natural frequency, f_n' natural frequency of the coupled system, Δ frequency shift due to the coupling of the two DOFs).

The following major limiting conditions were expected:

- The parameters of the bridge-vehicle mechanical system change according to the position of the vehicle. E.g., if a 10 s-long middle-section vibration sequence is needed for evaluation in the considered case, the fact has to be taken into account that due to the moving mass the bridge natural frequency changes during this short sequence by about 0.5 % at the considered speed of 0.1 m/s. Increased speed means a longer driving sequence and thus a greater frequency change.
- The spectral shift depends on the mass relation and the frequency distance of the two idealized DOFs. The effect is illustrated in Fig. 2. It follows that a measurable shift presumes a mass relation of at least 0.1 %.
- Road roughness has an influence on the measured data and will be examined further below.
- The reduction of the multi DOF system to two DOFs: The natural frequency of the moving spring-

mass has to be much closer to the traced (measured) bridge natural frequency than other bridge frequencies. Therefore, the most reliable case is when the frequency of the moving spring is lower than the first bridge frequency.

The RP was simulated according to the ISO standard 8608 applying appropriate model scales.

It was realized that the effect of the road roughness exceeds decisively the dynamic effect of the moving mass & spring-mass. However, the question is whether ISO 8608 is applicable to the low speeds that are preferable for the considered drive-by method. This can be confirmed only by experiments.

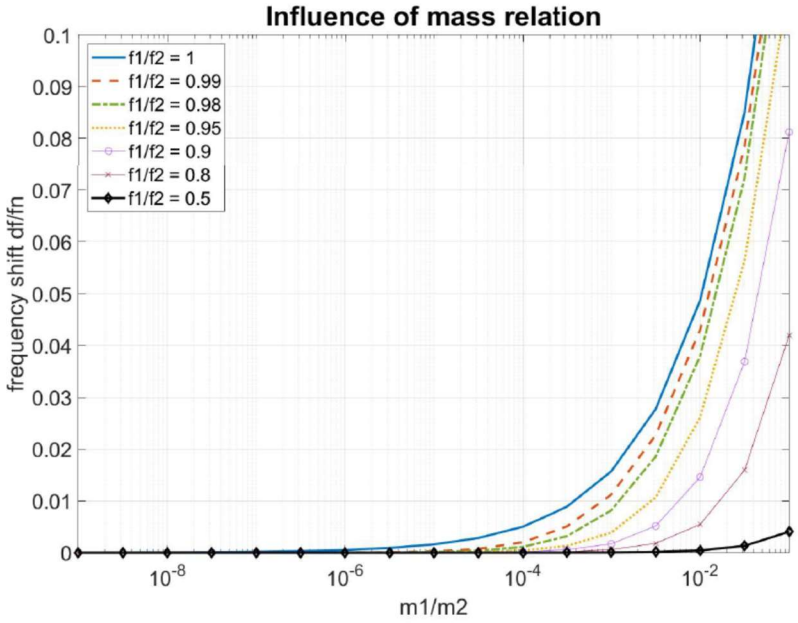

Fig. 2: Effect of the mass and frequency relation of a two DOF system on frequency shift.

The simulations of a moving spring-mass on a bridge showed that one of the peaks corresponding to a two DOF system may be missing in the response. In simulations with a RP, both of the peaks are usually recognizable. Another effect of a coarse RP is that the spectra of measured vibrations are split into many small irregular peaks that make the identification of the particular frequency peak quite difficult.

In order to assess how precise the identification of the peaks corresponding to spring-mass frequency and bridge frequency can be, 25 passage simulations for each parameter set were calculated considering RPs of classes "A" and "C".

m_1 [kg]	f_n(SM) [Hz]	f_n(B) [Hz]	$f_{n,est}'$(SM) [Hz]	$f_{n,est}'$(B) [Hz]	$f_{n,est}'$(SM) Err [%]	$f_{n,est}'$(B) Err [%]	Max. Err [%]
0.245	6.72	6.77	6.39	7.19	0.456	0.55	2.22
0.620	6.72	6.77	6.22	7.46	1.32	0.81	2.65
0.245	9.50	6.77	9.61	6.75	-0.228	1.06	3.34
0.620	9.50	6.77	9.80	6.69	-0.143	2.08	2.84

Tab. 2: Identified peaks $f_{n,est}$ from 25 simulations with RP class "C"(Err error, other symbols see Tab. 1).

4. Identification

A single-degree-of-freedom PSD response was fitted to the simulated (instead of measured) responses at manually pointed peaks using the "fmincon" optimization procedure in MATLAB. The fit result depends on the number of frequency lines considered, and suitable starting values are also essential for a good curve fit. In the case where the frequency peak is split into more peaks due to the road profile, the optimization result may envelop a number of peaks together or choose one of the peaks as dominant. The results presented in Tab. 2 for the RP of class "C" were achieved by choosing three frequency lines to the left

and right from a subjectively assumed center of a peak using a frequency resolution of 0.1 Hz. The results for the class "A" are only better by 0.3 % on average than for those presented in Tab. 2 for RP "C".

Knowing the two peaks in the vehicle response, the bridge frequency can be estimated using the theoretical model of the two DOF undamped system, which leads to Eqs. (1) and (2)

$$m_2 = \frac{\lambda m_1(k_1+k_2)-k_1k_2}{m_1\lambda^2-k_1\lambda}, \tag{1}$$

$$\omega_0^2 = \frac{m_1m_2\lambda_1^2-\lambda_1k_1m_1-\lambda_1k_1m_2}{(\lambda_1m_2m_1-k_1m_2)}, \tag{2}$$

where m_1 and k_1 are the known mass and stiffness of the moving spring mass, respectively, λ is the power of the peak circular frequency, m_2 and k_2 are the modal mass and stiffness of the bridge, respectively, and ω_0 is the natural bridge frequency.

A part of this estimation is identification of the bridge modal mass (m_2) which is quite sensitive to measurement error of the frequency peaks. An accurate estimate of the bridge modal mass from a theoretical model can increase the reliability of the bridge frequency estimation, or it can make it possible to estimate the bridge frequency from only the frequency shift of the vehicle, which is quite an appealing idea.

5. Conclusions

A new approach for drive-by identification was suggested and examined using simulations. The differences for rough road profile "C" in Tab. 2 together with the influence lines in Fig. 2 can help to define a relevant vehicle mass and vehicle frequency to be used in future applications of the method.

In spite of the fact that the method seems to require quite large vehicle masses or a small distance between the traced and vehicle frequencies, it might be suitable for e.g., approximate 1st bridge frequency estimation. In the case of frequent passages of the testing vehicle across a bridge, for example within the framework of public transport, there may be potential for more precise monitoring of bridge frequencies. Reducing the driving velocity to a minimum can also help to overcome the negative influence of road profile.

Acknowledgement

The sponsorship from grant GACR 21-32122J of the Czech Science Foundation and of the joint research project 109WFD0410468 of the Taiwan´s Ministry of Science and Technology are very much appreciated.

References

Bayer, J. (2023) Analysis suggestion for vehicle scanning method. In: *Proc. of Conf. Engineering Mechanics 2023*, Milovy, pp. 39–42.

Ormondroyd, J. and Den Hartog J. P. (1928) The theory of the dynamic vibration absorber. *Transactions of ASME*, 50(APM-50-7), 9–22.

Wang, Z. L., Yang, J. P., Shi, K., Xu, H., Qiu, F. Q. and Yang Y.-B. (2022) Recent Advances in Researches on Vehicle Scanning Method for Bridges. *Inter. Journal of Structural Stability and Dynamics*, vol. 22, no. 15.

Yang, Y. B., Lin, C. W and Yau J. -D. (2004) Extracting bridge frequencies from the dynamic response of a passing vehicle. *Journal of Sound and Vibration*, 272, 3–5, pp. 471–493.

Yang, Y.-B., Hao, X., Mo, X. Q., Wang, Z. L. and Wu Y. T. (2021) An effective procedure for extracting the first few bridge frequencies from a test vehicle. *Acta Mech.* 232, 1227–1251.

30th International Conference
ENGINEERING MECHANICS 2024
Milovy, Czech Republic, May 14 – 16, 2024

B-SPLINE BASED DENSITY ESTIMATION OF FATIGUE FAILURES IN SLM 18NI300 STEEL

Blacha Ł.*

Abstract: *The lack of probability-fatigue data is still a problem limiting the fatigue optimization of additively manufactured metallic materials. Modelling the probability density of fatigue life random variable is essential to predict the durability of structures. In the paper an experimental data for additively manufactured 18Ni300 maraging steel are studied fitting them to a proposed B-spline model. Parameters of the B-spline basis functions were obtained through a nonparametric density estimation technique. Obtained probability density functions were compared with maximum likelihood estimated Weibull density functions.*

Keywords: MS1 steel, fatigue failure probability, B-spline bases.

1. Introduction

Nowadays, reduction of energy consumption becomes the main engineering issue. The availability of additive manufacturing techniques have greatly increased the potential for mass design (directly connected with the reduction of energy consumption), overcoming the traditional constraints of manufacturing. Within the field of additive manufacturing, Selective Laser Melting (abbrev. SLM, alternatively: DMLS, direct metal laser sintering) becomes one of the most popular processes. In this powder-bed fusion process the desired shape is generated by a high-intensity laser which melts and fuses the metallic powder layer-by-layer. These features have made topology optimization (referred to as fatigue constraints) practical and providing another field of application for fatigue analysis. Topology optimization is an advanced methodology used to generate geometry configurations that are difficult to obtain using conventional processes. Due to the reduced material volume, the optimized geometry should be verified through analysis of the impact of the resulting modified stress tensor components on fatigue reliability. The prediction of fatigue reliability is inseparably linked to analysis of changes in density of fatigue lives at different load levels.

Density of a continuous random variable is a function able to provide a probability that the value of this variable would be equal any sample from the set of possible values. Estimation of probability density function (abbrev. PDF) is being practically applied not only in fatigue life estimation of solids but also in, e.g. reliability analysis. In case of the fatigue phenomena it is reasoned by the fact that fatigue damage process is stochastic in nature (e.g. Sobczyk and Spencer, 2012). The mathematical model behind it is a two-state stochastic process, described by the fatigue life random variable - preferably Weibull distributed in logarithmic space (Blacha and Karolczuk, 2016; Zhao and Liu, 2014; Schijve, 1993). Commonly, the tendency and scatter at the high-cycle fatigue regime are being described by the P-s-n (probability-stress-life) model, which means that scatter (as well as the sample space) is changing and depends on the stress level. It is the reason why the PDF will be shaped differently between each stress level and why probabilistic definition of the s-n field is crucial to ensure a reliable fatigue design of components, in particular for life prediction or failure hazard.

The approaches to density estimation could be divided into parametric and nonparametric. Parametric estimation requires a priori assumption regarding the probability distribution which results in PDF smooth along the entire sample space; an example of a parametric estimation technique is Maximum Likelihoo-

* Łukasz Blacha, PhD.: Opole University of Technology, Mikołajczyka 5 street; 45-271, Opole; PL, l.blacha@po.edu.pl

doi: 10.21495/em2024-050

Estimation (abbrev. MLE). In state of the art in fatigue reliability it can be found as the technique most frequently applied, often combined with the generalized extreme value distribution family of which the Weibull distribution is a part (the type III distribution) (Fernández Canteli et al., 2022). Nonparametric estimation makes minimal assumptions about the underlying distribution but specifically, the resulting PDF could easily become peaked or over-smoothed because the estimation result greatly depends on the number of sample points and span between them.

In the paper an alternative technique is proposed for nonparametric estimation of a smooth PDF for fatigue failure of additively manufactured 18Ni300 steel, combining kernel density estimation and B-spline interpolation bases. The proposed approach allows to define the PDF with relation only to the mean fatigue life and its scatter on the analyzed stress level.

2. Methodology

The paper investigates the possibility of nonparametric density estimation of fatigue failures in 18Ni300 maraging steel using a B-spline interpolation algorithm. In the first step, a MLE algorithm was used to estimate additional PDFs of a log fatigue-life random variable N_l (where $N_l = \lg(N)$ and N is a random number of load cycles to failure). The obtained results were then used to analyze and validate the B-spline PDF's estimated in the next step. The analysis involved fatigue lives corresponding to four stress levels in high-cycle fatigue loading. Entire investigation was based on the results of fatigue tests performed under controlled uniaxial constant-amplitude tension-compression loading, described further in this paper.

2.1. Fatigue tests

The fatigue tests were performed using specimens fabricated by selective laser melting (SLM) on an EOSINT M280 machine at Opole University of Technology, composition of the supplied powder can be found in Tab. 1. The specimens' geometry was designed according to the ASTM guidelines (ASTM E 466-15) and can be seen in Fig. 1.

Element	**Fe**	**Ni**	**Co**	**Mo**	**Ti**	**Al**	**Cr**
Min		17.00	8.50	4.50	0.60	0.05	-
Max		19.00	9.50	5.20	0.80	0.15	0.50
Element	**Cu**	**C**	**Mn**	**Si**	**P**	**S**	
Max	0.50	0.03	0.10	0.10	0.01	0.01	

Tab. 1: Chemical composition of powder used in manufacturing process (wt. %) (EOS, 2022).

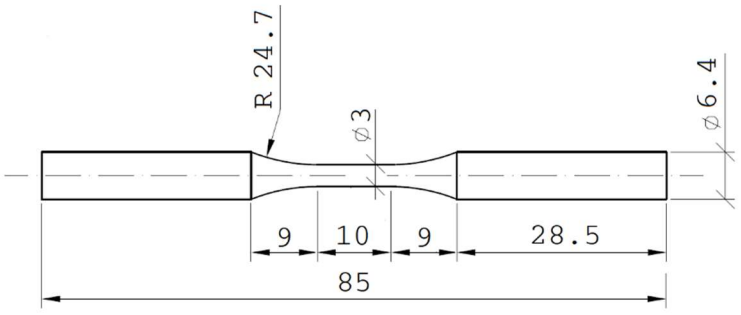

Fig. 1: Geometry of tested specimens.

The specimens were manufactured with a powder-layer thickness of 0.04 mm and 285/138/60 W laser powers for stripe/contour/edge scanning, respectively. During the process, new layers were added in the vertical direction with oxygen concentration in the process gas atmosphere less than 0.25 %. Finished specimens were cut by electrical band saw and heat-treated using a Nabertherm N41/H industrial furnace: maintained at 490 ºC for 4 hours and cooled for 48 hours. At the end, surfaces were bead-blasted in order to obtain a smooth finish (glass beads with diameters $\in$ <90, 150> μm).

The manufactured specimens were submitted to constant-amplitude uniaxial fully reversed fatigue loading. 20 specimens were tested at each of the σ_a stress amplitudes: 1 200, 1 000 and 800 MPa and 19 specimens were tested at σ_a = 520 MPa. The processed data required to reproduce the findings can be found in data repository (Blacha, 2023).

2.2. Maximum Likelihood Estimation

The test results were used to estimate the parameters of fatigue life distributions in a maximum likelihood estimation approach. PDF of the estimated distributions can be used to formulate and validate the assumptions underlying the proposed B-spline approach.

Maximum likelihood estimation (MLE) is a parametric technique based on an algorithm which evaluates the joint probability density at the observed data sample. The evaluation process determines the local maximum of the likelihood function L, parameterized by a multivariate parameter θ. Here, the likelihood function was represented by the Weibull PDF, assuming the random variable is Weibull distributed, $N_l \sim W(\alpha, \beta)$, where: $N_l = \lg(N)$). In such case, the maximum likelihood estimate $\hat{\theta}$ is a vector whose entries are the values of α and β that make the observed data most probable. Estimates of both distribution parameters, α and β (shape and scale parameter, respectively) can be seen in Tab. 2.

Stress amplitude σ_a, MPa	Shape parameter $\hat{\alpha}$	Scale parameter $\hat{\beta}$
1 200	45.606	3.355
1 000	53.047	3.761
800	59.985	4.215
520	41.868	4.937

Tab. 2: MLE-estimated parameters of Weibull distribution.

2.3. B-spline based density estimation

B-spline interpolation algorithm allows to derive smooth curves and surfaces on the basis of a sequence of limited data which values are known as control points. The curve is fitted in an iterative process with regards to these points and the basis functions N_{ip}, being a function of specific points called knots u, $u = \{u_0, u_1, \dots, u_m\}$ $(u_{i-1} < u_i)$:

$$N_{i,0}(u) = \begin{cases} 1 & if \quad u_i \le u \le u_{i+1} \\ 0 & else \end{cases}, \tag{1}$$

when $p > 0$:

$$N_{i,p}(u) = \frac{u - u_i}{u_{i+p} - u_i} N_{i,p-1}(u) + \frac{u_{i+p+1} - u}{u_{i+p+1} - u_{i+1}} N_{i+1,p-1}(u) \tag{2}$$

(where i is the ordinal and p denotes degree of the basis function).

Here it is assumed that PDF of a log-fatigue life can be modeled by a certain basis function with appropriately defined knots. In general, the more knots are defined, the higher degree is assumed and the shape of such function becomes more sigmoidal. Special care must be taken when defining the knot locations, especially the first and the last one (u_0 and u_m, respectively), as it has a major impact on the shape of this function. The undertaken simulations allowed to formulate the knot vector $U = [u_0\ u_1\ u_2\ u_3\ u_4\ u_5\ u_6]$ capable of estimating shape of the PDF for a continuous random variable N_l distributed on each of the tested stress levels. The following knot sequence was assumed and validated:

$$u_1 = \overline{n_l} - 2std,\ u_2 = \overline{n_l} + std,\ u_3 = u_2 + \Delta u,\ \dots,\ u_6 = u_2 + 4\Delta u \tag{3}$$

It should be mentioned that $U = [u_0 \dots u_6]$ knot vector results in 6th degree of the applied basis function, i.e. $N_{0,6}$. In the underlying assumption a nonparametric approach for PDF estimation can be used to locate the first and the last knot as well as the Δu interval. Application of kernel density estimation combined with sigmoidal kernel and Silverman's optimum estimate of the smoothing coefficient has provided a reasonable location of the boundary knots. The resulting basis function should be rescaled assuming $u = n_l$:

$$f(n_l) = \frac{N_{0,6}(u)}{\int_0^{\infty} N_{0,6}(u)\, du} \tag{4}$$

In this way, PDF of a log-fatigue life random variable can be obtained at a given load level, in nonparametric approach and on the basis of the mean value and standard deviation.

3. Results and conclusions

Densities obtained at the tested load levels according to the above approaches were compared and illustrated in Fig. 2.

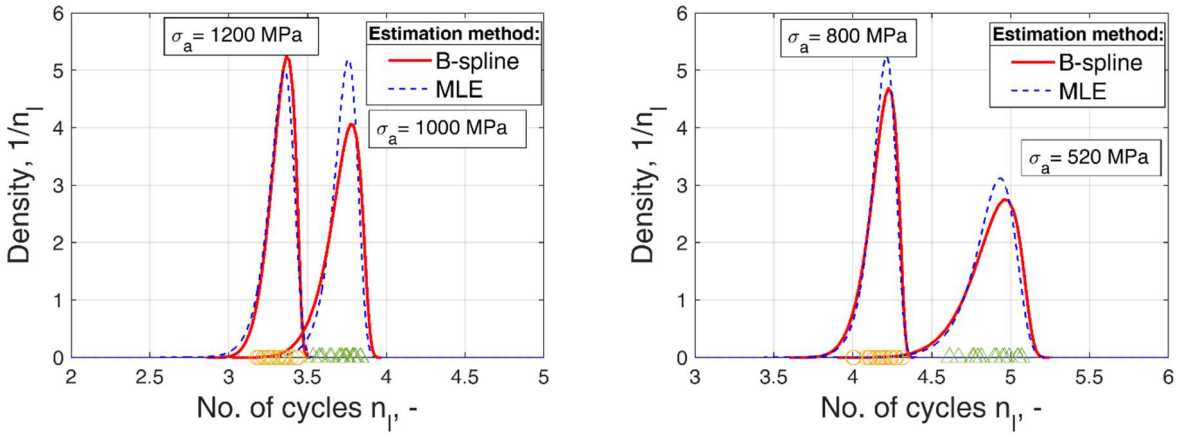

Fig. 2: Comparison between the PDFs estimated according to the proposed B-spline approach and MLE.

In view of Fig. 2 it can be seen that the proposed approach is capable of reflecting the trend in scatter growing along with mean fatigue life. Obtained density functions mostly reflect the derived Weibull densities, biggest discrepancy occurred at the load level where a slight movement outside the trend of stress-life relationship was observed (Blacha, 2023).

The results obtained for SLM-manufactured 18Ni300 steel evidenced the possibility of application of B-spline basis functions to an iterative, nonparametric estimation process of a smooth PDF. The findings can help in estimating a continuous fatigue failure probability distribution in high-cycle fatigue range, at the specified load level without the additional analysis of different load levels.

Acknowledgement

This work was financially supported by the Opole University of Technology under GAMMA project no. 155/22.

References

ASTM E 466-15 *Standard Practice for Conducting Force Controlled Constant Amplitude Axial Fatigue Tests of Metallic Materials*; ASTM International.

Blacha, Ł. (2023) *Fatigue Life for 18Ni300 Steel Under Uniaxial Fully Reversed Loading.* Mendeley Data, V1.

Blacha, Ł. and Karolczuk, A. (2016) Validation of the weakest link approach and the proposed Weibull based probability distribution of failure for fatigue design of steel welded joints. *Engineering Failure Analysis*, 67, pp. 46–62.

EOS Maraging Steel MS1 Material Data Sheet (2022). EU - EOS Store. ms-ms1-m290_material_data_sheet_06-22_en.pdf, 2022 (accessed 13 January 2024).

Fernández Canteli, A., Castillo, E., Blasón, S., Correia, J. A. F. O. and de Jesus, A. M. P. (2022) Generalization of the Weibull probabilistic compatible model to assess fatigue data into three domains: LCF, HCF and VHCF. *International Journal of Fatigue*, 159, art. 106771.

Schijve, J. (1993) A Normal Distribution or a Weibull Distribution for Fatigue Lives. *Fatigue & Fracture of Engineering Materials & Structures*, 16, pp. 851–859.

Sobczyk, K. and Spencer Jr, B. F. (2012) *Random Fatigue: From Data to Theory.* Academic Press, San Diego.

Zhao, Y. X. and Liu, H. B. (2014) Weibull modeling of the probabilistic S–N curves for rolling contact fatigue. *International Journal of Fatigue*, 66, pp. 47–54.

30th International Conference
ENGINEERING MECHANICS 2024
Milovy, Czech Republic, May 14–16, 2024

CGA-BASED SNAKE ROBOT CONTROL MODEL

Byrtus R.*

Abstract: *The snake robot is a nonholonomic mechanism composed of links equipped with passive wheels, connected by actuated joints whose motion mimics the locomotion of biological snakes. Control models intended for small-time local controllability are usually obtained by means of differential geometry, or, more recently, geometric algebra. Geometric algebras, also known as Clifford algebras, are an algebraic structure useful for modelling geometric objects and their transformations. We present an approach utilising the two-dimensional Conformal Geometric Algebra in order to derive the differential kinematics of the mechanism. A control model for small-time local controllability is created based on obtained differential kinematics, which is then used in visualization.*

Keywords: Geometric algebra, differential kinematics, snake robot, control model, nonholonomic mechanism.

1. Introduction

Let $\mathbb{R}^{3,1}$ be a vector space of dimension 4, with the orthogonal basis $\{\boldsymbol{e}_1, \boldsymbol{e}_2, \boldsymbol{e}_+, \boldsymbol{e}_-\}$ and an inner product such that $\boldsymbol{e}_1^2 = \boldsymbol{e}_2^2 = \boldsymbol{e}_+^2 = 1$ and $\boldsymbol{e}_-^2 = -1$. Define a new orthogonal basis $\{\boldsymbol{e}_1, \boldsymbol{e}_2, \boldsymbol{e}_0, \boldsymbol{e}_\infty\}$ with $\boldsymbol{e}_\infty = \boldsymbol{e}_- - \boldsymbol{e}_+$ and $\boldsymbol{e}_0 = \frac{1}{2}(\boldsymbol{e}_- + \boldsymbol{e}_+)$. The 2D Conformal Geometric Algebra (CGA) is the Clifford algebra $\mathbb{G}_{3,1}$, also denoted as $Cl_{3,1}$, with the basis $\{\boldsymbol{e}_1, \boldsymbol{e}_2, \boldsymbol{e}_0, \boldsymbol{e}_\infty\}$ along with the embedding Q of a point $[x, y] \in \mathbb{R}^2$ given by

$$Q : \mathbb{R}^2 \ni [x, y] \mapsto x\boldsymbol{e}_1 + y\boldsymbol{e}_2 + \frac{1}{2}(x^2 + y^2)\boldsymbol{e}_\infty + \boldsymbol{e}_0. \tag{1}$$

Denote the product on $\mathbb{G}_{3,1}$ as $\circ : \mathbb{G}_{3,1} \times \mathbb{G}_{3,1} \to \mathbb{G}_{3,1}$ (later on, we will omit $\circ$ for brevity). An important property that defines the structure of the algebra is that for any vector $\boldsymbol{a} \in \mathbb{R}^{3,1}$, its geometric product coincides with its inner product: $\boldsymbol{a} \circ \boldsymbol{a} = \boldsymbol{a} \cdot \boldsymbol{a}$. An element of $\mathbb{G}_{3,1}$ is called a *multivector*. $\mathbb{G}_{3,1}$ along with multivector addition and scalar multiplication has the structure of a vector space. The operation $\circ$ is associative and distributive. It is not the only product we can define in $\mathbb{G}_{3,1}$, in fact, for vectors $\boldsymbol{a}, \boldsymbol{b} \in \mathbb{R}^{3,1}$, it holds that

$$\boldsymbol{a} \circ \boldsymbol{b} = \boldsymbol{a} \cdot \boldsymbol{b} + \boldsymbol{a} \wedge \boldsymbol{b}, \tag{2}$$

where $\cdot$ is the inner product defined earlier and $\wedge$ is the outer product. The inner and outer products can be extended to an arbitrary multivector (note that the eq. (2) does not hold in general for any two multivectors). The linear combination of geometric products of k linearly independent basis vectors is called a k-vector; for example, $\boldsymbol{e}_1 \circ \boldsymbol{e}_2$ is a 2-vector (also called a bivector).

The advantage of utilising this algebraic structure lies in its connection to geometry, as the name implies. It can be shown that using the inner and outer products, we are able to express geometric entities from the embedded space (in this case $\mathbb{R}^2$) as the null-spaces of embedded points w.r.t. the respective product used. For the outer product, we have the so-called Geometric Outer Product Null Space (GOPNS) and for the inner product, the Geometric Inner Product Null Space (GIPNS); usually, the G is omitted, however it must be noted that in some literature, a distinction between IPNS and GIPNS (or OPNS and GOPNS) is made.

* Ing. Roman Byrtus: Institute of Mathematics, Brno University of Technology, Technická 2896; 616 69, Brno; CZ, roman.byrtus@vutbr.cz

doi: 10.21495/em2024-054

The geometric objects from $\mathbb{R}^2$ representable in CGA relevant to the scope of this paper are the embedded point $A_i = Q(x\boldsymbol{e}_1 + y\boldsymbol{e}_2)$, the point pair $P_i = A \wedge B$ given by the outer product of two embedded points A, B and the line $L = A \wedge B \wedge \boldsymbol{e}_\infty$ given by the wedge of points A, B and the null vector $\boldsymbol{e}_\infty$. In addition to geometric objects, there are elements of CGA that also represent transformations acting on these objects. In particular, let us introduce the *translator* T and the *rotor* R. The translator T represents translation in the direction of a vector $\boldsymbol{t} = x\boldsymbol{e}_1 + y\boldsymbol{e}_2$ and in exponential notation can be written as

$$T = e^{-\frac{1}{2}\boldsymbol{t}\boldsymbol{e}_\infty}. \tag{3}$$

Similarly, the rotor R representing rotation around an axis L (given by a unit bivector, for example, the axis representing rotation around the origin in $\mathbb{R}^2$ is given by $\boldsymbol{e}_{12}$) by an angle α is expressed in exponential notation as

$$R = e^{-\frac{1}{2}\alpha L}. \tag{4}$$

The transformations are applied to a multivector using the sandwich product. For example, for a rotation around the origin of the line L by angle α, the rotated line L_{rot} is given by $L_{rot} = RL\tilde{R}$, where $\tilde{R} = \boldsymbol{e}^{\frac{1}{2}\alpha L}$ is the *reverse* of R.

2. 2D Snake Robot Model

The snake robot consists of a series of links of length $2l$, connected by actuated joints, in our case revolute joints. Denote the configuration space of the mechanism as the manifold $Q \subset (\mathbb{R}^2 \times (S^1)^3)$ with point $\boldsymbol{q} = [x, y, \theta, \phi_1, \phi_2]$ representing a configuration of the mechanism at the time t, see Fig. 1. We thus track the coordinates of a head point (x, y), a global angle of orientation θ and relative rotation angles between links ϕ_1, ϕ_2. The centre of every link is given by the point $p_i = (x_i, y_i)$, where passive wheels are attached.

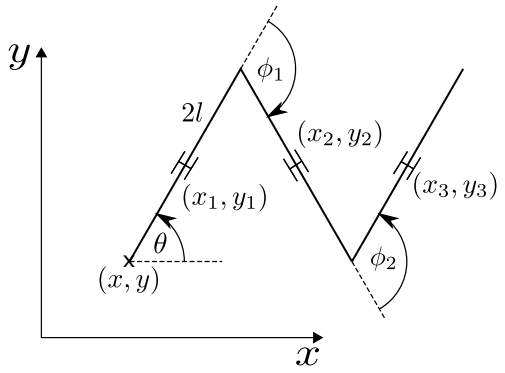

Fig. 1: A configuration of the mechanism.

The derivation of the control model is similar to the description given in Hrdina et al. (2016), but with the generalised transformations, we are able to model different mechanisms. The initial configuration of the i–th link of the mechanism is represented by point pairs $P_i^0 = A_i \wedge A_{i+1}$, where A_i are the edges of the links, see Fig. 2. We represent a general transformation M defined by bivector $L = L(\boldsymbol{q}(t))$ (depending state q at time t) as

$$M = e^{-\frac{1}{2}L(\boldsymbol{q}(t))},$$

and thus the reverse of M is $\tilde{M} = e^{\frac{1}{2}L(\boldsymbol{q}(t))}$.

A general configuration is then represented as a sequence of transformations applied to the initial configuration. Then the configuration of the i–th link at time t is given by

$$P_i = \prod_{j=k}^{1} M_j P_i^0 \prod_{j=1}^{k} \tilde{M}_j = T_{x,y} \prod_{j=i}^{1} R_j P_i^0 \prod_{j=1}^{i} (\tilde{R}_j)\tilde{T}_{x,y}, , \tag{5}$$

where M_j is the j–th transformation, $T_{x,y}$ is the translator from the origin to the head point and R_1 is the rotor representing the rotation w.r.t. global coordinate axes θ and the rotors R_2, R_3 represent the relative rotations ϕ_1, ϕ_2.

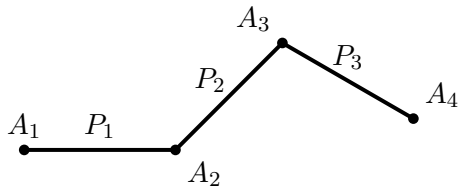

Fig. 2: A three-link snake robot represented in CGA.

To obtain the differential kinematics, we need to express the velocities of the state variables defining the mechanism's configuration, that is $\dot{x}, \dot{y}, \dot{\theta}, \dot{\phi}_1$ and $\dot{\phi}_2$. The constraint imposed on snake robots is the non-slip nonholonomic constraint, which limits the velocity of the i–th link to the direction defined by the point pair P_i. In terms of CGA, we can express this constraint as

$$\dot{p}_i \wedge P_i \wedge \boldsymbol{e}_\infty = 0 \tag{6}$$

where $\dot{p}_i$ is the velocity of the i–th point pair's centre p_i. In fact, this condition expresses the geometric fact that the velocity $\dot{p}_i$ coincides with the line $P_i \wedge \boldsymbol{e}_\infty$ passing through the point pair P_i. The centre p_i is obtained by the decomposition

$$p_i = P_i \boldsymbol{e}_\infty \tilde{P}_i. \tag{7}$$

Taking the derivative w.r.t. time of eq. (7), we get

$$\dot{p}_i = \partial_t (P_i \boldsymbol{e}_\infty \tilde{P}_i) = \dot{P}_i \boldsymbol{e}_\infty \tilde{P}_i + P_i \boldsymbol{e}_\infty \dot{\tilde{P}}_i. \tag{8}$$

Assuming the state of P_i is represented by k transformations, expressing $\dot{P}_i$ we arrive to

$$\dot{P}_i = \partial_t (\prod_{j=k}^{1} M_j P_i^0 \prod_{j=1}^{k} \tilde{M}_j). \tag{9}$$

The derivative of the general transformation M is then given by

$$\partial_t M = -\frac{1}{2} (\partial_t L(\boldsymbol{q}(t))) e^{-\frac{1}{2} L(\boldsymbol{q}(t))} = -\frac{1}{2} \dot{L}(\boldsymbol{q}(t)) M \tag{10}$$

and thus the derivative of the reverse is $\partial_t \tilde{M} = \frac{1}{2} \dot{L} \tilde{M}$. By chain rule

$$\dot{L} = \partial_t L(\boldsymbol{q}(t)) = \sum_{i=1}^{n} (\partial_{q_i} L) \dot{\boldsymbol{q}}_i. \tag{11}$$

Denoting $\partial_t M = \dot{M}$ and expanding eq. (9), we get

$$\dot{P}_i = \partial_t (\prod_{j=k}^{1} M_j P_i^0 \prod_{j=1}^{k} \tilde{M}_j) = \sum_{j=1}^{k} [P_i \cdot \dot{L}_j], \tag{12}$$

utilising Lemma 1 from Hrdina and Vašík (2015) in the last step, with $[P_i \cdot \dot{L}_j] = P_i \cdot L_j - L_j \cdot P_i$ being the commutator w.r.t. the inner product. Substituting eq. (12) into eq. (8) we can write $\dot{p}_i$ in the form of

$$\dot{p}_i = \sum_{j=1}^{k} [p_i \cdot \dot{L}_j]. \tag{13}$$

Finally, substituting Eq. (5) and Eq. (13) into the nonholonomic condition Eq. (6), we arrive to a set of three differential equations with multivector coefficients:

$$\begin{aligned}
&\Big(\dot{\theta} - 2\dot{x}\sin(\theta) + 2\dot{y}\cos(\theta)\Big)\boldsymbol{I} = 0,\\
&\Big(\dot{\phi}_1 + 2\dot{\theta}\cos(\phi_1) + \dot{\theta} - 2\dot{x}\sin(\phi_1+\theta) + 2\dot{y}\cos(\phi_1+\theta)\Big)\boldsymbol{I} = 0,\\
&\Big(2\dot{\phi}_1\cos(\phi_2) + \dot{\phi}_1 + \dot{\phi}_2 + 2\dot{\theta}\cos(\phi_2) + 2\dot{\theta}\cos(\phi_1+\phi_2) + \dot{\theta} -\\
&-2\dot{x}\sin(\phi_1+\phi_2+\theta) + 2\dot{y}\cos(\phi_1+\phi_2+\theta)\Big)\boldsymbol{I} = 0,
\end{aligned} \tag{14}$$

where $\boldsymbol{I} = \boldsymbol{e}_1\boldsymbol{e}_2\boldsymbol{e}_0\boldsymbol{e}_\infty$ is the pseudoscalar. Since $\boldsymbol{I}$ is nonzero, it holds that the coefficient of the pseudoscalar must be zero, and thus we have arrived to the dynamical system describing the differential kinematics of the 3–link robotic snake. We have obtained only three equations, meaning two more equations will have to be added in order to define the control system for the mechanism. Denote $u_1 = u_1(t), u_2 = u_2(t)$ as the control inputs. Then by adding two equations $\dot{\phi}_1 = u_1$, $\dot{\phi}_2 = u_2$, the forward kinematics are obtained. Note that the forward kinematics would be obtained by adding the equations $\dot{x} = u_1$, $\dot{y} = u_2$ instead. The final control system can be represented in vector form as

$$\dot{q} = X_1 u_1 + X_2 u_2, \tag{15}$$

where X_1, X_2 are control vector fields obtained by expressing $\dot{x}, \dot{y}, \dot{\theta}$ from eq. (14) along with the added control inputs u_1, u_2. Setting an initial configuration $\boldsymbol{q}_0$ as $\boldsymbol{q}_0 = [0, 0, 0, -\frac{\pi}{3}, \frac{\pi}{3}]$ and the controls as $u_1(t) = u_2(t) = 1$, the resulting motion can be seen in Fig. 3.

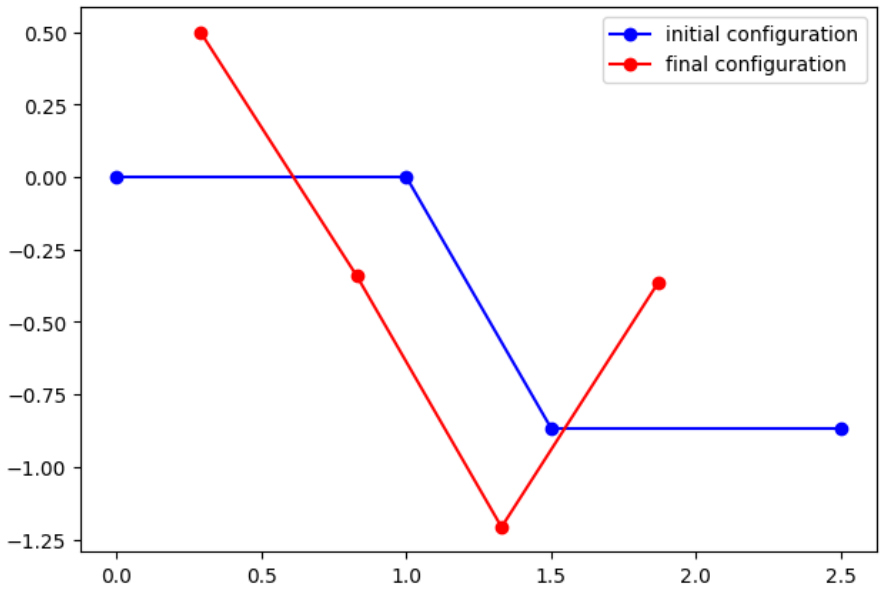

Fig. 3: The movement from the initial state in blue $\boldsymbol{q}_0$ into the final state $\boldsymbol{q}_f$ in red.

3. Conclusion

The application of geometric algebra in tasks involving geometry leads to a much more intuitive description of the underlying problems. Another advantage of using geometric algebra is that models are easily extended into higher dimensions - for example, in order to obtain the 3D planar locomotion model, it would be enough to add an extra dimension representing the z-axis, which leads to the 3D CGA. The extra dimension would appear in the relevant places (representation of the configuration, transformations having an extra dimension, etc.), but the formulas remain the same.

Acknowledgment

The author gratefully acknowledges financial support provided by FME BUT (project No. FSI-S-23-8161).

References

Hrdina, J., Návrat, A., and Vašík, P. (2016) Control of 3-link robotic snake based on conformal geometric algebra. *Advances in applied Clifford algebras*, 26, 3, pp. 1069–1080.

Hrdina, J. and Vašík, P. (2015) Notes on differential kinematics in conformal geometric algebra approach. In *Mendel 2015*, Cham. Springer International Publishing, pp. 363–374.

30th International Conference
ENGINEERING MECHANICS 2024
Milovy, Czech Republic, May 14 – 16, 2024

STRUCTURAL OPTIMIZATION USING BIOLOGICAL GROWTH METHOD IN ANSYS MECHANICAL, PART I

Čada Z.*, Černák M.**

Abstract: *This article focuses on a lesser-known alternative of structural shape optimization, based on morphing the mesh elements using the Biological Growth Method (BGM) and its implementation using the Ansys Mechanical program and newly developed software – M3Opti. The aim of these activities is to improve the properties of a structurally complex parts or assemblies, which requires an advanced materials models and contact or geometrical nonlinearities. The part I of the two-part paper presents the theoretical background and describes implementation in Ansys Mechanical.*

Keywords: Structural optimization, shape optimization, Ansys Mechanical, Biological Growth Method, FE mesh morphing.

1. Introduction

Nowadays a variety of optimization algorithms based on different principles are currently employed for structural optimization. Probably the most well-known is Topology Optimization (TO), which adjusts material distribution in given design space. However, TO is just a one group from wider structural optimization family. The second group is sizing optimization, and the third one is Shape Optimization (Bendsoe, 2004). Sizing optimization is based on modifying existing parametrized geometry via change of parameters. On the other hand, Shape Optimization is based on morphing existing geometry which does not have to be parametrized. From this point of view Shape Optimization is suitable for complex geometries which cannot be easily parametrized.

As for topology and sizing optimization, also for shape optimization there are several different specific algorithms. Proposed algorithms can be divided based on their principle into three categories (Hsu, 1994):

- Sequential Programming,
- Direct Search,
- Biological Growth.

Every proposed algorithm needs to determine structural performance of optimized problem to perform optimization steps. This is mainly achieved utilizing FEM and this step is common for all categories. Optimization procedures differ for different optimization algorithms, but they are regularly utilizing FEA to gain structural response.

Among all methods Biological growth Method (BGM) (Arutyunyan, 1988; Azegami, 1990; Mattheck, 1990; Mattheck, 1990; Porziani, 2020) has strong advantage because it does not require any mathematical programming techniques as Sequential Programming or Direct Search which often requires gradient calculation (Hsu, 1994). The term “Biological Growth Method” is quite broad and could refer to various processes or techniques used in biology for the growth, cultivation, or manipulation of biological organisms. In the context of structural optimization, biological principles can be applied to reduce stress

* Ing. Zdeněk Čada, PhD.: Development Department., SVS FEM s.r.o., Trnkova 117c; 628 00, Brno; CZ, zcada@svsfem.cz
** Ing. Martin Černák: Development Department., SVS FEM s.r.o., Trnkova 117c; 628 00, Brno; CZ, mcernak@svsfem.cz

doi: 10.21495/em2024-058

or other adverse properties in the surfaces of a structure, like the way bones or plants grow. In the more stressed regions of structures material swells simulating the growth mechanism of living organisms.

The reminder of part I presents implementation of Shape optimization utilizing BGM method in stand-alone software utilizing Ansys Mechanical. The principles and methods used in algorithm are described in Chapt. 2. Implementation is discussed in Chapt. 3. Application of this method is demonstrated and discussed in part II (Čada, 2024).

2. Methods

2.1. Mesh morphing

The principle of applying shape optimization with FEA isn't overly complicated. The main idea is based on mesh morphing as a mechanism for geometry change (Fig. 1), which is the simplest and fastest way to alter the shape of structurally complex parts.

It's necessary to determine the amount of shape change depending on the observed parameter (e.g. stress) which serves as objective function. Then, the change in shape of the structure can be achieved using mesh morphing. However, this method comes with limitations regarding the extent of shape change while preserving mesh topology. Each new mesh must meet quality criteria for elements and the adequacy of element density in a given area. If the criteria for mesh suitability are exceeded, remeshing (changing mesh topology) to a more suitable one is necessary. The direction of adding/removing material (movement direction of mesh nodes) is most suitable perpendicular to the surface of the structure.

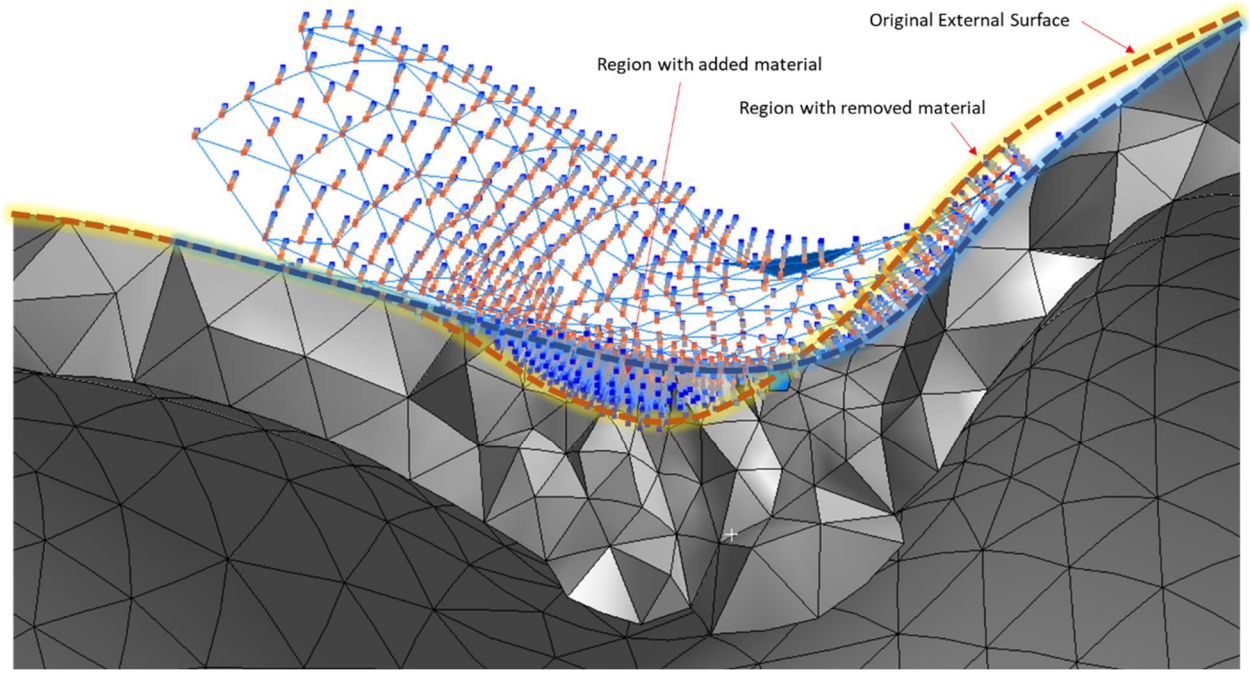

Fig. 1: Morphing example.

2.2. Application to structures

From the perspective of application to constructions, it's essential for the engineer to define areas of interest which will be modified. It's not always appropriate or possible to modify all regions of the structure together (Fig. 2). Furthermore, the engineer must define an objective function, meaning the result quantity such as von Mises stress, plastic strain, number of fatigue cycles, etc. and whether it needs to be minimized or maximized, as well as whether the dependency is linear, exponential, logarithmic, etc.

The threshold for determining whether material will be added or removed is often challenging to determine. From performed tests it has been found that the most suitable choose is based on a quantile of current values in the region of interest. Default threshold is calculated for each new design as 50 % quantile of nodal results which gives ratio how much material is added or removed, and this corresponds to moving distance of nodes (Fig. 3).

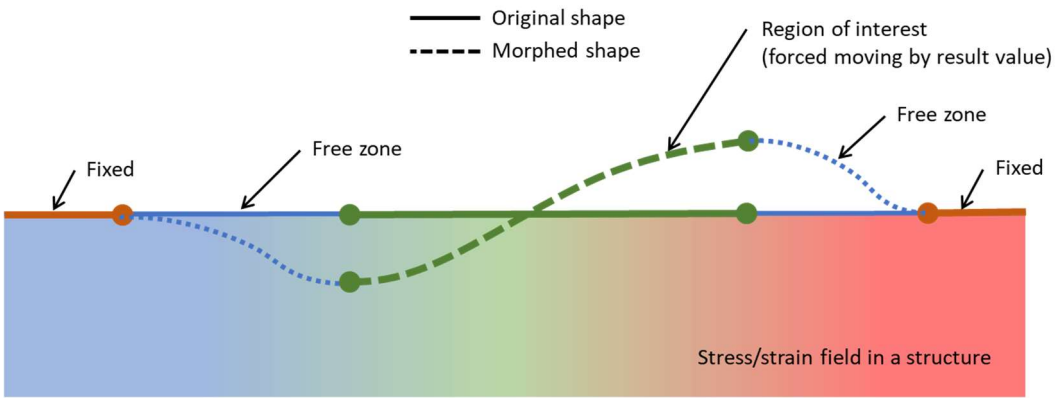

Fig. 2: Region of interest, morphing.

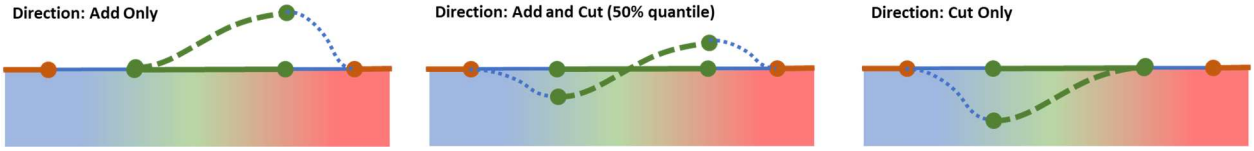

Fig. 3: Material adding or cutting.

The chosen result (quantity) as the source of values for calculating the objective function in the region of interest may not always be a continuous and smooth function, which can lead to undesirable shapes of the structure (Fig. 4). Therefore, it was deemed appropriate to perform additional smoothing. This approach to morphing has proven to be significantly more stable.

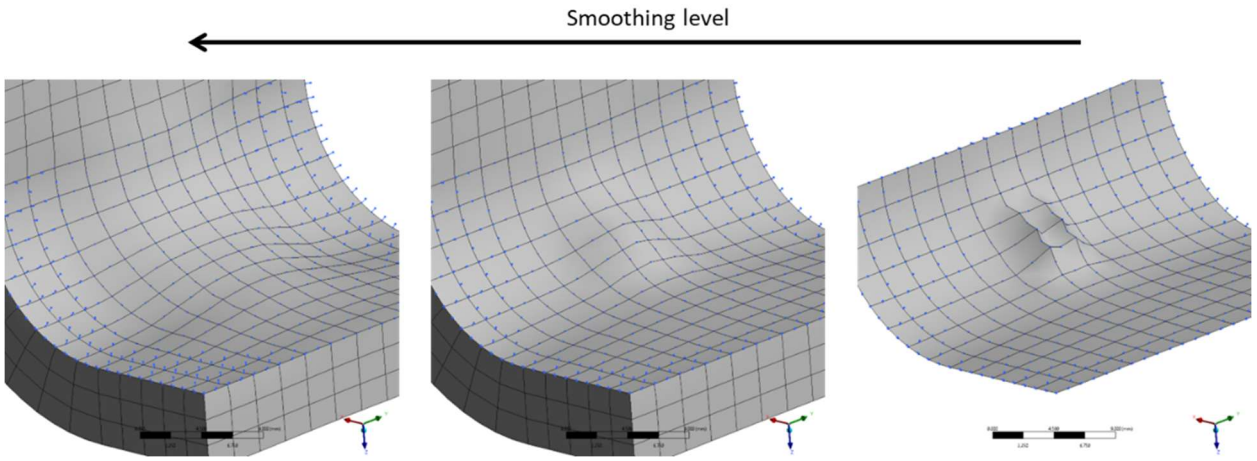

Fig. 4: Smoothing during morphing.

2.3. Iteration process, growth step size

In order to increase the stability of optimization calculations, various sizes of morphing steps (maximum node displacement) and the number of iterations were tested. The dependence on mesh size, morphing step, and the progression of improvement in the monitored variable within the chosen region were tracked. It was found that choosing a step size roughly ten percent of the size of adjacent elements typically resulted in decent stability in calculations, and the number of iterations to reach the optimum could be in the order of units (see Chapt. 3).

3. Ansys Mechanical implementation (M3Opti)

Software Ansys provides a several possibilities how to automate or customize calculation processes. The basic idea of customization is based on providing API of Ansys Mechanical (Ansys Help Documentation) which provides its object structure a can be used for controlling software programmatically.

Approach with standalone application has been chosen for implementing BGM algorithm for shape optimization. Main advantages of using stand-alone application over direct integration inside Ansys Mechanical are:

- application is alive while Mechanical is busy (not-responding),
- application can run on another computer than solver (Mechanical),
- postprocessing of optimization can be done without Mechanical.

Created application, which we named M3Opti (Mechanical Mesh Morph Optimization) controls Ansys Mechanical and uses its functionality for structural simulations and mesh morphing. It is a simple environment with GUI that allows users to set up a few necessary inputs and to display tables and charts during optimization. To achieve this, we have opted our own approach of port communication between Ansys Mechanical and M3Opti (ACT – Ansys Customization Toolkit).

Another approach which is possible for creating such an application is to use the newest technology for scripting and customization – PyAnsys (PyAnsys). This technology could be very useful for this purpose because it has embedded server-client communication and allows to communicate with Mechanical API directly from a standalone Python whit much less effort and programming experience required than in proposed solution.

References

ACT – Ansys Customization Toolkit. https://www.svsfem.cz/act. Accessed 13 February 2024.

Ansys Help Documentation. https://ansyshelp.ansys.com. Accessed 13 January 2024.

Arutyunyan, N. Kh. and Drozdov, A. D. (1988) Optimization problems in the mechanics of growing solids. *Mechanics of Composite Materials*, 24, 3, pp. 359–369.

Azegami, H. (1990) A Proposal of a shape-optimization method using a constitutive equation of growth: In the Case of a Static Elastic Body. *JSME international journal. Solid mechanics, strength of materials*, 33, 1, pp. 64–71.

Bendsoe, M. P. and Sigmund, O. (2004) *Topology Optimization: Theory, Methods and Applications*. Springer.

Čada, Z. and Černák, M. (2024) Structural optimization using Biological Growth Method in Ansys Mechanical, part II. In: *Proc. 30th Conference Engineering Mechanics*, Milovy, pp. 62–65.

Hsu, Y.-L. (1994) A review of structural shape optimization. *Computers in Industry*, 25, 1, pp. 3–13.

Mattheck, C. (1990) Design and growth rules for biological structures and their application to engineering. *Fatigue & Fracture of Engineering Materials & Structures*, 13, 5, pp. 535–550.

Mattheck, C. and Burkhardt, S. (1990) A new method of structural shape optimization based on biological growth. *International Journal of Fatigue*, 12, 3, pp. 185–190.

Porziani, S. and Biancolini, M. E. (2020) Bio-inspired Optimization Based on Biological Growth Method and Mesh Morphing Surface Sculpting. *Bioinspired Optimization Methods and Their Applications. BIOMA. Lecture Notes in Computer Science*, vol. 12438.

PyAnsys. https://docs.pyansys.com. Accessed 13 February 2024.

30th International Conference
ENGINEERING MECHANICS 2024
Milovy, Czech Republic, May 14 – 16, 2024

STRUCTURAL OPTIMIZATION USING BIOLOGICAL GROWTH METHOD IN ANSYS MECHANICAL, PART II

Čada Z.*, Černák M.**

Abstract: *This article focuses on a lesser-known alternative of structural shape optimization, based on morphing the mesh elements using the Biological Growth Method (BGM) and its implementation using the Ansys Mechanical program and newly developed software – M3Opti. The aim of these activities is to improve the properties of a structurally complex parts or assemblies, which requires an advanced materials models and contact or geometrical nonlinearities. The part II of the two-part paper presents the usage of developed software – M3Opti demonstrated on examples. Real-world applications are discussed.*

Keywords: Structural optimization, shape optimization, Ansys Mechanical, Biological Growth Method, FE mesh morphing.

1. Introduction

Presented work is the second part of the two-part paper dealing with structural optimization utilizing Shape optimization with Biological growth method. In the part I (Čada, 2024) the theoretical background and numerical implementation using Ansys Mechanical have been discussed. In the part II the usage of developed software M3Opti (ACT – Ansys Customization Toolkit) is demonstrated on examples and real-world applications of this tool are discussed.

The reminder of part II presents application of M3Opti for shape optimization of human bone (Sect. 2.1.) and valve housing (Sect. 2.2.). Real world usage and examples are discussed in Sect. 2.3. Suitability of proposed method and developed software are concluded in Chapt. 3.

2. Examples of shape optimization

2.1. Human bone

The first example we would like to demonstrate is optimization of human bone (Fig. 1). A model of tibia with isotropic linear-elastic material model has been used. Combined stress state has been assumed combining compression and bending. Region of interest, free zone and fixed zone of mesh are shown in Fig. 2. Objective function has been chosen as minimizing maximal principal stress in region of interest.

During the optimization maximal principal stress has been decreasing monotonically (see Fig. 3). After 9 iterations its value dropped from 4.5 MPa to 3.7 MPa which is almost an 18 % difference. Final geometry and corresponding stress distribution is shown in Fig. 3.

2.2. Valve housing

In the second example geometry of valve housing has been optimized. This concerns a thermo-structural analysis of a housing body, where the dominant loading is a thermal shock (transient thermal behaviour after heating by inner water). Bilinear isotropic elasto-plastic material model with isotropic hardening has

* Ing. Zdeněk Čada, PhD.: Development Department., SVS FEM s.r.o., Trnkova 117c; 628 00, Brno; CZ, zcada@svsfem.cz
** Ing. Martin Černák: Development Department., SVS FEM s.r.o., Trnkova 117c; 628 00, Brno; CZ, mcernak@svsfem.cz

doi: 10.21495/em2024-062

been used and the monitored variable has been accumulated plastic strain from three thermal cycles. Geometry with region of interest, fixed and free region are shown in Fig. 4.

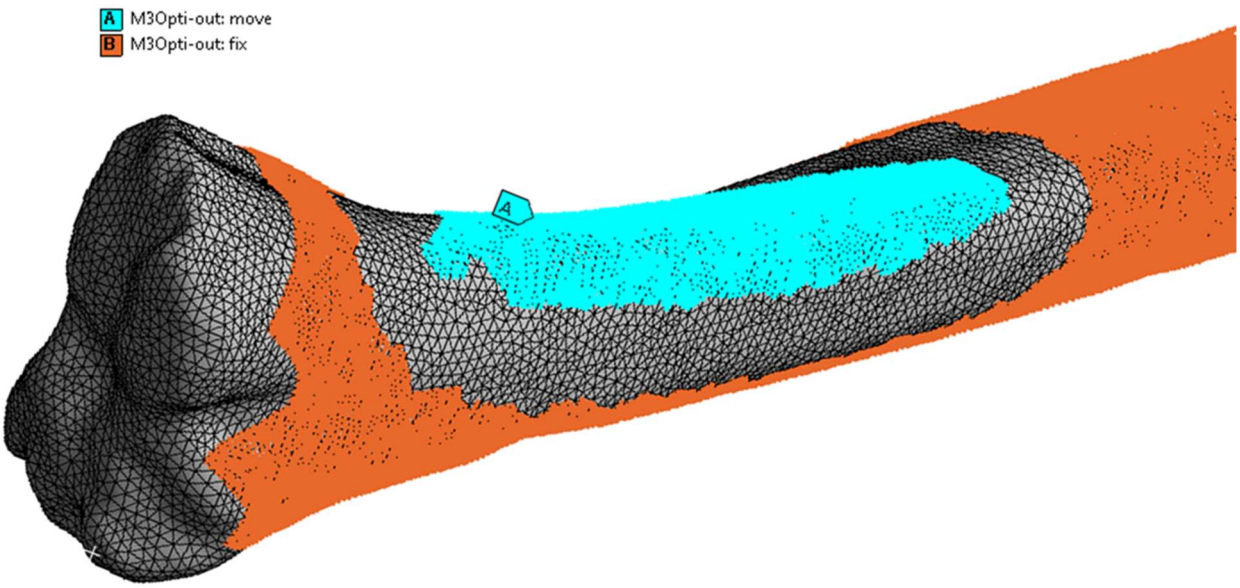

Fig. 1: Optimization of human bone – region of interest, free zone, fixed zone setup.

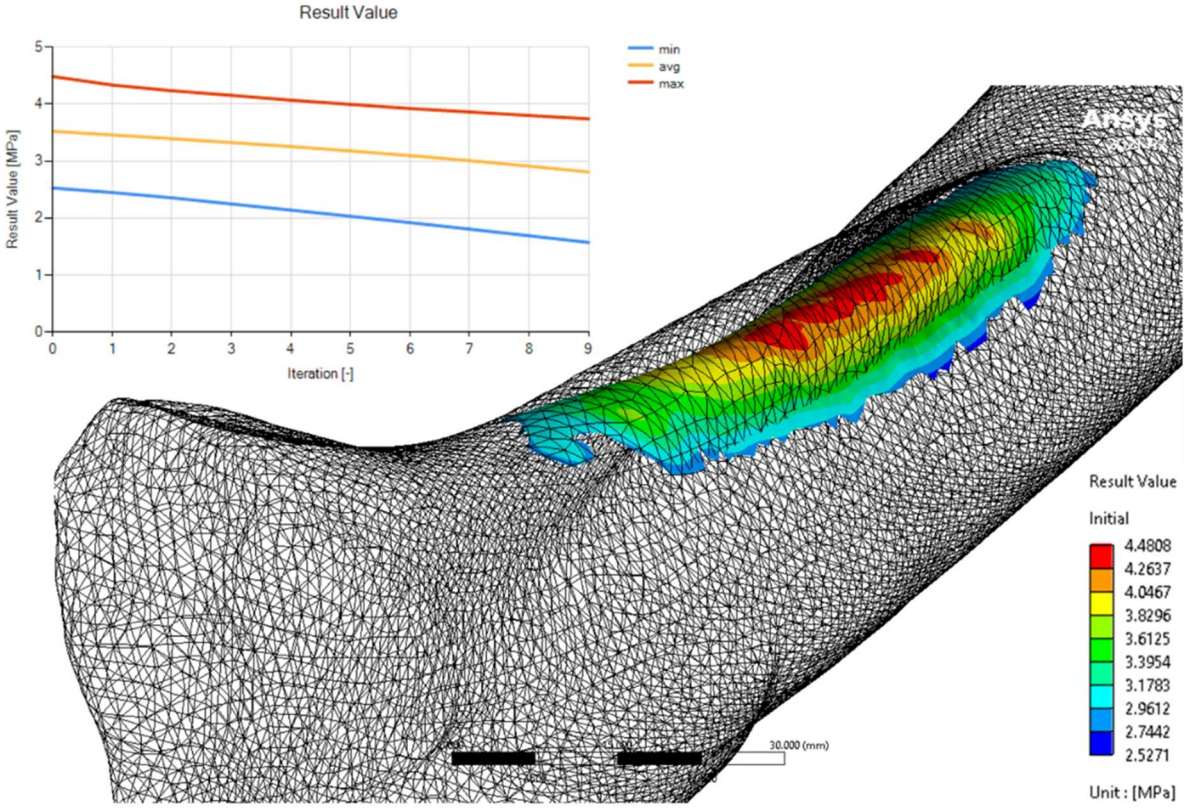

Fig. 2: Optimization of human bone – optimized shape.

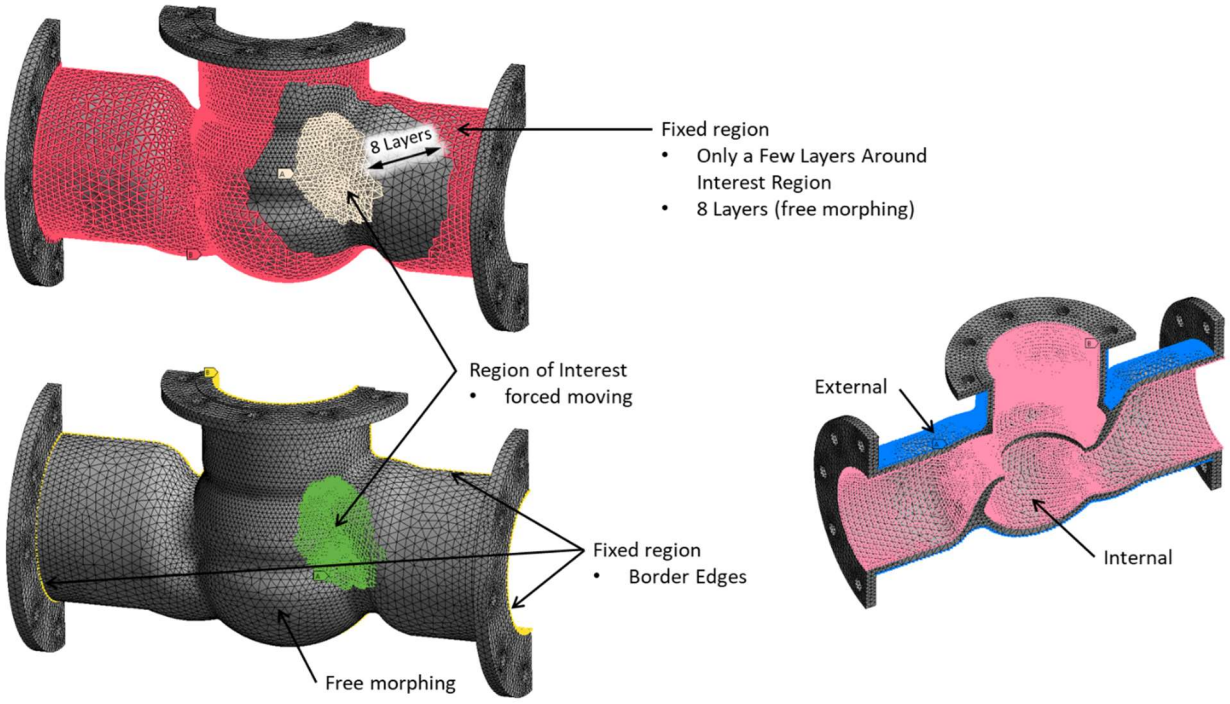

Fig. 3: Optimization of seal with using thermo-structural analysis – setup.

Result of optimization shown monotonical decrease of monitored variable – accumulated plastic strain. After 6 iterations accumulated plastic strain decreased from 0.010 to 0.0053 which is drop by almost 50 % (see Fig. 5). It is also clearly visible how was the region with maximal accumulated plastic strain becoming smaller during the iterations.

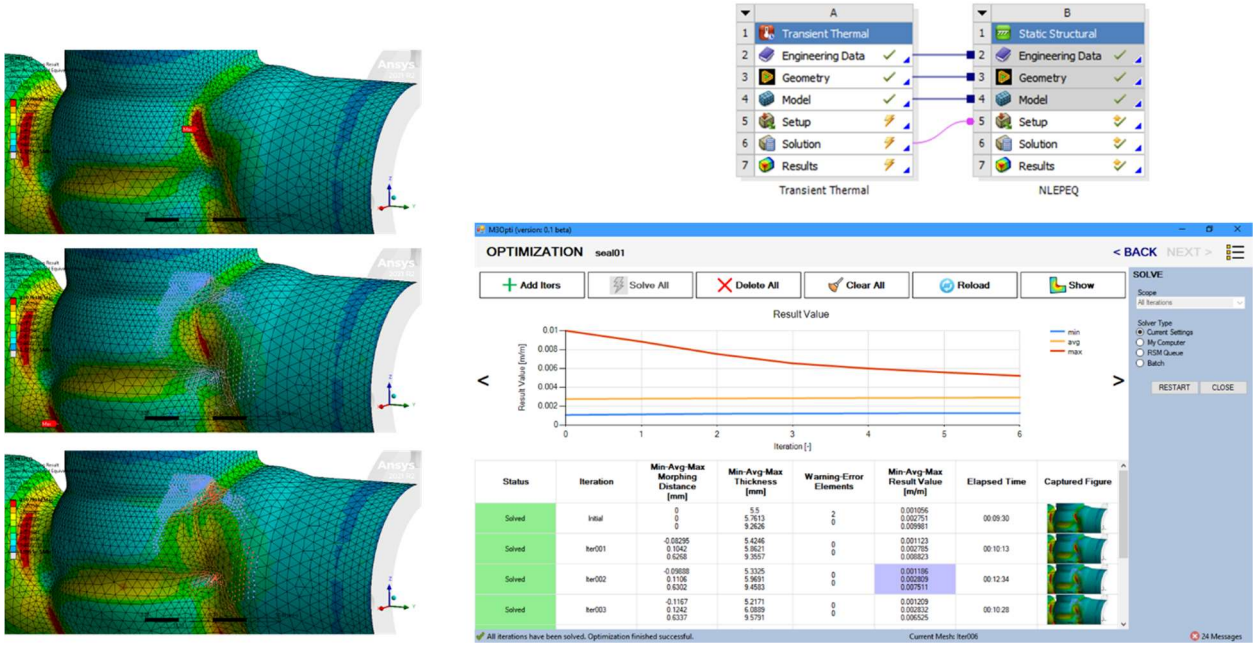

Fig. 4: Optimization of seal with using thermo-structural analysis – results.

Fig. 5 shows trajectory of nodes in part of the region of interest with highest accumulated plastic strain. Lines with dots corresponds by colour to the legend of accumulated plastic strain. As can be seen, a relatively small change in the outer surface of the seal housing led to a significant reduction in the maximum value of accumulated plastic strain.

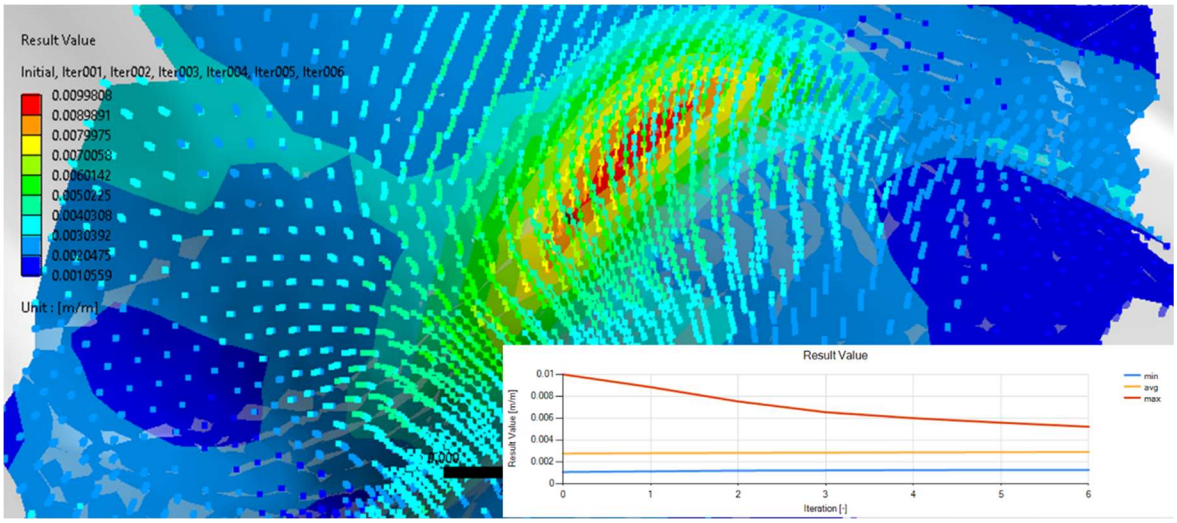

Fig. 5: Optimization of seal with using thermo-structural analysis – trajectories of nodes.

2.3. General examples, discussion

Two basic examples, mainly for demonstration purposes, has in introduced. However, authors see potential in more complicate models which some of the have already proved its usability in cooperation with commercial companies. The main advantage of developed software M3Opti implementing BGM method is its capability of using arbitrary model including all types of nonlinearities. Optimization can be based on any observable parameter which also gives opportunity to use M3Opti for various types of numerical simulation.

Here are some examples of proposed/tested analyses which are suitable for optimization:

- decreasing stress/strain in nonlinear static structural (material, contact and geometrical nonlinearities),
- decreasing stress/strain in nonlinear dynamic structural (transient, harmonic, spectral),
- decreasing heat flux in thermal analyses,
- increasing fatigue cycles in thermo-structural analysis including plastic material model (Chaboche). Real case tested in cooperation with Garrett Motion.

3. Conclusions

The paper demonstrates that Shape Optimization using the BGM is a very interesting method for subtly altering the shape of a structure by adding material in the most stressed areas, which can locally improve, properties of the entire structure. Observed variable used for optimization can be any output parameter such as stress, plastic strain, or fatigue life. Proposed solution has been implemented into computational software – M3Opti that uses functionality of Ansys Mechanical and allows users to easily set-up and optimize their numerical model.

The usage of this method for improving the mechanical properties of structures is mainly beneficial for structurally complex parts, which would be very difficult to parameterize at the CAD model level and can contain any type of nonlinearity. This goes hand in hand with the fact that for these structures, minor changes in shape are commonly tolerated both from an aesthetic and manufacturing process perspective.

Usage of M3Opti has been presented on two demonstration examples. Both shown significant increase in observed variable in relatively small number of iterations and with relatively small morphing of geometry which demonstrates usability of created software with BGM algorithm.

References

ACT – Ansys Customization Toolkit. https://www.svsfem.cz/act. Accessed 13 February 2024.

Čada, Z., Černák, M. (2024) Structural optimization using Biological Growth Method in Ansys Mechanical, part I. In: *Proc. 30th Conference Engineering Mechanics*, Milovy, pp. 58–61.

30th International Conference
ENGINEERING MECHANICS 2024
Milovy, Czech Republic, May 14 – 16, 2024

NEW DESIGN AND UPGRADE OF WHIRL FLUTTER AEROELASTIC DEMONSTRATOR

Čečrdle J.[*], Vích O.[**], Stárek J.[***], Vlach J.[†], Kolář M.[††], Šmíd M.[†††]

Abstract: *W-WING is aeroelastic demonstrator representing a half-wing with the nacelle, engine, and propeller. It was adapted from the former aeroelastic model of a commuter aircraft. The demonstrator is used for the experimental research of whirl flutter aeroelastic phenomenon. Two experimental campaigns were accomplished in the frame of the previous project. Currently, the demonstrator is intended for further experiments in the frame of the OFELIA project. For this purpose, the modification of the demonstrator design and other upgrades were proposed. Submitted paper describes the preparatory activities including the demonstrator design, instrumentation, and aerodynamic and structural analyses. Gained experimental results will be subsequently utilized for verification of the analytical models and computational tools that will be used for development of the new power plant system, characterized as an open-fan concept, utilized for a new generation short-medium range turboprop aircraft.*

Keywords: Flutter, whirl flutter, W-WING, OFELIA project.

1. Introduction

Whirl flutter is a specific type of aeroelastic flutter instability, discovered by Taylor and Browne (1938), which may appear on turboprop aircraft due to the effect of rotating parts, such as a propeller or a gas turbine engine rotor. The complicated physical principle of whirl flutter requires experimental validation of the analytically results obtained, especially due to the unreliable analytical solution of the propeller aerodynamic forces. Further, structural damping is a key parameter, to which whirl flutter is extremely sensitive and which needs to be validated. Therefore, aeroelastic models are used. A comprehensive description of whirl flutter experimental research is provided by Čečrdle (2023). VZLU's previous experimental activities included aeroelastic wind tunnel testing in the frame of the Czech aircraft structures certification. Aeroelastic models, that were formerly used for certification purposes, are currently often rebuilt, and utilized as research demonstrators for research of novel concepts, systems, methods, etc. The developed research demonstrator represents the half-wing and engine with a powered rotating propeller of a typical commuter turboprop aircraft structure.

2. W-WING whirl flutter aeroelastic demonstrator

Whirl flutter aeroelastic demonstrator (W-WING) was adapted from a half-wing with a span of 2.56 m with the engine of a former aeroelastic model of the commuter aircraft for 40 passengers. The total mass of the model is approximately 55 kg. The demonstrator was used for whirl flutter wind tunnel measurements in the frame of the previous project. Currently, the demonstrator is intended for further experiments in the frame of the OFELIA project. Based on the experience from the past activities, design modifications

[*] Ing. Jiří Čečrdle, PhD.: Czech Aerospace Research Centre (VZLU), Beranových 130; 199 05, Prague; CZ, cecrdle@vzlu.cz
[**] Ing. Ondřej Vích: Czech Aerospace Research Centre (VZLU), Beranových 130; 199 05, Prague; CZ, ondrej.vich@vzlu.cz
[***] Ing. Jan Stárek: Czech Aerospace Research Centre (VZLU), Beranových 130; 199 05, Prague; CZ, starek@vzlu.cz
[†] Ing. Jarmil Vlach: Czech Aerospace Research Centre (VZLU), Beranových 130; 199 05, Prague; CZ, vlach@vzlu.cz
[††] Ing. Martin Kolář: Czech Aerospace Research Centre (VZLU), Beranových 130; 199 05, Prague; CZ, kolar@vzlu.cz
[†††] Ing. Miroslav Šmíd: Czech Aerospace Research Centre (VZLU), Beranových 130; 199 05, Prague; CZ, smid@vzlu.cz

doi: 10.21495/em2024-066

and further upgrades of the demonstrator were proposed. The main change is the installation of the new motor with the sufficient power. Also, additional sensors and equipment are installed. In addition, the system of steady and unsteady flow field measurement was proposed for the dynamic response measurements. The baseline (i.e., unmodified) variant of the demonstrator is shown in Fig. 1. The wing and aileron stiffness is modeled by a duralumin spar of variable cross-section. The inertia characteristics are modeled by lead weights. The aileron is actuated by the electromagnetic shaker placed at the wing root via a push-pull rod.

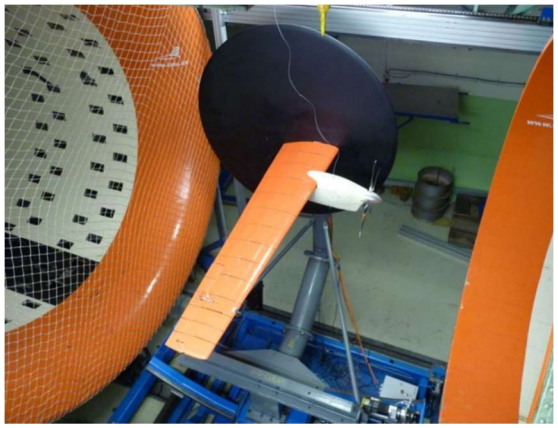

Fig. 1: W-WING baseline (unmodified) state.

The nacelle model has two DOFs (engine pitch and yaw). The stiffness parameters are modeled by means of cross-spring pivots. The leaf springs are changeable, and the stiffness parameters can be adjusted independently by replacing the spring leaves. Both pivots are independently movable in the direction of the propeller axis to adjust the pivot points of both vibration modes. The inertia of the engine is modeled by the replaceable and movable weight. The gyroscopic effect of the rotating mass is simulated by the mass of the propeller blades. Currently, two sets of blades made of duralumin and steel are available.

3. Propeller aerodynamic force analysis and motor selection

The most important modification is the installation of the new motor. The formerly used motor was selected assuming the propeller operation near the zero-thrust condition. Therefore, the required power was relatively low. Obviously, the operational slot for a specific blade angle of attack was limited in terms of the airflow velocity range. However, during the past tests, this range was found as too narrow and such an operation was found as ineffective. To avoid this practice, demonstrator was equipped with the new power plant system with the sufficient power to operate without limitations (as much as possible) in terms of the airflow velocities and propeller revolutions. New power plant enables to provide the test with real thrusted propeller using the fixed rpm thrusted mode of the propeller rotation. Using this approach, the evaluation of the thrust influence on the whirl flutter stability is applicable, contrary to the usage of the windmilling propeller as was typical practice in the past.

In order to predict the necessary power of the motor and operational margins of the propeller in terms of the revolutions and airflow velocities, the analytical study of the propeller aerodynamic forces was performed. The analyses were aimed at determining the areas of the propeller operation modes, i.e., thrust, reversal, zero-thrust and generator. The analyses were based on the CFD solver of the full NS equations for a viscous compressible flow based on the finite volume method. The rotating domain of 1/5 cylinder with the periodic condition was used. Solution included fully parallelized K-ω SST turbulence model with variable CFL. The example of results representing the required power vs. advance ratio is shown in Fig. 2.

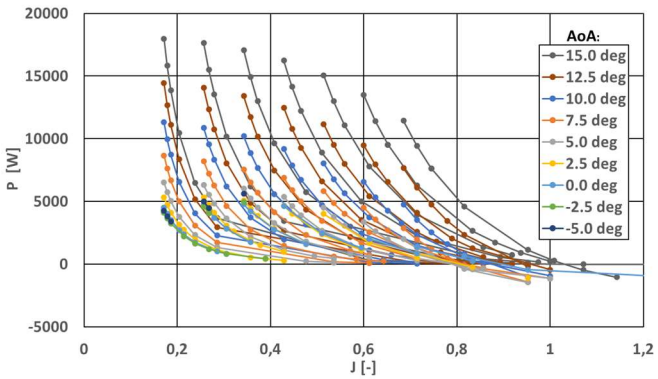

Fig. 2: Propeller power vs. advance ratio state.

Based on the results of analyses, and on further limitations (mass, dimensions, etc.), the selection of the appropriate motor has been done. The expected available operational power is 10–11 kW. This selection was the technical compromise with respect to obtain the maximal power and to keep the acceptable mass and dimensions.

4. New Demonstrator Nacelle Design

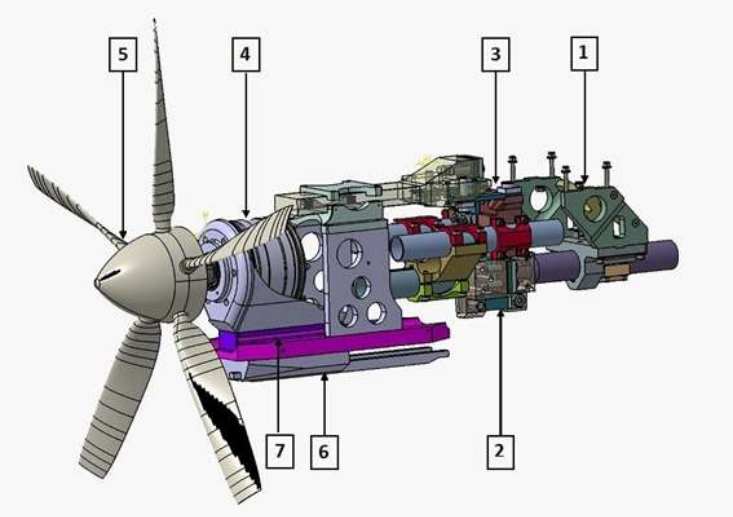

Fig. 3: Uncovered nacelle: (1) Wing mounting, (2) Yaw attachment, (3) Pitch attachment, (4) Motor, (5) Propeller, (6) Movable weight, (7) Thrust measurement cell.

The nacelle underwent an extensive redesign, particularly in the front part, while preserving the external contour of the fairing. The connection between the motor and the propeller was redesigned, and the motor was replaced by the more powerful, water-cooled, and larger one. Space was allocated for a load cell between the new motor console and the rest of the structure. A new thrust metering load cell was designed for this allocated space and the required range. The solution of the sliding weight compensating for the displacements of cross springs was reworked. The root part of the nacelle was reinforced. Fig. 3 shows the design model of the new nacelle with the description of the main parts while Fig. 4 shows the covered nacelle.

5. Strength Checks

The appropriate strength checks of the newly designed structure using FEM were performed. Calculations included:

1) Propeller blade attachment and propeller (shaft) strength check with respect to the propeller aerodynamic forces and centrifugal forces. Calculations included front and rear part of the propeller boss and the propeller blade mounting.
2) Propeller blade modal analysis. The purpose was to evidence the "rigidity" of the blade.
3) Thrust measurement cell analysis. Analyses included several load cases.
4) Stress analyses of cross-spring pivots and other parts of the assembly. Applied load included aerodynamic load generated by the propeller and the weight load. Analyses included all variants of cross-spring pivots (pitch and yaw). Static deformation of the assembly is compensated by means of special wedge-shaped washers placed under the leaves of the pitch spring attachment. Each set of leaves has the specific set of washers. This compensation eliminates static deformation theoretically to zero, in practice, some small deformation remains.

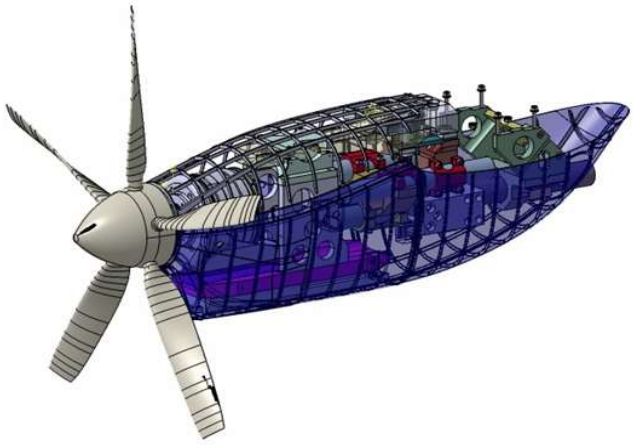

Fig. 4: Covered nacelle.

6. Demonstrator instrumentation

Propeller is powered by the motor with servo amplifier to manage and evaluate propeller revolutions, torque, and immediate power. In addition, independent (optical) rpm sensor is installed. Finally, balance cell for measurement of the propeller thrust is installed.

Demonstrator is equipped with the system of aerodynamic excitation by aileron flapping deflection. Various excitation signals (harmonic, sweep, impulse) are available. Aileron is actuated via push-pull rod using an

electromagnetic shaker (and amplifier) placed behind the splitter plate. Push-pull rod is instrumented by the deflection sensor for evaluation of aileron angular deflection and as safety guard to prevent damage of shaker and rod.

Mechanical instrumentation includes strain gauges in the root and half-span sections to measure the vertical bending, in-plane bending, and torsional deformations. Demonstrator is also equipped with 18 uniaxial accelerometers. Wing is instrumented at six spanwise sections and two positions chordwise for the vertical direction and at a single position in the wingtip for the in-plane (longitudinal) direction. Nacelle is instrumented in two sections (front and rear) for both vertical and horizontal directions and at the front section also for the longitudinal direction.

The data acquisition and processing are provided using in-house LabVIEW-based application. The application is also used to control the propeller rotation (constant or controlled rate ramp) and to manage the aerodynamic excitation by the aileron flapping (harmonic constant, harmonic sweep, impulse). The same application is also used for the calibration of sensors. Finally, the application provides a safeguard preventing the destruction of the demonstrator, provided the response at the critical points exceeds the preselected threshold, by turning off the propeller motor, the wind tunnel fan and, provided used, turning off the aerodynamic excitation by the aileron. The data acquired by the program consist of "slow" data (at a sampling frequency of 2 Hz), which include propeller revolutions and airflow velocity, and real-time data from the strain-gauges and selected accelerometers (2 000 Hz sampling frequency) depicted in the time domain as well as pre-processed into the form of the power spectral densities. The program also provides the immediate power and propeller revolutions signal from which the torque of the propeller is evaluated. Apart from the described application, the LMS TestLab system is used. The system acquires the continuous signals from all accelerometers and the airflow velocity signal. The amplitude evolution of the frequency components corresponding to the engine whirl motion are monitored in real-time. The data are then used for the assessment of the demonstrator vibration response using the methods of FFT and OMA.

Independently of the described measurement systems, the aerodynamic flow field measurement is provided. It gives pressure and velocity data on several points of the flow field. Acquisition will be done one location at a time. Sensors include Aeroprobe, L-shaped five-hole fast response 1kHz and Wire probe for CTA Dantec Streamline anemometer. The grid of measurement points for the steady aero measurement includes 15 points while the grid of measurement points for the unsteady aero measurement includes 17 points in total in four quadrants.

7. Conclusion and Outlook

The paper describes the mechanical concept and preparatory activities related to the aeroelastic demonstrator for experimental investigation into whirl flutter phenomenon. The demonstrator's concept allows adjusting of all main parameters influencing whirl flutter. A broad testing campaign in the VZLU 3 m-diameter wind tunnel is planned. The test schedule includes dynamic response and whirl flutter stability mechanical measurements and aerodynamic flow field measurements. The experimental results will be subsequently utilized for verification of the analytical models and computational tools (Dugeai et al., 2011) that will be used for development of the new power plant system, characterized as an open-fan concept, utilized for a new generation short-medium range turboprop aircraft.

Acknowledgement

Program and topic: HORIZON-JU-CLEAN-AVIATION-2022-01-SMR-01, Ultra Efficient Propulsion Systems for Short and Short-Medium Range Aircraft. Project nr. and title: 101102011, Open Fan for Environmental Low Impact of Aviation (OFELIA).

References

Taylor, E. S. and Browne, K. A. (1938) Vibration Isolation of Aircraft Power Plants, *J. Aerosp. Sci.*, 6(2):43–49.

Čečrdle, J. (2023) *Whirl Flutter of Turboprop Aircraft Structures.* 2nd ed., Elsevier Science, Oxford, UK.

Dugeai, A., Mauffrey, Y. and Sicot, F. (2011) Aeroelastic Capabilities of the elsA Solver for Rotating Machines Applications, In: *Int. Forum on Aeroelasticity and Structural Dynamics*, Paris, France.

30th International Conference
ENGINEERING MECHANICS 2024
Milovy, Czech Republic, May 14 – 16, 2024

THERMAL MANAGEMENT FOR MISSION CRITICAL AIRCRAFT EQUIPMENT

Červenka M.*, Koštial R.**

Abstract: *The operation of modern electronics under extremely low thermal conditions (below -50 °C) encounters a multitude of difficulties. The age of chip shortage limited available selection of state-of-the-art electronic components to only a fraction of previous offer. Automotive industry has gobbled most of the yet available stock while the aerospace-grade components are not available at all. In this paper we evaluate application of positive temperature coefficient heating strips as a means to keep the under-specified electronic devices in reasonable operational range while minimizing impact on the electronics design process. Our experimental results of PTC heaters testing suggest significant benefits compared to standard heaters used in the aerospace industry, but also some challenges, which are discussed in this paper.*

Keywords: Thermal management, heating strip, positive temperature coefficient, aviation, electronics.

1. Introduction

Integrated circuits (ICs) are fundamental to modern electronics, with their operation relying heavily on temperature. These circuits generate heat during operation due to energy losses manifested as heat in components, connections, wiring, or the printed circuit board (PCB). The greater the loss, the greater the excess heat generated. As the trend in electronic designs leans towards more compact devices with a greater concentration of components, IC packaging is becoming smaller but with poorer thermal properties. This is further compounded by the fact that component gates in semiconductor devices have been shrunk down to nanometer sizes, leading to a single die containing millions of gates formed from billions of transistors. Despite advancements in technology that allow for more compact and efficient devices, these new generations may face thermal-related problems in certain situations.

The operation of integrated circuits (ICs) at ultra-low temperatures, specifically below -50 °C, encounters a multitude of difficulties. A paramount issue originates from the differential coefficient of thermal expansion (CTE) between the components soldered to the circuit board and the circuit board itself. This discrepancy can engender considerable stress, especially upon the activation of the equipment. When hot components modify their shape due to this phenomenon, they might shatter brittle plastics, akin to what occurs when dry ice is introduced into a container constructed from brittle material such as an ice chest. An additional problem emerges when the equipment is transferred from extremely cold conditions to a warmer environment which may cause humidity condensation problems. Although these can be solved by application of protective varnish, there are even more serious problems.

Silicon dyes face several challenges when operated at extremely low temperatures. One of the main issues is the increase in resistance of semiconductors at lower temperatures as stated in Thompson (1961) and Jones (2003). Once the temperature drops below certain levels, the types of IC devices that can be used and their performance are significantly limited. Another problem is the decrease in electron mobility (quantized

* Ing. Miroslav Červenka, PhD.: Institute of Aerospace Engineering, Brno University of Technology, Technická 2896/2, 616 69 Brno; CZ, cervenka@fme.vutbr.cz

** Ing. Rostislav Koštial, PhD.: Institute of Aerospace Engineering, Brno University of Technology, Technická 2896/2, 616 69 Brno; CZ, kostial@fme.vutbr.cz

doi: 10.21495/em2024-070

vibrations of the atomic lattice) at lower temperatures. This problem occurs in most silicon dyes, leading to potential performance degradation - see Clark (1992) and Gurrum (2005).

Operating ICs at such low temperatures requires specialized packaging and treatment. However, even nowadays after the chip shortage is supposed to be over it is not possible to obtain certain specific components from any source. The manufacturers have simply quit production of ICs on ceramic substrates or even never encountered a requirement of a specific component to be used under extreme conditions.

Printed circuit boards (PCBs) made from FR4 face challenges when exposed to extreme temperatures. The glass transition temperature (Tg) of FR4, typically ranging from 130 °C to 140 °C, causes the material to lose its mechanical properties and soften at this threshold, especially under rapid temperature increase. High temperatures also lead to moisture absorption by FR4, causing swelling and distortion of the board and potentially damaging the components and causing connectivity issues described by Shreyas (2023). Additionally, the adhesive used to bond the FR4 layers can weaken and fail at high temperatures, leading to delamination. Potential solutions include using high Tg FR4, polyimide, PTFE (Teflon), metal-core PCBs (MCPCBs), and ceramic substrates, each with their own advantages and disadvantages depending on the application requirements. For instance, aluminum-core PCBs can aid excessive heat dissipation and external heat distribution, but require unconventional methods due to their reactivity - LaBar (2022). However, our main trouble is the lower end of the extreme temperatures.

The feasible solution to the all above described problems is to maintain the device temperature in the reasonable temperature range given by the components and other material specification requirements. Cooling or heating the device unevenly can cause additional issues, either electric or mechanical, therefore an exact and even heat delivery and distribution across the entire surface of the device under examination is of highest importance. The further text describes one such approach applicable in the aerospace industry.

2. Proposed method

Safety is still a major priority in the aviation industry. We use traditional heaters broadly throughout industries despite the numerous problems that have afflicted them. However, a possible solution to these problems exists: A Positive Temperature Coefficient (PTC).

2.1. Positive Temperature Coefficient Heating elements

PTC heaters are self-regulating heaters that work as open loop elements without outside regulation or/and control. Flexible PTC heaters use conductive inks layers printed on a flexible polymer-based matrix with at least two different conductive particles with different properties, for example carbon black with silica filler on siloxane elastomer-based polymer as element which we used for reference and testing as described in patent by Wachenfeldt (2008).

In addition, PTC elements are characterized by high reliability and durability, where partial function is maintained even after several damages as demonstrated in our previous study by Kostial (2019). PTC heaters are an excellent alternative for applicable in the aerospace industry. Their use ranges from the heating of critical electronics components that cannot be installed into a controlled environment (actuators, lights, etc.) to advanced self-regulating anti-icing systems, which we had already tested but the results are still under evaluation. Testing shows significant benefits compared to standard heaters used in the aviation industry, but also some challenges, which are discussed in the next section.

2.2. Application

In general, electronic components are manufactured at several grades. Consumer grade components are supposed to withstand temperatures ranging from 0 to +70 °C, automotive grade specifies range between -40 to +80 °C whereas aerospace requirements stretch from -55 °C up to +70 °C according to RTCA DO-160G specification (2010). The difficulties here can be seen in general availability and attainability of such components even for applications where the cost could be ignored. Hence, the goal of our sub-project is to keep an electronic PCB at reasonable levels to ensure temperature comfort for the components and also the entire PCB board itself. To ensure spatially-even heating effect for the electronic board two distinct heating strips were evaluated (Fig. 1).

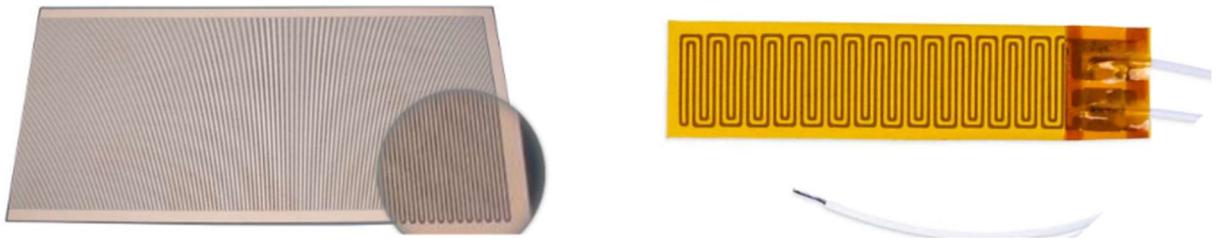

Fig. 1: Evaluated heating elements: A12WM Heating Foil (left), generic polyimide flexible heater (right).

Common method of heating (mainly smaller areas of) PCBs is to populate the board with passive or active components which in combination of analog or digital thermometer ICs and appropriate control ensure local temperature conditions. Use of the heating strips introduces the possibility for global thermal management across the entire area of interest. Compared to other methods of heating, the strips also have their own up and down sides but in general, the advantages and disadvantages of pre-assembled heating strips can be summarized as follows:

Pros	Cons
• Simplifies design process. • Optimal energy use and distribution. • High peak power. • Unaffected by voltage variations. • "Built-in" temperature control without any external components resulting in higher reliability.	• Fixed temperature setpoint given by the material composition. • Availability of custom geometries and temperature thresholds. • Cost of custom solutions. • PE/PET enclosure is not suitable for all scenarios.

Tab. 1: Heating strip advantages & disadvantages.

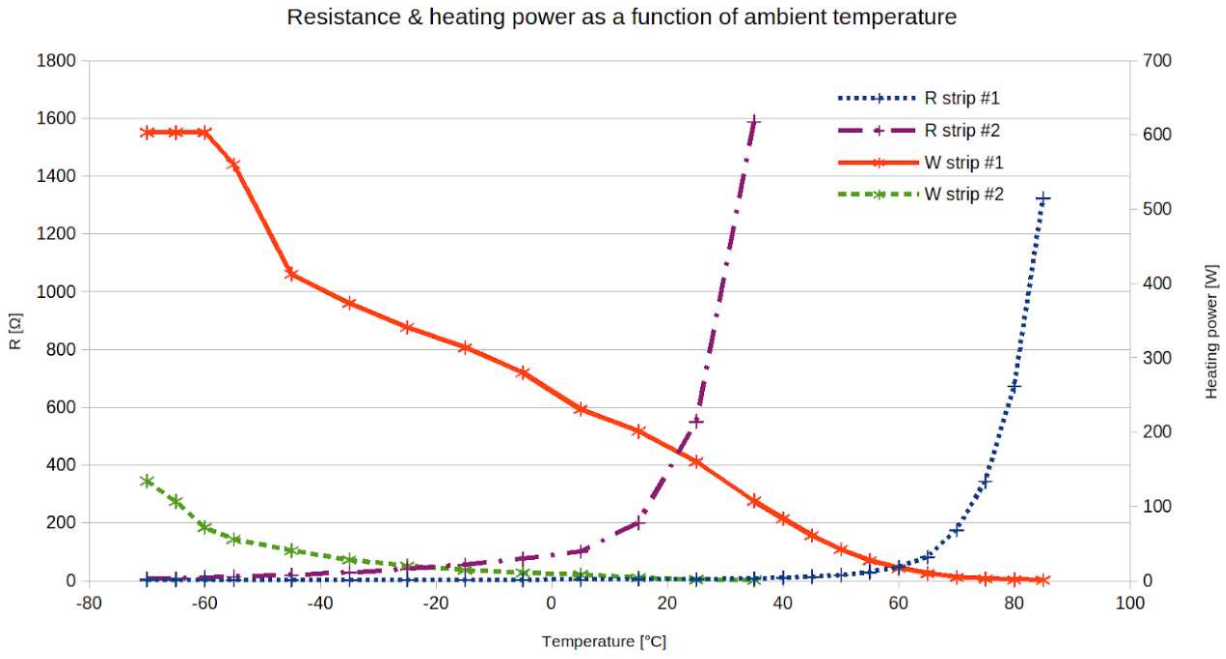

Fig. 1: Comparison of the reference strips in terms of resistance and heating power at Vcc = 28 V. The application would require the threshold temperature to be even lower than the strip #2; slightly negative values of the threshold would also be fully acceptable. The heating performance of strip #1 is too high whereas power output of strip #2 would be completely sufficient.

The evaluated PTC strip A12WM is manufactured to a specific fixed temperature setpoint which limits the heating temperature approximately to 70 °C as specified by the datasheet and also validated by a measurement in climatic/environmental chamber (see strip#1 in Fig. 2). (Over)heating the electronic

components to such high temperatures is very undesirable. All such available heating strips are designed to have the breaking temperature around this range which makes this behavior rather undesired. What we are currently looking for is a PTC strip whose characteristic is shown in Fig. 2 as suggested strip characteristic #2 Meaning with significantly limited power output (in tens of watts) and the breaking temperature at around 20 °C or even below threshold. Such a strip is manufacturable, but currently such an option is not offered for sale on the open market.

The most advantageous feature of the A12WM heating strip in comparison to the generic flexible heaters can be seen the fact that the area in which the temperature is already close or above the threshold (e.g. zones below and in vicinity of components like motor drivers and power mosfet transistors) is not heated by the strip. Material of the strip in that particular zone is already in a state of high-impedance and no excessive power is radiated in that area.

3. Conclusions

The aim of the paper was to briefly outline the problems we face today in the development of increasingly complex and sensitive electronics in aviation. Due to flight-levels of commercial traffic we are mainly dealing with very low temperatures of critical elements outside of environmentally controlled areas of the aircrafts. The solution proposed in this paper is to maintain electrical components and PCBs in an ideal temperature range using flexible PTC heaters. These are proving to be very suitable heating instruments due to their self-regulating material-based capabilities and long-term stability.

Acknowledgement

This document was created within the project TN02000009 - NaCCAS II, co-financed from the state budget by the Technology Agency of the Czech Republic within the National Centres of Competence Programme.

References

Thompson J. C. and Younglove B. A. (1961) Thermal conductivity of silicon at low temperatures, *Journal of Physics and Chemistry of Solids*, vol. 20, iss. 1–2, pp. 146–149.

Jones K. W. and Mitra A. K. (2003) Integrated Circuits and Thermal Issues: A Primer. *Journal of Aerospace, SAE Transactions*, vol. 112, sec. 1, pp. 123–146.

Clark W., El-Kareh B., Pires R., Titcomb S. and Anderson R. (1992) Low temperature CMOS-a brief review. Components, Hybrids, and Manufacturing Technology, *IEEE Transactions on,* 15, 397–404.

Shreyas S. (2023) FR4: Understanding the Material and Its Applications in PCB Design, online: https://www.wevolver.com/article/fr4-understanding-the-material-and-its-applications-in-pcb-design.

LaBar, M. (2022) *Material Properties of Fr-4 Laminates and Their Relative Effects on Thermal Reliability in Printed Circuit Boards*, California State University, Sacramento ProQuest Dissertations Publishing.

Gurrum S., Suman S. Yogendra J. and Fedorov, A. (2005). Thermal Issues in Next-Generation Integrated Circuits. Device and Materials Reliability, *IEEE Transactions on*. 4. 709–714.

Radio Technical Commission for Aeronautics Inc: RTCA/DO-160G, Environmental conditions and test procedures for airborne equipment, RTCA (2010) Inc: 1828 L Street, NW Suite 805 Washington, DC 20036, pp. 22-1-22-42.

Koštial R., Janhuba L. and Hlinka J. (2019) Aircraft leading edges minor damages detection based on thermographic survey of electrical anti-icing system. In: *13th Research and Education in Aircraft Design*, pp. 15–22.

Wachenfeldt F. (2008) *Heating element*, Patent No. WO2008048176A.

30th International Conference
ENGINEERING MECHANICS 2024
Milovy, Czech Republic, May 14 – 16, 2024

PERSPECTIVE WAYS OF HEAT TRANSFER ENHANCEMENT FOR HEAT EXCHANGERS IN FOULING CONDITIONS

Chudý D.*, Jegla Z.**

Abstract: *The paper discusses the possibilities of intensifying the heat transfer of liquid working fluids in heat exchangers under fouling conditions. It presents a perspective on heat exchangers according to the geometry of the heat exchanger surface. The shell and tube heat exchanger with the helical flow and plate heat exchanger with the spiral flow are introduced in greater detail. These two heat exchangers are compared concerning fouling and thermal-hydraulic behavior in industrial cases. The paper shows clear advantages of these flow structures for improving these aspects. The article places a strong recommendation on the use of spiral plate heat exchangers wherever the working conditions allow.*

Keywords: Heat transfer, fouling, thermal-hydraulic analysis, heat exchangers, spiral, helical.

1. Introduction

The research on heat exchangers currently focuses on optimizing known heat exchanger (HE) geometries. In addition, the thermal–hydraulic aspects of the use of nanoparticles in the working fluid are being investigated. The HE geometry can also be used as a criterion for dividing heat exchangers. The basic division of heat recovery HEs is according to the heat exchange surface based on tubular and plate. State-of-the-art heat exchanger designs are microchannel HEs. Opposite to these research trends are working fluids that exhibit significant heat transfer surface fouling. Fouling is a time-dependent phenomenon that negatively affects the thermal-hydraulic behavior of heat exchangers. In this work, the focus lies on liquid working fluid with fouling properties.

2. Tubular heat exchangers in fouling conditions of working liquids

For fouling conditions of liquid working fluids, shell and tube heat exchangers (STHEs) are commonly used. The deployment of SHTEs requires a more detailed structural design of the aiming. They are used for the most demanding applications in terms of pressure and temperature. A negative phenomenon is the formation of so-called dead zones, on the shell side close to segmental baffles (see Fig. 1). In dead zones, there is no required flow velocity, and therefore sufficient turbulence does not occur. Consequently, the heat exchange surface becomes fouled, thus impairing heat transfer, and leading to uneven structure loading.

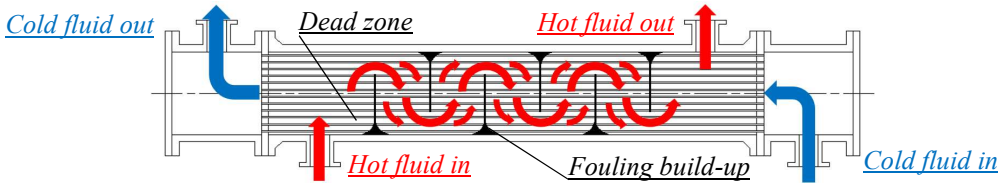

Fig. 1: Principle of shell-side fluid flow and dead zones in STHE.

* Ing. Dávid Chudý: Slovenské energetické strojárne (Slovak Energy Machines), SES a.s., Továrenská 210, 935 28 Tlmače, Slovak Republic, david_chudy@ses.sk

** Assoc. Prof. Ing. Zdeněk Jegla, PhD.: Institute of Process Engineering, Faculty of Mechanical Engineering, Brno University of Technology; Technická 2; 616 69, Brno; CZ, zdenek.jegla@vut.cz

doi: 10.21495/em2024-074

The following Tab. 1 shows the process data for the operation of the proposed STHE for cooling the vacuum side distillate pump around (VSDPA) stream by atmospheric residue (ATRES) stream to be heated.

Working fluid	VSDPA	ATRES
Side	Tube side	Shell side
Mass flow	31.2 kg/s	55.6 kg/s
Inlet temperature	274.3 °C	223.8 °C
Fouling factor	0.00053 $m^2 \cdot °C/W$	0.00088 $m^2 \cdot °C/W$

Tab. 1: Process data on STHE.

For the process data in Tab. 1, a thermo-hydraulic design of the STHE has been made considering the prescribed pressure losses, the working fluids, heat duty, and the position constraint, to get to basic design dimensions. Tab. 2 shows the main design parameters of the STHE for the shell side on which the fouling working fluid (ATRES) flows.

Shell internal diameter	**Tube length**	**Baffle spacing**	**Pressure drop**
1 200 mm	6 327 mm	516 mm	87 020 Pa

Tab. 2: Main results of shell side design data for STHE design.

There are several possibilities for heat transfer intensification in STHE (Akpomiemie and Smith, 2016). Intensification is implemented both on the shell side and on the tube side. On the tube side, these are mainly twisted tapes and coiled wires. Changing a baffle system can intensify heat transfer on the shell side. By tilting the baffles under a certain angle (5 ° to 45 °), a helical bypass of tubes is achieved (Stehlík et al., 1991), see Fig. 2.

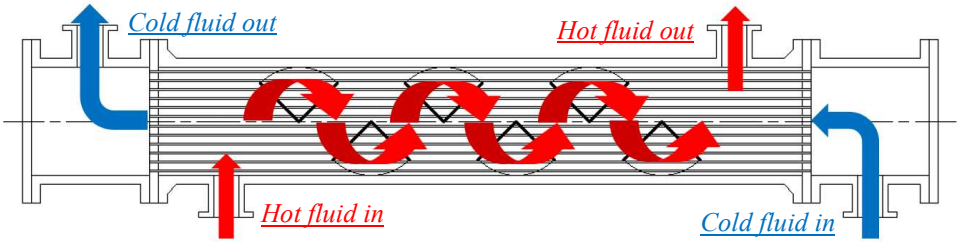

Fig. 2: Principle of inclined baffles and shell-side helical fluid flow in STHE.

According to the process data in Tab. 1, the optimal geometry of STHE with helical baffles was designed to minimize fouling on the shell side. Tab. 3 shows its main design data and the pressure drop on the shell side.

Shell inner diameter	**Tube length**	**Baffle inclination**	**Pressure drop**
1 200 mm	5 800 mm	15 °	81 894 Pa

Tab. 2: Main results of shell side design data for STHE design.

3. Plate heat exchanger

Tubular heat exchangers are predominant in process applications. However, they can be replaced by plate heat exchangers (PHE) with profiled plates, especially in processes where lower temperature and pressure are involved. The reason for choosing PHEs in new designs is their modular construction. Their deployment in processes with fouling agents has faced a lot of scrutiny.

In addition to the above-mentioned profiled plate design, PHEs also include spiral plate heat exchangers (SPHE). Spiral plate heat exchangers have, according to the manufacturer, a self-cleaning effect. The curvature of the channels of working fluids creates great turbulence along their entire length. If sediments appear, despite high turbulences, they are swept away because of the increased local velocity, i.e. the self-cleaning effect. A schematic of the SPHE is shown in Fig. 3.

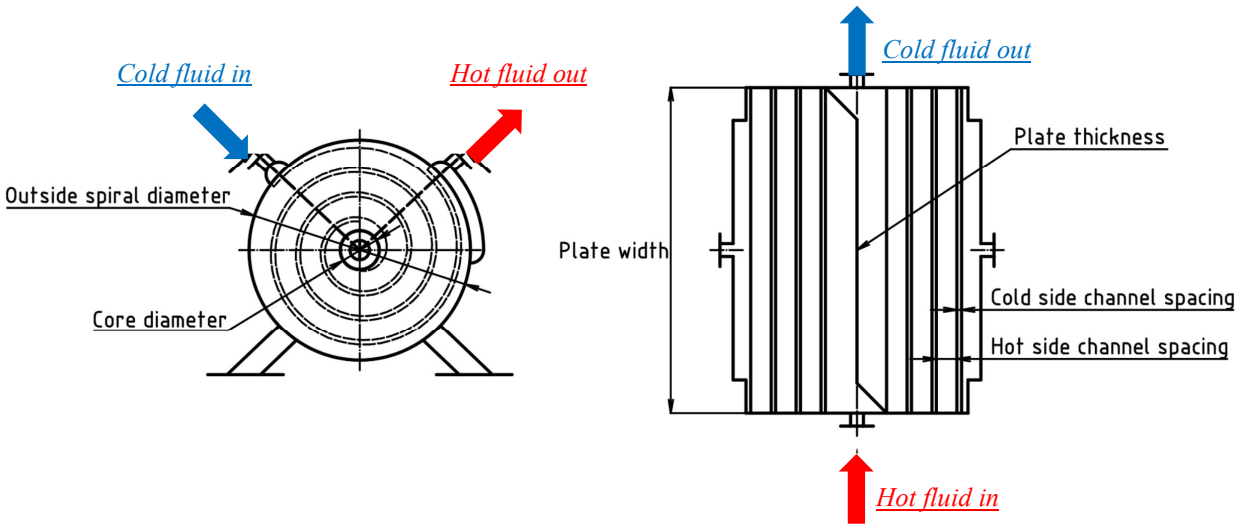

Fig. 3: Schematic drawing of a spiral plate heat exchanger.

Fig. 3 shows the principle of the SPHE function with a description of the basic geometry. The hot working fluid enters through the center of the unit and flows through a channel from the inlet toward the shell. The cold working fluid enters radially and flows towards the center. The arrangement of the working fluids in the SPHE is countercurrent, hence the correction factor to determine the mean temperature difference, $f = 1$ (Moretta, 2010). The heat exchange surface of the curved plate can be fitted with pins, which contribute to the intensification of heat transfer. To illustrate the characteristics of the SPHE, process data from an industrial case of heat recovery from hot wastewater for a 210 kW SPHE are presented in Tab. 4.

Working fluid	Hot wastewater	Cold feedwater
Mass flow	120 kg/s	20 kg/s
Inlet temperature	~25.4 °C	10 °C
Outlet temperature	25 °C	~12.6 °C
Fouling factor	0.000088 m².K/W	0 m².K/W

Tab. 4: Process data on SPHE.

The procedure in (Moretta, 2010) can be followed for SPHE design. In this procedure, the unknown is the heat transfer surface. The size of the heat exchange area is designed with an overdesign of 20 to 30 percent (Moretta, 2010). From the known width of the plate, the minimum length of the plate is determined and rounded to a value within the given overdesign range. In the present case, the overdesign is 28 %. The length of the plate is calculated using the Eq. (1) the outer diameter of SPHE, which for given process data together with other basic dimensions is given in Tab. 5 and recorded in Fig. 3.

$$D_S = \sqrt{15.36 \cdot L \cdot (S_h + S_c + 2 \cdot t) + C^2} \tag{1}$$

	Plate		**Channel spacing**		**Diameter**	
Thickness	**Width**	**Length**	**Hot side**	**Cold side**	**Core**	**Outside**
t	w	L	S_h	S_c	C	D_S
3 mm	1 000 mm	4 500 mm	60 mm	10 mm	125 mm	688 mm

Tab. 5: Main results for SPHE design.

4. Discussion of results

The two optimally designed STHEs presented in Chapt. 2 are identical in design except for the baffle system on the shell side. By changing the baffle system, fouling is reduced, and heat transfer is intensified. Both

designs were implemented to allow the STHE to transfer around 2.7 MW of heat. To achieve the same heat duty, a smaller heat transfer area is required in the case of the STHE with helical baffles, resulting in a reduced heat exchanger length (approx. 10 %). Comparing Tabs. 2 and 3, the pressure drop is reduced due to all the factors mentioned above in favor of the STHE with helical baffles.

The pressure drop of working fluids in the presented SPHE is calculated according to Eq. (2). Eq. (2) accounts for the fitting of 60 x 60 mm intensification pins on the heat exchange surface (Moretta, 2010). The pressure loss of both waste and feed water is around 15.3 kPa. The identity of achieved losses results from achieving the same flow velocity ($v = 2\ \mathrm{m/s}$) in differently sized channels (see Tab. 5), and at approximately the same densities (ρ) of both liquids.

$$\Delta P = \frac{1.45 \cdot (L \cdot v^2 \cdot \rho)}{1.705} \tag{2}$$

Lastly, a comparison of SPHE and STHE with helical baffles is made with the support of the in-house calculation program based on (Stehlík et al., 1991). The design of the new STHE with helical baffles is based on the case solved in Chap. 2 so that it meets the process data for SPHE in Tab. 4. The new inner diameter of the shell and length of the tubes have been set to maintain approximately the original ratio of these two dimensions and to achieve the stated heat duty of 210 kW.

$$p = 2 \cdot \sqrt{2} \cdot D \cdot \tan(\varphi) \tag{3}$$

Subsequently, according to Eq. (3), taken from (Stehlík et al., 1991), the baffle spacing (p) was calculated for the angle of baffle inclination (φ), which should be in the range of 40 to 60 percent of this value (Stehlík et al., 1991). The resulting dimensions of the STHE with helical baffles are given in Tab. 6 along with the pressure loss data.

Shell inner diameter	Tube length	Baffle inclination	Baffle spacing	Pressure drop	
				Shell	Tubes
400 mm	2 000 mm	15 °	150 mm	88 254 Pa	7 889 Pa

Tab. 6: Main results of shell side design data for STHE design.

The cold feedwater is placed on the tube side and the hot fouling wastewater on the shell side. The hydraulic loss of the fouling working fluid is lower in the SPHE than in the case of STHE with helical baffles.

5. Conclusions

The paper presents perspective ways to increase heat transfer in heat exchangers operating in fouling conditions of liquid working fluids. Industrial examples demonstrate these intensification methods. From the examples presented, it is possible to establish a clear superiority of spiral plate heat exchangers in terms of fouling rate, built-up area, and above all, pressure losses. The positive influence of helical and spiral flow on fouling and thermal-hydraulics behavior has also been demonstrated. Therefore, it seems promising to deal with such types of flows in the future and to investigate their influence on the presented aspects also for non-liquid working fluids and their operating conditions.

References

Akpomiemie, M. O. and Smith, R. (2016) Retrofit of Heat Exchanger Networks with Heat Transfer Enhancement Based on an Area Ratio Approach, *Applied Energy*, 165, pp. 22–35.

Stehlík, P., Kohoutek, J.n and Němčanský, J. (1991) *Heat Transfer Processes: Calculation of Heat Exchanger*. Script of Brno University of Technology, Publisher BUT (VUT) Brno (in Czech).

Moretta, A. A. (2010) Spiral Plate Heat Exchangers: Sizing Units for Cooling Non-Newtonian Slurries, *Chemical Engineering*, pp. 44–49.

30th International Conference
ENGINEERING MECHANICS 2024
Milovy, Czech Republic, May 14 – 16, 2024

WEAK IMPOSITION OF POTENTIAL DIRICHLET BOUNDARY CONDITIONS IN PIEZOELASTICITY: NUMERICAL STUDY

Cimrman R. *

Abstract: *Detailed modelling of piezoelastic structures often includes also an external circuit. This is tied with the need for a weak imposition of electric potential Dirichlet boundary conditions and questions of simulation accuracy arise. Several methods allowing the weak imposition, namely the non-symmetric Nitsche's method, penalty method and their combinations, are evaluated and their numerical convergence w.r.t. uniform mesh refinement for various finite element approximation orders is reported. The numerical study is performed on a geometry corresponding to a piezoelectric sensor.*

Keywords: Piezoelasticity, Dirichlet boundary conditions, weak imposition, numerical convergence.

1. Introduction

When performing and simulating experiments involving electro-active materials (piezoelectric, flexoelectric, etc.), such as reported in (Cimrman et al., 2023), the electric potential that arises on conductive electrodes is a key quantity to be measured and modeled. The presence of an external circuit (e.g. an oscilloscope) makes the constant potential on an electrode an additional unknown to be computed. As such, the usual potential Dirichlet boundary condition can be enforced only in a weak sense, because its value is not known.

The non-symmetric Nitsche's method without penalty term (Burman, 2012) seemed like a good candidate to be used in combination with the finite element method (FEM), but its slow convergence in our context of 3D piezoelasticity, numerically demonstrated below, motivated this ongoing research of simple and accurate methods for weak application of Dirichlet boundary conditions. We demand a sufficient accuracy even on relatively coarse meshes, because our main interest lies in dynamical simulations.

2. The Finite Element Model

We consider a piezoelastic disc $\Omega \subset \mathbb{R}^3$ whose FEM discretization is shown in Fig. 1. Under linear assumptions, the constitutive relations can be written as

$$\boldsymbol{\sigma} = \boldsymbol{C}^P \boldsymbol{\varepsilon} - \boldsymbol{e}^T \boldsymbol{E} \,, \quad \boldsymbol{d} = \boldsymbol{e}\boldsymbol{\varepsilon} + \boldsymbol{\kappa}\boldsymbol{E} \,, \quad \boldsymbol{\varepsilon} = \frac{1}{2}(\boldsymbol{\nabla}\boldsymbol{u} + \boldsymbol{\nabla}^T\boldsymbol{u}) \,, \quad \boldsymbol{E} = -\boldsymbol{\nabla} p \,, \tag{1}$$

where the mechanical stress $\boldsymbol{\sigma}$ (in Voigt notation vector ordering) and the electric displacement $\boldsymbol{d}$ are proportional to the mechanical strain $\boldsymbol{\varepsilon}$ and the electric field vector $\boldsymbol{E}$, $\boldsymbol{u}$ is the mechanical displacement vector, p the electric potential, $\boldsymbol{C}$ the matrix of elastic properties under constant electric field intensity, $\boldsymbol{e}$ the piezoelectric modulus and $\boldsymbol{\kappa}$ the permittivity under constant deformation. Denoting by Γ_b to bottom and Γ_t the top sides of the disc, where conductive electrodes are situated, the strong form of the problem is: Find p such that

$$\begin{aligned} -\boldsymbol{\nabla}\cdot\boldsymbol{\sigma} = \boldsymbol{b} \text{ in } \Omega \,, \quad \boldsymbol{\nabla}\cdot\boldsymbol{d} = 0 \text{ in } \Omega \,, \\ \boldsymbol{u} = 0 \text{ on } \Gamma_b \,, \quad p = 0 \text{ on } \Gamma_b \,, \quad p = \bar{p} \text{ on } \Gamma_t \,, \end{aligned} \tag{2}$$

* Robert Cimrman: Institute of Thermomechanics of the CAS, Prague & New Technologies - Research Centre and Faculty of Applied Sciences, University of West Bohemia, Plzeň; CZ, cimrman3@ntc.zcu.cz

doi: 10.21495/em2024-078

where $\boldsymbol{b}$ are the self-weight volume forces and $\bar{p}$ is a given potential to be enforced weakly. Zero Neumann boundary conditions are applied on the parts of the Ω boundary not mentioned above.

Let $V_0^u(\Omega) = \{\boldsymbol{u} \in [H^1(\Omega)]^3, \boldsymbol{u} = \boldsymbol{0} \text{ on } \Gamma_b\}$, $V_0^p = \{p \in H^1(\Omega), p = 0 \text{ on } \Gamma_b\}$. The weak form of (2) is then: Find p such that

$$\int_\Omega \boldsymbol{\varepsilon}(\boldsymbol{v})^T \boldsymbol{C} \boldsymbol{\varepsilon}(\boldsymbol{u}) - \int_\Omega \boldsymbol{\varepsilon}(\boldsymbol{v})^T \boldsymbol{e}^T \boldsymbol{\nabla} p - \int_\Omega \boldsymbol{v} \cdot \boldsymbol{b} = 0 \qquad \forall \boldsymbol{v} \in V_0^u(\Omega)\ , \tag{3}$$

$$\int_\Omega (\boldsymbol{\nabla} q)^T \boldsymbol{e} \boldsymbol{\varepsilon}(\boldsymbol{u}) + \int_\Omega (\boldsymbol{\nabla} q)^T \boldsymbol{\kappa} \boldsymbol{\nabla} p - \int_{\Gamma_t} (\boldsymbol{\kappa} \boldsymbol{\nabla} p) \cdot \boldsymbol{n} q = 0 \qquad \forall q \in V_0^p(\Omega)\ , \tag{4}$$

$$\boldsymbol{u} = 0\ , \quad p = 0 \qquad \text{on } \Gamma_b\ , \tag{5}$$

$$p = \bar{p} \qquad \text{on } \Gamma_t \text{ weakly, see below.} \tag{6}$$

Note that the last term in (4) would be zero if the condition $p = \bar{p}$ on Γ_t was applied as usual by modifying the definition of the test function space V_0^p. The above model is discretized using the FEM, leading formally to the same equations but with functions from appropriate finite element spaces.

3. Weak Imposition of Dirichlet Boundary Conditions

Numerous approaches exist for the weak imposition of Dirichlet boundary conditions, see e.g. (Lu et al., 2019). Here we consider only the non-symmetric (Freund and Stenberg, 1995) Nitsche's method (Nitsche, 1971) with or without penalty term (Burman, 2012). This method introduces additional terms to (4):

$$+ \int_{\Gamma_t} (\boldsymbol{\kappa} \boldsymbol{\nabla} q) \cdot \boldsymbol{n} (p - \bar{p}) + \int_{\Gamma_t} \beta q (p - \bar{p})\ , \tag{7}$$

where β is the penalty parameter. The pure penalty method can be obtained by omitting the first integral. According to (Babuška, 1973), $\beta = \beta_0 h^{-(2o+1)/3}$, see also (Lu et al., 2019), yields, in the case of the Laplace's problem, for a fixed β_0 the rate of convergence of the order $h^{(2o+1)/3}$ in the energy norm, where h is the element size and o the FE approximation order. For this reason results for the following Laplace's problem (electrostatics)

$$\int_\Omega (\boldsymbol{\nabla} q)^T \boldsymbol{\kappa} \boldsymbol{\nabla} p - \int_{\Gamma_t} (\boldsymbol{\kappa} \boldsymbol{\nabla} p) \cdot \boldsymbol{n} q = 0 \qquad \forall q \in V_0^p(\Omega)\ , \tag{8}$$

$$p = 0 \qquad \text{on } \Gamma_b\ , \tag{9}$$

$$p = \bar{p} \qquad \text{on } \Gamma_t \text{ weakly} \tag{10}$$

are also included in the next section for reference. Again the terms of (7) are added to (8) to enforce (10).

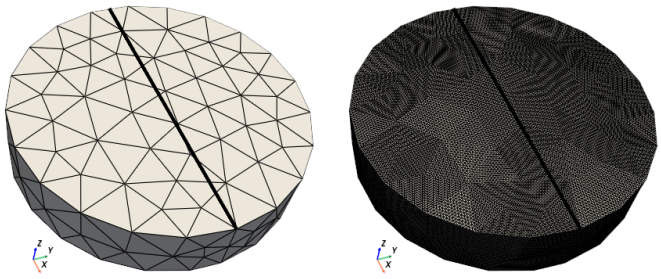

Fig. 1: The FE meshes and probe lines: basic mesh (left), $4\times$ uniformly refined mesh (right).

4. Numerical Convergence Results

The problems specified above were solved for approximation orders $o = \{1, 2, 3\}$ ($\boldsymbol{u}$ and p were approximated with the same order) and uniform mesh refinement levels $r = \{0, 1, 2, 3, 4\}$ with various values of β. The $r = 0$ (152 vertices, 382 elements) and $r = 4$ (280 177 vertices, 1 564 672 elements) meshes can

be seen in Fig. 1, together with probe lines along which the $p = \bar{p} = 555$ V satisfaction was checked. The geometry corresponds to a piezoelectric sensor PIC 181 from PI company.

The sensor has the following properties:

$$\text{in Voigt notation: } \boldsymbol{C}^P = \begin{bmatrix} 127.2050 & 80.2122 & 84.6702 & 0.0000 & 0.0000 & 0.0000 \\ 80.2122 & 127.2050 & 84.6702 & 0.0000 & 0.0000 & 0.0000 \\ 84.6702 & 84.6702 & 117.4360 & 0.0000 & 0.0000 & 0.0000 \\ 0.0000 & 0.0000 & 0.0000 & 22.9885 & 0.0000 & 0.0000 \\ 0.0000 & 0.0000 & 0.0000 & 0.0000 & 22.9885 & 0.0000 \\ 0.0000 & 0.0000 & 0.0000 & 0.0000 & 0.0000 & 23.4742 \end{bmatrix} \text{ GPa},$$

$$\boldsymbol{e} = \begin{bmatrix} 0.00000 & 0.00000 & 0.0000 & 0.0000 & 17.0345 & 0.0 \\ 0.00000 & 0.00000 & 0.0000 & 17.0345 & 0.0000 & 0.0 \\ -6.62281 & -6.62281 & 23.2403 & 0.0000 & 0.0000 & 0.0 \end{bmatrix} \text{ C/m}^2, \boldsymbol{\kappa} = \varepsilon^0 \begin{bmatrix} 1704.4 & 0.0 & 0.0 \\ 0.0 & 1704.4 & 0.0 \\ 0.0 & 0.0 & 1433.6 \end{bmatrix} \text{ F/m},$$

where $\varepsilon^0 = 8.8541878128 \cdot 10^{-12}$ F/m is the vacuum permittivity.

a) Laplace: p distribution

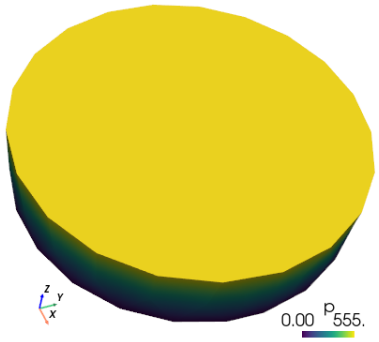

b) Piezoelasticity: p distribution (1 000× deformation)

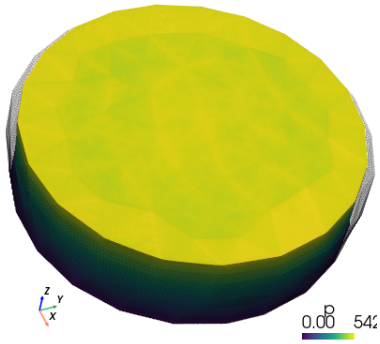

c) Laplace: probe

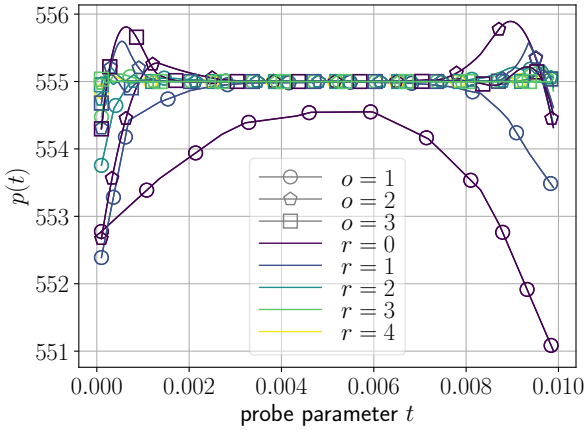

d) Piezoelasticity: probe

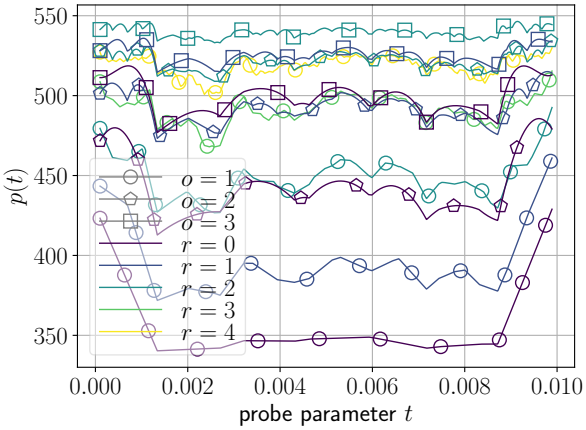

Fig. 2: Nitsche's method without penalty ($\beta = 0$): a) Laplace and b) piezoelasticity distributions of p for $o = 1$ and $r = 4$, c) Laplace and d) piezoelasticity probes of p along the lines in Fig. 1.

All results reported here were obtained using the Open Source finite element software SfePy (Cimrman et al., 2019; Cimrman, 2021). The results for the non-symmetric Nitsche's method without penalty term ($\beta = 0$), our first choice, are illustrated in Fig. 2. While the results for the Laplace's problem (Figs. 2 a) and 2 c) converge relatively well to the prescribed value 555 V, the piezoelasticity problem (Figs. 2 b and 2 d) have low accuracy even for the finest mesh ($r = 4$). Therefore the penalty term was added, either with a constant coefficient $\beta = 1$, or scaled by the local element size $\beta = h^{-(2o+1)/3}$. Overall convergence results are summarized in Fig. 3, where the error is defined as $||p(t) - \bar{p}||_2/N$, $N = 980$ being the fixed number of probe points along the probe line parameterized uniformly by t. The blue $\beta = 0$ lines correspond to the Nitsche's method without the penalty term discussed above. The orange lines show the influence of adding the penalty term, and finally the green dashed lines result from the pure penalty method with $\beta = 1$. When the h scaling of β is used, precision approaching machine limits seem to be reached, however the β values are large: the average values ranged from $5 \cdot 10^2$ ($o = 1$, $r = 0$) up to $2 \cdot 10^8$ ($o = 3$, $r = 3$) — that is significantly higher than in the constant case and it may spoil convergence of iterative solvers due to

a bad conditioning of the resulting matrix. The non-scaled $\beta = 1$ curves of the pure penalty method and the Nitsche's method with the penalty visually coincide, which indicates that the effect of the first integral of Eq. (7) is negligible in our setting (compare with the relatively lower accuracy of $\beta = 0$ lines).

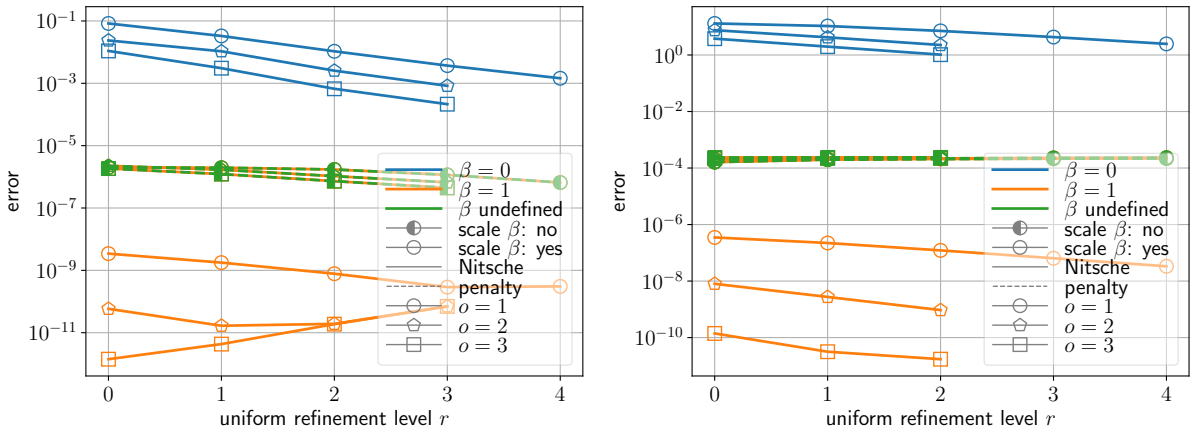

Fig. 3: The h-convergence of the Laplace's (left) and piezoelasticity (right) problems.

5. Conclusion

We have numerically evaluated the Nitsche's and penalty methods for weakly enforcing Dirichlet boundary conditions in the context of piezoelasticity, with the following outcomes. The non-symmetric Nitsche's method without penalty is not accurate enough by itself, only in combination with a penalty. The pure penalty method exhibits a sufficient accuracy even for coarse and low order approximations, although the error does not improve with the increasing order or h-refinement. However this does not present a practical problem in our piezo-elasto-dynamic application, where only second order elements are used to approximate the potential. The problem of bad conditioning with high values of the penalty β can be mitigated by using a direct solver. The influence of adding the Nitsche's method terms to the pure penalty method on the conditioning will be addressed in future.

Acknowledgment

This work has been supported by the grant 23-06220S of the Czech Science Foundation within institutional support RVO:61388998.

References

Babuška, I. (1973) The finite element method with penalty. *Mathematics of Computation*, 27, 122, pp. 221–228.

Burman, E. (2012) A penalty-free nonsymmetric nitsche-type method for the weak imposition of boundary conditions. *SIAM Journal on Numerical Analysis*, 50, 4, pp. 1959–1981.

Cimrman, R. (2021) Fast evaluation of finite element weak forms using Python tensor contraction packages. *Advances in Engineering Software*, 159.

Cimrman, R., Kolman, R., Musil, L., Kotek, V., and Kylar, J. (2023) Dynamics of a cantilever beam with piezoelectric sensor: finite element modeling. In *Proceedings of the 29th International Conference Engineering Mechanics 2023, Milovy, 2023*. pp. 51–54.

Cimrman, R., Lukeš, V., and Rohan, E. (2019) Multiscale finite element calculations in Python using SfePy. *Advances in Computational Mathematics*.

Freund, J. and Stenberg, R. (1995) On weakly imposed boundary conditions for second order problems. *Proceedings of the 9th International Conference on Finite Elements in Fluids*, pp. 327–336.

Lu, K., Augarde, C. E., Coombs, W. M., and Hu, Z. (2019) Weak impositions of dirichlet boundary conditions in solid mechanics: A critique of current approaches and extension to partially prescribed boundaries. *Computer Methods in Applied Mechanics and Engineering*, 348, pp. 632–659.

Nitsche, J. (1971) Über ein Variationsprinzip zur Lösung von Dirichlet-Problemen bei Verwendung von Teilräumen, die keinen Randbedingungen unterworfen sind. *Abhandlungen aus dem Mathematischen Seminar der Universität Hamburg*, 36, 1, pp. 9–15.

30th International Conference
ENGINEERING MECHANICS 2024
Milovy, Czech Republic, May 14 – 16, 2024

DESIGN OF A DEVICE FOR MEASURING THE RATE OF PARTICULATE FOULING OF HEAT TRANSFER SURFACES

Daxner J.[*], Jegla Z.[**], Zabloudil J.[***], Babička Fialová D.[†], Reppich M.[††]

Abstract: *This paper presents the process of designing an experimental device (TESTER) developed to test and assess the comprehensive rate of particulate fouling in various heat recovery processes. The evaluation can be used not only for direct flue gas heat recovery from combustion processes (e.g., process furnaces, water- or steam-boilers, etc.) but also for flue gas waste heat recovery processes (such as cement production, zinc dioxide production, etc.). The assessment of particulate fouling requires diverse operating conditions, including gas velocity, temperature, particles volume, size, and different types of TESTER geometry, such as tube diameter and arrangement. The main output of the experimental analysis is the identification of the optimal geometry or operating conditions of a heat exchanger and recommendation for the process operator.*

Keywords: Flue gas, waste heat recovery, heat exchanger, particulate fouling, fouling rate.

1. Introduction

Heat exchangers have an important role across the industry. They are used in power generation, chemical industry, waste treatment, etc. All recently stated processes can carry heat in flue gas regardless of whether flue gas are direct combustion products or merely waste heat stream (Jouhara et al., 2019). The primary goal of heat exchanger designers is to achieve maximum heat transfer rate while considering factors such as pressure drops, thermophysical properties of heat carriers, geometry configuration, etc. The main limitation in the design of heat exchangers for flue gas is the presence of particulate pollutants contained in the flue gas (Müller-Steinhagen et al., 2011). Despite research efforts, these add complexity to the heat exchanger design mainly because there is still a lack of information in predicting particulate fouling. The design of heat exchangers for fouling environments is therefore based only on the experience of the designer but lacks the knowledge of the actual fouling rate of the flue gas stream. Examples of processes that produce flue gas containing particulate matter are all processes where solid fuel (e.g. coal, biomass, municipal waste) is incinerated (Bott, 1995). On the other hand, there are processes where flue gas with solid particles are not direct products of combustion such as cement production, wood and pulp drying, or various chemical manufacturing methods (Bianchi et al., 2019).

Particulate fouling is caused by the deposition of colloidal solid particles, either organic or inorganic origin, present in the heat carrier. In gaseous media, the most common pollutants are by-products of combustion. They form deposits with varying mechanical and chemical properties depending on the type of fuel and combustion conditions (Trojan et al., 2019). Fig. 1 shows examples of heat exchangers fouled by ash.

[*] Ing. Ján Daxner: Institute of Process Engineering, Faculty of Mechanical Engineering, Brno University of Technology; Technická 2; 616 69, Brno; CZ, jan.daxner@vutbr.cz

[**] Assoc. Prof. Ing. Zdeněk Jegla, PhD.: Institute of Process Engineering, Faculty of Mechanical Engineering, Brno University of Technology; Technická 2; 616 69, Brno; CZ, zdenek.jegla@vut.cz

[***] Ing. Jan Zabloudil: Eveco Brno, s.r.o.; Hudcova 321/76d; 612 00, Brno; CZ, zabloudil@evecobrno.cz

[†] Ing. Dominika Babička Fialová, PhD.: Institute of Process Engineering, Faculty of Mechanical Engineering, Brno University of Technology; Technická 2; 616 69, Brno; CZ, dominika.fialova@vutbr.cz

[††] Prof. Dr.-Ing. Marcus Reppich: Faculty of Mechanical and Process Engineering, Augsburg University of Applied Sciences; An der Hochschule 1; 86161 Augsburg; DE, marcus.reppich@hs-augsburg.de

doi: 10.21495/em2024-082

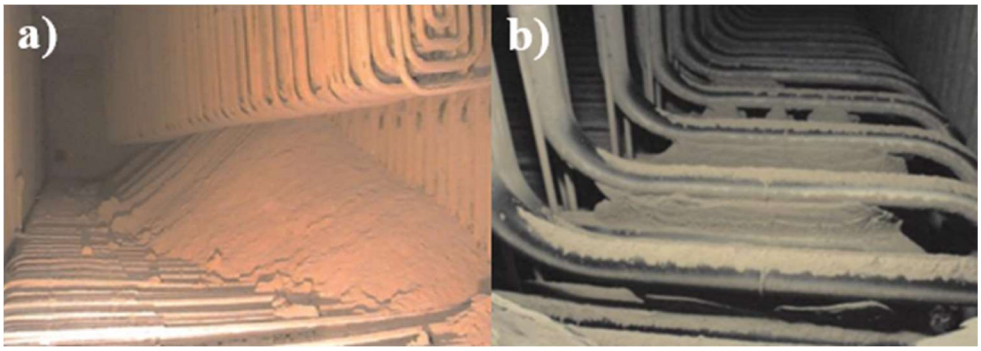

Fig. 1: Heavily fouled tubes of a) superheater and b) re-heater by ash (Trojan et al., 2019).

As mentioned, particulate fouling causes many problems in heat exchanger operation. Predicting fouling is challenging due to the low amount of experimental data which is usually the main reason for poor design of heat exchangers. For this reason, new ways for designing heat exchangers in fouling environments are being sought. This paper presents the design procedure of the experimental device TESTER, which will investigate the nature of fouling for a specific case and determine measures to mitigate fouling.

2. Design of the experimental device

The initial phase of the TESTER's technological design involved defining the experimental concept. The main parameter emphasized was the variability of the TESTER's geometry. Heat exchangers across the industry have various designs because there is no uniform heat exchanger concept for the use of heat from fouling flue gas. Flexibility in TESTER's geometry is crucial for approaching the complexity seen in practical solutions. Thus, it is necessary to be able to vary several most common types of geometries to mimic real industry solutions.

Alongside flexible geometry, mobility became a pivotal parameter in the TESTER's design. As is clear from the text, the main output of the TESTER's application will be a recommendation for operators of processes. For this reason, the tests must be carried out not only in laboratory (relevant) conditions but also in operational environments in already operating plants. Therefore, the device must be mobile, easy to transport, and simple to assemble, aligning with the practical demands of on-site experiments. These requisites were fundamental in our design consideration.

Considering these two parameters, the very first version of a TESTER was designed (see Fig. 2a), based on industry insights and expertise. Fig. 2b shows a cross-section of a TESTER. As shown in Fig. 2b, it is a cross-flow arrangement that corresponds most closely to industrially used heat exchanger designs, where one stream carries a heated medium and the second consists of flue gas with particulate matter. This initial version underwent subsequent modifications based on thermal-stress analysis and thermal-hydraulic calculations.

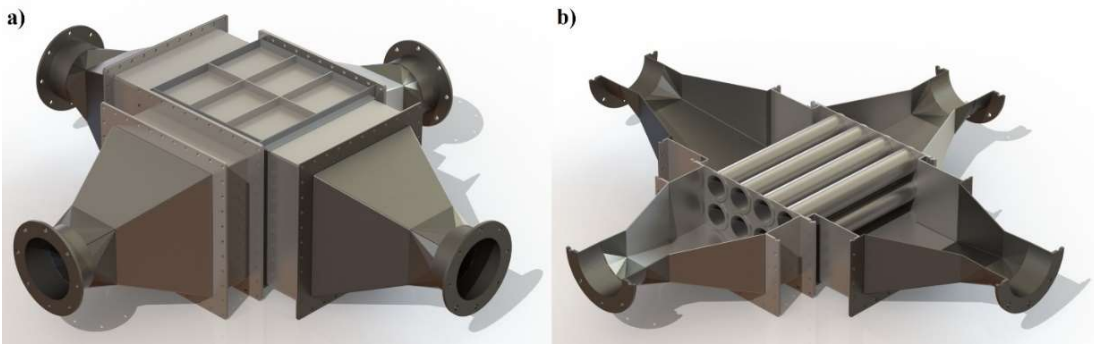

Fig. 2: a) First version of TESTER and b) first version of TESTER in cross-section.

The main purpose of the thermal-stress analysis was identifying and rectifying critical points within the TESTER's construction. This analysis used ANSYS Mechanical software (ANSYS Inc., 2023) to eliminate vulnerabilities and enhance TESTER's structure integrity. Consequently, for thermo-hydraulic calculations, the Heat Exchanger Design Handbook (Kuppan, 2013) was employed to optimize the fluid dynamics aspects of the TESTER.

2.1. Thermal Analysis

The first step of a thermal analysis was determining the maximum operating temperature at which the TESTER will be operated. Based on research and communication with industrial partners was this temperature determined to be 800 °C. Such a high temperature precludes the use of conventional structural steels due to the degradation of their material properties. For this reason, the individual components of the TESTER were made of durable materials, namely refractory steels 1.4841 and 1.4845. The inputs and assumptions for the thermal analysis are stated in Tab. 1. Fouling resistances were not considered.

Temperature TS (tube side)/SS (shell side) (°C)	800/15
Heat transfer coefficient TS/SS (W/(m^2·K))	80/35
Meshing size of the element through-thickness (mm)	1.5
Meshing size of the element on the surfaces (mm)	5
Thermal conductivity of refractory steel (W/(m.·K))	15

Tab. 1: Input parameters of a thermal analysis.

The thermal analysis results provided information about the temperature of individual parts of the TESTER and was used as the input parameter for stress analysis.

2.2. Stress Analysis

The thermal analysis was followed by a stress analysis performed in the same software ANSYS Mechanical (ANSYS Inc., 2023). Input parameters for stress analysis were results acquired in thermal analysis. All other input parameters were the same as stated in Sect. 2.1. As is shown in Fig. 3a, TESTER is symmetrical through all planes passing its center. This fact made it possible to perform cuts with all planes, resulting in 8 symmetrical parts of the TESTER (see Fig 3b) and only 1/8th of a TESTER was used for calculations. Subsequently, symmetry conditions were applied to the cutting surfaces. This modification ensured lower time requirement calculation and significantly reduced the required computing power.

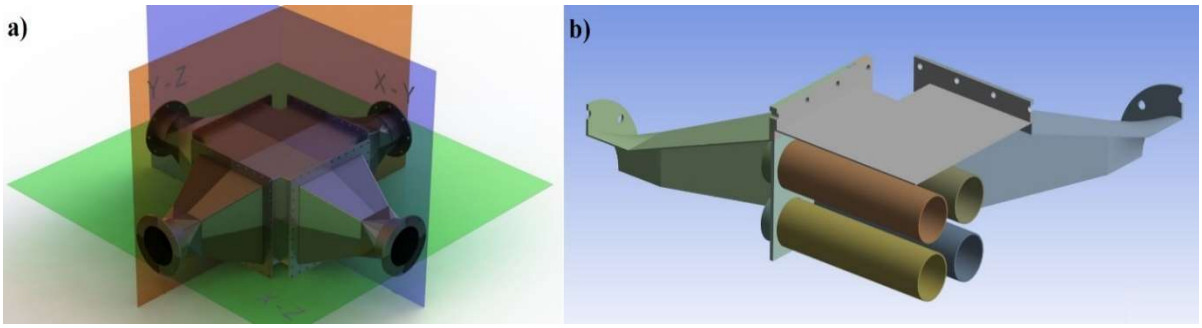

Fig. 3: a) TESTER's planes of symmetry, b) 1/8th of a TESTER created with cuts by planes.

Boundary conditions for all contact surfaces of individual parts have been set to bonded. When considering frictional connections, whose properties are closer to reality, computation difficulty increased extensively but differences between bonded and frictional connections were for subject analysis negligible. Fig. 4 shows critical areas of the structure revealed by thermal-stress analysis in terms of stress peaks.

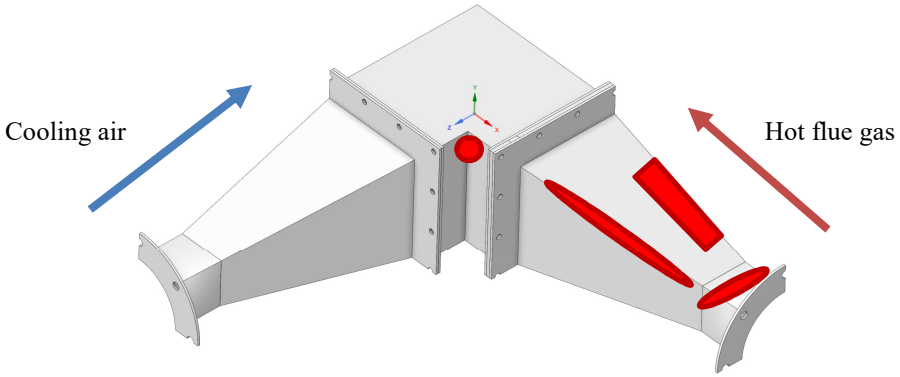

Fig. 4: Thermal-stress analysis of the very first version of a TESTER.

2.3. Thermal-hydraulic calculation

In contrast to the thermal stress analysis, a wider range of flue-gas flow conditions (an inlet temperature varying from 250 °C to 800 °C, the hot fluid located in the TS or SS) were analyzed using Heat Exchanger Design Handbook (Kuppan, 2013). Simultaneously, the most common tube bundle arrangements (in-line and staggered) were investigated. In addition to the geometrical parameters and inlet temperatures, the basic assumptions comprised the inlet pressure and the mean velocity of both fluids, flue gas, and air. The objective of the thermal-hydraulic calculations was to determine the flue gas and air flow rates, the heat duty of the clean TESTER (i.e., no fouling resistances were considered), and the pressure drops of both working fluids. Tab. 2 shows the results of a thermal-hydraulic analysis.

Temperature (°C)	250	400	600	800
Flow rate SS/TS (kg/s)	0.736/0.428	0.733/0.338	0.729/0.265	0.725/0.218
Pressure drop SS/TS (kPa)	0.079/0.088	0.083/0.070	0.086/0.055	0.090/0.045
Mean velocity SS/TS (m/s)	9.56/10.24	9.57/10.32	9.57/10.42	9.57/10.48

Tab. 2: Main output parameters of a thermal-hydraulic calculations with flue gas in tubes.

3. Conclusions

In this paper, the design procedure of the test heat exchanger (TESTER) for the investigation of the fouling rate of flue gas containing particulate matter has been presented. A key part of the overall design was performing thermal-stress analysis and thermal-hydraulic calculations. Those provided valuable results on which further modifications to the design of individual parts of the TESTER were based.

The TESTER is currently being assembled and commissioned in laboratory conditions. The results obtained by computational modeling and calculations will be experimentally verified in this step. At the same time, pilot fouling tests of the designed TESTER's geometry will be performed. Tests with industrial partners will start in the second half of 2024.

Acknowledgment

The authors gratefully acknowledge the financial support provided by the Technology Agency of the Czech Republic within the research project No. TK05020076 “Development of a mobile tester for safe and reliable heat recovery from fouling flue gases and an ammonia generator for their cleaning”, GA BUT within research project No. FSI-S-23-8173 and by the EU project Strategic Partnership for Environmental technologies and Energy Production, funded as project No. CZ.02.1.01/0.0/0.0/16_026/0008413 by Czech Republic Operational Programme Research, Development and Education.

References

ANSYS Inc. 2023 *ANSYS Mechanical User’s Guide, Release 2023 R2*. ANSYS, Inc., Canonsburg, PA, USA.

Bianchi, G., Panayiotou, G. P., Aresti, L., Kalogirou, S. A., Florides, G. A., Tsamos, K., Tassou, S. A. and Christodoulides, P. (2019) Estimating the waste heat recovery in the European Union Industry. *Energy, Ecology and Environment*, 4(5), 211–221.

Bott, T. R. (1995) *Fouling of heat exchangers*. Chemical engineering monographs, vol. 26, Amsterdam; New York: Elsevier.

Jouhara, H., Khordehgah, N., Almahmoud, S., Delpech, B., Chauhan, A. and Tassou, S. A. (2018) Waste heat recovery technologies and applications. *Thermal Science and Engineering Progress*, 6, 268–289.

Kuppan, T. (2013) *Heat exchanger design handbook*. 2nd edition. Mechanical engineering. Boca Raton.

Müller-Steinhagen, H., Malayeri, M. R. and Watkinson, A. P. (2011) Heat Exchanger Fouling: Mitigation and Cleaning Strategies. *Heat Transfer Engineering*, 32(3–4), 189–196.

Trojan, M., Taler, D. and Wielgus, S. (2019) On-line monitoring of the fouling of the boiler heating surfaces. *Thermal Science*, 23 (Suppl. 4), 1289–1300.

30th International Conference
ENGINEERING MECHANICS 2024
Milovy, Czech Republic, May 14 – 16, 2024

BATTERY CRASH SIMULATION IN ANSYS LS-DYNA

Dohnal J.*, Šebík M.**

Abstract: *Nowadays, lithium-ion batteries are considered as the most efficient source of power for electric vehicles (EVs). With the increasing utilization of EVs, the requirements for higher performance, lower weight and improved safety are also growing. These demands can be fulfilled by an improved battery design, which consists of decreased battery frame mass or higher number of battery cells. However, with these improvements come several negative aspects, such as higher risk of battery frame intrusion or lower heat dissipation due to reduction of space between the cells. Due to these factors, the risk of battery damage is rising, thus it is crucial to predict and better understand the behavior of the battery cells during critical situations, such as vehicle crash. Ansys LS-DYNA is a useful tool for the evaluation of battery cells during abusive scenarios. It offers the creation of multi-physics model that is able to predict coupled mechanical, electrical and thermal responses. This model is sufficient for the assessment of battery cell response to short-circuit, which can lead to uncontrollable, self-heating state called thermal runaway. This state poses the greatest safety risk for Li-Ion batteries. This paper focuses on risk assessment of traction battery during crash and overcharging simulations.*

Keywords: Battery, LS-DYNA, explicit, multi-physics, crash.

1. Introduction

Ansys LS-DYNA provides the capability to simulate battery cells under typical operating conditions, as well as in scenarios involving potential overloading and short-circuit events. LS-DYNA uses one-code strategy, integrating solvers cohesively. Particularly in battery simulations, the main utilized solver is the resistive heat solver. From the electromagnetic (EM) solver, the Joule energy term $\dot{q}_{joule}$ can be extracted (Ansys Inc., 2020):

$$\dot{q}_{joule} = \int_t^{t+1} \frac{j^2}{\sigma} dt, \tag{1}$$

which acts as a volumetric heat source term in the thermal equation:

$$\frac{\partial T}{\partial t} - \alpha \Delta^2 T = \dot{q}_{joule}, \tag{2}$$

where j is current density, is σ electrical conductivity and α is thermal diffusivity.

The electrochemical reactions within the battery cell are represented by a phenomenological model known as the Randles circuit. Despite its simplicity, this model suitably captures the behavior of the battery across various operational scenarios.

LS-DYNA offers several approaches to battery modeling. There are two micro-scale methods which are based on discretizing individual battery cell layers using solid or thick-shell elements. These models allow detailed analyses of single battery cells. However, due to the typically thin battery layers, the finite element mesh has small element dimensions along the cell thickness, thereby increasing computational time. Consequently, these methods prove inadequate for modeling battery modules or entire packs with numerous cells. In such cases, a global approach is favored, wherein the battery cell is considered as a homogeneous orthotropic continuum. This modeling strategy enhances computational efficiency.

* Ing. Jakub Dohnal.: SVS FEM s.r.o., Trnkova 117/c; 628 00, Brno; CZ, jdohnal@svsfem.cz

** Ing. Marek Šebík.: SVS FEM s.r.o., Trnkova 117/c; 628 00, Brno; CZ, msebik@svsfem.cz

doi: 10.21495/em2024-086

The risk of short-circuiting poses a significant threat to batteries, potentially resulting in catastrophic damage to the cell. This occurrence may arise from various factors. For example, overcharging the battery elevates its temperature, leading to possible damage to the separator layer, thereby initiating a short circuit and triggering a hazardous exothermic reaction known as thermal runaway. During thermal runaway, the temperature of the cell increases rapidly, presenting a considerable risk of fire or explosion. External heat sources can affect the battery cell in same negative manner. Furthermore, short-circuiting can be induced by physical deformation of the battery cell, such as nail penetration, causing mechanical harm to the cell separator and establishing an undesirable internal electrical connection between the electrodes.

This paper contributes to the SAFEBATT project, which is focusing on the advancement of a robust early warning system for battery failure and the design of a self-extinguishing and cooling system for battery packs to enhance its safety. In 2023, SVS FEM was tasked with conducting numerical simulations of the traction battery crash test in accordance with the ECE 100 standard, along with electro-thermal simulations. The results from these numerical simulations are presented within this paper.

2. Battery cell testing

The analyzed traction battery comprises 8 battery modules, each housing 24 cells. To calibrate and optimize the numerical model of a single battery cell, a series of mechanical, thermal, and electrical tests were conducted. Regarding the mechanical aspect of the battery, the cell consists of an inner series of diverse chemical compound layers, commonly referred to as the “jellyroll”, encased in an outer aluminum alloy casing. Four quasi-static mechanical tests were conducted to capture a broad spectrum of loading scenarios (see Fig. 1). Additionally, alongside force-displacement measurements, voltage and temperature were recorded to detect potential short-circuiting of the cell resulting from possible penetration of the separator layer.

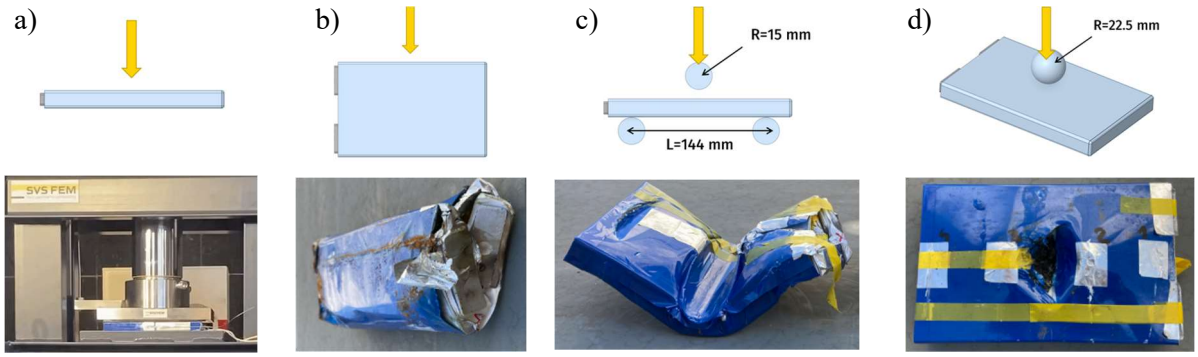

Fig. 1: Deformed specimens - a) flat compression, b) lateral compression, c) 3-point bending, d) punch.

The deformed cell shapes are depicted in Fig. 1. Short-circuiting was observed during the lateral compression test, coinciding with buckling deformation, culminating in battery ignition at the end of the loading sequence. Although thermal runaway was expected during the punch test, there was no notable sharp decline in the voltage that would consequently lead to an increase in temperature. A possible explanation for this phenomenon is the larger diameter of the spherical indenter, which only compresses the jellyroll layers without perforating them. Obtained force-displacement curves were utilized to calibrate the material model of the cell’s FE model.

Correctly defining the electrical and thermal properties within the numerical model of the cell is necessary for assessing voltage trend and heat conduction within the battery. Three electrical tests were conducted to acquire the parameters of the Randles circuit. One thermal test was executed. In this thermal test, the base of the cell was subjected to external heating until a short-circuit occurred, resulting in a cell explosion (see Fig. 2). The explosion happened because the cell was fastened by a thick rope encircling the upper section of the battery, preventing cell movement. However, due to this constrain on the upper surface, the accumulated internal pressure could not be adequately released through the top safety vent. It is assumed that in the event of pressure release, the battery will likely ignite.

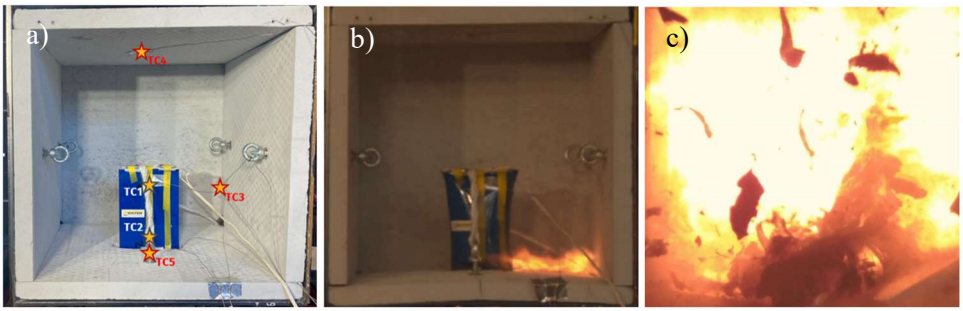

Fig. 2: Battery cell in the chamber a) with thermocouples, b) immediately before the explosion, c) during the explosion.

3. Crash simulation of traction battery

Based on the geometry, the finite element (FE) model of the entire traction battery was developed (see Fig. 4a). In most traction battery components, a bilinear material model was employed. Specifically, the bilinear material model was assigned to the battery cell's aluminum casing. Additionally, an orthotropic material model was applied to represent the homogeneous solid jellyroll of the cell. Parameters associated with these material models were iteratively adjusted to align with experimental results.

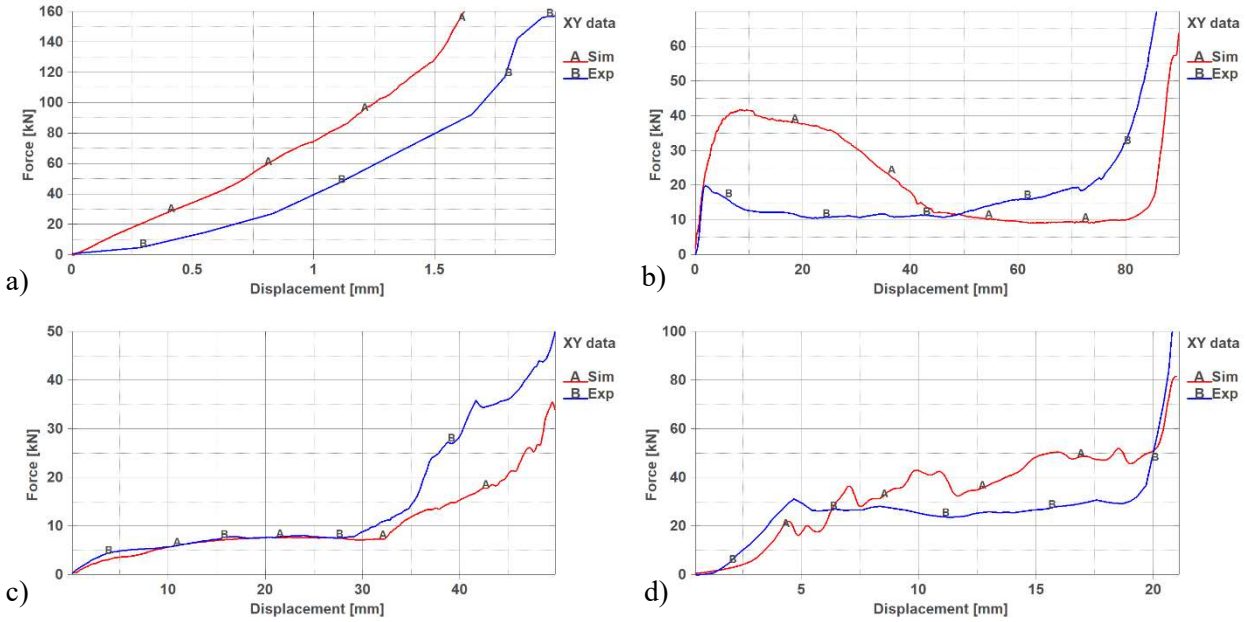

Fig. 3: Comparison of force-displacement curve between simulation and experiment a) flat compression, b) lateral compression, c) 3-point bending, d) punch.

Comparing the results obtained from simulations with experimental data, a perfect alignment between the force-displacement curves was not achieved (see Fig. 3). It is important to note that the jellyroll comprises numerous layers, each possessing different mechanical properties. Consequently, at the microscale level, local deformation processes (failure, buckling, delamination, etc.) within these layers cannot be accurately captured by a homogeneous model with a coarse mesh.

To date, only the structural part of the model has been solved in the crash simulation utilizing an explicit solver. However, the following phases of the project aim to incorporate electromagnetic (EM) and temperature solvers into the analysis.

An acceleration-time curve conforming to ECE 100 standard specifications was applied to the traction battery. Stress and strain distributions were evaluated across the battery frame, bolts, and individual cells. According to the findings of the numerical simulation, no compromising of structural integrity was observed within the traction battery. Moreover, cell deformation was negligible, thereby reducing the probability of an internal short-circuit event.

4. Electro-thermal simulation of battery module

In the current stage of the project, the battery cell is considered as rigid in terms of mechanical properties, since stress and deformation analyses of the cell/module are neglected in the electro-thermal simulations presented in this paper.

For the electromagnetic (EM) part of the model, a homogenized approach to the battery cell modeling is employed. Parameters such as the temperature at which short-circuiting occurs and the internal battery resistance were obtained from experimental data. Typically, a short-circuit event triggers an exothermic reaction accompanied by heat dissipation. However, this reaction was not observed in the overheating test due to aforementioned imperfections in battery mounting. Nevertheless, the exothermic reaction is still accounted for in the simulation, but the exothermic rise of the temperature, and post-short-circuit behavior are estimated.

Following the development of the FE model of the battery module, simulations were conducted to investigate the effects of overcharging cell number 1 (see Fig. 4b). Heat propagation within the battery module was monitored, revealing that the adjacent cell, number 2, also experienced heating due to the thermal runaway initiated by the first battery cell. Consequently, a short-circuit occurred in the cell number 2 area where the critical temperature was reached. Cell number 3, however, did not reach the critical temperature threshold, thus avoiding a short-circuit event.

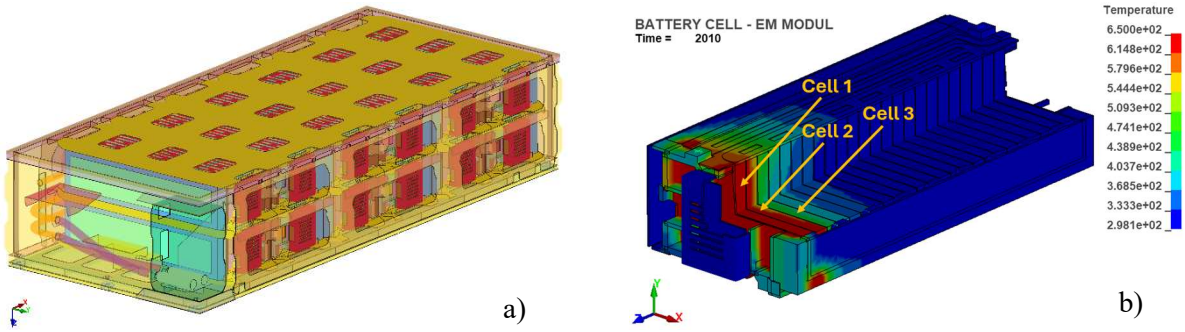

Fig. 4: a) Traction battery FE model for crash simulation, b) temperature of battery module during overcharging simulation – cut section view.

5. Conclusion

Ansys LS-DYNA was employed to create the FE model and conduct simulations of the battery under diverse loading conditions. A homogeneous battery cell modeling approach was adopted. To capture the multi-physics properties of the cell model, four quasi-static mechanical tests, one overheating test, and three electrical tests were conducted.

The FE model of the traction battery was developed to simulate mechanical crash test in accordance with ECE 100 standard. Stress and strain distributions across the entire battery and its individual cells were analyzed. According to the outcomes of the numerical simulation, no compromise of the structural integrity of the traction battery was observed. Moreover, there were no instances of cell penetration, reducing the probability of an internal short-circuit event.

In the electro-thermal simulation, a scenario involving the short-circuiting of one cell within the battery module was simulated, with subsequent observation of heat transfer within the module. In order to enhance electro-thermal simulation, additional experimental investigations are warranted to accurately characterize the thermal and electromagnetic aspects of the battery model, such as external shorting, heat propagation among multiple battery cells, or nail penetration. Furthermore, future considerations should include the effect of strain rate on resulting cell stresses.

References

Ansys Inc. (2020) *AnsysLearningHub.* Online. Ansys, Inc.

30th International Conference
ENGINEERING MECHANICS 2024
Milovy, Czech Republic, May 14 – 16, 2024

PIV MEASUREMENT OF WAKES PAST STATOR WHEEL INSIDE AIR TEST TURBINE VT-400 IN TWO AXIAL×TANGENTIAL PLANES

Duda D.[*], Uruba V.[**], Yanovych V.[***], Klimko M.[†], Tomášková T.[††], Jeřábek M.[†††], Žitek P.[‡], Milčák P.[‡‡]

Abstract: *VT-400 is a single-stage test turbine working with ambient air located at the University of West Bohemia in Pilsen. Inside this turbine, we perform a PIV (Particle Image Velocimetry) measurement of the flow field in two planes oriented in axial × tangential direction. There planes are located between the stator wheel and rotor wheel; first one is near the hub, second one at the middle of blade height. The spatial distribution of velocity fluctuations displays system of wakes and jets oriented diagonally over the studied area. The jets are represented by higher mean velocity and lower turbulence, the wakes oppositely. The spatial size of fluctuations is analyzed in terms of autocorrelation function: the size of correlated region is comparable with the wake width, additionally, there is apparent a wave in the stream-wise direction. At different turbine working parameters, we observed at least two distinct wavelengths. The neighboring wakes do not interact in the limits of studied areas.*

Keywords: Particle Image Velocimetry, turbine, stator wheel, wake, autocorrelation function.

1. Introduction

Steam turbines are still very important machines for energy production. They transform the energy from the form of high pressure and high enthalpy to the rotational kinetic energy (Burdin, 1824). Higher efficiency of is reached by adding the *stator wheel* before the rotor wheel. Its role is to deflect the direction of the flow from fully axial direction in a such way, that after the passage through rotor wheel, the fluid direction could be fully axial and thus having smallest kinetic energy (and thus larger fraction of energy being processed by the turbine rotor). The classical approach just takes into account the velocity deflection, but the stator is realized as a grid of high-lift blades, which naturally produce wakes – fluid region, which is significantly influenced by the previous presence of solid body. Typically, the mean flow velocity is slower and fluctuations stronger inside the wake region (in comparison with the region between wakes – jets).

[*] Assoc. Prof. Daniel Duda, PhD.: Department of Power System Engineering, University of West Bohemia in Pilsen, Univerzitní 22; 306 14, Pilsen; CZ, dudad@fst.zcu.cz

[**] Prof. Václav Uruba, CSc.: Institute of Thermomechanics, Czech Academy of Sciences; Dolejškova 5; 180 00, Prague; CZ, uruba@fst.zcu.cz

[***] Assoc. Prof. Vitalii Yanovych, DSc.: Výzkumný a zkušební ústav Plzeň s.r.o., Tylova 1581/46, 301 00 Pilsen,; CZ, yanovych@fst.zcu.cz

[†] Ing. Marek Klimko, PhD.: Department of Power System Engineering, University of West Bohemia in Pilsen, Univerzitní 22; 306 14, Pilsen; CZ, klimko@fst.zcu.cz

[††] Ing. Tetjana Tomášková, PhD.: Department of Mathematics, Physics and Technology, University of West Bohemia in Pilsen, Klatovská 51; 306 14, Pilsen; CZ, tomaskot@kmt.zcu.cz

[†††] Ing. Matěj Jeřábek: Department of Power System Engineering, University of West Bohemia in Pilsen, Univerzitní 22; 306 14, Pilsen; CZ, jerabekm@fst.zcu.cz

[‡] Ing. Pavel Žitek, PhD.: Department of Power System Engineering, University of West Bohemia in Pilsen, Univerzitní 22; 306 14, Pilsen; CZ, zitek@fst.zcu.cz

[‡‡] Ing. Petr Milčák, PhD.: Doosan Škoda Power, Tylova 1/57, 301 28, Pilsen; CZ, petr.milcak@doosan.com

doi: 10.21495/em2024-090

In the past, the flow inside turbines has been explored mainly numerically (Denton and Pullan, 2012; Sieverding and Manna, 2020) or by using pressure measurements (Klimko and Okresa, 2016; Ilieva, 2017; Klimko et al., 2021; Porreca et al., 2007). Our recent work uses Particle Image Velocimetry to map flow in some selected planar area past the rotor (Duda et al., 2021) or stator wheel (Duda et al., 2024). Very interesting apparatus exists at Baltimore university: their experimental configuration uses turbines made of transparent materials (Chow et al., 2002; Uzol et al., 2002).

2. Methods

The current contribution focuses to the axial × tangential plane past the stator wheel of single-stage test turbine VT-400 (Klimko and Okresa, 2016). The plane is studied at two heights – approx. 4.5 mm above the endwall and second approximately in the middle of blade height, see Fig. 1. Due to perspective effects, the bottom plane covers slightly larger area than the upper one. Both, illumination and observation is done through a *groove* in the turbine body, which usually serves for traversing pressure probes. The illumination lasersheet has to be reflected by a mirror placed inside the turbine but above the wheels, therefore we hope, that it does not affect the flow field. For other details about the camera, laser, particle seeding, etc., we refer our previous work (Duda et al., 2024), which is published in "open-access" mode.

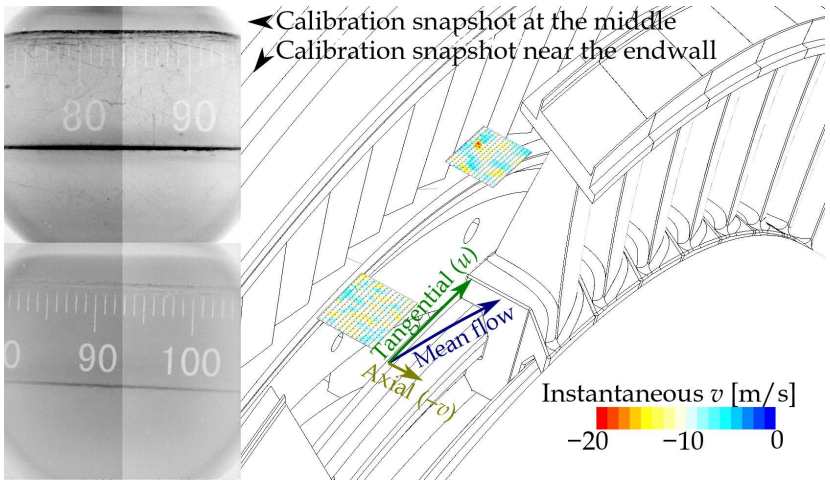

Fig. 1: Sketch of the position of studied planes inside the turbine with negatives of calibration snapshots.

3. Results

The measurements have been performed at two rotational speeds of the turbine rotor and at five pressure gradients. These gradients were adapted for the output angle α to match the values of $-40\,°$ to $+40\,°$. Unfortunately, it was not possible to measure three states at the middle plane because the mirror inside the turbine become dirty by some oil (surprisingly it was not Safex used as tracer particles). The droplets on the mirror surface caused uneven reflections, which caused the horizontal strip of extremely high fluctuations at the panel in third column and second line in Fig. 2. The rest of the column was too damaged for some data processing – this is the reason for white space in the Figs. 2 and 3.

The spatial size of fluctuations can be shown by the autocorrelation, Fig. 3. Single point in the wake has been chosen as the reference point, which automatically correlates with its neighborhood (blue spot). We observe the wavy character of fluctuations displayed as the near areas of anticorrelation. We do not observe any crosstalk with the neighboring wakes, which suggests that the fluctuation source is at the stator wheel, not in the inlet large-scale turbulence. Note the presence of two wavelengths: e.g. in the middle plane at lower speed (left column of Fig. 3) the wave is longer at $\alpha = -20\,°$, while at $\alpha = 0\,°$, the wave is half and later at $\alpha = +20\,°$, there appears a longer wave again, but now it is modulated by the shorter wave.

Acknowledgement

We acknowledge the support of project SGS-2022-023 of the University of West Bohemia in Pilsen.

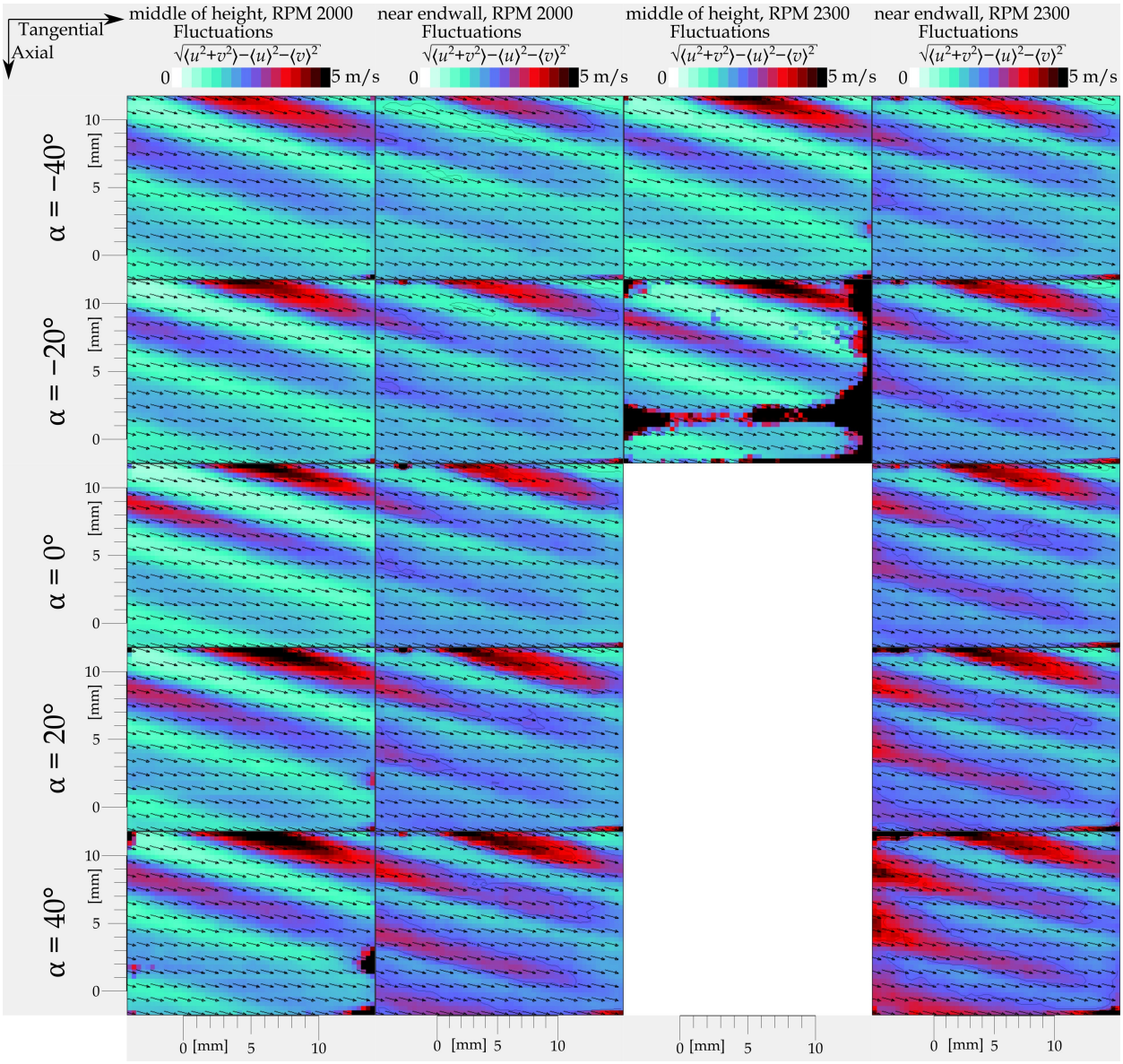

Fig. 2: Spatial maps of the measured standard deviation of the in-plane velocity, $\sqrt{\sigma_u^2+\sigma_v^2}$. The limits of the colormap are from 0 to 5 m/s. It is important to note, that the contribution from fluctuations in radial direction is not measured. First and second columns display the results at turbine rotational speed of 2 000 rpm, the third and fourth one at 2 300 rpm. The first and third show the plane near the middle, the second and fourth column display the plane near hub.

References

Burdin, C. (1824) Hydraulic turbines or high-speed rotary machines. *Annales de chimie et de physique, 24*(?), 207–217, (in French).

Chow, Y.-C., Uzol, O., Katz, J. and Meneveau, C. (2002) An Investigation of Axial Turbomachinery Flows Using PIV in an Optically Unobstructed Facility. In: *9th Int. Symposium on Transport Phenomena and Dynamics of Rotating Machinery,* Honolulu, pp. 10–14.

Denton, J. and Pullan, G. (2012) A Numerical Investigation Into the Sources of Endwall Loss in Axial Flow Turbines. In: *Proc. of ASME Turbo Expo*, GT2012(1), 69173.

Duda, D., Jelínek, T., Milčák, P., Němec, M., Uruba, V., Yanovych, V. and Žitek, P. (2021) Experimental Investigation of the Unsteady Stator/Rotor Wake Characteristics Downstream of an Axial Air Turbine. *International Journal of Turbomachinery Propulsion and Power*, 6(3), 22.

Duda, D., Klimko, M., Milčák, P., Jeřábek, M., Uruba, V., Yanovych, V. and Žitek, P. (2024) Wakes and secondary structures past stator wheel in test turbine VT-400 observed by PIV. *European Journal of Mechanics*, B/Fluids, pp. 151–163.

Ilieva, G. (2017) A Deep Insight to Secondary Flows. *Defect and Diffusion Forum*, 379(1), 83–107.

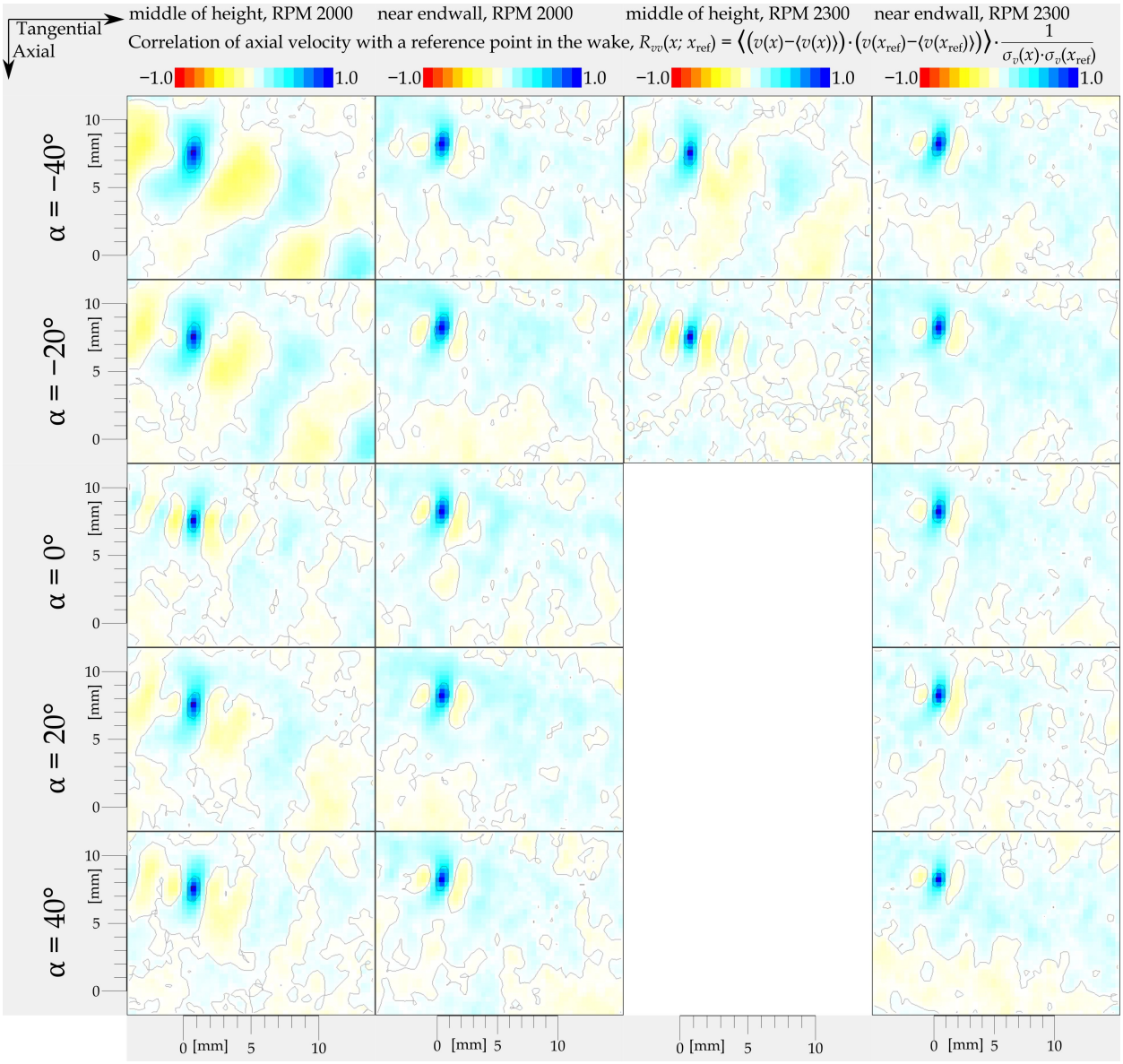

Fig. 3: Autocorrelation function of the axial velocity with a point inside the wake (comp. Fig. 2). Blue areas represent the region, where the fluctuations correlate with the fluctuations in the probed point. The yellow means anticorrelation, i.e. the wave nature of fluctuations in the wake. The more distant areas of light blue and yellow do not correlate, but the experimental noise causes, that the calculated correlation is never zero exactly.

Klimko, M. and Okresa, D. (2016) Measurements on the VT 400 Air Turbine. *Acta Polytechnica*, 56(2), 118–125.

Klimko, M., Lenhard, R., Žitek, P.and Kaduchová, K. (2021) Experimental Evaluation of Axial Reaction Turbine Stage Bucket Losses. *Processes*, 9(10), 1816.

Porreca, L., Hollenstein, M., Kalfas, A. and Abhari, R. (2007) Turbulence measurements and analysis in a multistage axial turbine. *Journal of Propulsion and Power*, 23, 227–234.

Sieverding, C. and Manna, M. (2020) A Review on Turbine Trailing Edge Flow. *International Journal of Turbomachinery Propulsion and Power*, 5(2), 10.

Uzol, O., Chow, Y.-C., Katz, J. and Meneveau, C. (2002) Experimental Investigation of Unsteady Flow Field Within a Two-Stage Axial Turbomachine Using Particle Image Velocimetry. *Journal of Turbomachinery*, pp. 542–552.

30th International Conference
ENGINEERING MECHANICS 2024
Milovy, Czech Republic, May 14 – 16, 2024

PROBABILITY LIMITS OF THE CRITICAL ROTOR SPEEDS

Dupal J.*

Abstract: *Rotors are manufactured with certain tolerances, implying that both outer and inner diameters of the rotor can be treated as random parameters (RP). This paper focuses on an approach for estimating the mean and variance of the critical speeds of rotors. These values allow for probabilistic determination of the upper and lower limits of critical speeds. The mean of critical speeds has to be derived iteratively due to the frequency (revolution) dependence of gyroscopic and circulation matrices. Subsequently, the critical speed is approximated using two terms of Taylor's expansion at the mean value of critical speed. It is essential to conduct sensitivity analysis of the critical speed concerning RP. This approximate approach avoids the necessity of knowing the probability function of randomly valued diameters, respecting the validity of Chebyshev's inequality. Rotor discretization in this study is achieved using the Finite Element Method.*

Keywords: Critical speed, probability, FEM, sensitivity analysis, rotor dynamics.

1. Introduction

The discretized mathematical model of the rotating rotor without external excitation can be represented by well known equation of motion (system of the n differential equations of the 2nd order) (e.g. Dimarogonas, (1996))

$$\mathbf{M}\ddot{\mathbf{q}}(t)+\left[\mathbf{B}+\omega\mathbf{G}\right]\dot{\mathbf{q}}(t)+\left[\mathbf{K}+\omega\mathbf{K}_c\right]\mathbf{q}(t)=\mathbf{0}. \tag{1}$$

where **M, B, G, K,** $\mathbf{K}_c$ is matrix of mass, damping, gyroscopic effect, stiffness and circulation, respectively, all of order n. The quantity $\mathbf{q}(t)$ corresponds to vector of generalized displacements and its differentiations are marked by dots. Adding the trivial identity

$$\mathbf{M}\dot{\mathbf{q}}(t)-\mathbf{M}\dot{\mathbf{q}}(t)=\mathbf{0}, \tag{2}$$

to (1) we can come after simple rearrangements to the equation (system of the $2n$ differential equations of the 1st order)

$$\dot{\mathbf{u}}(t)=\mathbf{A}(\omega)\mathbf{u}(t), \tag{3}$$

where

$$\mathbf{A}(\omega)=\begin{bmatrix}\mathbf{0}, & \mathbf{I}\\ -\mathbf{M}^{-1}\left(\mathbf{K}+\omega\mathbf{K}_c\right), & -\mathbf{M}^{-1}\left(\mathbf{B}+\omega\mathbf{G}\right)\end{bmatrix},\quad \mathbf{u}(t)=\begin{bmatrix}\mathbf{q}(t)\\ \dot{\mathbf{q}}(t)\end{bmatrix}. \tag{4}$$

The Eq. (3) leads to the eigenvalue problem

$$\left[\mathbf{A}(\omega)-\lambda\mathbf{I}\right]\mathbf{v}=\mathbf{0}, \tag{5}$$

which can be solved for ith critical speed in the iteration way respecting some starting chosen initial value by iteration way

* Prof. Dr. Ing. Jan Dupal: University of West Bohemia in Pilsen, Univezitni 22, 30614 Plzen; CZ, dupal@kme.zcu.cz

doi: 10.21495/em2024-094

$$\begin{aligned}&\left[\mathbf{A}\left(\omega_i^{(r-1)}\right)-\lambda_i^{(r)}\mathbf{I}\right]\mathbf{v}_i^{(r)}=\mathbf{0}\ \Rightarrow\ \lambda_i^{(r)}=?\\&\omega_i^{(r)}=\mathrm{Im}\left\{\lambda_i^{(r)}\right\}\ \Rightarrow\ \omega_{crit,i}=\lim_{r\to\infty}\left\{\mathrm{Im}\left[\lambda_i^{(r)}\right]\right\}\end{aligned}. \tag{6}$$

Each critical speed can be alternatively assessed by Campbell's diagram, too.

2. Probability approach

Let us assemble the independent input random parameters (RP) to the vector of RP and apply the expectation operator. We can come to the mean vector of RP

$$\boldsymbol{\mu}_{\mathbf{p}}=E\left\{\left[p_1,\ p_2,\ \ldots,\ p_s\right]^T\right\}\in\mathbf{R}^{s,1}. \tag{7}$$

Let us introduce the critical eigenvalue vector in form

$$\boldsymbol{\lambda}_{crit}=\left[\lambda_1,\quad \lambda_2,\quad \ldots,\quad \lambda_b,\right]^T\in\mathbf{C}^{b,1} \tag{8}$$

real part of which corresponds to the vector of critical angular speeds. There is a well-known method to calculate derivatives of one eigenvalue e.g. $\lambda_j=\lambda_{crit,i}$ with respect to some parameter e.g. p_k. Let us derivate the equation

$$\left[\mathbf{A}\left(\omega_{crit,j}\right)-\lambda_j\mathbf{I}\right]\mathbf{v}_j=\mathbf{0} \tag{9}$$

with respect to parameter p_k and pre-multiply by $\mathbf{v}_j^{*T}$. Now we can write

$$\mathbf{v}_j^{*T}\frac{\partial\mathbf{A}\left(\omega_{crit,j}\right)}{\partial p_k}\mathbf{v}_j-\frac{\partial\lambda_i}{\partial p_k}\underbrace{\mathbf{v}_j^{*T}\mathbf{v}_j}_{1}+\underbrace{\mathbf{v}_j^{*T}\left[\mathbf{A}\left(\omega_{crit,j}\right)-\lambda_j\mathbf{I}\right]}_{\mathbf{0}}\frac{\partial\mathbf{v}_j}{\partial p_k}=0,$$

$$\Downarrow$$

$$\frac{\partial\lambda_j}{\partial p_k}=\mathbf{v}_j^{*T}\frac{\partial\mathbf{A}\left(\omega_{crit,j}\right)}{\partial p_k}\mathbf{v}_j. \tag{10}$$

Let us assemble the elements (10) into the sensitivity matrix

$$\frac{\partial\boldsymbol{\lambda}_{crit}}{\partial\mathbf{p}}=\left\{\frac{\partial\lambda_j}{\partial p_k}\right\}_{j,k}. \tag{11}$$

The relation between derivatives $\frac{\partial\lambda_j}{\partial p_k}$ and $\frac{\partial\Omega_{Dj}}{\partial p_k}$ can be obtained by ($\Omega_{Dj}=\Omega_{crit,j}=\omega_{crit,j}$)

$$\lambda_j=-D_j\Omega_j+i\underbrace{\Omega_j\sqrt{1-D_j^2}}_{\Omega_{Dj}}=\left(\frac{-D_j}{\sqrt{1-D_j^2}}+i\right)\Omega_{Dj}, \tag{12}$$

and then the derivatives of the j^{th} critical angular speed with respect to k^{th} RP has form

$$\frac{\partial\Omega_{Dj}}{\partial p_k}=\frac{\dfrac{\partial\lambda_j}{\partial p_k}}{\dfrac{\partial\lambda_j}{\partial\Omega_{Dj}}}=\frac{1}{\left(\dfrac{-D_j}{\sqrt{1-D_j^2}}+i\right)}\frac{\partial\lambda_j}{\partial p_k}. \tag{13}$$

The eigenfrequencies of un-damped system and damping ratios can be obtained according to following relations (Ω_j corresponds to the *j*-th eigenfrequency of un-damped system)

$$\left.\begin{aligned}\Omega_{Dj} = \mathrm{Im}\left\{\lambda_j\right\} = \Omega_j\sqrt{1-D_j^2}\\ -D_j\Omega_j = \mathrm{Re}\left\{\lambda_j\right\}\end{aligned}\right\} \Rightarrow D_j = \frac{-\mathrm{Re}\left\{\lambda_j\right\}}{\left|\lambda_j\right|}, \quad \Omega_j = \left|\lambda_j\right|.$$

These quantities are depicted in Fig. 1

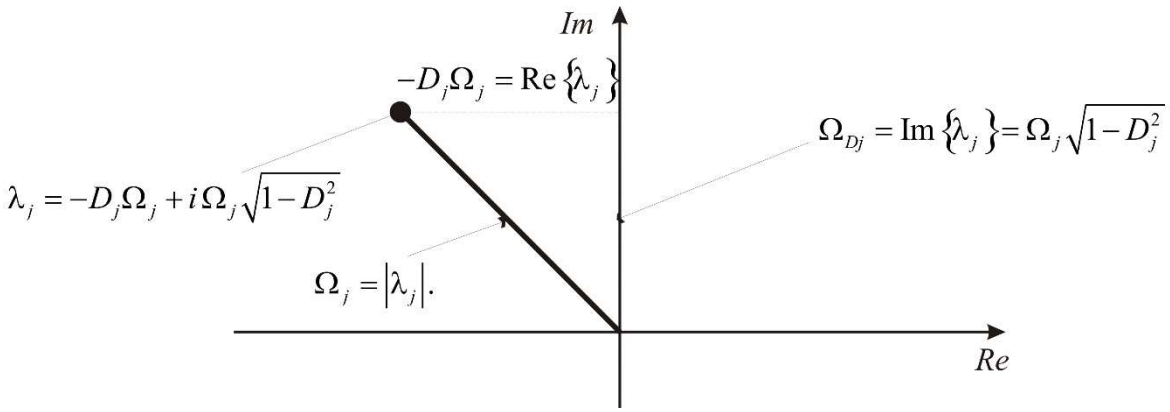

Fig. 1 Complex eigenvalues.

Let us introduce diagonal complex matrix $\mathbf{D} = diag\left\{\left(\frac{-D_j}{\sqrt{1-D_j^2}} + i\right)^{-1}\right\}$, enabling rewrite the Eq. (13) into the compact form

$$\frac{\partial \boldsymbol{\Omega}_D}{\partial \mathbf{p}} = \mathbf{D}\frac{\partial \boldsymbol{\lambda}_{crit}}{\partial \mathbf{p}}. \tag{14}$$

Let us express the vector of critical angular speeds by means of the first two terms of Taylor's series about mean vector of RP (Dupal, 2008). We can come to brief form (only the 1st derivatives)

$$\boldsymbol{\Omega}_D \doteq \boldsymbol{\Omega}_D\left(\boldsymbol{\mu}_\mathbf{p}\right) + \left.\frac{\partial \boldsymbol{\Omega}_D}{\partial \mathbf{p}}\right|_{\mathbf{p}=\boldsymbol{\mu}_\mathbf{p}}\left(\mathbf{p}-\boldsymbol{\mu}_\mathbf{p}\right) = \boldsymbol{\Omega}_D\left(\boldsymbol{\mu}_\mathbf{p}\right) + \frac{\partial \boldsymbol{\Omega}_D}{\partial \mathbf{p}}\left(\mathbf{p}-\boldsymbol{\mu}_\mathbf{p}\right). \tag{15}$$

The terms containing the 2nd derivatives and higher were left out respecting linear transformation relation between diameters of shafts and their eigenvalues. Applying expectation operator $E\left\{\boldsymbol{\Omega}_D\right\}$ to the Eq. (15) we obtain approximate relation for mean value of vector of critical angular speeds in form

$$\boldsymbol{\mu}_{\boldsymbol{\Omega}_D} \doteq \boldsymbol{\Omega}_D\left(\boldsymbol{\mu}_\mathbf{p}\right). \tag{16}$$

Applying variance operator $E\left\{\left(\boldsymbol{\Omega}_D - \boldsymbol{\mu}_{\boldsymbol{\Omega}_D}\right)\left(\boldsymbol{\Omega}_D - \boldsymbol{\mu}_{\boldsymbol{\Omega}_D}\right)^T\right\}$ to the Eq. (15) respecting (16) we can come to the covariation matrix of critical speed vector in form

$$\boldsymbol{\Sigma}_{\boldsymbol{\Omega}_D} = E\left\{\frac{\partial \boldsymbol{\Omega}_D}{\partial \mathbf{p}}\left(\mathbf{p}-\boldsymbol{\mu}_\mathbf{p}\right)\left(\mathbf{p}-\boldsymbol{\mu}_\mathbf{p}\right)^T\frac{\partial \boldsymbol{\Omega}_D^T}{\partial \mathbf{p}}\right\} = \frac{\partial \boldsymbol{\Omega}_D}{\partial \mathbf{p}}E\left\{\left(\mathbf{p}-\boldsymbol{\mu}_\mathbf{p}\right)\left(\mathbf{p}-\boldsymbol{\mu}_\mathbf{p}\right)^T\right\}\frac{\partial \boldsymbol{\Omega}_D^T}{\partial \mathbf{p}} = \frac{\partial \boldsymbol{\Omega}_D}{\partial \mathbf{p}}\boldsymbol{\Sigma}_\mathbf{p}\frac{\partial \boldsymbol{\Omega}_D^T}{\partial \mathbf{p}}. \tag{17}$$

The last relation can be rearranged by means of (14) into form

$$\boldsymbol{\Sigma}_{\boldsymbol{\Omega}_D} = \mathbf{D}\frac{\partial \boldsymbol{\lambda}_{crit}}{\partial \mathbf{p}}\boldsymbol{\Sigma}_\mathbf{p}\frac{\partial \boldsymbol{\lambda}_{crit}^T}{\partial \mathbf{p}}\mathbf{D}, \tag{18}$$

where $\boldsymbol{\Sigma}_\mathbf{p}$ is covariation matrix of input RP (when parameters are independent this matrix is diagonal).

3. Application

Random parameters: D_1, D_2 from the left hand side, probability density function-normal (Gauss), variances $\sigma_{D_i}^2 = 1e-7m, i = 1, 2.$ $\mathbf{\Sigma_p} = diag\left\{\sigma_{D_i}^2\right\}$. Mean values $\mu_{D_1} = 0.012\ m$, $\mu_{D_2} = 0.016\ m$.

Results: $\sigma_{\Omega_{D1}}^2 = 0.8149\ (rad/s)^2$, $\sigma_{\Omega_{D2}}^2 = 0.8332\ (rad/s)^2$.

Monte Carlo $\sigma_{\Omega_{D1}}^2 = 0.8149\ (rad/s)^2$, $\sigma_{\Omega_{D2}}^2 = 0.8390\ (rad/s)^2$

$P\left\{\mu_{\Omega_{Di}} + 3\sigma_{\Omega_{Di}} \le \Omega_{Di} \le \mu_{\Omega_{Di}} + 3\sigma_{\Omega_{Di}}\right\} = 0.9973$ (Gauss), Monte Carlo simulation relative frequency of the inequality satisfaction is 0.9972.

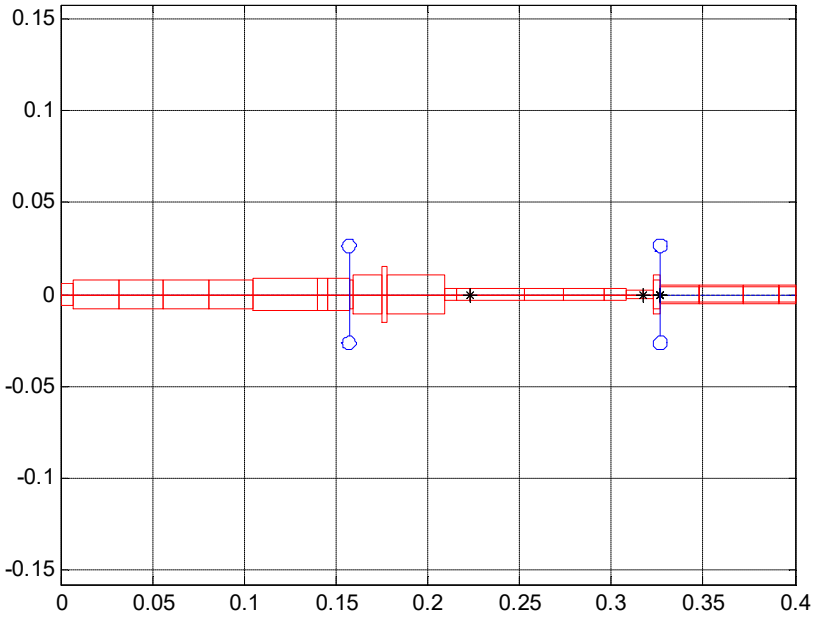

Fig. 2 Spindle of the textile machine.

4. Conclusions

Numerous numerical experiments were conducted, involving various values of random parameters governed by different probability density functions. Selected combinations will be demonstrated during the presentation. In line with the Central Limit Theorem, the results tend to converge towards the normal probability function as the number of RPs increases. The presented approach could be enhanced by incorporating more terms from Taylor's series into the eigenvalue expression. Based on the results of Monte Carlo simulations, the accuracy of the presented approach seems to be satisfactory.

Acknowledgement

This publication was supported by the project TAČR No. FW06010052

References

Dupal, J. (2008) *Mechanics of stochastic systems.* Handbook of University of West Bohemia, (in Czech).

Dimarogonas, A. (1996) *Vibration for engineers.* Prentice Hall, Upper Saddle River, New Jersey 07458.

30th International Conference
ENGINEERING MECHANICS 2024
Milovy, Czech Republic, May 14 – 16, 2024

SOLUTION METHODS FOR AN AEROELASTIC PROBLEM WITH COMBINED HARMONIC AND STOCHASTIC EXCITATION

Fischer C.*, Náprstek J.**

Abstract: *Assessing responses in slender engineering structures facing both deterministic harmonic and stochastic excitation is often based on an approximation by the single-degree-of-freedom van der Pol-type nonlinear model. Determining the response probability density function involves solving the Fokker-Planck equation, which is generally a challenging task. Hence, semi-analytical and numerical methods come into play. This contribution reviews several possible techniques and spotlights the exponential-polynomial-closure method. The shown results are limited, as the paper reflects an early stage of the relevant research direction.*

Keywords: Fokker-Planck equation, stochastic averaging, numerical solution, Galerkin approximation, van der Pol-type oscillator, partial amplitudes, exponential-polynomial-closure method.

1. Introduction

Slender engineering structures, such as footbridges, masts, and power lines, are prone to excessive vibration. This tendency is particularly notable in the interplay between natural and excitation frequencies. In the lock-in region, where the structure's response stabilizes within a specific frequency range, it exhibits stationarity characterized by a dominant frequency and several superharmonic frequencies. Beyond this boundary, the response transforms into a non-stationary quasi-periodic state, with new frequencies emerging in a fan-shaped plot. Introducing additive random noise further complicates the scenario, the response process is stochastic. Understanding these dynamics is crucial for the design of slender structures, providing insights into their complex vibrational patterns and aiding in the development of effective mitigation strategies.

Exploring nonlinear dynamic systems under random excitation has long been an important subject with applications in various scientific and engineering domains. Researchers have developed analytical, semi-analytical, and numerical methods to obtain stationary PDFs or statistical moments, particularly focusing on systems influenced by Gaussian white noise. In contrast to the stationary response case, where usable solution procedures are often available, the non-stationary response case remains the subject of intensive research, presenting significant challenges even in scenarios limited to additive excitation.

The physical model utilized in this paper is the SDOF oscillator of the van der Pol type. This model is commonly used to depict transverse wind-generated vibrations under additive excitation, combining deterministic and random components. The normal form of this model is given as follows:

$$\dot{u} = v\,, \qquad \dot{v} = (\eta - \nu u^2)v - \omega_0^2 u + P\omega^2 \cos\omega t + h\xi(t)\,, \tag{1}$$

where: u, v are the displacement $[\mathrm{m}]$ and velocity $[\mathrm{ms}^{-1}]$; η, ν are the parameters of the linear and quadratic damping, respectively $[\mathrm{s}^{-1}, \mathrm{s}^{-1}\mathrm{m}^{-2}]$; ω_0, ω are the eigen-frequency of the linear SDOF system and frequency of the vortex shedding $[\mathrm{s}^{-1}]$; $f(t)$ represents external excitation: $f(t) = P\omega^2 \cos\omega t + h\xi(t)$; $P\omega^2$ and $\xi(t)$ are the amplitude of the harmonic excitation force $[\mathrm{ms}^{-2}]$ and the broadband Gaussian random process $[1]$; and h is the multiplicative constant $[\mathrm{ms}^{-2}]$.

* RNDr. Cyril Fischer, PhD.: Institute of Theoretical and Applied Mechanics, Prosecká 76, 190 00 Prague 9, fischerc@itam.cas.cz

** Ing. Jiří Náprstek, DSc.: Institute of Theoretical and Applied Mechanics, Prosecká 76, 190 00 Prague 9, naprstek@itam.cas.cz

doi: 10.21495/em2024-098

Using the Itô stochastic calculus, the response PDF is governed by the FPE:

$$\frac{\partial p(\mathbf{x},t)}{\partial t} = -\frac{\partial}{\partial x_j}\left(\kappa_j(\mathbf{x},t)\cdot p(\mathbf{x},t)\right) + \frac{1}{2}\frac{\partial^2}{\partial x_j \partial x_k}(\kappa_{jk}(\mathbf{x},t)\cdot p(\mathbf{x},t))\,. \tag{2}$$

Parameters $\kappa_j(\mathbf{x},t)$ and $\kappa_{jk}(\mathbf{x},t)$ represent the first and second derivative moments, generally referred to as drift and diffusion coefficients, respectively. In the stationary case, the left-hand side of Eq. (2) vanishes, resulting in a reduced FPE that is solvable in many particular cases (Lin and Cai, 1988). However, in the general non-stationary case, finding a solution for the complete FPE remains a challenging problem.

2. State of the art

According to Er (1998a), the solution of non-linear second order systems dates back to Kramers (1940), who presented solution of an one-dimensional undamped system with a non-linear stifness and an additive white noise excitation. Actually, the motivation in that paper was the first excursion problem in the theory of the velocity of chemical reactions, when the particle is originally caught in a potential hole but may escape in the course of time by passing over a potential barrier. If the function representing the potential barrier is smooth a reliable solution for any value of the viscosity is obtained.

The method of equivalent linearisation (Caughey, 1959), is the simplest solution method for non-linear systems with random excitation. Its approach can be regarded as the first approximation. In this reference the author studies the response of a nonlinear string to random excitation. It is shown that if the loading force is represented by truncated Gaussian white noise with uncorrelated Fourier coefficients, the mean squared deflection at every point is smaller than that for the equivalent linear string. The paper illustrates modification of the linearisation method, which is used for deterministic differential equations, for the stochastic case. The method of equivalent linearisation has been popular for over 65 years. However, there have been some missteps in its history, including an early conjecture by one of the pioneers that proved to be false, and an alternative to the standard procedure that went unrecognised for 27 years. Numerous reviews on method variants and applications are available; e.g. refer to the text by Elishakoff and Crandall (2016) and the papers cited therein.

Wen (1975) presents an approximate method for nonstationary solution of systems under random excitation, where the studied systems are supposed to include polynomial restoring force and the (filtered) shot noise type excitation. Using the Galerkin approach based on a time-dependent Hermite-series expansion, the Fokker-Planck equation (FPE) is is reduced to a system of first-order ordinary differential equations. Alternatively, when the excitation is non-white or when the FPE is difficult to solve, the perturbation method (Crandall, 1963) or statistical linearisation techniques (Caughey, 1959, 1963) are recommended, as reviewed also by Iwan and Yang (1972). Analogous procedure was used by the authors, (Náprstek and Fischer, 2024), and is illustrated by the numerical example in Chapt. 3.

Iyengar and Dash (1978) propose a technique which is capable to adopt the non-Gaussian excitation. Their approach belongs to the class of closure techniques. The individual methods in this class differ by different assumptions made about the statistical structure of the response. Even in cases where the response may be non-Gaussian, it would be possible to find a function of the response which can be approximated in terms of the Gaussian distribution via error minimization. The method due to Iyengar and Dash (1978), the Gaussian closure technique, automatically leads to an associated linear system driven by a Gaussian input. This, in fact, implies similarity of the method with the statistical linearisation techniques.

When the system is highly non-linear, or when multiplicative random excitations are present, i.e., when the probability distribution of the system response is far from being Gaussian, more response moments than two has to be approximated. This generalization leads to non-Gaussian closure methods as that used by Assaf and Zirkle (1976). In this highly instructive paper authors approximate the PDF of the response via the Edgeworth-type expansion. It is a rearrangement of the Gram-Charlier expansion so that the accuracy increases with the natural order of the terms (Cramér, 1946). The PDF is assumed in the form

$$p(x) = p_0(x)\left[1 + \frac{1}{3!}\frac{\lambda_3}{\sigma_x^3}\,H_3\!\left(\frac{x-m_x}{\sigma_x}\right) + \frac{1}{4!}\frac{\lambda_4}{\sigma_x^4}\,H_4\!\left(\frac{x-m_x}{\sigma_x}\right) + \frac{10}{6!}\frac{\lambda_3^2}{\sigma_x^6}\,H_6\!\left(\frac{x-m_x}{\sigma_x}\right) + \ldots\right] \tag{3}$$

where $p_0(x)$ is the Gaussian PDF and m_x, σ_x are the mean value and the standard deviation of x, $H(\cdot)$ are the Chebychev-Hermite polynomials, and λ_i the ith-order semi-invariants. The authors claim that four

terms in the expansion are usually sufficient. On the other hand, the obtained series can lead to negative probabilities as pointed out by Grigoriu (1991).

Cai and Lin (1988) and Cai et al. (1992) have developed a new approximation procedure in which a given non-linear system is replaced by another non-linear system belonging to the class of generalized stationary potential (Lin and Cai, 1988) for which the exact stationary solutions are obtainable. The replacement is based on the premise of preservation of the average energy dissipation in the replacing and the original systems.

For weakly non-linear systems with weak excitations, the stochastic average method, (Roberts and Spanos, 1986), represents a powerful alternative. The perturbation method, due to Crandall (1963), belongs to this category as well. For systems with random additive excitation, moment equations derived from the Itô's derivative rule can be used to compute the statistical moments instead of the FPE. Introduction of the central-moment closure or cumulant-neglect closure to the moment equations creates the hierarchy of equations limited to a desired level, (Wu and Lin, 1984).

The exponential-polynomial-closure (EPC) method was initially published by Er (1998b). In the original stationary setting, it assumes the sought PDF of an approximate solution in the form of an exponential polynomial:

$$p(\mathbf{x};\mathbf{a}) = C\exp\left(Q_n(\mathbf{x};\mathbf{a})\right) \tag{4}$$

Here, $\mathbf{x}$ is the state vector, $\mathbf{a}$ is the unknown parameter vector, and $Q_n(\mathbf{x};\mathbf{a})$ is a polynomial function. The algebraic system for the unknown parameters $\mathbf{a}$ results from the Galerkin approximation with respect to basis functions $h_k(\mathbf{x}) = x_1^{k_1}\ldots x_{n_x}^{k_{n_x}} f_N(\mathbf{x})$, where $k = k_1 + \ldots + x_{n_x}$ and f_N is the PDF solution using Gaussian closure.

Since then, variants of the EPC method have been proposed for different settings of the stationary PDF solutions of nonlinear stochastic oscillators. Modifications for the non-linear, non-stationary case have only recently emerged, implicitly allowing for non-Gaussian excitation (Guo et al., 2020). A further modification by Wang et al. (2023) claims superior performance with respect to smaller errors at the PDF tails compared to the results of Monte-Carlo simulations.

3. Numerical example

The response of the van der Pol oscillator in Eq. (1) is stationary in the lock-in region, which corresponds to interval $\omega \in (0.85, 1.35)$ with respect to natural frequency $\omega_0 = 1$, parameters $\eta = 1/2$, $\nu = 1/4$, $P = 1$, and the stochastic parameters $h = 1$, $S = 1$. In order to use the stochastic averaging method, (Náprstek and Fischer, 2024), the response variables are expressed in the trigonometric form as follows

$$u(t) = a_c\cos\omega t + a_s\sin\omega t\,, \quad v(t) = -a_c\omega\sin\omega t + a_s\omega\cos\omega t\,, \quad \dot{a}_c\cos\omega t + \dot{a}_s\sin\omega t = 0\,.$$

New parameters a_c, a_s are random variables representing the *partial amplitudes* of the response. In the stationary case, they are described by the reduced FPE. It is solvable analytically for zero detuning ($\Delta = 0$) between excitation and natural frequency. For $0 < \Delta$, the solution was sought using the Galerkin approach (Náprstek and Fischer, 2024). The result is illustrated in Fig. 1. PDFs with respect to partial amplitudes a_c, a_s is shown for $M = 2$ and a non-negligible value of detuning $\delta = 0.10$. The contour plot of the estimated cross-PDF $p(a_c, a_s)$ is shown on the left. The middle plot depicts the sections of the PDF for fixed values $a_c = \{-3/2.0, 3/2\}$ and the right-hand plot illustrates the sections for the selected values $a_s = \{2, 3, 4\}$. The sections and the corresponding colors are indicated as horizontal/vertical lines in the left-hand plots. The dashed curves show the basic analytical solution which is valid for the case zero no

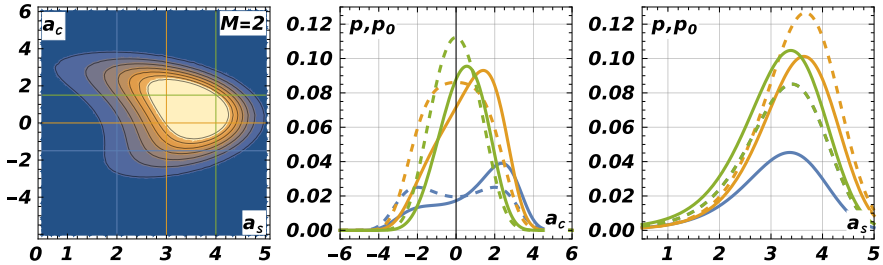

Fig. 1: The Galerkin approximation of the stationary cross-PDF for $M = 2$ (number of stochastic moments) and detuning value $\Delta = 0.10$.

detuning is assumed. The estimates including the $M = 2$ Galerkin approximations are shown in solid. It can be confirmed than corrections for $M > 2$ do not bring visible improvement.

4. Concluding remarks

The study of nonlinear dynamic systems under random excitations is an attractive and widely applicable topic in various scientific and engineering domains. Nonlinearity in the mathematical model can result in a non-zero mean of the response, even when the excitation mean is zero. As the PDFs obtained by different methods are only approximative, their behaviours at the tail positions poses a challenging problem. This contribution, based on a just started research, presented a historical and state-of-the-art review of available methods and some preliminary results regarding the stationary nonlinear state based on the stochastic averaging and subsequent Galerkin approach. However, the final target is the fully non-linear non-stationary case, which is still subject of an ongoing area of research.

Acknowledgment

The kind support of Czech Science Foundation project No. 24-13061S and of the RVO 68378297 institutional support are gratefully acknowledged.

References

Assaf, S. H. A. and Zirkle, L. D. (1976) Approximate analysis of non-linear stochastic systems. *Int. J. Control*, 23, 4, pp. 477–492.

Cai, G. Q. and Lin, Y. K. (1988) A new approximate solution technique for randomly excited non-linear oscillators. *Int. J. Non Linear Mech.*, 23, 5–6, pp. 409–420.

Cai, G. Q., Lin, Y. K., and Elishakoff, I. (1992) A new approximate solution technique for randomly excited non-linear oscillators–II. *Int. J. Non Linear Mech.*, 27, 6, pp. 969–979.

Caughey, T. K. (1959) Response of a nonlinear string to random loading. *J. Appl. Mech.*, 26, 3, pp. 341–344.

Caughey, T. K. (1963) Equivalent linearization techniques. *J. Acoust. Soc. Am.*, 35, 11, pp. 1706–1711.

Cramér, H. (1946) *Mathematical Methods of Statistics*. Princeton University Press, Princeton.

Crandall, S. H. (1963) Perturbation techniques for random vibration of nonlinear systems. *J. Acoust. Soc. Am.*, 35, pp. 1700–1705.

Elishakoff, I. and Crandall, S. H. (2016) Sixty years of stochastic linearization technique. *Meccanica*, 52, 1–2, pp. 299–305.

Er, G. K. (1998a) Multi-Gaussian closure method for randomly excited non-linear systems. *Int. J. Non Linear Mech.*, 33, 2, pp. 201–214.

Er, G. K. (1998b) A new non-Gaussian cloasure method for the PDF solution of non-linear random vibrations. In: *Proceedings of The 12th ASCE Engineering Mechanics Conference*, La Jolla, California. ASCE, Reston, VA, pp. 1403–1406.

Grigoriu, M. (1991) A consistent closure method for non-linear random vibration. *Int. J. Non Linear Mech.*, 26, 6, pp. 857–866.

Guo, S. S., Shi, Q., and Xu, Z. D. (2020) Stochastic responses of nonlinear systems to nonstationary non-Gaussian excitations. *Mech. Syst. Sig. Process.*, 144, pp. 106898.

Iwan, W. D. and Yang, I. M. (1972) Application of statistical linearization techniques to nonlinear multidegree-of-freedom systems. *J. Appl. Mech.*, 39, 2, pp. 545–550.

Iyengar, R. N. and Dash, P. K. (1978) Study of the random vibration of nonlinear systems by the Gaussian closure technique. *J. Appl. Mech.*, 45, 2, pp. 393–399.

Kramers, H. A. (1940) Brownian motion in a field of force and the diffusion model of chemical reactions. *Physica*, VII, 4, pp. 284–304.

Lin, Y. K. and Cai, G. Q. (1988) Equivalent stochastic systems. *J. Appl. Mech.*, 55, 4, pp. 918–922.

Náprstek, J. and Fischer, C. (2024) Averaging-based characteristics of the response induced by combined random and harmonic excitation. In: *Proceedings of the 15th International Conference on Vibration Problems. ICoVP 2023*, Singapore. Springer, Lecture Notes in Mechanical Engineering. in print.

Roberts, J. B. and Spanos, P. D. (1986) Stochastic averaging: An approximate method of solving random vibration problems. *Int. J. Non Linear Mech.*, 21, 2, pp. 111–134.

Wang, K., Wang, J., Jia, S., Zhu, Z., Yu, Z., and Xu, L. (2023) Non-stationary nonzero mean probabilistic solutions of nonlinear stochastic oscillators subjected to both additive and multiplicative excitations. *Chin. J. Phys.*, 81, pp. 64–77.

Wen, Y. K. (1975) Approximate method for nonlinear random vibration. *Journal of the Engineering Mechanics Division*, 101, 4, pp. 389–401.

Wu, W. F. and Lin, Y. K. (1984) Cumulant-neglect closure for non-linear oscillators under random parametric and external excitations. *Int. J. Non Linear Mech.*, 19, 4, pp. 349–362.

30th International Conference
ENGINEERING MECHANICS 2024
Milovy, Czech Republic, May 14 – 16, 2024

ASSESSMENT OF MECHANICAL PROPERTIES OF TITANIUM SAMPLES, MANUFACTURED WITH THE USE OF ADDITIVE TECHNOLOGIES

Gzik-Zroska B.[*], Joszko K.[**], Stradomski G.[***], Piątek A.[†], Wolański W.[††], Kawlewska E.[†††]

Abstract: *This work determines the endurance of titanium alloy samples Ti-6Al-4V, made by the incremental technique using LENS technology, and evaluated how the direction of specimen placement on the 3D printer work platform affects these properties. A static tensile test was carried out with simultaneous application of a digital image correlation system. The tests performer showed the effect of the direction of specimens alignment during printing process on the maximum stress at break. Printing direction had no significant effect on parameters such as maximum force at break, Young's module, strain and Poisson's ratios.*

Keywords: Titanium, 3D printing, Young's modulus, LENS.

1. Introduction

With the use of various chemical compositions, metal alloys are characterized by a wide range of properties and have found wide application. Titanium alloys are characterized by low density, good corrosion resistance and biocompatibility. It is due to these features that interest among producers from various industries is growing, resulting in a constant desire to improve this material and adapt it to the needs of the consumer. The dynamically developing medical industry has also drawn attention to the advantages of titanium, in particular its biocompatibility, good corrosion resistance in the tissue environment and much lower density compared to iron. To influence the properties of titanium alloy, attempts are made to modify its chemical composition and processing parameters. In the era of technological development, incremental techniques involving the layered creation of a three-dimensional object based on its geometric notation in CAD software are becoming increasingly important. One of the 3D printing methods is the LENS method (laser engineered net shaping), which involves local application of material in the form of spherical metal, ceramic or metal-ceramic powders and sintering it with a high-power laser (Oosthuizen, 2011; Arthur, 2018). The input in the form of spherical powders with a gradation of 44 to 150 μm should be characterized by high purity, chemical uniformity, and no defects. This met can be used both to produce new models and to supplement existing ones (Mellor, 2015; Razavi, 2018). The work, which aims to assess the mechanical properties of titanium samples made of the Ti-6Al-4V alloy by using LENS technology, will present

[*] Eng. Bożena Gzik-Zroska, PhD.: Department of Biomaterials and Medical Devices Engineering, Silesian University of Technology, Roosevelta 40, 41-800, Zabrze, PL; bozena.gzikzroska@polsl.pl

[**] Eng. Kamil Joszko, PhD.: Department of Biomechatronics, Silesian University of Technology, Roosevelta 40; 41-800, Zabrze; PL; kamil.joszko@polsl.pl

[***] Prof. Grzegorz Stradomski: Faculty of Production Engineering and Materials Technology, Czestochowa University of Technology, 42-201 Częstochowa, PL; grzegorz.stradomski@pcz.pl

[†] Eng. Agata Piątek: Student club "Biokreatywni", Silesian University of Technology, Roosevelta 40; 41-800, Zabrze; PL; agatpia347@student.polsl.pl

[††] Eng. Edyta Kawlewska, PhD.: Department of Biomechatronics, Silesian University of Technology, Roosevelta 40; 41-800, Zabrze; PL; edyta.kawlewska@polsl.pl

[†††] Prof. Wojciech Wolański: Department of Biomechatronics, Silesian University of Technology, Roosevelta 40; 41-800, Zabrze; PL; wojciech.wolanski@polsl.pl

doi: 10.21495/em2024-102

the results obtained during a static tensile test with the simultaneous use of a digital image correlation system.

2. Methods

The assessment of mechanical properties was carried out using the MTS Insight 2 static testing machine and micro-correlation by Dantec Dynamic. The MTS Insight 2 static testing machine used enables static tensile, compressive and bending tests to be performed with computer registration of force and elongation measurements. The DIC digital micro-correlation system used by Dantec Dynamic is a technique for measuring displacements and strains in real time, based on the analysis of high-resolution images performed while loading the test element. Images with an appropriate speckle structure (the technique requires imposing a structure on the tested surface) are archived during loads and then analyzed by specialized Istra 4D software. The results are presented in the form of colorful maps of displacements and deformations, which makes it possible to verify the formulated numerical models. The measurement system is fully compatible with MTS testing machines by synchronizing measurement points between the machine and the correlation system. This connection ensures full control over research, acquisition and processing of the obtained measurement data. During measurements, not only static images are obtained, but it is also possible to visualize the deformation process in the form of animations. In addition to measuring the values of the tested parameters, this gives the opportunity to analyze the deformation process itself, including observing the processes of cracking, crack propagation and destruction on a micro scale. The research material consisted of 12 paddle-shaped samples with dimensions of 65×10×2 mm, made using the LENS method from powdered titanium alloy Ti-6Al-4V. The samples were printed in two different orientations on the build plate: horizontally (X samples) and vertically (Y samples). All samples were annealed in an oven at 920 °C for 4 hours to eliminate internal stresses. Then they were rinsed twice in an ultrasonic bath for 60 minutes using waves with a frequency of 37 kHz and dried for 60 minutes. Finally, each surface was mechanically ground and polished. Then, a special speckled structure was applied to each sample using aerosol paints (white, black) in order to identify deformations by the digital image correlation system (Fig. 1).

a)

b)

Fig. 1: Example of a test sample: a) before painting, b) after painting.

Before starting the research, the digital image correlation system was calibrated using a specialized calibration plate provided by the system manufacturer. Each sample was subjected to a static tensile test at a speed of 5 [mm/min] at room temperature (Fig. 2, Fig. 3). In order to calculate the Poisson number, the value of longitudinal and transverse strains in the range of elastic strains was recorded for the tested samples.

Fig. 2: Test stand.

Fig. 3: Sample after the test.

3. Results

The values obtained during the tests, such as the maximum force and stress at break, were read from the testing machine, and the strain and Young's modulus were read from the digital image correlation system (Fig. 4). The results are presented in Tabs. 1 and 2. Fig. 5 shows the stress-strain curves for the tested samples.

Sample number	Peak Load [kN]	Ultimate tensile stress [MPa]	Young's modulus [GPa]	Strain at Break [%]
x1	18.9	946.9	-	15.8
x2	19	950.4	116.6	15.6
x3	18.9	945.3	114.3	14.6
x4	18,9	943.5	114	16.6
x5	19	948.6	113.9	17.6
x6	18.1	903.5	117.3	15.5
Average	18.8 ± 0.3	939.7 ± 17.9	115.2 ± 1.6	16 ± 1

Tab. 1: Test results for samples X.

Sample number	Peak Load [kN]	Ultimate tensile stress [MPa]	Young's modulus [GPa]	Strain at Break [%]
y1	18.5	925.7	113.8	14.1
y2	18.6	928.8	113.2	15.8
y3	18.6	931.3	114.3	17.5
y4	18.6	928.1	113.8	18.1
y5	18.6	932.1	117.6	15,8
y6	18.4	919.2	119.9	17.1
Average	18.6 ± 0.1	927.5 ± 4.7	115.4 ± 2.7	16.4 ± 1.5

Tab. 2: Test results for samples Y.

a)

b)

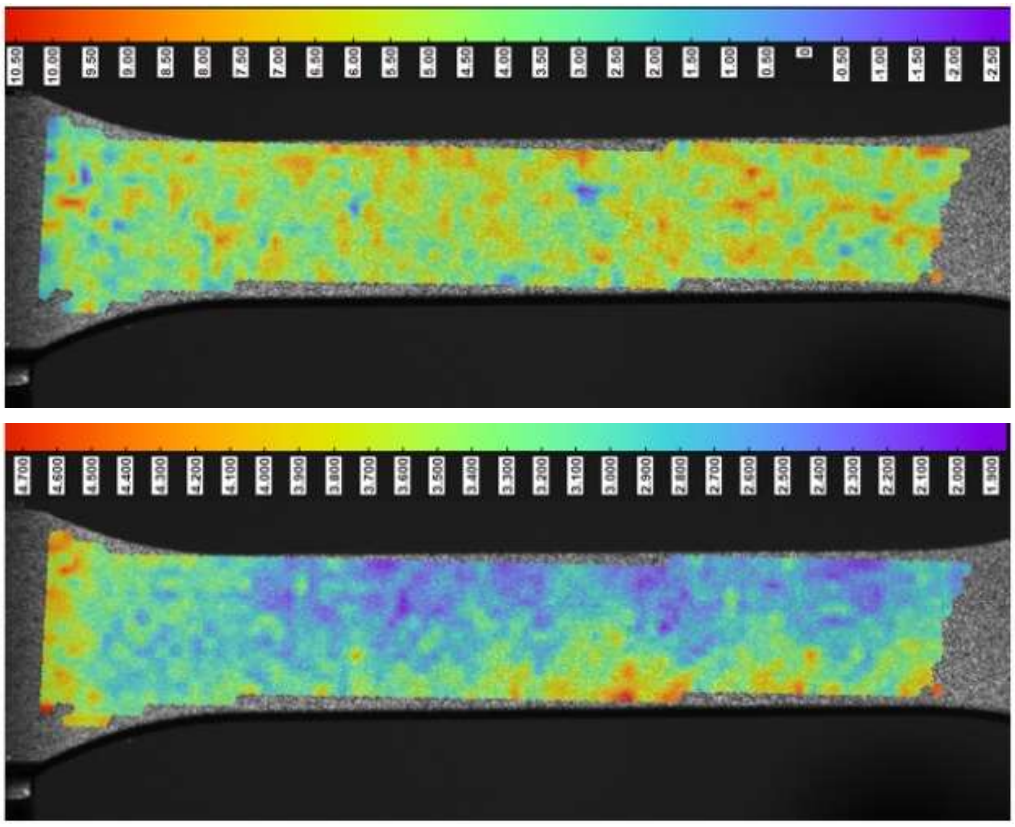

Fig. 4: Strain maps for an example sample x2: a) along the sample axis, b) perpendicular to the sample axis.

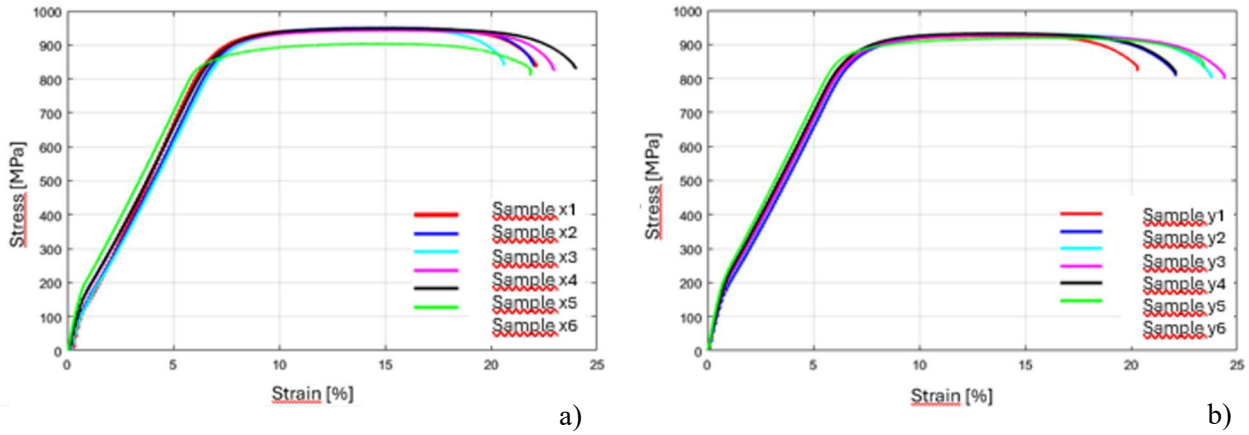

a) b)

Fig. 5: Stress-strain curve of samples: a) samples X, b) samples Y.

Analyzing the influence of printing direction on the average values of maximum ultimate tensile stress, higher values were observed in the case of horizontal orientation of the print - 939.7 [MPa] compared to vertical arrangement - 927.5 [MPa]. The average maximum peak load was higher for horizontal samples compared to vertical ones and amounted to 18.8 and 18.6 [kN], respectively. However, the average values of Young's moduli and strain at break were higher for the vertical direction than for the horizontal direction and were 115.4 and 115.2 [MPa] and 16.4 [%] and 16 [%], respectively. Fig. 4 shows example strain maps obtained from the digital image correlation system for a plane parallel to the direction of sample stretching and for a perpendicular plane. The strain values read for two mutually perpendicular directions were then used to calculate the Poisson number. The average value of Poisson's number for samples X was 0.3 and for samples Y it was 0.4.

4. Conclusions

The tests carried out showed the influence of the printing direction on the maximum value of stress at break. A greater result was observed in the horizontal than in the vertical position. However, the printing direction did not have a significant impact on parameters such as maximum force at break, Young's modulus, strain and Poisson's ratios.

Acknowledgement

This publication is supported by the Excellence Initiative – Research University program implemented at the Silesian University of Technology, years 2022-2024.

References

Arthur, N. K. and Pityana, S. (2018) Microstructure and material properties of LENS fabricated Ti-6Al-4V components. *R&D Journal*, 34, pp. 33–36.

Mellor, I., Grainger, L., Rao, K., Deane, J., Conti, M., Doughty, G. and Vaughan, D. (2015) Titanium powder production via the Metalysis process. *Titanium powder metallurgy*, pp. 51–67.

Oosthuizen, S. J. (2010) In search of low cost titanium: the Fray Farthing Chen (FFC) Cambridge process. *Journal of the Southern African Institute of Mining and Metallurgy*, 111(3), pp. 199–202.

Razavi, S. M. J., Bordonaro, G. G., Ferro, P., Torgersen, J. and Berto, F. (2018) Fatigue behavior of porous Ti-6Al-4V made by laser-engineered net shaping. *Materials*, 11(2), 284.

30th International Conference
ENGINEERING MECHANICS 2024
Milovy, Czech Republic, May 14 – 16, 2024

AUGMENTED M5 GEOMETRY OF HUMAN VOCAL FOLD IN PHONATORY POSITION – PILOT RESULTS

Hájek P.[*], **Horáček J.**[**], **Švec J. G.**[***]

Abstract: *The presented contribution deals with a newly designed parametric planar geometry of the vocal fold – the augmented M5 model – which is fitted to a real-shaped human vocal fold. The real shape of the vocal fold during a phonatory position for* 112 Hz *was obtained from a plaster cast and was digitized by optical scanning. The geometry model of the vocal fold surfaces was constructed based on the data from the optical scanner and the augmented M5 model was fitted to a coronal slice of the selected vocal fold surface. The equations of the augmented M5 model are explained and its parameters, tuned to the real vocal fold geometry, are provided. The fitting is done in Python 3.8.5 using the* `scipy.optimize.curve_fit` *package, which contains non-linear least squares method. It is shown that the augmented M5 model fits the real data with coefficient* R^2 *close to* 1 *and the tuned parameters are in a good agreement with the overall vocal fold dimensions and with the parameters of the original 2D M5 model.*

Keywords: Vocal fold, M5 geometry, non-linear least squares, curve fitting, phonatory position.

1. Introduction

Computational modeling of human phonation is a demanding task requiring knowledge of the underlying physics, interactions between the vocal folds and fluid flow, materials of the soft tissues and warmer humid air and the geometry of the human larynx. The latter is often simplified to an idealized parametric geometry. Such a parametric geometry of the human vocal fold can be implemented in a code, there is a possibility to tune its parameters, but it can also be physically inaccurate.

There have been numerous attempts, *e.g.* in Titze (1989); Alipour and Scherer (2000); Scherer et al. (2001); Alipour-Haghighi and Scherer (2015); Li et al. (2012); Xue et al. (2014); Wu and Zhang (2016, 2019); Chen et al. (2020), to define the geometry of the human vocal fold using highly simplified geometries as well as relatively complex ones – each was suitable for different approaches in computational or experimental modeling. One of the most widely used geometries is the three-parametric M5 shape of the vocal fold (Scherer et al., 2001). The key part of the planar geometry consists of two circular arcs with a tangent line between them. Although this shape fits the real vocal fold well, the other two tangents representing upper and lower boundary of the vocal fold are too simplified to fit the real shape of the vocal fold. To overcome this limitation, an augmented 2D M5 vocal fold shape is constructed and presented here.

2. Methods

The augmented M5 geometry is based on a plaster cast of the human larynx in the phonatory position at the vocal folds self-oscillation frequency of 112 Hz, which was obtained and described in our previous

[*] Ing. Petr Hájek, PhD.: Institute of Solid Mechanics, Mechatronics and Biomechanics, Brno University of Technology, Technická 2896/2; 616 69, Brno; CZ; Voice Research Laboratory, Department of Experimental Physics, Palacký University Olomouc; 17. listopadu 1192/12; 779 00, Olomouc; CZ, hajek.p@fme.vutbr.cz

[**] Ing. Jaromír Horáček, DSc.: Institute of Thermomechanics of the Czech Academy of Sciences; Dolejškova 1402/5; 182 00, Prague; CZ, jaromirh@it.cas.cz

[***] Prof. RNDr. Jan G. Švec, PhD. et PhD.: Voice Research Laboratory, Department of Experimental Physics, Palacký University Olomouc; 17. listopadu 1192/12; 779 00, Olomouc; CZ, jan.svec@upol.cz

doi: 10.21495/em2024-106

study (Šidlof et al., 2008). The plaster cast (see Fig. 1a) was digitized with an accuracy of $0.1\,\mathrm{mm}$ using the SHINING 3D EinScan-SE optical scanner, see Fig. 1b). The resulting stereolithography (STL) geometry model was cut, cleaned and smoothed in GOM Inspect to extract the vocal folds (Fig. 1c) and to obtain the final STL surfaces of the left and right vocal folds in 3D (Fig. 1d).

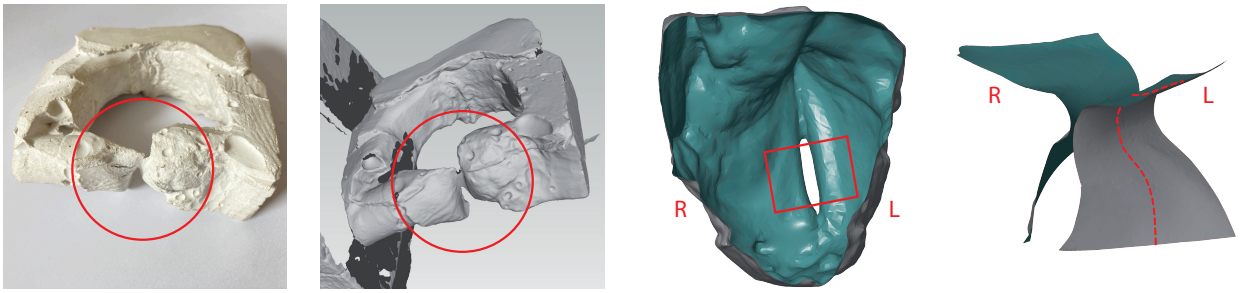

Fig. 1: Stages of digitalization of the plaster cast: a) plaster cast of the human vocal folds (encircled); b) raw digitized geometry of the plaster cast; c) view from the cranio-caudal direction of the extracted vocal folds (cut part is marked) and d) cleaned and smoothed surfaces of the vocal folds (representative slice is marked on the left vocal fold). Left and right vocal folds are labeled.

The left vocal fold from the Fig. 1d) was then processed in Python 3.8.5 using the `numpy-stl` package. The loaded surface of the vocal fold was sliced by the frontal plane to obtain a representative slice of the vocal fold surface. The surface was finally fitted by the augmented M5 geometry model. The fitting was performed using the non-linear least squares method from the `scipy.optimize.curve_fit` package.

2.1. Augmented M5 geometry as a fitting function

Unlike the original three-parametric M5 model (Scherer et al., 2001), the augmented M5 model has eight parameters: R_o, T, Ψ (these are the original M5 parameters, see Fig. 2a) that fully control the geometry between points B–E and R_{AB}, α_{AB}, R_{EF}, β_{EF} and β (these are the added parameters) that control the lower and upper boundary of the vocal fold, which are designed as two circular arcs, see Fig. 2b). Like the original M5 model, also the augmented M5 geometry forms a smooth curve with tangency between each line or arc.

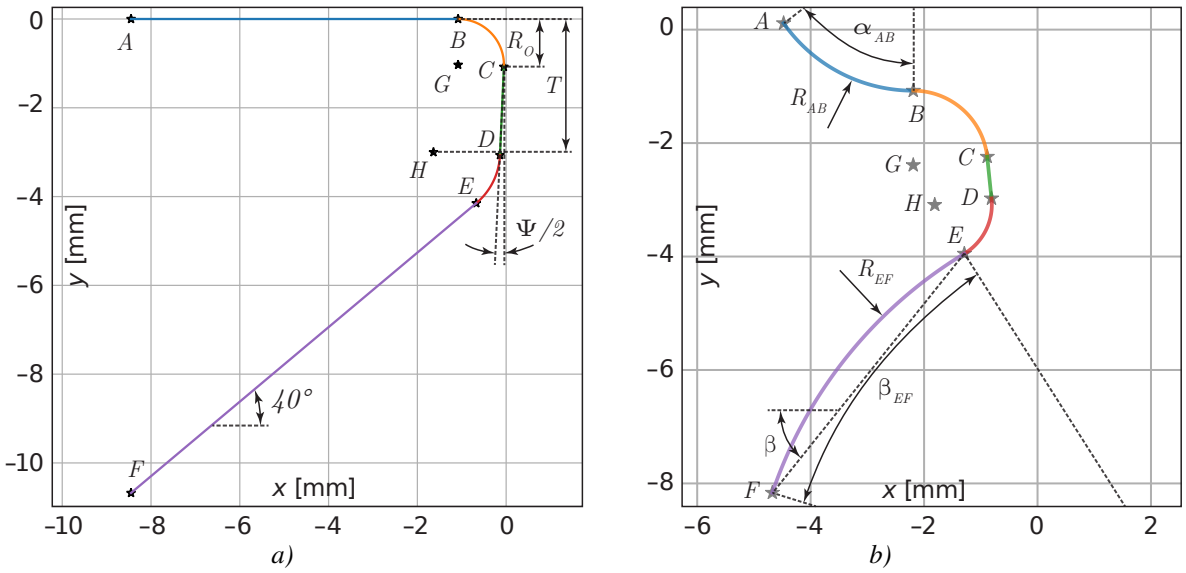

Fig. 2: Development of the augmented M5 model: a) the original M5 geometry with: $R_o = 0.987\,\mathrm{mm}$, $T = 3.000\,\mathrm{mm}$ and $\Psi = 5\,°$ and b) the augmented M5 geometry with the remaining parameters: R_{AB}, α_{AB}, R_{EF}, β_{EF} and β.

The fitting function is a piecewise-defined function with arcs and a straight line between points A–F. Points G and H are the centers of the two arcs from the original M5 model, see Fig. 2b). The centers of the arcs between points A and B and between E and F are not shown in Fig. 2b), but are labeled by points I and J,

respectively. Since the geometry is planar, each point has two coordinates in x and y denoted by a subscript. The equations of the point coordinates are as follows:

$$A_x = -\left(\frac{W_G}{2} + \frac{R_o}{1-\sin\Psi/2}\right) - R_{AB}\cdot\sin\alpha_{AB}, \tag{1}$$

$$A_y = Y_{off} + R_{AB}\cdot(1-\cos\alpha_{AB}), \tag{2}$$

$$B_x = -\left(\frac{W_G}{2} + \frac{R_o}{1-\sin\Psi/2}\right), \tag{3}$$

$$B_y = Y_{off}, \tag{4}$$

$$C_x = -\left(\frac{W_G}{2} + \frac{R_o}{1-\sin\Psi/2}\right)\cdot(1-\cos\Psi/2), \tag{5}$$

$$C_y = Y_{off} - \frac{R_o}{1-\sin\Psi/2}\cdot(1+\sin\Psi/2), \tag{6}$$

$$D_x = -\left\{\frac{W_G}{2} + \left[T\cdot\left(1+\frac{\sin\Psi/2}{2}\right) - \frac{R_o}{1-\sin\Psi/2}\right]\cdot\tan\Psi/2\right\}, \tag{7}$$

$$D_y = Y_{off} - T\cdot\left(1+\frac{\sin\Psi/2}{2}\right), \tag{8}$$

$$E_x = D_x - T\cdot\left(\frac{\cos\Psi/2}{2} - \frac{\sin\beta}{2}\right), \tag{9}$$

$$E_y = Y_{off} - T\cdot\left(1+\frac{\cos\beta}{2}\right), \tag{10}$$

$$F_x = E_x + R_{EF}\cdot[\sin\beta - \cos(\pi/2-\beta-\beta_{EF})], \tag{11}$$

$$F_y = E_y - R_{EF}\cdot[\cos\beta - \sin(\pi/2-\beta-\beta_{EF})], \tag{12}$$

$$G_x = B_x, \tag{13}$$

$$G_y = Y_{off} - \frac{R_o}{1-\sin\Psi/2}, \tag{14}$$

$$H_x = D_x - T\cdot\frac{\cos\Psi/2}{2}, \tag{15}$$

$$H_y = Y_{off} - T, \tag{16}$$

$$I_x = B_x, \tag{17}$$

$$I_y = Y_{off} + R_{AB}, \tag{18}$$

$$J_x = E_x + R_{EF}\cdot\sin\beta, \tag{19}$$

$$J_y = E_y - R_{EF}\cdot\cos\beta. \tag{20}$$

These equations are derived for programming purposes rather than being in the most elegant form. Besides the eight parameters that control the geometry, there are two parameters W_G (width of the *glottis*) and Y_{off} (y offset) that control an offset of the entire geometry in x and y directions, respectively, and which are necessary for a correct fit with respect to a chosen reference point. The complete geometry is placed in the third quadrant of a plane. The line and the arcs between the points from Eqs. (1) to (20) can be constructed very easily using linear equation and Pythagorean theorems, respectively.

3. Results and Discussion

The fit from a representative slice in the center of the selected vocal fold is shown in Fig. 3 together with the resulting parameters. The augmented M5 geometry (the multicolored line in Fig. 3) fits the real shape (the blue dots in Fig. 3) with coefficient $R^2 = 0.999$. *Glottis* is in a divergent shape with $\Psi < 0$. The angle β is sharper than the angle of $40\,^\circ$ in the original M5 geometry (recall Fig. 2a). The parameters R_{AB} and R_{EF} describe the curvatures of the lower and upper boundaries of the vocal fold and are of the order of mm. The parameters α_{AB} and β_{EF} define the length of the arc of the upper and lower boundary and are at the upper limit of the bounds given in the non-linear least squares method. The parameters R_o, T and Ψ are close to the original parameters stated in Scherer et al. (2001).

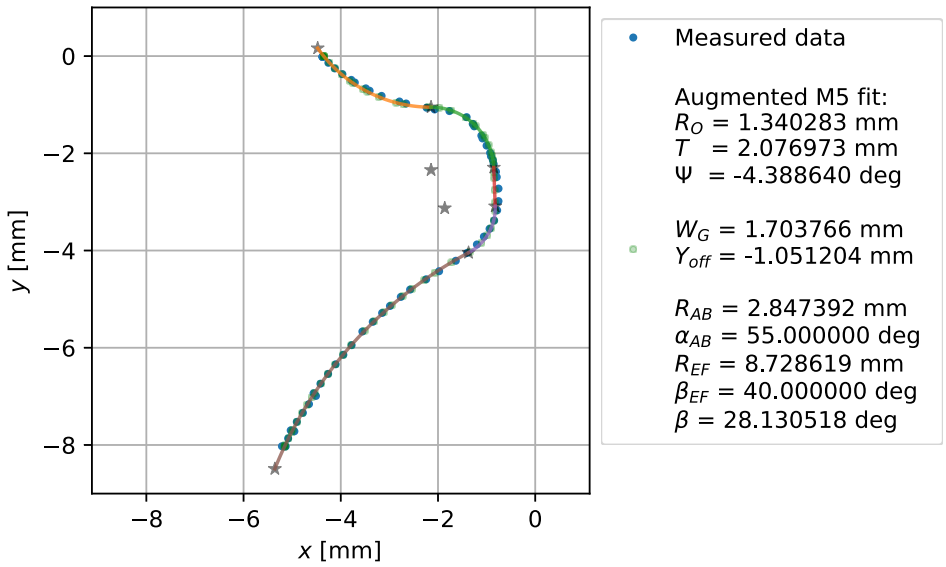

Fig. 3: The augmented M5 geometry fitted on data from the real vocal fold (left) with the resulting parameters (right).

4. Conclusions

The augmented M5 geometry of the vocal fold presented here fits the real shape of the human vocal fold very well, with R^2 better than 0.99. This geometry can be reconstructed from Eqs. (1) to (20) and the resulting parameters given in Fig. 3 and can be used for subsequent numerical or experimental analyses of the human voice production. The fitting code is available on `https://github.com/hajekpc/Augmented-M5-geometry.git`.

Acknowledgment

The study was supported by a grant from the Czech Science Foundation: No. 24-11121S "Redistribution of acoustic energy output in human voice and its effect on vocal folds loading using computer and physical modeling".

References

Alipour, F. and Scherer, R. C. (2000) Vocal fold bulging effects on phonation using a biophysical computer model. *Journal of Voice*, 14, 4, pp. 470–483.

Alipour-Haghighi, F. and Scherer, R. C. (2015) Time-Dependent Pressure and Flow Behavior of a Self-oscillating Laryngeal Model with Ventricular Folds. *Journal of Voice*, 29, 6, pp. 649–659.

Chen, Y., Li, Z., Chang, S., Rousseau, B., and Luo, H. (2020) A reduced-order flow model for vocal fold vibration: From idealized to subject-specific models. *Journal of Fluids and Structures*, 94, pp. 102940.

Li, S., Scherer, R. C., Wan, M., and Wang, S. (2012) The effect of entrance radii on intraglottal pressure distributions in the divergent glottis. *The Journal of the Acoustical Society of America*, 131, pp. 1371–1377.

Scherer, R. C., Shinwari, D., De Witt, K. J., Zhang, C., Kucinschi, B. R., and Afjeh, A. A. (2001) Intraglottal pressure profiles for a symmetric and oblique glottis with a divergence angle of 10 degrees. *The Journal of the Acoustical Society of America*, 109, 4, pp. 1616–1630.

Šidlof, P., Švec, J. G., Horáček, J., Veselý, J., Klepáček, I., and Havlík, R. (2008) Geometry of human vocal folds and glottal channel for mathematical and biomechanical modeling of voice production. *Journal of Biomechanics*, 41, 5, pp. 985–995.

Titze, I. R. (1989) A Four-Parameter Model of the Glottis and Vocal Fold Contact Area. *Speech Communication*, 8, pp. 191–201.

Wu, L. and Zhang, Z. (2016) A parametric vocal fold model based on magnetic resonance imaging. *The Journal of the Acoustical Society of America*, 140, 2.

Wu, L. and Zhang, Z. (2019) Voice production in a MRI-based subject-specific vocal fold model with parametrically controlled medial surface shape. *The Journal of the Acoustical Society of America*, 146, 6, pp. 4190–4198.

Xue, Q., Zheng, X., Mittal, R., and Bielamowicz, S. (2014) Subject-specific computational modeling of human phonation. *The Journal of the Acoustical Society of America*, 135, 3, pp. 1445–1456.

30th International Conference
ENGINEERING MECHANICS 2024
Milovy, Czech Republic, May 14 – 16, 2024

ANALYTICAL INVESTIGATION OF MARS DRONE CONCEPTUAL DESIGN

Havran E.*

Abstract: *An analysis of Mars rotary wing aircraft was done, regarding a quadcopter design. A mission profile was proposed, that could be generalized to multiple mission goals. Energy requirements for such a mission were computed and then a mass sizing of the drone was calculated. This resulted in various design points of Mars drones, in accordance with what initial conditions (for example rotor count) were chosen. Next, using blade element momentum theory, an analytical model of the rotors was calculated and implemented to the drone, so as to create a conceptual design for later research and development use.*

Keywords: Mars drone, conceptual design, mass sizing, blade element momentum theory.

1. Introduction

As Mars exploration picks up its pace, with multiple planned missions in the next decades, the exploration and possible colonization of the planet will require more advanced technologies. A capability gap exists between immobile landers, mobile rovers that can nevertheless cover only a small distance in comparison with the surface of the planet and orbiting satellites that can cover large swaths of it at the expense of resolution of the pictures when dealing with surface mapping, or inability to take samples from interesting areas. Mars aircraft, especially ones with vertical take-off landing capabilities, offer a huge opportunity to bridge this gap, as was laid out by Young (2000). In recent years a technological demonstrator- the Ingenuity Mars Helicopter, was designed and tested on Mars, proving the applicability of rotary wing aircraft usage on the planet. However, Ingenuity only had a small size with no scientific payload and as such, larger Mars drones are being developed. While only in the conceptual phases, examples could include the work by NASA published for example in Johnson and Withrow-Maser (2020) or work by Aoki et al. (2018). Both used slightly different conceptual design principles to create the concept and as such there was slight variation of the results. For creating a new conceptual design of a Mars drone, utilizing both of these design processes and implementing knowledge of the blade element momentum theory of helicopters, a qualitative and quantitative analysis of a general Mars drone could have been created. The author utilized this as part of his diploma thesis (Havran, 2023).

Mars has a different environment than Earth. For rotary wing aircraft this is mainly noticeable in the very thin atmosphere, which also has a different composition. This results in a very low Reynolds number and Mach number of the flows, creating a specific case not encountered on Earth, explained by Koning et al. (2018). The decrease in rotor performance thanks to the thin atmosphere is alleviated a little by the lower gravitational acceleration on Mars.

2. Mission profile and energy requirement

Before a Mars drone could be designed, a mission profile needed to be created. A study by Balaram and Daubar (2019) listed possible mission goals. To design a concept, that can be utilized for multiple mission goals, considering a general mission profile without a specific mission goal was beneficial.

* Ing. Edmund Havran: Institute of Aerospace Engineering, Brno University of Technology, Technická 2896/2; 616 69, Brno; CZ, edmund.havran@vut.cz

doi: 10.21495/em2024-110

It consisted of the following parts: 1) Wake-up from sleep and preparation for flight; 2) Take-off; 3) Climb to altitude of 200 meters; 4) Flight for a distance of 1 000 meters with forward speed of 5 m/s; 5) Hovering for 2 minutes; 6) Descend to 0 meters; 7) Landing; 8) Recharge and sleep for 1 sol till the next mission. Energy requirements for one day of operations were calculated in accordance with Dorling et al. (2017) for the in-flight part. Landed energy consumption assumed a steady power usage of 10 W. Total energy required for the drone for 1 sol is shown in Fig. 1. in relationship with the assumed drone mass M_{total}.

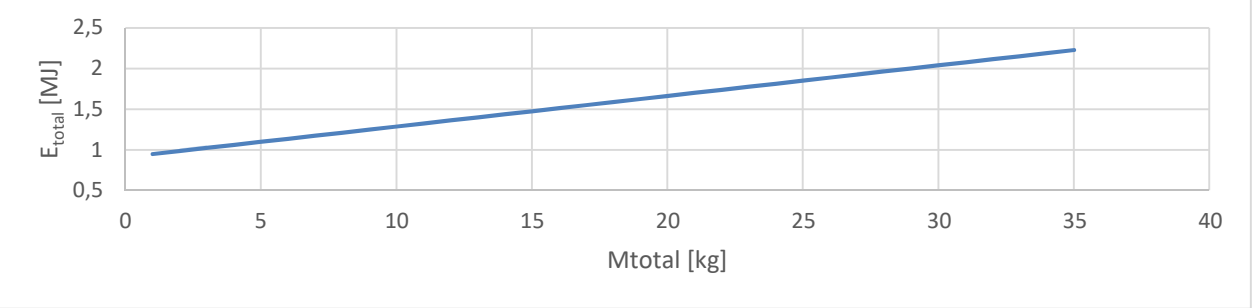

Fig. 1: Total energy required for 1 sol in relationship with total drone mass.

2.1. Mass sizing

Two methods for mass sizing were evaluated. Method 1 stemmed from Johnson (2020) and method 2 from Aoki et al. (2018). For the sake of brevity, only method 1 is described in this paper. Before both could be utilized, drone rotor disk count had to be decided. Four cases were studied: a tricopter, quadcopter, hexacopter and octacopter. A design assumption of variables is given in Tab. 1 approximated from other Mars drone concepts listed in Havran (2023). Drone masses from 1 to 35 kg were considered.

Coefficient of thrust	C_T	0.02	[-]
Coefficient of torque	C_Q	0.0023	[-]
Solidity	σ	0.18	[-]
Rotor tip speed	V_{tip}	0.7	Mach

Tab. 1: Assumed variables.

Rotor tip speed was limited to only 0.7 Mach to create a large cushion of possible improvement in forward speed and rotor performance in following studies and ensure appropriate results in the concept design phase. For method 1, total blade area A_b, masses of the blade, supporting arms from the fuselage to the rotor housing, fuselage, landing gear, motors and battery were first calculated. As these values used rotor radius and blade area, different results could have been achieved by having different rotor counts. For simplicity's sake, only the quadrotor was further analyzed.

$$A_b = \sigma \cdot A \tag{1}$$

$$M_{blade} = 1.1 \cdot A_b \tag{2}$$

$$M_{arm} = 0.2 \cdot r_{rotor} \tag{3}$$

$$M_{fuselage} = 28 \cdot \left(\frac{M_{total}}{1000}\right)^{\frac{2}{3}} \tag{4}$$

$$M_{gear} = 0.067 \cdot M_{total} \tag{5}$$

$$M_{motor} = \frac{P_{Fhove}}{\rho_{motor}} + M_{controller} \tag{6}$$

$$M_{bat} = \frac{1.3 \cdot E_{total}}{\rho_{bat}} \tag{7}$$

Controller mass was assumed to be 0.11 kg. Power density of the motor ρ_{motor} was chosen in accordance with off-the shelf components available for RC airplanes as 2 500 W/kg. Battery power density ρ_{bat} of 218.5 Wh/kg including the battery management system and assuming end of life cycle was chosen. This value was commercially available in high end products. To prolong the battery life, it was necessary to ensure energy reserves both on top and low ends of the battery charge. This was achieved by adding

30 % to the total required energy. Recharging the battery was done by solar panels. Their size depended on recharge time and rate, so a total time in direct sunlight during 1 sol was calculated as 35 % of a sol, about 5.6 hours. From this the needed charging power of the solar panels was calculated.

$$P_{solar} = \frac{E_{total}}{0.35 \cdot t_{sol}} \tag{8}$$

Taking the values introduced in Johnson (2020) for solar cell power density of 21.9 W/m^2 and mass density of 2 kg/m^2 allowed solar cell mass to be calculated.

$$M_{solar} = 2 \cdot A_{solar} \tag{9}$$

Two additional constant masses added were for avionics at 1.2 kg, including navigational and communicational equipment and a payload reserve of 2.02 kg without specification. The total mass M_{total} was first assumed to the values of 1 to 35 kg.

Results are shown in Fig. 2. These also included a version with 15 % added mass as a buffer, because it could be expected that empirical formulas used for mass assumption were not accurate. Msum corresponds to the mass calculated from above formulas. Mass divergence shows the difference between the calculated M_{total} and initially assumed M_{total}. If the initially assumed mass and calculated one are the same – the divergence is 0- then a design point was formed. Changing the required payload, or flight profile changed the design point too and thus a large array of values could have been quickly evaluated.

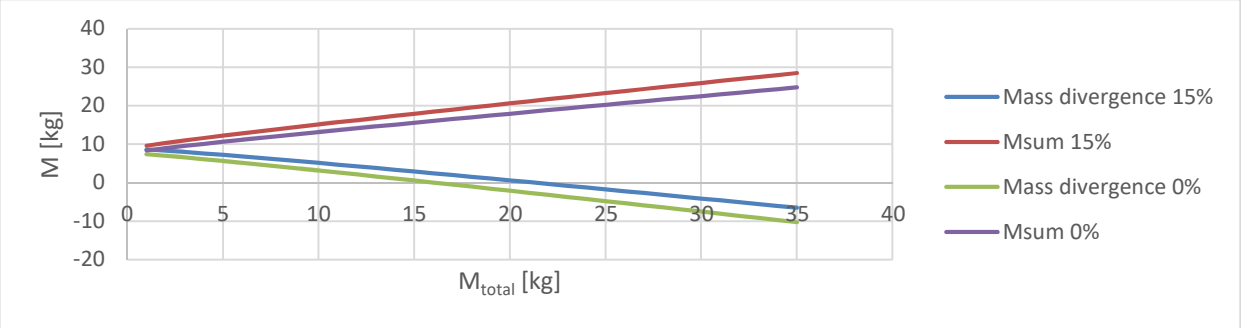

Fig. 2: Mass convergence graph.

2.2. Aerodynamics of rotors

Aerodynamic analysis using blade element momentum theory (BEMT) was utilized. The principle of BEMT was that a nondimensional rotor induced inflow ratio λ in hover could be computed, assuming a linear lift polar curve shape of an airfoil. A known and tested triangle airfoil by Suwa et al. (2012) was assumed, where a clearly linear part of its lift polar was narrowed down. The blade was also assumed to be of rectangular planform and with constant pitch angle along its span. The calculations used by BEMT were widely published, for example in Leishman (2008).

Flow around the rotor blade was influenced by induced flow and this resulted in different real angles of attack of the flow on the blade. Thanks to the induced inflow ratio, the final effective angle of attack α along the blade was calculated from the pitch angle of the blade (a given geometrical property of the blade). Fig. 3 shows the effective angle of attack along the blade radius r for different pitch angles of the blade. This was shown for a drone mass of 15 kg. Fig. 4 on the other hand shows the effective angle of attack for pitch angle of 2 ° for various drone design points.

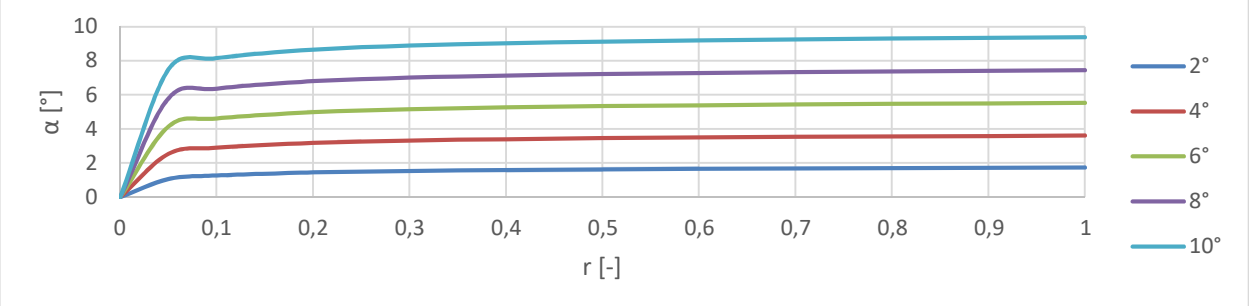

Fig. 3: Effective angle of attack for different pitch angles for a drone with a mass of 15 kg.

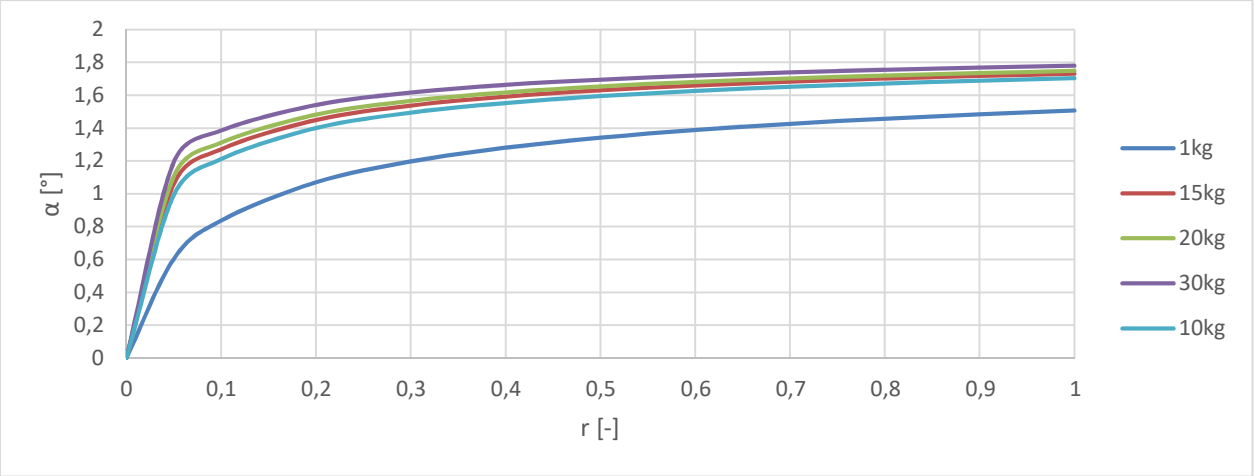

Fig. 4: Effective angle of attack for different drone masses for a blade pitch angle of 2 °.

3. Conclusions

Utilizing aerodynamic characteristics of the rotors, drone mass and a components list, a finalized conceptual design of the drone was created. As the used airfoil was not optimized and the blade was assumed to be of rectangular shape, the resulting drone performance could be vastly improved upon by a specifically designed and optimized rotor blade using better airfoils. As such, the resulting graphs are useful for the conceptual design phase of a Mars multicopter and could be used with little modifications to provide a base for more advanced and specific research and development of a Mars rotary wing vehicle in multiple possible configurations and mission goals.

Acknowledgement

This work has been supported by the project No. FSI-S-23-8163 funded by The Ministry of Education, Youth and Sport (MEYS, MŠMT in Czech) institutional support.

References

Aoki, R. et al. (2018) Conceptual Helicopter Design for Exploration of Pit Craters and Caves on Mars, In: *AIAA Atmospheric Flight Mechanics Conference*, AIAA SPACE Forum, Orlando, FL.

Balaram, J. et al. (2019) Helicopters on Mars: Compelling Science of Extreme Terrains Enabled by an Aerial Platform, *9th International Conference on Mars*, Pasadena, 6277.

Dorling, K., Heinrichs, J., Messier, G.G. and Magierowski, S. (2017) Vehicle Routing Problems for Drone Delivery, *IEEE Transactions on Systems, Man, and Cybernetics: Systems*, 47(1), pp. 70–85.

Havran, E. (2023) *Mars Drone conceptual design*. Diploma thesis, Brno University of Technology, Faculty of Mechanical Engineering, Institute of Aerospace Engineering.

Johnson, W. and Withrow-Maser, S. (2020) *Mars Science Helicopter Conceptual Design*. Moffet Field, CA, Ames Research Center.

Koning, W. J. F., Allan, B. G. and Johnson W. (2018) Generation of Mars Helicopter Rotor Model for Comprehensive Analyses, In: *AHS Specialists´ Conference on Aeromechanics Designs for Transformative Vertical Flight*, San Francisco, CA, 22 p.

Leishman, J. G. (2008) *Principles of helicopter aerodynamics*. 2nd edition, Cambridge University Press, Aerospace Series, Cambridge.

Suwa, T., Nose, K., Numata, D., Nagai, H. and Asai, K. (2012) Compressibility Effects on Airfoil Aerodynamics at Low Reynolds Number, In: *30th AIAA Applied Aerodynamics Conference*, AIAA, Reston, VA.

Young, L. A. (2000) *Vertical Lift – Not Just For Terrestrial Flight*. Moffet Field, CA, Ames Research Center.

30th International Conference
ENGINEERING MECHANICS 2024
Milovy, Czech Republic, May 14 – 16, 2024

ON DIFFUSION, REACTION, AND FLOW OF HIGH-CONCENTRATION MULTICOMPONENT GAS MIXTURES

Hlavatý T.[*], **Isoz M.**[**]

Abstract: *Heterogeneous catalysis contributes to producing more than 80 % of all chemical products in the world. Industrial heterogeneous catalysis is a complex process that combines fully three-dimensional mass, momentum, and energy transport on several scales. In the present work, we leverage our previously developed CFD solver for non-isothermal heterogeneously catalyzed reactive flow based on the finite-volume method and extend it with multicomponent Stefan-Maxwell diffusion description to handle high-concetration multicomponent mixtures. The resulting framework is verified and validated on the simple Stefan tube experiment, for which an analytical solution is available.*

Keywords: Stefan-Maxwell diffusion, high concentration reactive flow, OpenFOAM.

1. Introduction

Heterogeneous catalysis plays a crucial role in numerous industrial chemical processes, ranging from mobile applications in catalytic converters for automotive exhaust gas aftertreatment to stationary large industrial reactors for natural gas conversion (Tischer et al., 2001) or ethylene oxychlorination. In the case of mobile catalysts, the active catalytic material is usually coated in the form of a porous layer on the walls of monolith channels (Blažek et al., 2021). For the fixed-bed reactors, the catalyst is deposited on and inside catalyst-carrying particles.

However, there is still significant room for optimization of such processes (Fechete et al., 2012). The efficiency of an arbitrary heterogeneous catalyzed process is strongly dependent on all the transport processes inside the system. In particular, focusing onto mass transport, the following needs to be taken into account, (i) global transport of reactive species inside the reactor, i.e., to and from porous media coated with catalytic material, (ii) local diffusive transport inside the porous structure of the catalyst, and (iii) adsorption of reactants onto active sites and subsequent reaction followed by desorption of products. Furthermore, despite the fact that the proper description of the high-concentration-mixture diffusion, which is common in the real-life industrial processes, is well known for a long time (Taylor and Krishna, 1993), the most of the newly developed computational fluid dynamics (CFD) solvers for coupled momentum and multicomponent mass transfer, e.g. (Chandra et al., 2020), rely on simplified (linear) Fick's diffusion.

The main goal of the present work is to extend our previously developed solver for heterogeneously catalyzed reactive flow (Hlavatý et al., 2023b) by the Stefan-Maxwell diffusion description to deal with the high-concentration mixtures commonly present in the industrial chemical reactors.

2. Model description

The presented model stems from our previously published OpenFOAM solver for the heterogeneously catalyzed reactive flow for the simulations of the catalytic filters in the automotive exhaust gas aftertreatment (Hlavatý et al., 2023b). Non-isothermal reactive flow of an ideal gas in the heterogeneous domain Ω

[*] Ing. Tomáš Hlavatý: University of Chemistry and Technology, Technická 5; 166 28, Prague; CZ, and Institute of Thermomechanics, CAS, Dolejškova 1402/5; 182 00, Prague; CZ, hlavaty@it.cas.cz

[**] Ing. Martin Isoz, PhD.: Institute of Thermomechanics, CAS, Dolejškova 1402/5; 182 00, Prague; CZ, isozm@it.cas.cz

doi: 10.21495/em2024-114

is assumed, while the heterogeneity of Ω is ensured by dividing Ω in free space ($\Omega_{\rm fs}$) and porous media ($\Omega_{\rm pm}$), such that $\Omega = \Omega_{\rm fs} \cup \Omega_{\rm pm}$ and $\Omega_{\rm fs} \cap \Omega_{\rm pm} = \emptyset$, and by using (i) effective diffusion coefficients, and (ii) piece-wise continuous right hand side of governing equations, see (Hlavatý et al., 2022, 2023a,b).

Assuming a Newtonian gas, neglecting heat mechanical sources, and marking the velocity $\boldsymbol{u}$, the mass density ρ, the pressure p, and the temperature T, the steady-state momentum, mass, and heat transfer can be, in order, described by the following set of balances,

$$\nabla \cdot [\rho \boldsymbol{u}\boldsymbol{u}^{\intercal}] - \nabla \cdot [\mu \left(\nabla \boldsymbol{u} + (\nabla \boldsymbol{u})^{\intercal}\right)] = -\nabla p + \rho \boldsymbol{s}^{\boldsymbol{f}} \,, \tag{1}$$

$$\nabla \cdot (\rho \boldsymbol{u}) = 0 \,, \tag{2}$$

$$\nabla \cdot (\boldsymbol{u} \rho \omega_i) - \nabla \cdot \left(\dot{\boldsymbol{m}}_i^{\rm D}\right) = s_i^r, \quad i = 1, \ldots, n-1 \,, \tag{3}$$

$$\nabla \cdot (\rho \boldsymbol{u} c_{\rm p} T) - \nabla \cdot \left(\lambda^{\rm eff} \nabla T\right) = s^h \,, \tag{4}$$

where μ is the dynamic viscosity of the gas, $\lambda^{\rm eff}$ is the effective heat conductivity, and $c_{\rm p}$ is the heat capacity. For more information on parameters' computations see (Hlavatý et al., 2023a). The source term $\rho \boldsymbol{s}^{\boldsymbol{f}}$ describes the resistivity of the flow through the porous medium ($\Omega_{\rm pm}$) and is defined based on the Darcy permeability model (Kočí et al., 2019). Reactions are assumed to occur only in the catalytic material, and the chemical-reactions and enthalpy sources are, in order, defined in the form

$$s_i^r = \begin{cases} 0 & \text{in } \Omega_{\rm fs} \\ \nu_i \varphi_c \, s^r \, M_i & \text{in } \Omega_{\rm pm} \end{cases}, \quad s^h = \varphi_c \, s^r (-_{\Delta} H_r) \,, \tag{5}$$

where ν_i is the i-th component stoichiometric coefficient, φ_c is the volumetric fraction of the catalyst, and s^r is the reaction rate computed from a rate law considering the local gas temperature and composition.

The gas mass density is assumed to be linked with pressure, and temperature via the ideal gas law $(6)_1$, where $\mathrm{R}^{\rm g}$ is the universal gas constant and $M^{\rm g}$ is the composition-dependent molar mass of the gas $(6)_2$, where ω_i, and M_i are the i-th chemical specie mass fraction, and the molar mass, respectively. Supposing a gas mixture of n species, the mass fraction of the n-th component can be expressed using $(6)_3$,

$$\rho = \frac{p \, M^{\rm g}}{\mathrm{R}^{\rm g} \, T} \,, \quad M^{\rm g} = \frac{1}{\sum_{i=1}^{n} \omega_i / M_i} \,, \quad \omega_n = 1 - \sum_{i=1}^{n-1} \omega_i \,. \tag{6}$$

The main contribution of the present work lies in an extension of the specie diffusion mass flux calculation, $\boldsymbol{m}_i^{\rm D}$. In our previous implementations, the diffusive mass flux was computed using Fick's law valid for small concentrations. In the present work, universal Stefan-Maxwell description of the diffusive fluxes is utilized and implemented within the developed solver. Working in the mass-average frame, the Stefan-Maxwell relations can be expressed in a compact matrix form as;

$$\left[\dot{\boldsymbol{m}}^{\rm D}\right] = \rho \, \left[D^0\right] \, [\nabla \boldsymbol{\omega}] \,, \tag{7}$$

where $\left[\dot{\boldsymbol{m}}^{\rm D}\right]$ is the matrix of the diffusive mass fluxes of the $(n-1)$ chemical species, i.e. in three spatial dimensions $\left[\dot{\boldsymbol{m}}^{\rm D}\right] \in \mathbb{R}^{(n-1,3)}$, and $[\nabla \boldsymbol{\omega}]$ is the matrix of the mass fraction gradients, of the same dimension (Taylor and Krishna, 1993). The symbol $\left[D^0\right]$ stands for the $(n-1, n-1)$ dimensional matrix of the multicomponent diffusion coefficients in the mass average frame, which can be calculated as suggested by Taylor and Krishna (1993),

$$\left[D^0\right] = [B^{\rm ou}] \, \mathrm{diag} \, (\boldsymbol{\omega}/\boldsymbol{y}) \, \left[B^{-1}\right] \, \mathrm{diag} \, (\boldsymbol{y}/\boldsymbol{\omega}) \, [B^{\rm uo}] \,, \tag{8}$$

where $[B^{\rm ou}]$, and $[B^{\rm uo}]$ are mutually inverse matrices of the transformation from the mass to molar average frame and vice versa, respectively. The used form of the transformation matrix is,

$$[B^{\rm ou}]_{i,k} = \delta_{i,k} - \omega_i \left(1 - \frac{\omega_n \, y_k}{y_n \, \omega_k}\right), \; i, k = 1, \ldots, n-1 \,, \tag{9}$$

where y_i is the molar fraction of the i-th specie, and $\delta_{i,k}$ is Kronecker delta.

Diagonal matrices $\mathrm{diag}\,(\boldsymbol{\omega}/\boldsymbol{y})_{i,i} = \omega_i/y_i$ and $\mathrm{diag}\,(\boldsymbol{y}/\boldsymbol{\omega})_{i,i} = y_i/\omega_i$ are ratio of the mass (ω) to the molar fraction (y) and vice versa. Finally, the matrix of the diffusion coefficients in the molar average frame $\left[B^{-1}\right]$ is computed as the inversion of the $(n-1, n-1)$ dimensional matrix $[B]$, whose coefficients are defined as follows,

$$[B]_{i,i} = \frac{y_i}{\mathcal{D}_{i,n}} + \sum_{k=1, i\neq k}^{n} \frac{y_k}{\mathcal{D}_{i,k}}\,, \tag{10}$$

$$[B]_{i,j} = -y_i \left(\frac{1}{\mathcal{D}_{i,j}} - \frac{1}{\mathcal{D}_{i,n}}\right)\,. \tag{11}$$

Note that the matrix of the diffusion coefficients $\left[D^0\right]$ is composition-dependent, which means that the Stefan-Maxwell diffusion leads to a non-linear problem.

In general, it is difficult to determine the Stefan-Maxwell binary diffusion coefficients $\mathcal{D}_{i,j}$. However, considering the ideal gas and heterogenous domain, $\Omega = \Omega_{\mathrm{fs}} \cup \Omega_{\mathrm{pm}}$, we can assume that the Stefan-Maxwell binary diffusion coefficients are equal to the effective Fick binary diffusion coefficients, $\mathcal{D}_{i,j} = D^{\mathrm{eff}}_{i,j}$, whose calculation is taken from (Hlavatý et al., 2023a).

3. Numerical results

The new implementation of the diffusive flux was validated on the well known benchmark case of the Stefan tube with the high concentration diffusive mass transfer.

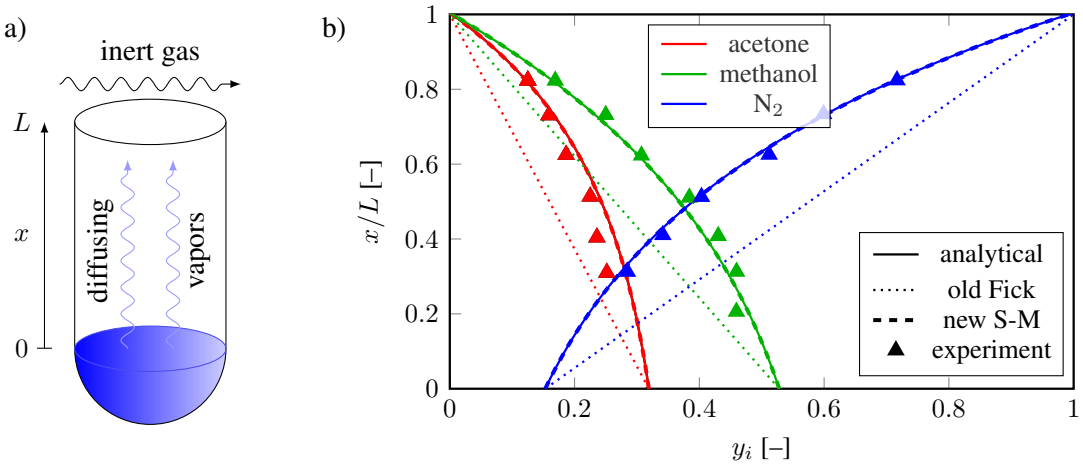

Fig. 1: a) Schematics of the Stefan tube, b) comparison of molar fraction profiles in the Stefan tube computed with different implementations of the custom solver with the experimental data by Carty and Schrodt (1975).

The Stefan tube is a simple device schematically depicted in Fig. 1a. At the bottom of the tube, there is a level of the acetone/methanol mixture. The vapor evaporates and diffuses to the top of the tube. A stream of the inert gas flows across the top of the tube, which keeps the mole fraction of diffusing vapors close to zero there (Taylor and Krishna, 1993). As the diffusion to the top of the tube is a relatively slow process, the change of the liquid level is slow and we can assume a pseudo-steady state. With such an assumption, the boundary conditions for the molar fractions of all the acetone and methanol are Dirichlet and constant,

$$y_i(0) = \frac{p_i^{\mathrm{s}}}{p}\,, \quad y_i(L) = 0\,, \tag{12}$$

where p_i^{s} is the saturated vapor pressure and the system of mass balances (3) can be reduced to the set of the ordinary differential equations with the analytical solution. Furthermore, Carty and Schrodt (1975) published experimental data on the diffusion of acetone/methanol mixture in pure nitrogen. This allowed us to compare new solver concentration profiles (dashed lines) with the analytical solution (solid lines), experiment (triangles), and the old solver implementation (dotted lines) in Fig. 1b.

Let us emphasize three things: (i) the old solver-implementation (old Fick), which assumes constant molar mass of the gas, is not capable resolving cross-diffusion effects occurring in the Stefan tube with a high concentration of the diluted gases, (ii) the new solver-implementation (new S-M) predicts results almost identical to the analytical solution, and (iii) they provide quite good agreement with the experiment.

4. Conclusion

In the present contribution, we delineated fundamental principles of a solver applicable to the simulation of heterogeneously-catalyzed reactive flows. The new solver allows for the simulations of non-diluted reactive mixtures with simultaneous momentum, heat, and mass transfer, while the mass transfer treatment comprises the Stefan-Maxwell approach to multi-component diffusion. For the simplified case of a mass transfer in a Stefan tube, the new solver provides results in a perfect agreement with both the experiment and the available analytical solution. The proposed solver extension allows one to properly describe and optimize complex industrial processes, such as ethylene oxichlorination which is descibed in detail in (Hlavatý et al., 2023a) and illustrated in Fig. 2.

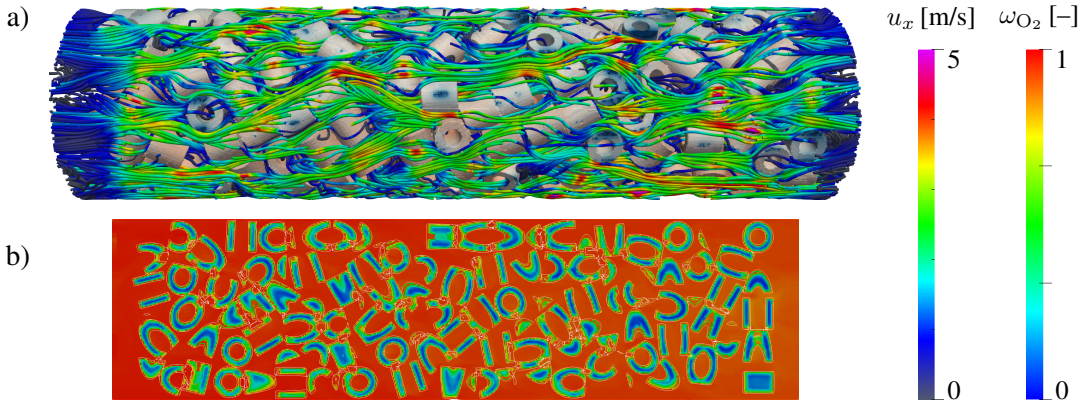

Fig. 2: a) Streamlines colored by streamwise velocity component in industrial packed bed, b) oxygen mass fraction (ω_{O_2}) contours on longitudinal cut through the geometry.

Acknowledgments

The work was financially supported by the institutional support RVO:61388998, by the grant project with No. TN02000069/001N of the Technology Agency of the Czech Republic, and the grant project with No. QL24010110 of the National Agency for Agricultural Research (NAAR).

References

Blažek, M., Žalud, M., Kočí, P., York, A., Schlepütz, C., Stampanoni, M., and Novák, V. (2021) Washcoating of catalytic particulate filters studied by time-resolved X-ray tomography. *Chemical Engineering Journal*, 409, pp. 128057.

Carty, R. and Schrodt, T. (1975) Concentration profiles in ternary gaseous diffusion. *Industrial & Engineering Chemistry Fundamentals*, 14, 3, pp. 276–278.

Chandra, V., Peters, E., and Kuipers, J. (2020) Direct numerical simulation of a non-isothermal non-adiabatic packed bed reactor. *Chemical Engineering Journal*, 385, pp. 123641.

Fechete, I., Wang, Y., and Védrine, J. C. (2012) The past, present and future of heterogeneous catalysis. *Catalysis Today*, 189, 1, pp. 2–27.

Hlavatý, T., Isoz, M., and Khýr, M. (2023a) Simulation of heterogeneously-catalyzed non-isothermal reactive flow in industrial packed beds. pp. 44–51.

Hlavatý, T., Isoz, M., and Kočí, P. (2022) Developing a coupled cfd solver for mass, momentum and heat transport in catalytic filters. pp. 79–86.

Hlavatý, T., Kočí, P., Isoz, M., Deka, D., and Partridge, W. (2023b) Balanced fast-spacims capillary configurations provide practically noninvasive channel-average measurements in catalytic monoliths. *Chemical Engineering Science*, 282, pp. 119272.

Kočí, P., Isoz, M., Plachá, M., Arvajová, A., Václavík, M., Svoboda, M., Price, E., Novák, V., and Thompsett, D. (2019) 3D reconstruction and pore-scale modeling of coated catalytic filters for automotive exhaust gas aftertreatment. *Catalysis Today*, 320, pp. 165–174.

Taylor, R. and Krishna, R. (1993) *Multicomponent mass transfer*, 2. John Wiley & Sons.

Tischer, S., Correa, C., and Deutschmann, O. (2001) Transient three-dimensional simulations of a catalytic combustion monolith using detailed models for heterogeneous and homogeneous reactions and transport phenomena. *Catalysis Today*, 69, 1, pp. 57–62.

30th International Conference
ENGINEERING MECHANICS 2024
Milovy, Czech Republic, May 14 – 16, 2024

TEMPERATURE FIELD EVALUATION USING INJECTION MOLD THERMAL INSERTS

Holesovský F.*, Hejna M.**

Abstract: *This article deals with thermal inserts in injection molds and their effect on the mechanical properties of crystalline plastics. Description and solution of the temperature field, mathematical-physical analysis of the solution of temperature fields, methods of temperature measurement, non-contact temperature measurement, touch temperature measurement, course of temperature fields in the injection mold, evaluation of the effect of thermal inserts on the distribution of the temperature field in the injection mold are given. Methods of evaluating the temperature field are presented here. In this part, the measurement of temperature fields in an injection mold containing thermal inserts is also performed.*

Keywords: Thermal inserts, temperature field, injection mold.

1. Introduction

The processing of plastics is currently a field that is still developing, mainly because their processing is cheap and at the same time productive. The great development of the use of plastics is mainly in engineering, especially in the automotive industry, electrical engineering, construction and packaging technology (Hejna, 2004).

In practice, more and more demands are placed on the product to be as cheap as possible, produced in the shortest possible time and have the appropriate properties. These demanding requirements are met by the processing of plastics using injection technology. This technology can produce products with good dimensional and shape accuracy. Other advantages also include the high utilization of processed material, thus meeting the requirements for waste-free technology. However, the purchase price of both the machinery and the injection mold is quite high, which is why this technology is suitable for large-scale and mass production (Hejna, 2004).

The injection molding process can be shortened mainly by the cooling time, i.e. by removing heat from the shaped cavity of the mold, this can be achieved by tempering the injection molds. One of the many methods of tempering injection molds is the use of thermal inserts, which remove heat from the mold cavity. Whether this method of tempering will affect the mechanical properties of crystalline plastics is discussed in this article (Hejna, 2004).

2. Temperature field in injection form

2.1. Description and solution of the temperature field

The process of cooling the injection mold is a non-stationary, cyclically repeating process that takes place in the temperature range from the melt temperature to the mold temperature. This temperature system creates a cyclic three-dimensional temperature field, which is most influenced by the choice, construction,

* Prof. Dr. Ing. František Holešovský: University of West Bohemia in Pilsen, Street Univerzitni 2732/8; 301 00, Pilsen; CZ, holesovf@fst.zcu.cz

** Ing. Marek Hejna: University of West Bohemia in Pilsen, Street Univerzitni 2732/8; 301 00, Pilsen; CZ, marek78@fst.zcu.cz

doi: 10.21495/em2024-118

method of location and efficiency of the temperature system, or Tempering agent, mold and product material.

Taking into account the characteristics of the injection molding, cooling should take place uniformly and at the same speed in all parts of the injection mold. However, this depends on the design of the tempering system and the distribution of the temperature fields in the tool. In the ideal case, which cannot be achieved in practice due to very rapid changes in temperature over time, the spray should have the same temperature during cooling at all points in the layer at the same distance from the surface. Uneven distribution of temperatures in the mold cavity and on the surface of the injection, i.e. an inhomogeneous temperature field, results in the risk of dimensional and shape deviations of the injection. Temperature differences between individual injection areas cannot be avoided, but due to knowledge of the distribution of temperature fields, they can be influenced so that they are within acceptable limits and reproducible in each cycle.

The temperature field in the jet is clearly determined by its geometry (shape and dimensions), material properties, temperature distribution at a certain moment and conditions of heat transfer over the entire surface of the body and during the investigated phase. If we use rectangular coordinates x, y, z, the 3D non-stationary temperature field (temperatures at points with coordinates x, y, z are functions of time) at time t is generally described by the following function (Hejna, 2004):

$$T = T(x, y, z, t) \tag{1}$$

where: T … temperature [K],
x, y, z … Cartesian coordinates [m],
t … time [s].

The uneven distribution of temperature in the body results in a heat flow in the direction of decreasing temperature:

$$q = -\lambda \, . \, grad \, T \tag{2}$$

where: λ … coefficient of thermal conductivity [W/m.K],
grad T … temperature gradient in form [K/m].

Injection molds are most often metal, and for other solutions it can be considered that the material forms a homogeneous environment and heat is shared in it by conduction. Non-stationary heat conduction in the body (in our case in injection and injection form) is described by the partial differential Fourier equation (3). This equation describes the temperature distribution in the injection mold at any instant of time.

$$\frac{\partial T(x,y,z,t)}{\partial t} \, . \rho . c_v = \frac{\partial T(x,y,z,t) . \partial T(x,y,z,t)}{\partial t . \partial t} \, . \lambda_x + \frac{\partial T(x,y,z,t) . \partial T(x,y,z,t)}{\partial t . \partial t} . \lambda_y + \frac{\partial T(x,y,z,t) . \partial T(x,y,z,t)}{\partial t . \partial t} . \lambda_z + q_{zdr} \tag{3}$$

For a homogeneous environment ($\lambda_x = \lambda_y = \lambda_z = \lambda$) of the mold material, the following relation applies:

$$\frac{\partial T}{\partial t} = a . \left(\frac{\partial T . \partial T}{\partial t . \partial t} + \frac{\partial T . \partial T}{\partial t . \partial t} + \frac{\partial T . \partial T}{\partial t . \partial t} \right) + \frac{q_{zdr}}{\rho . c_v} \tag{4}$$

where: $\frac{\partial T}{\partial t}$… temperature change with time [K/s],
a… coefficient of thermal conductivity [m^2/s] defined by the relation: $a = \lambda/\rho.c_v$,
ρ… density [kg/m^3],
c_v… specific heat capacity at constant volume [$J/kg^3.K$],
t… time [s],
$\lambda_x, \lambda_y, \lambda_z$ … thermal conductivity coefficient of the form in the direction (x,y,z) [W/m.K],
q_{zdr}… heat output of internal sources [W/m^2].

The term q_{zdr} is added to the right side of Eq. (3) when heat is released in the material of the body as a result of chemical or physical changes. It represents the specific heat output of internal sources.

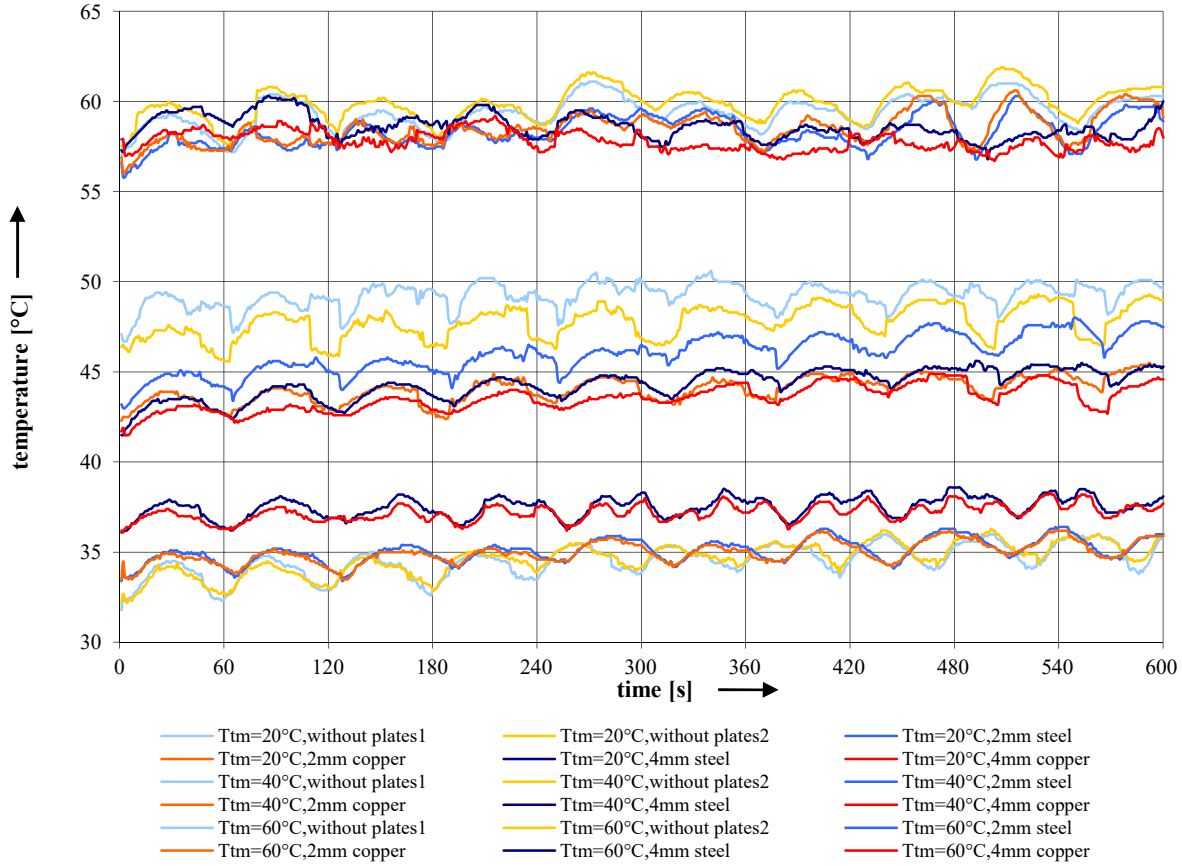

Fig. 1: Temperature field in the injection mold with different methods of tempering and different temperatures of the tempering medium (Hejna, 2004).

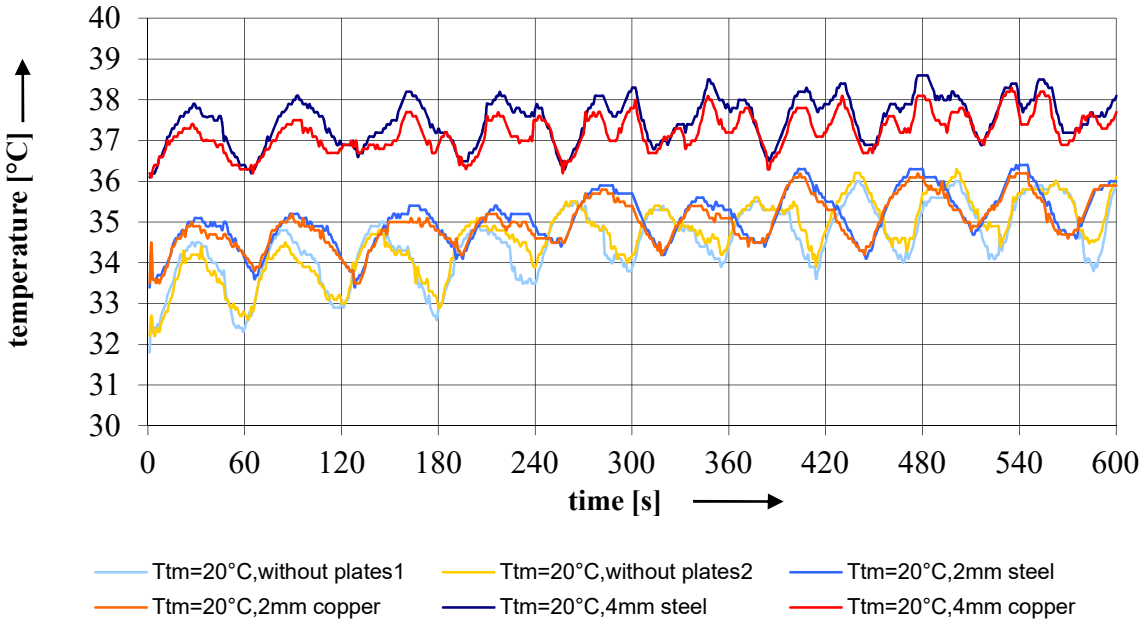

Fig. 2: Temperature field in the injection mould for different tempering methods at Ttm = 20 °C (Hejna, 2004).

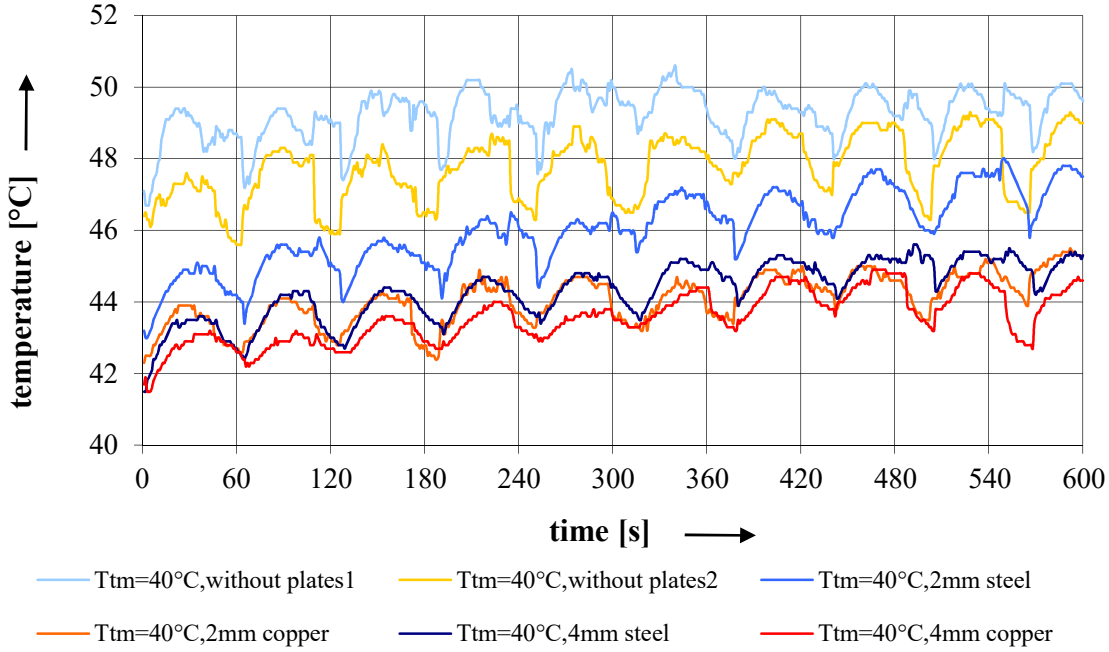

Fig. 3: Temperature field in the injection mould for different tempering methods at Ttm = 40 °C (Hejna, 2004).

3. Conclusions

From the time dependences of temperatures (see Figs. 1–3) it can be seen that when using thermal inserts in the injection mold, heat was removed from the shaped cavity of the injection mold in both measured locations, due to their greater ability to accumulate heat than the mold material. At the temperature of the tempering medium Ttm = 20 °C, more heat was removed from the shaped cavity of the injection mold than at the temperature Ttm = 40 °C and Ttm = 60 °C. There is also slightly greater heat dissipation with copper thermal inserts than with steel ones, which is due to the higher thermal conductivity of copper (Hejna, 2004).

An interesting and important finding is the finding that when thermal inserts are used in the tool, the difference between the maximum and minimum temperature of the mold decreases.

Disadvantages of measuring the temperature field in the injection mold by the non-contact method using thermocouples include the disturbing effects of the hydraulic mechanism of the injection press. Although a galvanically isolated converter was used and the thermocouples were placed in a steel jacket, it was not possible to eliminate these effects. Among the other external influences that caused the course of the curves to oscillate, we can consider the opening of the barrier in the closing unit of the injection press, the operation of the pump during the plasticization of a new batch of material and, in particular, the movement of the moving part of the mold. Unfortunately, even after the introduction of additional filtering of the measured values to suppress interfering signals, the adverse effects were not eliminated (Hejna, 2004).

Acknowledgement

First of all, I would like to thank my parents for their full support during my doctoral studies at the University of West Bohemia in Pilsen.

I also thank all the members of the Department of Machining Technology. In particular, I would like to thank Professor Holešovský for his professional guidance in writing this article, for his valuable comments and suggestions for its publication.

References

Hejna, M. (2004) *Thermal inserts in injection moulds and their effect on mechanical properties*. Diploma thesis, TU Liberec.

30th International Conference
ENGINEERING MECHANICS 2024
Milovy, Czech Republic, May 14 – 16, 2024

STRESS-STRAIN ANALYSIS OF THE EFZ–22 SAND FILTER PRESSURE VESSEL

Houfek M.*, Šimáček F.**

Abstract: *Non-heat able pressure vessels appear on a large scale in engineering practice. In the field of water supply, i.e. in water treatment plants, this is one of the basic characteristics for a closed filter container. It is therefore obvious that there is a need to devote more attention to this discipline in terms of construction, calculations of individual shapes, attachments, penetrations and the establishment of these structural devices. The company Envites (www.envites.cz) is engaged in the market from designing, calculating up to the in-house production of individual products that serve as technologies for water and sludge treatment. One of the main aspects is the separate calculation of the pressure part of the vessel. In many cases, it is a pressurized, insoluble container of larger volumes and weights. In this post, we will deal with the calculation for three pressure vessels and show the calculation procedure on one of these vessels. These two containers are designed as sand filters for industrial water filtration, which is used in industrial facilities.*

Keywords: Envites, pressure vessel, shell, numerical calculation, EFZ–22 sand filter.

1. Introduction

One of the essential raw materials for industry is water. In the field of industry, however, it is not water that is obtained only from wells or rivers. It is necessary to adjust this water so that it meets the specified input parameters for possible further use in engineering. It is thus the removal of unwanted elements, minerals and microbes from the water, which under the given conditions lead to damage or the subsequent disposal of machinery. Another possible source of water is from waste parts of the operation. The water obtained in this way needs to be technologically processed so that its parameters correspond to the input requirements for the given technology. One of the basic and suitable treatments is pressure sand filtration. The efficiency of vertical pressure filters is determined by the grain size of the sand used as filling. The grain size ranges from 0.6 mm to 1.2 mm. The average capture of impurities in the given grain size range is up to 40 μm. In order for the equipment designed in this way to work flawlessly, it is necessary to design the steel pressure vessel correctly. The basic dimensions of the pressure vessel are determined by the input parameters, which are the filter area, the working pressure and the required volume of the filtered medium. These parameters will affect both the size and the thickness of such a container.

Another influence on the pressure vessel is given by the technical location of the vessel, connection holes (necks), weight, etc. All the required input parameters were taken when the design was entered.

2. Methods

The design of the steel part of the pressure filter was carried out in two design steps. The ČSN EN 13445-3 (2018, 2021) standard was used for the design and analytical calculation, where the rough design of the pressure part of the vessel, which is the cylindrical shell and toro spheric bottoms, was carried out using empirical relationships (1–10).

* Ing. & Ing. Martin Houfek, PhD.: Envites company, water, construction department, Vídeňská 120b, Brno 619 00, houfek@envites.cz

** Ing. František Šimáček: Company Envites, Managing Director of Envites, Vídeňská 120b, Brno 619 00, simacek@envites.cz

doi: 10.21495/em2024-122

Calculation of the nominal wall thickness of the pressure vessel:

$$e = \frac{p \cdot D_i}{2 \cdot f \cdot z - p} \tag{1}$$

For the geometry given p_{max}:

$$p_{max} = \frac{2 \cdot f \cdot z \cdot e_a}{D_m} \tag{2}$$

$$e_a = (e_{min} - c) \tag{3}$$

$$e_{min} = (e_{ex} + c + e) \tag{4}$$

Toro spherical bottom:

$$e_s = \frac{p \cdot R}{2 \cdot f \cdot z - 0{,}5 \cdot p} \tag{5}$$

$$e_y = \frac{\beta \cdot p \cdot (0{,}75 \cdot R + 0{,}2 \cdot D_i}{f} \tag{6}$$

$$e_b = (0{,}75 \cdot R + 0{,}2 \cdot D_i) . \left[\frac{p}{111 \cdot f_b} \cdot \left(\frac{D_i}{r} \right)^{\left(\frac{1}{1{,}5} \right)} \right] \tag{7}$$

Pressure loading of the toro spherical bottom:

$$p_s = \frac{2 \cdot f \cdot z \cdot e_a}{R + 0{,}5 \cdot e_a} \tag{8}$$

$$p_y = \frac{f \cdot e_a}{\beta \cdot (0{,}75 \cdot R + 0{,}2 \cdot D_i)} \tag{9}$$

$$p_b = 111 \cdot f_b \cdot \left(\frac{e_a}{0{,}75 \cdot R + 0{,}2 \cdot D_i} \right)^{1{,}5} \cdot \left(\frac{r}{D_i} \right)^{0{,}825} \tag{10}$$

The geometry designed in this way needs to be verified by numerical calculation. An analysis of critical or risk points on the vessel's pressure jacket was performed using the finite element method. The identified locations were the junction of the cylindrical shell with the toro spheric bottoms and the large flanges that were inserted into the pressure vessel shell and into the toro spheric bottom. These openings can affect the stiffness of the designed geometry and a numerical calculation must be performed to determine whether it is necessary to propose a local increase in the thickness of the pressure vessel in the given areas, see Fig. 1. Discretization of the container was carried out, see Fig. 2. The results of the stress-strain analysis (Ondracek, 2006) were evaluated and entered in Tab. 1. Further, the individual results of stress and deformation of critical points on the pressure vessel are shown in Figs. 3–9.

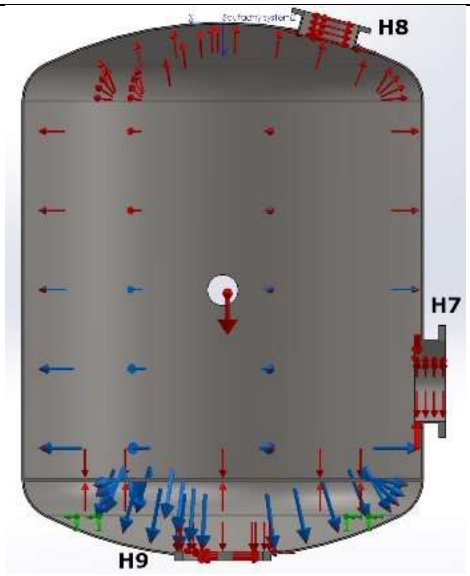

Fig. 1: Defined boundary conditions.

Fig. 2: Container discretization.

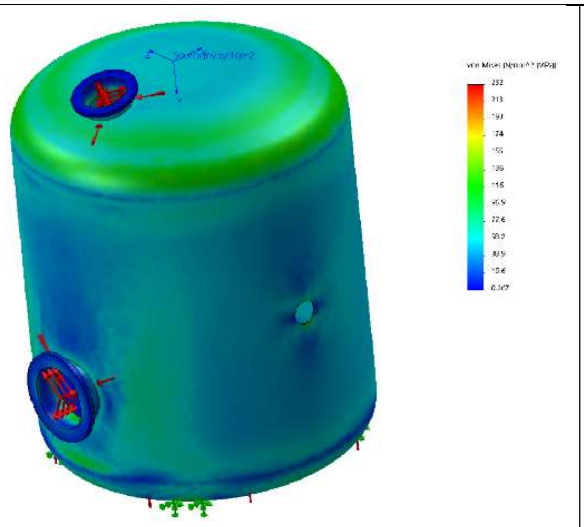

Fig. 3: Von Mises stress on the filter shell – overpressure 0.5 MPa.

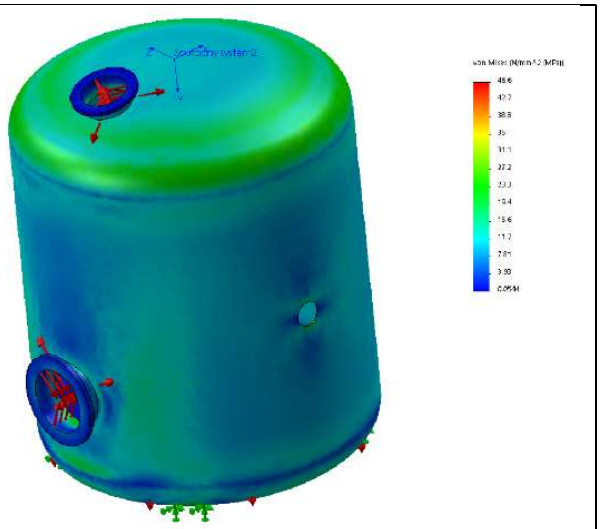

Fig. 4: Von Mises stress on the filter shell – vacuum 0.1 MPa.

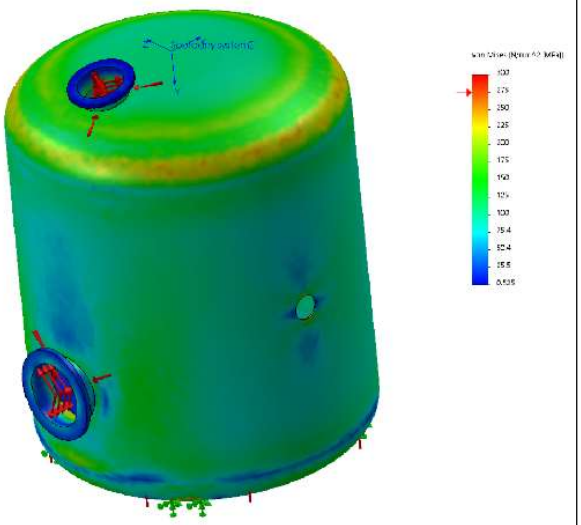

Fig. 5: Von Mises stress on the filter shell – overpressure 0.95 MPa.

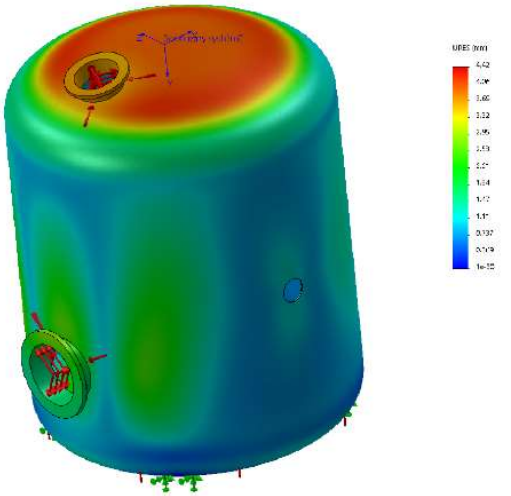

Fig. 6: Total deformation on the filter shell – overpressure 0.95 MPa.

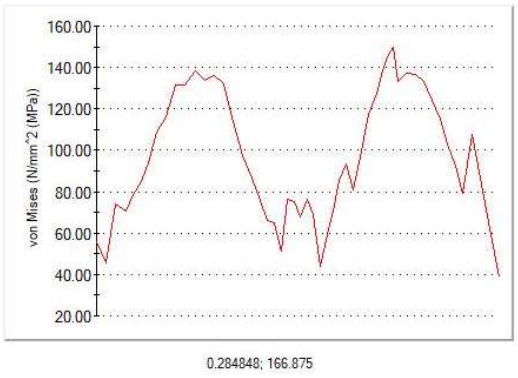

Fig. 7: Von Mises stress around the circumference of the H7 flange – overpressure 0.95 MPa

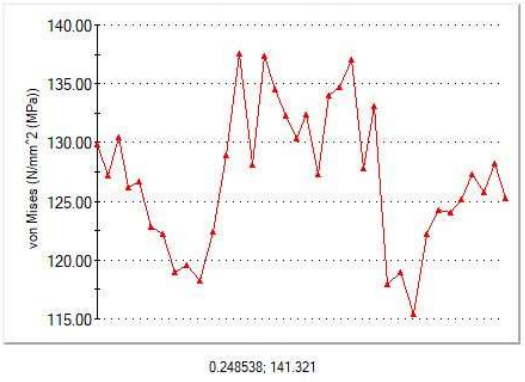

Fig. 8: Von Mises stress around the circumference of the H8 flange – overpressure 0.95 MPa.

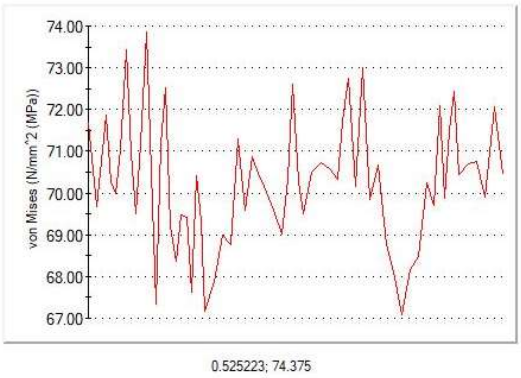

Fig. 9: Von Mises stress around the circumference of the H9 flange – overpressure 0.95 MPa.

Load states	Flange H7	Flange H8	Flange H9
	[MPa]	[MPa]	[MPa]
Overpressure 0.5 MPa	120	120	38.9
Vacuum 0.1 MPa	15.8	7.76	14.5
Test pressure 0.95 MPa	150	135.5	73.8
Test pressure 0.95 MPa + hydro. pressure + gravity	152	137	74.1

Tab. 1: Maximum von Mises stress values on flanges H7, H8, H9 (see Figs. 3–5).

3. Conclusions

From the obtained results of the numerical simulation evaluated in Tab. 1, it can be seen that at an operating overpressure of 0.5 MPa, in the critical places of the necks H7, H8 are below the determined yield limit of the material by 36 %, and at the neck H9, the value of the stress relative to the yield is 12 %. The value of the yield strength of the material used according to the documented material sheets is 340 MPa. The percentage difference is due to the construction of the H9 neck, which is reinforced with a strong ring. At full load (test pressure 0.95 MPa + hydro. pressure + own weight), the stress on the H7, H8 Throat increased by a percentage of 17 %. As can be seen from the numerical simulation results, the stress values are far below the yield point. During the design, a weld joint coefficient of 0.7 was assumed, which is the value when the weld does not pass NDT, and thus the main weld joints on the pressure vessel move in the safe area. At maximum load, the total deformation on the pressure part of the vessel is 4.27 mm, see Fig. 6. The calculated nominal thickness of the pressure part of the container was determined according to the normative results to a value of 5 mm.

Acknowledgement

In this way, I would like to thank the company Envites spol. s.r.o., Vídeňská 264/120b, 619 00 Brno for allowing me to prepare a contribution and financing the necessary costs associated with this contribution.

References

ČSN EN 13445-3 *Non-heatable pressure vessels – Part 3: Design and calculation* (2018), Office for Technical Standardization, Metrology and State Testing, 700 p., (in Czech).

ČSN EN 13445-3 *Non-heatable pressure vessels – Part 5: Inspection and testing* (2021) Office for Technical Standardization, Metrology and State Testing, 87 p., (in Czech).

Ondracek, E., (2006) *Mechanics of bodies: elasticity and strength II*. 4th edition, reprint, *Academic Publishing House CERM*. Brno, (in Czech).

30th International Conference
ENGINEERING MECHANICS 2024
Milovy, Czech Republic, May 14 – 16, 2024

GALLOPING OF INSULATED BUNDLED OVERHEAD LINE SIMPLIFIED ANALYSIS

Hračov S.*, Macháček M.**

Abstract: *Our paper provides an analysis of the susceptibility of a particular bundled overhead line to galloping. It presents a case study of an aerial bundled cable, consisting of four conductors insulated by polyethylene, and used for low-voltage power lines. The susceptibility to loss of stability is analyzed for cable without and with simulated icing observed on similar real conductors. In the first case, the proneness to galloping was excluded based on the results of CFD simulation and the Den Hartog criterion. In latter case, the possible occurrence of galloping was confirmed. The critical wind velocity for the ice-covered cable was calculated utilizing quasi-steady theory. Finally, the amplitudes of limit cycle oscillation for supercritical wind speeds were estimated based on simplified numerical analysis.*

Keywords: Aerial bundled cable, wind effects, galloping, limit cycle oscillation.

1. Introduction

Due to the wind action, electrical overhead conductors often lose their aeroelastic stability in the form of galloping. Galloping is a low-frequency self-excited oscillation with amplitudes reaching up to several times the sag, most often in a plane perpendicular to the wind direction see Holmes (2018). Galloping generally cannot occur at conductors with symmetrical circular cross sections. However, especially in the winter ice accretion can significantly change their geometric cross-sections leading to a loss of stability and excessive amplitudes of limit cycle oscillation. According to a document by EPRI (2006), the occurrence of galloping was most often observed in mode shape with one to three loops.

In this paper, the specific insulated bundled cable with very low tension force is analyzed in terms of proneness to galloping with and without the effect of icing see Fig.1. The properties of this short-span low - voltage bundled line consisting of four main conductors are summarized in Tab. 1

Fig. 1: Bundled overhead line – axonometric view, cross-section and ice-covered cross-section.

2. Assessment of proneness to galloping

The necessary condition for the occurrence of self-excited oscillation – galloping, based on quasi-steady theory of a general profile, can be expressed by the Den Hartog criterion:

$$C_D(\alpha) + \frac{dC_L}{d\alpha}(\alpha) < 0 \tag{1}$$

* Ing. Stanislav Hračov, PhD.: Institute of Theoretical and Applied Mechanics of the Czech Academy of Sciences, Prosecká 809/76; 190 00, Prague; CZ, hracov@itam.cas.cz

** Ing. Michael Macháček, PhD.: Institute of Theoretical and Applied Mechanics of the Czech Academy of Sciences, Prosecká 809/76; 190 00, Prague; CZ, machacek@itam.cas.cz

doi: 10.21495/em2024-126

where C_D and C_L represent the aerodynamic drag and lift coefficients, respectively, and α represents the angle of attack, which is defined in Fig. 2.

Parameter	Value
Horizontal distance of suspension points	21.1 m
Vertical distance of suspension points	1.55 m
Diameter of circumscribed circle of bundled line (D)	38 mm
Cross-sectional are of line	465.28 mm^2
Young's modulus (E)	57 GPa
Mass per unit length of line (with ice accretion)	1.69 kg/m (2.09 kg/m)
Horizontal component of tension force for: -5 °C (-5 °C with ice accretion)	930.3 N (1 149.5 N)

Tab. 1: Geometrical and mechanical properties of electric line (AES 4 x 120).

These aerodynamic coefficients of the cable related to various α are depicted in Fig. 2. The left part of this figure presents coefficients for the cable without ice accretion, while the right part values for the ice-covered line. The data related to the cable itself were determined by CFD simulation in Comsol MultiPhysics, while the aerodynamic coefficients for the cable with icing were adopted from Desai et al. (1995). The assessment of susceptibility to galloping was evaluated for several angles of attack by means of the Den Hartog criterion, which is also graphically represented in Fig. 2 by the black line. The results indicate that the conductor without icing is not prone to galloping, as shown in Fig. 2, where the black line is above the zero for the entire range of angles α. On the other hand, angular intervals of possible instability can be found for the iced-covered cable. The minima of the curve in Fig. 2 representing the Den Hartog criterion correspond to the angles of attack, which are related to the lowest critical wind speeds. The angles α_c = 40.0 °, 179.3 ° and 187.5 ° were determined as critical from the viewpoint of the onset of galloping.

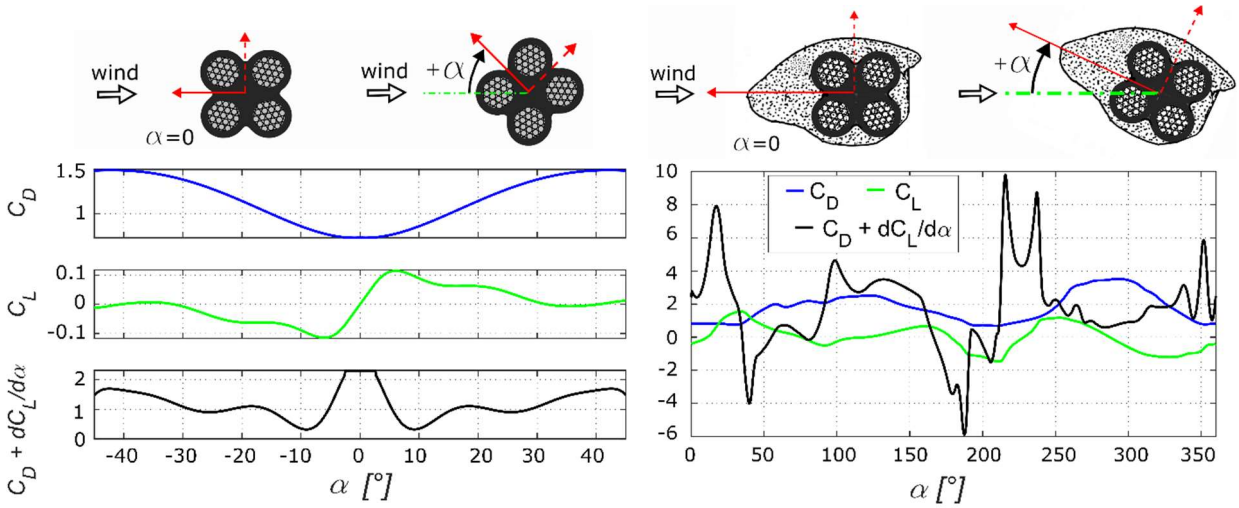

Fig. 2: Aerodynamic drag and lift coefficients, C_D and C_L , and the Den Hartog criterion for line without and with ice accretion as the functions of angle of attack α.

The estimate of critical wind speeds for the onset of self-excited transversal galloping-type oscillations of the line with icing having the cross-section related to angles α_c can be determined, as outlined in Païdoussi et al. (2010):

$$V_c(\alpha_c) = \frac{4 \cdot m \cdot \zeta \cdot 2\pi \cdot f_n}{-\left(\frac{dC_L}{d\alpha}(\alpha_c) + C_D(\alpha_c)\right) \cdot \rho \cdot D} \tag{2}$$

where m is the mass per unit length, ζ is the structural damping ratio, f_n is the natural frequency related to the in-plane natural mode i.e. mode in the plane of the static sag, ρ stands for air density and D represents the diameter of circumscribed circle of the bundled line. The wind direction is assumed horizontal.

The lowest critical wind velocity corresponds to the natural frequency of the lowest in-plane natural mode. For our bundled overhead line with ice accretion, it is the first asymmetric in-plane mode, which is depicted in Fig. 3 and corresponds to a very low frequency f_n = 1.105 Hz. This mode and its natural frequency were determined according to the solution in Madugula (2001), which is valid for taut cables with sag-to-span ration 1:8 or lower. In our case, this ratio is approximately 1:17. It should be noted that due to low tension force, the natural frequency of the first symmetric in-plane mode is higher than the above stated lowest in-plane natural frequency.

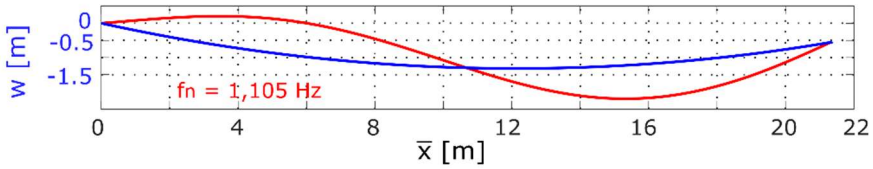

Fig. 3: Sag of the cable w, (blue curve) and the lowest natural in-plane mode (red curve).

Tab. 2 summarizes the estimated critical wind speeds for this lowest in-plane mode for three critical angles α_c. The structural damping ratio of the cable was assumed by low value $\zeta = 0.5$ %. The observed critical velocities are very low, so there is a realistic assumption of the occurrence of self-excited oscillation.

Angle of attack	α_c = 40.0 °	α_c = 179.3 °	α_c = 187.5 °
Critical wind speed	1.59 m/s	1.85 m/s	1.08 m/s

Tab. 2: Critical wind speeds V_c for galloping of bundled overhead line with ice accretion.

3. Simplified calculation of limit cycle oscillation

The simplified calculation of the post-critical steady response is based on the assumptions of the quasi-steady theory. The harmonic oscillation of the line in the plane of the sag i.e. perpendicular to the direction of the wind in the lowest in-plane natural mode $y_n(x)$ is considered:

$$y(x,t) = A \cdot y_n(x) \cdot \sin(2\pi \cdot f_n \cdot t) \tag{3}$$

where A is amplitude of the limit cycle, x is longitudinal coordinate of the rope, $x \in (0, L)$, L is the length of the rope and t stands for time. Only in-plane motion of the cable is thus assumed, so the axial and along-wind motions as well as rotation are neglected. The Max normalization of natural mode $y_n(x)$ is used in Eq. (3). The estimation of the level of steady oscillation of the line at supercritical wind speeds is based on the assumption of equality of work, W_d, done by the structural dissipative forces, F_d, and work, W_w, done by the aerodynamic forces, F_y, acting on the oscillating line during one natural period T_n:

$$W_d = \int_0^L \int_0^{Tn} F_d\left(\dot{y}(x,t)\right) \cdot dy(x,t) \cdot dx = W_w = \int_0^L \int_0^{Tn} F_y\left(\dot{y}(x,t)\right) \cdot dy(x,t) \cdot dx \tag{4}$$

The structural damping force acting on a differential length of the cable dx at point x is considered viscous, i.e. proportional to the line velocity $\dot{y}(x,t)$:

$$F_d\left(\dot{y}(x,t)\right) \cdot dx = 4\pi \cdot f_n \cdot \zeta \cdot m \cdot \dot{y}(x,t) \cdot dx \tag{5}$$

The aerodynamic force acting on a differential length dx at point x in the direction perpendicular to the wind direction can be expressed as

$$F_y\left(\dot{y}(x,t)\right) \cdot dx = 0{,}5 \cdot \rho \cdot V^2 \cdot D \cdot \left(-\sec\left(\alpha_r(x,t)\right) \cdot \left(C_L\left(\alpha_c + \alpha_r(x,t)\right) + C_D\left(\alpha_c + \alpha_r(x,t)\right) \cdot \tan\left(\alpha_r(x,t)\right)\right)\right) \cdot dx \tag{6}$$

where V represents the supercritical wind speed, which is considered constant along the whole cable and $\alpha_r(x,t)$ is the angle of attack of the relative wind at point x:

$$\alpha_r(x,t) = \tan^{-1}\left(\dot{y}(x,t)/V\right) \tag{7}$$

By substituting the expressions from Eq. (5) and Eq. (6) and differential $dy(x,t)$

$$dy(x,t) = 2\pi \cdot f_n \cdot A \cdot y_n(x) \cdot \cos(2\pi \cdot f_n \cdot t) \cdot dt \tag{8}$$

into Eq. (4), the supercritical wind speed V can be numerically evaluated from Eq. (4) for the chosen value of the amplitude, A. The oscillation amplitudes, as functions of wind speed for selected critical angles α_c of the analyzed line from Tab. 2, calculated according to this approach are shown graphically in Fig. 4.

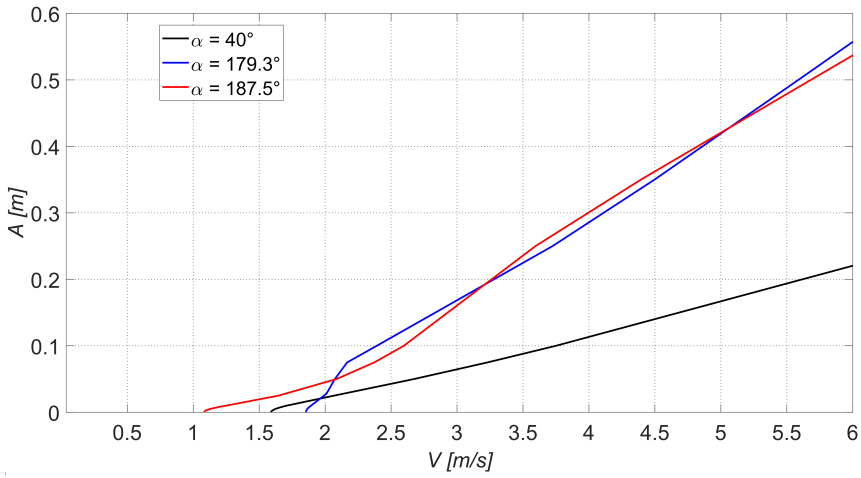

Fig. 4: Amplitude of limit cycle oscillation as function of wind speed.

4. Discussion of the results and conclusions

The numerical simulations confirmed the predicted critical wind speeds given in Tab. 2. The calculated amplitudes of the steady-state response are significant even for low wind speeds. Especially, the predicted wind effects for both angles around 180 ° are extreme, and the amplitudes in these cases reach almost half of the static sag for wind speed around 6 ms^{-1}. However, considering the very low static forces of this cable, it is rather impossible to assume that such amplitudes for higher wind velocities will be reached. During these predicted substantial limit-cycle oscillations, the dynamic normal forces in the cable are not negligible compared to static tensile force. This fact completely changes the prerequisite of harmonic character of the response and mainly the assumption of linearity of the mechanical system. A more sophisticated 3D FEM model, respecting the geometrical nonlinearity of the system, must be used to solve the self-excited excited vibration of this low-tensioned cable. The outputs from the simplified analysis with a linearized model used in this paper can serve only for the estimation of the onset of galloping-type instability.

The results of this analysis nevertheless served also for controlling, comparative purposes and calibrations during the creation of 3D FEM model. This complex model includes geometrical nonlinearity of the problem and incorporates bending stiffness, which improves the stability of calculations and the precision of results. Detailed information about the model and comparison with the results of this simplified approach are presented in another paper of authors; see Macháček and Hračov (2024).

Acknowledgement

The kind support of Czech Scientific Foundation project No. 24-13061S is gratefully acknowledged.

References

Desai, Y. M., Yu, P., Popplewell, N. and Shah, A. H. (1995) Finite element modelling of transmission line galloping, *Computers & Structures*, 57, 3, pp. 407–420.

EPRI (2006) *Transmission Line Reference Book - Wind Induced Conductor Motion.*

Holmes, J. D. (2018) *Wind Loading Structures*, CRC Press, 3rd edition.

Madugula, M. K. S. (2001) *Dynamic Response of Lattice Towers and Guyed Masts*, ASCE.

Macháček, M. and Hračov, S. (2024) Galloping of insultated bundled overhead line – Nonlinear numerical analysis in time domain, In: *Proc. of 30th Con*ference *Engineering mechanics 2024.* Milovy, pp. 190–193.

Païdoussis M., Price S. J., de Langre E. (2010) Fluid-Structure Interactions: Cross-Flow-Induced Instabilities. Cambridge University Press.

30th International Conference
ENGINEERING MECHANICS 2024
Milovy, Czech Republic, May 14 – 16, 2024

MANIPULATOR TRAJECTORY AND WORKSPACE IN THE MATLAB AND MSC ADAMS ENVIRONMENTS

Hroncová D.[*], Delyová I.[**], Sivák P.[***], Prada E.[†]

Abstract: *The contribution is dedicated to computer modelling and its application in the design of mechanical systems with a focus on manipulator and robot models. This article discusses the use of Matlab/Simulink and MSC Adams/View programs in the design and subsequent analysis of a robot model. Attention is given to direct and inverse kinematics. We provide an example of solving inverse and direct kinematics, as well as an example of using the Adams program in the design and simulation of a mobile robot.*

Keywords: Direct kinematics, inverse kinematics, simulation, trajectory, workspace.

1. Introduction

The first steps in robotics were robots with a fixed platform for manipulation tasks (Fig. 1a). The mechanisms of industrial robots and manipulators consist of bodies that form various types of kinematic chains. This has been addressed by numerous authors (Siciliano and Khatib, 2008; Murray et al., 1994; Khalil and Dombre, 2002). In most cases, these mechanisms represent open or mixed kinematic chains. Two bodies of a kinematic chain interconnected so that their mutual mobility is limited form a kinematic pair (Fig. 1a–c). Depending on the type of kinematic constraint in the kinematic pair, kinematic chains are composed of translational or rotational kinematic pairs. When designing mechanisms such as industrial robots, reliable calculation of the relevant kinematic quantities is necessary. These quantities then allow further scaling of individual parts of the mechanism. To achieve this goal, we use simulation models and computer modelling (Swevers et al., 2007).

In the first part of the paper, we delve into the theory of simple open kinematic chains, which are utilised in the construction of various manipulators and robots. We describe the method of determining angular quantities of an open kinematic chain with two links by solving inverse kinematics. The trajectory of the end effector is determined by a fifth-degree polynomial. Subsequently, the angular quantities are determined by solving inverse kinematics. The direct kinematic task is used to determine the workspace. Workspaces are provided for various angular constraints at the manipulator's joints.

In the second part, MSC Adams-View software is used for the design and optimization of the trajectory of a two-link robotic arm (Frankovský et al., 2012, Delyová et al., 2014). Simulation software like MSC Adams is an excellent tool for dynamic analysis of various complex interconnected mechanical systems, being fast and very efficient (Vavro et al., 2017). It allows for evaluating the results in graphical form (Tedeschi et al., 2017). In the final section of the paper, we assess the results of the kinematic analysis.

[*] Ing. Darina Hroncová, PhD.: Faculty of Mechanical Engineering, Technical University of Košice, Letná 9; 042 00, Košice; SK, darina.hroncova@tuke.sk

[**] Assoc. Prof. Ing. Ingrid Delyová, PhD.: Faculty of Mechanical Engineering, Technical University of Košice, Letná 9; 042 00, Košice; SK, ingrid.delyova@tuke.sk

[***] Assoc. Prof. Ing. Peter Sivák, PhD.: Faculty of Mechanical Engineering, Technical University of Košice, Letná 9; 042 00, Košice; SK, peter.sivak@tuke.sk

[†] Ing. Erik Prada, PhD.: Faculty of Mechanical Engineering, Technical University of Košice, Letná 9; 042 00, Košice; SK, erik.prada@tuke.sk

doi: 10.21495/em2024-130

2. Direct and inverse analysis

This part of the paper demonstrates the solution to the direct and inverse kinematic tasks. The model of a two-link robotic arm is used. This two-link manipulator can be found, for example, in Scara manipulators shown in Fig. 1b). The manipulator workspace is also illustrated. The inverse kinematics task is to determine the angular coordinates of the actuators given the coordinates of the end effector position. Eqs, (1) and (2) are used. The solved Scara model belongs, in terms of kinematics, to simpler models and we can solve it analytically. The solution will be based on the scheme of the two-link robotic arm in Fig. 2a–c and Eqs. (1) and (2).

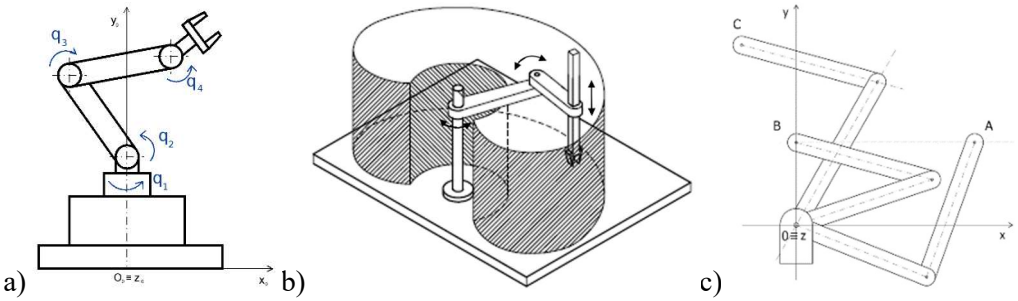

Fig. 1: a) Model of the 4R manipulator, b) Scara manipulator with workspace, c) two link manipulator.

The manipulator consists of arms with lengths $L_1 = 0.22$ [m] and $L_2 = 0.19$ [m], fixed to a solid base. This could be a stand or the arms could be on a mobile chassis, if it were a service robot. A manipulator with a fixed base and two arms has 2 degrees of freedom. We will investigate the motion of the two arms of the manipulator in the plane in Fig. 2a–b.

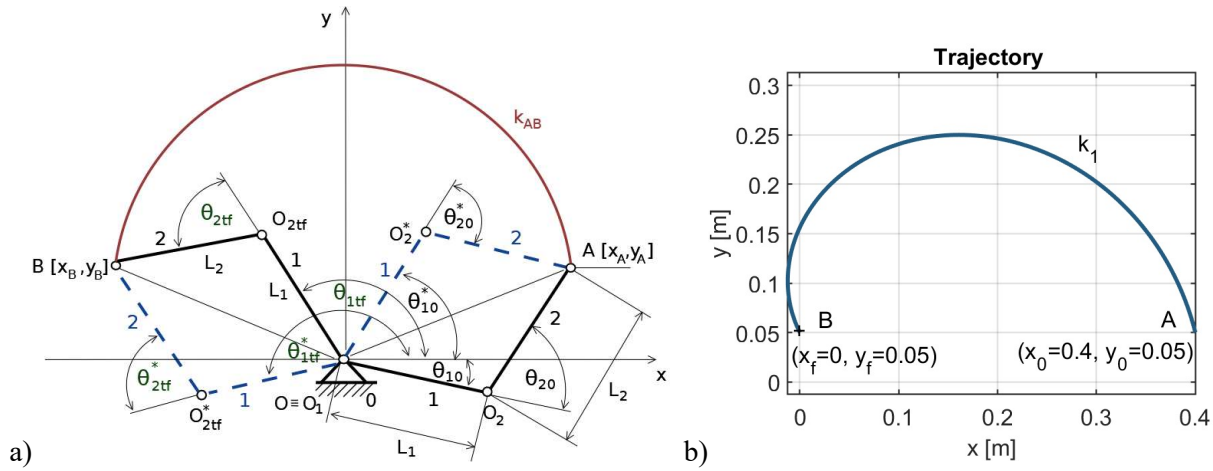

Fig. 2: Model of the two arm manipulator with angles θ_{1t0}, θ_{2t0}, θ_{1tf}, θ_{2tf} and with trajectory k_{AB}.

The rotation angle in individual kinematic pairs is denoted by angles θ_1, θ_2 according to Fig. 2a. Each link is assigned a coordinate system 0_i, x_i, y_i, z_i, and each joint is assigned a generalized coordinate q_i, which is defined along the axis of rotation (Fig. 2a). Generalized coordinates determine the instantaneous position of the body. We denote them as q_1, q_2 (Fig. 2a). It holds for generalized coordinates $q_1 = \theta_1$, $q_2 = \theta_2$. We assume that the drives are located in rotational kinematic pairs.

To determine the angles, we will use the Eqs. (1) and (2) provided below. There is typically more than one solution, as seen in Fig. 2a. We will address the task during the movement of the end effector of the second arm, between the individual points A, B, C, D, E according to Fig. 3a–c. The conversion of coordinates x_A, y_A using generalized coordinates θ_1, θ_2 stems from the geometry shown in Fig. 1a:

$$x_A = L_1 \cdot cos(\theta_1) + L_2 \cdot cos(\theta_1 + \theta_2) \tag{1}$$

$$y_A = L_1 \cdot sin(\theta_1) + L_2 \cdot sin(\theta_1 + \theta_2) \tag{2}$$

With the known position of x_A and y_A, the solution for the two unknown angles θ_1 and θ_2 is determined by solving the two equations (1) and (2). This involves solving the inverse kinematics problem.

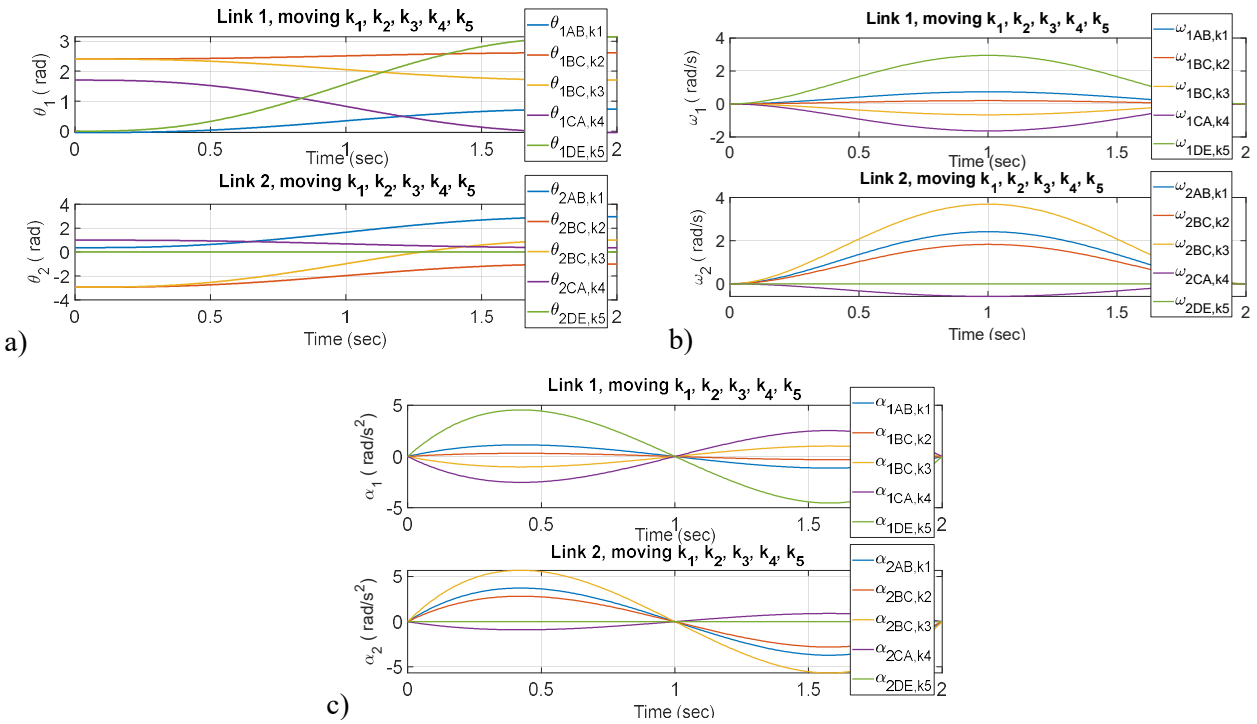

Fig. 3: The progression of angular quantities during individual movements along curves k_1 to k_5.

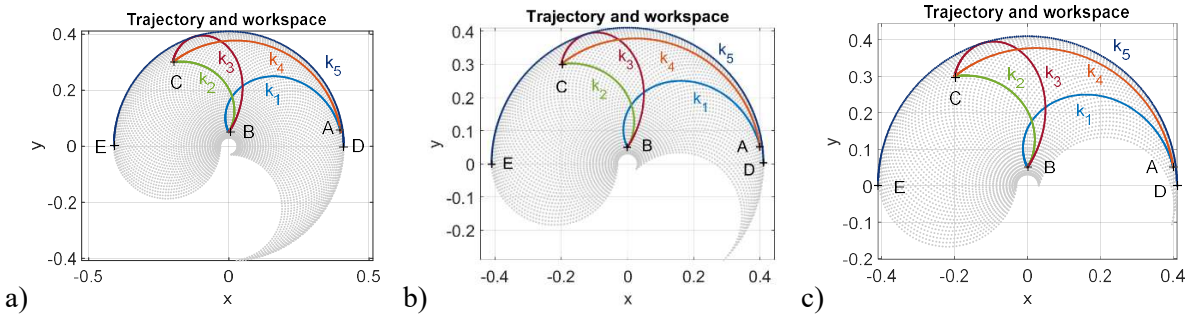

Fig. 4: The diagram of the trajectories k_1, k_2, k_3, k_4, k_5 and the workspace.

3. Simulation using MSC Adams

The improvement in computing technology has led to the development of computer methods in the field of complex spatial mechanical systems. MSC Adams employs an object-oriented programming environment with animated simulation. It simulates complex mechanical systems with multiple degrees of freedom. Models are defined directly by the geometry of individual bodies and their kinematic constraints, driving forces, and motion generators. We present a simulation of a robot in MSC Adams.

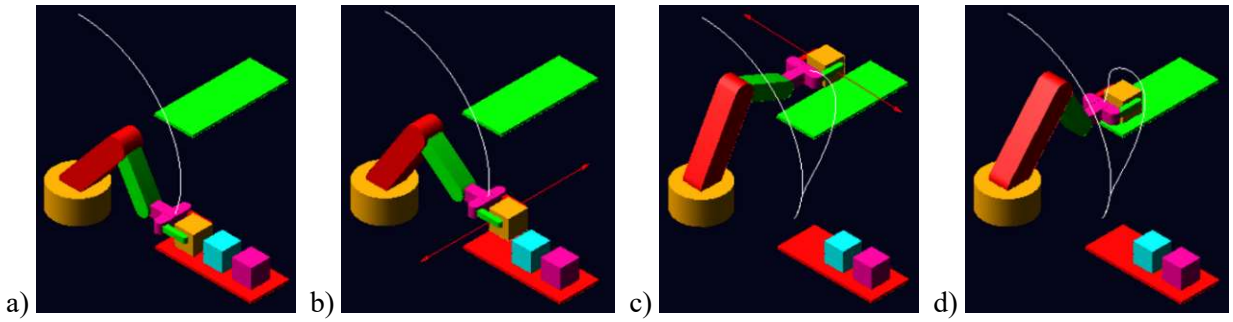

Fig. 5: Time plots of trajectories.

Computer modelling of prototypes is a highly convenient tool for creating, processing, editing, and presenting simulation results in the form of graphs. Graphs of output variables allow for viewing real-time values of measured quantities during the simulation itself (Fig. 6a-d). With multibody modelling

software, there's no need to solve mathematically described motion with equations of motion. We only utilize information about the geometric parameters of the designed model. An example of a manipulator model is shown in Fig. 6a-d, illustrating various views of the manipulator simulation model in the MSC Adams View program during multibody modelling with depicted end-point trajectories.

The progression of angular rotation and angular velocity determined by simulation in the program is processed by the Postprocessor, and the graphs are shown in Fig. 6.

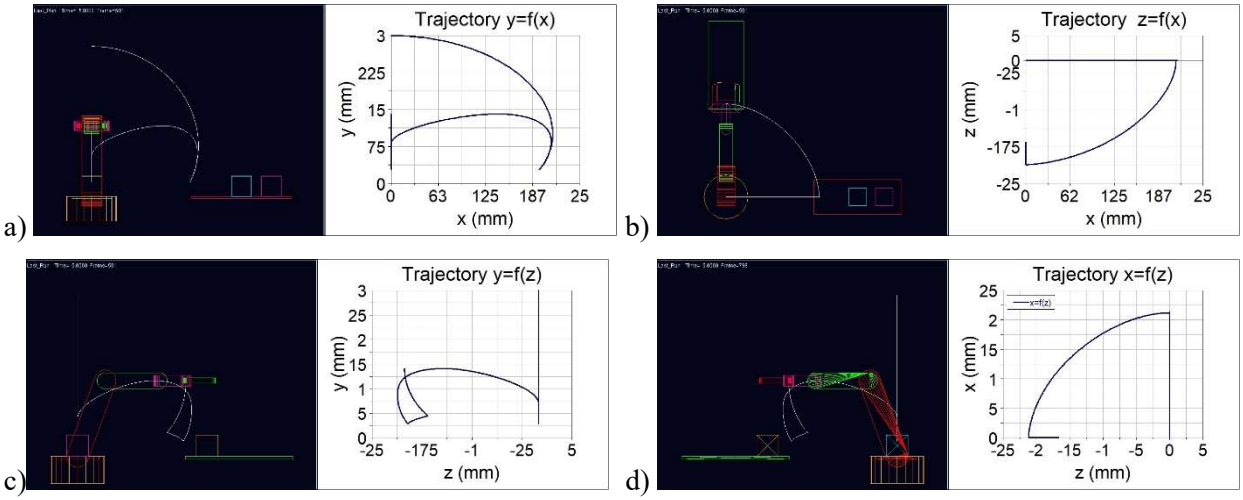

Fig. 6: Relations of kinematic quantities of member 1 of the bound system.

4. Conclusion

The article presented the kinematic analysis of a two-link manipulator using simulation in Matlab and MSC Adams/View. The direct and inverse tasks are solved in Matlab. The results are depicted in the form of time diagrams of the investigated variables. The trajectories of motion and workspace are shown. MSC Adams provides tools for virtual prototyping, model visualization, and easier evaluation of the obtained results. It allows simulating the motion of multibody mechanical systems, making it a suitable aid for teaching and practice. The contribution of this work is mainly didactic, particularly in the field of applied mechanics and mechatronics, presenting the possibility of computer simulation.

Acknowledgement

This work was supported by the Ministry of Education of Slovakia Foundation under Grant project VEGA No.1/0342/24, VEGA No.1/0152/24, VEGA No.1/0436/22, KEGA No.027 TUKE-4/2022.

References

Delyová, I., Hroncová, D. and Frankovský, P. (2014) Analysis of simple mechanism using MSC Adams. *Manufacturing Technology*, 14(2), 141–145.

Delyová, I., Hroncová, D., Sivák, P. and Beliško, M. (2013) The dynamic analysis of cam mechanism. *American Journal of Mechanical Engineering*, 1(7), 266–270.

Frankovský, P., Hroncová, D., Delyová, I. and Hudák, P. (2012) Inverse and forward dynamic analysis of two link manipulator. *Procedia Engineering*, 48, 158–163.

Khalil, W. and Dombre, E. (2002) Modeling, Identification and Control of Robots. London: Hermes Penton Ltd.

Mickoski, H., Mickoski, I. and Djidrov, M. (2018) Dynamic modeling and simulation of three-member robot manipulator. *Mathematical Models in Engineering*, 4(4), 183–190.

Murray, R. M., Li, Z. and Sastry, S. S. (1994) *A Mathematical Introduction to Robotic Manipulation*. California. University of California. CRC Press.

Siciliano, B. and Khatib, O. (2008) *Handbook of Robotics*. Heidelberg, Berlin Springer-Verlag.

Swevers, J., Verdonck, W. and De Schutter, J. (2007) Dynamic model identification for industrial robots. *IEEE control systems magazine*, 27(5), 58–71.

Tedeschi, F. and Carbone, G. (2017) Design of a novel leg-wheel hexapod walking robot. *Robotics*, 6(4), 40.

Vavro jr, J., Vavro, J., Kováčiková, P., Bezdedová, R. and Híreš, J. (2017) Kinematic and dynamic analysis and distribution of stress in items of planar mechanisms by means of the MSC ADAMS software. *Manufacturing technology*, 17(2), 267–270.

30th International Conference
ENGINEERING MECHANICS 2024
Milovy, Czech Republic, May 14 – 16, 2024

MODELLING OF LEADING EDGE MORPHING BY USING GEOMETRICALLY EXACT BEAM THEORY

Hrstka M.[*], **Bajer J.**[**], **Hadaš Z.**[***], **Sharif Khodaei Z.**[†], **Aliabadi F.**[††], **Kotoul M.**[†††]

Abstract: *The goal of the presented work is to demonstrate a capability of a non-linear computational model for a leading edge morphing based on the geometrically exact Timoshenko beam theory implemented in the finite element method. The leading edge topology is divided into outer surface with various bending and tension response along the element centre line and kinematic mechanism. Their interconnection is realized by joints, in the computational model realized by the Lagrange multiplier technique. Loading is realized by prescribed moment in one mounting node which represents an electric servomotor. In the results section, beam resultants dependent on the various initial configuration of the kinematic mechanism are analysed.*

Keywords: **Morphing wing, geometrically exact beam, finite element method, non-linear analysis, Lagrange multiplier method, meta-materials.**

1. Introduction

Wing morphing has been used in aeronautical engineering since the Wright brothers controlled the course of their Flyer by manually manipulating wing surfaces. Generally, wing morphing is a concept of the airfoil shape modification in order to improve aerodynamic properties and system performance over the aircraft's nominal flight envelope. There are various morphing concepts, such as camber or wingspan modifications, active twist or sweep changes. The presented study is focused on the leading edge morphing of one wing segment, where the construction on the airfoil includes three main parts – a central box, a leading edge and a trailing edge (see Fig. 1a). There are numerous approaches dealing with wing morphing, e.g. topological optimization Gu et al. (2021); Achleitner et al. (2019); Dexl et al. (2020) or design of a kinematic mechanism with non-zero degrees of freedom Li et al. (2022); Sun et al. (2022). The usage of classical materials in aeronautical engineering as aluminium alloys or Duralumin are limited by bending deflection which relies on the yield strength and the cross section thickness. This is sometimes in contrast with other requirements, e.g. with ability to withstand aero-static and aerodynamic loads and with bending rigidity or buckling. This contradictory requirements can be treated by using meta-material structures with mechanical properties that can be tailored according to the operational conditions, Olympio and Gandhi (2010a,b). This work focuses on the design of the kinematic mechanism (the topology and functional principle is depicted in Fig. 1c) by using simplified geometrically exact beam model where the non-linear problem is solved by the finite element method, based on the studies of Reissner (1972); Simo (1985); Wood and Zienkiewicz (1977).

[*] Ing. Miroslav Hrstka, PhD.: Institute of Solid Mechanics, Mechatronic and Biomechanics, Brno University of Technology, Technická 2896/2; 616 69, Brno; CZ, miroslav.hrstka1@vutbr.cz

[**] Ing. Jan Bajer: NCC MESTEC - Cybernetics and Robotics Division, Brno University of Technology, Technická 2896/2; 616 69, Brno; CZ, Jan.Bajer@vutbr.cz

[***] Assoc. Prof. Zdeněk Hadaš, PhD.: Institute of Automation and Computer Science, Brno University of Technology, Technická 2896/2; 616 69, Brno; CZ, hadas@fme.vutbr.cz

[†] Prof. Zahra Sharif Khodaei, PhD.: Department of Aeronautics, Imperial College London, Exhibition Rd, SW7 2AZ South Kensington, London, UK, z.sharif-khodaei@imperial.ac.uk

[††] Prof. M H Ferri Aliabadi, FRAeS, FIMA, CEng, CMaths: Department of Aeronautics, Imperial College London, Exhibition Rd, SW7 2AZ South Kensington, London, UK, m.h.aliabadi@imperial.ac.uk

[†††] Prof. RNDr. Michal Kotoul, DSc.: Institute of Solid Mechanics, Mechatronic and Biomechanics, Brno University of Technology, Technická 2896/2; 616 69, Brno; CZ, kotoul@fme.vutbr.cz

doi: 10.21495/em2024-134

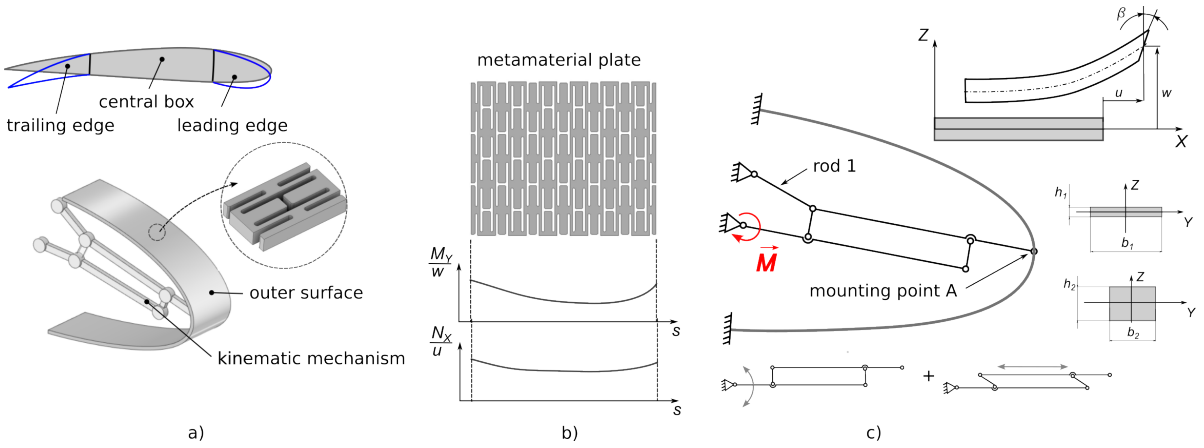

Fig. 1: a) NACA 2412 airfoil and leading edge geometry and mechanism illustration, b) meta-material plate with varying cell bending response, c) wire model of the morphing wing assembly.

2. Methods

Implementing meta-materials in the morphing wing design requires multi-disciplinary modelling approach due to the generally anisotropic and heterogeneous behaviour of these structures. They are valuable for their large bending flexibility. An example of such meta-material in shown in Fig. 1b. The graphs below show dependence of the bending and tensional stiffness along the meta-material plate. Thus, when a optimization is used to find an optimal material properties of the outer surface and topology of the kinematic mechanism dependent on the prescribed external loading, it is convenient to find a suitable simplification of the computational model to speed-up the process and suppress the model quantities that can be designed afterwards.

The presented computational model deals with morphing of the the leading edge. The wing segment geometry is depicted in Fig. 1c. The leading edge is simplified into two regions - the outer surface and the kinematic mechanism, mounted at the central box.

The solution process of the design loop within the BAANG project and resides in determination of the optimal material properties, i.e. a bending and axial stiffness of the outer surface and topology of the kinematic mechanism and its mounting points position according to the desired morphed airfoil shape resulting from the aero-elastic optimization. The presented study represent the initial part, i.e. determination of the mechanical response.

The mechanical behaviour of both outer surface and kinematic mechanism are simulated with the finite element method (FEM) by using geometrically exact Timoshenko beam and finite strain theory, as the nominal deflections are significant. Let us consider a leading edge geometry in the X-Z plane represented by beams with material parameters and geometry of the cross section (see Fig. 1c). No out-plane loading is considered. The geometry is meshed with the prescribed element length. Every element is then represented by a straight beam spatially oriented in the reference coordinate system X-Z. Motion of the beam to the deformed coordinate system (denoted by x-z) is described in Simo (1985); Reissner (1972)

$$x = X + u(X) + Z\sin\beta(X), \quad y = Y, \quad z = w(X) + Z\cos\beta(X), \tag{1}$$

where $u(X)$, $w(X)$ are axial deformation and deflection in the reference coordinate system and $\beta(X)$ is the cross section rotation. The deformation gradient, the Green-Lagrange strain tensor and the second Piola-Kirchhoff stresses are computed as

$$F_{iI} = \begin{bmatrix} [1 + u_{,X} + Z\beta_{,X}\cos\beta] & 0 & \sin\beta \\ 0 & 1 & 0 \\ [w_{,X} - Z\beta_{,X}\sin\beta] & 0 & \cos\beta \end{bmatrix}, \quad \mathbf{E} = \frac{1}{2}(\mathbf{F}^T\mathbf{F} - \mathbf{I}), \quad \mathbf{S} = \frac{1}{\det(\mathbf{F})}\mathbf{F}^{-1}\sigma\mathbf{F}^{-T}. \tag{2}$$

Where $(,X)$ is the derivative with respect to the coordinate X and σ is the Cauchy stress. There are only two non-zero components of (2c), i.e.

$$\begin{aligned} E_{XX} &= u_{,X} + \frac{1}{2}(u_{,X}^2 + w_{,X}^2) + Z\Lambda\beta_{,X} = E_0 + ZK^{\mathrm{b}}, \\ 2E_{XZ} &= (1 + u_{,X})\sin\beta + w_{,X}\cos\beta = \Gamma, \quad \Lambda = (1 + u_{,X})\cos\beta - w_{,X}\sin\beta. \end{aligned} \tag{3}$$

The variational form for the beam can be written as

$$\delta\Pi = \int_\Omega (\delta E_{XX} S_{XX} + 2\delta E_{XZ} S_{XZ}) \mathrm{d}V - \delta\Pi_{\mathrm{ext}}, \tag{4}$$

where $\delta\Pi_{\mathrm{ext}}$ is the variation of external forces. By considering a quadratic three-node element, the finite element approximation for the displacements and their shape functions for nodes $a = 1, 2, 3$ are

$$\begin{Bmatrix} u \\ w \\ \beta \end{Bmatrix} = N_a(X) \begin{Bmatrix} \hat{u}_a \\ \hat{w}_a \\ \hat{\beta}_a \end{Bmatrix}, \quad N_1 = \frac{1}{2}\xi(1-\xi),\ N_2 = 1-\xi^2,\ N_3 = \frac{1}{2}\xi(1+\xi),\ \xi \in < -1, 1 > . \tag{5}$$

Performing the standard linearization of the non-linear weak form, the problem can be written in the incremental form as

$$\mathbf{K}_{\mathrm{T}} \mathrm{d}\mathbf{u} = \Psi(\mathbf{u}) = -(\mathbf{f}_{\mathrm{int}} - \mathbf{f}_{\mathrm{ext}}), \tag{6}$$

where $\mathbf{f}_{\mathrm{int}}$, $\mathbf{f}_{\mathrm{ext}}$ are internal and external forces, respectively. The tangent stiffness matrix is defines as

$$(\mathbf{K}_{\mathrm{T}})_{ab} = \int_L \mathbf{B}_a^T \mathbf{D}_T \mathbf{B}_b \, \mathrm{d}X + (\mathbf{K}_{\mathrm{G}})_{ab}, \quad (\mathbf{K}_{\mathrm{G}})_{ab} = \int_\Omega \frac{\partial \mathbf{B}_a}{\partial \mathbf{u}} \sigma_b \, \mathrm{d}V, \quad \mathbf{u} = \begin{Bmatrix} u \\ w \\ \beta \end{Bmatrix}, \tag{7}$$

where

$$\mathbf{D}_{\mathrm{T}} = \begin{bmatrix} EA & 0 & 0 \\ 0 & \kappa GA & 0 \\ 0 & 0 & EI \end{bmatrix}, \quad \mathbf{B}_a = \begin{bmatrix} (1+u_{,X})N_{a,X} & w_{,X}N_{a,X} & 0 \\ \sin\beta N_{a,X} & \cos\beta N_{a,X} & \Lambda N_a \\ \beta_{,X}\cos\beta N_{a,X} & -\beta_{,X}\sin\beta N_{a,X} & (\Lambda N_{a,X} - \Gamma\beta_{,X} N_a) \end{bmatrix}, \tag{8}$$

where the Saint-Venant material type is considered and E is the Young modulus, G is the shear modulus, I is the second moment of inertia of the cross section and A is the cross section area. The expression of the geometric stiffness matrix $\mathbf{K}_{\mathrm{G}}$ can be found in Zienkiewicz and Taylor (2005), Chapter 17.

The non-linear equation (6) was solved by the Newton-Raphson method and accelerated by the line-search technique, where the i-th iteration factor η_i in $\mathbf{u}_{i+1} = \mathbf{u}_i + \eta_i \mathrm{d}\mathbf{u}_i$ is determined in order to minimize the projection

$$G_i \equiv (\mathrm{d}\mathbf{u}_i)^T \mathbf{\Psi}(\mathbf{u}_i + \eta_i \mathrm{d}\mathbf{u}_i) = 0. \tag{9}$$

Since the geometry is generally spatially oriented, the element quantities have to be transformed to the global coordinate system by standard transformation relations (see Zienkiewicz and Taylor (2005). Governing matrices of the system are then assembled by using

$$\mathbf{K}_T^s = \sum_{\mathrm{elements}} \mathbf{K}_T^g, \quad \mathbf{f}_{\mathrm{int}}^s = \sum_{\mathrm{elements}} \mathbf{f}_{\mathrm{int}}^g. \tag{10}$$

Both outer surface and kinematic mechanism are represented by beam elements with defined parameters. Their interconnection is modelled by the Lagrange multiplier technique. In the connection nodes, the degrees of freedom u and w are coupled, by which a revolute kinematic pair is simulated. Equation (6) is expanded to the form of

$$\begin{bmatrix} \mathbf{K}_T + \lambda_a \mathbf{H}_a & \mathbf{G}^T \\ \mathbf{G} & \mathbf{0} \end{bmatrix} \begin{Bmatrix} \mathrm{d}u \\ \mathrm{d}\lambda \end{Bmatrix} = \begin{Bmatrix} -(\mathbf{f}_{\mathrm{int}} - \mathbf{f}_{\mathrm{ext}}) - \lambda^T \mathbf{G} \\ -\mathbf{g} \end{Bmatrix}, \quad \mathbf{f}_{\mathrm{int}} = \int_L \mathbf{B}_a^T \mathbf{S} \, \mathrm{d}X, \quad a = 1, 2, 3$$
$$\begin{matrix} g_X = u_a - u_b, \\ g_Z = w_a - w_b \end{matrix}, \quad G_I = \frac{\partial g_I}{\partial u_a}, \quad H_I = \frac{\partial^2 g_I}{\partial u_a \partial u_b}, \quad I = 1, 2, ..., n_c, \quad n_c \text{ is the node count.} \tag{11}$$

3. Results

The capabilities of the presented model were tested on three cases of the rod 1 mounting position (see Fig. 1c). Initial geometry and deformation of the case 1, case 2 and case 3 are depicted in Fig. 2a. Input parameters were $E = 200$ GPa, $\mu = 0.3$, $G = E/(2(1+\mu))$, $b_1 = 20$ mm, $h_1 = 1$ mm, $b_2 = 5$ mm, $h_2 = 5$ mm, $\kappa = 5/6$, $I = bh^3/12$. The kinematic mechanism is loaded by the moment $M = 2$ Nm. The FEM model has 70 quadratic elements and 147 nodes. The beam resultants are depicted in Fig. 2. The axial force N_x, shear force T_z and bending moment M_o are computed from the integral (11) and are mapped to the deformed geometry. It can be seen that the character of the beam resultants can be governed by changing the position the rod 1, setting the relative motion of the mounting point A to positive or negative (causing compression or tension in the beam).

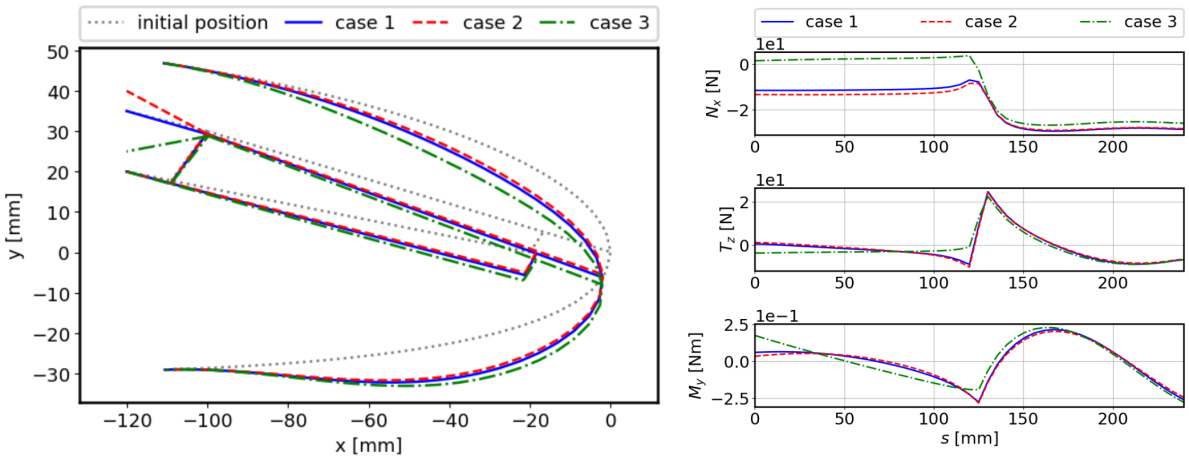

a) b)

Fig. 2: a) The initial geometry and deformations of three rod 1 mounting positions, b) beam resultants: axial force N_x, shear force T_z, bending moment M_y mapped on the deformed geometry.

4. Conclusions

The geometrically exact beam theory applied to the problem on the leading edge morphing has been investigated. The main goal of the paper was to prove the capability and parametrization of the computational algorithm for future optimization of the material parameters and desired morphed outer surface position as a output from aero-elastic analysis. Also solving methods of the non-linear finite element method were implemented, as line-search technique for the Newton-Raphson method. Nevertheless, the parameters in the material matrix (8) are to be modified in the subsequent work according to he meta-material response, as is depicted in Fig. 1b.

Acknowledgment

Computational resources were provided by the e-INFRA CZ project (ID:90254), supported by the Ministry of Education, Youth and Sports of the Czech Republic. The authors acknowledge the supports by Horizon Europe via the project HORIZON-WIDERA-2021-ACCESS-03, SEP-210806308.

References

Achleitner, J., Rohde-Brandenburger, K., von Bieberstein, P. R., Sturm, F., and Hornung, M. (2019) Aerodynamic design of a morphing wing sailplane. *AIAA Aviation 2019 Forum*.

Dexl, F., Hauffe, A., and Wolf, K. (2020) Multidisciplinary multi-objective design optimization of an active morphing wing section. *Structural and Multidisciplinary Optimization*, 62, 5, pp. 2423–2440.

Gu, X., Yang, K., Wu, M., Zhang, Y., Zhu, J., and Zhang, W. (2021) Integrated optimization design of smart morphing wing for accurate shape control. *Chinese Journal of Aeronautics*, 34, 1, pp. 135–147.

Li, Y., Ge, W., Zhou, J., Zhang, Y., Zhao, D., Wang, Z., and Dong, D. (2022) Design and experiment of concentrated flexibility-based variable camber morphing wing. *Chinese Journal of Aeronautics*, 35, 5, pp. 455–469.

Olympio, K. R. and Gandhi, F. (2010a) Flexible skins for morphing aircraft using cellular honeycomb cores. *Journal of Intelligent Material Systems and Structures*, 21, 17, pp. 1719–1735.

Olympio, K. R. and Gandhi, F. (2010b) Zero poisson's ratio cellular honeycombs for flex skins undergoing one-dimensional morphing. *Journal of Intelligent Material Systems and Structures*, 21, 17, pp. 1737–1753.

Reissner, E. (1972) On one-dimensional finite-strain beam theory: The plane problem. *Zeitschrift für angewandte Mathematik und Physik ZAMP*, 23, 5, pp. 795–804.

Simo, J. C. (1985) A finite strain beam formulation. The three-dimensional dynamic problem. Part I. *Computer Methods in Applied Mechanics and Engineering*, 49, 1, pp. 55–70.

Sun, J., Li, X., Xu, Y., Pu, T., Yao, J., and Zhao, Y. (2022) Morphing Wing Based on Trigonal Bipyramidal Tensegrity Structure and Parallel Mechanism. *Machines*, vol. 10.

Wood, R. D. and Zienkiewicz, O. C. (1977) Geometrically nonlinear finite element analysis of beams, frames, arches and axisymmetric shells. *Computers & Structures*, 7, 6, pp. 725–735.

Zienkiewicz, O. C. and Taylor, R. (2005) *Finite Element Method for Solids and Structural Mechanics*. Elsevier B. H., Burlington, 6th edition.

30th International Conference
ENGINEERING MECHANICS 2024
Milovy, Czech Republic, May 14 – 16, 2024

IMPACT OF DIFFERENT DISINFECTION SOLUTIONS ON MECHANICAL PROPERTIES OF ORTHODONTIC IMPRESS SILICONE MATERIAL

Hrubanová A.[*], Thomková B.[**], Košková O.[***], Richtrová M.[†], Borák L.[††], Štourač P.[†††], Marcián P.[‡]

Abstract: *This study explores the influence of disinfection on silicone material used in cleft protection and orthodontic impressions. A series of uniaxial tensile tests were conducted to evaluate the mechanical properties after disinfection. Statistical analysis of stress-strain curves at various stress levels using one-way ANOVA showed no significant differences, supporting the hypothesis that disinfection does not compromise the material properties of the silicone used for the cleft protection with obturators. Additionally, the study explores the utilization of 3D printing for creating a casting mold used in the manufacturing of silicon-based products.*

Keywords: Orthodontic, silicone material, uniaxial tensile test, disinfection, ANOVA.

1. Introduction

Silicone materials are employed for cleft protection during anesthesia with obturators (Richtrova et al., 2023). The obturators are disinfected prior to insertion. The primary objective of this study is to assess the impact of various disinfectants on silicone material on its mechanical properties through uniaxial tensile testing. We hypothesize that disinfection will not induce any changes in the mechanical properties as was previously shown by (Guntupali et al., 2022) with same silicon material but different disinfectants. Consequently, a secondary goal is to evaluate the efficacy of manual mixing of two-component silicone and the utilization of 3D printing for creating a casting mold. This research aims to contribute valuable insights into the compatibility of silicone with disinfection processes and explore innovative manufacturing techniques for producing casting molds.

2. Methods

Three commonly used disinfectants, Softasept N (*B Braun Medical*; propanol and ethalon base), Octenisept (*Schulke*; Octenidine dihydrochloride and phenoxyethanol base), and Cutasept F (*Hartmann-Rico*; propanol base), were selected for this study. To assess their impact on mechanical properties, uniaxial tensile testing was conducted.

[*] Ing. Anna Hrubanová: Institute of Solid Mechanics, Mechatronics and Biomechanics, Faculty of Mechanical Engineering, Brno University of Technology, Technická 2896/2, 616 69 Brno, Czech Republic; CZ, anna.hrubanova@vutbr.cz, Brno PhD. Talent Scholarship Holder

[**] Ing. Barbora Thomková: Institute of Solid Mechanics, Mechatronics and Biomechanics, Faculty of Mechanical Engineering, Brno University of Technology, Technická 2896/2, 616 69 Brno, Czech Republic; CZ, barbora.thomkova@vutbr.cz

[***] MUDr. Olga Košková, PhD.: Department of Burns and Plastic Surgery, Faculty of Medicine, Masaryk University, Jihlavská 340/20, 625 00 Brno, Czech Republic; CZ, koskova.olga@fnbrno.cz

[†] MUDr. Michaela Richtrová: Department of Paediatric Anaesthesiology and Intensive Care Medicine, Masaryk University, Černopolní 212/9, 662 63 Brno, Czech Republic; CZ, 60032@mail.muni.cz

[††] Ing. Libor Borák, PhD.: Institute of Solid Mechanics, Mechatronics and Biomechanics, Faculty of Mechanical Engineering, Brno University of Technology, Technická 2896/2, 616 69 Brno, Czech Republic; CZ, xmborak01@vutbr.cz

[†††] Prof. MUDr. Petr Štourač, PhD., MBA, FESAIC.: Department of Paediatric Anaesthesiology and Intensive Care Medicine, Masaryk University, Černopolní 212/9, 662 63 Brno, Czech Republic; CZ, stourac@med.muni.cz

[‡] Ing. Petr Marcián, PhD.: Institute of Solid Mechanics, Mechatronics and Biomechanics, Faculty of Mechanical Engineering, Brno University of Technology, Technická 2896/2, 616 69 Brno, Czech Republic; CZ, marcian@fme.vutbr.cz

doi: 10.21495/em2024-138

2.1. Specimen preparation

Specimens for the experiments were created using molds prepared on a 3D printer (Prusa i3 MK3S+). The mold was constructed from a commonly used 3D printing material PLA (polylactic acid), a thermoplastic monomer derived from renewable organic sources. The mold for sample preparation was designed according to CSN 527-2 and consisted of two parts. A drainage channel was incorporated into the lower part for the eventual removal of excess material, as shown in Fig. 1a. During mold fabrication, the infill density was set at 50 %, ensuring adequate rigidity when the mold was compressed during sample production.

The samples were produced from Zhermack Elite HD+ silicone impression material. This material is commonly used for impressions of upper palates in orthodontic laboratories. The material was prepared by mixing catalyst and base in a 1-to-1 ratio, precisely weighted using precision scale Lesak HD112 (0.001 g, Lesak). The two components were then manually mixed, placed in a mold and compressed. After the material solidified within 210 seconds, the samples were extracted and inspected.

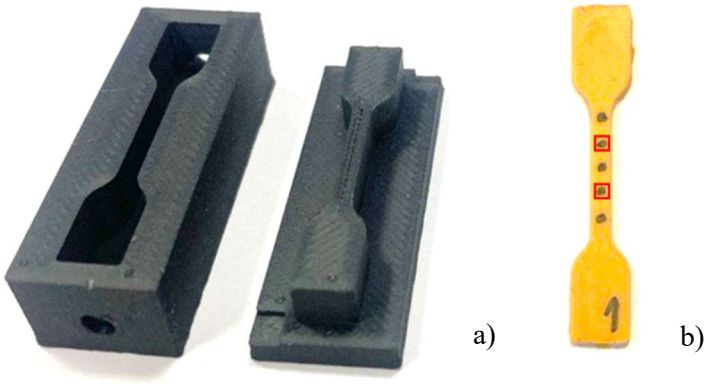

Fig. 1: 3D printed mold used for specimen preparation a), uniaxial tensile specimen with markers for deformation evaluation b); those marked in red in were employed for deformation tracking.

All specimens were prepared 24 hours before mechanical testing to mitigate the impact of specimen aging. Before testing, black markers were applied to the neck area of each specimen to track the deformation during testing (Fig. 1b). All specimens were categorized into four groups, consisting of three groups subjected to different disinfection procedures and one reference group without any disinfection.

2.2. Testing and evaluation

All tests were conducted on a customized computer-controlled testing device (Camea, s.r.o., CZ). The device is equipped with linear-stepped motor that enables mechanical displacement of clamps. In the case of uniaxial testing, a single motor was employed, and the specimen was gripped by two spring clamps with serrations to prevent slippage during testing. The force was measured by a load cell (max. 20 N) mounted on one actuator axis allowing the controlled displacement. The specimen was captured by a CCD camera with a resolution of 0.02 mm/pixel, positioned perpendicular to the testing area. To ensure a good visibility of the markers, the measured area was illuminated by two external lights. The specimen thickness was measured by a dial indicator at 3 locations on each specimen, and the mean value was used for further analysis.

Before undergoing tensile testing, each specimen (except that from the reference group) was immersed in one of the three different disinfection solutions (Softasept N, Octenisept, Cutasept F) for 60 seconds. Subsequently, the specimens were air-dried before being subjected to uniaxial tension testing. This simulated pre-operative conditions, where the surgeon immerses the prosthesis in the disinfectant for approx. 1 minute and allows it to air-dry before inserting into the patient's body. After clamping a pre-tension of 0.1 N was applied to each specimen to ensure its flatness. The testing was displacement-controlled, with a displacement speed set to 0.333 mm/s. Uniaxial specimens were loaded until failure occurred at the neck area.

The evaluation of the test was conducted in software Tibixus (Turčanová et al., 2023), which analyzes the images captured by the CCD camera. The first captured image served as a reference, and the

deformation was assessed through digital image correlation (DIC). The calculation of the first Piola-Kirchhoff (engineering) stress was carried out using Eq. (1):

$$\sigma = \frac{F_{exp}}{b\,T}, \tag{1}$$

where F_{exp} is the force measured by the load cell, b is the initial (undeformed) width of the specimen and T is the measured mean thickness.

2.3 Statistical Analysis

To compare the difference between the four groups (3 disinfectants and 1 control group), thirteen datasets were created by interpolating the strain value of stress-strain curves at thirteen stress-levels (Lisický et al., 2021), ranging from 0.1 MPa up to 1.3 MPa and sorted into four groups by the disinfectant used. At each stress level a one-way ANOVA test was conducted to determine whether there is a significant difference between the various disinfectant groups and the reference group. The significance was assumed for $p < 0.05$.

The normalization of data was used for clearer data representation using Eq. (2):

$$\varepsilon_N = \frac{\varepsilon_i - \bar{\varepsilon}}{S_\varepsilon}, \tag{2}$$

where ε_N is the normalized strain data, ε_i is the strain value before normalization, $\bar{\varepsilon}$ is the mean value and S_ε is the standard deviation.

3. Results and discussion

The resulting stress-strain curves are shown in Fig. 2.

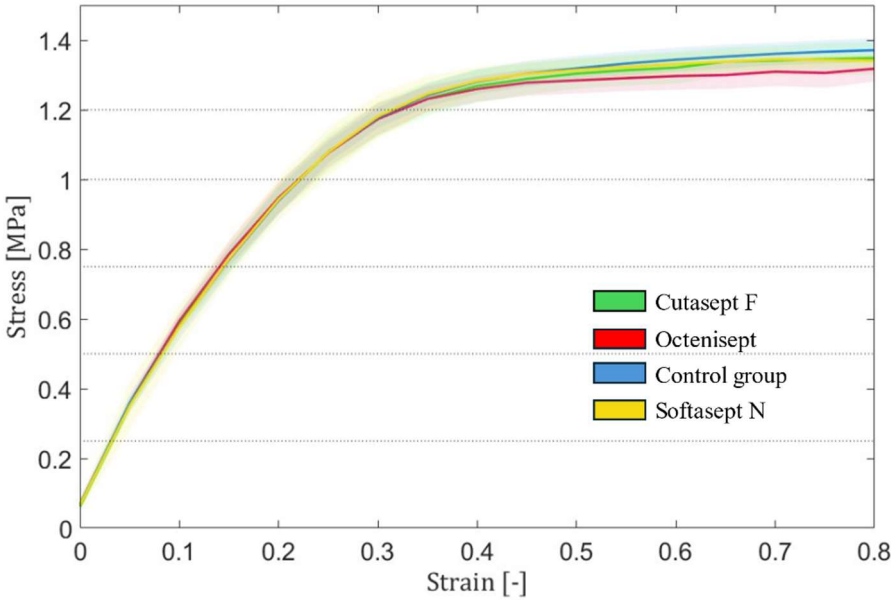

Fig. 2: Average stress-strain curve (solid line) with standard deviation of the uniaxial tensile tests for each of the 4 groups. The specimens cured with Softasept N are displayed in yellow, the specimens cured with Octenisept are shown in red, the ones cured with Cutasept F are green and the group shown in blue is the reference group which wasn't immersed in any disinfectant.

The results indicate no significant difference between the four groups, as the mean values for each group fall within the interquartile range of the others (Fig. 3). To validate this hypothesis, a one-way ANOVA test was conducted. The resulting p-values are summarized in Tab. 1. All the p-values are above the significance level of 0.05, meaning that the null hypothesis about the equality of mean cannot be rejected.

This suggests that there indeed is not a statistically significant difference between the disinfectant and that the effect of plunging the silicon into any of these three disinfectants does not change its material properties.

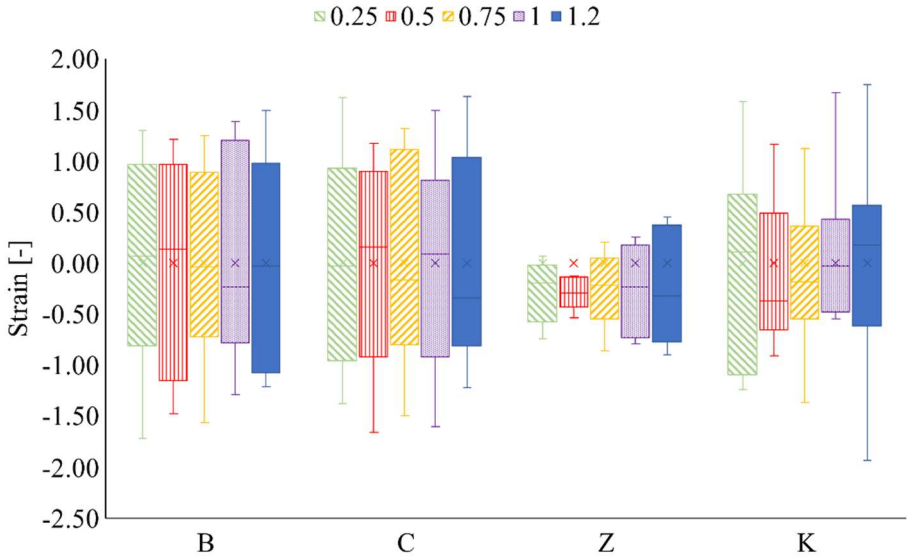

Fig. 3: Box plot of normalized strain data for different stress levels (used stress levels are shown in Fig. 2) Each disinfectant group is marked by letter (B – Cutasept F; C – Octenisept; Z – SoftaseptN; K – reference group), each stress level is differentiated by color and pattern.

Stress-level [MPa]	P-value	Stress-level [MPa]	P-value	Stress-level [MPa]	P-value
0.1	0.941	0.6	0.137	1	0.672
0.2	0.335	0.7	0.821	1.1	0.502
0.3	0.941	0.8	0.754	1.2	0.326
0.4	0.86	0.9	0.697	1.3	0.438
0.5	0.87				

Tab. 1: Resulting p-values of one way ANOVA test for different stress levels.

4. Conclusion

The aim of this study was to assess the effect of three disinfectants on the mechanical properties of Zhermack Elite HD+, a silicone material commonly used for orthodontic impressions. A series of uniaxial tensile tests were conducted, and the resulting stress-strain curves were compared using one-way ANOVA at various stress levels. The results revealed no statistically significant differences in the tensile responses, suggesting that the immersion of the material in the disinfectant should not alter its material properties.

Acknowledgement

The research was supported by the AZV - Czech Health Research Council (NU23-06-00301).

References

Richtrova, M. et al. (2023) Use of computer-aided design and 3D printing for airway management in paediatric patients with a cleft facial defect: a pilot study. *British Journal of Anaesthesia*, 130, 65, e469–e471.

Turcanová, M. et al. (2023) Biaxial stretch can overcome discrepancy between global and local orientations of wavy collagen fibres. *Journal of Biomechanics*, 161, 111868.

Lisický O. et al. (2021) Interpretation of experimental data is substantial for constitutive characterization of arterial tissue. *ASME J. Biomech Eng.*, 143(10): 104501.

Guntupali Y. et al. (2022) Effect of disinfectants on the tear strength of addition silicone impression material – An in vitro study. *J. Adv. Pharm. Technol. Res.*, 458–461.

30th International Conference
ENGINEERING MECHANICS 2024
Milovy, Czech Republic, May 14 – 16, 2024

USING FINITE VOLUME METHOD TO SIMULATE LASER SHOCK PEENING OF 7050 AL ALLOY

Isoz M.[*], **Gruber P.**[**], **Ježek O.**[***], **Kubíčková L.**[†], **Gabriel D.**[††], **Kaufman J.**[†††], **Brajer J.**[‡]

Abstract: *Laser shock peening (LSP) is a modern alternative to standard peening processes such as shot peening. In general, peening is used to improve the strength and fatigue resistance of components by hardening their surface. In LSP, a laser-induced shockwave is used to harden the material to a depth of the order of* 1 *mm, that is, roughly twice as deep as can be achieved with shot peening. Frameworks for LSP simulation have been developed since the end of the 1990s and are exclusively based on the finite element method (FEM). The critical component of the framework is the dynamic simulation of the elastoplastic shockwave that subjects the component material to a strain rate of the order* $10^{-7}\ s^{-1}$*. In this contribution, we present a simulation framework for LSP based on the finite volume method (FVM) that allows for modeling the strain-rate hardening of the material. The framework is used to simulate the LSP of the 7050 aluminum alloy. Using a comparison of our FVM results with the FEM data available in the literature, we found that FVM can be applied to LSP simulation with the same success as the more traditional FEM.*

Keywords: Laser shock peening, modeling, simulation, finite volume method, OpenFOAM.

1. Introduction

In Fig. 1, we show fundamentals of the LSP process, particularly of its water-confined variant with ablative coating applied (Scius-Bertrand et al., 2020), which is of interest in this paper. First, a high power density laser is used to convert the ablative coating (also known as the sacrificial layer) to plasma. The expanding plasma is confined by the transparent overlay and for a duration of tens of nanoseconds loads the component surface by a pressure in order of GPa. This loading generates a shockwave that propagates through the component and plasticizes its material, resulting in an affected zone with induced compressive residual stresses that are beneficiary for the fatigue resistance or surface hardness of the component.

Due to its industrial potential, attempts on numerical simulation of the laser shock peening (LSP) have been made since the end of the 1990s; see, e.g. (Braisted and Brockman, 1999; Hfaiedh et al., 2015; Sun et al., 2022). All simulations reported in the literature were performed using the finite element method (FEM). However, the critical element of the simulation appears to be the propagation of the elastoplastic shockwave. Interestingly, the finite volume method (FVM) was reported by Berezovski et al. (2014) to achieve results with no post- or pre-shock spurious oscillations for elastic wave propagation, especially when flux limiters are applied. Such a behavior is crucial for LSP simulation where spurious oscillations may lead to unphysical plastic zones and residual stresses in the material. In this contribution, we build on our previous work (Isoz et al., 2023) where we presented an FVM-based simulation framework for

[*] Ing. Martin Isoz, PhD.: Institute of Thermomechanics, Czech Academy of Sciences (CAS), Dolejškova 1402/5; 182 00, Prague; CZ, isozm@it.cas.cz

[**] Ing. Pavel Gruber, PhD.: Institute of Thermomechanics, CAS, Dolejškova 1402/5; 182 00, Prague; CZ

[***] Ing. Ondřej Ježek: Institute of Thermomechanics, CAS, Dolejškova 1402/5; 182 00, Prague; CZ

[†] Ing. Lucie Kubíčková: Institute of Thermomechanics, CAS, Dolejškova 1402/5; 182 00, Prague; CZ

[††] Ing. Dušan Gabriel, PhD.: Institute of Thermomechanics, CAS, Dolejškova 1402/5; 182 00, Prague; CZ

[†††] Ing. Jan Kaufman, PhD.: HiLASE Centre, Institute of Physics, CAS, Za Radnicí 828; 252 41, Dolní Březany; CZ

[‡] Ing. Jan Brajer, PhD.: HiLASE Centre, Institute of Physics, CAS, Za Radnicí 828; 252 41, Dolní Březany; CZ

doi: 10.21495/em2024-142

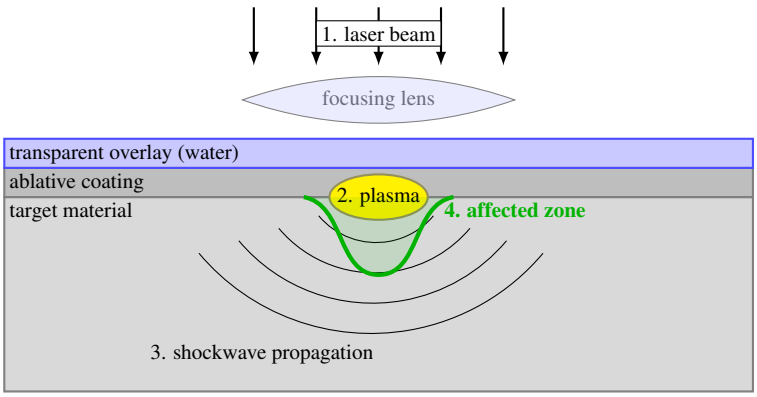

Fig. 1: Fundamentals of the laser shock peening process.

LSP implemented in the open-source C++ library OpenFOAM (OpenCFD, 2007). Here, the framework is extended by the Jonson-Cook model (Johnson and Cook, 1983) to simulate strain-rate hardening and used to recompute the study by (Sun et al., 2022), which is focused on LSP of the 7050 aluminum alloy.

2. Simulation framework fundamentals

The complete laser shock peening of the component consists of a series of individual steps, LSP shots, illustrated in Fig. 1. As stated above, the pressure loading during the shot lasts $\mathcal{O}(10^1)$ ns. Then, the shockwave looses energy required for the material plastization in $\mathcal{O}(10^3)$ ns. In-between shots, the component is repositioned, resulting in a delay of order $\mathcal{O}(10^{-1})$ s = $\mathcal{O}(10^8)$ ns. In the simulation framework, this splitting of temporal scales is reflected, in a standard manner (Braisted and Brockman, 1999; Sun et al., 2022), by simulating each shot as dynamic plastic wave propagation followed by a pseudo-static relaxation. The formal description of the process is given in (Isoz et al., 2023). Here, we will only summarize the fundamentals and focus on the new developments.

Both the dynamic and relaxation sub-steps are simulated under small-strain settings $\varepsilon = \frac{1}{2}\left(\nabla \boldsymbol{u} + \boldsymbol{u}\nabla\right)$ with damping effects and body forces neglected. The dynamic wave propagation is solved as elasto-plastic with the component internal state represented by the plastic strain ε_p. Newly, the plastic strain evolves under the isothermal Johnson and Cook (1983) yield criterion

$$\sigma_y = \left(A + B\varepsilon_\mathrm{p}^n\right)\left(1 + C\ln\left(\frac{\dot{\varepsilon}_\mathrm{p}}{\dot{\varepsilon}_\mathrm{p,ref}}\right)\right), \tag{1}$$

where $\dot{\varepsilon}_\mathrm{p}$ is the rate of the plastic strain, A is the static material yield strength and B, n, C are empirical parameters of which C is relevant only to the selected reference strain rate $\dot{\varepsilon}_\mathrm{p,ref}$. The pseudo-static relaxation is treated as perfectly elastic. However, with ε_p encoding the internal state of the component taken into account.

With respect to the boundary conditions used, the laser-induced loading is represented by a prescribed pressure that varies spatially and temporally. On the rest of the component surface, the boundary conditions used can correspond, for example, to the component clamping. Finally, only the surface layer of the material is directly affected by the shockwave propagation. On the other hand, residual stresses from the static substep reach significantly further. As a result, it is computationally profitable to solve the dynamic-sub step only in the directly affected part of the computational domain.

The problem governing partial differential equations are spatially discretized using the finite volume method as described in (Cardiff et al., 2017). The discretization schemes are usually selected to be as close as possible to second order, which is the highest global method order available in OpenFOAM (OpenCFD, 2007). Still, application of high-order schemes with flux limiting is often profitable for divergence terms. The explicit temporal integration of the shockwave propagation is performed using the standard central differencing.

3. Comparison of FVM and FEM on 7050 Al alloy

In the present contribution, our aim is to evaluate the capabilities of our FVM-based simulation framework against the state-of-the-art FEM framework. As the reference solution, the recent paper by Sun et al. (2022)

on single-shot LSP of 7050 aluminum alloy was selected, as it contains data on both the residual stresses in the material and on elasto-plastic shockwave propagation.

Simulation set-up In the FVM-based simulations, we followed the paper (Sun et al., 2022) with respect to the (i) material (7050 Al alloy), (ii) sample geometry (hexahedron of dimensions $30 \times 30 \times 8$ mm), (iii) and spatio-temporal laser-induced pressure loading. A different computational mesh, more suitable to FVM, was used. Still, the number of degrees of freedom was approximately $1.5 \cdot 10^6$ in both the FEM and FVM simulations. Used pressure profiles and details on the material are given in Fig. 2. Comparison of the computational meshes used are shown in Fig. 3.

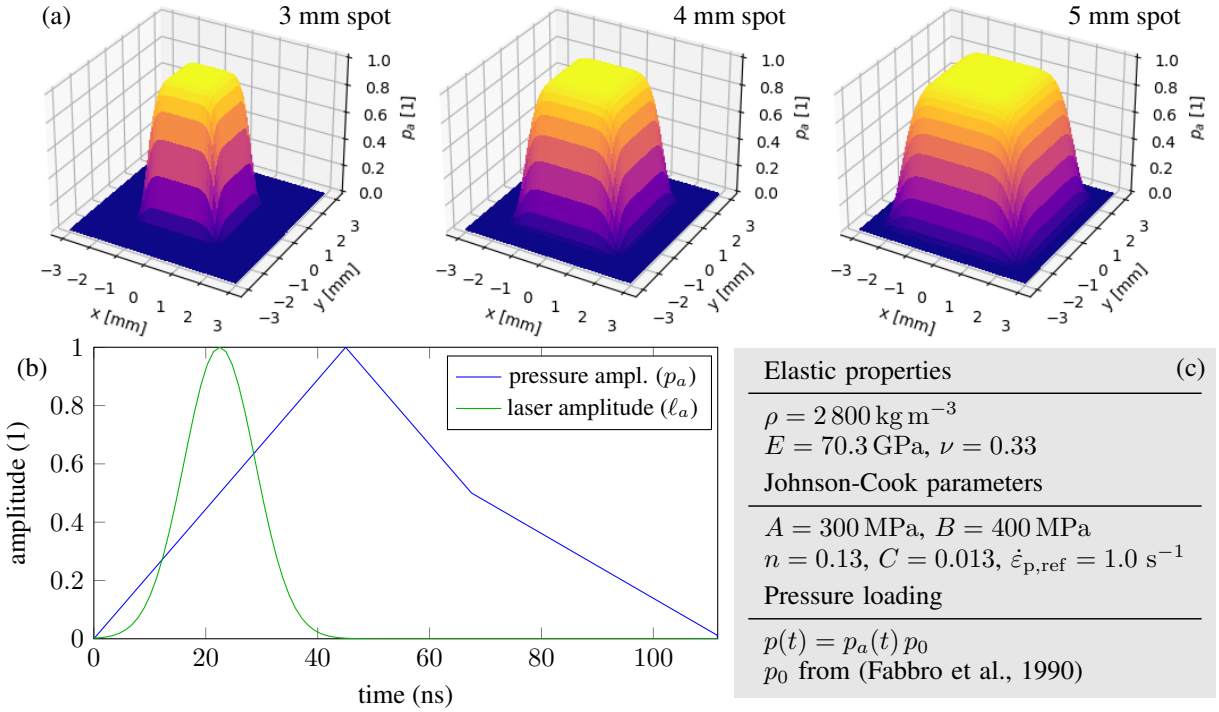

Fig. 2: Simulation set-up. a) spatial pressure profiles – three spot sizes were tested, b) temporal pressure and laser amplitude profiles, c) model parameters.

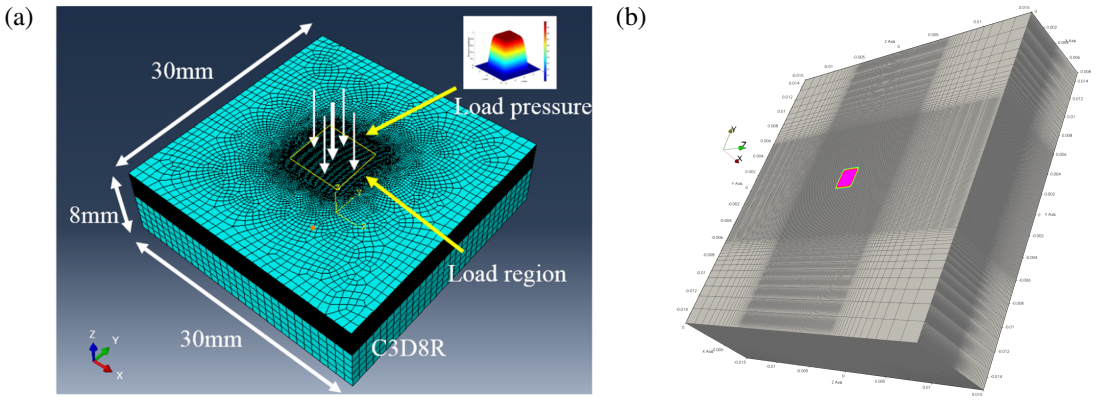

Fig. 3: Used computational meshes. a) Sun et al. (2022), b) this work.

Shockwave propagation Results for shockwave propagation at 100, 200, 400, and 600 ns and for the three spot sizes were compared with (Sun et al., 2022). In Fig. 4a, we show examples for the smallest and the biggest spots at 400 ns and 200 ns, respectively. These results were selected as they exhibit qualitatively different wave systems. However, the differences between FEM and FVM are negligible. Qualitatively different results between FEM and FVM were obtained at 600 ns. However, we contribute this difference to the fact that there is a sharp transition from a fine to a coarse mesh in FEM, see Fig. 3a. At 600 ns, the wave already passed this transition, which may have skewed the results in (Sun et al., 2022).

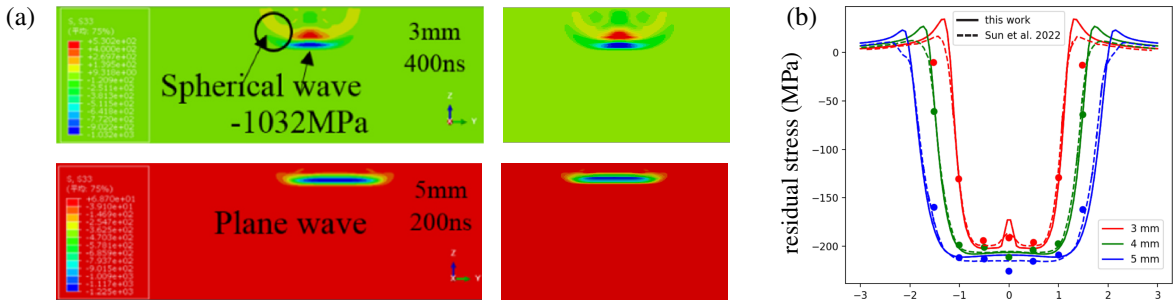

Fig. 4: Comparison of simulation results. a) shockwave propagation; same contours and same ranges are always displayed, b) residual stresses on material surface.

Residual stresses In Fig. 4b, we show a comparison of the residual stresses calculated and measured on the line on the sample surface and passing through the spot center. There are only small discrepancies between FEM and FVM while both methods agree with the experimental data rather well.

4. Conclusions

We extended our previously developed FVM-based framework for LSP simulations by the Johnson-Cook model to model the strain-rate hardening. The extended framework was used to reproduce FEM-based results of Sun et al. (2022) who dealt with simulation of a single shot LSP on 7050 aluminum alloy. It was found that both frameworks give comparable results with respect to (i) the dynamic simulation, and (ii) the final residual stresses. Future developments will be aimed at implementation of boundary conditions for pressure loading capable of mimicking those induced by imperfect industrial lasers.

Acknowledgments

The work was financially supported by the institutional support RVO:61388998 and by the grant project with No. TM04000048 of the Technology Agency of the Czech Republic.

References

Berezovski, A., Kolman, R., Blažek, J., Kopačka, J., Gabriel, D., and Plešek, J. (2014) Comparative study of finite element method, isogeometric analysis, and finite volume method in elastic wave propagation of stress discontinuities. *e-Journal of Nondestructive Testing*, 19, pp. 16321.

Braisted, W. and Brockman, R. (1999) Finite element simulation of laser shock peening. *International Journal of Fatigue*, 21, pp. 719–724.

Cardiff, P., Tukovic, Z., Jaeger, P. D., Clancy, M., and Ivankovic, A. (2017) A Lagrangian cell-centred finite volume method for metal forming simulation. *International Journal For Numerical Methods In Engineering*, 109, pp. 1777–1803.

Fabbro, R., Fournier, J., Ballard, P., Devaux, D., and Virmont, J. (1990) Physical study of laser-produced plasma in confined geometry. *Journal of Applied Physics*, 68, pp. 775–784.

Hfaiedh, N., Peyre, P., Song, H., Popa, I., Ji, V., and Vignal, V. (2015) Finite element analysis of laser shock peening of 2050-t8 aluminium alloy. *International Journal of Fatigue*, 70, pp. 480–489.

Isoz, M., Gruber, P., Schmidt, J., Kubíčková, L., Štefan, J., Kaufman, J., Brajer, J., and Gabriel, D. (2023) Calibrated finite volume method-based simulation framework for laser shock peening. In *Proc. of the Conf. Engineering Mechanics*, IT CAS, Milovy, Czech Republic, pp. 103–106.

Johnson, G. and Cook, W. (1983) A constitutive model and data for metals subjected to large strains, high strain rates, and high temperatures. In *Proc. 7th International Symposium on Ballistics*, pp. 541–547.

OpenCFD (2007) *OpenFOAM: The Open Source CFD Toolbox. User Guide Version 1.4, OpenCFD Limited*. Reading UK.

Scius-Bertrand, M., Videau, L., Rondepierre, A., Lescoute, E., Rouchausse, Y., Kaufman, J., Rostohar, D., Brajer, J., and Berthe, L. (2020) Laser induced plasma characterization in direct and water confined regimes: new advances in experimental studies and numerical modelling. *Journal of Physics D: Applied Physics*, 54, pp. 055204.

Sun, B., Zhao, J., Qiao, H., and Lu, Y. (2022) Effects of square spot size and beam quality on residual stress of 7050 aluminum alloy by laser shock peening. *Materials Chemistry and Physics*, 284, pp. 126023.

30th International Conference
ENGINEERING MECHANICS 2024
Milovy, Czech Republic, May 14 – 16, 2024

INFLUENCE OF SIMPLIFYING THE GEOMETRY OF THE FE MODEL OF THE VEHICLE FRONTAL FULL BARRIER CRASH TEST

Jančář, R.*, Dlugoš, J., Fridrichová, K.*****

Abstract: *The deformation of the vehicle as a result of the accident serves as the input for determining the impact speed for the purposes of the expert report. One possibility of calculating the impact speed is by means of a verified finite element analysis (FEA) of the vehicle impact. However, to develop such a sufficiently accurate finite element (FE) model requires a significant financial and time investment. Such a model contains a number of key simplifications that are difficult to detect without prior experience. Fortunately, there are at least a few freely available detailed FE vehicle models that have been experimentally verified. On these it is possible to investigate the effect of different modelling methods on observed parameters such as overall deformation. This paper is specifically concerned with the sensitivity of FEA results to different levels of vehicle geometry modelling. A Chevrolet Silverado 1500, model year 2014, is used as a detailed FE vehicle model.*

Keywords: Finite element analysis, crash simulation, crashworthiness, accident reconstruction.

1. Introduction

In accident analysis, a number of methods are used to determine crash conditions. The Energy Equivalent Speed (EES) is used to quantify the deformation energy of the vehicle that caused the plastic deformation. The EES value can be determined in various ways such as by expert estimation, comparison, correlation diagram, energy grid, from crash test values and the CRASH3 method. Each of these methods is described in detail by Bucsuházy et al. (2023).

When a vehicle hits a barrier or another vehicle, kinetic energy is converted into deformation energy. This is a system of bodies that can be modelled using the finite element method (FEM). Among the first, this was attempted by Winter et al. (1981) on a DeLorean DMC-12 vehicle. Damage analysis of a 2010 model year Toyota Yaris vehicle using FEM was performed by Numata (2018). Numata investigated the distribution of the deformation energy as a function of the overlap ratio in a frontal impact. Burg (2013) used the results of the finite element analysis (FEA), which he visually compared with the real deformed shape of the vehicle. Based on this, he determined the impact speed. A similar approach was used by Görtz (2016), who compared the deformation depths in a frontal impact on a column determined by FEA and measured on a real vehicle.

Creating a finite element (FE) model of a vehicle for the purpose of assessing its crash deformation energy can be a costly and time-consuming process. Therefore, the objective of this paper is to determine which geometric features have the greatest influence on the results.

* Bc. Radek Jančář: Institute of Automotive Engineering, Brno University of Technology, Technická 2896/2; 616 69, Brno; CZ, radek.jancar@vut.cz

** Ing. Jozef Dlugoš, PhD.: Institute of Automotive Engineering, Brno University of Technology, Technická 2896/2; 616 69, Brno; CZ, jozef.dlugos@vut.cz

*** Ing. Kateřina Fridrichová: Institute of Automotive Engineering, Brno University of Technology, Technická 2896/2; 616 69, Brno; CZ, katerina.fridrichova@vut.cz

doi: 10.21495/em2024-146

2. Methods

A detailed FE model of the Chevrolet Silverado 1500, model year 2014, was created as part of Project No. DTNH22-13-C-00329 (Singh, 2012) between NHTSA and EDAG, INC. (Fig. 1). The project focused on exploring full-size pickup truck lightweighting options with production processes available between 2020 and 2030. Investigation of the impact of vehicle lightweighting was observed on the verified FE model mentioned above. This model was created using reverse engineering tools such as 3D scan, CAD model reconstruction, material property measurements on real vehicle samples and others. Verification was performed using results from crash tests such as NHTSA test no. 8456 or test no. 8316, by comparing the natural frequencies of the cab or by using torsional and flexural stiffness of the body and frame. This resulted in a FE model containing over 1 400 components and nearly 3 million elements. Glued joints and spot welds were modeled by advanced methods with failure considerations based on e.g. Malcolm (2007).

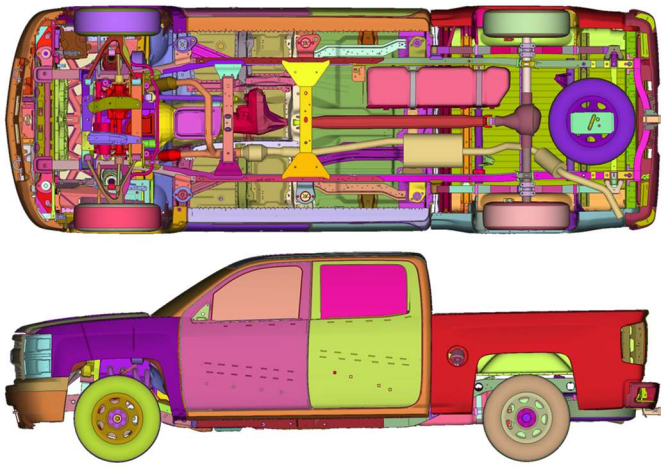

Fig. 1: Detailed FE model of Chevrolet Silverado 1500 (Singh, 2012).

The effect of geometry simplification (Drapal, 2016) on the results is investigated on this FE model. The simplification consists of reducing a discretized component or group of components to a mass point that is connected to adjacent parts by RBE3 (Fig. 2). The geometry modifications are divided into the following groups:

- The body group includes the windshield and rear glass, the cab doors and bucket doors, the front grille and the headlights.
- The accessories group includes exhaust, spare tire, tow bar, tank and tow hooks.
- The interior group includes the dashboard, front seats, steering wheel and pedals.
- The suspension group includes front suspension springs, airbag model tires and brakes.
- The engine bay group includes the battery, radiator and steering.
- All of the above groups at the same.

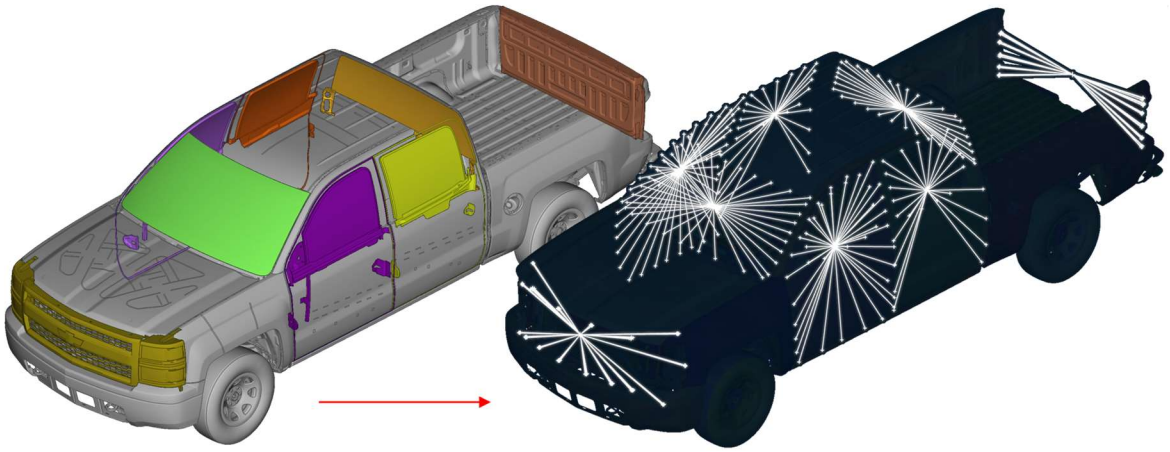

Fig. 2: The body group: replacement of the parts by mass points and RBE3.

The NCAP Frontal Full Barrier Test is simulated. The evaluated outcome parameter is the total longitudinal deformation of the vehicle at 56 km·h^{-1}. From the results of the FEA, it is evident (Fig. 3) that the longitudinal deformation is generally not linearly dependent on the impact speed. This is due to the nonlinearity of the model due to the nonlinear materials and the significant amount of contacts. This nonlinearity is more dominant for higher impact velocities (Bucsuházy et al., 2023; Görtz, 2018). Therefore, in addition to the total longitudinal deformation of the vehicle, the parameter representing speed change required to increase the longitudinal deformation by 1 mm is also investigated. This parameter is determined as a slope of the deformations for speeds of 42 km·h^{-1} and 56 km·h^{-1}.

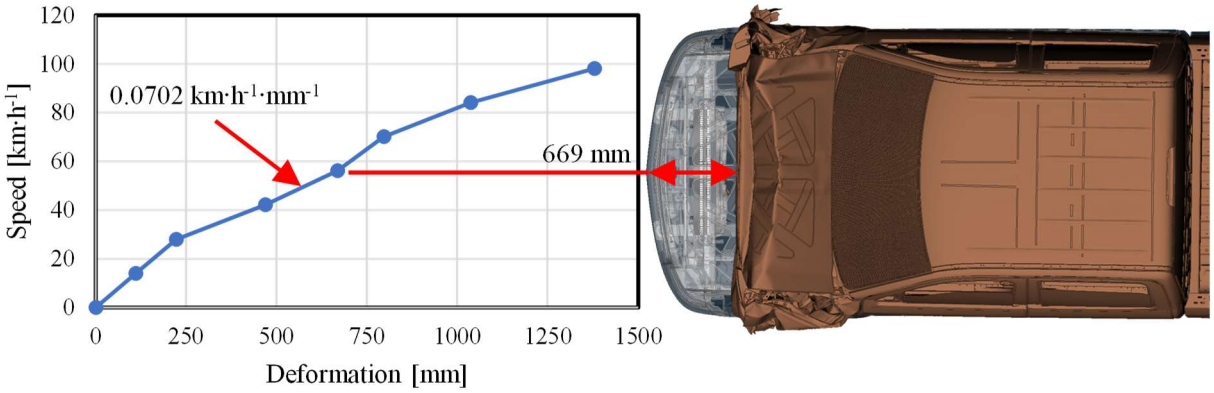

Fig. 3: Output parameters evaluated; the total longitudinal deformation 669 mm and the slope 0.0702 km·h^{-1}·mm^{-1} for the full FE model.

3. Results

The results of the simplified geometry models are shown in Tab. 1. The combination of all groups at once leads to the largest difference from the results of the full FE model. The absence of selected parts and their replacement with mass points and RBE3 reduces the stiffness of the vehicle, leading to an increase in the total longitudinal deflection from 669 mm to 700 mm (an increase of 4.62 %). The engine bay group contributes the most to this decrease in stiffness by reducing components in the front area of the vehicle (battery, radiator and steering). These components are subject to the largest deformations. The radiator, in particular, contributes to a significant change in the overall deformation. In the case of a full FE model, contact between the powertrain and the radiator occurs during the impact. In the absence of the radiator, the powertrain moves significantly further due to the new clearance. This phenomenon can be seen by comparing the deformed shapes of the front of the vehicle at the same time for the FE model with and without the radiator (Fig. 4).

The accessories group has the smallest effect on the deformation. The components such as exhaust, spare tyre, towing bracket, tank and towing hooks do not contribute too much to the vehicle's stiffness. Their influence is primarily through added mass.

FE model	Deformation [mm]	Difference [%]	Slope [km·h^{-1}·mm^{-1}]	Difference [%]
Full	669	-	0.0702	-
All groups bellow	700	4.62	0.0623	-11.33
The body group	672	0.37	0.0708	0.78
The accessories group	670	0.14	0.0708	0.82
The interior group	648	-3.13	0.0726	3.39
The suspension group	679	1.43	0.0758	7.99
The engine bay group	695	3.89	0.0641	-8.65

Tab. 1: Results of the impact of geometry simplification.

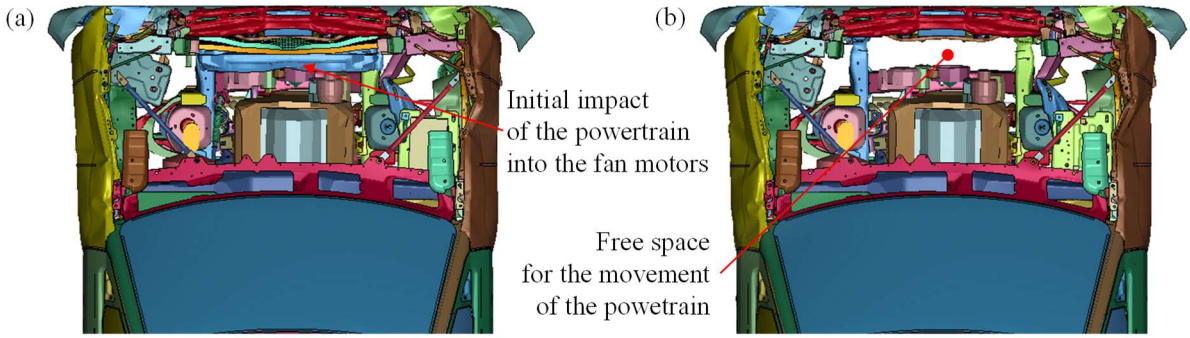

Fig. 4: Deformation of the front of the vehicle at 27.5 ms: a) model with radiator – the full model, b) model without radiator – the engine bay group.

4. Conclusions

In FEA of a vehicle frontal impact, the most important aspect from the geometry model point of view is to capture the area closest to the deformed zone as detailed as possible. This is confirmed by the results of the sensitivity analysis i.e., the engine bay group. The absence of the radiator causes an increase in the total longitudinal deformation of 3.89 %. However, if the parts involved are made of very compliant material such as the plastic front grille or the headlights (the body group), the reduction of these parts to mass points has a minimal effect on the results. The reduction of parts (even sufficiently rigid ones) in the areas far from the most deformed zone using mass points and RBE3 does not significantly degrade the results (the body group and the accessories group).

Interesting results arose when reducing the interior group. In this group, the dashboard (represented by a cross brace), front seats, steering wheel and pedals were replaced by mass points. The RBE3 connection should not result in a stiffer cabin, yet the results provide 3.13 % less deformation compared to the full model. The explanation for this phenomenon requires further investigation.

To better understand the sensitivity of the detailed FE model, it would be useful to investigate other influences such as the material model. The detailed FE model contains materials with multilinear stress diagrams for different strain rates. Further, it would be useful to investigate the influence of shell element formulation, mass scaling settings, and different methods of joining individual parts.

Acknowledgement

The authors gratefully acknowledge the funding from the specific research on BUT FSI-S-23-8235. The authors wish to thank NHTSA for providing Chevrolet Silverado FE model publicly available that enabled this research to be made.

References

Bucsuházy, K., Moravcová, P., Semela, M. et al. (2023) *Vehicle Crush Investigation: A Guidebook to Documentation and Analysis*. 1st edition. Brno.

Burg, H. (2013) Zur Einstufung von EES-Werten bei außergewöhnlichen Unfällen. In: *15 AREC Meeting*, Wildhaus.

Drapal, L. and Voparil, J. (2016) Shape Design of a Piston Ring. In: *Proc. of 20th Int. Sci. Conf. Transport Means*, Juodkrante, Lithuania. Kaunas Univ. of Technology, pp. 767–771.

Görtz, M. (2016) 3D-Vermessung von Schäden an Fahrzeugkarosserien, In: *16. Aachen Interdisziplinäres Verkehrssymposium*. Aachen.

Görtz, M. (2018) *Model for determining deformation energies on vehicles after traffic accidents*. Dissertation, Žilina: UZVV UNIZA, (in Slovak).

Malcolm, S. and Nutwell, E. (2007) Spotweld Failure Prediction using Solid Element Assemblies, In: *6th European LS-DYNA Users' Conference.* Gothenburg, pp. 47–56.

Numata, S. and Okumura, D. (2018) Validation of Crush Energy Calculation Methods for Use in Accident Reconstructions by Finite Element Analysis. *SAE Int. Journal of Transportation Safety*, 6, 2, pp. 133–146.

Singh, H. (2012) Mass Reduction for Light-Duty Vehicles for Model Years 2017-2025. Report No. DOT HS 811 666, Program Reference: DOT Contract DTNH22-11-C-00193. Contract Prime: Electricore.

Winter, R., Mantus, M. and Pifko, A. B. (1981) Finite Element Crash Analysis of a Rear-Engine Automobile (No. 811306). SAE Technical Paper.

30th International Conference
ENGINEERING MECHANICS 2024
Milovy, Czech Republic, May 14 – 16, 2024

VIBRATION DIAGNOSTICS IN THE ASSESSMENT OF THE VEHICLES BODYWORK TECHNICAL STATE PROCEDURE

Kałaczyński T.*, Łukasiewicz M., Liss M.***, Mazurkiewicz A.†**

Abstract: *An integral part of every vehicle, the car body plays an important role in aspects such as safety, aerodynamics, aesthetics and comfort. Studies of the dynamic properties of mechanical structures using modal analysis methods are now very widespread. The essence of this analysis is to obtain information about the object in the form of the so-called modal model, which consists of modes of natural vibrations, natural frequencies and damping coefficients, mass and dynamic stiffness. The paper presents the possibilities of implementing vibration diagnostics in the assessment of the vehicle structure technical state with modal analysis.*

Keywords: Modal analysis, vehicle bodywork, vibration diagnostics, technical state.

1. Introduction

Modern vehicles in new condition provide only a certain guarantee of proper behavior in extreme road conditions. Of course, each vehicle is subject to natural degradation processes over the time of its operation, which cause individual mechanisms and systems to lose their full technical efficiency and a significant part of the vehicle's structure to wear out. An equally important factor influencing the strength of the structure is the advancing corrosion process. In addition, all kinds of accident damage and the manner and quality of post-accident repairs also affect the technical condition. Current methods of diagnosing the load-bearing structure of vehicles are to a large extent based only on the organoleptic assessment of its condition, which is burdened with a large error in the assessment of its strength, durability, and thus the level of safety, both for the driver and other road users. Thanks to proper technical service, as well as the implemented systems for monitoring the technical state allowing for early detection of potential damage, it is possible to maintain or even extend the good technical state of the structure. Maintenance consists of a set of technological activities necessary to maintain the vehicle's mechanisms in a state of maximum technical readiness throughout its entire life (Żółtowski et al., 2015). Technological activities in the extensive maintenance process are supported by measurement methods supporting the assessment of the current vehicle technical state.

A local change in stiffness occurring in a mechanical structure is in many cases caused by damage. This situation has a direct impact on the form of the modal parameters of the modal model.

The assessment of stiffness changes on the basis of the modal model can be made in such a situation on the basis of the knowledge of the correlation between the model of the structure without damage and the model created on the real object after some time of exploitation (Kałaczyński et al., 2018)

* Tomasz Kałaczyński, PhD.: Faculty of Mechanical Engineering, Bydgoszcz University of Science and Technology, Al. prof. S. Kaliskiego 7, Bydgoszcz; PL, kalaczynskit@pbs.edu.pl

** Marcin Łukasiewicz, PhD.: Faculty of Mechanical Engineering, Bydgoszcz University of Science and Technology, Al. prof. S. Kaliskiego 7, Bydgoszcz; PL, mlukas@pbs.edu.pl

*** Michał Liss, PhD.: Faculty of Mechanical Engineering, Bydgoszcz University of Science and Technology, Al. prof. S. Kaliskiego 7, Bydgoszcz; PL, michal.liss@pbs.edu.pl

† Assoc. Prof. Adam Mazurkiewicz: Faculty of Mechanical Engineering, Bydgoszcz University of Science and Technology, Al. prof. S. Kaliskiego 7, Bydgoszcz; PL, adam.mazurkiewicz@pbs.edu.pl

doi: 10.21495/em2024-150

2. Methods

Applying the modal analysis method in the assessment of the selected vehicle body elements state practice, the system under test must meet the relevant conditions and assumptions (Żółtowski et al., 2015):

- the system is linear and its dynamics can be described using a linear system of ordinary or partial differential equations. From the assumption of linearity of the system, we can formulate the principle of superposition of the system;
- the system satisfies Maxwell's principle of reciprocity; as a result of this condition, we obtain symmetrical matrices of masses, stiffness, damping and frequency characteristics;
- the damping in the system is small or proportional to the mass or elasticity;
- the system is observable and it is possible to measure all the characteristics that are necessary to know the model.

The analysis of body dynamics is possible either on the basis of a structural model (e.g. FEM) or through appropriate tests on a real object. For the purposes of this study, a comparison of the applied experimental modal analysis for two elements of the structure of the car body, shown in Fig. 1, is presented.

a) b)

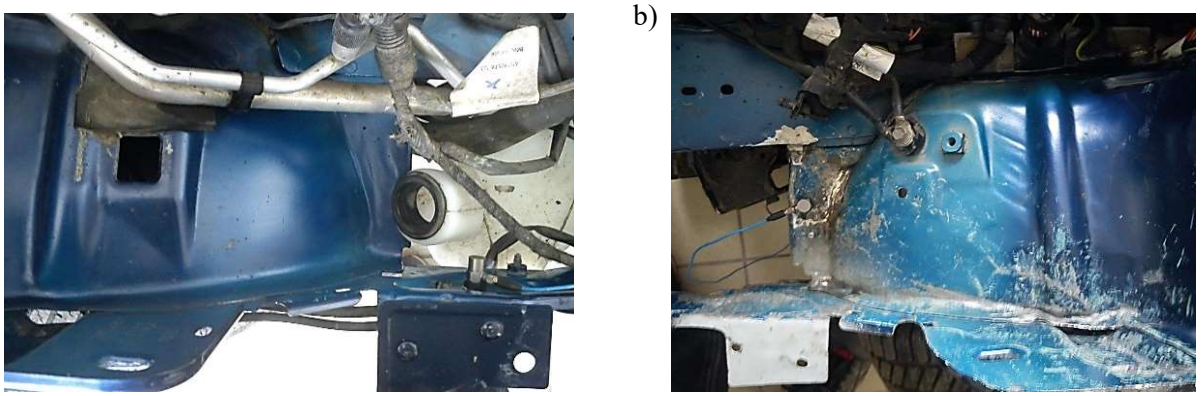

Fig. 1: a) An undamaged part of the vehicle body structure, b) damaged part of the vehicle body structure.

Assuming that the conditions have been met, the next stage of the research is to analyze the structure by stimulating it to vibrate by impulse excitation. This kind of excitation can be inflicted with a modal hammer or a vibration inductor. Fig. 2 shows the attachment of the response sensor and how to force the structure with a modal hammer. Arrangement of the measuring points show in Fig. 3.

Fig. 2: Modal analysis experiment example.

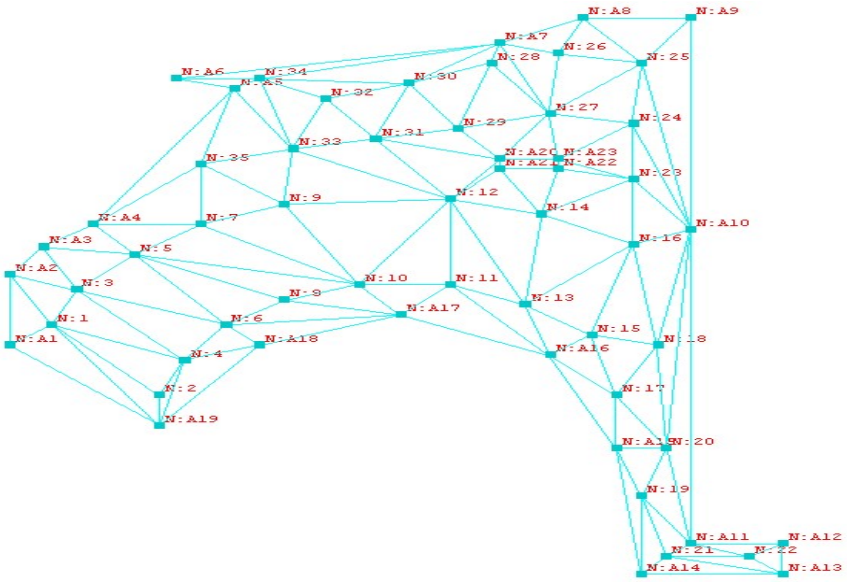

Fig. 3: Arrangement of measuring points on the test object.

The vibrational forms of the structure under study take different forms depending on the frequency of excitation. Each of the natural resonant frequencies corresponds to a specific form of vibration, often also called vibration modes. Selected mods are shown in Figs. 4 and 5.

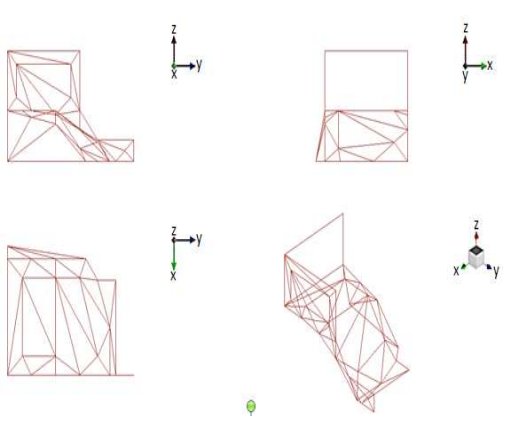

Fig. 4: Modeled geometry of the actual mode undamaged object.

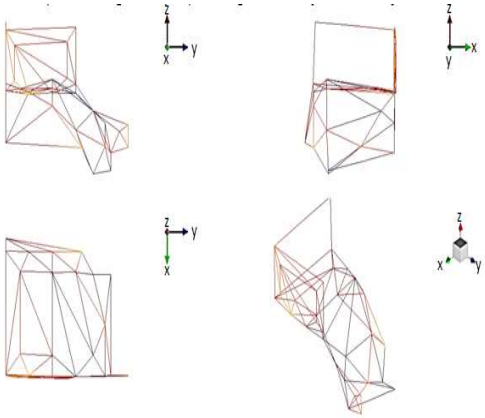

Fig. 5: Visualization of the selected mode of the body element as a response to the extortion inflicted.

One of the basic models of mechanical structures used for diagnostic purposes are finite element models. The results obtained from the simulation of the tuned model are compared with the model obtained from the measurement on a real object. If the correlation between the results of the model without damage and the results of the model derived from the experiment is close to unity, then the mechanical structure is not defective. A low or decreasing correlation value between the models indicates a specific type of damage or a progressive degradation of the mechanical structure (Łukasiewicz et al., 2014).

This type of structural diagnosis is based on the study of changes in the elements of the stiffness or elasticity matrix. The stiffness and elasticity matrices are closely related to the parameters of the modal model by the following relationships (Olatunbosun et al., 2010):

$$K = M(\sum_{i=1}^{n} \omega_i^2 \Psi_i \Psi_i^T)M, \tag{1}$$

$$S = \sum_{i=1}^{n} \frac{1}{\omega_i^2} \Psi_i \Psi_i^T, \tag{2}$$

where: n – Number of degrees of freedom, M – mass matrix, K – stiffness matrix, S – elastic matrix, ω_i – eigenfrequency, Ψ_i – vector of natural vibration modes.

As a result of the experiment, individual parameters of the modal model were obtained, which are summarized in Tab. 1.

	Natural frequency of vibrations [Hz]	Damping factor [%]	Order of the modal model
Undamaged element	146.010	0.81	23
	241.241	3.53	37
	357.726	3.77	27
	563.986	1.99	39
	613.041	1.71	26
	867.667	2.12	40
Damaged element	257.297	2.53	42
	426.802	1.97	34
	443.474	1.97	42
	759.213	2.26	37
	835.186	1.61	28
	913.352	1.34	24

Tab. 1: Summary of the obtained modal model parameters.

3. Conclusions

The problem of vehicle body parts degradation on Polish roads is still of importance. This is influenced not only by difficult climatic conditions, but also by the tendencies of vehicle users, who are largely interested in cars after more than ten years of operation, as well as post-accident cars, in which repair processes affect the dynamic properties of the repaired car components. In this type of vehicle group, the degradation of the body occurs to a large extent as a result of corrosion processes. This raises another problem with the assessment of the corrosion degree, which is still based only on organoleptic methods. Analyzing the available literature, it can be seen that several solutions to this problem have been developed, while the proposed methods are still very complicated and difficult to implement during the mandatory simple technical inspection.

An attempt to apply modal analysis methods for this purpose may shed a completely new light on the existing problem, and even become a viable solution that can also be applied to more common use.

Acknowledgement

This paper has been achieved under the research project “Hybrid multimedia mobile stage are a chance for decisive innovation” No. POIR.04.01.04-00-0045/17-00.

References

Kałaczyński, T., Łukasiewicz, M., Musiał, J., Polasik, R., Szczutkowski, M., Dluhunovych, N., Wilczarska, J. and Kasprowicz, T. (2018) Analysis of the diagnostic potential research thermovision in the technical state of combustion engine injectors assessment. In: *24th International Conference on Engineering Mechanics*, vol. 24, pp. 357–360.

Żółtowski, M., Liss, M., Żółtowski, B., and Melcer, J. (2015) Truss harbor cranes modal design elements research, *Polish Maritime Reasearch*, no. 4 (88), vol. 22, pp. 84–92.

Łukasiewicz, M., Kałaczyński, T., Musiał, J. and Shalapko, J. (2014) Diagnostics of buggy vehicle transmission gearbox technical state based on modal vibrations. *Journal of Vibroengineering*, nr. 16, vol. 6, pp. 3137–3145.

Olatunbosun, O. A., Gauchia, A., Boada, L. J. M. and Diaz, V. (2010) *Dynamic performance analysis of a light van body in white structure*, Automobile Engineering, London.

Żółtowski, B. and Kałaczyński, T. (2013) *Machine diagnostics. Lecture and exercises*, Bydgoszcz Wydawnictwo Uczelniane Uniwersytetu Technologiczno– Przyrodniczego (in Polish).

30th International Conference
ENGINEERING MECHANICS 2024
Milovy, Czech Republic, May 14 – 16, 2024

DATA-DRIVEN APPROACH TO ESTIMATING SOOT DISTRIBUTION INSIDE CATALYTIC FILTERS IN AUTOMOTIVE EXHAUST GAS AFTERTREATMENT

Khýr M.*, Plachá M., Hlavatý T.***, Isoz M.†**

Abstract: *The performance and the necessary regeneration frequency of catalytic filters (CFs) used in the treatment of automotive exhaust gases depend strongly on the solid matter accumulated within their porous walls. Reliable predictions of solid matter (soot) accumulation are crucial in the development and optimisation of CFs. In this contribution, we exploit the tools of artificial intelligence (AI) to estimate the distribution of soot directly in the porous microstructure of CFs. Specifically, our AI model uses deep neural networks (DNNs) and convolutional autoencoders (CAEs) to predict the soot distribution from information about the microstructure and the initial velocity field. To provide the model with training and validation data, we used our previously developed transient numerical model of particle deposition in the CF walls to calculate soot distribution in a dataset of artificial 2D geometries. The results of the developed AI model are in good agreement with simulation regarding the total amount of accumulated soot. However, the accuracy in the spatial distribution of the soot is not optimal, and consequently, using estimated particle deposits to simulate the pressure drop in the artificial microstructure results in 35 % accuracy.*

Keywords: AI, DNN, CFD, OpenFOAM, catalytic filters.

1. Introduction

The ever-tightening regulation of pollutants in automotive exhaust gas requires more efficient and complex gas aftertreatment systems. Particulate matter in the gas has to be filtered out and pollutant gases have to be converted. These two steps can be combined in one component, the catalytic filter (CF), thus reducing the heat losses and spatial requirements of the aftertreatment process (Kočí et al., 2019). The filtration efficiency and overall pressure drop of the CF are severely affected by the deposition of particulate matter (soot) within its porous walls. Filtration simulations can benefit microstructure design by predicting the distribution of soot.

In our previous work, we studied gas flow and pollutant gas conversion Kočí et al. (2019) and particulate matter filtration (Plachá et al., 2024) at a pore-scale level utilising tools of computational fluid dynamics (CFD). The CFD-based pore-scale numerical solver by Plachá et al. (2024) uses a partially two-way coupled Eulerian-Lagrangian approach to model the transport of solid particles in flowing gas. The solver is capable of predicting the accumulated soot distribution resolved in space and time in good agreement with the experimental data. In this work, we attempt to circumvent the main computational bottleneck of the numerical model, namely the computational cost of particle tracking during the soot deposition modelling. We propose a data-driven approach to estimating the soot distribution, and whilst our ultimate goal is to estimate the spatio-temporal distribution in real-world three-dimensional microstructures, at present we focus solely on soot distribution in two-dimensional artificial geometries at an a priori selected time step.

* Matyáš Khýr: Institute of Thermomechanics, Czech Academy of Sciences (CAS), Dolejškova 1402/5; 182 00, Prague; CZ, khyrm@it.cas.cz

** Ing. Marie Plachá, PhD.: Department of Chemical Engineering, Faculty of Chemical Engineering, University of Chemistry and Technology, Technická 5; 166 28, Prague; CZ

*** Ing. Tomáš Hlavatý: Institute of Thermomechanics, CAS, Dolejškova 1402/5; 182 00, Prague; CZ

† Ing. Martin Isoz, PhD.: Institute of Thermomechanics, CAS, Dolejškova 1402/5; 182 00, Prague; CZ

doi: 10.21495/em2024-154

In the following text, we will briefly introduce the numerical model by Plachá et al. (2024) and present the developed AI model focussing first on the structural parts; deep neural networks (DNNs) and convolutional autoencoders (CAEs); and then on the complete architecture. Next, we describe the generation of the artificial model dataset and, finally, we show examples of predicted soot distributions and compare the simulated pressure drop between the microstructures with the simulated and estimated soot deposits.

2. Mathematical model

Full-order numerical model. The training and validation dataset for AI was prepared using the numerical model by Plachá et al. (2024) which was created for simulation of the accumulation of soot within the CF. The model combines two approaches; Eulerian and Lagrangian. The Eulerian approach is used to calculate the flow within the CF microstructure, and the effect of particles on the flow is neglected. The calculated velocity field is then used to simulate the transport of the particulate matter by tracking individual particles via the Lagrangian approach. Interactions between particles are not taken into account, given their small sizes and low concentrations. The two approaches are partially coupled, since the deposited matter is introduced into the computational domain via an algorithm of Isoz and Plachá (2022) where the matter creates a porous zone obstructing the flow and a probabilistic particle trap. Hence, the flow field can be recomputed iteratively and the newly deposited particulate matter is reflected by adjusting the domain.

The SIMPLE algorithm, as implemented in OpenFOAM (OpenCFD, 2007), is used to solve the Navier-Stokes equations in a form describing a steady-state incompressible laminar flow of a Newtonian fluid. The computational domain Ω considered here can be divided into three respective sub-domains containing; free pores (Ω_P), catalytic coating (Ω_C), and deposited soot (Ω_s). The governing equations can be written as

$$\begin{aligned} \nabla\cdot(\boldsymbol{u}\otimes\boldsymbol{u}) - \nabla\cdot(\nu\nabla\boldsymbol{u}) &= -\nabla\tilde{p} + \boldsymbol{s} \\ \nabla\cdot\boldsymbol{u} &= 0 \end{aligned} \quad , \quad \boldsymbol{s} = \begin{cases} 0 & \text{in } \Omega_\mathrm{P} \\ -\frac{\nu}{\kappa_\mathrm{C}}\boldsymbol{u} & \text{in } \Omega_\mathrm{C} \\ -\phi_\mathrm{s}\frac{\nu}{\kappa_\mathrm{s}}\boldsymbol{u} & \text{in } \Omega_\mathrm{s} \end{cases} \tag{1}$$

where $\boldsymbol{u}$ is the gas velocity, ν kinematic viscosity and $\tilde{p}$ the kinematic pressure. The source term $\boldsymbol{s}$ is active only in the catalytic coating (Ω_C) and in the deposited soot (Ω_s), as it accounts for additional resistance in these porous regions, calculated based on the Darcy permeability model. Particle tracking implementation reflects Newton's second law of motion

$$m\frac{\mathrm{d}^2\boldsymbol{r}}{\mathrm{d}t^2} = \boldsymbol{F}_\mathrm{D} + \boldsymbol{F}_\mathrm{B}\,, \tag{2}$$

where $\boldsymbol{r}$ is the particle position and m the particle mass. Two forces acting on the particles are assumed; the drag $\boldsymbol{F}_\mathrm{D}$ and the Brownian force $\boldsymbol{F}_\mathrm{B}$; other forces are negligible. To calculate the drag, the Stokes law with Cunningham slip correction is used (Plachá et al., 2024). The Brownian force is calculated as in Li and Ahmadi (1993). Furthermore, the model implements the effect of adhesion of the soot via a probabilistic trap. When a particle comes into contact with the walls of the CF or the coating, the probability is set to $\mathcal{P} = 1$. In cells with deposited soot, a particle is trapped with probability $\mathcal{P} = \phi_\mathrm{s}$, where ϕ_s is the volume fraction of soot in the cell. The model is implemented in the OpenFOAM open-source C++ library (OpenCFD, 2007) and its detailed description can be found in Plachá et al. (2024); Isoz and Plachá (2022).

The numerical model was used by Plachá et al. (2024) to perform simulations in $500\,\mu\mathrm{m}$ long segments of the wall of the CF channel, see Fig. 1a. A two-dimensional square cutout with size $80\,\mu\mathrm{m}$ was created as a model geometry for the AI. The cutout captures a single channel the inner dimensions of which were parameterised. Namely, the number of substrate and coating layers on the walls were changed to ensure that the model dataset includes geometries with various structural characteristics, see examples in Fig. 1c.

Data-driven soot estimation model. The neural network design stems from our objective to estimate the soot distribution function $\phi_\mathrm{s}^t : \Omega \subset \mathbb{R}^d \to [0,1]$, $d = 2,3$ at an a priori selected time $t \in (0,T]$ via an approximation of an operator $\mathcal{G}$. The operator's arguments are the binary microstructure function $\boldsymbol{Z} : \Omega \to \{0,1\}^2$ and the initial velocity field $\boldsymbol{u} : \Omega \to \mathbb{R}^d$ in a clean CF. Fundamentally, this approach is inspired by the DeepONet of Shukla et al. (2024). In particular, discrete approximations of $\boldsymbol{Z}$ and $\boldsymbol{u}$ are processed and a discrete approximation of ϕ_s^t is returned, i.e., we pursue a discrete approximation of $\mathcal{G}$.

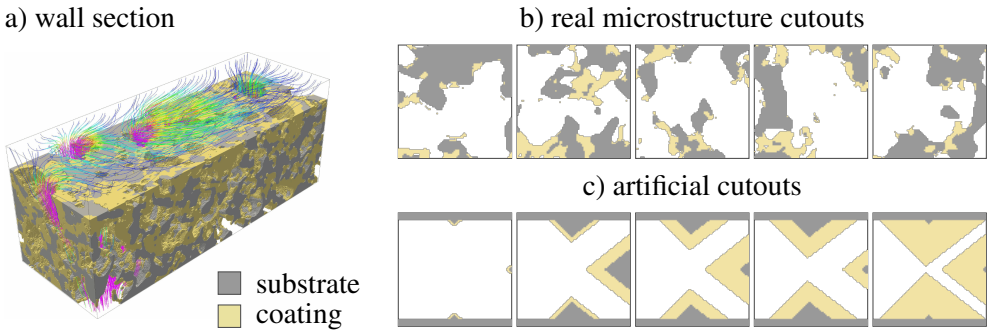

Fig. 1: a) CF wall segment from (Plachá et al., 2020); b) and c) examples of microstructure cutouts.

To efficiently process high-dimensional data, separately trained fully-connected deep neural network and three convolutional autoencoders are used in the model. The microstructure data including substrate ($\boldsymbol{Z}_\mathrm{S}$) and catalytic coating ($\boldsymbol{Z}_\mathrm{C}$) are processed by the first autoencoder, the velocity field ($\boldsymbol{u}$) by the second and the soot volume fraction field (ϕ_s^t) by the third. Note that all the fields in the present work are considered to be of dimension $d = 2$. Lastly, the field of the volume fraction of soot is estimated by the deep neural network.

Deep neural networks (DNNs) consist of layers of small units, so-called *neurons*. Each neuron represents a function, the function of the j-th neuron in the i-th layer can be written as $o_{ij} = f_{ji}(\boldsymbol{x})$. The input of the function ($\boldsymbol{x} = \boldsymbol{o}_{i-1}$) is the vector of outputs of neurons forming the $(i-1)$-th layer. The output is a part of inputs to each neuron in the $(i+1)$-th layer. The function f_{ij} is a composed parametric function $a_{ij}(\boldsymbol{w}_{ij}^\mathsf{T}\boldsymbol{o}_{i-1})$, where a is the activation function and $\boldsymbol{w}$ the weight vector. In matrix-vector notation, the parametric function for i-th layer can be written as

$$f_i(\boldsymbol{o}_{i-1}) = \boldsymbol{a_i}(\boldsymbol{W}_i^\mathsf{T}\boldsymbol{o}_{i-1})\,, \tag{3}$$

where $\boldsymbol{a}$ is generally non-linear and applied in an element-wise manner on the product of the weight matrix $\boldsymbol{W}$ and the previous layer output $\boldsymbol{o}_{i-1}$ representing an affine transformation. Training a neural network means adjusting the network weights to minimise the error in fitting the given data.

A convolutional autoencoder is formed of two parts; an encoder and a decoder. The role of the encoder is to gradually reduce the dimensionality of the input data, and it commonly consists of a combination of convolutional and downsampling layers. On the other hand, the decoder uses transposed convolutional layers with strides and/or upsampling to reconstruct high-dimensional data from the low-dimensional representation.

The complete architecture of the AI model comprises two encoders for transforming the high-dimensional input data into low-dimensional latent representations, a DNN for work in the latent space and, a decoder for transformation of the DNN output back. The approximated operator $\mathcal{G}$ then works in several branches. In the first one, the two matrices $\boldsymbol{Z}_\mathrm{S}$ and $\boldsymbol{Z}_\mathrm{C}$ representing the microstructure are given to the pre-trained encoder and they are converted into their latent representation. In the second branch, the flow field data $\boldsymbol{u}$ are processed similarly to the first branch. Thereafter, the DNN estimates the latent representation $\tilde{\phi}_\mathrm{S}$ of the desired field ϕ_s. Lastly, the two-dimensional ϕ_s is reconstructed by the pre-trained decoder. The architecture described and data examples are depicted in Fig. 2a.

Data transfer between full-order model and AI. The cells of the initial coarse orthogonal computational mesh correspond one-to-one to the elements of the binary matrices $\boldsymbol{Z}$. However, during simulation, the mesh is refined near the edges and in regions with accumulated soot. This leads to a locally refined unstructured mesh from which the results cannot be used directly as input to the encoders. The data from the unstructured mesh must first be mapped back onto a coarse structured orthogonal mesh, and then the cell-centre values can be read and stored in rectangular matrices. Similarly, the estimated values $\hat{\phi}_\mathrm{s}$ are mapped back onto a coarse mesh and, subsequently, the mesh is refined and used in the simulation to compute the pressure drop.

3. Results

Examples of soot distribution estimates compared to simulation together with pressure fields in model geometries calculated with estimated and simulated soot deposits are shown in Fig. 2b. Although the network

was able to capture the general shape of accumulated soot, the mean squared error (MSE) in the estimated soot distributions across the validation dataset is larger than 50 %, since the estimated distributions are more diffuse. This also affects the pressure fields and the calculated pressure drop, which has a mean error 35 % across selected samples.

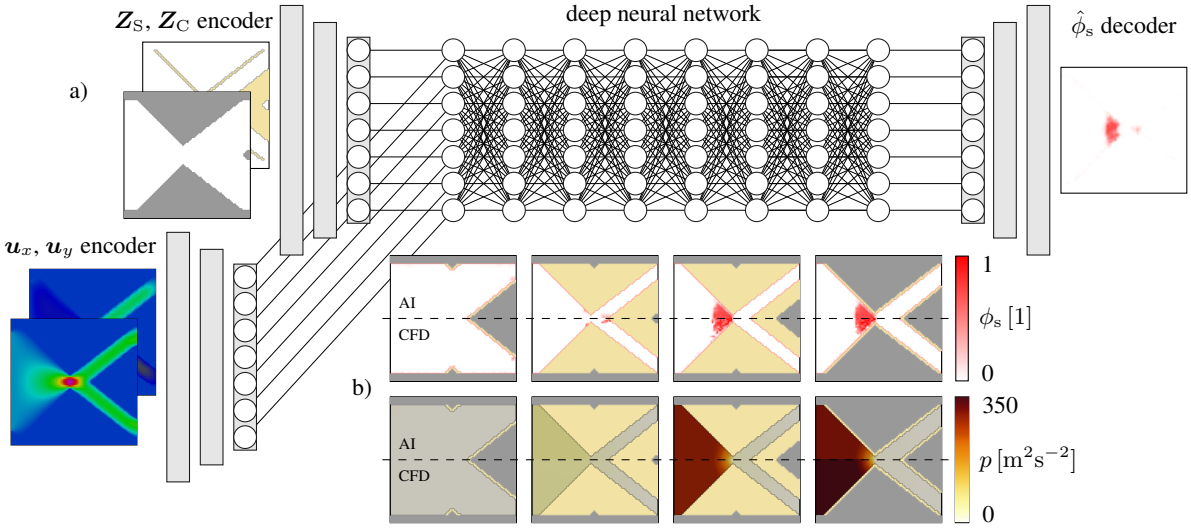

Fig. 2: a) AI model architecture and b) examples of soot distributions and pressure fields in model geometries.

4. Conclusions

We presented the design of a neural network capable of estimating the soot distribution in the catalytic filter walls. We used an existing numerical model to create an artificial model dataset that was then used for network training and validation. We have demonstrated the model's ability to process structural data and provide qualitative estimates of the soot distribution, which are accurate in the total amount of accumulated soot but lack the sharp spatial distribution. Since the smearing present in AI estimates affects the pressure drop, we are currently working to address this before extending the model to three-dimensional geometries.

Acknowledgments

The work was financially supported by the institutional support RVO:61388998, by the Czech Science Foundation (GA 22-12227S) and by the grant project with No. TN02000069/001N of the Technology Agency of the Czech Republic.

References

Isoz, M. and Plachá, M. (2022) A parallel algorithm for flux-based bounded scalar redistribution. In *Proceedings of the conference Topical Problems of Fluid Mechanics*. Institute of Thermomechanics of the Czech Academy of Sciences, pp. 87–94.

Kočí, P., Isoz, M., Plachá, M., Arvajová, A., Václavík, M., Svoboda, M., Price, E., Novák, V., and Thompsett, D. (2019) 3D reconstruction and pore-scale modeling of coated catalytic filters for automotive exhaust gas aftertreatment. *Catalysis Today*, 320, pp. 165–174.

Li, A. and Ahmadi, G. (1993) Computer simulation of deposition of aerosols in a turbulent channel flow with rough walls. *Aerosol Science and Technology*, 18, pp. 11–24.

OpenCFD (2007) *OpenFOAM: The Open Source CFD Toolbox. User Guide Version 1.4, OpenCFD Limited*. Reading UK.

Plachá, M., Isoz, M., Kočí, P., Jones, M., Svoboda, M., Eastwood, D., and York, A. (2024) Particle accumulation model in 3D reconstructed wall of a catalytic filter validated with time-resolved X-ray tomography. *Fuel*, 356, pp. 129603.

Plachá, M., Kočí, P., Isoz, M., Svoboda, M., Price, E., Thompsett, D., Kallis, K., and Tsolakis, A. (2020) Pore-scale filtration model for coated catalytic filters in automotive exhaust gas aftertreatment. *Chemical Engineering Science*, 226, pp. 115854.

Shukla, K., Oommen, V., Peyvan, A., Penwarden, M., Plewacki, N., Bravo, L., Ghoshal, A., Kirby, R. M., and Karniadakis, G. E. (2024) Deep neural operators as accurate surrogates for shape optimization. *Engineering Applications of Artificial Intelligence*, 129, pp. 107615.

30th International Conference
ENGINEERING MECHANICS 2024
Milovy, Czech Republic, May 14 – 16, 2024

DYNAMIC PROPERTIES OF PRESSURE COMPENSATED PUMP

Kolář D.*

Abstract: *The aim of the study is to evaluate the dynamic properties of a variable displacement pump. It is a pressure compensated axial piston pump with swash plate. The dynamic properties will be evaluated for transient response. The transient response will be induced by the rapid closure of the directional valve located at the pump outlet. The consequence of the directional valve rapid closure is the regulation of the displacement. The main motivation of this paper is to determine, if the pump speed and the set pump displacement affect the control time in and the overshoot. A methodology for measuring the dynamic properties during the transient response is presented in this paper. The experimental circuit used to measure the dynamic properties is described. Subsequently, the time dependence of the pressure at the pump outlet is evaluated when the directional valve at the pump outlet is rapidly closed. The measurements are then used to evaluate the overshoot and the control time in as a function of the pump speed and the pump relative displacement. The results will be further used to create a mathematical model of a pressure compensated pump.*

Keywords: Dynamic properties, pressure compensated pump, overshoot, control time in.

1. Introduction

Pressure compensated pumps are used in many industrial applications. Pressure compensated pumps are used in energy saving systems as shown in (Vašina et al., 2018). The pressure compensated pump works on the following principle. When the pressure in the circuit reaches to the value set on the pressure compensator, the pump displacement is regulated to the minimum value. From this perspective, two basic states can be defined for the pressure compensated pump. In the first state, the pressure at the pump outlet has not reached the value, which is set on the pressure compensator. The pump displacement is maximal and the pump generates the maximal flow rate. In the second state, the pressure at the pump outlet has reached the value, which is set on the pressure compensator. The pump displacement is minimal and the pump generates the minimal flow rate. This minimal flow rate covers the flow losses of the pump to maintain a constant pressure at the pump outlet. If there is a sudden increase in hydraulic resistance in the circuit, the pressure will also increase. This can be demonstrated, for example, by the rapid closure of the directional valve at the pump outlet. The decrease of pump displacement occurs over a certain settling time. In the meantime, the pressure at the pump outlet also rises above the value, which is set at the pressure compensator. In terms of the transient response, it is desirable to avoid pressure peaks in the system and to keep the settling time as short as possible. The dynamic properties of a pressure compensated pump are examined by (Mondal et al., 2022; Mondal et al., 2018). They investigate how the closing speed of the valve at the pump outlet affects the pressure peak. From their results, it can be observed that as the closing time increases, the pressure peak in the system decreases, but the settling time increases. Subsequently, (Saleh et al., 2006) examine whether the pump speed has an effect on overshoot and settling time. They concluded that as the pump speed increases, the overshoot increases and the settling time decreases. The knowledge of these properties is important for the development of the mathematical model of pressure compensated pump.

* Ing. David Kolář: VŠB-TUO, Faculty of Mechanical Engineering, Department of Hydromechanics and Hydraulic Equipments, 17. listopadu 2172/15, 708 00, Ostrava, CZ, david.kolar@vsb.cz

doi: 10.21495/em2024-158

2. Methods

An experimental circuit was designed and assembled to measure the dynamic properties of the pressure compensated pump. A scheme of the circuit is shown in Fig. 1. The main part of the circuit is the pressure compensated pump (HP+PC). The pump has a set screw, which can be used to limit the displacement. The source of mechanical energy for the pump is the electric motor (M). The electric motor speed is control by a frequency converter (FC). A relief valve (RV) is connected in parallel to the pump to ensure the safety function. The pump is loaded by a proportional relief valve (PRV). A directional valve (DV), which is located before the proportional relief valve, is used to close the pump outlet. In order to keep the oil viscosity constant, a cooler (C) is placed in the circuit. A temperature of 53 °C ± 1 °C is maintained in the circuit. The oil purity is maintained by the filter (F). The circuit is further contained a pump outlet pressure sensor (PS), a flow rate sensor (FS), a speed sensor (SS) and a temperature sensor (TeS). The tank (T) is a reservoir for the oil.

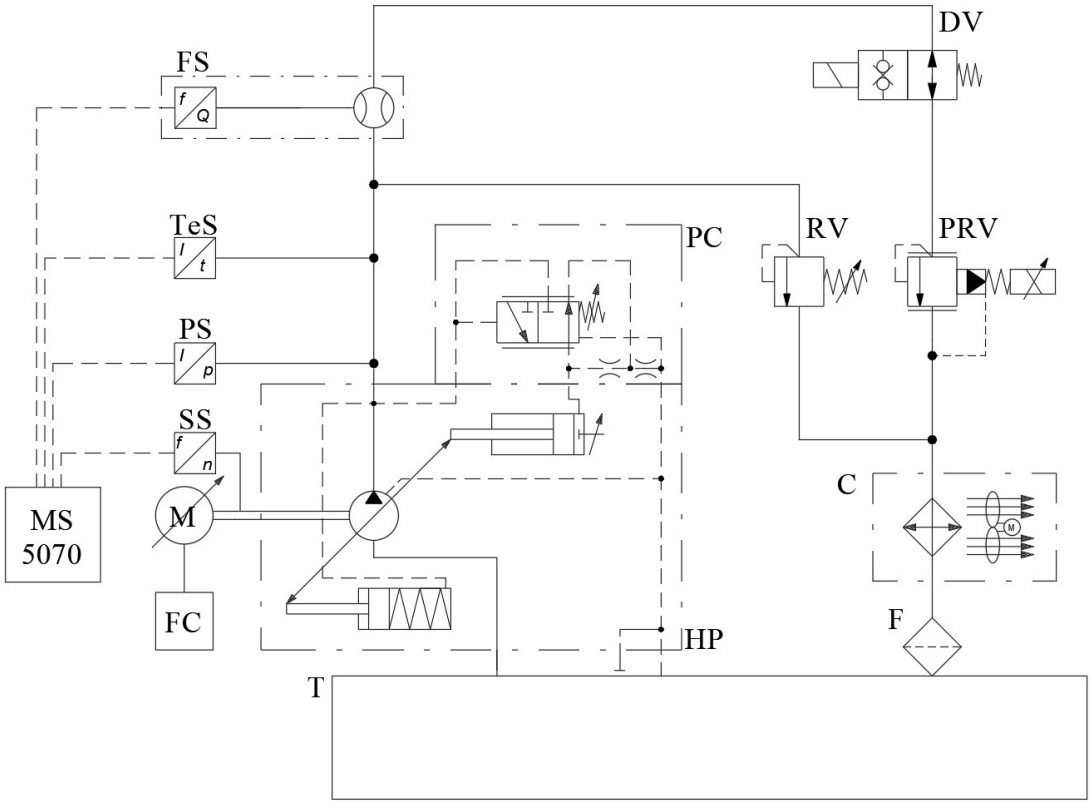

Fig. 1: Experimental circuit scheme.

Measurement procedure

The relief valve (RV) was fully open. The directional valve (DV) was closed and at the pressure compensator (PC) was set the maximal pressure. The speed of electric motor (M) was set to value n = 1 500 min^{-1}. The pressure at the relief valve was set to value p_{RV} = 250 bar. The pressure at the pressure compensator was set to value p_{PC} = 110 bar. Then the directional valve (DV) was opened. The pressure at the proportional relief valve was set to value p_{PRV} = 40 bar. Then, time recording of the variables was performed with a time of 3 s and a sampling rate of 0.0001 s. At time t = 0.5 s, the directional valve (DV) was closed. This process was repeated for pump speed n = (1 250; 1 000; 750; 500) min^{-1} and pump relative displacement β = (0.75; 0.50; 0.25). The pump relative displacement β is the ratio between the set pump displacement and the maximal pump displacement.

3. Results

If the directional valve is closed rapidly, a transient response will occur. The result of the transient response is a pressure peak, which is determined by the kinetic energy of the oil, the oil bulk modulus, the oil viscosity, etc. (Bureček et al., 2015; Hružík et al., 2017). In this research, the time dependencies of pressure

p at the pump outlet during the rapid closure of the directional valve were evaluated. The control time in t_{SE} was evaluated from each time dependence. The control time in t_{SE} is the time, which is elapsed from the moment, when the directional valve is closed to the moment, when maximal pressure is reached at the pump outlet, see (RE 92 712). Subsequently, the pressure peak p_{max} was evaluated from each time dependence. Furthermore, the time dependencies of pressure p at the different pump speeds n are shown in Fig. 2a and also the time dependencies of pressure p at different pump relative displacements β are shown in Fig. 2b. In Fig. 2a is shown an example of the control time in t_{SE} (s) and pressure peak p_{max} (bar) evaluation. Subsequently, the overshoot x (%) was evaluated for each pressure peak p_{max}, according to:

$$x = \frac{p_{max}}{p_{PC}} \cdot 100 - 100, \tag{1}$$

where p_{max} is the pressure peak (bar) and p_{PC} is the pressure set at the pressure compensator (bar).

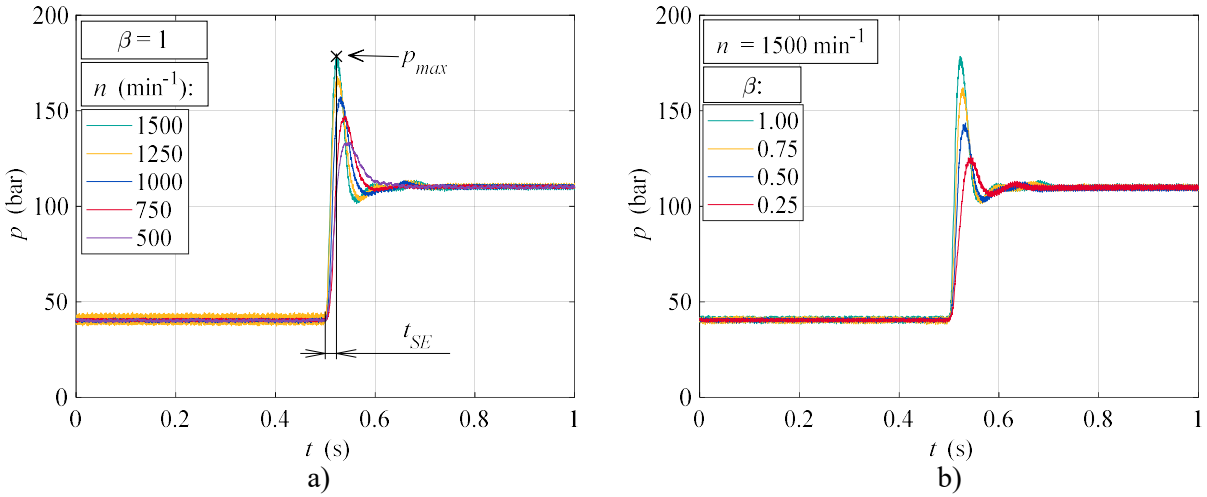

Fig. 2: Time dependencies of pressure p:
a) for different pump speeds n, b) for different pump relative displacements β.

The dependencies of the control time in t_{SE} on the pump speeds n at the different pump relative displacements β were evaluated, see Fig. 3a. Subsequently, the dependencies of overshoot x on the pump speeds n at the different pump relative displacements β were also evaluated, see Fig. 3b.

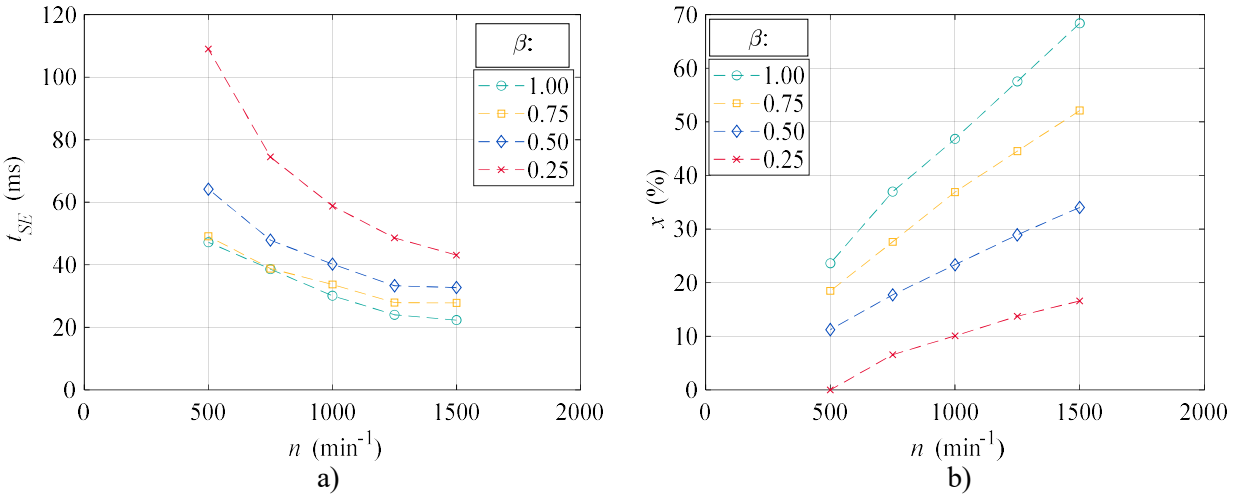

Fig. 3: Dependencies on the pump speeds n at the pump relative displacements β:
a) of the control time in t_{SE}, b) of the overshoot x.

Fig. 3a shows the control time in t_{SE} decreases with an increasing pump speed n and the control time in t_{SE} decreases with an increasing pump relative displacement β. Fig. 3b shows the overshoot x increases with an increasing pump speed n and the overshoot x increases with an increasing pump relative displacement

β. These evaluated control times in t_{SE} can be burdened with a deviation of up to 3 ms, which is due to the effect of different closing times of the directional valve at different flow rates Q.

In Tab. 1 are evaluated values of control time in t_{SE} and overshoot x at different pump speeds n and different pump relative displacements β.

	n = 1 500 min^{-1}		n = 1 250 min^{-1}		n = 1 000 min^{-1}		n = 750 min^{-1}		n = 500 min^{-1}	
	t_{SE} [ms]	x [%]	t_{SE} [ms]	x [%]	t_{SE} [ms]	x [%]	t_{SE} [ms]	x [%]	t_{SE} [ms]	x [%]
β = 1.00	22.3	68.4	24.0	57.5	30.1	46.8	38.6	37.0	47.2	23.6
β = 0.75	27.8	52.1	27.9	44.5	33.7	36.9	38.8	27.6	49.1	18.5
β = 0.50	32.7	34.0	33.3	28.9	40.2	23.3	47.9	17.7	64.2	11.2
β = 0.25	43.1	16.6	48.6	13.7	58.8	10.1	74.5	6.6	109.0	0.0

Tab. 1: Evaluated values of control time in t_{SE} and overshoot x.

4. Conclusions

The aim of this study was to assess the effect of the pump speed and pump relative displacement on the dynamic properties of the pressure compensated axial piston pump with a swash plate. The measurements were carried out at different pump speeds and different pump relative displacements. The main monitored variables were control time in and overshoot. It was found, when the pump speed increases the control time in decreases and the overshoot increases. It was also found, when the pump relative displacement increases the control time in decreases and the overshoot increases. The results will be used to develop and verify the mathematical model of the pressure compensated pump. Also, the results can be used to compare the dynamic properties of pressure compensated pumps of other design types. In the future, the time dependence of torque on the pump shaft will be measured.

Acknowledgement

This work was supported by the European Regional Development Fund in the Research Centre of Advanced Mechatronic Systems project, project number CZ.02.1.01/0.0/0.0/16_019/0000867 within the Operational Programme Research, Development and Education.

The work presented in this paper was supported by a grant SGS „Operational properties of fluid mechanisms and their mathematical predictions.” SP2024/019.

References

Vašina, M., Hružík, L. and Bureček, A. (2018) Energy and Dynamic Properties of Hydraulic Systems. *Tehnicki Vjesnik-Technical Gayette*, vol. 25, no. 2, pp. 382–390.

Mondal, N., Saha, R. and Sanyal, D. (2022) An Experimental Exploration on Pressure-Compensated Swash Plate-Type Variable Displacement Axial Piston Pump. *Journal of The Institution of Engineers*: Series C, vol. 103, iss. 3, pp. 267–277.

Mondal, N., Saha, R. and Sanyal, D. (2018) An Experimental Study on Variable Displacement Pressure Compensated Yoke Typ Axial Piston Pump. In: *Proc. of the 7th International and 45th National Conference on Fluid Mechanics and Fluid Power* (FMFP), IIT Bombay, 4 p.

Saleh, T. A., Rabie, M. G. and Abdou, S. E. (2006) Investigation of Static and Dynamic Behavior of Pressure Compensated Variable Displacement Swash Plate Axial Piston Pump. In: *Proc. of the 12th AMME Conference*, Military Technical College Cairo, pp. 315–333.

Datasheet Bosch-Rexroth: Variable displacement pump A10VSO18 RE 92 712/10.07.

Bureček, A., Hružík, L. and Vašina, M. (2015) Determination of Undissolved Air Content in Oil by Means of a Compression Method, *Strojnicki Vestnik-Journal of Mechanical Engineering*, vol. 61, no. 7–8, pp. 477–485.

Hružík, L., Bureček, A. and Vašina, M. (2017) Effect of Oil Viscosity on Pulsating Flow in Pipe. *Advances in Mechanism Design II*, vol. 44, pp. 137–143.

30th International Conference
ENGINEERING MECHANICS 2024
Milovy, Czech Republic, May 14 – 16, 2024

DESIGN OF CABLE-NETS FOR GLASS FAÇADES

Komlev V.*, Machacek J.**

Abstract: *The studies of cable-nets supporting glass façades are presented. Numerical modelling of the net, point-fixed bolted (spider) attachment and glass panes is described in some details using ANSYS software. Basic entry data concerning geometry, glass and cable properties are introduced based on current European Standards. Commonly recommended cable prestressing and the transverse wind loading in accordance with Eurocode 1 are employed. Partial results of large parametric studies are presented, covering various cable-net geometry, set of glass thicknesses and cable diameters. Finally, the study of a failure of some cables and robustness of the cable-net is demonstrated.*

Keywords: Cable-net, prestressing, glass façade, nonlinear analysis, anchorage failure, robustness.

1. Introduction and analysis

Large-scale glass façades are frequently supported by prestressed cable-net systems using point-fixed fittings to attach glass panes, see Fig. 1. The systems and basic elements (laminated or insulated glass units, point-fixed bolted (spider) or clamped fittings, prestressed stainless steel cables incl. anchors) are described in some details by Komlev and Machacek, 2022, 2023.

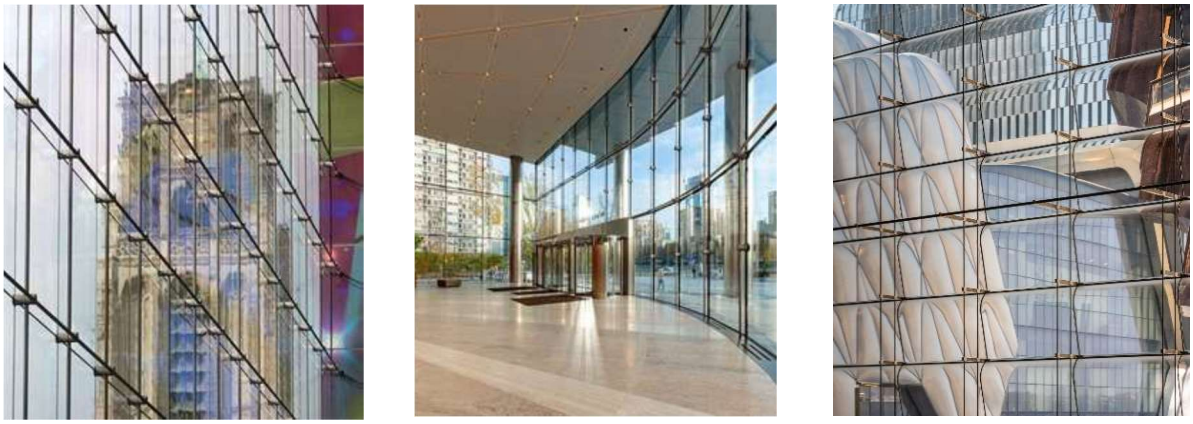

Fig. 1: Market Hall Rotterdam (2014), Mennica Tower Warsaw (2019), Hudson Yard 20 N. Y. (2018).

The typical cable-nets with laminated glass panes attached by spider fittings were analysed by the authors using software ANSYS 2021/R2 and facilitating by use of the Python code. FE modelling employed elements SOLID 186 (glass), SOLID 187 (spiders) and BEAM 188 (cables). Frictional contact surfaces were introduced in the all mentioned elements. The prestressing was applied on each cable at its one end in the direction of the cable axis. The transverse loading represents wind loads in accordance with EN 1991-1-4 (region III, terrain III, force coefficients for suction -1.2) as a characteristic pressure of F_{wk} =1 kPa (in case of the serviceability limit states, i.e. for deflections) and design pressure of F_{wd} =1.5 kPa (in case

* Mgr. Vitalii Komlev: Czech Technical University in Prague, Faculty of Civil Engineering, Thakurova 7; 166 29, Prague; CZ, vitalii.komlev@fsv.cvut.cz

** Prof. Ing. Josef Macháček, DSc.: Czech Technical University in Prague, Faculty of Civil Engineering, Thakurova 7; 166 29, Prague; CZ, machacek@fsv.cvut.cz

doi: 10.21495/em2024-162

of ultimate limit states, i.e. for stresses and cable loads). These loadings were applied as the uniform area loadings following the cable prestress in the next, final loading step.

After the successful validating of the modelling using experiments by Yussof (2015) and verification using data by Shang (2014) (for details see Komlev and Machacek (2023)) this paper presents results of parametric studies concerning the realistic configurations of cable nets, laminated glazing and robustness of the façades after failures of some cables.

2. Basic data

The studies cover an arbitrary chosen façades with cable-nets according to Fig. 2. The glass panes are attached by spider point-fixed bolted fixing, while the 5 mm gap among the panes for silicon sealing is considered.

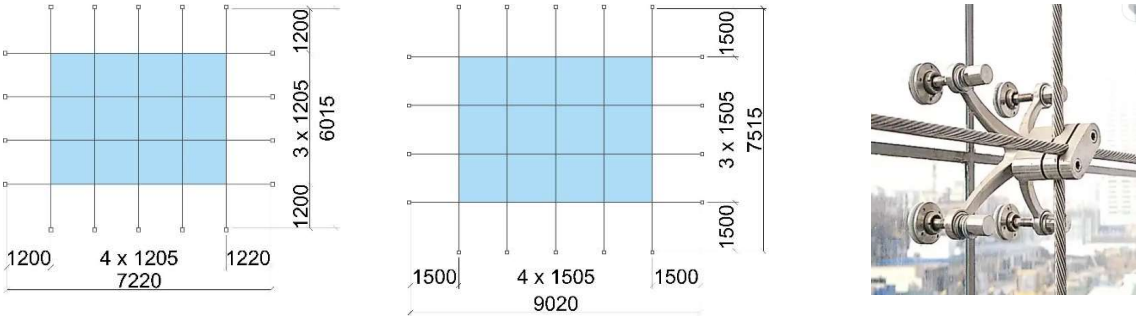

Fig. 2: Cable-nets analysed in the study and "spider" fixing of the glass panes.

The laminated glass was considered from two glass panes of various thickness with PVB (polyvinylbutyral) 0.76 mm interlayer. In accordance with standards EN 16612 (Glass in buildings - Determination of the lateral load resistance of glass panes by calculation, CEN, 2019) and CEN/TS 19100-2 (Design of glass structures - Part 2: Design of out-of-plane loaded glass components, EN-CENELEC, 2021) the equivalent thicknesses for numerical analysis were established (see Tab. 1), while shear factor taking PVB into account was considered as $\omega = 0.3$.

Laminated glass	Equivalent thickness for deflections [mm]	Equivalent thickness for stresses [mm]
4+0.76+4	6.63	7.32
6+0.76+6	9.75	10.74
8+0.76+8	12.86	14.15
10+0.76+10	15.98	17.57
12+0.76+12	19.10	20.98

Tab. 1: Laminated glass used in the study.

Glass properties according to EN 16612: modulus of elasticity 70 GPa, density 2 500 kg/m^3, compression strength 1 000 MPa, Poisson's ratio 0.23 and the design bending strength for the thermally toughened safety glass follows from the standard formulas based on class CC3 consequences (see EN 19100-1) for $\gamma_{MA} = 2.0$ and $\gamma_{MV} = 1.3$. Resulting design bending strength gives $f_{gd} = 75.7$ MPa.

Stainless steel Macalloy cables 1 x 19 with modulus of elasticity 107 GPa, diameters, breaking and design loads according to Tab. 2 were considered in the study. The prestressings were assumed to be 30 % of the design loads in accordance with the published recommendations.

The deflections in the serviceability limit states (for the characteristic loadings) are limited in accord with EN 16612 either to $L/65$ or 50 mm, with L as the shorter span. The absolute value seems to be rather strange in respect to the net dimensions and so only limit $L/65$ was taken into account. The respective value for the 1 200 x 1 200 [mm] net gives 92.5 mm and for the 1 500 x 1 500 [mm] net results in 115.6 mm.

Diameter [mm]	Breaking load [kN]	Design load [kN]	Prestressing load [kN]
14	139	92.7	27.8
16	182	121.3	36.4
19	212	141.3	42.4
22	285	190.0	57.0
26	398	265.3	79.6

Tab. 2: Stainless steel strands Macalloy 1 x 19 used in the study.

3. Results of studies

3.1. Strengths and deflections

Results of parametric studies with the net of 1 200 x 1 200 [mm] is presented in Tab. 3, of the net 1 500 x 1 500 [mm] in Tab. 4. The nets not satisfying either glass design bending stress (< 75.7 MPa) or limit deflections (for the net 1 200 x 1 200 < 92.5 [mm] and for the net 1 500 x 1 500 < 115.6 [mm]) are shown in italics (Note: not satisfying nets with even lower dimensions were in these tables excluded).

Laminated glass [mm]	Cable diameter [mm]	Cable prestress [kN]	Maximal cable force [kN]	Maximal glass stress [kN]	Maximal deflection [kN]
10+0.76+10	*14*	*27.8*	*36.1*	*55.3*	*102.5*
4+0.76+4	16	36.4	42.2	75.7	91.5
6+0.76+6		36.4	42.5	58.6	87.0
10+0.76+10		36.4	43.9	51.8	83.6
4+0.76+4	19	42.4	48.9	68.9	79.3
6+0.76+6		42.4	48.0	40.3	74.9
10+0.76+10		42.4	49.8	37.7	72.4

Tab. 3: Results for net 1 200 x 1 200 [mm].

Laminated glass [mm]	Cable diameter [mm]	Cable prestress [kN]	Maximal cable force [kN]	Maximal glass stress [kN]	Maximal deflection [kN]
12+0.76+12	*19*	*42.4*	*57.6*	*62.0*	*120.7*
8+0.76+8	22	57.0	69.3	64.3	102.0
10+0.76+10		57.0	69.6	61.4	99.1
12+0.76+12		57.0	70.2	58.8	97.5
8+0.76+8	26	79.6	89.9	59.6	80.4
10+0.76+10		79.6	90.4	57.4	78.1
12+0.76+12		79.6	90.9	56.2	76.8

Tab. 4: Results for net 1 500 x 1 500 [mm].

The maximal cable forces seem to be rather low in comparison with the design cable load given in Tab. 2. Therefore, in spite of generally recommended prestressing value of 30 % much higher prestressing seems to be appropriate.

3.2. Failure of anchors and net robustness

A failure of the anchorage of various cables in the 1 500 x 1 500 [mm] façade cable-net was studied and the decisive case is presented in Fig. 3.

The cable-net with cables of Ø 22 mm and laminated glass panes 10+0.76+10 [mm] under the above specified wind loading and full prestressing according to Tab. 4 demonstrated the worst total behaviour with failure of the mid vertical cable (V3), resulting in increasing the deflection of 11 % (109.9/99.1), glass stressing of 19 % (73.2/61.4) and the neighbouring cable forces increase of 12 % (69.4/61.8).

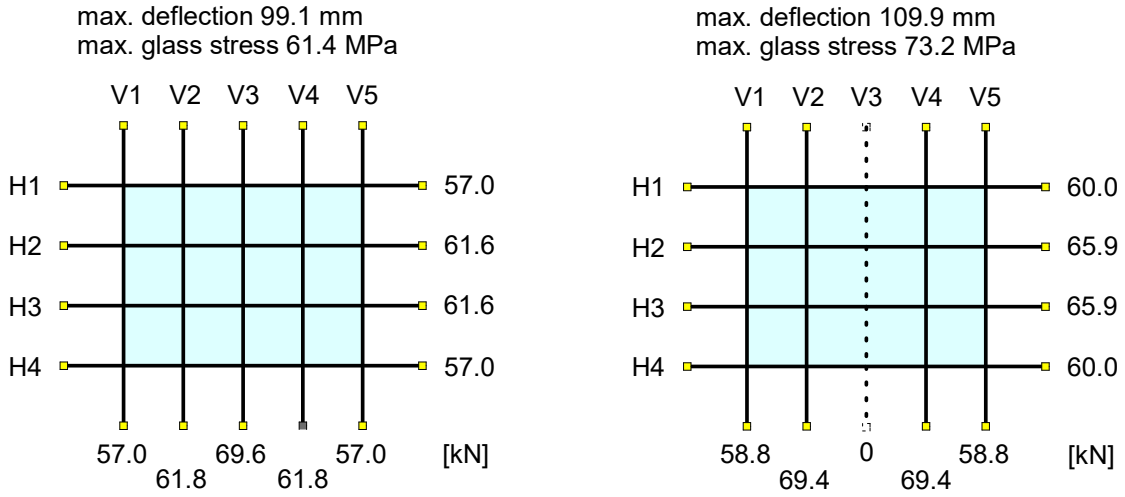

Fig. 3: Cable-net 1 500 x 1 500 [mm]: Full prestressing (left) and failure of cable anchorage V3 (right).

Potential failures of other cables in the above cable-net under the wind loading show the substantial increase of the most loaded vertical cable V3: a failure of the V2 cable gives the increase of 9 %, a failure of the V1 cable gives 3 %, a failure of the H2 cable gives 13 % and a failure of H1 cable gives the increase of 11 %.

Partial loss of the 1/3 or 2/3 of the original prestressing was also studied, including the decrease of prestressing of all cables or each of the individual cables. The results of these studies will be published elsewhere.

4. Conclusions

The paper follows up the previous papers of authors (Komlev and Machacek, 2022, 2023) with presenting results of parametric studies concerning strength and deflections of realistic façade prestressed cable-nets covered by laminated glass panes attached by fixed-point bolted fittings under wind loading.

The study also presents some results of individual cable failures. It is obvious, that the impact of failure of mid cables is decisive, while failures of the edge cables are less dangerous. The full study covers both partial and full loss of the prestressing and will be presented elsewhere.

The following studies of the authors (under way) investigate the optimal prestressing values, thermal effects influencing the façade cable-nets and dynamic behaviour of the cable-nets.

Acknowledgement

Support of the Czech Technical University grant SGS22/141/OHK1/3T/11 is gratefully acknowledged.

References

Komlev, V. and Machacek, J. (2022) Cable-net systems supporting glass façades. In: *Conf. Engineering Mechanics,* Milovy, pp. 205–208.

Komlev, V. and Machacek, J. (2023) Analysis of cable-net systems for glass façades. In: *Int. Conf. Engineering Mechanics*, Milovy, pp. 123–126.

Yussof, M. M. (2015) *Cable-net supported glass façade systems.* PhD Thesis, University of Surrey, 279 p.

Shang, C. D. (2014) *Numerical simulation and analysis of the mechanical behaviour of cable supported glass façades.* PhD Thesis, UPC University of Barcelona, 171 p.

Komlev, V. and Machacek, J. (2023) *Cable nets for glass façades – Design and parametric studies*, TZB-info, steel structures, 11 p. (in Czech).

30th International Conference
ENGINEERING MECHANICS 2024
Milovy, Czech Republic, May 14 – 16, 2024

INFLUENCE OF BERKOVICH INDENTER TILT ON THE PROJECTED CONTACT AREA AT NANOINDENTATION TEST

Kovář J.*, Fuis V.**

Abstract: *At the nanoindentation test, the tilt of the indenter or specimen surface can occur. This deviation influences the projected contact area, which is important for the evaluation of the Young modulus and hardness. This paper is aimed on the derivation of the analytical expressions for the projected contact area if the indenter is tilted in 3D space. Then the projected contact area is the same as the area of indenter cross-section by the plane corresponding to the specimen surface. The calculated results for tilted and ideal indenter were compared and the influence of the indenter tilt was evaluated. The cross-sections were plotted for few indenter tilts to better describe the change of the projected contact area. The results show that indenter tilt can have significant impact on the results if the indenter tilt is big enough.*

Keywords: Berkovich indenter, tilt, nanoindentation, projected contact area, shape function.

1. Introduction

The nanoindentation test is well-known method for determination of the Young modulus and hardness of the tested specimen (Oliver, 1992). To obtain correct results, the projected contact area to the specimen surface has to be known. This area is influenced by the indenter or the specimen tilt in 3D space. When the specimen is tilted, the projected contact area is the same as the area of indenter cross-section by a plane of specimen surface. The analytical expressions for the area of the sections of mostly used Berkovich indenter (Fig. 1), which has the shape of the three-sided pyramid, were already derived (Shi, 2013). However, simplifications, which could have influence to the calculated results, were used; therefore, derivation of expressions will be done without these simplifications in this paper to evaluate the influence of the specimen tilt on the projected contact area and results of nanoindentation more precisely.

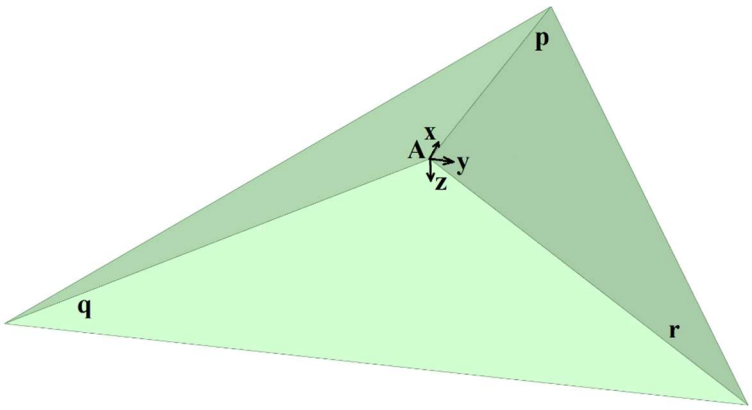

Fig. 1: Berkovich indenter.

* Ing. Jaroslav Kovář, PhD.: Institute of Solid Mechanics, Mechatronics and Biomechanics, Brno University of Technology, Technická 2896/2; 616 69, Brno; CZ, jaroslav.kovar@vut.cz

** Assoc. Prof. Ing. Vladimír Fuis, PhD.: Centre of Mechatronics – Institute of Thermomechanics of the Czech Academy of Sciences – branch Brno and Faculty of Mechanical Engineering, Brno University of Technology, Technická 2896/2; 619 69, Brno, CZ, fuis@it.cas.cz

doi: 10.21495/em2024-166

2. Derivation of the analytical expressions

The modified Berkovich indenter, here referred to as Berkovich indenter, is defined by only one parameter, which is the angle between the z-axis and the center of the side of the indenter at the section of the indenter (α in Fig. 2). The commonly used value of this parameter is $\alpha = 65.3\,°$ (Borodich, 2003). To make the following derivation more clear, the opposite angle (φ) was used. The relation between these parameters is given by (1).

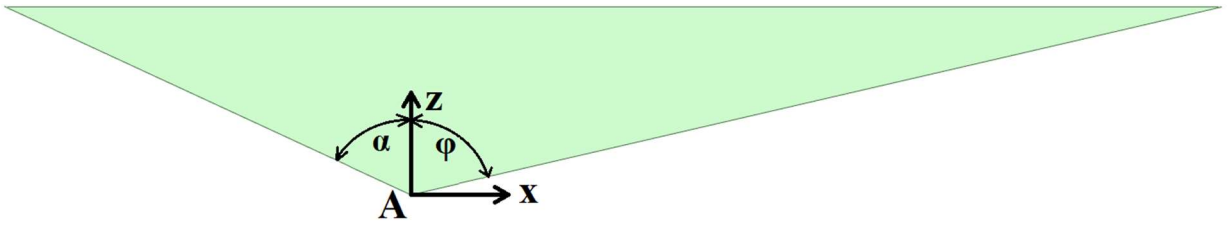

Fig. 2: Section of the Berkovich indenter by xz-plane.

$$\tan\varphi = 2 \cdot \tan\alpha \tag{1}$$

2.1. Parametrization of the indenter edges

If the indenter is cut by a plane, the cross-section is triangular, with the apexes at the intersection of the cutting plane with indenter edges. From the geometry of the indenter (Figs. 1 and 2), the unit vectors of indenter edges were derived and because all edges come out from the origin of the coordinate system (point A), the parametric equations of the edges can be expressed by (2) ÷ (4). The parameter can reach the infinity, because the indenter was expected as unbounded from the upper side.

$$p: \quad x = \frac{\tan\varphi \cdot p_1}{\sqrt{\tan^2\varphi + 1}}; \quad y = 0; \quad z = \frac{p_1}{\sqrt{\tan^2\varphi + 1}} \qquad p_1 \epsilon \langle 0; \infty) \tag{2}$$

$$q: \quad x = \frac{-\tan\varphi \cdot \sin 30° \cdot p_2}{\sqrt{\tan^2\varphi + 1}}; \quad y = \frac{\tan\varphi \cdot \cos 30° \cdot p_2}{\sqrt{\tan^2\varphi + 1}}; \quad z = \frac{p_2}{\sqrt{\tan^2\varphi + 1}} \qquad p_2 \epsilon \langle 0; \infty) \tag{3}$$

$$r: \quad x = \frac{-\tan\varphi \cdot \sin 30° \cdot p_3}{\sqrt{\tan^2\varphi + 1}}; \quad y = \frac{-\tan\varphi \cdot \cos 30° \cdot p_3}{\sqrt{\tan^2\varphi + 1}}; \quad z = \frac{p_3}{\sqrt{\tan^2\varphi + 1}} \qquad p_3 \epsilon \langle 0; \infty) \tag{4}$$

2.2. Parametrization of the section plane

The next step was the obtaining of the equation for the slice plane ρ. This plane was created from the plane xy, which was firstly rotated by angle ε around the x-axis, then about λ around y-axis and finally moved in the way of z-axis about the value of the contact depth (h_c) which is depending on the indentation depth (Oliver, 1992). For this plane, the unit vectors were derived and the normal vector was derived by its cross product (5). When the normal vector was known, the equation of the section plane (6) was derived.

$$\overrightarrow{n_\rho} = (\cos\varepsilon \cdot \sin\lambda; -\cos\lambda \cdot \sin\varepsilon; \cos\lambda \cdot \cos\varepsilon) \tag{5}$$

$$\rho: \quad \cos\varepsilon \cdot \sin\lambda \cdot x - \sin\varepsilon \cdot \cos\lambda \cdot y + \cos\varepsilon \cdot \cos\lambda \cdot z - \cos\varepsilon \cdot \cos\lambda \cdot h_c = 0 \tag{6}$$

2.3. Determination of the edges of cross-section

From the parametric equations of the edges (2 ÷ 4) and the equation of the plane (6), the coordinates of the apexes of the triangular cross-section were derived (7 ÷ 9) (B, C, and D in Fig. 3). These coordinates are dependent on the values of parameters from (2 ÷ 4), which can be determined in the intersection of the edges and plane according to (10 ÷ 12).

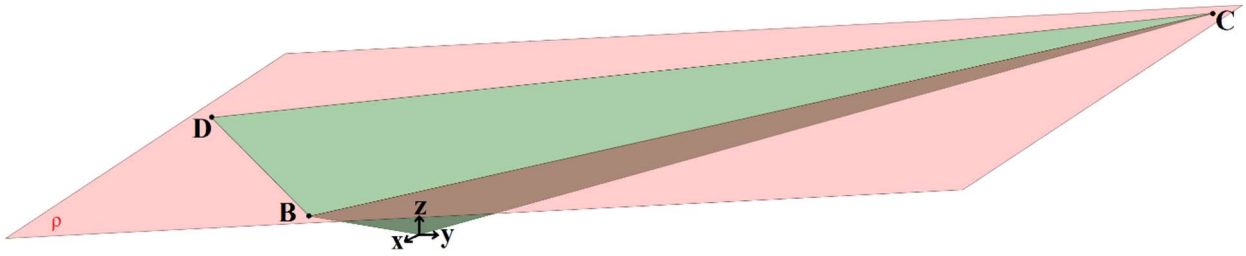

Fig. 3: Section of the Berkovich indenter by tilted plane.

$$B = \left[\frac{\tan\varphi \cdot p_1'}{\sqrt{\tan^2\varphi+1}}; 0; \frac{p_1'}{\sqrt{\tan^2\varphi+1}}\right] \quad (7)$$

$$C = \left[\frac{-\tan\varphi \cdot \sin 30° \cdot p_2'}{\sqrt{\tan^2\varphi+1}}; \frac{\tan\varphi \cdot \cos 30° \cdot p_2'}{\sqrt{\tan^2\varphi+1}}; \frac{p_2'}{\sqrt{\tan^2\varphi+1}}\right] \quad (8)$$

$$D = \left[\frac{-\tan\varphi \cdot \sin 30° \cdot p_3'}{\sqrt{\tan^2\varphi+1}}; \frac{-\tan\varphi \cdot \cos 30° \cdot p_3'}{\sqrt{\tan^2\varphi+1}}; \frac{p_3'}{\sqrt{\tan^2\varphi+1}}\right] \quad (9)$$

$$p_1' = \frac{h_c \cdot \sqrt{\tan^2\varphi+1}}{\tan\lambda \cdot \tan\varphi+1} \quad (10)$$

$$p_2' = \frac{h_c \cdot \sqrt{\tan^2\varphi+1}}{-\sin 30° \cdot \tan\lambda \cdot \tan\varphi - \cos 30° \cdot \tan\varepsilon \cdot \tan\varphi+} \quad (11)$$

$$p_3' = \frac{h_c \cdot \sqrt{\tan^2\varphi+1}}{-\sin \quad ° \cdot \tan\lambda \cdot \tan\varphi + \cos 30° \cdot \tan\varepsilon \cdot \tan\varphi+1} \quad (12)$$

2.4. Derivation of the surface of cross-section

From the known apexes of the triangle (7–9), the area of the cross-section was calculated. The two vectors corresponding to the edges of the triangle were created and then the cross-section area was determined as the half of its cross product size. The resulting expression (13) was depended on the values p_1', p_2', and p_3' (10–12). When these parameters were substituted to the (13), the final equation (14) was derived by Matlab with the relation between parameters φ and α from (1).

$$A_c = \frac{\sqrt{3}\cdot\tan\varphi}{4\cdot(\tan^2\varphi+1)} \cdot \sqrt{\left(2\cdot p_2'\cdot p_3' - p_1'\cdot p_2' - p_1'\cdot p_3'\right)^2 + 3\cdot\left(p_1'\cdot p_3' - p_1'\cdot p_2'\right)^2 + \tan^2\varphi\cdot\left(p_1'\cdot p_2' + p_2'\cdot p_3' + p_1'\cdot p_3'\right)^2} \quad (13)$$

$$A_c = 3^{\frac{3}{2}} \cdot h_c^2 \cdot \tan^2\alpha \cdot \sqrt{\frac{\tan^2\varepsilon+\tan^2\lambda+1}{(2\cdot\tan\alpha\cdot\tan\lambda+\ \ )^2\cdot\left(2\cdot\tan\alpha\cdot\tan\lambda-1+\tan^2\alpha\cdot(3\cdot\tan^2\varepsilon-\tan^2\lambda)\right)^2}} \quad (14)$$

The cross-section for the untilted Berkovich indenter can be determined by (15) (Oliver, 1992). Then the ratio between the cross-sectional areas of the tilted and untilted indenter can by determined by (16). Ratio is dependent only on the angles of tilt (ε and λ) and the indenter angle α.

$$A_{c0} = 3^{\frac{3}{2}} \cdot h_c^2 \cdot \tan^2\alpha \quad (15)$$

$$\frac{A_c}{A_{c0}} = \sqrt{\frac{\tan^2\varepsilon+\tan^2\lambda+1}{(2\cdot\tan\alpha\cdot\tan\lambda+1)^2\cdot\left(2\cdot\tan\alpha\cdot\tan\lambda-1+\tan^2\alpha\cdot(3\cdot\tan^2\varepsilon-\tan^2\lambda)\right)^2}} \quad (16)$$

3. Results and discussion

The Berkovich indenter was cut by the plane at the indentation depth 100 nm, the section plane was tilted and the areas of cross-sections were calculated according to (14). The relative differences between the areas obtained by tilted and untilted section planes are shown in Fig. 4. The plotted surface shows that the difference is symmetrical for the positive and negative values of the tilt in *x*-axis. This is due to the same symmetry of the indenter. The calculated results show difference against the expression determined by (Shi, 2013), due to the simplifications which were used in their derivation. The Berkovich indenter was modelled in the 3D CAD software Autodesk Inventor and the areas of its cross-sections by tilted plane were measured and compared with the results of analytical calculations. Both methods gave the same values. To better depiction of the tilt influences, the tilted and untilted planes were plotted for few combinations of the angles ε and λ in Fig. 5. The values of angles were chosen according to Fig. 4. All calculations assumed tilted surface of the tested specimen (section plane), as the indenter is tilted, the contact depth needs to be corrected for the influence of the indenter tilt.

4. Conclusion

The analytical expressions for the calculation of the cross-section of Berkovich indenter by tilted plane were derived. These expressions were applied to the calculation of projected contact area at the nanoindentation of the tilted specimen by the Berkovich indenter. The results show that tilt lower than 1 ° gives relative difference in contact areas lower than 1 %. As the Berkovich indenter is symmetrical, the tilt

around *x*-axis, which lies in the plane of symmetry, causes the symmetrical influence of the contact area. The future work could be aimed on the determination of the projected contact area of the blunted indenter.

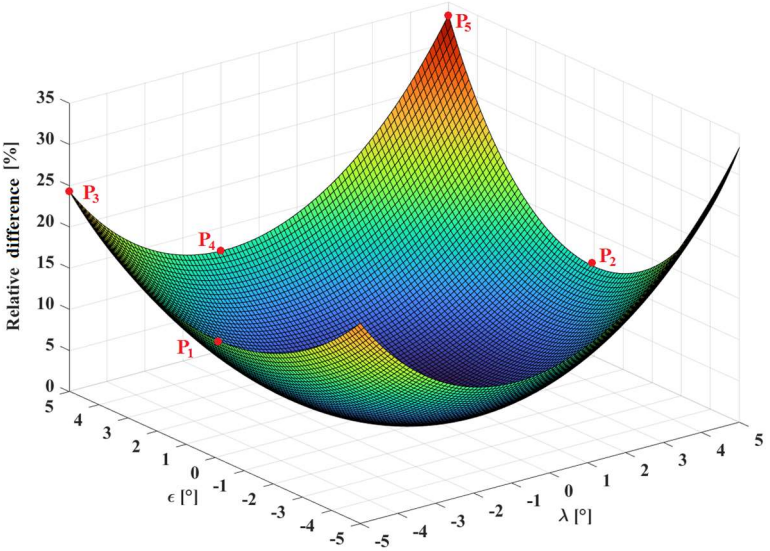

Fig. 4: Relative difference of the areas of cross-section by tilted and untilted planes at the indentation depth 100 nm (ε – tilt in x-axis, λ – tilt in y-axis).

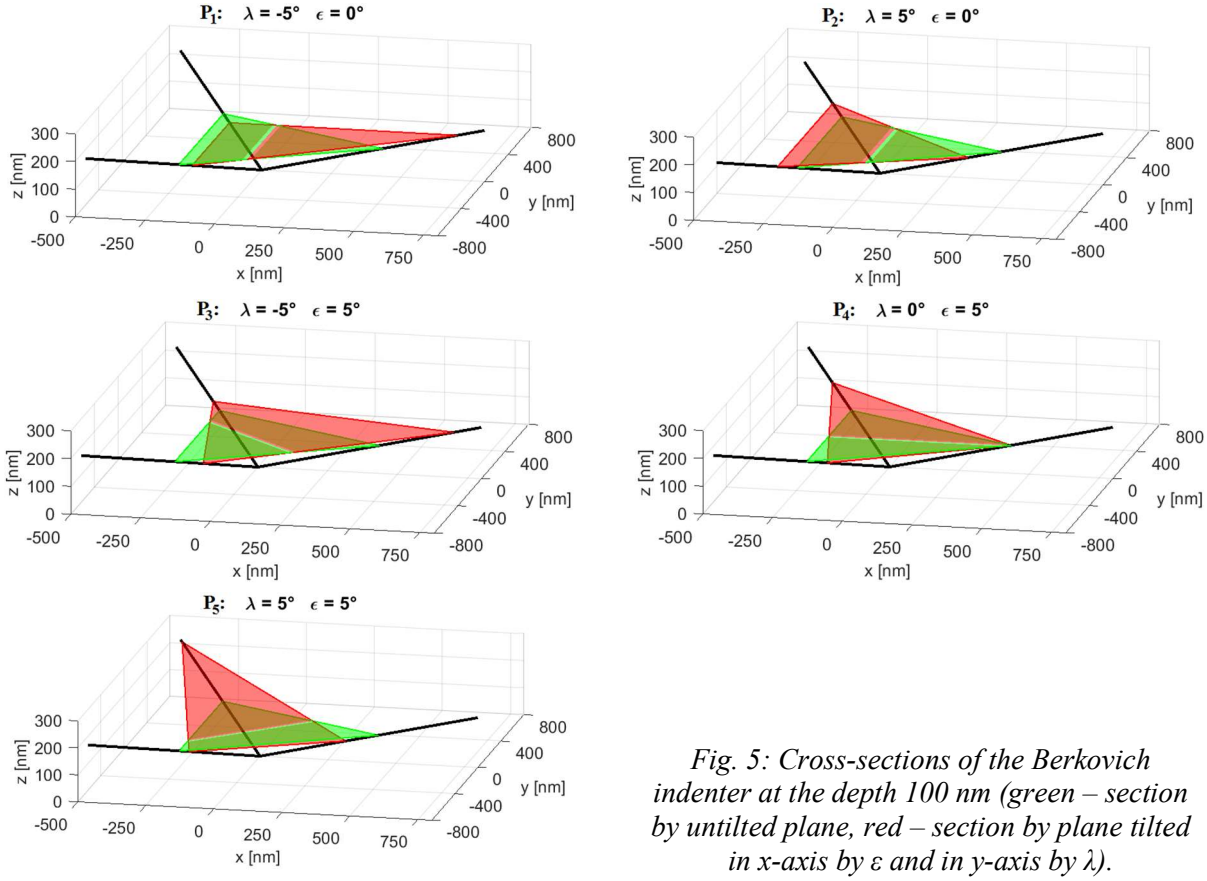

Fig. 5: Cross-sections of the Berkovich indenter at the depth 100 nm (green – section by untilted plane, red – section by plane tilted in x-axis by ε and in y-axis by λ).

Acknowledgement

This study was realized with the support by the grant FSI-S-23-8186 and with the institutional support RVO: 61388998.

References

Borodich, F. M., Keer, L. M. and Korach, C. S. (2003) Analytical study of fundamental nanoindentation test relations for indenters of non-ideal shapes. *Nanotechnology*, 14(7), 803–808.

Oliver, W. C. and Pharr, G. M. (1992) An improved technique for determining hardness and elastic modulus using load and displacement sensing indentation experiments. *Journal of Materials Research*, 7(06), 1564–1583.

Shi, C. et al. (2013) Effects of indenter tilt on nanoindentation results of fused silica: an investigation by finite element analysis. *Materials Transactions*, 54(6), 958–963.

30th International Conference
ENGINEERING MECHANICS 2024
Milovy, Czech Republic, May 14 – 16, 2024

MOTION ANALYSIS OF CZECH SIGN LANGUAGE ALPHABET CNN BASED CLASSIFIER VIA OPTICAL FLOW

Krejsa J.*, Věchet S., Šnajder J.*****

Abstract: *Single hand sign language alphabet letters can be successfully detected and classified from a single still image using convolution neural networks (CNN). Czech variant of the alphabet uses specific motions to add diacritics to the letters. The paper deals with determination of such a motion using optical flow analysis of image sequences.*

Keywords: Diacritics detection, sign language, gesture recognition.

1. Introduction

Sign language is fully developed language with its own grammar and lexicon, used as primary communication mean by hearing impaired (Sandler, 2006). Sign languages are not universal nor mutually intelligible, but all are based on manual articulation combined with non-manual markers, such as facial expressions. Sign language alphabet (or fingerspelling) is a subset of sign language used to express words that do not have a specific sign, such as names.

Several methods were proposed to automatically detect and classify particular signs, some using special instrumentation such as accelerometers on gloves/hands of the gesturer, see e.g. (González, 2018), or 3D sensing technology (Dong, 2015; Ma, 2016). With the development of machine learning techniques, the recent focus is on the classification using monocular images as the solely source of input. Czech sign language single hand alphabet was successfully classified by convolution neural network (CNN), see (Krejsa, 2020). Another successful approach by (Šnajder, 2022) combines feature detection using MediaPipe framework with common fully connected multilayer classification neural network.

Czech sign language alphabet has to deal with interesting peculiarity as it contains diacritics (accents) in certain letters. Diacritics is expressed by motion of the hand gesturing the letter and therefore can not be classified from a single image, but from the sequence of images. Czech language uses three types of diacritics. The first one is acute (letter A with acute is written as Á), used for prolonging the length of vowels. Second is caron (letter C with acute is written as Č), this diacritics often completely changes the meaning of the word, eg. “prát” (to wash or to fight) and “přát” (to wish). The last one is diacritic ring that is used only with letter “u” and prolongs it, while it can only be used in middle or end of the word.

When detecting the diacritics from a sequence of images, there are basically two approaches, the first one is to use machine learning tailored to processing the sequences. Such approach was used by (Šnajder, 2023) where Long Short-Term Memory (LSTM) architecture was used successfully applied on the task reaching 87 % accuracy of detection.

* Assoc. Prof. Ing. Jiří Krejsa PhD.: Institute of Thermomechanics of the Czech Academy of Sciences, Brno department, Czech Republic, krejsa@fme.vutbr.cz

* Assoc. Prof. Ing. Stanislav Věchet, PhD.: Institute of Thermomechanics of the Czech Academy of Sciences, Brno department, Czech Republic, vechet.s@fme.vutbr.cz

** Jan Šnajder: Faculty of Mechanical Engineering, Brno University of Technology, Czech Republic, snajder@fme.vutbr.cz

doi: 10.21495/em2024-170

The second approach, further investigated in this paper, is to use CNN for classification of letters and image processing techniques for the analysis of motion and subsequently for accent recognition. In particular, the optical flow is used, as it is proved to be usable for gesture recognition, see (Nagy, 2020) for details.

2. Materials and methods

2.1. Still image classification

The classification of particular letter from a single image (not counting the diacritics) is performed by the convolution neural network. Training data were gathered from both sign language interpreters and hearing impaired. Data were augmented (translation, rotation, both uniform and non-uniform scaling). Network topology consisted of 8 convolution layers interlaced with pooling layers, followed by a single fully connected classification layer. Latest accuracy tests exhibit 93 % successful classification on test set. For the details please refer to (Krejsa, 2020). Mentioned CNN was used for the classification during the experiments.

2.2. Optical flow

Optical flow is a method of motion estimation in a sequence of subsequent images. If we take two subsequent images (called frames) into account, we can observe some regions of the image to change position. Depending on the way the sequence was recorder, it might be the change of the recording device position, or actual motion within the scene. We assume the steady position of the observer (the camera) and static (or slowly changed) lighting conditions, therefore the difference between consecutive frames corresponds to the motion of objects observed. Optical flow method outputs the vector field on the domain of the image (the direction and magnitude of motion for each part of the image). All further described experiments were made using Lucas-Kanade method (Lucas 1981), implemented in OpenCV library.

2.3. Data acquisition

Several sentences were prepared and sign language interpreter gestured them in a single take for each sentence. Several takes of the same sentence were recorded, varying in gesturing speed and amount of motion used for diacritics. The recording was taken by two simultaneously running cameras positioned about 50 cm from each other horizontally to capture the images from different angle. An example of the image sequence for a single letter with caron is shown in Fig. 1 (left).

2.4. Data processing

Whole sentence (approximately 1 000 images) was sequentially fed into CNN that outputs the probabilities of each letter in the alphabet. Two consecutive images were fed into the optical flow implementation, outputting the vector field for given image pair.

Fig. 1: Composite image of subsequent images of letter Ř (left). The composite is organized in rows, tope left is where the sequence starts, bottom right is where it ends. Corresponding heat map of motion vectors (right).

During the experiments the optical flow was calculated for each pair of images, regardless the CNN output. The vector field is visualized in Fig. 1 (right), where the intensity corresponds to the length of the vector (displacement in the image domain) and the color corresponds to the direction of the vector.

In order to detect the accents, the mean of optical flow vectors for each pair of images was calculated, giving the overall motion between the images. The means were summed up along the whole time sequence, resulting in motion trajectory.

The identification of diacritics works as follows: Each trajectory results in 4 parameters: W = width of bounding box of trajectory, H = height of the bounding box, DX = horizontal distance between the first and the last point in trajectory and DY = vertical distance of the same. For particular diacritics then

$$\text{If } (W>W_{high}) \text{ AND } (H>H_{high} \text{ AND } (DY < H/2) \text{ AND } (DX > W/2) \text{ then CARON} \quad (1)$$

$$\text{If } (W<W_{low}) \text{ AND } (H>H_{high}) \text{ AND } (DY > H/2) \text{ then ACUTE} \quad (2)$$

$$\text{If } (W>W_{high}) \text{ AND } (H>H_{high}) \text{ AND } (DY < H/2) \text{ AND } (DX < W/2) \text{ then RING} \quad (3)$$

The method was tested on 7 sentences with the total of 49 diacritics letters. All of them were tested independently on both sequences from two cameras horizontally distant. For each sentence there were several takes, resulting in 362 diacritics to be identified in total.

3. Results

An example of the motion detected over the whole sentence is shown in Fig. 2. The sentence in particular is "Žlutý papoušek přeletěl keř ve Žďáru nad Sázavou.", it contains 41 letters, 7 with caron and three with acute. On the figure one can see the motion in both vertical and horizontal axis. Actual letters and diacritics positions are denoted by red and magenta lines (its values on y-axis have no other meaning). Particular trajectories for both letters with/without diacritics are shown in Fig. 3, where blue trajectories correspond to letters without diacritics and black and red are two different instances of the ones with.

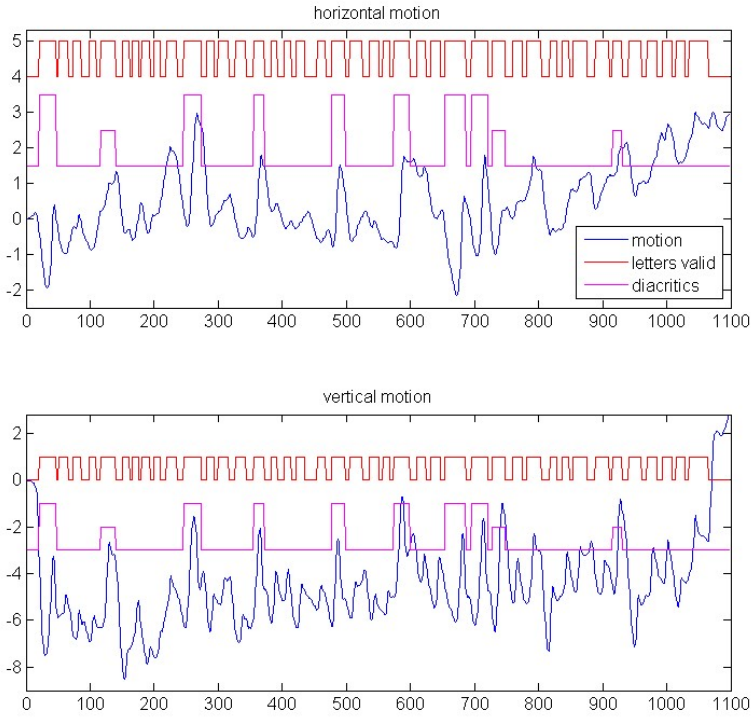

Fig. 2: Detected motion during the sentence. X-axis denotes frame number, Y-axis the amount of motion. Valid letters are shown in red, those with diacritics in magenta.

Out of 362 letters with diacritics the twelve were misclassified by CNN, and in 37 cases the diacritics itself was misjudged by the system, giving over 86 % correct classification rate in total. No significant difference between the values taken by left and right camera were found in diacritics part of the task, however all 12 misclassifications by CNN were made on the data from one of the cameras.

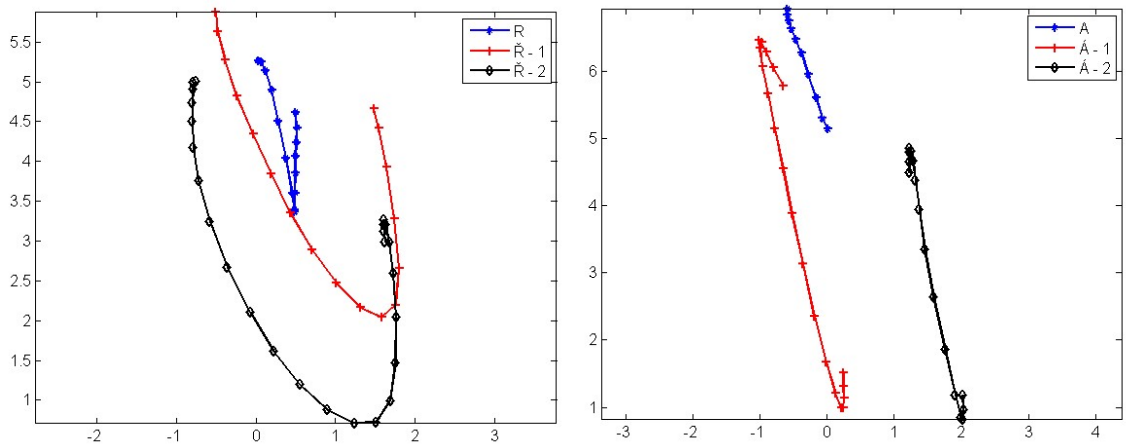

Fig. 3: Detected trajectories for R vs Ř (left) and A vs Á (right).

4. Discussion and conclusions

The main advantage of described approach is that it avoids the retraining of the neural networks used for sequences analysis. Using only the motion detected within the image sequence makes the diacritics detection and classification independent on the gesturer and can easily be extended for any other diacritics in other languages simply by adding different criteria to the trajectory evaluation part. Furthermore, for known letters not containing the diacritics the calculation can be paused, saving the computational means.

The main drawback is the requirement of static observer position and low background motion. The method in its simplest form will inevitably fail when the background has a lot of motion. This could be dealt with using independent background motion analysis and using hand detection techniques for limiting the area the vector field results are used for the diacritics evaluation, however, the authors feel that such extension would increase the number of parameters necessary to fine-tune the method thus decreasing its robustness and contradicting its main advantages.

Future work will be focused on testing the method on larger test data set and further fusion of CNN output sequence with optical flow results.

Acknowledgement

The results were obtained with institutional support RVO 61388998 of the Institute of Thermomechanics AS CR v.v.i. Authors would like to express their gratitude to sign language interpreters.

References

Sandler, W. and Lillo-Martin, D. (2006) *Sign Language and Linguistic Universals*. Cambridge University Press.

González, G. S. et al. (2018) Recognition and Classification of Sign Language for Spanish, *Computación y Sistemas*, vol. 22, no. 1, pp. 271–277.

Dong, C. Leu, M. and Yin, Z. (2015) American sign language alphabet recognition using microsoft Kinect. In: *Proc. of the IEEE Conference on Computer Vision and Pattern Recognition Workshops*, pp. 44–52.

Ma, L. and Huang, W. (2016) A static hand gesture recognition method based on the depth information, In: *Intelligent Human-Machine Systems and Cybernetics (IHMSC), 8th International Conference*, vol. 2, pp. 136–139.

Krejsa, J. and Vechet, S. (2020) Czech Sign Language Single Hand Alphabet Letters Classification. In: *19th International Conference on Mechatronics - Mechatronika (ME)*, Prague.

Šnajder, J. and Bednařík, J. (2022) Czech Single Hand Alphabet Classification with MediaPipe, In: *Proc. of the 28th Conference Engineering Mechanics*, Milovy, pp. 381–384.

Šnajder, J. and Krejsa, J. (2023) Classification of Czech Sign Language Alphabet Diacritics via LSTM. In: *20th International Conference on Mechatronics - Mechatronika (ME)*, Pilsen.

Nagy, D. Z. and Piller, I. (2020) An Optical Flow-based Gesture Recognition Method, *Acta Marisiensis*, vol. 17, no. 1, pp 22–26.

Lucas, B and, Kanade, T. (1981) An iterative image registration technique with an application to stereo vision. *Proc. of Imaging Understanding Workshop*, pp. 121–130.

30th International Conference
ENGINEERING MECHANICS 2024
Milovy, Czech Republic, May 14 – 16, 2024

REYNOLDS-AVERAGED SIMULATION OF TURBULENT FLOWS WITH IMMERSED BOUNDARIES

Kubíčková L.[*], **Isoz M.**[**]

Abstract: *Simulating turbulent flows in complex real-life geometries faces two major problems. First, direct simulation of turbulent flow is extremely costly. Second, a complex geometry-conforming mesh is required, and such mesh presumably suffers from several mesh-quality related problems lowering the solution accuracy and prolonging the simulation time. To solve the first problem, phenomenological turbulence models based on, e.g. Reynolds-averaging, are commonly utilized. To address the second one, a variant of an immersed boundary (IB) method can be used where the complex geometry is projected onto a simple mesh by an indicator field and adjustment of governing equations. Consequently, a connection of Reynolds-averaging and an immersed boundary method shall resolve both the problems and provide a simulation approach favorable for e.g. optimizations. However, such a connection is not common. In this contribution, we utilize our custom IB variant, the hybrid fictitious domain-immersed boundary method (HFDIB) and aim on extending the HFDIB by tools of the Reynolds-averaged simulation (RAS). In comparison with standard simulation approaches, the new HFDIB-RAS approach shows acceptable results in wide range of flow Reynolds numbers and in several testing geometries.*

Keywords: Immersed boundary method, computational fluid dynamics, Reynolds-averaged simulation, wall functions.

1. Introduction

In the modern world, engineers are increasingly using simulation tools to design, test and optimize devices and components. Moreover, with more affordable and always growing computational power, the tested geometries can be more complex, and simulations more accurate and faster. However, simulations of complex geometries affected by turbulent flows are still problematic and require specific approaches to be computationally feasible.

One problem is with the turbulent flow itself. Direct numerical simulation of such a flow is extremely costly, since the number of required mesh nodes grows steeply with the Reynolds number of the flow (Wilcox, 2006). To alleviate simulation costs, several turbulence modeling approaches have been developed. In this work, we focus on the Reynolds-averaged simulation (RAS) approach extended by the Boussinesq hypothesis and wall functions for boundary layer modeling. Despite the assumptions adopted and the consequent inaccuracies of the approach, its low computational cost makes it a prominent part of the engineering toolbox. The value of RAS is the most apparent in optimizations or parametric studies, where trends in the solution are of the most importance.

Another problem related to simulations of industrial flows is the complexity of the geometry and mesh construction. A standard in computational fluid dynamics (CFD) is to create the mesh to be geometry-conforming. Consequently, the complexity and irregularity of the real-life geometry is reflected in the mesh and may lead to lower mesh quality. In particular, high nonorthogonality and skewness of the mesh lead to lower solution robustness and accuracy. An answer to this problem may be a kind of an immersed boundary

[*] Ing. Lucie Kubíčková: Institute of Thermomechanics, Czech Academy of Sciences, Dolejškova 1402/5; 182 00, Prague; CZ (ITCAS), and Department of Mathematics, Informatics, and Cybernetics, University of Chemistry and Technology, Technická 5; 166 28, Prague; CZ (DMICUCT), luciekub@it.cas.cz

[**] Ing. Martin Isoz, PhD.: ITCAS, and DMICUCT

doi: 10.21495/em2024-174

(IB) method. In the IB method, the geometry-conforming mesh is replaced by a simple one and the complex geometry is projected onto it using a scalar indicator field and adjustment of governing equations. Moreover, in optimizations and parametric studies, the IB method has a clear advantage, since for different geometries, only the scalar field has to be redefined and no remeshing is required, saving large amounts of computational time (Kubíčková and Isoz, 2022).

Ultimately, for simulations of turbulent flows in or around complex geometries, the connection of the RAS turbulence modeling approach and the IB method would be favorable. However, such a connection is not common (Verzicco, 2023). Several attempts have been reported in the literature; see e.g. (Capizzano, 2011; Troldborg et al., 2022). The methods showed acceptable solution accuracy, but to stabilize the computation, they mostly used mesh refinement near the immersed boundary. Such refinements are costly and may locally reduce the quality of the mesh, lowering the IB-inherent advantage to be used in geometry optimization.

In this contribution, we present recent advances in the development of a connection of the RAS approach and our custom IB method variant, the hybrid fictitious domain-immersed boundary method (HFDIB), see (Isoz et al., 2022). The main motivation is application of the resulting HFDIB-RAS approach in an automated geometry optimization. Therefore, we focus on robustness and general applicability of the approach. The approach combines the HFDIB method with two-equation RAS turbulence models and wall functions. Compared with standard CFD approaches, the HFDIB-RAS shows good accuracy in a variety of verification and validation tests.

2. Description of HFDIB-RAS

The presence of the solid body in the computational domain is indicated by a scalar field λ, see Fig. 1a. This field is constructed given the distance from the body surface and surface normal. In HFDIB-RAS, the λ field is used to divide mesh cells into three groups, in-solid cells, boundary cells and free-stream cells, see Fig. 1b. Each group is then treated differently in the construction of IB-induced sources.

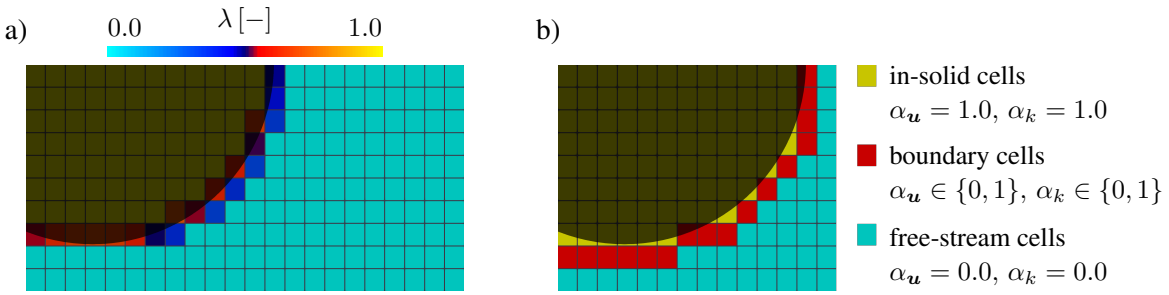

Fig. 1: a) Scalar field λ indicating presence of a solid body (cylinder). b) Division of mesh cells based on the λ field. Values of α fields are given.

The used governing equations stem from the Reynolds-averaged Navier-Stokes equations with the Boussinesq hypothesis. To close the problem, we focus on two-equation turbulence models to compute the turbulent viscosity. In short form, the equations can be written as:

$$\begin{aligned} \mathcal{M}(\boldsymbol{u}) = -\nabla\hat{p} + \boldsymbol{f}_{\mathrm{ib}}, \quad \boldsymbol{f}_{\mathrm{ib}} = \alpha_{\boldsymbol{u}}(\lambda)\,[\,\mathcal{M}(\boldsymbol{u}_{\mathrm{ib}}) + \nabla\hat{p}\,], \quad \nabla\cdot\boldsymbol{u} = 0 \\ \mathcal{N}(k) = S_{\mathrm{ib}}, \quad S_{\mathrm{ib}} = \alpha_k(\lambda)\,\mathcal{N}(k_{\mathrm{ib}}), \quad \mathcal{P}(\omega|\varepsilon) = 0 \end{aligned} \tag{1}$$

where $\hat{p}$ is the turbulence pressure, $\boldsymbol{u}$ the velocity, k the turbulence kinetic energy, ω the specific rate of dissipation of k and ε the rate of dissipation of k. The operator $\mathcal{M}$ contains terms of the momentum equation where $\boldsymbol{u}$ is present, operator $\mathcal{N}$ sums up the k conservation equation and $\mathcal{P}$ the ω or ε ($\omega|\varepsilon$) conservation equation (based on the chosen turbulence model). Exact definitions of the operators may be found in Kubíčková and Isoz (2023).

The effect of the solid body on flow is accounted for by two source terms, $\boldsymbol{f}_{\mathrm{ib}}$ and S_{ib}. These source terms are switched on and off based on the fields $\alpha_{\boldsymbol{u}}$ and α_k. The α fields are non-zero in cells where the body has the greatest effect on the flow behavior; see Fig. 1b. The calculation of the source terms is based on the prescribed values of the respective fields $\boldsymbol{u}_{\mathrm{ib}}$ and k_{ib}. These immersed values are then enforced in the most affected cells by iterative solution of the equations. Lastly, the effect of the solid body on ω or ε cannot be accounted for by source terms, because the fields go to infinity near the solid surface. Still, the values of $\omega_{\mathrm{ib}}|\varepsilon_{\mathrm{ib}}$ are computed, but to enforce them, direct matrix manipulation is utilized.

In each group of cells, the immersed values are computed differently. In the in-solid cells, it is considered that $\boldsymbol{u}_{\mathrm{ib}} = \mathbf{0}$, $k_{\mathrm{ib}} = 0$, $\omega_{\mathrm{ib}}|\varepsilon_{\mathrm{ib}} = \max(\omega^{\mathrm{old}}|\varepsilon^{\mathrm{old}})$. In the boundary cells, wall functions in the forms given by Kalitzin et al. (2005) are used to calculate the values of $\omega_{\mathrm{ib}}|\varepsilon_{\mathrm{ib}}$. For k_{ib}, the wall functions cannot be used directly, since it severely deteriorates the stability and accuracy of the solution. Instead, there is a switch for cases with a resolved and unresolved boundary layer. In resolved cases, the wall functions are used to give the value at the solid surface and a simple polynomial interpolation is used to compute the value in the boundary cell center. In the unresolved case, α_k is set to zero and the k behavior is corrected by $\omega|\varepsilon$.

Lastly, the values of $\boldsymbol{u}_{\mathrm{ib}}$ are treated similarly to those of k_{ib}. Only in cases with resolved boundary layer, the value at the surface is given by the no-slip boundary condition. In unresolved cases, the turbulent viscosity, computed from k and $\omega|\varepsilon$ corrects the velocity behavior near the body surface.

3. Verification & validation tests

Several verification and validation tests were conducted. In each test, two similar meshes were created: (i) one simple and structured mesh for the HFDIB-RAS method and (ii) one geometry-conforming mesh for simpleFoam solver available in OpenFOAM (Weller et al., 2021). The simpleFoam solver is used to provide referential solutions and geometry-conforming meshes were made to fit a surface-representing contour of the λ fields. This ensures that simpleFoam works with the same geometries as HFDIB-RAS even with non-ideal λ field generation.

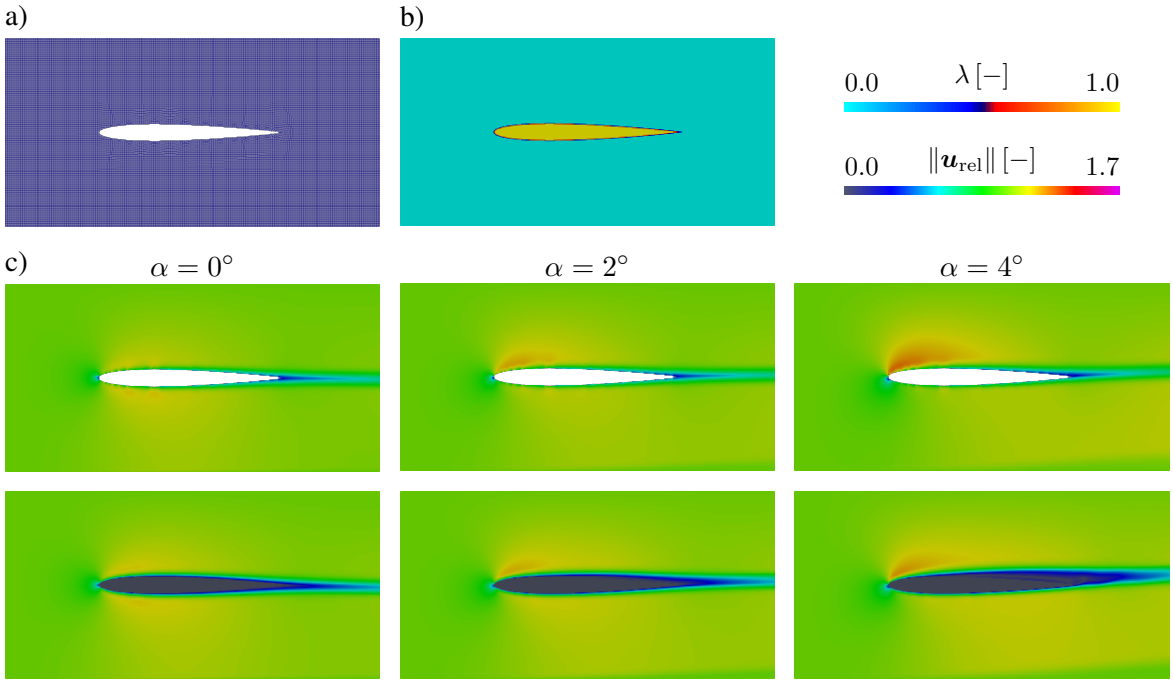

Fig. 2: Verification test on NACA-0009 airfoil with $\mathrm{Re} = 200\,000$. *a) Mesh used for simpleFoam. b)* λ *field used for HFDIB-RAS. c) Comparison of velocity fields for different angles of attack* α. *Colored by magnitude of relative velocity* $\boldsymbol{u}_{\mathrm{rel}} = \boldsymbol{u}/\|\boldsymbol{u}_{\mathrm{inlet}}\|$.

One chosen verification test and one validation test is presented. In the verification test, simulations of flow around a NACA-0009 airfoil with $\mathrm{Re} = 200\,000$ were performed for several angles of attack. The results are depicted in Fig. 2. As a validation test, a backward facing step benchmark was selected with experimental data provided by Driver and Seegmiller (1985). The results achieved are presented in Fig. 3. In both tests, the agreement is not perfect; the HFDIB-RAS overestimates the boundary layer thickness. However, for use in optimization, the HFDIB-RAS behavior is considered acceptable, since it captures the trends sufficiently well.

4. Conclusions

In this work, we introduce the HFDIB-RAS approach, which is a connection of our custom immersed boundary method variant and the Reynolds-averaged simulation approach. In particular, two-equation turbulence models with wall functions for boundary layer modeling. The code with illustrative tutorials is available from https://github.com/techMathGroup/openHFDIBRANS. Moreover, we present recently

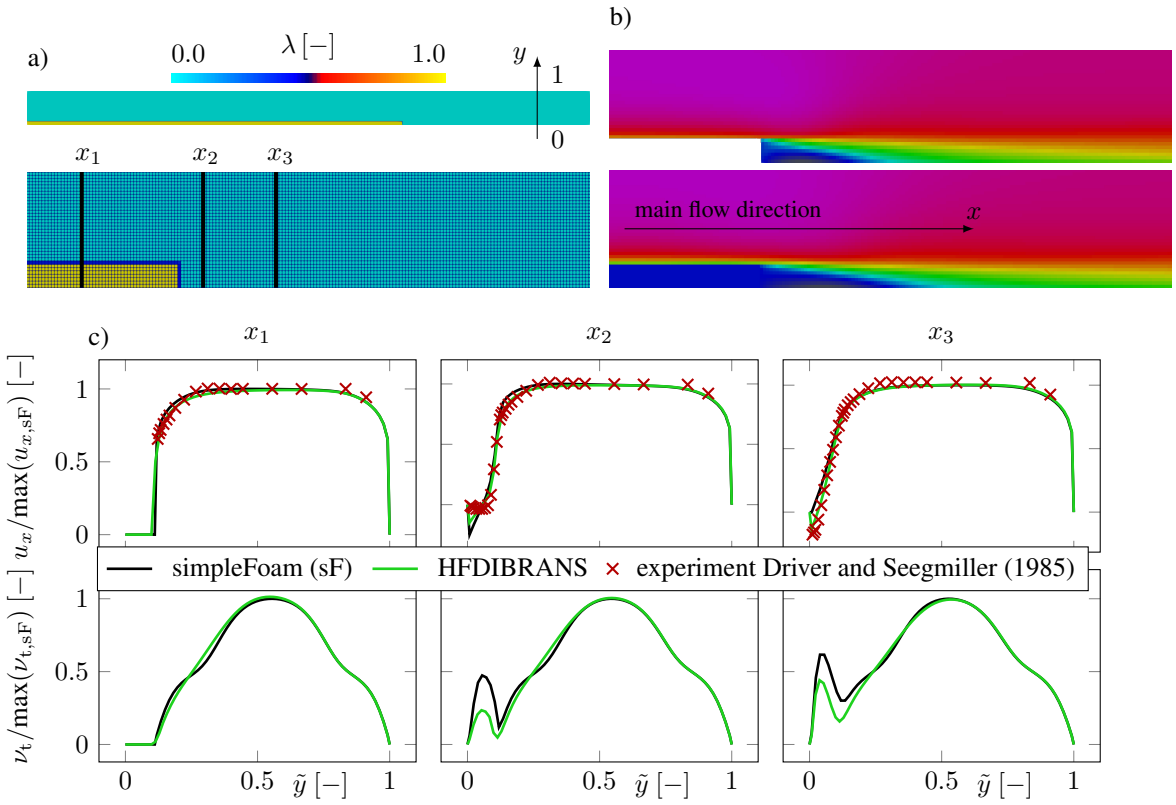

Fig. 3: Validation test on the backward facing step benchmark. a) Used λ field with highlighted sampling lines. b) Velocity field from the simpleFoam (top) and HFDIB-RAS (bottom) simulations. c) Comparison of $\boldsymbol{u}$ and ν_t profiles along sampling lines.

achieved HFDIB-RAS results that show good agreement with standard computational fluid dynamics approaches. In future development, the HFDIB-RAS will be used in geometry optimization.

Acknowledgments

The work was financially supported by the institutional support RVO:61388998 and by the grant project with No. TN02000069/001N of the Technology Agency of the Czech Republic. The authors acknowledge the financial support provided by the Ministry of Education, Youth, and Sports of the Czech Republic via the project No. CZ.02.01.01/00/22_008/0004591 (Ferroic Multifunctionalities), co-funded by the European Union. This work was supported from the grant of Specific university research – grant No. A2_FCHI_2024_022.

References

Capizzano, F. (2011) A turbulent wall model for immersed boundary methods. *AIAA J.*, 49, 11, pp. 2367–2381.

Driver, D. and Seegmiller, H. (1985) Features of a reattaching turbulent shear layer in divergent channel flow. *AIAA Journal*, 23, 2, pp. 163–171.

Isoz, M., Kotouč Šourek, M., Studeník, O., and Kočí, P. (2022) Hybrid fictitious domain-immersed boundary solver coupled with discrete element method for simulations of flows laden with arbitrarily-shaped particles. *Computers & Fluids*, 244, pp. 105538–1–105538–22.

Kalitzin, G., Medic, G., Iaccarino, G., and Durbin, P. (2005) Near-wall behavior of rans turbulence models and implications for wall functions. *Journal of Computational Physics*, 204, pp. 265–291.

Kubíčková, L. and Isoz, M. (2022) Hybrid fictitious domain-immersed boundary method in CFD-based topology optimization. In *Proceedings of Topical Problems of Fluid Mechanics 2022*. IT CAS, pp. 119–126.

Kubíčková, L. and Isoz, M. (2023) On Reynolds-averaged turbulence modeling with immersed boundary method. *Topical Problems of Fluid Mechanics 2023*, pp. 104–111.

Troldborg, N., Sørensen, N. N., and Zahle, F. (2022) Immersed boundary method for the incompressible reynolds averaged navier–stokes equations. *Computers and Fluids*, 237, pp. 105340.

Verzicco, R. (2023) Immersed boundary methods: Historical perspective and future outlook. *Annual Review of Fluid Mechanics*, 55, pp. 129–155.

Weller, H., Greenshields, C., and Bainbridge, W. (2021) The OpenFOAM foundation.

Wilcox, D. (2006) *Turbulence modeling for CFD*. DCW Industries, USA, 3rd edition.

30th International Conference
ENGINEERING MECHANICS 2024
Milovy, Czech Republic, May 14 – 16, 2024

FREE AXISYMMETRIC VIBRATION OF ELASTICALLY RESTRAINED POROUS ANNULAR PLATE USING HAAR WAVELETS

Kumar Y.*

Abstract: *Free axisymmetric vibration analysis of a porous annular plate is presented in this paper. Both the edges of the plate are elastically restrained against rotation and translation. The classical plate theory is used to develop the mathematical model. The mechanical properties are varying in thickness direction. The Haar wavelets are used in the analysis. The highest order derivative is approximated by Haar wavelets and a generalized eigenvalue problem is obtained. The first three frequencies for different combinations of restraint parameters, radii ratio and porosity coefficient are obtained. The present analysis is validated by a convergence study. The frequencies for classical boundary conditions are obtained by assuming particular values of restraint parameters and compared with those available in the literature. A close agreement of results is observed.*

Keywords: Axisymmetric, restrained, porous, annular, Haar wavelets.

1. Introduction

Free vibration of structures has been a topic of research for a long time. Porous plates, being lightweight, find applications in many fields. There is a need of research on dynamic behavior of structures made of porous material. This paper considers free axisymmetric vibration of porous annular plate elastically restrained along the inner and outer boundaries. The mechanical properties of the plate material are assumed to be varying along thickness direction. The Haar wavelets are used to calculate first three frequencies. The effects of porosity and restraint coefficients are studied on the frequencies. The results in special cases are compared with those available.

2. Mathematical model

Consider a porous annular plate of uniform thickness h with inner radius b and outer radius a (Fig. 1). The top and bottom surfaces are $z = h/2$ and $z = -h/2$, respectively. The material properties are assumed to be graded in the thickness direction.

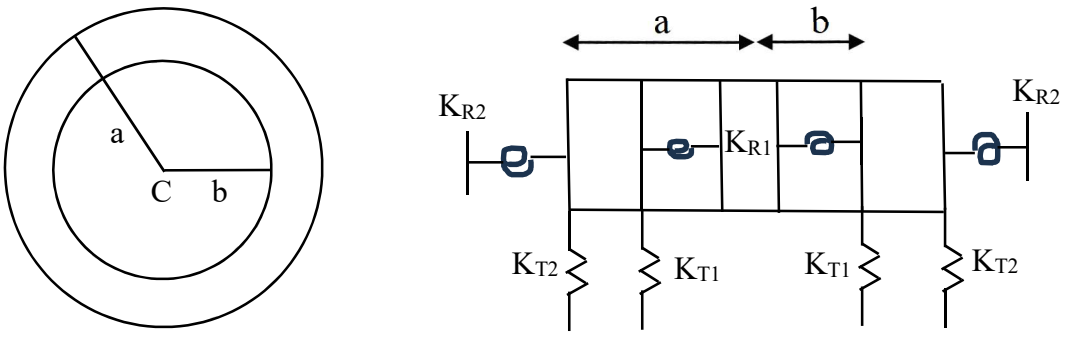

Fig. 1 a) Geometry of the porous annular plate, b) annular plate with constraints at the edges.

* Dr. Yajuvindra Kumar, PhD.: Government Girls Degree College Behat, India, yaju_saini@yahoo.com

doi: 10.21495/em2024-178

The equation of motion governing axisymmetric vibration of such plate is given as follows (Shariyat and Alipour, 2011):

$$D\frac{\partial^4 w}{\partial r^4}+\left\{\frac{2D}{r}+2\frac{dD}{dr}\right\}\frac{\partial^3 w}{\partial r^3}+\left\{\frac{(2+\upsilon)}{r}\frac{dD}{dr}+\frac{d^2D}{dr^2}-\frac{D}{r^2}\right\}\frac{\partial^2 w}{\partial r^2}+\left\{\frac{D}{r^3}-\left(\frac{1}{r^2}\frac{dD}{dr}-\frac{\upsilon}{r}\frac{d^2D}{dr^2}\right)\right\}\frac{\partial w}{\partial r}+\rho h\frac{\partial^2 w}{\partial t^2}=0, \tag{1}$$

where w is the transverse displacement, $D=Eh^3/12(1-\upsilon^2)$ is the flexural rigidity, υ is the Poisson ratio and ρ is the mass density. For free vibrations, solution of Eq. (1) may be taken as:

$$w(r,t)=\bar{W}(r)\,e^{i\omega t}. \tag{2}$$

Using Eqs. (2) and (1) becomes:

$$D\frac{d^4\bar{W}}{dr^4}+\left\{\frac{2D}{r}+2\frac{dD}{dr}\right\}\frac{d^3\bar{W}}{dr^3}+\left\{\frac{(2+\upsilon)}{r}\frac{dD}{dr}+\frac{d^2D}{dr^2}-\frac{D}{r^2}\right\}\frac{d^2\bar{W}}{dr^2}+\left\{\frac{D}{r^3}-\left(\frac{1}{r^2}\frac{dD}{dr}-\frac{\upsilon}{r}\frac{d^2D}{dr^2}\right)\right\}\frac{d\bar{W}}{dr}-\rho h\omega^2\bar{W}=0. \tag{3}$$

The variation of Young's modulus and mass density per unit volume in the thickness plane is taken as follows:

$$E(z)=E_{max}\left[1-e_1\cos\left\{\frac{\pi(z+0.5h)}{2h}\right\}\right],\ \rho(z)=\rho_{max}\left[1-e_1\cos\left\{\frac{\pi(z+0.5h)}{2h}\right\}\right] \tag{4}$$

where $e_1=1-\frac{E_{min}}{E_{max}}$ is the coefficient of plate porosity, defined as void volume to bulk volume ratio, and $0<e_1<1$. The E_{min}, E_{max} are the Young's moduli and ρ_{min}, ρ_{max} are the mass densities at $z=h/2$ and $z=-h/2$, respectively. The Poisson's ratio $\upsilon=0.3$ is considered to be constant throughout the thickness.

Using the non-dimensional variables $R=\frac{r}{a}, W=\frac{\bar{W}}{h}$ and Eqs. (4) and (3) becomes:

$$A_0\frac{d^4W}{dR^4}+A_1\frac{d^3W}{dR^3}+A_2\frac{d^2W}{dR^2}+A_3\frac{dW}{dR}+A_4W=0, \tag{5}$$

where $A_0=f(e_1)\,R^3$, $A_1=2f(e_1)R^2, A_2=-f(e_1)R, A_3=f(e_1), A_4=-\Omega^2\frac{(\pi-2e_1)}{\pi}R^3,$

$$f(e_1)=\frac{\pi^3-6(\pi^2+8\pi-32)e_1}{\pi^3}.$$

By letting $\epsilon=b/a$ and using the transformation $S=(R-\epsilon)/(1-\epsilon)$, the domain $[\epsilon, 1]$ gets converted into the domain $[0, 1]$ of applicability range of Haar wavelets and Eq. (5) takes the following form:

$$B_0\frac{d^4W}{dS^4}+(1-\epsilon)B_1\frac{d^3W}{dS^3}+(1-\epsilon)^2B_2\frac{d^2W}{dS^2}+(1-\epsilon)^3B_3\frac{dW}{dS}+(1-\epsilon)^4B_4W=0, \tag{6}$$

in which $B_0=f(e_1)\{\epsilon+(1-\epsilon)S\}^3, B_1=2f(e_1)\{\epsilon+(1-\epsilon)S\}^2,\ B_2=-f(e_1)\{\epsilon+(1-\epsilon)S\},$

$$B_3=f(e_1),\ B_4=-\Omega^2\frac{(\pi-2e_1)}{\pi}\{\epsilon+(1-\epsilon)S\}^3,\ D_0=\frac{E_{max}h^3}{12(1-\upsilon^2)}, \Omega=\omega a^2\sqrt{\frac{\rho_{max}h}{D_0}}$$

and Ω is the frequency parameter.

3. Haar wavelets and integrals

The Haar wavelet transform was proposed by Alfred Haar in 1909. The Haar wavelet is discontinuous and resembles a step function (Hein and Feklistova, 2011). The Haar wavelet family on $[0, 1]$ is defined as

$$h_i(S)=\begin{cases}1 & S\in[S_1,S_2)\\ -1 & S\in[S_2,\ S_3]\\ 0 & elsewhere\end{cases} \tag{7}$$

where $S_1=\frac{k}{m};\ S_2=\frac{k+0.5}{m};\ S=\frac{k+1}{m}; m=2^j;\ j=0,1,2,\ldots\ldots,J$ is the scaling factor; $k=0,1,2,\ldots\ldots,m-1$ is the delay factor; $i=m+k+1$. Integer J is the maximal level of resolution.

The first four integrals of the wavelets $h_i(x)$ are (Lepik, 2007):

$$p_{1,i}(S)=\begin{cases}S-S_1 & S\in[S_1,\ S_2]\\ S_3-S & S\in[S_2,\ S_3]\\ 0 & elsewhere\end{cases}, \tag{8}$$

$$p_{2,i}(S)=\begin{cases}\dfrac{(S-S_1)^2}{2} & S\in[S_1,\,S_2]\\ \dfrac{1}{4m^2}-\dfrac{(S_3-S)^2}{2} & S\in[S_2,\,S_3]\\ \dfrac{1}{4m^2} & S\in[S_3,\,1]\\ 0 & S\in[0,S_1]\end{cases}, \tag{9}$$

$$p_{3,i}(S)=\begin{cases}\dfrac{(S-S_1)^3}{6} & S\in[S_1,\,S_2]\\ \dfrac{S-S_2}{4m^2}-\dfrac{(S_3-S)^3}{6} & S\in[S_2,\,S_3]\\ \dfrac{S-S_2}{4m^2} & S\in[S_3,\,1]\\ 0 & S\in[0,S_1]\end{cases} \tag{10}$$

and

$$p_{4,i}(S)=\begin{cases}\dfrac{(S-S_1)^4}{24} & S\in[S_1,\,S_2]\\ \dfrac{(S-S_2)^2}{8m^2}-\dfrac{(S_3-S)^2}{24}+\dfrac{1}{192m^4} & S\in[S_2,\,S_3]\\ \dfrac{(S-S_2)^2}{8m^2}+\dfrac{1}{192m^4} & S\in[S_3,\,1]\\ 0 & S\in[0,S_1]\end{cases}. \tag{11}$$

The collocation points are defined as

$$S_l=\frac{l-0.5}{2M},\qquad l=1,2,\dots\dots,2M \tag{12}$$

where $M=2^J$.

4. Boundary conditions

Boundary conditions at the edges are given as follows:

at S = 0

$$\epsilon\frac{d^2w}{dS^2}+(1-\epsilon)\left\{\upsilon-\frac{\epsilon K_{R1}}{f(e_1)}\right\}\frac{dw}{dS}=0, \tag{13}$$

$$\epsilon^2\frac{d^3w}{dS^3}+\epsilon(1-\epsilon)\frac{d^2w}{dS^2}-(1-\epsilon)^2\frac{dw}{dS}+\epsilon^2(1-\epsilon)^3\frac{K_{T1}}{f(e_1)}w=0 \tag{14}$$

and at S = 1

$$\frac{d^2w}{dS^2}+(1-\epsilon)\left\{\upsilon+\frac{K_{R2}}{f(e_1)}\right\}\frac{dw}{dS}=0, \tag{15}$$

$$\frac{d^3w}{dS^3}+(1-\epsilon)\frac{d^2w}{dS^2}-(1-\epsilon)^2\frac{dw}{dS}-\ (1-\epsilon)^3\frac{K_{T2}}{f(e_1)}w=0. \tag{16}$$

The Eq. (6) is a fourth order ordinary differential equation with variable coefficients which is solved for using Haar wavelets. According to Chen and Hsiao (2007), the highest order derivative $\frac{d^4W}{dS^4}$ of transverse displacement W is expanded into the Haar series as follows:

$$\frac{d^4W}{dS^4}=\sum_{i=1}^{2M}a_ih_i(S) \tag{17}$$

where a_i are unknown wavelet coefficients.

Integrating (17) four times, it yields that

$$\begin{aligned}\frac{d^3W}{dS^3}&=\sum_{i=1}^{2M}a_i\,p_{1,i}(S)+\frac{d^3W(0)}{dS^3},\\ \frac{d^2W}{dS^2}&=\sum_{i=1}^{2M}a_i\,p_{2,i}(S)+\frac{d^3W(0)}{dS^3}S+\frac{d^2W(0)}{dS^2},\\ \frac{dW}{dS}&=\sum_{i=1}^{2M}a_i\,p_{3,i}(S)+\frac{d^3W(0)}{dS^3}\frac{S^2}{2}+\frac{d^2W(0)}{dS^2}S+\frac{dW(0)}{dS},\end{aligned} \tag{18}$$

and $$W = \sum_{i=1}^{2M} a_i \, p_{4,i}(S) + \frac{d^3W(0)}{dS^3}\frac{S^3}{6} + \frac{d^2W(0)}{dS^2}\frac{S^2}{2} + \frac{dW(0)}{dS}S + W(0).$$

The quantities $\frac{d^3W(0)}{dS^3}, \frac{d^2W(0)}{dS^2}, \frac{dW(0)}{dS}, W(0)$ in Eq. (18) are obtained using boundary conditions (13–16).

5. Results

Expressing displacement function W in terms of Haar wavelets and discretizing Eq. (6) at different grid points, we obtain a generalized eigenvalue problem. This eigenvalue problem is solved for first three frequencies using a computer program developed in MATLAB. The convergence of frequency parameter Ω for different values of various parameters (porosity coefficient e_1 and restraint parameters (K_{R1}, K_{R2}, $K_{T1,}$ K_{T2}) is shown in Tab. 1. Comparison of frequencies of clamped (C) and simply supported (S) annular plate is shown in Tab. 2. A close agreement of results is observed.

	J					
Mode	2	3	4	5	6	7
I	16.001	15.986	15.983	15.982	15.981	15.981
II	32.311	32.263	32.251	32.248	32.247	32.247
III	85.802	85.18	85.029	84.991	84.982	84.979

Tab. 1: Convergence of frequency parameter Ω of elastically restrained porous annular plate for first three modes for $\epsilon = 0.3, e_1 = 0.1,\ K_{R1} = K_{R2} = K_{T1} = K_{T2} = 100$.

				Mode		
Boundary condition	$K_{R1} = K_{R2}$	$K_{T1} = K_{T2}$	**Reference**	**I**	**II**	**III**
Clamped-Clamped	10^9	10^9	Lal and Sharma (2004)	45.3462	125.3621	246.1563
			Present	**45.303**	**125.950**	**246.900**
Supported-Supported	0	10^9	Selmane and Lakis (1999)	21.0790	81.7370	182.54
			Present	**21.107**	**82.064**	**183.08**

Tab. 2: Comparison of frequency parameter Ω of isotropic annular plate for $e_1 = 0, \epsilon = 0.3$.

References

Lepik, Ü. (2007) Application of the Haar wavelet transform to solving integral and differential equations. *Proc. of Estonian Academy of Sciences. Physics. Mathematics*. 56, 1, pp. 28–46.

Shariyat, M. and Alipour, M. M. (2011) Differential transform vibration and modal stress analyses of circular plates made of two-directional functionally graded materials resting on elastic foundations. *Archive of Applied Mechanics*, 81, pp. 1289–1306.

Hein, H. and Feklistova, L. (2011) Free vibrations of non-uniform and axially functionally graded beams using Haar wavelets. *Engineering Structures*, 33, pp. 3696–3701.

Lokavarapu, B. R. and Chellapilla, K. R. (2014) Frequency analysis of annular plates with inner and outer edges elastically restrained and resting on Winkler foundation. *International Journal of Mechanical Sciences*, 81, pp. 184–194.

Xianjie, S., Dongyan, S., Wen, L. L. and Quinshan, W. (2014) A unified method for free vibration analysis of circular, annular and sector plates with arbitrary boundary conditions. *Journal of Vibration and Control*, pp. 1–15.

Chen, C. F. and Hsiao, C. H. (1997) Haar wavelet method for solving lumped and distributed-parameter systems. *IEE Proceedings - Control Theory and Applications*. 144, 1, pp. 87–94.

Lal, R. and Sharma, S. (2004) Axisymmetric vibrations of non-homogeneous polar orthotropic annular plates of variable thickness. *Journal of Sound and Vibration*, 272, pp. 245–265.

Salmane, A., and Lakis, A. A. (1999) Natural frequencies of transverse vibrations of nonuniform circular and annular plates. *Journal of Sound and Vibration*, 220, pp. 225–249.

30th International Conference
ENGINEERING MECHANICS 2024
Milovy, Czech Republic, May 14 – 16, 2024

LES SIMULATIONS OF AIRFLOW AROUND RECTANGLE WITH SIDE RATIO 2:1 AND THEIR COMPARISION WITH EXPERIMENTS

Ledvinková B.[*], Hračov S.[**], Macháček M.[***]

Abstract: *Our contribution is focused on the comparison of the experimental investigations and of the numerical 3D LES simulations of the airflow around sharply edged rectangle with side ratio 2:1. The rectangle object was exposed to the airflow having a given velocity at different angles of the wind attack in the wind tunnel with the aim to obtain the curves of the aerodynamic coefficients and Strouhal number depending on the impact angle. The comparative numerical 3D simulations of the wind tunnel testing were performed using COMSOL Multiphysics and OpenFoam both incorporating the Large Eddy Simulation (LES) method.*

Keywords: Rectangle 2:1, wind tunnel, LES simulation, aerodynamic characteristics.

1. Introduction

The flow around U-profiles with the constant side ratio 2 differing in the inner depth of their vertical sides and the effect of the porosity or their flanges at different attack angles were studied in the wind tunnel by Hračov and Macháček (2020). Ledvinková et al. (2021) and Ledvinková et al. (2022) with the aim to compare simulated results with the experimental ones performed the 2D URANS simulations with the same geometry and conditions. The qualitative compliance between the simulated and experimental aerodynamic mean coefficients was achieved, however 2D URANS simulations are not capable to describe realistically the flow characteristics.

In this work we thus proceed to the 3D modelling and as the first verifying study the turbulent air flow around the bluff body having rectangular cross section with side ratio 2:1 using Large Eddy Simulation method is modelled. Our aim is to evaluate aerodynamics coefficients, to investigate the flow characteristics for different attack angles and to compare computed results with the experimental ones.

2. Computational settings

Large Eddy Simulation method (LES) solves explicitly large eddies whereas the effect of small eddies is accounted via the sub-grid scale model. The implementations of the LES method with standard Smagorinsky sub-grid model in Comsol Multiphysics simulation platform based on the Finite Element Method (FEM) and OpenFoam open source code using the finite volume method were used.

The investigated rectangle body (30 x 15cm) was placed into the larger square computational domain 7.5 x 7.5 m as apparent from Fig. 1. The size of the computational domain was chosen in such a way so that the blockage effect is negligible. Due to the time demanding computations for the inlet flow velocity 14m/s used in the wind tunnel experiments (Hračov and Macháček, 2020), the velocity of the inlet flow was chosen to be 2.8 m/s (corresponding to the Reynold's number Re = 2.7e4) for the most of performed

[*] Ing. Blanka Ledvinková, PhD.: Institute of Theoretical and Applied Mechanics of the Czech Academy of Sciences, Prosecká 809/76; 190 00, Prague; CZ, ledvinkova@itam.cas.cz

[**] Ing. Stanislav Hračov, PhD.: Institute of Theoretical and Applied Mechanics of the Czech Academy of Sciences, Prosecká 809/76; 190 00, Prague; CZ, hracov@itam.cas.cz

[***] Ing. Michael Macháček, PhD.: Institute of Theoretical and Applied Mechanics of the Czech Academy of Sciences, Prosecká 809/76; 190 00, Prague; CZ, machacek@itam.cas.cz

doi: 10.21495/em2024-182

simulations. Periodic boundary conditions were imposed on side and lower-upper surfaces (cf. Fig. 1). The spanwise length of the computational domain was set to be 0.3 m. This value equals to the along wind dimension of the rectangle object and fulfils the requirement for the spanwise length suggested by Tamura et al. (1998).

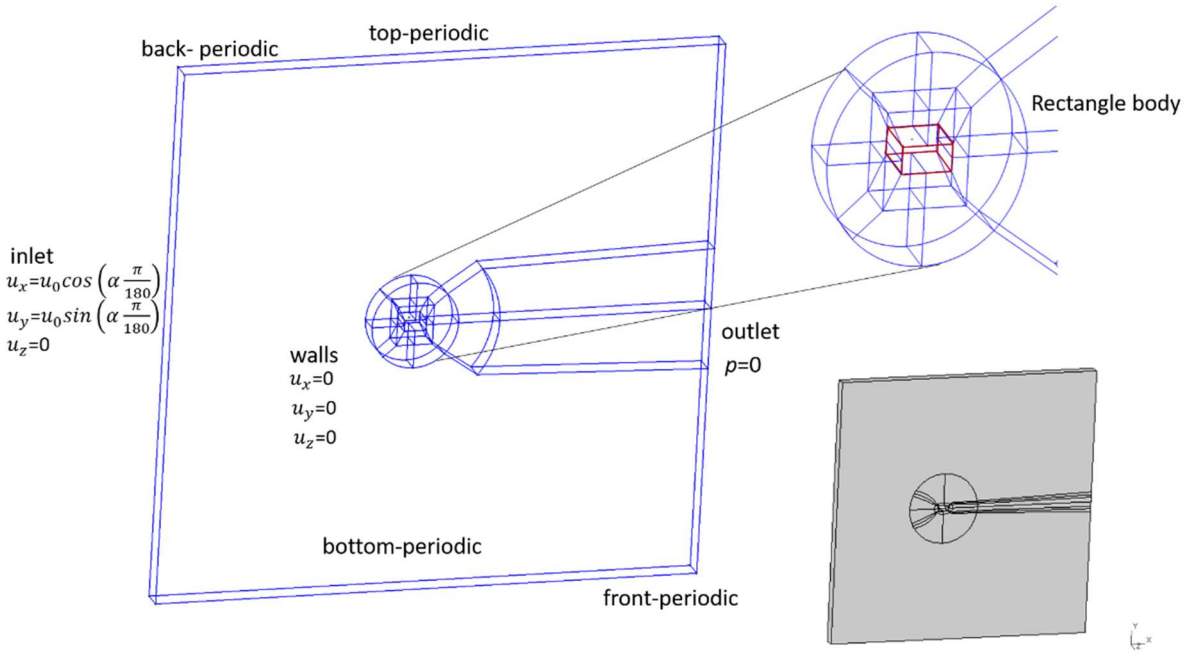

Fig. 1: a) Computational domain for OpenFoam calculations with initial and boundary conditions, b) Computational domain for Comsol Multiphysics calculations.

The computational meshes are not identical for Comsol Multiphysics and OpenFoam computations (due to the different meshing software and various requirements of FEM/FVM method) but they have similar structure. The rectangle body is surrounded by the structured boundary layer having 6 cell layers, the width of the first cell layer is 1.0e-4 m and the expansion ratio is 1.2 in the x-y plane. The domains in the circle surrounding of the rectangle object and in the wake area are also covered by structured mesh, the cell size increases continuously with the increasing distance from the body as shown in Fig. 2. The rest of the computational domain is covered with unstructured mesh, cf. Fig. 2. The described 2D mesh was extruded along the z-dimension by 24 uniformly distributed cells. The mesh for Comsol calculations consists of 900 000 elements, while the total cell number for OpenFoam calculations is about 3.5 million.

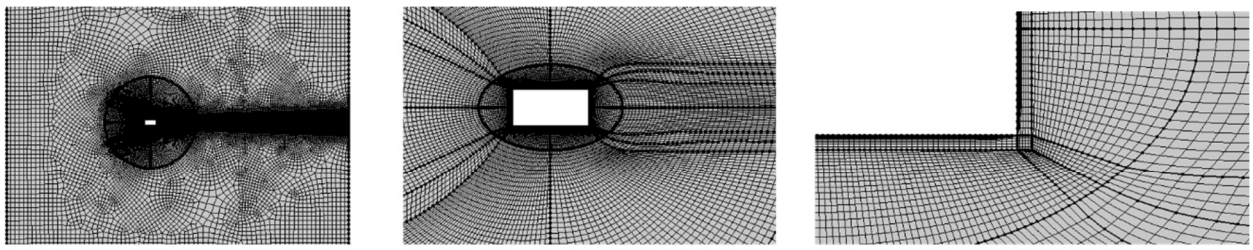

Fig. 2: Computational mesh for Comsol calculations- projection into x-y plane –a) whole domain, b) proximity of the rectangle body, c) detail of the corner of the rectangle.

For the OpenFoam calculations, the second-order centred differentiation scheme is used for diffusive terms and convective terms are approximated by Linear Upwind Stabilised Transport scheme (LUST). Time progress is managed by the backward differentiation formula (BDF) approach (inspired by Bruno et al., 2010). The PIMPLE algorithm with the automatic time step regulation was used, maximum Courant number was set to be 2.4.

Calculations in Comsol Multiphysics software are performed by the Algebraic Multigrid method using GMRES solver and generalized α method for the time discretization. In order to achieve reasonable computational time P1+P1 fluid discretization assuming linear elements for both pressure and velocity field.

3. Results

The values of the drag and the lift forces were evaluated by the integration of the *x*-and *y* components of the total stress force over all the walls of the investigated body for several angles of wind attack α. The reference dimension for the calculation of coefficients is across wind dimension 0.15 m.

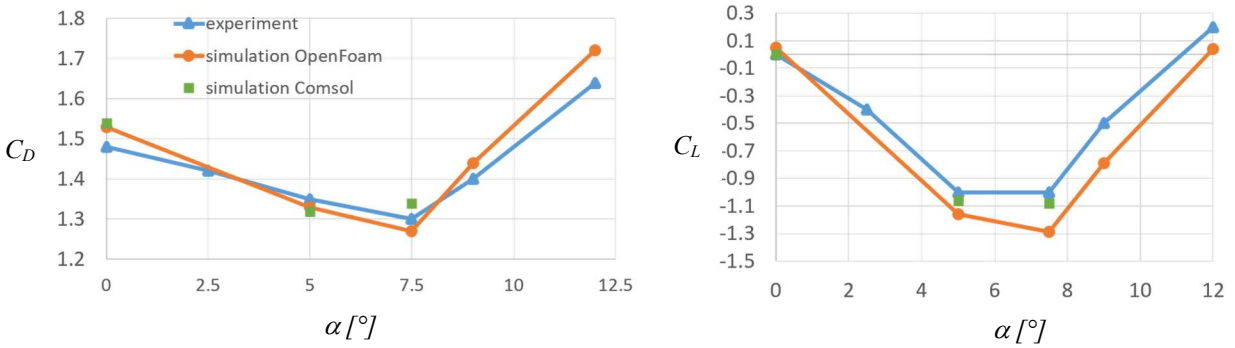

Fig. 3: Mean drag and lift coefficient for the rectangle with side ratio 2 depending on the impact angle - comparison of the results obtained from the simulations performed in Comsol Multiphysics and OpenFoam and from the experiments in the wind tunnel.

The comparison of the calculated and experimental mean aerodynamic coefficients for several positive values of the angle of attack is shown in Fig. 3. As apparent, the simulated and measured values show qualitatively same trends and the position of the minimum corresponds approximately to the same impact angle.

The values of Strouhal number related to the vortex shedding frequency for the zero angle of attack and two different wind velocities are listed in Tab. 1. Strouhal number seems to be only slightly velocity dependent, the values calculated by Comsol Multiphysics correspond better to the measured ones.

	v = 2.8 m/s	v = 14 m/s
experiment	0.087	0.092
simulation-Comsol Multiphysics	0.078	0.080
simulation- OpenFoam	0.068	not calculated yet

Tab. 1: Experimentally and numerically determined Strouhal number for the wind velocity v=2.8 m/s and v = 14 m/s and zero impact angle.

The experimental dependence of Strouhal number on the impact angle is shown in Fig. 4a. Its value fluctuates around 0.09 for small impact angles $\alpha < 5$ °, in the proximity of the angle $\alpha = 5$ ° the frequency spectrum is ambiguous and there is a step increase for angles $\alpha > 7$ °. This rise was observed also in simulations. The calculated time dependencies of the lift coefficient and the values of Strouhal numbers for three values of impact angles are shown in Fig. 4b–d.

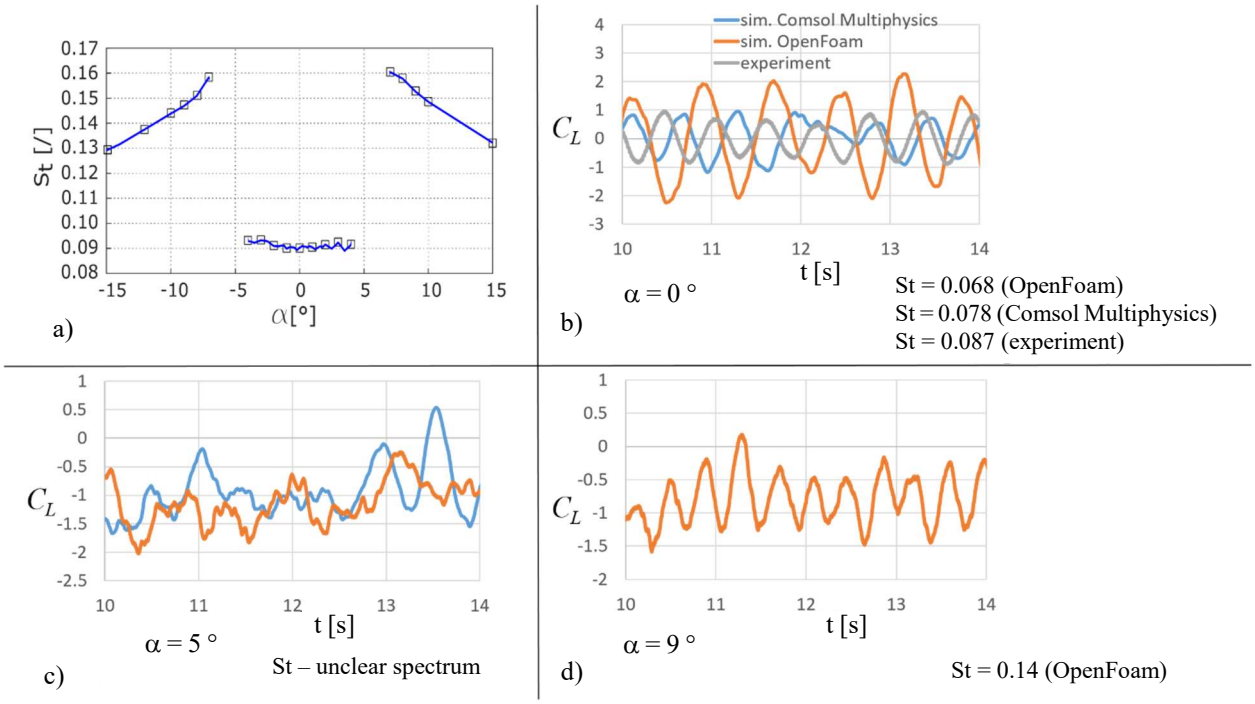

Fig. 4: a) Dependence of Strouhal number on impact angle obtained experimentally for v = 12.8 m/s, b–d) time dependence of lift coefficient and Strouhal number for various angles of attack obtained from OpenFoam and Comsol Multiphysics simulations.

4. Conclusions

The results of our simulations show qualitatively same trends for the mean aerodynamics coefficients and for Strouhal number depending on the impact angle as the experimental results obtained by the static measurement in the wind tunnel. However, the numerical results provided by Comsol Multiphysics simulations correspond better with experiments than those obtained from OpenFoam simulations.

Acknowledgement:

The kind support of Czech Scientific Foundation project No. 24-13061S is gratefully acknowledged.

Computational resources were provided by the e-INFRA CZ project (ID:90254), supported by the Ministry of Education, Youth and Sports of the Czech Republic.

The cooperation with Ing. Martin Kožíšek from HUMUSOFT s.r.o. is gratefully acknowledged.

References

Holmes, J. D. (2018) *Wind Loading Structures*, CRC Press, 3rd edition.

Hračov, S. and Macháček, M. (2020) Susceptibility of U-profiles with different geometry and porosity to galloping. *EASD Procedia EURODYN*, pp. 621–630.

Ledvinková, B., Hračov, S. and Macháček, M. (2021) Numerical study of the air flow around the U-profile. In: *Proc. of Computational Mechanics*, Srní, pp. 138–141.

Ledvinková, B., Hračov, S. and Macháček, M. (2022) Determination of aerodynamic coefficients for air flow around U-profiles with different flange porosities. In: *Proc. of the 28th Conference* Engineering *mechanics,* Milovy, pp. 237–240.

Bruno, L., Francos, D., Coste, N. and Bosco, A. (2010) 3D flow around a rectangular cylinder: A computational study. *J. Wind Eng. Ind. Aerodyn.*, 98, pp. 263–276.

Tamura, T., Miyagi, T. and Kitagishi, T. (1998) Numerical prediction of unsteady pressures on a square cylinder with various corner shapes. *J. Wind Eng. Ind. Aerodyn.*, 35, pp. 275–298.

30th International Conference
ENGINEERING MECHANICS 2024
Milovy, Czech Republic, May 14 – 16, 2024

EFFICIENT COMPUTATIONAL ALGORITHM FOR SOLVING TWO-SCALE PROBLEMS OF LARGE DEFORMING HETEROGENEOUS PERIODIC STRUCTURES

Lukeš V.[*], **Rohan E.**[**]

Abstract: *We propose an efficient computational algorithm for solving coupled two-scale problems of large deforming heterogeneous hyperelastic media with periodic structure. Our algorithm is based on clustering points in the deformation space and the approximating material coefficients with the help of the sensitivity analysis method. The effectiveness of the proposed approach is compared with the standard FE^2 computational scheme in a simple 2D example.*

Keywords: Homogenization, hyperelasticity, model order reduction, finite element method.

1. Introduction

We consider a heterogeneous hyperelastic medium with a periodic structure subjected to large deformations. The updated Lagrangian formulation and the two-scale homogenization method are employed to get the coupled macro-micro system of equations, which must be solved in an iterative loop. The standard two-scale finite element approach for nonlinear problems leads to the FE^2 computational strategy, see e.g. Schröder (2014); Lukeš (2023), where the local microscopic problems are computed at all quadrature points of the macroscopic domain. This strategy is very computationally demanding and difficult to use in practical applications. In this paper, we propose using the K-means clustering algorithm, employed e.g., in Benaimeche et al. (2022), and sensitivity analysis techniques, see Rohan (2003), to reduce the number of local problems that need to be solved during macroscopic iterations and loading steps. We demonstrate the proposed approach in 2D numerical simulations, where we measure the computational time and observe the error induced by the approximation.

2. Two-scale model of hyperelastic structures

We use the neo-Hookean hyperelastic material model to describe the nonlinear behavior of compressible heterogeneous structures. The Cauchy stress in such a structure can be expressed as

$$\boldsymbol{\sigma} = K(J-1) + \mu J^{-5/3}\,(\boldsymbol{b} - \mathrm{tr}(\boldsymbol{b})/3\boldsymbol{I}), \tag{1}$$

where, μ is the shear modulus, K is the bulk modulus, $\boldsymbol{F}$ is the deformation gradient, $J = \det(\boldsymbol{F})$, $\boldsymbol{b} = \boldsymbol{F}\boldsymbol{F}^T$, and $\boldsymbol{I} = (\delta_{ij})$ is the Kronecker symbol. The constitutive equation (1), together with the equilibrium equation (∇ is the gradient operator and $\boldsymbol{f}$ stands for external forces)

$$-\nabla \cdot \boldsymbol{\sigma} = \boldsymbol{f} \tag{2}$$

define the nonlinear problem that is linearized using the updated Lagrangian formulation. The linearized incremental form of the problem is treated by the homogenization procedure, which results in the coupled

[*] Ing. Vladimír Lukeš, PhD.: Department of Mechanics, Faculty of Applied Sciences, University of West Bohemia, Univerzitní 2732/8; 301 00, Plzeň; CZ, vlukes@kme.zcu.cz

[**] Prof. Dr. Ing. Eduard Rohan, DSc.: Department of Mechanics, Faculty of Applied Sciences, University of West Bohemia, Univerzitní 2732/8; 301 00, Plzeň; CZ, rohan@kme.zcu.cz

doi: 10.21495/em2024-186

system of macroscopic and microscopic equations. At the macroscopic level, we must solve the following equilibrium equation for the unknown macroscopic displacement increments $\delta \boldsymbol{u}^0$

$$\int_\Omega \boldsymbol{\mathcal{A}} \nabla_x \delta \boldsymbol{u}^0 : \nabla_x \boldsymbol{v} = L^{new}(\boldsymbol{v}) - \int_\Omega \boldsymbol{\mathcal{S}} : \nabla_x \boldsymbol{v}, \qquad \text{for all } \boldsymbol{v} \in \boldsymbol{V}_0(\Omega). \tag{3}$$

L^{new} involves all forces applied in the current loading step, $\boldsymbol{\mathcal{A}}$ and $\boldsymbol{\mathcal{S}}$ are the homogenized coefficients arising from the solution of a microscopic subproblem, $\boldsymbol{V}_0(\Omega)$ is the set of admissible functions that are equal to zero on the Dirichlet boundary of Ω, and ∇_x denotes the gradient operator with respect to the macroscopic scale x.

For a given macroscopic deformation $\boldsymbol{F}(x)$, we solve the local problem at the deformed locally periodic reference cell $Y(x)$ (see Lukeš (2023)) to find the characteristic responses $\boldsymbol{\chi}$:

$$\int_{Y(x)} \mathbb{A} \nabla_y (\boldsymbol{\chi}^{ij} + \boldsymbol{\Pi}^{ij}) : \nabla_y \boldsymbol{v} = 0, \qquad \text{for all } \boldsymbol{v} \in \boldsymbol{H}^1_\#(Y). \tag{4}$$

By $\boldsymbol{H}^1_\#(Y)$ we denote the functional space of $Y(x)$ locally periodic functions, $\Pi^{ij}_k = y_j \delta_{ik}$, and $\mathbb{A}$ is the fourth-order tangential stiffness tensor (Truesdell rate of the Kirchhoff stress). The microscopic configuration $Y(x)$ is updated at each iteration step using the macroscopic (incremental) deformation $\nabla_x \delta \boldsymbol{u}^0$ and the microscopic response $\boldsymbol{\chi}^{ij}$ as: $Y^{new}(x) = Y^{old}(x) + (\boldsymbol{\chi}^{ij} + \boldsymbol{\Pi}^{ij}) \frac{\partial \delta u^0_i}{\partial x_j}$.

The homogenized stiffness coefficients $\boldsymbol{\mathcal{A}}$ and the averaged Cauchy stress $\boldsymbol{\mathcal{S}}$ are given by

$$\boldsymbol{\mathcal{A}} = \frac{1}{|Y|} \int_Y \mathbb{A} \nabla_y (\boldsymbol{\chi}^{ij} + \boldsymbol{\Pi}^{ij}) \nabla_y (\boldsymbol{\chi}^{ij} + \boldsymbol{\Pi}^{ij}), \quad \boldsymbol{\mathcal{S}} = \frac{1}{|Y|} \int_Y \boldsymbol{\sigma}. \tag{5}$$

3. Approximation of homogenized coefficients

Solving the nonlinear macroscopic problem by the finite element method requires knowing the tangent modulus and stress tensors at all quadrature points $\hat{x}$ of Ω at each iteration step. To avoid the computational bottleneck of the FE^2 approach, we propose the following algorithm reducing the number of computed local subproblems. In the first step, the polar decomposition of the macroscopic deformation $\boldsymbol{F}(\hat{x}) = \hat{\boldsymbol{R}}\hat{\boldsymbol{U}}$ is employed to decompose the deformation into the rotation tensor $\boldsymbol{R}$ and the symmetric stretch tensor $\boldsymbol{U}$. Then, $\hat{\boldsymbol{U}}$ is used to express the symmetric strain tensor $\hat{\boldsymbol{e}} = \hat{\boldsymbol{U}} - \boldsymbol{I}$, which components represent a point in the 3 (for 2D) or 6 (for 3D) dimensional space of deformations. Using the K-means clustering method, see Lloyd (1982) for details, we can find a minimal number of sets $O^k = \{\hat{\boldsymbol{e}} : |\hat{\boldsymbol{e}} - \mathring{\boldsymbol{e}}^k| < \rho\}$, such that $\bigcup_k O^k$ includes all strains $\hat{\boldsymbol{e}}$, where $\mathring{\boldsymbol{e}}^k$ is the mean value (center) of points in O^k, and ρ is a given parameter. Now, instead of solving the local microscopic subproblems (4) for all macroscopic deformations $\boldsymbol{F}(\hat{x})$, we solve the subproblems only for a reduced number of deformations $\mathring{\boldsymbol{F}} = \mathring{\boldsymbol{e}}^k + \boldsymbol{I}$ to get the homogenized coefficients $\mathring{\boldsymbol{\mathcal{A}}}$ and $\mathring{\boldsymbol{\mathcal{S}}}$. The choice of the ρ parameter affects the number of sets O^k (we call them centroids) and the accuracy of the resulting approximation. The centroids are constructed on the fly during the macroscopic iterations when newly appeared deformations $\hat{\boldsymbol{e}}$ cannot be covered by the existing centroids.

Approximation of the homogenized coefficients in the quadrature points $\hat{x}$ is made with the help of the sensitivity analysis technique as suggested in Rohan (2003). The coefficient sensitivities $\delta\mathring{\boldsymbol{\mathcal{A}}}$, $\delta\mathring{\boldsymbol{\mathcal{S}}}$ with respect to deformations can be evaluated using the already computed characteristic responses $\boldsymbol{\chi}$, see Rohan (2003), so there is no need to solve any additional microscopic problem. The following approximation scheme for the homogenized coefficients is used

$$\boldsymbol{\mathcal{A}}(\hat{x}) \approx \hat{\boldsymbol{R}}^T \left(\sum_i \left(\mathring{\boldsymbol{\mathcal{A}}}^i + \delta\mathring{\boldsymbol{\mathcal{A}}}^i(\hat{\boldsymbol{g}}^i) \right) w_i \right) \hat{\boldsymbol{R}}, \qquad \boldsymbol{\mathcal{S}}(\hat{x}) \approx \hat{\boldsymbol{R}}^T \sum_i \left(\mathring{\boldsymbol{\mathcal{S}}}^i + \delta\mathring{\boldsymbol{\mathcal{S}}}^i(\hat{\boldsymbol{g}}^i) \right) w_i, \tag{6}$$

where the summation is performed for all centroids to which $\hat{\boldsymbol{e}}$ belongs, $\hat{\boldsymbol{g}}^i$ is the relative strain of $\hat{\boldsymbol{e}}$ with respect to $\mathring{\boldsymbol{e}}^i$, and w_i are the weights reflecting the distance $|\hat{\boldsymbol{e}} - \mathring{\boldsymbol{e}}^i|$, $\sum_i w_i = 1$.

4. Numerical simulation

The suggested reduction strategy is demonstrated in a simple 2D example. We consider a rectangular macroscopic domain of shape 0.4×0.25 m fixed on its left edge and displaced on the right edge as depicted in

Fig. 1 left. The total prescribed displacement $\bar{\boldsymbol{u}} = [0.05, -0.05]^T$ m is applied uniformly in six loading steps. The microscopic periodic unit cell Y consisting of two hyperelastic parts, see Fig. 1 right, is defined by the following material parameters: $K = 1\,000$ Pa, $\mu = 100$ Pa in Y_1 and $K = 1\,000$ Pa, $\mu = 10$ Pa in Y_2.

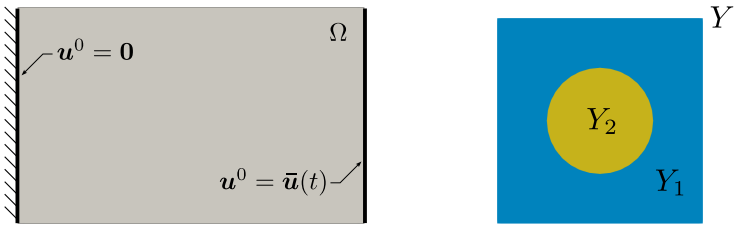

Fig. 1: Macroscopic domain Ω and the applied boundary conditions (left), periodic cell $Y = Y_1 \cup Y_2$ (initial configuration, right).

The deformed macroscopic sample and the deformed microscopic cells in selected macroscopic points are shown in Fig. 2. To be able to measure the approximation error of the proposed algorithm, we choose three quadrature points of the macroscopic domain, labelled in Fig. 2 left by symbol $\circ$, in which the extra local problems are solved, and the exact values of the homogenized coefficients are evaluated.

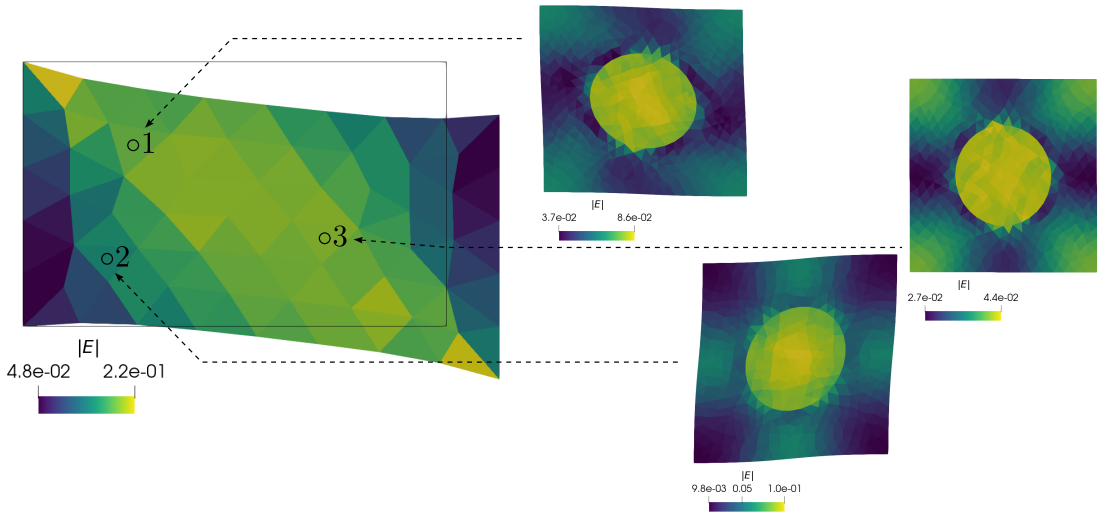

Fig. 2: Deformed macroscopic domain (left), deformed microscopic configurations at the macroscopic checkpoints (right).

The coefficient components $\mathcal{A}_{1111}$, $\mathcal{S}_{11}$ are compared for different parameters ρ in Fig. 3. We label the exact values by superscript ^{exact} and the approximated values by ^{approx}.

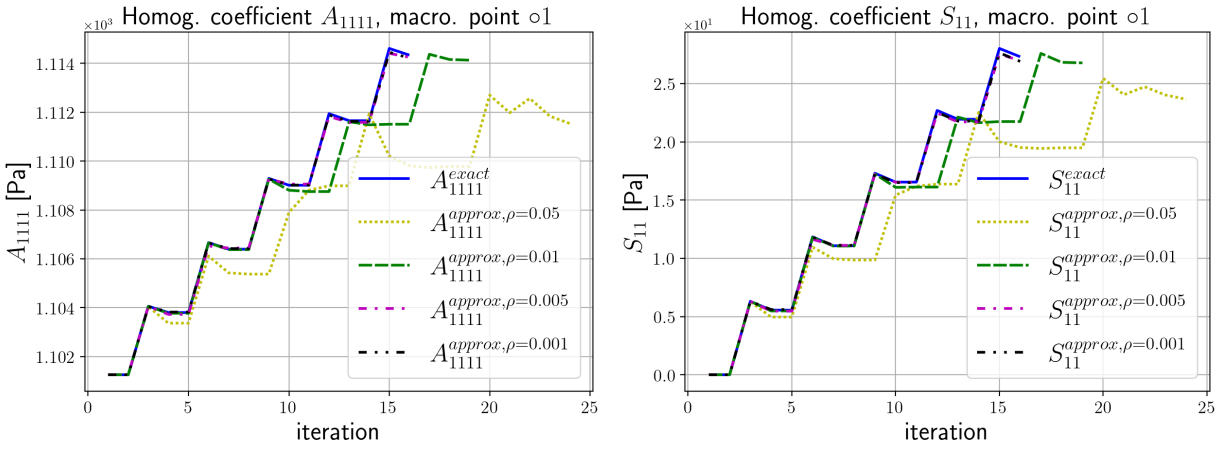

Fig. 3: Comparison of components $\mathcal{A}_{1111}$, $\mathcal{S}_{11}$ calculated for $\rho = 0.05, 0.01, 0.005, 0.001$ with the exact solution.

The efficiency of our new algorithm is apparent from Fig. 4, where we compare the computation time of the coupled two-scale simulations and the number of solved local microproblems for various ρ with the full FE^2 simulation without any reduction (denoted by "No approx"). The computation time of the full simulation is less than the reduced simulation for $\rho = 0.001$ in our case. This result occurs because the computation time of our simple 2D local problem is very small, and it is comparable to the time required to evaluate the sensitivities and for the approximation of the coefficients. For more complex geometries at the microscopic level and for 3D problems, the solution time of (4) will grow much more than the overhead associated with sensitivity analysis and approximation.

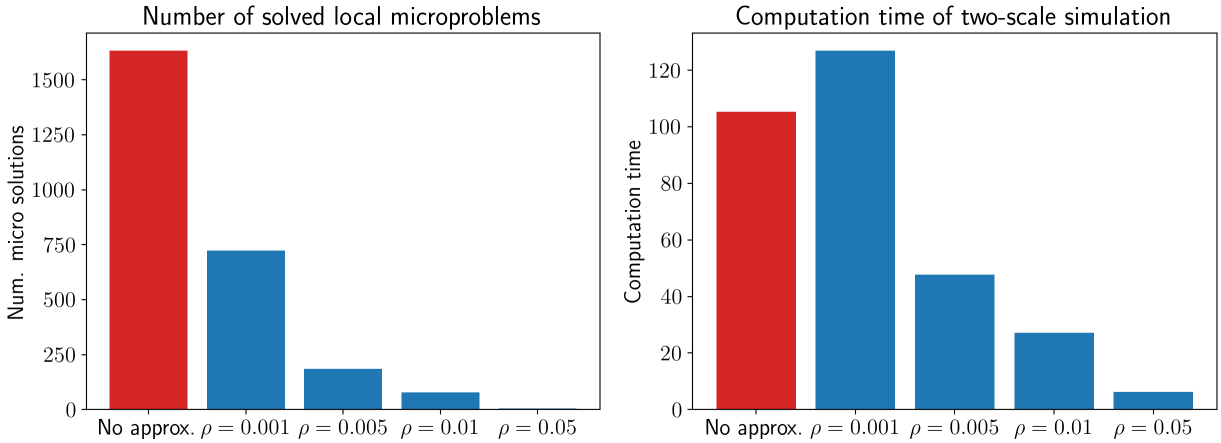

Fig. 4: Number of solved local microproblems (left), computation time of the simulation (right).

The two-scale numerical simulation has been implemented in SfePy (Simple Finite Elements in Python), see Cimrman (2023), which allows to solve the local problems efficiently using parallel computing on multiple cores or processors.

5. Conclusion

The proposed algorithm can efficiently reduce the computational complexity of the coupled two-scale problems arising from the homogenization of heterogeneous structures undergoing large deformations. The problem reduction efficiency can be controlled by the parameter ρ, which, for a particular application, should be chosen in such a way as to minimize the number of centroids associated with sets O^k while keeping the approximation error below the given limit. In the case of the presented 2D simulation, for $\rho = 0.005$, we achieve less than half the computational time with a relative error of the order of 10^3.

Acknowledgment

The research has been supported by the project GACR GL22-00863K of the Czech Science Foundation.

References

Cimrman, R., Lukeš, V. and Rohan E. (2019) Multiscale finite element calculations in Python using Sfepy. *Advances in Computational Mathematics*, 45, 4, pp. 1897–1921.

Lloyd, S. (1982) Least squares quantization in PCM. *IEEE Transactions on Information Theory*, 28, 2, pp. 129–137.

Lukeš, V. and Rohan E. (2022) Homogenization of large deforming fluid-saturated porous structures. *Computers & Mathematics with Applications*, 110, pp. 40–63.

Rohan, E. (2003) Sensitivity strategies in modelling heterogeneous media undergoing finite deformation. *Mathematics and Computers in Simulation*, 61, 3, pp. 261–270.

Benaimeche, M. A., Yvonnet, J., Bary, B. and He, Q.-C. (2022) A k-means clustering machine learning-based multiscale method for anelastic heterogeneous structures with internal variables. *International Journal for Numerical Methods in Engineering*, 123, 9, pp. 2012–2041.

Schröder, J. (2014) A numerical two-scale homogenization scheme: the FE2-method, In: *Plasticity and Beyond: Microstructures, Crystal-Plasticity and Phase Transitions*, Springer, Vienna, pp. 1–64.

30th International Conference
ENGINEERING MECHANICS 2024
Milovy, Czech Republic, May 14 – 16, 2024

GALLOPING OF INSULATED BUNDLED OVERHEAD LINE - NONLINEAR NUMERICAL ANALYSIS IN TIME DOMAIN

Macháček M.*, Hračov S.**

Abstract: *Our contribution focuses on a 3D numerical nonlinear analysis of galloping in a specific bundled overhead line with ice accretion. We studied the susceptibility to this self-excited oscillation, critical onset wind speeds, and global dynamic response of a very low-tensioned line with simulated icing observed on similar real conductors. Due to the highly nonlinear mechanical behavior of such a flexible cable, we employed the Newmark integration method combined with the iterative Newton-Raphson method. We analyzed two numerical models of the overhead line loaded by the wind: one assuming nonlinearity only in the wind load, while retaining the linearity of the mechanical system itself, and the other representing a fully nonlinear system including geometrical nonlinearity. Our analysis revealed that the determined critical wind speeds for the onset of galloping are in relatively close ranges for both models. However, numerical simulations with the fully nonlinear system indicated significantly lower amplitudes of limit cycle oscillations, especially at higher wind speeds, compared to the linear model of the line. This underscores the necessity of using fully nonlinear models during the design stage of such low-tensioned aerial conductors.*

Keywords: Aerial bundled conductors, wind effects, galloping, limit cycle oscillation.

1. Introduction

Wind action on the electrical conductors can cause a loss of their aeroelastic stability called galloping. Galloping is a low frequency, self-excited vibration, usually in a plane perpendicular to the wind direction, see Holmes (2018) with large amplitudes. The most often observed vibration mode shapes has one to three loops; higher modes have been detected only sporadically, see EPRI (2006). A necessary condition for the emergence of galloping is a rotationally asymmetric cross-section of the line. Power lines are generally rotationally symmetrical, but ice accretion can cause the significant changes in their shapes. The amplitudes of galloping oscillations can reach, in some cases, more than ten times the diameter of the cable. Such deformations lead to substantial axial stresses in the lines, which can be crucial not only for the safe design of supporting structures, but also for fatigue life of the lines. This article presents outcomes from a fully nonlinear 3D numerical analysis of galloping of a very low-tensioned bundled overhead line with ice accretion. The power line consists of four conductors covered by polyethylene insulation see Fig. 1.

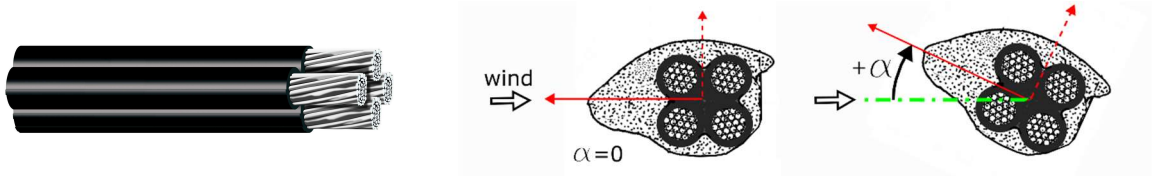

Fig. 1: Bundled overhead line – axonometric view and ice-covered cross-section.

* Ing. Michael Macháček, PhD.: Institute of Theoretical and Applied Mechanics of the Czech Academy of Sciences, Prosecká 809/76; 190 00, Prague; CZ, machacek@itam.cas.cz

** Ing. Stanislav Hračov, PhD.: Institute of Theoretical and Applied Mechanics of the Czech Academy of Sciences, Prosecká 809/76; 190 00, Prague; CZ, hracov@itam.cas.cz

doi: 10.21495/em2024-190

In all cases the wind direction is perpendicular to the sag plane and α is the angle of ice accretion with respect to the wind. By varying the angle of ice accretion it is possible to find the lowest critical wind speed for loss stability at galloping, see Fig. 1. The simulated icing observed on similar real conductors was adopted from Desai et al. (1995). Both cable ends are supported against torsion and all three directions of linear movements. The geometrical and mechanical properties of the electrical cable are shown in Tab. 1. The elastic polyethylene makes it difficult to define the stress transfer between the aluminium cores. For this paper, torsional stiffness was calculated as the arithmetic mean between minimum and maximum torsional hypothetical stiffness. Minimum torsional stiffness was calculated as four single acting aluminium circular rods and maximum torsional stiffness was calculated as a group of four circular rods using Steiner's theorem.

Parameter	Value	Parameter	Value
Horizontal distance of suspension points	21.1 m	Vertical distance of suspension points	1.55 m
Length of line	21.588 m	Cross-sectional are of line	0.00046528 m^2
Young's modulus	57 GPa	Shear modulus	25.5 GPa
Diameter circumscribed circle of power-line	0.038 m	Mass moment of rotational inertia unit length of line (with ice accretion)	4.6504e $\cdot 10^{-4}$ kg·m^3
Viscous damping ratio of dynamic system	0.5 %	Polar moment of inertia of the cross section	2.7502 10^{-8} m^4
Mass per unit length of line (with ice accretion)	2.09 kg/m	Horizontal component of tension force for: -5 °C with ice accretion	1 149.5 N

Tab. 1: Geometrical and mechanical properties of electric line (AES 4 x 120).

2. Proneness of ice-coated cable to galloping

The susceptibility to galloping can be assessed using the Den Hartog criterion, which is based on the quasi-steady theory. This criterion can be expressed as:

$$C_D(\alpha) + \frac{dC_L}{d\alpha}(\alpha) < 0 \tag{1}$$

where C_D a C_L are drag and lift coefficients and α is the angle of wind attack. Aerodynamic coefficients for analysed ice-covered line adopted from Desai et al. (1995) are depicted as functions of α in Fig. 2. The drag coefficient is represented by the red line, the lift coefficient by the blue line and the torsion (moment) coefficient by the green line. The Den Hartog criterion is also expressed for all α in Fig. 2 by the black line. The negative values of this black curve indicate the angles of wind attack α for which the instability can occur. The angles α = 40.0 ° and 179.3 ° were determined as critical angles from the point of view of the onset of galloping and the character of the response.

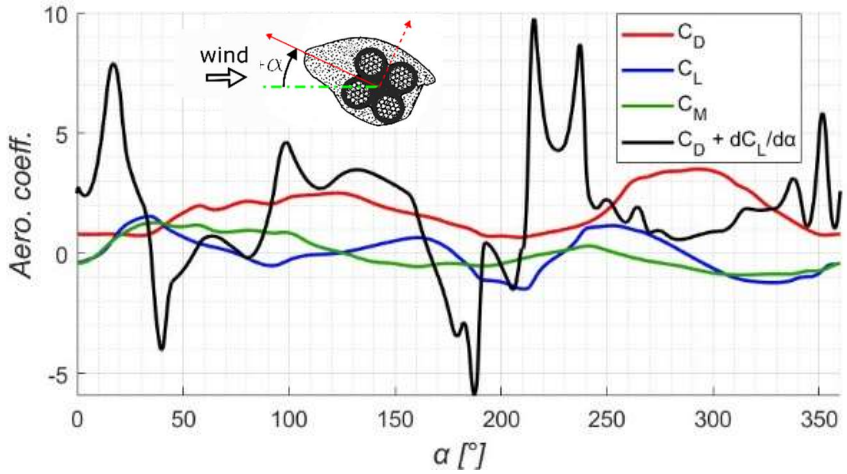

Fig. 2: Aerodynamic drag, lift and moment coefficients, C_D, C_L, C_M, and Den Hartog criterion of line.

3. Description of used numerical methods and computational model

CALFEM, finite element toolbox for Matlab was used for the analysis of the effects of wind on the bundled overhead line. The necessary modifications of this toolbox consist of an adaptation of the geometrical nonlinearity to achieve a better approximation of the real cable behavior. Because of the geometrical nonlinearity and the nonlinearity in the wind load, which depends on the velocity of the cable motion, we used the Direct Integration Time-history analysis in combination with the incremental iterative Newton-Raphson method to solve the differential equations of motion.

The finite element model of the overhead line was built using the modified bar element in 3D space. This adjustment involves adding torsional stiffness to the previously completely flexible joint (connection) between every two elements. Therefore, it is a finite element that can be loaded by and carry only normal forces and torsional moments. This modification ensures a more realistic numerical simulation of a perfectly flexible cable with the required torsional stiffness. The entire finite element model consisted of 100 modified bar elements.

The correctness of the used 3D FEM model was initially verified by comparing the results of the static nonlinear numerical analyses with the simplified analytical solutions. Subsequently, the results from modal analysis of this linearized 3D model were successfully compared with analytical solutions in Madugula (2001), which are valid for tensioned cables with a sag-to-span ratio of 1:8 or less. In our case, this ratio is approximately 1:17. The lowest in-plane natural mode, crucial for galloping susceptibility, was determined from modal analysis and is shown in Fig. 3. The corresponding frequency for this mode is 1.105 Hz.

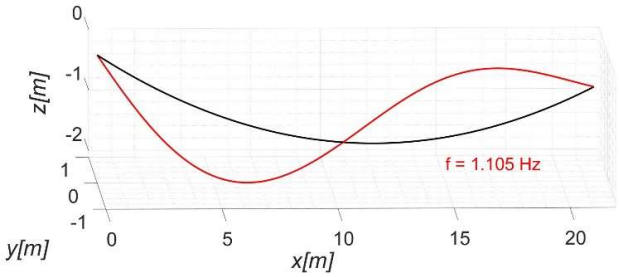

Fig. 3: Sag of the cable (black curve) and the lowest natural in-plane mode (red curve).

4. Time-Domain numerical analysis of galloping

The amplitude of the limit cycle oscillation and the global dynamic response for selected wind speeds ranging from 0 to 6 m/s were evaluated using the Newmark integration method with a constant time step of 0.001 s and the iterative Newton-Raphson method performed at each time step. The responses of three modifications of a fully nonlinear computational model of the power line were analyzed and compared.

The first simplest model, FEM - 1D model, allows vibrations only in the perpendicular plane to the wind direction, i.e., only the aerodynamic nonlinear forces in this plane are considered. The linearity of the cable is assumed, i.e., its structural matrices remain constant during the numerical calculations. An extended version of this model, the second model, FEM - 3D model, differs from the first model only by allowing the line to move in three-dimensional space and by incorporating all three components of aerodynamic wind load. The third model, FEM - 3D – nonlinear model, represents the fully nonlinear model in 3D, with the structural matrices being reassembled at each time step according to the actual deformed state.

The calculated amplitudes of the limit cycle oscillation are shown in Fig. 4 as functions of the wind velocity for each model and for two critical angles of wind attack. From the graphs in this figure, it is evident that the numerical simulations with all the models described above provide almost similar and accurate estimations of the critical galloping onset wind velocity. The graphs in Fig. 4 also demonstrate good agreement between the outcomes from the simplified galloping analysis of the same overhead line represented by the black line, and the results of numerical simulations with the simplified model, FEM - 1D, indicated in this figure by the red diamonds. This fact confirms the equivalence of both models when considering identical model assumptions. The amplitudes of limit cycle oscillations related to the FEM - 3D model, marked in Fig. 4 by blue squares, reach higher values than for the FEM - 1D model. This effect is especially pronounced for the angle of wind attack equal to 40 °. It is caused by the torsional load introduced into the 3D model, which significantly contributes to the increase in the galloping effect.

The fully nonlinear solution of the response of the bundled line is shown in Fig. 4, marked by green dots. Nonlinear numerical simulations indicate that the amplitudes cannot increase beyond a certain level. In our case, a maximum amplitude of 35 mm was identified. The inclusion of geometric nonlinearity into the model causes significant oscillations of the normal forces, especially for higher wind speeds and amplitudes, leading to substantial changes in the stiffness matrix during a vibration period. This phenomenon results in amplitude limitation and changes in the dominant vibration frequency and the shape of the forced oscillation mode.

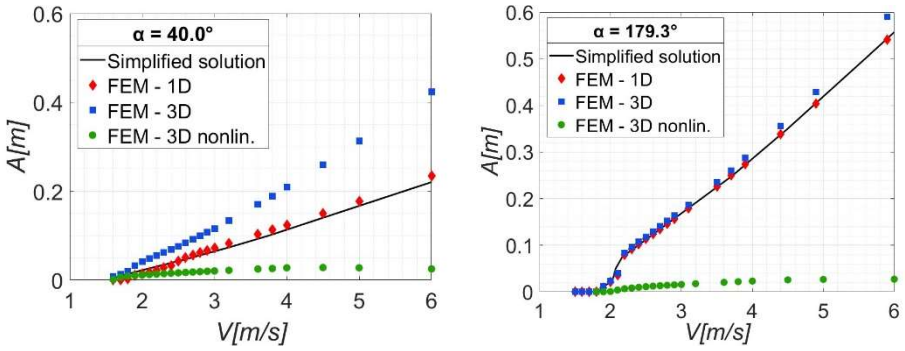

Fig. 4: Amplitude of limit cycle oscillation as function of wind speed.

The selected calculated trajectories of the antinode of the cable during one period of limit cycle oscillation related to various wind speeds are shown in Fig. 5. The elliptical trajectory at the onset of galloping instability is very similar for the geometrically linear and nonlinear approaches see Fig. 5a. However, the trajectory at higher wind speeds for the nonlinear model is no longer elliptical see Fig. 5b. The substantial flattening of the trajectory at the lower edge demonstrates the increase in stiffness when the cable moves downwards and the tensile forces increase. The inclination of the elliptic oscillation depends on the slope of all aerodynamic coefficients, especially the drag coefficient. This is demonstrated on trajectories related to angles of wind attack α = 40.0 ° and 179.3 ° in Fig. 5, which have oppositely inclined elliptical shapes due to their reversed slope of the drag coefficient.

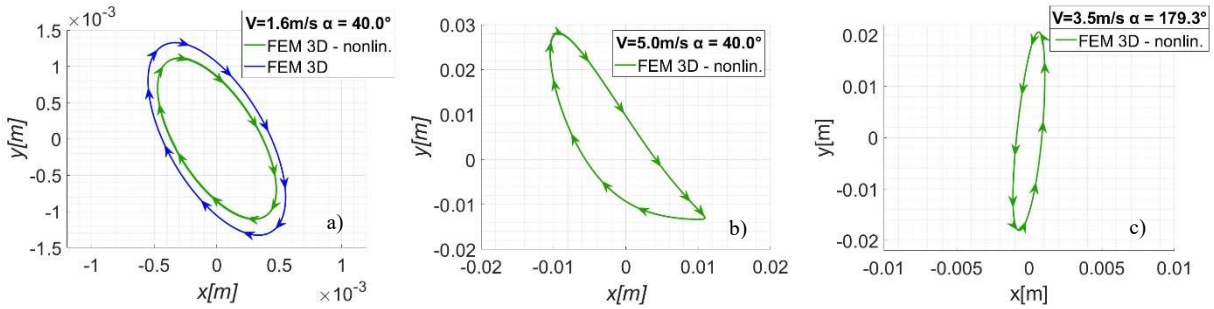

Fig. 5: Trajectory of amplitude of limit cycle oscillation.

5. Conclusions

The presented numerical analysis has proved the necessity of adopting a fully nonlinear model for predicting the dynamic response in the case of such low-prestressed electric lines. This approach will ensure a more realistic estimate of the maximal stress in the line and supporting structures, resulting in a safer and, in some cases, more economical design.

Acknowledgement

The kind support of Czech Scientific Foundation project No. 24-13061S is gratefully acknowledged.

References

Desai, Y. M., Yu, P., Popplewell, N. and Shah, A. H. (1995) Finite element modelling of transmission line galloping, *Computers & Structures*, 57, 3, pp. 407–420.

EPRI (2006) Transmission Line Reference Book - Wind Induced Conductor Motion.

Holmes, J. D. (2018) *Wind Loading Structures*, CRC Press, 3rd edition.

Madugula, M. K. S. (2001) *Dynamic Response of Lattice Towers and Guyed Masts*, ASCE.

30th International Conference
ENGINEERING MECHANICS 2024
Milovy, Czech Republic, May 14 – 16, 2024

STRUCTURAL DAMAGE DETECTION BY PSO METHOD

Marton M.*, Sokol M., Lamperová K.*****

Abstract: *Detecting structural damage is necessary for ensuring the safety and long service life of civil infrastructure. In this paper, a method for structural damage detection and localization utilizing the Particle Swarm Optimization (PSO) technique is proposed. Through numerical simulations, the effectiveness of PSO-based damage detection in detecting structural damage has been demonstrated. This study contributes to the advancement of structural health monitoring practices, highlighting the potential of PSO in improving structural integrity assessment. This study underscores the potential of the PSO method as a powerful tool for enhancing the reliability and efficiency of structural health monitoring systems, thereby contributing to the advancement of structural integrity assessment and maintenance practices in civil engineering.*

Keywords: PSO method, FEM model, damage detection.

1. Introduction

Civil infrastructure plays a key role in sustaining modern society, which includes a vast network of bridges, buildings, and other structures important for transportation, commerce, and public safety. However, infrastructure aging and exposure to various environmental loads pose significant challenges to its integrity, necessitating effective monitoring and maintenance strategies to ensure continued functionality and safety (Farrar and Worden, 2007; Hester and González, 2017; Sofi et al., 2022; Sohn et al., 2001).

Structural damage resulting from factors such as material degradation, environmental deterioration or extreme loading is a critical threat to the performance and safety of civil infrastructure (Ároch et al., 2016), (Lamperová et al., 2020; Venglár, 2018). Detection and assessment of structural damage in its early stages is essential to prevent catastrophic failures and minimizing the risk of loss of life and property (Nicoletti et al., 2022).

Over the years, considerable research efforts have been focused on developing advanced techniques for structural damage detection and health monitoring (Marwala, 2010; Sofi et al., 2022). Traditional methods, including visual inspection, finite element analysis, and modal analysis, have limitations in terms of accuracy, efficiency, and applicability to real-time monitoring (Marwala, 2010; Ventura et al., 2005). Consequently, there is a growing interest in the use of computational intelligence and optimization algorithms for enhancing the effectiveness of structural health monitoring systems (Kang et al., 2012; Zhang et al., 2014).

One such optimization algorithm that has gained prominence in recent years is the Particle Swarm Optimization (PSO) method (Kenedy and Eberhart, 1995). Inspired by the social behavior of organisms such as bird flocking and fish schooling, PSO is a population-based stochastic optimization technique that

* Ing. Martin Marton, PhD.: Department of Structural Mechanics, Slovak University of Technology, Faculty of Civil Engineering, Radlinského 11; 810 05, Bratislava; SK, martin.marton@stuba.sk

** Prof. Ing. Milan Sokol, PhD.: Department of Structural Mechanics, Slovak University of Technology, Faculty of Civil Engineering, Radlinského 11; 810 05, Bratislava; SK, milan.sokol@stuba.sk

*** Ing. Katarína Lamperová, PhD.: Department of Structural Mechanics, Slovak University of Technology, Faculty of Civil Engineering, Radlinského 11; 810 05, Bratislava; SK, katarina.lamperova@stuba.sk

doi: 10.21495/em2024-194

iteratively updates the position and velocity of particles within a search space to converge towards an optimal solution (Kennedy and Mendes, 2002; Krohling, 2005; Marton et al., 2021).

The inherent parallelism and global search capabilities of PSO make it particularly suitable for addressing complex optimization problems, including structural damage detection. By integrating sensor data with computational models, PSO can effectively identify and localize damage within a structure, offering advantages such as robustness to noise, uncertainties, and nonlinearities (Li et al., 2014).

In this paper, a new approach for structural damage detection using the PSO method is proposed. The paper is focused on the numerical simulation of damage to the truss beam and demonstrates the effectiveness of PSO-based damage detection in the accurate identification and localization of this damage. This study contributes to the advancement of structural health monitoring by exploiting the potential of PSO to increase the reliability and efficiency of damage detection techniques.

2. Methodology

2.1. Particle Swarm Optimization (PSO)

Particle Swarm Optimization (PSO) is a metaheuristic optimization algorithm inspired by the social behavior of bird flocks or fish schools. It operates by iteratively updating the position and velocity of a population of particles within a search space to converge towards an optimal solution (Kenedy and Eberhart, 1995). In PSO, each particle represents a potential solution, and its movement is guided by its own experience (personal best) and the collective knowledge of the swarm (global best).

2.2. Finding solution based on the objective function.

Structural damage detection using PSO involves comparing the eigenfrequencies and eigenmodes in an objective function. This comparison allows to identify inconsistencies caused by structural damage, which is manifested by changes in stiffness parameters. The goal is to minimize the difference between the frequencies and the eigenmodes obtained from the numerical model for each iteration with the reference data. In this case, the damage was applied to the undamaged numerical model to obtain the reference data (simulated damage). At each iteration, the positions of the PSO swarm particles are updated and the value of the fitness function is evaluated - the best position within the iteration is selected. This gradually approaches the optimal solution, which represents the sought parameters and at the same time corresponds to the eigenfrequencies and eigenmodes obtained from the reference model. The fitness of the objective function is mathematically defined as

$$Fitness = \sum_i wf_i \left(\frac{FC_i - F_i}{FD_i}\right)^2 + \sum_i wms_i \left(\frac{\left(1-\sqrt{MAC_i}\right)^2}{MAC_i}\right), \quad (1)$$

where:

wf_i is the weight factor for the i^{th} frequency,

$\left(\frac{FC_i - F_i}{FD_i}\right)^2$ is the quadratic difference between the calculated frequency FC_i and the frequency FD_i, from damaged model normalized with respect to the frequency FD_i from damaged model,

MAC_i is the Modal Assurance Criterion for the i^{th} frequency (Pastor et al., 2012),

wms_i is the weight factor of each MAC_i,

$\left(\frac{\left(1-\sqrt{MAC_i}\right)^2}{MAC_i}\right)$ is the MAC comparison.

3. Case study

The case study investigates a two-span steel truss consisting of 12 sections, with the first span consisting of 8 sections and the second span consisting of 4 sections. A numerical finite element model of this structure was created. In this case, structural damage was intentionally introduced to sections 3, 8, and 9 (0). the Young's modulus E of these sections was reduced by 30 % by multiplying by the stiffness coefficient (values of k_3, k_8 and k_9 were 0.7) (Lamperova et al., 2023; Lehký et al., 2023).

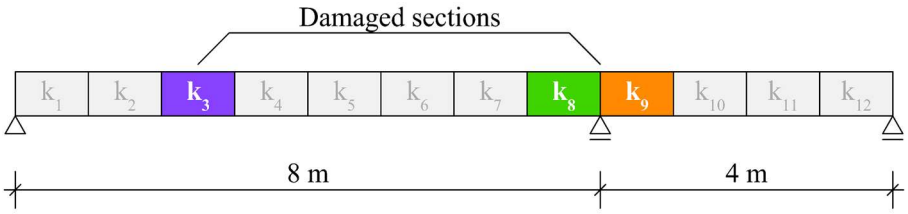

Fig. 1: Numerical model of a double-span truss.

Further information on the progress and results of the optimization is shown in 0, which shows the evolution of the objective function and the stiffness coefficient of each section of the truss beam. It is clear from the figure that the optimization process produced promising results that show good agreement with the objectives of the study. It is essential to emphasize that these simulations were performed exclusively in a theoretical framework using numerical models to evaluate the structural response to damage.

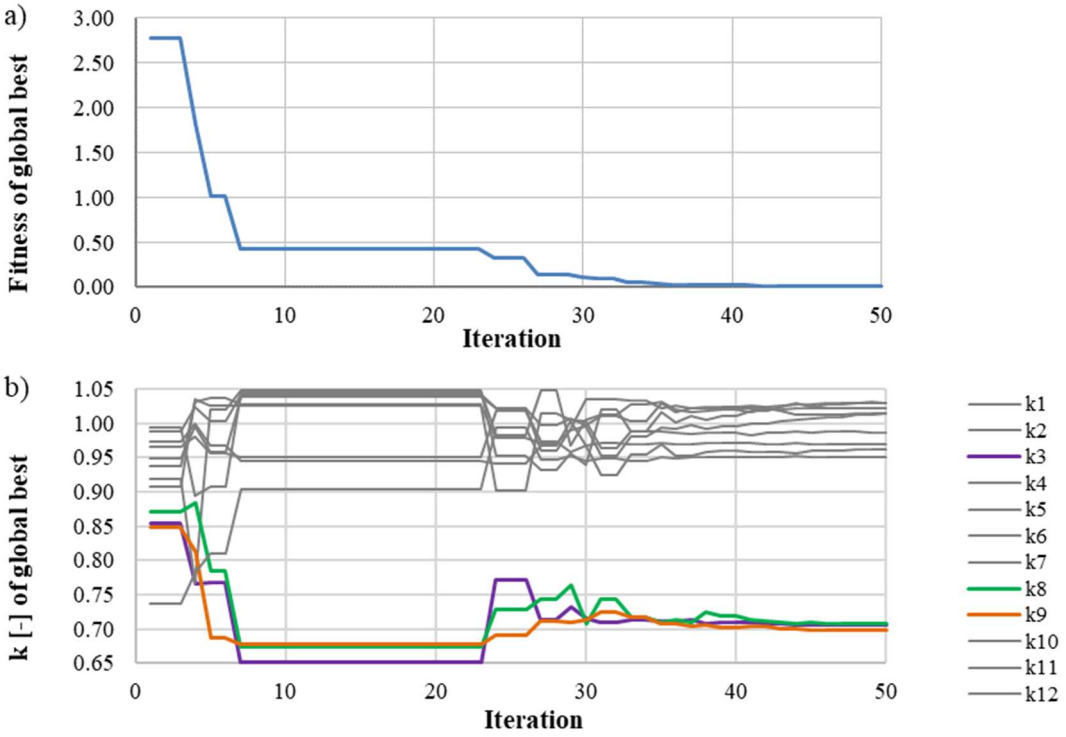

Fig. 2: Evolution of a) the objective function, b) the stiffness coefficients.

4. Conclusions

In this paper, a new approach for structural damage detection using the Particle Swarm Optimization (PSO) method applied to a double-span steel truss was presented. Through numerical simulations, the effectiveness of the proposed methodology was demonstrated in the accurate identification and localization of structural damage.

The research was aimed at optimizing the stiffness parameters of the truss structure by comparing the eigenfrequencies and eigenmodes obtained from the numerical models with those from the damaged model. By formulating the optimization problem within the framework of PSO, satisfactory agreement was achieved in simulated scenario with artificially induced damage. The results obtained from the case studies show the potential of PSO-based damage detection techniques in enhancing the reliability and efficiency of structural health monitoring systems. By leveraging computational intelligence and optimization algorithms such as PSO, challenges associated with traditional methods can be mitigated and the accuracy of damage detection in civil infrastructure can be improved.

Looking to the future, further research efforts should explore the application of PSO and other optimization algorithms in real-world scenarios with complex structural geometries and varying environmental conditions.

In conclusion, this study contributes to the growing body of knowledge in structural health monitoring and optimization techniques and offers valuable insights for engineers and researchers seeking to increase the safety and resilience of civil infrastructure.

Acknowledgement

This paper has been supported by the grant No. 1/0230/22 provided by VEGA Agency of Ministry of Education, Science, Research and Sport of the Slovak Republic and by the grant No. APVV-22-0431 provided by the Slovak Research and Development Agency (SRDA).

References

Ároch, R., Sokol, M. and Venglár, M. (2016) Structural Health Monitoring of Major Danube Bridges in Bratislava. *Procedia Engineering*, *156*, 24–31.

Farrar, C. R. and Worden, K. (2007) An introduction to structural health monitoring. *Philosophical Transactions of the Royal Society A: Mathematical, Physical and Engineering Sciences*, *365*(1851), 303–315.

Hester, D. and González, A. (2017) A discussion on the merits and limitations of using drive-by monitoring to detect localised damage in a bridge. *Mechanical Systems and Signal Processing*, 90, 234–253.

Kang, F., Li, J. J. and Xu, Q. (2012) Damage detection based on improved particle swarm optimization using vibration data. *Applied Soft Computing Journal*, 12(8), 2329–2335.

Kenedy, J. and Eberhart, R. (1995) *Particle Swarm Optimization*. *The Industrial Electronics Handbook - 5 Vol. Set*, 1942–1948.

Kennedy, J. and Mendes, R. (2002) Population structure and particle swarm performance. In: *Proc. of the Congress on Evolutionary Computation,* CEC 2002, 2, 1671–1676.

Krohling, R. A. (2005) Gaussian particle swarm with jumps. In: *IEEE Congress on Evolutionary Computation*, 2, 1226-1231, vol. 2.

Lamperova, K., Lehky, D. and Slowik, O. (2023) Structural damage identification using optimization-based FE model updating. In: *Current Perspectives and New Directions in Mechanics, Modelling and Design of Structural Systems - Proc. of the 8th International Conference on Structural Engineering, Mechanics and Computation,* 1844–1850.

Lamperová, K., Sokol, M. and Timková, B. (2020) Identification of Bearings State on the Bridge Checked by Dynamic Tests. *Strojnicky Casopis*, 70(2), 67–76.

Lehký, D., Šplíchal, B., Lamperová, K. and Slowik, O. (2023) Inverse Analysis and Optimization-based Model Updating for Structural Damage Detection. *Ce/Papers*, 6(5), 1228–1233.

Li, W. M., Jiang, Z. H., Wang, T. L. and Zhu, H. P. (2014) Optimization method based on Generalized Pattern Search Algorithm to identify bridge parameters indirectly by a passing vehicle. *Journal of Sound and Vibration*, 333(2), 364–380.

Marton, M., Sokol, M., Bekö, A. and Maosen, C. (2021) Identification of Damage on Stringers By the PSO Method. *Slovak Journal of Civil Engineering*, 29(3), 9–14.

Marwala, T. (2010) *Finite-element-model Updating using Computational intelligence Techniques* (vol. 148).

Nicoletti, V., Arezzo, D., Carbonari, S. and Gara, F. (2022) Vibration-Based Tests and Results for the Evaluation of Infill Masonry Walls Influence on the Dynamic Behaviour of Buildings: A Review. *Archives of Computational Methods in Engineering*, 29(6), 3773–3787.

Pastor, M., Binda, M. and Harčarik, T. (2012). Modal assurance criterion. *Procedia Engineering*, 48, 543–548.

Sofi, A., Jane Regita, J., Rane, B. and Lau, H. H. (2022) Structural health monitoring using wireless smart sensor network – An overview. *Mechanical Systems and Signal Processing*, 163, 108113.

Sohn, H., Farrar, C. R., Hemez, F. and Czarnecki, J. (2001) A Review of structural health. *Library Lanl. Gov*, 1–7.

Venglár, M. (2018) Dynamic Tests and System Identification of Bridges. *Dissertation Thesis*, 129.

Ventura, C. E., Lord, J. F., Turek, M., Brincker, R., Andersen, P. and Dascotte, E. (2005) FEM updating of tall buildings using ambient vibration data. In: *Proc. of the 6th European Conference on Structural Dynamics*, 4–7.

Zhang, J., Cai, J., Meng, Y. and Meng, T. (2014) Genetic algorithm particle swarm optimization based hardware evolution strategy. *WSEAS Transactions on Circuits and Systems*, 13, 274–283.

30th International Conference
ENGINEERING MECHANICS 2024
Milovy, Czech Republic, May 14 – 16, 2024

ASPECTS OF ADAPTATION OF FLANGE JOINTS FOR MODERN LOW-CARBON ENERGETICS

Michálková A.[*], Jegla Z.[**], Krišpín J.[***], Gross A.[†], Reppich M.[††]

Abstract: *This study investigates the possible need for flange joint design adaptation when dealing with hydrogen. The study focuses on the comparison of flange joint design with two different leakage rates representing the need for higher tightness due to the leak-prone nature of hydrogen molecules. The model calculation following the European standard EN 1591-1 based on an industrial flange joint in a natural gas pipeline outlines the impact of changing tightness class on load ratios for bolts, gasket and flanges. While the operation remains safe in the specific case studied, the findings underscore the need for careful consideration in flange joint design when switching to natural gas hydrogen blends or pure hydrogen, ensuring both the safety and reliability of the processes in modern low-carbon energetics.*

Keywords: Flange joint tightness, hydrogen, gasket suitable for hydrogen.

1. Introduction

Bolted flange joints are widely used across various industries, particularly in situations where joint dismantling is necessary for example due to periodical maintenance. The reliability of flange joints is vital to ensure the safety and reliability of the entire process or system. One of the consequences of an improper design and subsequent failed flange joint is the leakage of operating media posing a significant impact on the environment and also personnel safety. Therefore, high demands are placed on the joints not only to withstand pressure and other mechanical and thermal loads safely but also to maintain sufficient tightness to avoid potentially dangerous leaks. The design and evaluation of bolted flange joints according to European standard EN 1591-1 (The Czech Office for Standards, Metrology and Testing [OSMT], 2015) enable the leakage rate estimation based on gasket test data according to standard EN 13555 (Czech Standardization Agency [CSA], 2021).

2. Discussion of engineering aspects of hydrogen utilization

With the increasing emphasis on sustainable energy sources and mitigating carbon emissions to achieve the 2050 carbon neutrality commitment, hydrogen is widely researched as a clean source of energy. Hydrogen can be used as fuel or an energy carrier and storage. However, the utilization of hydrogen presents unique challenges including hydrogen damage mechanisms (hydrogen-induced cracking, hydrogen embrittlement, hydrogen blistering), changes in equipment operating conditions and also the need for higher equipment tightness as hydrogen molecules are extremely small and therefore susceptible to higher rates of leaking. Proper design of flange joint with regard to its tightness becomes imperative as hydrogen

[*] Ing. Anežka Michálková: Institute of Process Engineering, Faculty of Mechanical Engineering, Brno University of Technology (BUT), Technická 2896/2; 616 69, Brno; CZ, anezka.michalkova@vutbr.cz

[**] Assoc. Prof. Ing. Zdeněk Jegla, PhD.: Institute of Process Engineering, Faculty of Mechanical Engineering, Brno University of Technology (BUT), Technická 2896/2; 616 69, Brno; CZ, zdenek.jegla@vut.cz

[***] Ing. Jan Krišpín: ORGREZ, a.s.; Hudcova 76; 612 00, Brno; CZ, jan.krispin@orgrez.cz

[†] Ing. et Ing. Arnošt Gross: Veolia Energie ČR, a.s.; 28. října 3337/7; 702 00, Ostrava; CZ, arnost.gross@veolia.com

[††] Prof. Dr.-Ing. Marcus Reppich: Faculty of Mechanical and Process Engineering, Augsburg University of Applied Sciences; An der Hochschule 1; 86161, Augsburg; DE, marcus.reppich@hs-augsburg.de

doi: 10.21495/em2024-198

is odourless, colourless, tasteless and flammable and potentially explosive. Hydrogen leaks are especially dangerous indoors, in a poorly ventilated spaces, where the gas cannot be quickly diluted into a non-flammable concentration.

This study focuses on the comparison of two versions of the same flange joint – one designed with a lower Tightness Class and the other one designed with a stricter Tightness Class representing the need for higher tightness when dealing with hydrogen. The typical design of a bolted flange joint with two weld-neck flanges with raised face and flat gasket is shown in Fig. 1. This topic was inspired by a high number of scientific articles exploring the possibility of using existing natural gas pipeline network to transport natural gas hydrogen blends or pure hydrogen. However, most of these articles are general and lack specific details such as flange joints. The general consensus is that blends up to about 20 vol. % of hydrogen should not have a significant impact on the pipeline (Erdener et al., 2023). This appears to be confirmed by a research project in Germany, where 20 % hydrogen blend was transported in the natural gas grid to regular households with no significant technical issues or leaks (Dörr et al., 2023).

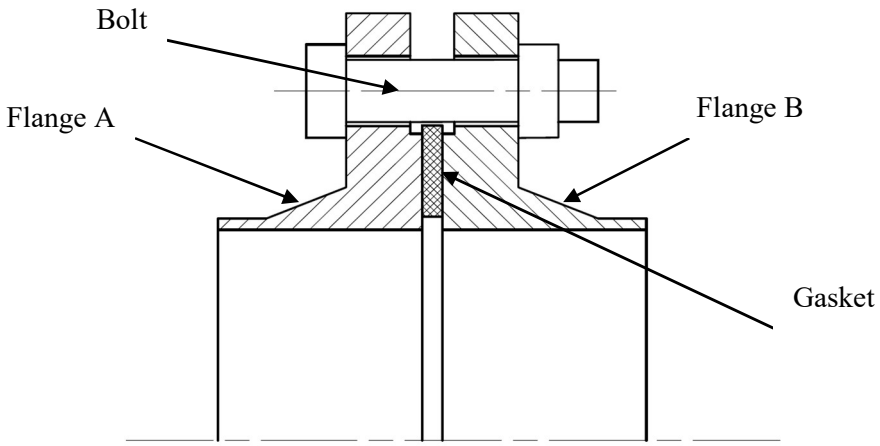

Fig. 1: Sketch of a typical bolted flange joint with a flat gasket.

2.1. Design of flange joints with leakage rate estimate

The calculation method outlined in European standard EN 1591-1 (OSMT, 2015) satisfies both leak tightness and strength criteria of flange joint design. If a selected leakage rate is to be achieved, the gasket properties have to be assumed from test results performed according to European standard EN 13555 (CSA, 2021) with helium as the operating medium. The calculation involves an elastic analysis of the load and deformation response between bolts, flanges and gasket, considering potential plasticity of gasket material during assembly. This calculation method considers both internal and external loads and loading of the flange joint must be axisymmetric as must be the geometry. Other assumptions on which the mechanical model is based in this calculation method include: only circumferential stress and strain in the flange ring is considered and gasket–flange contact is an annular area. This method does not take bolt bending into account.

Annex I of EN 1591-1 (OSMT, 2015) outlines the procedure for leakage rate conversion from reference (test) to actual operating conditions. However, this procedure cannot be used to determine the actual on-site leakage rate due to the incomplete understanding of leakage mechanisms. Therefore, this annex only provides a summary of the general correlations and should be considered indicative only if used. Therefore, this calculation would not be performed.

2.2. Gaskets suitable for hydrogen utilization

The material of the selected gasket must be chemically resistant to hydrogen. Gasket manufacturers usually conduct a series of additional tests to prove chemical resistance. For long-term leak tightness in a hydrogen environment, gasket materials based on elastomers or PTFE are not suitable due to elastomer embrittlement over time and the time-dependent creep of PTFE as reported by SGL Carbon GmbH (2022). These gasket materials show significant increase in leakage over time. However, gaskets from flexible graphite do not demonstrate this kind of behavior and leakage rate remains constant over time as shown in Fig. 2.

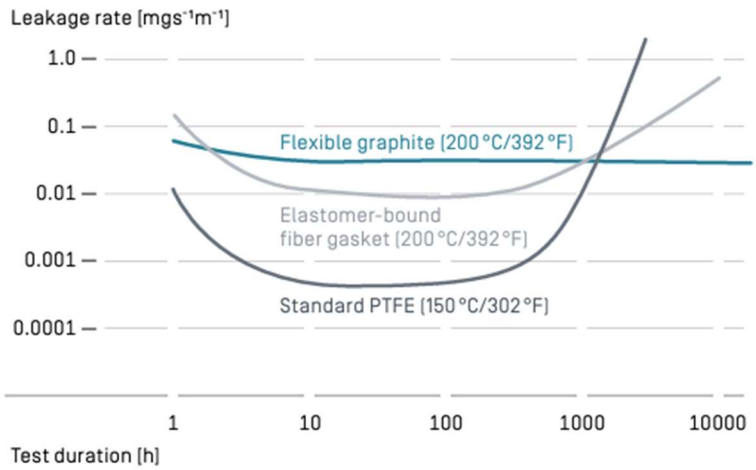

Fig. 2: Leakage rate over time of different gasket materials (SGL Carbon GmbH, 2022).

3. Model calculation of the hydrogen effect on the design of flange joint tightness

The model calculation is based on an industrial flange joint used to incorporate a flow meter into a pipeline transporting natural gas for combustion in a furnace. The flange joint consists of two similar DN100 PN16 weld-neck flanges as given in EN 1092-1 (Czech Standardization Agency [CSA], 2019) with tongue/groove flange facings. The minimum required gasket surface pressure at assembly $Q_{\min(L)}$ and minimum required gasket surface pressure in subsequent service conditions $Q_{S\min(L)}$ for Sigraflex Universal PRO gasket for Tightness Classes $L_{0.01}$ and $L_{0.001}$ are shown in Tab. 1, where Q_A is gasket surface pressure at assembly prior to unloading.

L	$Q_{\min(L)}$	$Q_{S\min(L)}$ $[MPa]$			
$[mg/(s \cdot m)]$	$[MPa]$	$Q_A = 20\ MPa$	$Q_A = 30\ MPa$	$Q_A = 40\ MPa$	$Q_A = 60\ MPa$
0.01	11	5	5	5	5
0.001	27	-	18	9	5

Tab. 1: Minimum required gasket surface pressure for different tightness classes, valid for PN16 (16 bar) (Münster University of Applied Sciences, 2019).

Materials used for flanges and bolts are P250GH and C45E, respectively. Assessment of the suitability of these materials for hydrogen operation was not the subject of this work. The service conditions are given in Tab. 2.

	Assembly	**Hydraulic test**	**Operating conditions**
Pressure [MPa]	0	2.288	1.6
Temperature [°C]	20	20	50
Axial force [N]	0	0	0
Bending moment [N.m]	0	0	0
Radial force [N]	0	0	0
Torsional moment [N.m]	0	0	0

Tab. 2: Service conditions.

Both calculations were based on the minimum required pressure limits. The required bolt force is 80 kN and 150 kN respectively for the two tightness classes. The resulting load ratios are given in Tab. 3.

		Assembly	Hydraulic test	Operating conditions
Bolts	$L_{0.01}$	27.2 %	13.9 %	19.4 %
	$L_{0.001}$	51.1 %	27.9 %	41.0 %
Gasket	$L_{0.01}$	10.9 %	2.5 %	3.3 %
	$L_{0.001}$	20.5 %	9.0 %	10.1 %
Flange	$L_{0.01}$	20.1 %	14.3 %	18.6 %
	$L_{0.001}$	37.7 %	26.4 %	36.7 %

Tab. 3: Flange joint load ratios.

The change in tightness class resulted in higher load ratios for bolts, gasket and flange. As none of the load ratios exceed 100 %, the operation of the flange joint is still safe after the tightness change. However, this model calculation highlights the possibility of a load ratio exceeding 100 % due to the higher minimum force required for a higher tightness class. In that case, the replacement of the flanges could be needed to withstand higher mechanical load.

4. Conclusions

This study describes the possible need for flange joint design adaptation in connection to modern low-carbon energetics, focusing on hydrogen and the challenges connected to switching to natural gas hydrogen blends in the existing natural gas pipeline network. The comparison of two flange joint designs, differing in leakage rates, serves as a practical example of adapting engineering solutions to the specific demands of hydrogen applications such as the need for higher tightness of process equipment. With a lower allowable leakage rate, the load ratios of bolts, gasket and flanges are higher due to the higher required gasket surface pressure.

Acknowledgement

This research was conducted with the state support of the Technology Agency of the Czech Republic as part of the project "Technical solutions for low-emission energy" of the program "National Center for Energy II" (TN02000025) and was supported by funds from GA BUT within research project FSI-S-23-8173 and by the EU project Strategic Partnership for Environmental technologies and Energy Production, funded as project No. CZ.02.1.01/0.0/0.0/16_026/0008413 by Czech Republic Operational Programme Research, Development and Education.

References

Czech Standardization Agency (2019) *Flanges and their joints – Circular flanges for pipes, valves, fittings and accessories, PN designated – Part 1: Steel flanges* (ČSN EN 1092-1). Prague (in Czech).

Czech Standardization Agency (2021) *Flanges and their joints – Gasket parameters and test procedures relevant to the design rules for gasketed circular flange connections* (ČSN EN 13555). Prague.

Dörr H., Brandes A., Kronenberger M., Janßen N., Gehrmann S. (2023) Wasserstoff in der Gasinfrastruktur: DVGW/Avacon-Pilotvorhaben mit bis zu 20 Vol.-% Wasserstoff-Einspeisung in Erdgas – H2-20. Deutscher Verein des Gas- und Wasserfaches e. V., Bonn (in German).

Erdener B.C., Sergi B., Guerra O. J., Chueca A. L., Pambour K., Brancucci C. and Hodge B. (2023) A review of technical and regulatory limits for hydrogen blending in natural gas pipelines. *International Journal of Hydrogen Energy*, 48, 14, pp. 5595–5617.

Münster University of Applied Sciences (2019) Sigraflex Universal Pro V20010C2I-P (2 mm) https://gasketdata.org/en/SGL-Carbon-GmbH/Sigraflex-Universal-Pro-V20010C2I-P/detail/334/

SGL Carbon GmbH (2022) Long-term safe sealing of hydrogen with SIGRAFLEX ® https://www.sglcarbon.com/data/pdf/SGL-Technical-Info-SIGRAFLEX-Hydrogen-EN.pdf

The Czech Office for Standards, Metrology and Testing (2015) Flanges and their joints – Design rules for gasketed circular flange connections – Part 1: Calculation (ČSN EN 1591-1). Prague (in Czech).

30th International Conference
ENGINEERING MECHANICS 2024
Milovy, Czech Republic, May 14 – 16, 2024

MODELING OF A QUARTER-CAR MODEL PASSING AN OBSTACLE USING LAPLACE TRANSFORMS, MATLAB/SIMULINK AND SIMSCAPE

Miková Ľ.[*], Šarga P.[**], Vagaš M.[***], Prada E.[†], Brada L.[††]

Abstract: *In this paper, the possibilities of modelling a quarter model of a car as it passes over an obstacle are presented. The Laplace transform was first used to solve the differential equations that describe this dynamic action. As the next option the solution of the derived differential equations is using Matlab/Simulink and finally the results were verified using a model that was created in the Matlab/Simulink/Simscape environment.*

Keywords: Laplace transform, dynamics modelling, Matlab, Simscape, physical modelling.

1. Introduction

Knowledge from practice is that a large group of problems solved in engineering practice is related to the solution of linear differential equations. These can be used to describe the amount of money in a savings bank, the orbit of a spacecraft, the amount of deformation of elastic structures, the description of radio waves, the size of a biological population, the current or voltage in an electrical circuit, etc. In fact, differential equations can be used to explain and predict new facts about anything that is constantly changing. In more complex systems, we do not use just one differential equation, but a system of differential equations, as in the case of an electrical network of multiple circuits or in a chemical reaction with several interacting chemicals. Differential equations with constant coefficients can then be solved using the Laplace transform to obtain their solution, which is a mathematical description of dynamical systems, see Yang (2017) and Harris (2014). In the present paper, the procedure of solving differential equations using Laplace transform is described on a quarter car model, Kmec (2022). In the following section, a solution to the same problem is then shown using modern simulation techniques. In the first case, a differential equation model was created in the Matlab/Simulink environment, which was then compared with the model created in the Matlab/Simulink/Simscape environment, Dvorak (2023) and Slough (2021).

2. Laplace transform

Solving differential equations often encounters problems, especially in terms of time. Integral transformations can be used to solve differential equations with constant coefficients in certain cases, Hroncova (2012). Equations defined in the time domain can be modified into qualitatively different

[*] Assoc. Prof. Ing. Ľubica Miková, PhD.: Faculty of Mechanical Engineering, Technical University of Košice, Letná 9; 042 00, Košice; SK, lubica.mikova@tuke.sk

[**] Assoc. Prof. Ing. Patrik Šarga, PhD.: Faculty of Mechanical Engineering, Technical University of Košice, Letná 9; 042 00, Košice; SK, patrik.sarga@tuke.sk

[***] Assoc. Prof. Ing. Marek Vagaš, PhD.: Faculty of Mechanical Engineering, Technical University of Košice, Letná 9; 042 00, Košice; SK, marek.vagas@tuke.sk

[†] Ing. Erik Prada, PhD.: Faculty of Mechanical Engineering, Technical University of Košice, Letná 9; 042 00, Košice; SK, erik.prada@tuke.sk

[††] Ing. Leo Brada, PhD.: Faculty of Mechanical Engineering, Technical University of Košice, Letná 9; 042 00, Košice; SK, leo.brada@tuke.sk

doi: 10.21495/em2024-202

equations, determined by so-called pairs of the original equations in a completely different domain, e.g. the frequency domain. The mathematical manipulation of the pairs is then considerably easier. Solving in this domain is finding the pair of the solution of a differential equation. After determining the search variables in the domain of their pairs, we adjust them in the opposite way again to the original time domain and obtain the resulting solution. The transformation of differential equations (originals) into algebraic equations (pairs), that is, the transformation is very convenient, since whole large dictionaries of originals and their corresponding pairs are available. The Laplace one-sided transform is a functional integral transform, introduced by Laplace and defined for t ≥ 0 by the relation:

$$F(s) = L\{f(t)\} = \int_0^\infty f(t)\, e^{-st} dt, \tag{1}$$

where: L is the Laplace operator, f(t) is a function of time which is called the original, $F(s)$ is the Laplace pair of the original, s is the argument of the Laplace transform, it is a complex variable.

3. Vehicle crossing an obstacle

A quarter car model will be considered, which is constructed from two masses M, which represents the mass of the sprung body section, and mass m, which represents the mass of the axle, wheel and tire (Fig. 1). The constant B is the viscous damping constant, K is the spring stiffness constant of the main suspension and k is the tire stiffness constant. The deflections y1(t) and y2(t) represent the displacements from the equilibrium positions.

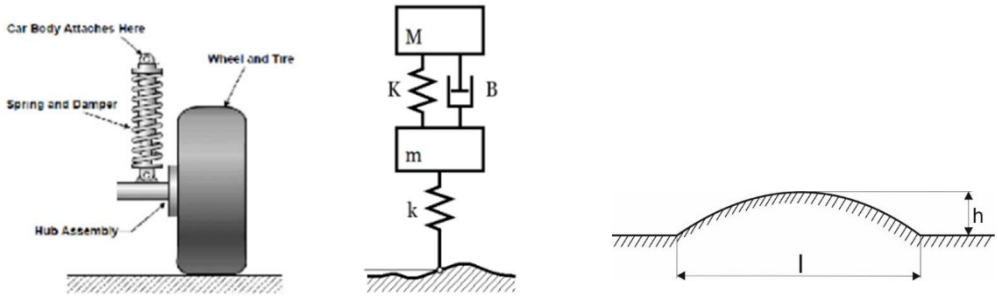

Fig. 1: Dynamic model of the vehicle and the obstacle.

The roughness of the terrain can be described by the equation:

$$s = s(\lambda), \tag{2}$$

where λ is the vehicle path at constant speed.

The equations of motion of a dynamic system can be written in the form:

$$m\ddot{y}_1 + By_1 - By_2 + (K + k)y_1 - Ky_2 = ks(\lambda), \tag{3a}$$

$$M\ddot{y}_2 + By_2 - By_1 - Ky_1 + Ky_2 = 0. \tag{3b}$$

The obstacle equation is:

$$s = hsin\, \frac{\pi}{l}\lambda \quad pre\ \lambda \in \langle 0{,}1\rangle. \tag{4}$$

In the next step, damping B will not be considered, so the equations of the dynamical system will be:

$$m\ddot{y}_1 + (K + k)y_1 - Ky_2 = ks(\lambda), \tag{5a}$$

$$M\ddot{y}_2 - Ky_1 + Ky_2 = 0. \tag{5b}$$

The partial solutions of these equations are assumed to be of the form:

$$y_j = a_j \sin(\Omega t + \gamma), \tag{6}$$

where a_j are the amplitudes of the displacements y_1 a y_2 from the equilibrium position. After substituting (6) into Eqs. (5a) and (5b) and adjusting:

$$[(k_1 + k_2) - m_1\Omega^2]a_1 - k_2a_2 = ks(\lambda), \tag{7a}$$

$$-k_2a_1 + (k_2 - m_2\Omega^2)a_2 = 0. \tag{7b}$$

Solving these equations using the determinant yields a frequency equation for calculating the natural angular frequencies Ω_1 *a* Ω_2:

$$\Omega_{1,2} = \sqrt{\frac{[m_1k_2+m_2(k_1+k_2)]\pm\sqrt{[m_1k_1+m_2(k_1+k_2)]^2-4m_1m_2k_1k_2}}{2m_1m_2}}. \tag{8}$$

Laplace transform of the equations of the dynamical system (5) under zero initial conditions:

$$ms^2Y_1(s) + (K+k)Y_1(s) - KY_2(s) = k\frac{h}{s}, \tag{9a}$$

$$Ms^2Y_2(s) - KY_1(s) + KY_2(s) = 0. \tag{9b}$$

Transfer functions are:

$$Y_1(s) = \frac{kh(K+Ms^2)}{s[Mm(s^2+\Omega_1^2)(s^2+\Omega_2^2)]},\ Y_2(s) = \frac{kK\ )}{s[Mm(s^2+\Omega_1^2)(s^2+\Omega_2^2)]}. \tag{10}$$

The inverse transformation is performed by decomposing the functions $Y_1(s)$ and $Y_2(s)$:

$$Y_1(s) = \frac{kh(K+Ms^2)}{s[Mm(s^2+\Omega_1^2)(s^2+\Omega_2^2)]} = \frac{kh}{Mm}\left[\frac{K}{\Omega_1^2\Omega_2^2}\frac{1}{s} + \frac{K-M\Omega_1^2}{\Omega_1^2(\Omega_1^2-\Omega_2^2)}\frac{s}{s^2+\Omega_1^2} + \frac{M\Omega_1^2-K}{\Omega_2^2(\Omega_1^2-\Omega_2^2)}\frac{s}{s^2+\Omega_2^2}\right], \tag{11a}$$

$$Y_2(s) = \frac{kK}{s[Mm(s^2+\Omega_1^2)(s^2+\Omega_2^2)]} = \frac{kKh}{Mm}\left[\frac{1}{\Omega_1^2\Omega_2^2}\frac{1}{s} + \frac{1}{\Omega_1^2(\Omega_1^2-\Omega_2^2)}\frac{s}{s^2+\Omega_1^2} + \frac{1}{\Omega_2^2(\Omega_1^2-\Omega_2^2)}\frac{s}{s^2+\Omega_2^2}\right]. \tag{11b}$$

Inverse Laplace transform of Eqs. (11a) and (11b):

$$y_1(t) = \frac{kh}{Mm}\left[\frac{K}{\Omega_1^2\Omega_2^2} + \frac{K-M\Omega_1^2}{\Omega_1^2(\Omega_1^2-\Omega_2^2)}\cos\Omega_1(t) + \frac{M\Omega_1^2-K}{\Omega_2^2(\Omega_1^2-\Omega_2^2)}\cos\Omega_2(t)\right], \tag{12a}$$

$$Y_2(s) = \frac{kK}{Mm}\left[\frac{1}{\Omega_1^2\Omega_2^2} + \frac{1}{\Omega_1^2(\Omega_1^2-\Omega_2^2)}\cos\Omega_1(t) + \frac{1}{\Omega_2^2(\Omega_1^2-\Omega_2^2)}\cos\Omega_2(t)\right]. \tag{12b}$$

The solution of the differential equations of the quarter car model using the Laplace transform was then verified using Matlab, where two methods were used:

- solving the differential equations using their models in Simulink - in this method it is necessary to know the differential equations describing the problem to be solved (Fig. 2),
- in the second case, the Model Based Design approach was used using the Simscape superstructure, where physical modelling is involved and in this case, it is not necessary to know the differential equations describing the problem to be solved (Fig. 2).

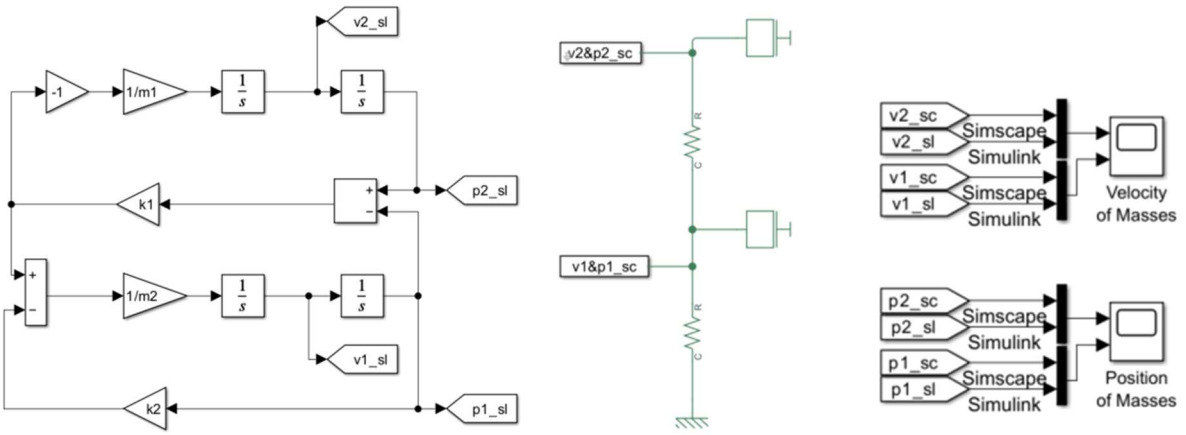

Fig. 2: Simulink model of the differential equation and physical model of vehicle.

In the following figures showing the velocities and positions of the two masses, you can see the correspondence between the solution of the differential equations in the Simulink environment compared to the solution using the physical modelling environment in Simscape (Fig. 3).

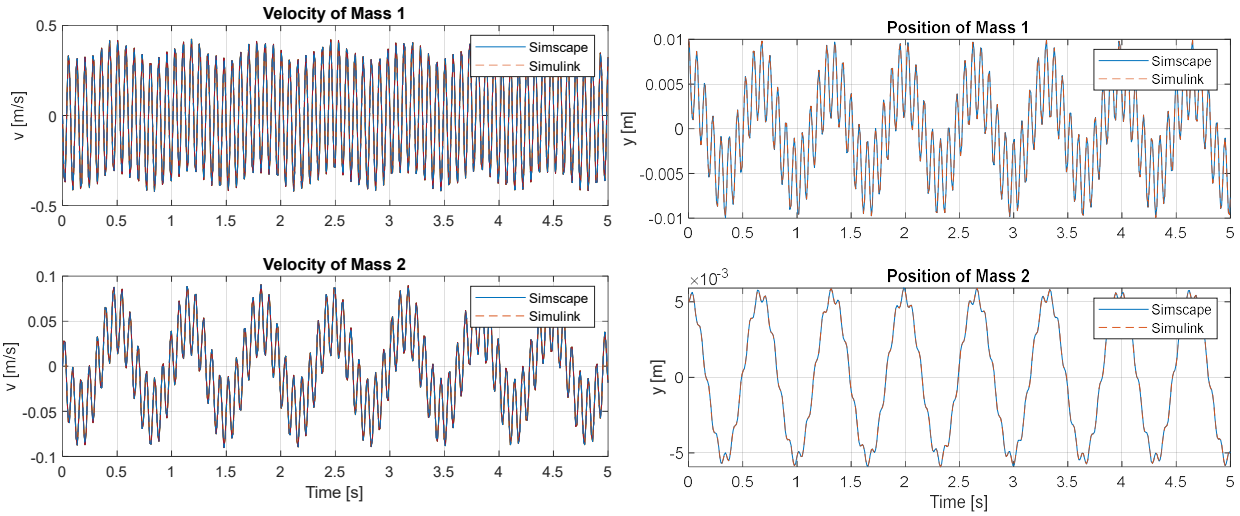

Fig. 3: Final velocity and position of the mass 1 and 2.

4. Conclusions

In this paper, a method for solving differential equations using the Laplace transform and using modern simulation methods is presented. These approaches have been applied to the example of solving a vehicle passing over an obstacle. A quarter car model was created and differential equations were developed for this case. The solution using Laplace transform represents a classical solution to such a problem, which is time consuming and presents a higher error generation rate. Subsequently, two procedures for solving the differential equations were implemented using Matlab. The first method requires knowledge of the differential equations describing the problem to be solved, which can be problematic in some cases. The second method used consists of physical modelling, where the main advantage is that we do not need to know the differential equations and the resulting model consists of real components. Such a solution represents a simpler way of solving the problem, especially when it is necessary to solve more complex systems, in which it is often complicated to set up and then solve differential equations.

Acknowledgement

This work was supported by the Ministry of Education of Slovakia Foundation under Grant project 1/0436/22, VEGA 1/0201/21, KEGA 027TUKE-4/2022, KEGA 031TUKE-4/2022.

References

Yang, X. S. (2017) *Laplace Transform*. Engineering Mathematics with Examples and Applications. 23 p.

Harris, E. F. (2014) Integral Transforms, *Mathematics for Physical Science and Engineering.* Chapter 13, 453–486.

Hroncova, D., Šarga, P. and Gmiterko, A. (2012) Simulation of Mechanical System with Two Degrees of Freedom with Bond Graphs and MATLAB/Simulink, In: *Procedia Engineering: MMaMS 2012: Modelling of Mechanical and Mechatronics Systems*, pp. 112–232.

Kmec J., Pavelka J. and Soltes, J. (2022) Determination of stiffness and damping parameters from a vehicle model in a frontal impact into the rigid barrier using the Matlab. *MM Science Journal*, 5651–5655.

Dvorak, L., Fojtasek, K. and Dyrr, F. (2023) Experimental verification of pneumatic elements mathematical models in Matlab-Simulink Simscape. *MM Science Journal*, 6359–6366.

Slough, J. Belcher, M., Tsui, T. and Bhattacharya, S. (2021) Modeling and Simulation of Electric Vehicles Using Simulink and Simscape. In: *IEEE Vehicular Technology Conference Proceedings.* pp. 1–6.

30th International Conference
ENGINEERING MECHANICS 2024
Milovy, Czech Republic, May 14 – 16, 2024

RECONSTRUCTION OF DUO ROLLING MILL

Mrkos J.*, Horký P., Formánek M.*****

Abstract: *Shown are design concepts for the reconstruction of an adjustable UD rolling mill (from the 90s) for a section mill train at domestic customer´s place. A finite element method was used to discretize the models in the elastic field using spatial elements. The strength evaluation consists in the assessment of assumed critical cross-sections and points from the point of view of a possibility of emergence of ductile, fatigue and sudden fractures, including the propagation of cracks. The SKALA program fully utilizes the results of the elasticity solution by the MARC system in the linear field, and the generalized Neuber principle is applied to a wide extent to determine the plastic deformations necessary for the assessment of service life (Pospíšil, 1976).*

Keywords: Design concept, DUO rolling mill, reconstruction, FEM, elasticity and strength evaluation.

1. Introduction - Device Description

In this paper is described a structural revision during the reconstruction of the DUO (two horizontal working rolls) rolling mill (Fig. 1). The rolling mill is used to shaping hot steel bars. In the DUO rolling mill, holes for anchors got worn (ovality, plastic deformations) in the lower frame (frame material 42 2712.5, R_m = 500 MPa, R_e = 280 MPa), where it was necessary to press on the bushings (to be lined - bushings made of material 42 CrMo 4 + QT , R_m = 700 MPa, R_e = 500 MPa) so that all the original linked-up components can be kept and thereby the costs saved. In the vicinity of the opening of the lower frame, there are potential critical points such as threads (M24) for shims and an inlet for cooling (Fig. 2). The design modification consists in enlarging the opening, pressing-on the bush and working it to the original internal dimension (Fig. 3).

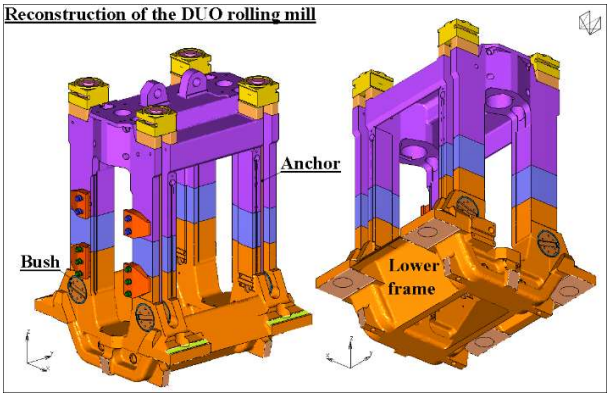

Fig. 1: The DUO rolling mill.

2. Boundary Conditions

The boundary conditions of the UD rolling mill are as follows (Fig. 4). Three different loading modes after pressing-on the bushings were calculated:

- The first loading was considered with self-weight and pre-loaded anchors, bolts, as the var. UDS15R, lower condition.
- The second loading was considered centric with self-weight and pre-loaded anchors, bolts, as var. UDS16R, upper condition.
- The third loading was considered eccentric with self-weight and pre-loaded anchors, bolts, as var. UDS17R upper condition.

* Ing. Josef Mrkos: ŽĎAS, a.s.: Strojírenská 6; 591 71, Žďár; CR, josef.mrkos@zdas.cz
** Ing. Pavel Horký: ŽĎAS, a.s.: Strojírenská 6; 591 71, Žďár; CR, pavel.horky@zdas.cz
*** Ing. Michael Formánek: ŽĎAS, a.s.: Strojírenská 6; 591 71, Žďár; CR, michael.formanek@zdas.cz

doi: 10.21495/em2024-206

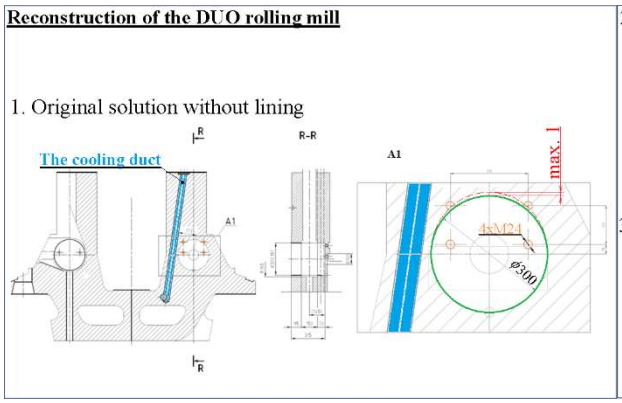

Fig. 2: Initial shape of the opening of the lower frame.

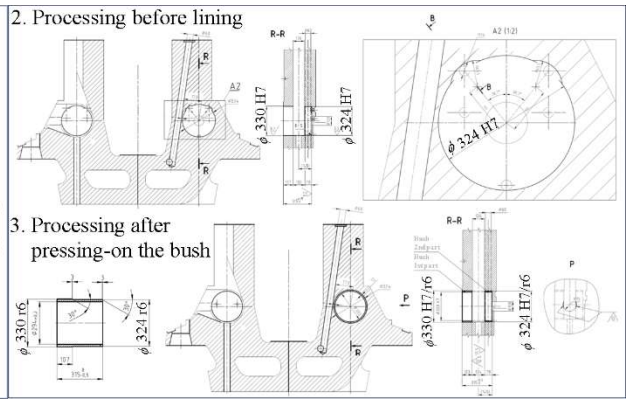

Fig. 3: Working before and after pressing the bushing into the lower frame.

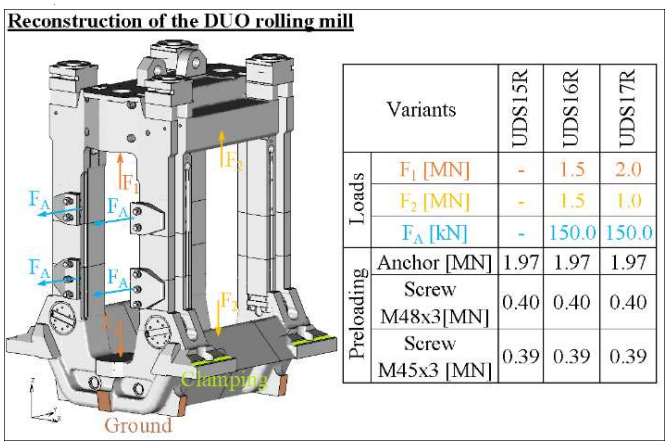

	Variants	UDS15R	UDS16R	UDS17R
Loads	F_1 [MN]	-	1.5	2.0
	F_2 [MN]	-	1.5	1.0
	F_A [kN]	-	150.0	150.0
Preloading	Anchor [MN]	1.97	1.97	1.97
	Screw M48x3[MN]	0.40	0.40	0.40
	Screw M45x3 [MN]	0.39	0.39	0.39

Fig. 4: Boundary conditions of the DUO rolling mill.

3. Results of elasticity calculation

Displacement in the Z-axis direction are in the Fig. 5. The figures show differences between individual variants. Hole deformations:

- var. UDS15R range from -0.021 to 0.014 mm.
- var. UDS16R range from -0.060 to -0.015 mm.
- var. UDS17R range from -0.127 to -0.017 mm.

The values correspond to the predicted results.

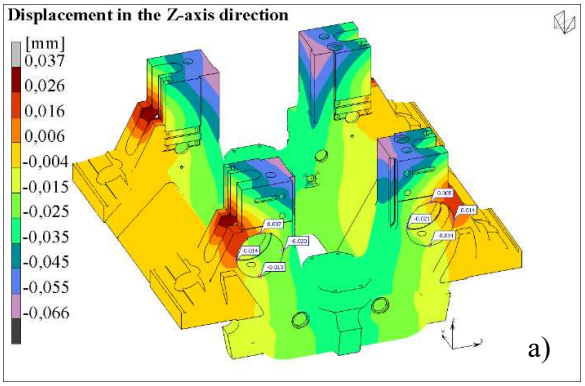

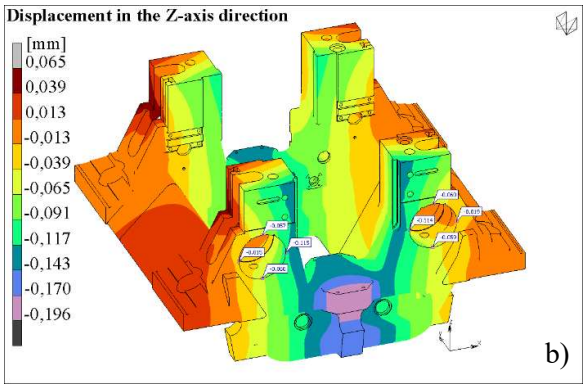

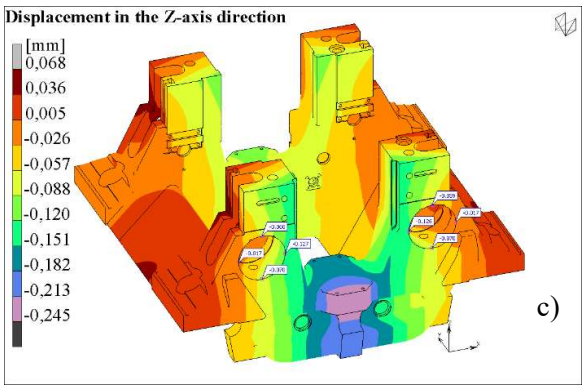

Fig. 5: Displacement in the Z of the lower frame for the loading variant a) UDS15R, b) UDS16R and c) UDS17R.

The first principal stress, design (reduced) stress SV (according to HMH) are shown in Figs. 6–9. On the basis of the first principal stress and design (reduced) stress (according to HMH), the places for strength assessment were selected and they will be assessed for strength in the following chapter.

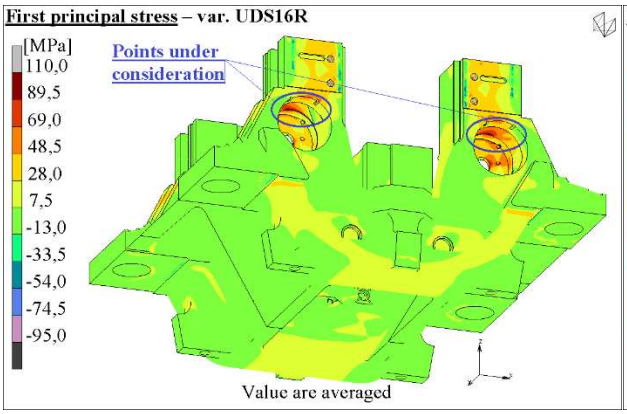

Fig. 6: The first principal stress for the loading var. UDS16R.

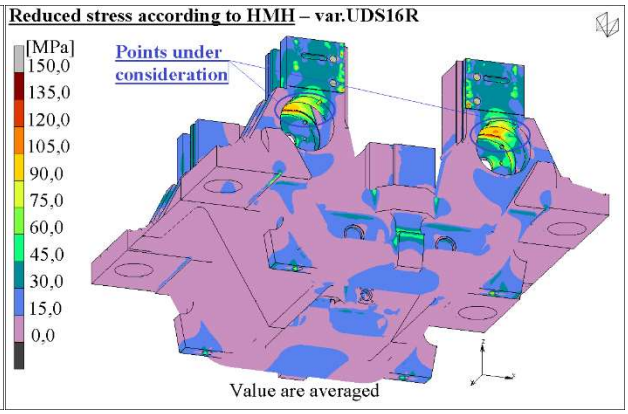

Fig. 7: Reduced stress according to HMH for the loading var. UDS16R.

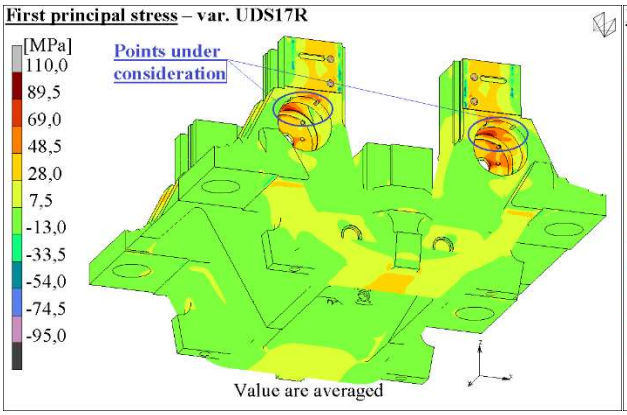

Fig. 8: The first principal stress for the loading var. UDS17R.

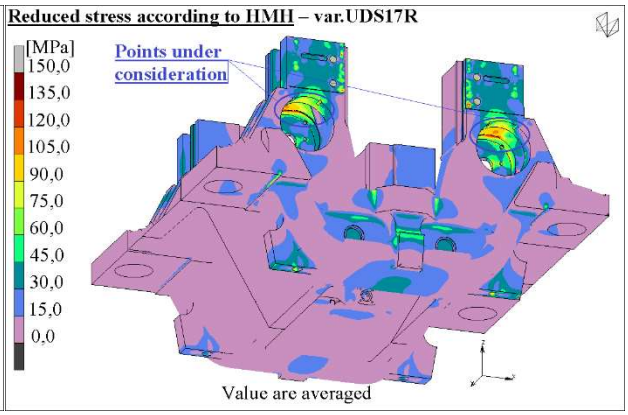

Fig. 9: Reduced stress according to HMH for the loading var. UDS17R.

4. Strength Assessment

Two locations (KM1, KM2) were selected from the results of the flexibility calculation (by the Marc Mentat 2023.3 program) for assessment. The SKALA program assessed the possibility of ductile, fatigue and sudden fracture, including crack propagation, at both locations. The SKALA program makes full use of the results of the elasticity solution in the linear field, and the generalized Neubér's principle is used to determine the plastic deformations necessary for the lifetime assessment.

Description of the points to be assessed:

a) KM1 - The tensile area of the recess of the M24 thread on the lower frame (Figs. 10 and 11) - (HS – UDS17R, DS – UDS15R) - taken for the higher upper state of load from UDS16R and UDS17R.

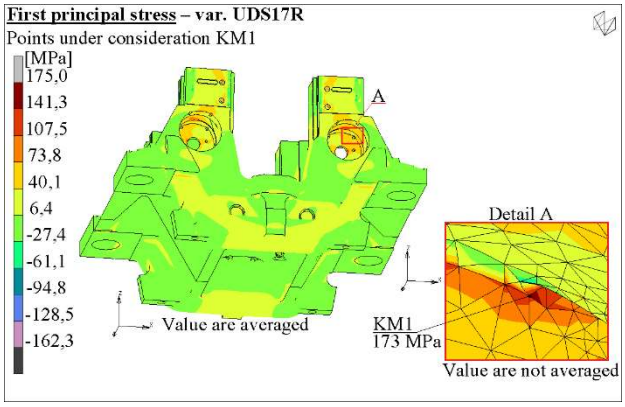

Fig. 10: First principal stress at the recess of the M24 thread for the loading var. UDS17R.

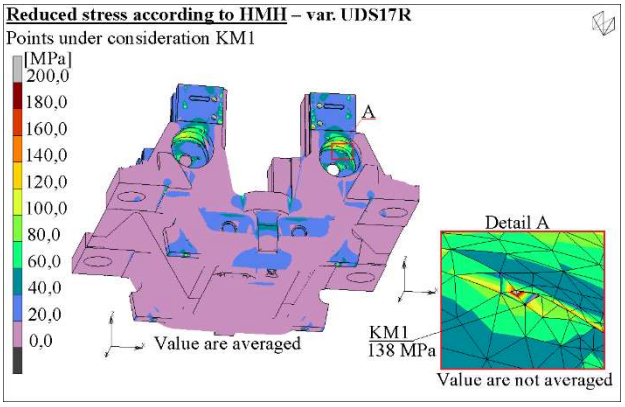

Fig. 11: Reduced stress at the recess of the M24 thread for the loading var. UDS17R.

b) KM2 - The tensile area of the M24 drilled-off thread on the lower frame (Figs. 12 and 13) - (HS – UDS16R, DS – UDS15R) - taken for the higher upper state of load from UDS16R and UDS17R.

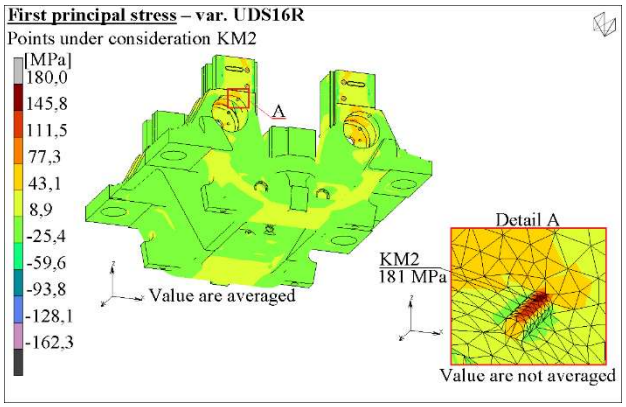

Fig. 12: The first principal stress of the M24 drilled-off thread for the loading var. UDS16R.

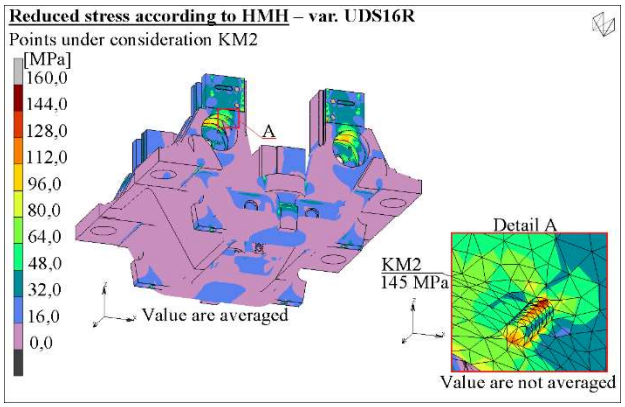

Fig. 13: Reduced stress of the M24 drilled-off thread for the loading var. UDS16R.

Brief overview of the strength evaluation results is shown in Tab. 1, where:

- ND - the number of permitted loading cycles,
- n_σ - the security against the occurrence of the limit state of fatigue (formation of a crack having conventional depth of 1 mm),
- n_{Rm}, n_{Rk} - the degree of safety against the ultimate strength and/or yield point in the block of ultimate state of ductile fracture,
- n_{sig}, n_{def} - the degree of safety against the strain of force or force plus deformation origin in the block of the limit state of sudden fracture,
- N_{kr}, (N_f) - the number of cycles with the crack propagation from the initial depth of 1 mm and/or from the depth L_p to the critical L_{kr} or functional (L_f) depth,
- L_k, L_{kr} - the critical depth of a crack at the critical point (node) L_k and/or L_{kr} during its propagation; when they are reached, a sudden fracture occurs in the critical cross-section,
- L_f - functionally permissible crack depth.

Variants of calculation	Point under consideration	Ductile fracture n_{Rm} [-] n_{Rk} [-]	Fatigue N_D [cycle] n_σ [-]	Sudden fracture n_{sig} [-] n_{def} [-]	Sudden fracture L_k [mm]	Crack propagation N_{kr} [cycle] (N_f [cycle])	Crack propagation L_{kr} [mm] (L_f [mm])
	Material 42 2712.5 (R_m = 500 MPa, R_e = 280 MPa)						
UDS17R/ UDS15R	KM1	Satisfactory 2.1 1.3	>1.00E7 2.419	3.710 3.530	10.0	- (110E6)	- (15)
UDS16R/ UDS15R	KM2	Satisfactory 2.1 1.3	>1.00E7 3.108	5.512 3.418	9.25	- (12.2E6)	- (10)

Tab. 1: Strength evaluation results for the assessed points.

5. Conclusions

According to the results of the elasticity and strength calculation of the design changes of the DUO rolling mill, it can be stated that, for the specified maximum operating loads and the above-mentioned materials, the specified design variant with pressing-on the bushings in the rolling mill meets the usually required safety limit states of both ductile and sudden fracture at assessed points KM1 and KM2 with sufficient reserve. Furthermore, for the specified maximum possible operating cyclic loads and the above-mentioned materials, the specified design variant with pressing-on the bushings in the rolling mill meets the limit state of fatigue (N_D > 1.0E7 cycles - permanent life) with sufficient reserve at the assessed points KM1 and KM2 from the point of view of usually required safety. The design revision can be used.

References

Pospíšil, B. (1976) *Evaluation of strength and durability of machine components*. ČVTS Praha (in Czech).

30th International Conference
ENGINEERING MECHANICS 2024
Milovy, Czech Republic, May 14 – 16, 2024

STOCHASTIC VERSION OF THE ARC-LENGTH METHOD

Náprstek J.[*], **Fischer C.**[**]

Abstract: *The solution of a nonlinear algebraic system using the incremental method, based on pre-defined loading steps, fails in the vicinity of local extrema as well as around bifurcation points. The solution involved the derivation of the so-called 'Arc-Length' method. Its essence lies in not incrementing the system parameter or any of the independent variables but rather the length of the response curve. The stochastic variant of this method allows for working with a system where system parameters include random imperfections. This contribution presents a variant that tracks the first two stochastic moments. Even in this simple case, interesting phenomena can be observed, such as the disappearance of the energy barrier against equilibrium jump due to random imperfections in the system.*

Keywords: Random imperfection, stochastic arc-length method, continuation, numerical method.

1. Introduction

In the study of slender and flexible structures, the amplitudes of deflections or vibrations, and consequently the corresponding deformations, can reach values that cannot be approximately considered linear. Mathematical models must account for the arising nonlinearity, introducing significant complications in mathematical processing. Finding the equilibrium state requires solving nonlinear systems. There can exist multiple equilibrium states, which in themselves can be stable or unstable. Transitions between them occur spontaneously or through the breakthrough of energy barriers. Such a process may be entirely local and insignificant for the overall system, allowing its loading to continue, or, alternatively, it may signify partial or complete collapse of the system.

The general formulation of the problem in static analysis reads:

$$\mathbf{F}(\mathbf{r}, \mathbf{u}, \lambda) = 0\,, \tag{1}$$

where $\mathbf{r}$ represents the internal parameters of the system (describing geometry, physical properties, etc.) with m components; $\mathbf{u}$ is the displacement vector of nodes in the network with n components; λ is the load parameter. The function $\mathbf{F}$ is assumed as sufficiently continuous.

A similar concept can be applied when seeking the stationary response of dynamic systems. If some form of averaging is employed, it is possible to formulate the corresponding differential equation in slow time, where the characteristic feature for the stationary solution is a zero differential part.

The solution of the system (1) using the incremental method with pre-defined loading steps $\Delta\lambda$, see for example (Jagannathan et al., 1975; Bergan, 1980), fails around the extremum of any of the curves $u^i(\lambda)$ and further in the vicinity of a bifurcation point. After many attempts to find a solution, each with only a limited range of applicability, a more universal method was proposed by Riks (1979), which was named the "Arc-Length" method. Its essence lies in not incrementing λ or any of the components of $\mathbf{u}$ but rather the length of the response curve arc. The length of the vector $|\Delta\mathbf{u}^t, \Delta\lambda|$ is specified, assuming that it does not differ

[*] Ing. Jiří Náprstek, DSc.: Institute of Theoretical and Applied Mechanics, Prosecká 76, 190 00 Prague 9, naprstek@itam.cas.cz

[**] RNDr. Cyril Fischer, PhD.: Institute of Theoretical and Applied Mechanics, Prosecká 76, 190 00 Prague 9, fischerc@itam.cas.cz

doi: 10.21495/em2024-210

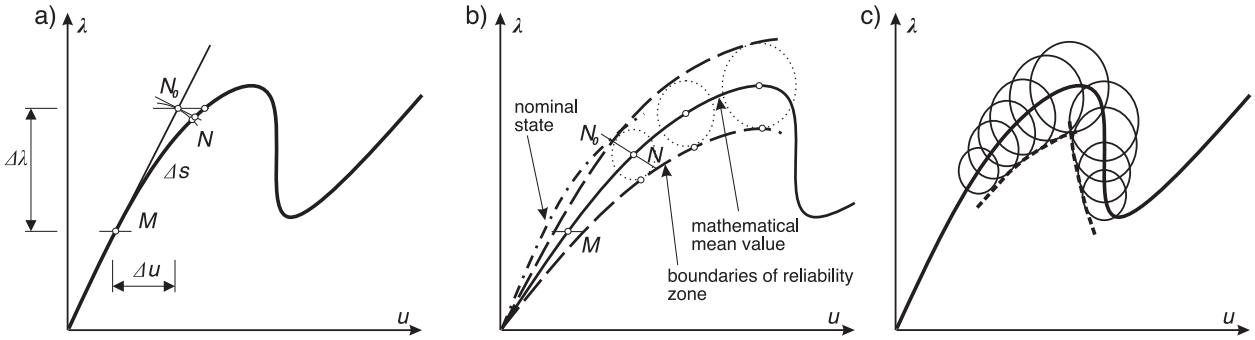

Fig. 1: a) Incremental and Arc-Length method, b) stochastic Arc-Length method, c) mathematical expectation and reliability zone.

significantly from the actual length of the arc as a curve. Thus, the increment of the load parameter is one of the unknowns, rather than a predetermined quantity.

It turns out that the fundamental idea of the Arc-Length method can be extended to the domain of systems with random imperfections, as shown by Náprstek (1994, 1999).

2. The stochastic arc-length method

In the stochastic case, the perturbed parameters $\mathbf{r}$ should be understood as the sum of the deterministic and stochastic component:

$$\mathbf{r} = \mathbf{r}_d + \mathbf{r}_\varepsilon \,, \tag{2}$$

where $\mathbf{r}_d$ represents the nominal values of system parameters, and $\mathbf{r}_\varepsilon$ denotes parameter perturbations as Gaussian random processes in suitable coordinates. The system (1) thus transforms into a system of stochastic equations. Its solution will be formulated in weak stochastic sense.

Let $\partial_{\mathbf{u}}\mathbf{F}^t(\mathbf{r}, \mathbf{u}_{N_j}, \lambda_{N_j})$ denote the incremental matrices in the j-th approximation step to the point N, where the coordinates statistically sufficiently satisfy the system (1). This point is approached from the initial point M by incrementing the arc length by Δs, as depicted in Fig. 1a:

$$\partial_{\mathbf{u}}\mathbf{F}^t(\mathbf{r}, \mathbf{u}_{N_j}, \lambda_{N_j}) = \mathbf{C}^t_{N_j} \quad ; \quad \partial_\lambda \mathbf{F}(\mathbf{r}, \mathbf{u}_{N_j}, \lambda_{N_j}) = \mathbf{\Lambda}_{N_j} \,. \tag{3}$$

Matrices $\mathbf{C}N_j$ and $\mathbf{\Lambda}N_j$ describing the local stiffness state at point N_j are influenced by imperfections $\mathbf{r}_\varepsilon$. The linear stochastic approximation of parameter deviations from the nominal state can be introduced as linear combinations of suitable deterministic basis functions. The coefficients of this linear combination are random processes. The basis functions can encompass, for example, systems of cones with vertices at individual nodes of the mesh in case of discretized system, values of Fourier coefficients representing the expansion of imperfect surfaces, etc. Consequently, imperfections are modeled as m random scalar processes entering into (1) or (2). This implies that the local stiffness matrices (3) can be expressed in the form

$$\mathbf{C}_{N_j} = \mathbf{C}^0_{N_j} + \sum_{i=1}^{m} \mathbf{C}^i_{N_j} r^i_\varepsilon \quad ; \quad \mathbf{\Lambda}_{N_j} = \mathbf{\Lambda}^0_{N_j} + \sum_{i=1}^{m} \mathbf{\Lambda}^i_{N_j} r^i_\varepsilon \,. \tag{4}$$

where $\mathbf{C}^0_{N_j}, , \mathbf{\Lambda}^0_{N_j}$ represent the local stiffness matrices at point N_j of the system in the nominal state, $\mathbf{C}^i_{N_j}$, $\mathbf{\Lambda}^i_{N_j}$ denote the increments of matrices $\mathbf{C}^0_{N_j}$, $\mathbf{\Lambda}^0_{N_j}$ due to a "unit" imperfection, and r^i_ε is the value of the i-th imperfection (a Gaussian-centered random process).

The increments of displacements and loads are expressed in a similar form, i.e., as linear combinations of certain vectors, where the coefficients of these combinations are the same random processes r^i_ε as in the case of (4):

$$\Delta\mathbf{u}_{N_j} = \Delta\mathbf{u}^0_{N_j} + \sum_{i=1}^{m} \Delta\mathbf{u}^i_{N_j} r^i_\varepsilon \quad ; \quad \Delta\lambda_{N_j} = \Delta\lambda^0_{N_j} + \sum_{i=1}^{m} \Delta\lambda^i_{N_j} r^i_\varepsilon \,. \tag{5}$$

The solution of the response of the imperfect system is based on the incremental form of the system (1) supplemented by the constant arc-length condition $\Delta s = \text{const}$. This means that the increment of the load is

unknown; it is one of the unknowns, just like all the increments of displacements at the nodes. The advance from point M to point N on the response hyperplane proceeds in two steps, as shown in Fig. 1b.

The initial step involves moving in the tangential direction towards point N_0. This is accomplished by solving a linear system that is generated as follows: starting with the incremental operation (1), subsequent substitutions as per (3), (4), (5) (where point N_j is substituted with point M), and then applying the mathematical expectation operator $\mathcal{E}\cdot$. This process yields the first part of the solution; the part which describes the mathematical expectation and generalized coordinates of the stochastic component of the response during the first step from point M to point N_0:

$$\begin{aligned}
&\mathbf{C}^0_M \Delta\mathbf{u}^0_M + \mathbf{\Lambda}^0_M \Delta\lambda^0_M + \sum_{i=1}^{m}\sum_{k=1}^{m}\left(\mathbf{C}^i_M \Delta\mathbf{u}^k_M + \mathbf{\Lambda}^i_M \Delta\lambda^k_M\right) K^{ik} = 0\,, \\
&\Delta\mathbf{u}^{0t}_{M^-} \Delta\mathbf{u}^0_M + \Delta\lambda^0_{M^-} \Delta\lambda^0_M + \sum_{i=1}^{m}\sum_{k=1}^{m}\left(\Delta\mathbf{u}^{it}_{M^-} \Delta\mathbf{u}^k_M + \Delta\lambda^i_{M^-} \Delta\lambda^k_M\right) K^{ik} = \Delta s^{(2)}\,,
\end{aligned} \tag{6}$$

where it was used:

$$\mathsf{E}\{r^i_\varepsilon \cdot r^k_\varepsilon\} = K^{ik} \quad ; \quad \mathsf{E}\{r^i_\varepsilon\} = 0\,. \tag{7}$$

The second step of the calculation aims to reach point N on the response curve through successive iterations, with the goal of achieving the best possible accuracy. This is done to ensure the following equations are optimally satisfied:

$$\mathsf{E}\{\mathbf{F}(\mathbf{u}_N, \lambda_N)\} = 0 \quad ; \quad \mathsf{E}\{r^i_\varepsilon \cdot \mathbf{F}(\mathbf{u}_N, \lambda_N)\} = 0\,. \tag{8}$$

In the j-th step, that is, at point N_j, however, these equations are not satisfied, and the following holds:

$$\mathsf{E}\{\mathbf{F}(\mathbf{u}_{N_j}, \lambda_{N_j})\} = \mathbf{\Phi}_{N_j}\ ; \quad \mathsf{E}\{r^i_\varepsilon \cdot \mathbf{F}(\mathbf{u}_{N_j}, \lambda_{N_j})\} = \mathbf{\Psi}^i_{N_j}\ ; \quad i = 1, .., m\ ;\ j = 0, 1, .. \tag{9}$$

The iteration will take place in the hyperplane perpendicular to the previous tangent (line MN_0) of the surface (1), or along the hypersphere with the center at point M (depending on whether the linear or quadratic version of the Arc-Length method is used). Similar steps as in the first step deliver the algebraic system of $(1+m)(n+1)$ equations for the unknown increments $\Delta\mathbf{u}^0_{N_j}$, $\Delta\lambda^0_{N_j}$, $\Delta\mathbf{u}^k_{N_j}$, $\Delta\lambda^k_{N_j}$ $(k = 1, \ldots, m)$:

$$\begin{aligned}
&\mathbf{C}^0_{N_j} \Delta\mathbf{u}^0_{N_{j+1}} + \mathbf{\Lambda}^0_{N_j} \cdot \Delta\lambda^0_{N_{j+1}} + \sum_{i=1}^{m}\sum_{k=1}^{m}\left(\mathbf{C}^i_{N_j} \cdot \Delta\mathbf{u}^k_{N_{j+1}} + \mathbf{\Lambda}^i_{N_j} \cdot \Delta\lambda^k_{N_{j+1}}\right) K^{ik} = -\mathbf{\Phi}_{N_j}\,, \\
&\Delta\mathbf{u}^{0t}_{N_j} \Delta\mathbf{u}^0_{N_{j+1}} + \Delta\lambda^0_{N_j} \Delta\lambda^0_{N_{j+1}} + \sum_{i=1}^{m}\sum_{k=1}^{m}\left(\Delta\mathbf{u}^{it}_{N_j} \Delta\mathbf{u}^k_{N_{j+1}} + \Delta\lambda^i_{N_j} \Delta\lambda^k_{N_{j+1}}\right) K^{ik} = 0\,,
\end{aligned} \tag{10}$$

$$\begin{aligned}
&\sum_{i=1}^{m}\left(\mathbf{C}^i_{N_j} \Delta\mathbf{u}^0_{N_{j+1}} + \mathbf{\Lambda}^i_{N_j} \Delta\lambda^0_{N_{j+1}}\right) K^{li} + \sum_{k=1}^{m}\left(\mathbf{C}^0_{N_j} \Delta\mathbf{u}^k_{N_{j+1}} + \mathbf{\Lambda}^0_{N_j} \Delta\lambda^k_{N_{j+1}}\right) K^{lk} = -\mathbf{\Psi}^l_{N_j}\,, \\
&\sum_{i=1}^{m}\left(\Delta\mathbf{u}^{it}_{N_j} \Delta\mathbf{u}^0_{N_{j+1}} + \Delta\lambda^i_{N_j} \Delta\lambda^0_{N_{j+1}}\right) K^{li} + \sum_{k=1}^{m}\left(\Delta\mathbf{u}^{0t}_{N_j} \Delta\mathbf{u}^k_{N_{j+1}} + \Delta\lambda^0_{N_j} \Delta\lambda^k_{N_{j+1}}\right) K^{lk} = 0\,.
\end{aligned} \tag{11}$$

Based on these calculations, the overall response of the system during one step of the Arc-Length method from point M to point N can be described as

$$\mathbf{u}_N = \mathbf{u}_M + \sum_{j=0}^{\mu}\left(\Delta\mathbf{u}^0_{N_j} + \sum_{i=1}^{m}\Delta\mathbf{u}^i_{N_j} r^i_\varepsilon\right)\,. \tag{12}$$

Hence, the value of the mathematical expectation and mutual correlation of the individual response component at point N read

$$\mathsf{E}\{\mathbf{u}_N\} = \mathbf{u}_M + \sum_{j=0}^{\mu} \Delta\mathbf{u}_{N_j}^0 \,, \tag{13}$$

$$\mathsf{E}\{\mathbf{u}_N \cdot \mathbf{u}_N^t\} - \mathsf{E}\{\mathbf{u}_N\} \cdot \mathcal{E}\{\mathbf{u}_N^t\} = \sum_{k=0}^{\mu}\sum_{j=0}^{\mu} \left(\sum_{i=1}^{m}\sum_{l=1}^{m} \Delta\mathbf{u}_{N_j}^i \Delta\mathbf{u}_{N_k}^{lt} \cdot K^{il} \right) \,. \tag{14}$$

Formulas (13), (14) enable tracing the curves of the most probable response (mathematical mean) and the corresponding dispersion zone. Properties (e.g. diameter) of this zone indicates how much the critical load level needs to be reduced due to introduced imperfections.

The outcomes of the entire calculation can be understood with reference to Fig. 1c. For every point along the curve of the mathematical mean response, there is a corresponding curve depicting the probability density distribution of deviations from the mathematical mean at individual nodes or degrees of freedom. Given that the analysis was confined to the first two stochastic moments, each of these curves represents a Gaussian distribution with a variance derived from the second-moment calculation.

Consequently, upper and lower bounds are established, forming a region on both sides of the curve which represents the most probable response. This region is known as the reliability region. It ensures that, with the specified probability and imperfection statistics, the system's response will not fall outside this defined area. The process of deriving both upper and lower bound curves can result in a complex profile, as suggested in Fig. 1c. This complexity indicates that certain sections of these curves may not be relevant for the original purpose. Both upper and lower curves may exhibit inflection points and various special properties, necessitating evaluation methods that exploit the particular characteristics of their geometry.

3. Concluding remarks

Tthe stochastic Arc-Length method is a powerful tool for addressing the challenges posed by uncertainties and nonlinearities in structural analysis, providing insights into the reliability of structures under stochastic conditions. It uses the arc length as a parameter to trace the response of the structure. This allows for efficient tracking of nonlinear responses, especially in situations where traditional methods may encounter convergence issues. While the method often focuses on the first few stochastic moments, higher moments may be considered for a more comprehensive stochastic analysis.

Acknowledgment

The kind support of Czech Science Foundation project No. 24-13061S and of the RVO 68378297 institutional support are gratefully acknowledged.

References

Bergan, P. (1980) Solution algorithms for nonlinear structural problems. *Computers and Structures*, 12, 4, pp. 497–509.

Jagannathan, D. S., Epstein, H. I., and Christiano, P. (1975) Nonlinear analysis of reticulated space trusses. *Journal of the Structural Division*, 101, 12, pp. 2641–2658.

Náprstek, J. (1994) Influence of random characteristics on static stability of the non-linear deformable system. In: *Steel Structures and Bridges '94*. STU Bratislava, pp. 175–180.

Náprstek, J. (1999) Strongly non-linear stochastic response of a system with random initial imperfections. *Probabilistic Engineering Mechanics*, 14, 1–2, pp. 141–148.

Riks, E. (1979) An incremental approach to the solution of snapping and buckling problems. *International Journal of Solids and Structures*, 15, 7, pp. 529–551.

30th International Conference
ENGINEERING MECHANICS 2024
Milovy, Czech Republic, May 14 – 16, 2024

MICRO-SCALE CREEP OF CEMENTITIOUS MATERIALS

Němeček J.*, **Němečková J.****, **Němeček J.*****

Abstract: *Nowadays, micro-scale creep properties are accessible via nanoindentation tests. The paper aims to investigate various analytical expressions used to estimate micro-scale visco-elastic properties of cement paste. Five analytical methods based on various assumptions were tested. The necessity of taking plastic deformations into account was shown. Creep compliance evaluated for a short-term load duration (tens of seconds) was found in the order of usual uniaxial creep tests of cement pastes or concretes that take place on a much longer time scale (tens to hundreds of days). However, the creep response has the same logarithmic nature. Using different evaluation methods exhibited high scatter and direct comparison to uniaxial data does not give a clue how to select the best fitting method.*

Keywords: Cement, creep, visco-elasticity, nanoindentation.

1. Introduction

Creep of cementitious materials is an important phenomenon influencing the long-term performance of concrete structures. For many decades, creep has been studied on a macroscale using large-scale specimens. With the development of techniques such as electron microscopy or nanoindentation, the creep of cementitious matrix has also been accessed at micro-scale. Various theories on the creep mechanisms have been published. The main mechanisms employ sliding of C-S-H globules or C-S-H sheets, their compaction and water movements under conditions of sustained loading (Kai et al., 2021).

The logarithmic kinetics of creep is generally observed after days on concrete samples in the lab or even after years on concrete bridges. Interestingly, creep experiment conducted in a nanoindenter exhibits logarithmic kinetics already in the scale of seconds (Baronet et al., 2022). But, significantly higher stresses are applied by an indenter compared to usual macroscopic testing. Routinely used shapes of sharp indenters such as Berkovich, cube corner or Vickers cause both high stresses and volumetric compaction under the tip. This paper makes a comparison of various analytical approaches used for evaluation of creep parameters from nanoindentation performed on main hydration products of cement pastes (C-S-H gels) at the sub-micrometer level.

2. Theory and methods

Nanoindentation is a technique which uses a sharp (usually diamond) tip that is pressed into the material while accurately recording the force, P, and the tip displacement, h. There are four principal deformations caused by an indenter: elastic, viscous, plastic and fracture. The amount of individual deformation types depends strongly on the acuity of the indentation tip. While flat or spherical indenters tend to produce only elastic or visco-elastic deformations, sharper indenters cause further elasto-plastic or visco-elasto-plastic deformations. Indentation load-displacement ($P - h$) curves of cementitious materials usually contain all

* Prof. Ing. Jiří Němeček, PhD., DSc.: Czech Technical University in Prague, Faculty of Civil Engineering, Thákurova 7; 166 29, Prague 6; CZ, jiri.nemecek@fsv.cvut.cz

** Ing. Jitka Němečková, PhD.: Czech Technical University in Prague, Faculty of Civil Engineering, Thákurova 7; 166 29, Prague 6; CZ, jitka.nemeckova@fsv.cvut.cz

*** Ing. Jiří Němeček, PhD.: Czech Technical University in Prague, Faculty of Civil Engineering, Thákurova 7; 166 29, Prague 6; CZ, jiri.nemecek.1@fsv.cvut.cz

doi: 10.21495/em2024-214

kinds of viscous-elastic and plastic deformations. For higher stresses, fracture deformation may be observed as sudden burst in $P-h$ curves. The experimental $P-h$ curve usually contains three segments (see Fig. 1a). The first is the loading phase, during which all kinds of deformations occur. This is followed by the holding phase, in which the load is kept constant and the unloading part is final. Purely elastic behavior of the material can be assumed in the unloading part of the $P-h$ curve form which the indentation (reduced) modulus is derived (Oliver and Pharr, 1992) as $E_r = \frac{S\sqrt{\pi}}{2\sqrt{A_c}}$ where S is the contact stiffness and A_c is a contact area. A general relationship between the time-dependent indentation load, $P(t)$, and displacement, $h(t)$, for a step loading of a visco-elastic solid can be expressed as

$$h^m(t) = \kappa P_{max} J(t) \tag{1}$$

where $J(t)$ is the creep compliance function, m and κ are geometric constants (e.g. $m = 2$ and $\kappa = \frac{\pi}{2\tan\alpha}$ for cone or pyramid), P_{max} is the maximum load. Using Kelvin chain model, $J(t)$ can be approximated as

$$J(t) = \frac{1}{E_{r,0}} + \sum_{i=1}^{N} \frac{1}{E_{r,i}} \left(1 - e^{-\frac{t}{\tau_i}}\right) RCF_i \tag{2}$$

where $E_{r,0}$ is the instantaneous reduced modulus, E_i and τ_i are elastic moduli and retardation times of respective Kelvin units and RCF_i are ramp correction factors defined as $RCF_i = \frac{\tau_i}{t_R}\left(e^{t_r/\tau_i} - 1\right)$ with t_R being the ramping time (Oyen and Cook, 2009). If the load is instantaneously applied the $RCF_i = 1$, otherwise it accounts for a finite load ramping.

2.1. Effect of plastic deformation

In many materials including cement paste, nanoindenters equipped with sharp tips (especially the cube corner tip) cause non-negligible plastic strains that evolve mainly over loading period. Ignoring the strains and related add-on deflections to Eq. (1), respectively, result in overestimation of creep compliance values as confirmed both experimentally and numerically (Vandamme et al., 2012). Based on the assumption that plastic deformations appear only at the loading period, a relationship between contact compliance and the testing parameters can be established (Vandamme and Ulm, 2013) as

$$J(t) = \frac{1}{E_r} + \frac{2a_c \Delta h(t)}{P_{max}} = \frac{1}{E_r} + \frac{ln(1 + t/\tau)}{C} \tag{3}$$

where $\Delta h(t)$ is the increment of indenter's penetration depth during holding phase, $a_c = \sqrt{\frac{A_c}{\pi}}$ is the radius of contact. A logarithmic function fitting $\Delta h(t)$ from experiments was proposed by Vandamme and Ulm (2013) leading to the second expression in Eq. (3), where C is the creep modulus and τ is the characteristic time. Němeček et al. (2023) used a simple correction of plastic deformations by adding an additional fitting parameter, h_0, directly to Eq. (1) such that

$$(h(t) - h_0)^m = \kappa P_{max} J(t). \tag{4}$$

This formula leads to a successful fitting of the short-term experimental data. One of the advantages of this simple method is that it allows to estimate the amount of plastic deformation appearing in the loading phase depending on the type of an indenter.

3. Experiments and methods

Nanoindentation (using Hysitron TI-700) was performed on hydrated cement paste CEM I-42,5R (water/binder = 0.40) aged for 1.5 year in lime water. Two types of sharp indenter tips (Berkovich and cube corner) were used. The loading protocol was prescribed as follows: linear loading for 1 s; 40 s holding at 1.5 mN maximum force; linear unloading for 1 s. Always, a representative $P-h$ curve received from well hydrated phases of the cementitious matrix (C-S-H) was selected for each tip (Fig. 1a). Then, the analytical approaches described in Sect. 2. were applied. This included non-linear least square regression

of the depth-time data by: (I) standard visco-elastic model assuming the step load (i.e. neglecting finite ramping, Eq. (2) with $RCF_i = 1$); (II) visco-elastic model with ramp correction (Eq. (2); (III) visco-elastic model with h_0 correction (Eq. (4) with RCF_i=1); (IV) visco-elastic model with h_0 and RCF_i correction (Eq. (4); (V) logarithmic fit (Eq. (3). Where applicable, using of two Kelvin units was sufficient in fitting the short-term data. Since the fitting procedure is very sensitive to the data in the beginning of the curve, the first 1 s of the holding (fitted) period was ommited and the data from 1–40 s interval were taken into consideration. Then, creep functions $J(t)$ were constructed for each of the model variant.

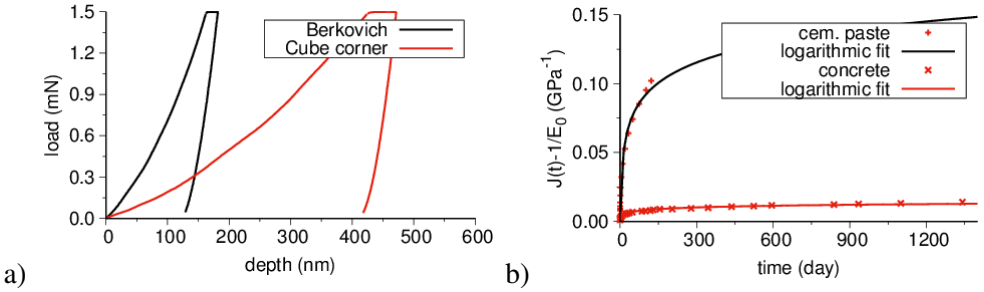

Fig. 1: a) Nanoindentation $P - h$ curves. b) Macroscopic uniaxial tests after Zhang et al. (2014).

4. Results and discussion

Despite receiving of relatively good fits of the experimental data (depth-time data) for every model, very large differences in the $J(t)$ predictions were obtained. It can be seen from Fig. 2 that results from the cube corner tip gave systematically higher estimates, leading to the conclusion that this tip causes non-negligible plastic strains that can hardly be filtered out by any of the methods. The stresses caused by the tip are also higher compared to less acute Berkovich tip and may already lie in the region of non-linear creep. Regardless of the tip used, the highest estimate of compliance was given by standard visco-elastic model assuming the step load and neglecting the plastic deformation. This was especially significant if the sharper cube corner tip was used. The ramp correction decreased the compliance prediction to one half in the case of Berkovich tip. When the h_0 correction was used, the lowest compliance prediction was received, regardless of the RCF_i correction. The logarithmic creep model provides intermediate predictions of $J(t)$. Parameters of different model variants are summarized in Tabs. 1 and 2.

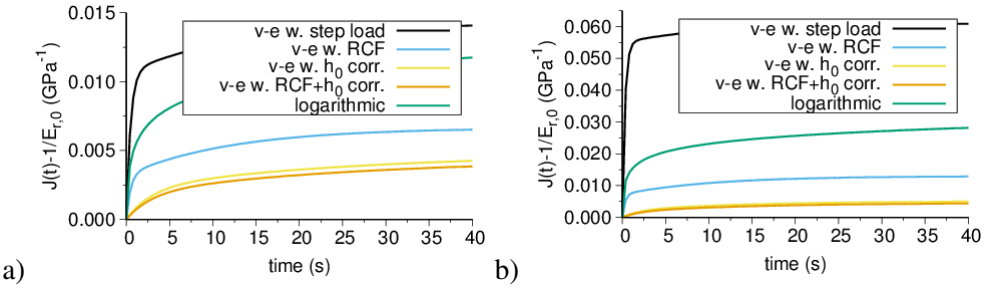

Fig. 2: J(t) functions for a) Berkovich tip, b) cube corner tip.

Deciding on what short-term compliance prediction is correct is a non-trivial task. One can compare the short-term functions with the standard macroscopic uniaxial tests done either on cement paste samples with millimeter dimensions or even on concrete specimens already containing large aggregates Zhang et al. (2014). Examples of such functions are given in Fig. 1b for a comparable cement paste and concrete having a comparable cementitious matrix. It is evident from Fig. 1b and also Tabs. 1 and 2 that the functions predict the creep in a similar order like from nanoindentation but on a completely different time scale.

5. Conclusions

From this study, it can be concluded that utilizing sharp nanoindentation is a feasible technique for quantifying the micro-scale creep of cementitious materials. So far, the methodology for estimation of the short-term

	Berkovich					Cube corner			
Method	$E_{r,0}$ (GPa)	τ_1 (s)	E_1 (GPa)	τ_2 (s)	E_2 (GPa)	τ_1 (s)	E_1 (GPa)	τ_2 (s)	E_2 (GPa)
1	40	0.5	93.9	12.3	281.1	0.1	18.2	3.6	165.4
2	40	0.5	309.2	12.3	292.8	0.1	138.4	3.5	173.6
3	40	2.9	444.9	26.4	389.3	0.6	451.3	8.0	338.7
4	40	2.9	531.4	26.4	396.8	0.6	590.0	8.0	350.5

Tab. 1: Parameters of Kelvin chain based creep compliance functions.

Parameter	**Berkovich**	**Cube corner**	**Uniaxial creep of paste**	**Uniaxial creep of concrete**
C (GPa)	564.5	274.9	46.5	565.8
τ	0.05 (s)	0.02 (s)	1.4 (day)	0.98 (day)

Tab. 2: Parameters of logarithmic creep compliance functions.

creep compliance is not standardized. It follows from the study that the available analytical estimates perform very differently based on their assumptions and the exact experimental methodology applied (e.g. tip or loading protocol selection). It seems that using the most acute tips (cube corner) leads to overestimation of the creep compliance due to significant stresses imposed to the material. Less acute tips (Berkovich) seem to give more reasonable predictions. Plastic strains developed during loading under the indenter cannot be ignored. But, even if the plastic deformations are taken into account, the analytical methods differ in their prediction by more than 100 %. Short-term creep data from nanoindentation provide reasonable creep compliance predictions and can be successfully used for comparisons of local visco-elastic behavior. However, direct linking of the short-term creep data to the uniaxial creep on a higher scale can hardly be achieved and further research in this direction is necessary.

Acknowledgment

Financial support of the Grant Agency of the Czech Republic (project No. 23-05435S) is gratefully acknowledged.

References

Baronet, J., Sorelli, L., Charron, J.-P., Vandamme, M., and Sanahuja, J. (2022) A two-scale method to rapidly characterize the logarithmic basic creep of concrete by coupling microindentation and uniaxial compression creep test. *Cement and Concrete Composites*, 125, pp. 104274.

Kai, M., Zhang, L., and Liew, K. (2021) New insights into creep characteristics of calcium silicate hydrates at molecular level. *Cement and Concrete Research*, 142, pp. 106366.

Němeček, J., Trávníček, P., Keppert, M., Halodová, P., Rosnecký, V., and Němeček, J. (2023) Nanomechanical analysis of gamma-irradiated cement paste exposed to different humidities. *Construction and Building Materials*, 393, pp. 131969.

Oliver, W. and Pharr, G. (1992) An improved technique for determining hardness and elastic modulus using load and displacement sensing indentation experiments. *Journal of materials research*, 7, 6, pp. 1564–1583.

Oyen, M. L. and Cook, R. F. (2009) A practical guide for analysis of nanoindentation data. *Journal of the Mechanical Behavior of Biomedical Materials*, 2, 4, pp. 396–407.

Vandamme, M., Tweedie, C., Constantinides, G., Ulm, F.-J., and Van Vliet, K. (2012) Quantifying plasticity-independent creep compliance and relaxation of viscoelastoplastic materials under contact loading. *Journal of Materials Research*, 27.

Vandamme, M. and Ulm, F.-J. (2013) Nanoindentation investigation of creep properties of calcium silicate hydrates. *Cement and Concrete Research*, 52, pp. 38–52.

Zhang, Q., Le Roy, R., Vandamme, M., and Zuber, B. (2014) Long-term creep properties of cementitious materials: Comparing microindentation testing with macroscopic uniaxial compressive testing. *Cement and Concrete Research*, 58, pp. 89–98.

30th International Conference
ENGINEERING MECHANICS 2024
Milovy, Czech Republic, May 14 – 16, 2024

DESIGN OF AN INDEXING GEARBOX WITH RADIAL CAMS

Ondrášek J.*

Abstract: *Indexing gearboxes are used to convert the uniform rotary motion of the input camshaft into a required non-uniform rotary motion with clearly defined dwell portions of an output shaft. The indexing gearbox with conjugate cams consists of a pair of radial cams and an indexing turret follower fitted with rollers that are mounted on both sides and rolled. The favourable properties of polygon joints are advantageously used in the design of the indexing gearbox with radial cams. The joint profile formed by the polygon has very low, if not negligible, notch effects. For this reason, the fatigue strength of the respective connection is significantly increased. The geometric shape of the follower roller crown in cam mechanisms has also a significant effect on the contact stress due to the load and inertial effects in the surface layers of the general kinematic pair. Together with the design changes of the existing design of indexing gearboxes, modern coating methods can be used, which have become an integral part of industrial practices. Coatings extend the lifetime of sliding and rolling surfaces.*

Keywords: Indexing gearbox, cam mechanism, radial cam, polygon connection, indexing turret follower.

1. Introduction

The company VÚTS, a.s. (VÚTS, a.s., 2024) is a research organization with long-time experience in the design and calculation of cams and cam mechanisms among other things. For this purpose, computational programs and procedures for the analysis and synthesis of combined cam mechanisms were developed here, see (Koloc and Václavík, 1993; Norton, 2009; Ondrášek, 2019). As part of its research and development activities, VÚTS, a.s. ensures the production of cams and cam mechanisms for domestic and foreign customers.

2. Indexing gearboxes with conjugate cams

The company VÚTS, a.s. is also a producer of indexing gearboxes with conjugate cams of the KP series, which consists of a pair of radial cams with an axial disc star fitted with double-sided mounted rollers, see Fig. 1. In these types of the indexing gearboxes, the input and output shafts are arranged parallel to each other. The indexing gearboxes are used to convert the uniform rotary motion of the input camshaft to the unidirectional rotary motion with clearly defined dwell portions of the mechanism output shaft (intermittent rotary motion). We can denote the gearbox output member with the term indexing turret follower.

2.1. Displacement law

Indexing cam mechanisms belong to the mechanisms with non-periodic displacement laws. The shape of the cam contour is determined by the synthesis which goes on the basis of the knowledge of a displacement law $w = f(\tau)$ of the given indexing gearbox and its dimensional parameters. The movement of the driving member – camshaft is described by the independent motion function $\tau(t)$ and the movement of the indexing turret follower by the dependent motion function $w(t)$. The displacement law $w(\tau)$ of an indexing gearbox with a rotating cam increase the functions with dwell portions, with individual rises (indexes) following each other with a period of 2π. Displacements on each motion interval may be

* Ing. Jiří Ondrášek, PhD.: VÚTS, a.s.; Svárovská 619, 460 01 Liberec, Czech Republic; jiri.ondrasek@vuts.cz

doi: 10.21495/em2024-218

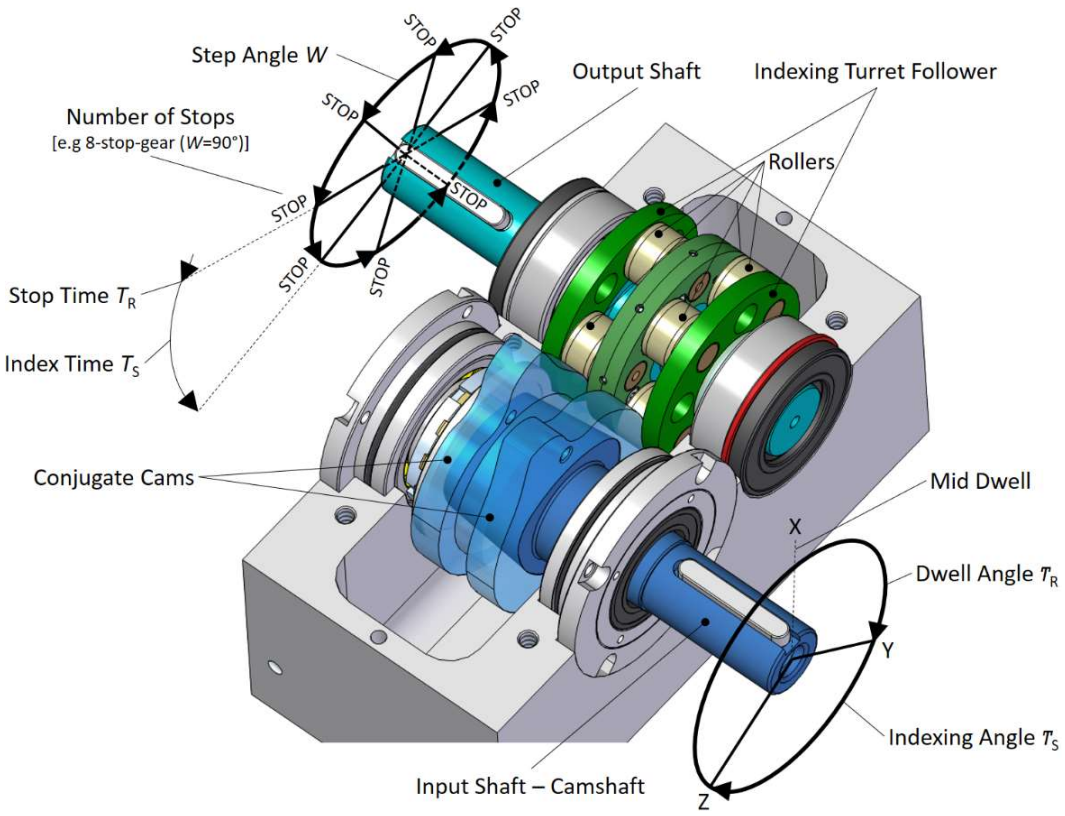

Fig. 1: Indexing gearbox with conjugate cams.

different in a maximum total rise W and an expression of the normalized form where the displacement $\eta = \eta(\xi)$ and the range are in unity. The variables ξ_k ,η_k of k^{th} motion interval are in linear correlation with the original variables τ, w and are expressed as:

$$\xi_k = \frac{\tau-\tau_{0k}}{T},\ \eta_k(\xi_k) = \frac{w(\tau)-w_{0k}}{W},\ \xi_k \in \langle -\tfrac{1}{2};\ \tfrac{1}{2}\rangle,\ \eta_k \in \langle -\tfrac{1}{2};\ \tfrac{1}{2}\rangle. \tag{1}$$

The coordinates τ_{0k}, w_{0k} determine the position of the origin O_k of the motion interval coordinate system $O_k\xi_k\eta_k$, while in the following step it is given by the coordinates:

$$\tau_{0(k+1)} = \tau_{0k} + 2\pi,\ w_{0(k+1)} = w_{0k} + W. \tag{2}$$

The derivatives in the original variables τ, w and normalized variables ξ_k, η_k are related by the relations:

$$w' = \frac{dw}{d\tau} = \frac{W}{T}\cdot\frac{d\eta_k}{d\xi_k} = \frac{W}{T}\eta_k'(\xi_k),\ w'' = \frac{d^2w}{d\tau^2} = \frac{W}{T^2}\cdot\frac{d^2\eta_k}{d\xi_k^2} = \frac{W}{T^2}\eta_k''(\xi_k). \tag{3}$$

If the variable $\tau = f(t)$ is a function of time t, then the following relations are valid:

$$\dot{w} = \frac{W}{T}\eta_k'(\xi_k)\dot{\tau},\ \ddot{w} = \frac{W}{T}\left(\frac{1}{T}\eta_k''(\xi_k)\dot{\tau}^2 + \eta_k'(\xi_k)\ddot{\tau}\right). \tag{4}$$

VÚTS, a.s. produces indexing gearboxes with radial cams, whose displacement law of the motion interval is mathematically defined by a standardized form that expresses a 5 ° polynomial function:

$$\eta(\xi) = \frac{1}{8}\xi[15 - 10(2\xi)^2 + 3(2\xi)^4],\ \eta'(\xi) = \frac{15}{8}[1-(2\xi)^2]^2,\ \eta''(\xi) = -30\xi[1-(2\xi)^2]. \tag{5}$$

The numerical parameters of the motion interval and dwell intervals are contained in Tab. 1. An example of the course of such the displacement law of a indexing cam gearbox is shown in Fig. 2.

Boundary Points	**1**	**2**	**3**	**4**
$\tau-(k-1)\cdot 360$ [°]	0	220	320	360
W [°]	0	0	90	90

Tab. 1: Numerical parameters of the displacement law intervals.

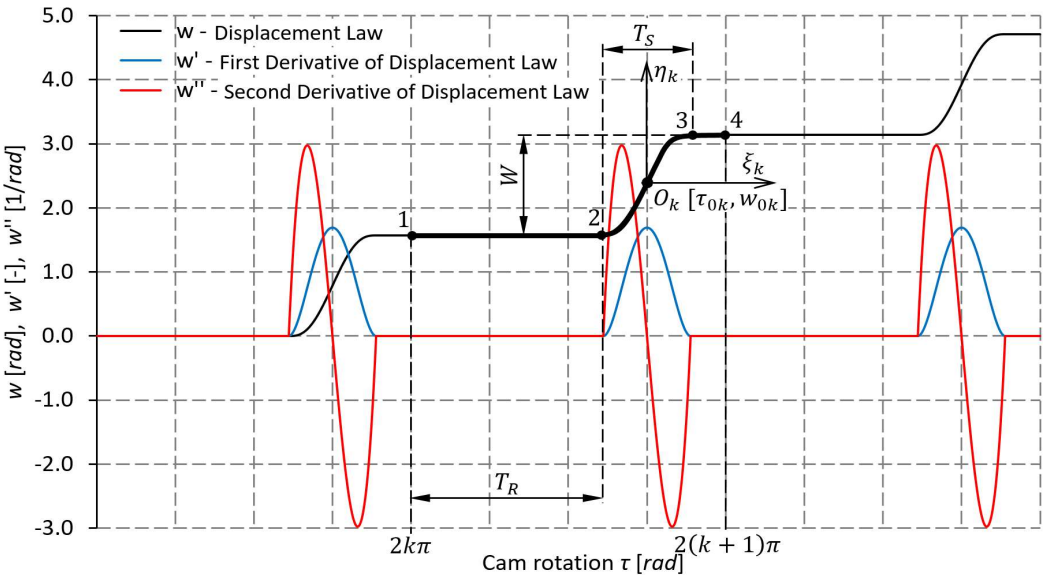

Fig. 2: Displacement law of indexing gearbox.

2.2. Design of a camshaft and an indexing turret follower

In the design process of the input (camshaft) and output member (indexing turret follower) of the indexing gearbox, the favorable properties of conical polygon connections were used, see Fig. 3. In the design process of the camshaft and the indexing turret follower of the indexing gearbox, the favorable properties of the conical polygon connections were used. The joint profile formed by the polygon is characterized by a transmission of large, variable and shock torques, possibility of defining the mutual rotation of the cams of the cam pair and their axial position on the shaft, self-centering, simple backlash elimination between the cams and the camshaft and the discs and the indexing turret follower shaft, simple assembly and disassembly. In the case of indexing turret follower production, there is a saving of material because the indexing turret follower body used to be made from a piece of semi-finished product.

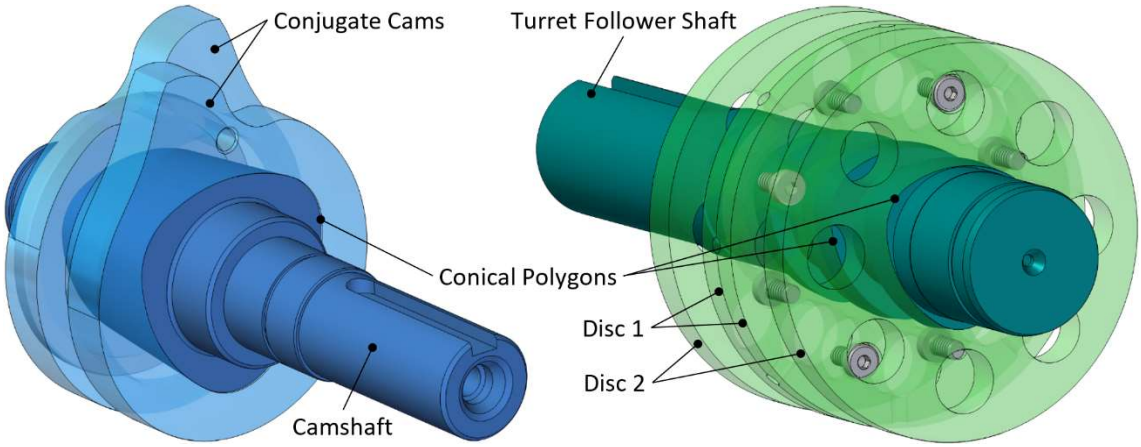

Fig. 3: Camshaft and body of indexing turret follower.

2.3. Optimization of roller shape of a cam follower

The geometric shape of the crown of the follower roller has a significant effect on the contact stress due to the load and inertial effects in the surface layers of the general kinematic pair. In the case of a cylindrical roller, there are discontinuities at the intersections of the cylindrical profile with the cam profile. The mentioned discontinuities cause a very sharp increase in the pressure distribution in the respective contact surfaces of the bodies. These local increases in pressure distribution can exceed the ultimate strength of the material and thus cause plastic deformations, occurrence of residual stresses in material or eventually steel hardening. A possible variant how to ensure a more even distribution of the contact stress is a structural change in the shape of the axial cross-section of the roller crown. This is one of the reasons for the practical application of the roller with convex segments of the crown while the middle section of the crown being

cylindrical, see Fig. 4. The characteristic dimensions of such a roller are diameter D, width l_e, radius R of the crown convex part, width w of the convex part and radius r of edge rounding. The optimization parameters of such a crown profile are the radius R of the convex region and its width w. The entire optimization of the crown profile is carried out in order to distribute the contact stress as evenly as possible with the largest possible load generated by the effects of the force N.

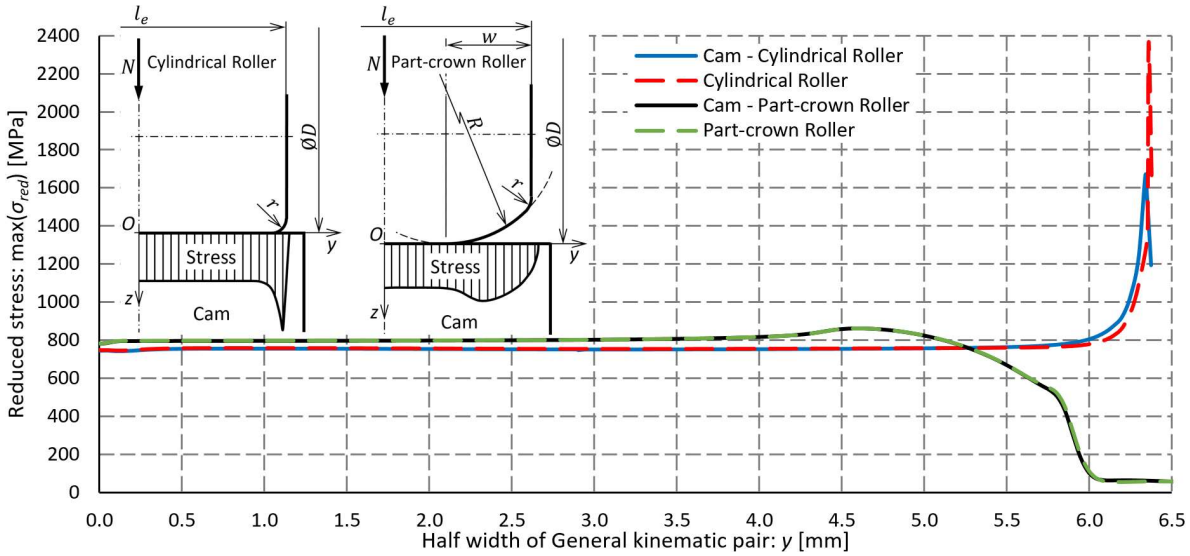

Fig. 4: Stress distribution in general kinematic pair.

3. Conclusions

In the case of an indexing drive of KP series, a conical polygonal connection was used to mount the conjugate cams on the camshaft and the lever discs on the lever shaft. In the case of this type of connection, the exact position of the cams on the camshaft is ensured. The profile of the connection formed by the conical polygon has very low, even negligible notch effects, this means a significant increase in the fatigue strength of the respective connection. These connections are used to transmit large, variable and shock torques. Patent CZ 306709 protects this arrangement of the cams on the camshaft and lever discs on the lever shaft.

The rollers have an optimized shape, thanks to which the service life of the indexing gearbox is extended. This is because there is no increase in the values of the contact stresses in critical regions when the cam and roller are in contact.

Another result of the development is the use of modern technologies from the areas of coating. Parts that form sliding pairs are coated, and another solution would be technologically too demanding, i.e. rollers and pins on which the rollers are sliding seated. In the case of rollers, this is the surface that is in contact with the cams. The coated pins allow clean sliding of the rollers. Coatings extend the lifetime of the sliding and rolling surfaces and help reduce the required power consumption while simultaneously increasing performance. Coatings are generally used to improve hardness, wear resistance and oxidation of contact surfaces.

Acknowledgement

This publication was supported by the Ministry of Industry and Trade (MPO) within the framework of institutional support for long-term strategic development of the research organization - provider MPO, recipient VÚTS, a. s.

References

Koloc, Z., Václavík, M. (1993) *Cam Mechanisms*. Elsevier, Amsterdam.

Norton, R., L. (2009) *Cam Design and Manufacturing Handbook*. Industrial Press, Inc., New York.

Ondrášek, J. (2019) The General Kinematic Pair of a Cam Mechanism, *Kinematics - Analysis and Applications, IntechOpen*, London, pp. 17–38.

VÚTS, a.s. (2024) Available from URL<https://www.vuts.cz/>.

30th International Conference
ENGINEERING MECHANICS 2024
Milovy, Czech Republic, May 14 – 16, 2024

ELASTOPLASTIC MODELS FOR INTERPRETING INDENTATION RESULTS

Panfilov I. A.*, Aizikovich S. M., Vasiliev A. S.*****

Abstract: *One of the current and widely used non-destructive testing methods for monitoring and determining the elastic properties of materials is indentation. For interpretation of the test results, a non-trivial task of constructing an adequate mathematical model of the indentation process arises. In numerous cases, analytical formulas are used that are obtained from an elastic linear formulation of problems on the indentation of a non-deformable punch into a homogeneous elastic half-space. Currently, the numerical formulation of the problem makes it possible to obtain and use a numerical solution obtained taking into account the complete plastic nonlinear behavior of the material. In this work, a study of contact problems on the introduction of a spherical and conical indenter into an elastoplastic homogeneous half-space was carried out. To verify the numerical solution, the problem of introducing a spherical and conical indenter into an elastic homogeneous half-space was also solved and compared with known analytical solutions. Issues of convergence and tuning of numerical methods, the influence of plasticity and the applicability of analytical solutions were explored. Problems were solved numerically using the finite element method in the Ansys Mechanical software package.*

Keywords: Continuous contact, contact mechanic, contact problem, indentation, conical indenter, spherical indenter, finite element method.

1. Introduction

Indentation is used for non-destructive testing of materials and obtaining mechanical characteristics (Bulychev and Alekhin, 1990; Golovin, 2009): hardness, elastic properties of bulk materials and coatings, etc. The essence of the method is to press a more rigid punch, called indenter (usually made of diamond or hard alloys) into the surface of the test sample and obtain diagrams of force depending on the indentation depth on a nanometer scale. The elastic properties of materials and coatings under study are determined from the analysis of the force-displacement diagram at the unloading stage. The Field-Swain (spherical indenter) (Field and Swain, 1993) and Oliver-Pharr (Berkovich indenter) (Pharr and Oliver, 1992) methods are based on solutions to contact problems of theory of elasticity for spherical and parabolic punches (Hertz, 1881; Johnson, 1989). In (El-Sherbiney and Halling, 1996; Sadyrin et al., 2020 and Vasiliev et al., 2020), approximate analytical solutions of axisymmetric contact problems on indentation of a spherical, conical and cylindrical punch into an elastic half-space with a functionally graded coating were constructed.

2. Methods

The hypothesis of small indenter movements used in the presented works imposes serious restrictions on the use of analytical applied formulas, since even a small indenter displacement causes the development of plastic deformations. The indentation force and contact area differ significantly from the analytical results.

* Prof. Ivan Panfilov, PhD.: Don State Technical University, 1 Gagarin Square, Rostov on Don, RU; mechanic_rgu@mail.ru

** Prof. Sergei Aizikovich, Dr. Sci.: Don State Technical University, 1 Gagarin Square, Rostov on Don, RU; saizikovich@gmail.com

*** Dr. Andrey Vasiliev, PhD.: Don State Technical University, 1 Gagarin Street, Rostov on Don, RU; andre.vasiliev@gmail.com

doi: 10.21495/em2024-222

The present paper examines the problems of indentation of spherical and conical indenters into an elastoplastic half-space, in a static axisymmetric statement. To implement plastic deformation, a bilinear material model with an elastic modulus (Young's modulus) and a tangential elastic modulus was used. The indenter is made of elastic diamond. The half-space is made of aluminum. The Young's modules of the indenter and half-space material were 1 000 GPa and 70 GPa, respectively. The yield strength and tangential elastic modulus for the bilinear half-space material were 0.28 GPa and 0.5 GPa, respectively.

Contact problems are nonlinear problems due to the changing status of the contact and the stiffness matrix, and require special attention to the accuracy and convergence of the solution. Below are the settings of the numerical methods used in the Ansys finite element analysis package and applied in this calculation.

To implement the contact problem, the "Augmented Lagrange" contact algorithm was used. This is a modified contact algorithm of the common "Pure Penalty" method ("penalty function method"), characterized by the presence of an additional term λ in the expression of the contact force:

$$F_n = k_n \cdot x_p + \lambda, \tag{1}$$

The value of the contact stiffness k_n has a major influence on accuracy and convergence. A large value of stiffness provides high accuracy, but degrades convergence and vice versa. Using the additional term λ allows one to reduce the sensitivity of the algorithm to the contact stiffness k_n, and allows one to obtain acceptable results with the value k_n = 1, but also requires a larger number of iterations. To "recognize" contacts, the "Gauss point detection" method was used, in which additional points were added on the edges of the elements. To improve convergence, "Normal from Contact" recognition was used with an increase in the number of calculations.

In the present work, to construct a finite element mesh, an 8-node element PLANE183 was used - a high-order element with intermediate nodes. In the area of contacts, the meshes were refined. For indenters, a larger mesh was used. In this case, the reference parameters, relative to which the mesh dimension and linear dimensions of the half-space should be set, are the contact area (indentation depth). Thus, the used partition, for example, in the elastic problem provided about 30 elements in the contact area for a spherical indenter, and 10 elements for a conical one.

For the problem of a spherical punch indentation, refinement of the mesh will obviously lead to more accurate results, and the problem will converge. For the cone indentation problem, setting up the mesh was a much more difficult task because a singularity was formed at the center of the cone. In other words, refinement of the mesh in the center of the cone lead to a direct increase in stress and divergence of the problem. Also, for the problem with a conical indenter, the shape of the elements in the center of the contact was quite important - the shape and size of the elements should have provided greater deformation and prevented the cells from "collapsing". One way to deal with numerical singularity is to create a rounding at the tip of the cone, or to use plasticity models.

For contact surfaces, elements such as CONTA172 and TARGE169 were used with automatic recognition and limitation of the contact area. Moreover, since the indenter rigidity was several times greater than the rigidity of the indented material, the TARGE169 elements were applied specifically to the indenter. Ansys also allows one to take into account geometric nonlinearity for large deformations by including in the calculation the nonlinear strain tensor $\boldsymbol{\varepsilon}(x, y, z)$ with respect to the derivative displacements $\boldsymbol{u}'(x, y, z)$ ("Large deflection"). Thus, in contrast to analytical theories, where only contact nonlinearity was taken into account under the hypothesis of small deformations, we were able to numerically realize all three types of nonlinearity: contact, geometric (large deformations) and physical (plasticity) ones.

Analytical results for comparison were taken from the well-known formulas (2)–(8) for the indentation of rigid punches (Johnson, 1989):

$$a_s = (Rd)^{\frac{1}{2}}, \tag{2}$$

$$a_c = \frac{2d}{\pi \cdot \tan(\varphi)}, \tag{3}$$

$$F_s = \frac{4}{3} E^* R^{\frac{1}{2}} d^{\frac{3}{2}}, \tag{4}$$

$$F_c = \frac{2}{\pi} E \cdot \frac{d^2}{\tan(\varphi)}, \tag{5}$$

$$p_s = p_0\left(1-\frac{r^2}{a^2}\right)^{\frac{1}{2}},\ p_0 = \frac{2}{\pi}E^*\left(\frac{d}{R}\right)^{\frac{1}{2}}, \tag{6}$$

$$p_c = \frac{Ed}{(1-\nu^2)\pi a}\ln\left(\frac{a}{r}-\left(\left(\frac{a}{r}\right)^2-1\right)^{\frac{1}{2}}\right), \tag{7}$$

$$E^* = \frac{E}{1-\nu^2}. \tag{8}$$

To take into account the rigidity of a diamond spherical indenter in expressions (2)–(8) for effective rigidity E^*, the following formula was used:

$$\frac{1}{E^*} = \frac{1-\nu_1^2}{E_1}+\frac{1-\nu_2^2}{E_2}. \tag{9}$$

Here $\boldsymbol{a}$ is the contact radius, $\boldsymbol{d}$ is the indentation depth, $\boldsymbol{\varphi}$ is the angle between the horizontal and lateral planes of the cone, $\boldsymbol{r}$ is the vertical coordinate, $\boldsymbol{E_1, E_2}$ and $\boldsymbol{\nu_1, \nu_2}$ are Young's moduli and Poisson's ratios of the indenter and half-space, respectively, $\boldsymbol{F}$ is the vertical force, $\boldsymbol{p}$ – pressure in the contact area. The indices *s* and *c* here and below in the graphs indicate membership in a sphere and a cone, respectively. The error increased with increasing deformation and for maximum values was about 2 % for the vertical force.

3. Results

Figs. 1 and 2 show the results for spherical and conical indentation into an elastic aluminum half-space. It is worth noting that these loads for the elastic problem significantly exceed the permissible ones in terms of the yield strength and were considered as model problems for comparing models. Within the limits of elastic deformations, the error in the numerical results was less than 0.1 %. When solving an elastoplastic problem numerically, we observed linear unloading area, which was used for estimation of Young's modulus using non-destructive testing methods (nanoindentation).

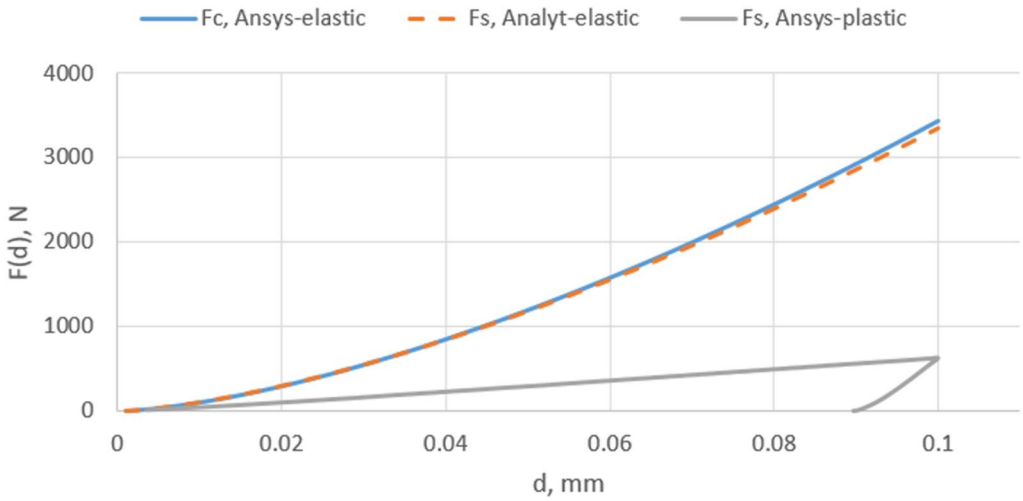

Fig. 1: Vertical force from displacement for a spherical indenter d.

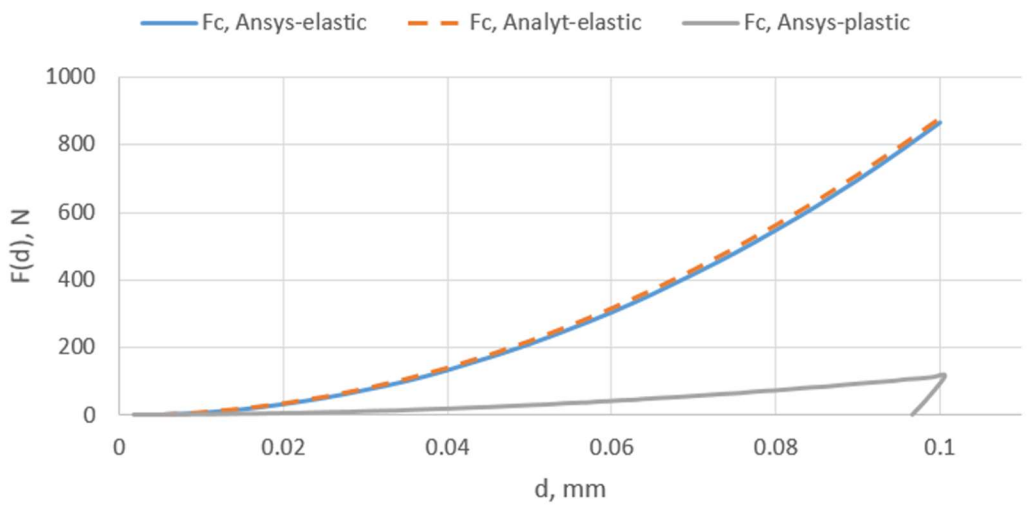

Fig. 2: Vertical force from displacement for a conical indenter d.

4. Conclusions

The contact area for the elastic model and the elastoplastic model was demonstrated to be significantly different. During plasticity stage, the material was "squeezed out" from under the indenters and significantly increased the contact area. For a spherical indenter for maximum displacement, the difference in contact radius was about 30 %, for a conical indenter – 45 %. In general, the use of an elastic model can serve as a model problem for verification and calibration of numerical methods. However, for large deformations, it is recommended to use an elastoplastic deformation model, and also a nonlinear strain tensor model (large deformation model). These studies can effectively be used to evaluate the accuracy and analysis of models used in identifying the properties of graded, multilayer and coated materials.

Acknowledgement

This work was supported by the Russian Science Foundation grant No. 22-19-00732.

References

Bulychev, S. I. and Alekhin, V. P. (1990) *Testing of materials by continuous indentation of an indenter*. Mashinostroyeniye, Moscow, 224 p.

El-Sherbiney, M. G. D. and Halling, J. (1996) The Hertzian Contact of Surfaces Covered with Metallic Films. *Wear*, 40, pp. 325–337.

Field, J. S. and Swain, M. V. (1993) A simple predictive model for spherical indentation. *Journal of Materials Research* 8, pp. 297–306.

Golovin, Y. I. (2009) *Nanoindentation and its capabilities: a practical guide*. Mashinostroenie, Moscow (in Russian).

Hertz, H. (1881) Üeber die Berührung Fester Elastischer Körper, *J. Reine u. Angew. Math.,* 92, pp. 156–171 (in German).

Johnson, K. L. (1989) *Mechanics of contact interaction*. Mir, Moscow (Russian translation).

Pharr, G. M. and Oliver, W. C. (1992) An improved technique for determining hardness and elastic modulus using load and displacement sensing indentation experiments. *J. Mater. Res.,* 7, 6, pp. 1564–1583.

Sadyrin, E., Vasiliev, A. and Volkov, S. (2020) Mathematical modeling of experiment on Berkovich nanoindentation of ZrN coating on steel substrate. *Acta Polytechnica CTU Proceedings*, 27, pp. 18–21.

Vasiliev, A. S., Volkov, S. S., Sadyrin, E. V. and Aizikovich, S. M. (2020) Simplified analytical solution of the contact problem on indentation of a coated half-space by a conical punch. *Mathematics,* 8, 6, p. 983.

30th International Conference
ENGINEERING MECHANICS 2024
Milovy, Czech Republic, May 14 – 16, 2024

PREDICTION OF NON-STATIONARY DEFORMATION OF GAS TURBINE USING MACHINE LEARNING APPROACH COUPLING BETWEEN CFD AND FEM MODEL

Pařez J.*, Vampola T.**

Abstract: *After shutdown, the gas turbine rotor system cooling primarily through natural convection and radiation. It is presenting a common engineering challenge prevalent across various applications. In power engineering, this phenomenon has long been acknowledged and addressed through gradual startup and shutdown procedures of the rotor system. However, within the aircraft engine domain, this issue is more necessary due to the variable operating conditions and temperatures changes by flight modes or engine shutdown events. Moreover, engine aftercooling proves particularly arduous owing to the intricate geometry and equipment constraints. This paper delves into the application of a developed Finite Element Method (FEM) tool for predicting rotor thermal bow induced by temperature discrepancies between the upper and lower sides of the rotor. The paper meticulously elucidates the mathematical model of the FEM tool and expounds upon the calculation methodology for rotor deflection based on the selected geometry.*

Keywords: Rotor thermal bow, natural convection, gas turbine engine, 3D FEM.

1. Introduction

The operational temperature, trend monitoring, and control system of parts and components have a substantial impact on their reliability and lifespan across various industries. This impact is particularly pronounced in aviation, where it directly influences flight safety. The temperatures of aircraft engines, such as turboprop engines, and their adjacent components are influenced by internal engine mechanisms (compressor, combustion chamber, turbine) as well as external devices within the nacelle that dissipate heat. This paper discusses the prediction of rotor bow resulting from non-uniform temperature distribution in turbine engines. Previous studies by Pařez et al. (2022a, 2021) have addressed the issue of heat transfer during engine cooling via natural convection and radiation. While initial studies utilized a 1D Finite Element Method (FEM) solver (Pařez et al., 2022b), it was insufficient for comprehensive rotor system analysis, leading to the development of a 2D FEM solver (Pařez et al., 2022c). However, relying solely on a 2D solver does not accurately represent the real 3D geometry and physical principles, necessitating the development of a complete 3D FEM solver to accurately model temperature distribution and strain.

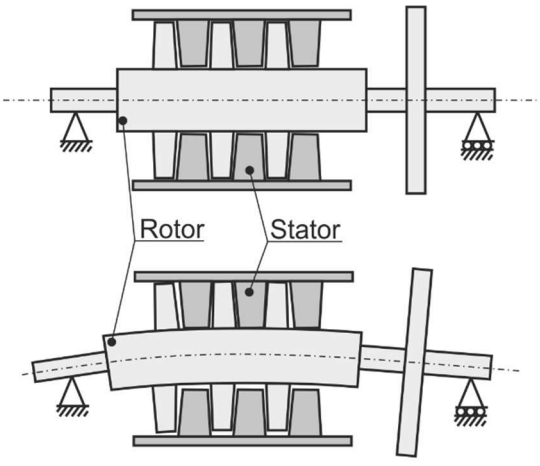

Fig. 1: Effect of "rotor thermal bow".

* Ing. Jan Pařez: Department of Mechanics, Biomechanics and Mechatronics, Faculty of Mechanical Engineering, Center of Aviation and Space Research, Czech Technical University in Prague; Technicka 4; 160 00, Prague 6; Czech Republic, jan.parez@fs.cvut.cz

** Prof. Dr. Ing. Tomáš Vampola: Department of Mechanics, Biomechanics and Mechatronics, Center of Aviation and Space Research, Faculty of Mechanical Engineering, Czech Technical University in Prague; Technicka 4; 160 00, Prague 6; Czech Republic, tomas.vampola@fs.cvut.cz

doi: 10.21495/em2024-226

Research on understanding thermal bow in turbomachinery has been conducted by Deepthikumar et al. (2014), while Yuan et al. (2009) employed Computational Fluid Dynamics (CFD) to model thermal bow resulting from convective airflow within compressor shafts. Marinescu and Ehrsam (2012) conducted a similar analysis on a steam turbine, highlighting the significant cooling time required. Due to computational complexity, they initially worked with a 2D simulation and adjusted the results to account for 3D effects. Pennacchi and Vania (2004) focused on model-based diagnostic techniques to detect thermal sag in generators, while Penara et al. (2015) studied the numerical determination of temperature distribution dependence on rotor vibration stability. Although literature touches on aeronautical applications, the presence of thermal bow in aircraft gas turbines is marginally discussed, including in works by Deepthikumar et al. (2014) and recent studies by Smith and Neely (2013) on aircraft engine compressors, which also delved into rotor dynamics and vibration.

2. Mathematical method

The Finite Element Method (FEM) solver operates through a series of Matlab scripts. The control script systematically executes various stages of the calculation process. Initially, input data regarding the computational mesh geometry, material properties, physical characteristics, and boundary conditions for temperatures and node supports are gathered. Based on this information, the computational mesh is generated. Subsequently, a calculation scope is determined, encompassing tasks such as temperature distribution, structural analysis, or dynamic property assessment.

The generation of the computational node mesh commences by discretizing the rotating component, adhering to specified node counts along the circumference and radial layers. Within this mesh, the computation domain is delineated based on the rotor system boundaries, with boundary edge points being included. This straightforward mesh structure facilitates the calculation of trapezoidal elements. These elements, comprising five sets of four points delineating the front, back, and middle planes in a counter clockwise orientation, are iteratively created for all relevant points within the calculation domain.

The calculation first determines the temperature distribution in the geometry based on the input boundary temperatures. The boundary temperatures are entered using a machine learning approach. Temperature distributions where non-stationary ambient airflow primarily due to natural convection affects the surface temperature as shown in Fig. 2. Thus, the temperatures are entered by a correlation function for specific correlation parameters and prescribed to the edge nodes of the geometry in Fig. 3.

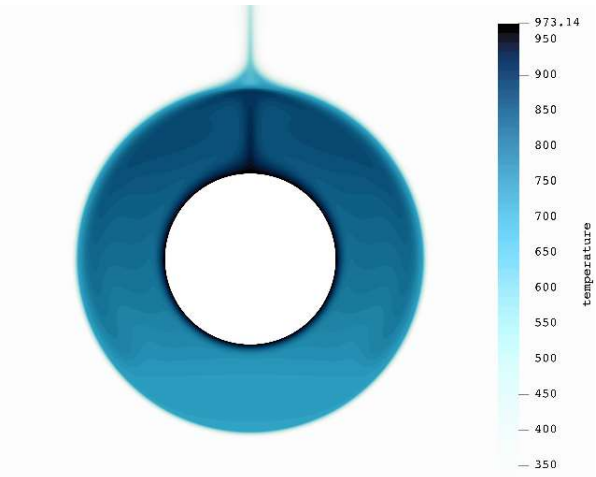

Fig. 2: Temperature distribution in single annular for flow path temperature 700 [°C].

The temperature field and deformations are calculated through a multi-step process. Initially, the temperature field is computed by constructing a heat conduction matrix for sub-elements, which are subsequently assembled into a comprehensive matrix incorporating the entire geometry and boundary conditions. Solving this matrix yields the temperature distribution for each node within the mesh. Once the temperature field distribution is established, a stiffness matrix is similarly constructed for the entire geometry, comprising the sub-elements. The displacement of each node within the computational mesh is determined by solving this stiffness matrix. The entire calculation process is conducted through linear calculations.

3. Computational model

The computational model of the rotor system simplifies the geometry into an annular cylindrical shape. The 3D mesh comprises 9 000 equally spaced elements along the inner radius, with 10 radial layers and 6 axial planes. The rotor system is supported by two-bearing supports: one fixed to prevent radial displacement, while the other allows axial displacement to compensate for thermal expansion. It's the same with an aircraft rotor. The rotor material, conventional steel, is characterized by known properties. The temperature field

distribution is based on measurements obtained from the double annulus under engine cooling conditions after-shutdown, with initial values set at 700 °C for edge nodes. This is followed by cooling by natural convection. The numerical analysis aims to ascertain the temperature field distribution within the geometry, incorporating prescribed boundary conditions at the edges. Additionally, the analysis seeks to determine the deformation history and its maximum values, depicted in Fig. 3 below.

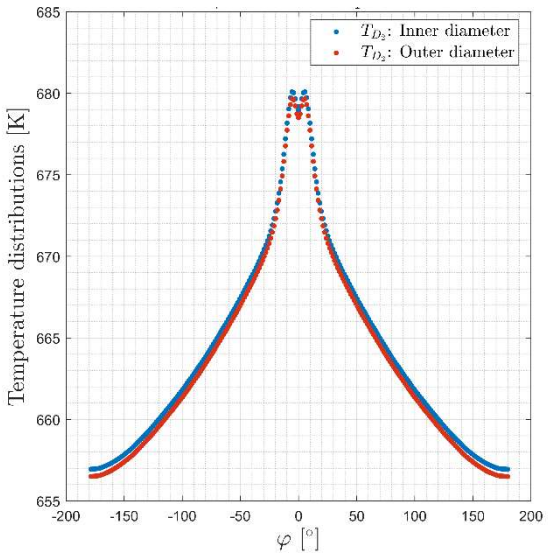

Fig. 3: Machine learning predicted temperatures for edge nodes at time $t > 0$.

The results from the developed FEM model of the rotor system highlight the significant impact of the non-uniform temperature field distribution. This is plotted in Figs. 4–7. Effect of asymmetrical deformation of upper and lower part leads to deflection in the rotor system, known as Rotor Thermal Bow.

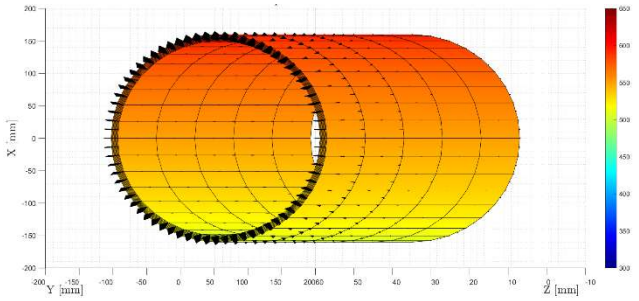

Fig. 4: Temperature field in time t_1.

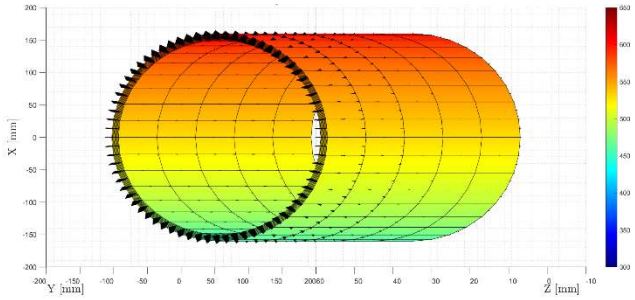

Fig. 5: Temperature field in time t_2.

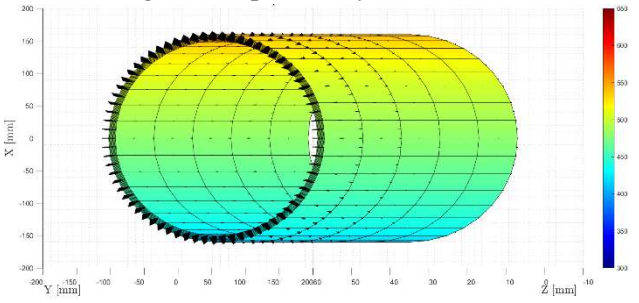

Fig. 6: Temperature field in time t_3.

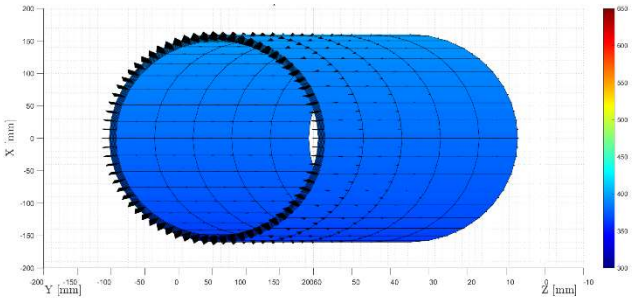

Fig. 7: Temperature field in time t_4.

3. Conclusions

The calculation of the rotor system deformation under natural convection conditions using the developed finite element model was studied. The mathematical model of the FEM tool and the choice of its meshing and creation of computational elements were described. The geometry was simplified into a rotor, and the temperature field distribution was calculated based on boundary conditions. Furthermore, the rotor was chosen to be supported in two bearings, one allowing axial displacement due to thermal expansion second support is fixed. Next, the total deformations were studied. The temperature differences generate

an additional deformation which results in the deflection of the whole shaft. The results of the temperature field distribution and an indication of the deformation vectors were plotted in the Fig. 8.

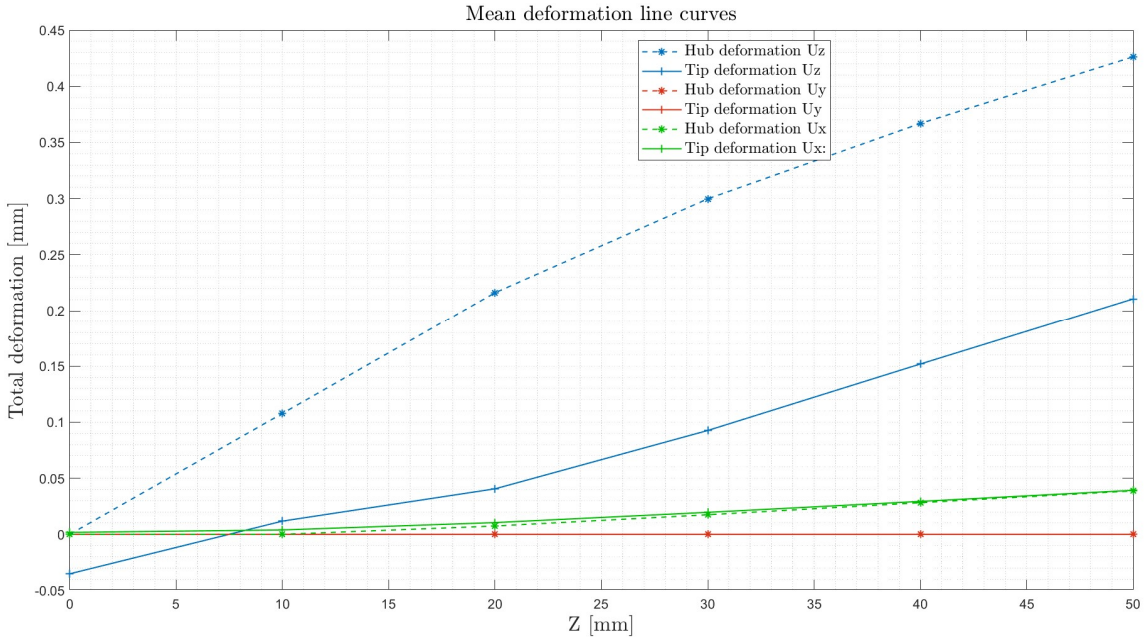

Fig. 8: Deformation for time t_2.

Acknowledgement

Authors acknowledge support from the ESIF, EU Operational Programme Research, Development and Education, and from the Center of Advanced Aerospace Technology (CZ.02.1.01/0.0/0.0/ 16_019/0000826), Faculty of Mechanical Engineering, Czech Technical University in Prague. This work was supported by the Grant Agency of the Czech Technical University in Prague, grant No. SGS22/151/OHK2/3T/12.

References

Deepthikumar, M. B., Sekhar, A. S. and Srikanthan, M. R. (2014) Balancing of flexible rotor with bow using transfer matrix method. *Journal of Vibration and Control*, 20(2), pp. 225–240.

Marinescu, G. and Ehrsam, A. (2012) Experimental Investigation Into Thermal Behavior of Steam Turbine Components: Part 2–Natural Cooling of Steam Turbines and the Impact on LCF Life. *Turbo Expo: Power for Land, Sea, and Air*, vol. 44700, pp. 1111–1120. American Society of Mechanical Engineers.

Penara, D., Baldassarre, L., Griffin, D., Mattana, A., Panconi, S. and Meli, E. (2015) Numerical prediction and experimental validation of rotor thermal instability. In: *Proc. of the 44th Turbomachinery Symposium. Turbomachinery Laboratories*, Texas A&M Engineering Experiment Station.

Pařez, J., Tater, A., Polanský, J. and Vampola, T. (2022a) Experimental and numerical study of natural convection in 3D double horizontal annulus. *EDP Sciences*. vol. 264, p. 01027.

Pařez, J., Rohan, P. and Vampola, T. (2021) Heat Transfer in Double Annular due to Natural Convection. *IOP Conference Series: Materials Science and Engineering*. vol. 1190, no. 1, p. 012002.

Pařez, J. and Vampola, T. (2022b) Numerical 1D Stiffness Matrix Model of Thermal Bowed Rotor. In: *30th Workshop of Applied Mechanics*. Prague, pp. 39–42.

Pařez, J., Kovář, P. and Vampola, T. (2022c) Sensitivity Analysis of Thermodynamical Parameters on the Thermal Bowed Rotor Using 2D Finite Element Mode. In: *Proc. of Computational Mechanics*. Plzeň: University of West Bohemia, pp. 103–106.

Pennacchi, P. and Vania, A. (2004) Accuracy in the identification of a generator thermal bow. *Journal of Sound and Vibration*, 274(1-2), pp. 273–295.

Smith, E. O. and Neely, A. (2013) Shaft thermal bow modelling in gas turbines-an initial study. In: *Proc. 21st International Symposium on Air Breathing Engines*, pp. 9–13.

Yuan, H. Q., Zhu, X. Z., Li, D. and Wen, B. C. (2009) Dynamic characteristics of transient thermal starting up of a rotor system. Zhendong yu Chongji, *Journal of Vibration and Shock*, 28(7), pp. 33–37.

30th International Conference
ENGINEERING MECHANICS 2024
Milovy, Czech Republic, May 14 – 16, 2024

ROLE OF SUBMEMBRANE SPACES IN THE CONTROL OF TRANSMEMBRANE ION FLUX AND CELLULAR INOTROPIC STATE IN A MODEL OF HUMAN VENTRICULAR CARDIOMYOCYTE

Pásek M.*, Bébarová M., Christé G.*****

Abstract: *We have recently developed a model of human ventricular cardiomyocyte incorporating the t-tubular and surface submembrane spaces and restricted ion exchange between these spaces and cytosol. After incorporating the experimental finding that majority of Na^+-Ca^{2+} exchanger proteins are located at the t-tubular membrane of human ventricular cardiomyocytes, we explored the consequences of ion concentration changes in the submembrane spaces on the electrophysiological activity of these cells. Consistently with the experimental and modelling studies published so far, our model predicts an increased Ca^{2+} extrusion during the action potential. However, our model also predicts a significant reduction of Ca^{2+} extrusion throughout the diastole, which can ultimately lead to an increase of cellular inotropy.*

Keywords: Human ventricular cardiomyocyte, t-tubules, submembrane spaces, submembrane Ca^{2+} gradient, Na^+-Ca^{2+} exchanger, mathematical model.

1. Introduction

In our previous modelling studies, we showed that activity-induced ion concentration changes in t-tubules and extracellular clefts of ventricular cardiomyocytes may be large enough to significantly modulate membrane ionic currents, cellular electrical activity, and cellular inotropic state (Pásek et al., 2003, 2006, 2008, 2012; Hrabcová et al., 2013). However, the magnitude and functional consequences of ion concentration changes that occur in submembrane spaces at the inner side of ventricular cardiomyocytes are still unclear. In 2002, Weber et al. found out that, upon excitation of ventricular cardiomyocyte, the transient increase of Ca^{2+} concentration (so-called Ca^{2+} transient) in intracellular submembrane spaces is substantially higher (>3.2 μM in peak value) than that in bulk cytosol (~1.2 μM). In their novel model of rabbit ventricular cardiomyocytes, Shannon et al. (2004) formulated a new submembrane compartment allowing proteins on the inner side of the membrane to sense ion concentrations that differ from those in the bulk cytosol. They showed that the elevated Ca^{2+} concentration in the submembrane spaces may substantially promote the Ca^{2+} extrusion from the myocyte via Na^+-Ca^{2+} exchanger. Nevertheless, a deeper analysis of the impact of ion concentration changes in the submembrane spaces on action potential (AP) and cytosolic Ca^{2+} transient (CaT_c) has not been done yet.

To fill this gap and translate the impact observed in the animal model to human cardiac electrophysiology, we used our recently published model of human ventricular cardiomyocyte (Synková et al., 2021). Our simulations revealed that the alterations of ion concentrations in the submembrane spaces may play a role in modulating the cellular electrical activity and inotropic state.

* Assoc. Prof. Michal Pásek, PhD.: Institute of Thermomechanics, Czech Academy of Science, Dolejškova 5; 182 00, Prague; CZ and Department of Physiology, Faculty of Medicine, Masaryk University, Kamenice 5; 62500; Brno; CZ, pasek.avcr@centrum.cz

** Assoc. Prof. Markéta Bébarová, PhD.: Department of Physiology, Faculty of Medicine, Masaryk University, Kamenice 5; 625 00; Brno; CZ, mbebar@med.muni.cz

*** Dr. Georges Christé.: Laboratoire de Neurocardiologie, EA4612, Université Lyon 1, F-69003; Lyon; F, christe.georges@laposte.net

doi: 10.21495/em2024-230

2. Methods

The schematic diagram of our model is illustrated in Fig. 1. The t-tubular fractions of ion transporters are the same as in the original published model (Synková et al., 2021) except for the t-tubular fraction of Na^+-Ca^{2+} exchanger ($f_{NaCa,t}$) that was increased from 0.56 to either 0.8 or 0.9 to respect the experimental finding by Hong et al. (2012) indicating that a great majority of Na^+-Ca^{2+} exchange proteins (roughly 80–90 %) are located at the t-tubular membrane in human ventricular cells. Our 2021 model already included the surface and t-tubular submembrane spaces (see Fig. 1) with time constants controlling the ion fluxes between them and the cytosol being $\tau_{ssc} = 2.8$ ms and $\tau_{stc} = 2.7$ ms, respectively. To reveal the physiological role of these spaces, we compared the simulations on the model with its modified version, in which their function was disabled by multiplying the time constants τ_{ssc} and τ_{stc} by a factor 10^{-6}.

The simulations were performed using the computational system MATLAB 7.2 (MathWorks, Natick, MA, USA) and the solver for stiff systems ODE-15s. To achieve a dynamic steady-state, the model was paced for 600 s of equivalent cell lifetime under all conditions. The standard ion concentrations in the extracellular bulk space $[Na^+]_b$, $[K^+]_b$, and $[Ca^{2+}]_b$ were set to 140, 5.4, and 2 mM, respectively. The basic units in which the equations were solved were mV for the membrane potential, mA for membrane currents, mM for ion concentrations, ml for volumes, and s for the time. The Matlab code of the model is available at https://www.it.cas.cz/en/d3/l033/.

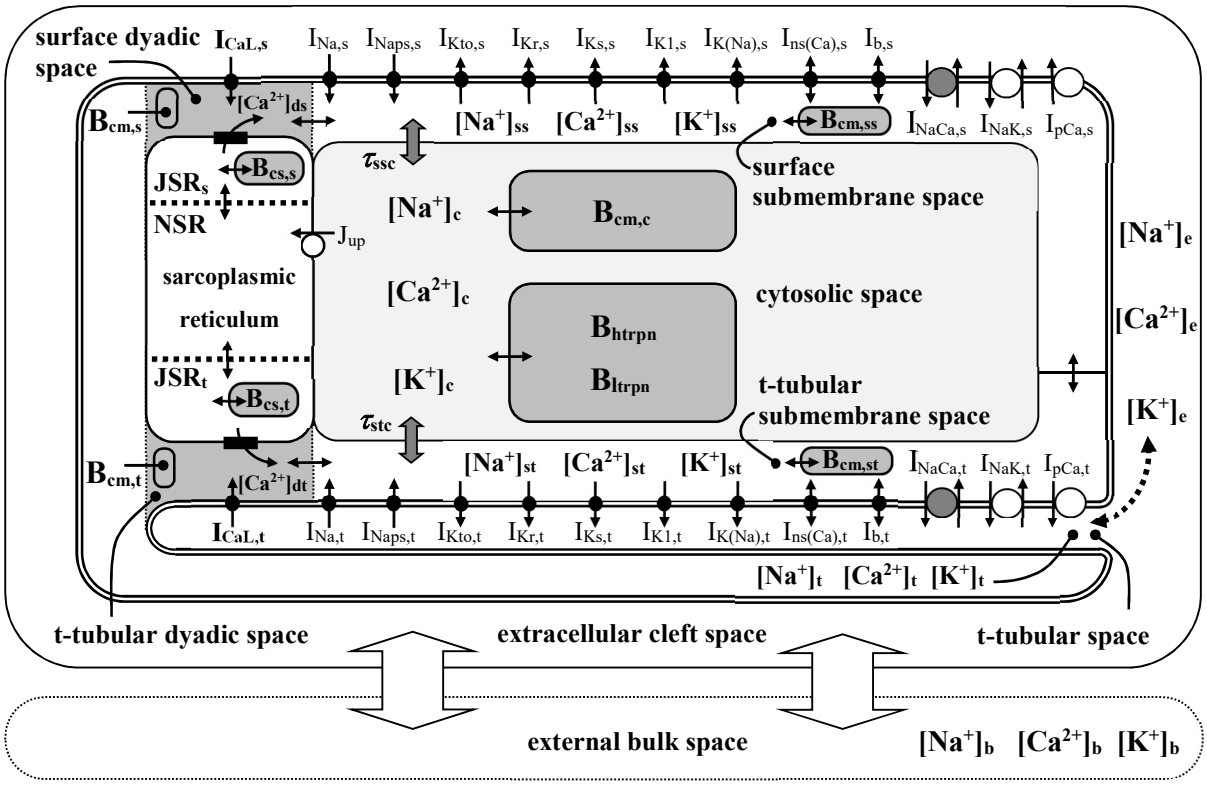

Fig. 1: Schematic diagram of the model of human ventricular cell. Description of electrical activity of the surface (s) and t-tubular (t) membranes comprises formulations of the following ion currents: fast sodium current (I_{Na}), persistent sodium current (I_{Naps}), L-type calcium current (I_{CaL}), transient outward potassium current (I_{Kto}), rapid and slow components of delayed rectifier potassium current (I_{Kr} and I_{Ks}), inward rectifying potassium current (I_{K1}), background currents (I_b), sodium-activated potassium current ($I_{K(Na)}$), calcium-activated non-specific current ($I_{ns(Ca)}$), sodium-calcium exchange current (I_{NaCa}), sodium-potassium pump current (I_{NaK}), and calcium pump current (I_{pCa}). The intracellular space contains the cytosolic space (c), surface and t-tubular submembrane spaces (ss, st), surface and t-tubular dyadic spaces (ds, dt), and network and junctional compartments of sarcoplasmic reticulum (NSR, JSR_s, JSR_t). J_{up} represents Ca^{2+} flow via SR Ca^{2+} pump and the small filled rectangles in JSR membrane ryanodine receptors. The small black and grey bi-directional arrows denote intracellular ion diffusion. Ion diffusion between the t-tubular and cleft spaces is represented by the dashed arrow, and between the cleft and external bulk spaces by the thick white arrows.

3. Results

Fig. 2 shows the simulated time course of APs, I_{Ca}, I_{NaCa}, $I_{ns(Ca)}$ and Ca^{2+} concentrations in NSR, surface and t-tubular submembrane spaces and cytosol in the original model versus the model with disabled function of both submembrane spaces. As follows from the figure, the presence of functional submembrane spaces led to a substantial increase of Ca^{2+} transients in these spaces (see the increase of amplitude in $[Ca^{2+}]_{ss}$ and $[Ca^{2+}]_{st}$) and, consequently, to the activation of inward I_{NaCa} and of $I_{ns(Ca)}$ at the beginning of AP. The activation of $I_{ns(Ca)}$ resulted in AP shortening (by 5.3 % at 90 % of repolarisation) and, consequently, to a slight decrease of Ca^{2+} intake via I_{Ca} (by 3.1 %). Despite that, the steady-state SR Ca^{2+} load at the end of the cycle and the peak value of CaT_c increased (by 11–16 % and 5.3–8.7 %, respectively, see the graphs of $[Ca^{2+}]_{NSR}$ and $[Ca^{2+}]_c$), which was the consequence of a lower inward I_{NaCa} during the diastolic phase of the stimulation cycle (see the less negative values of I_{NaCa} after the termination of AP). Hence, the performed simulations show that the limited Ca^{2+} diffusion between the submembrane spaces and cytosol in human ventricular cardiomyocytes underlies the substantially higher transient changes in $[Ca^{2+}]_{st}$ and $[Ca^{2+}]_{ss}$ versus those in $[Ca^{2+}]_c$, which promote the higher I_{NaCa}-mediated Ca^{2+} extrusion at the beginning of AP. On the other hand, after the termination of AP, the limited submembrane Ca^{2+} diffusion coupled with a high $f_{NaCa,t}$ (0.8 or 0.9) reduces the level of $[Ca^{2+}]_{st}$

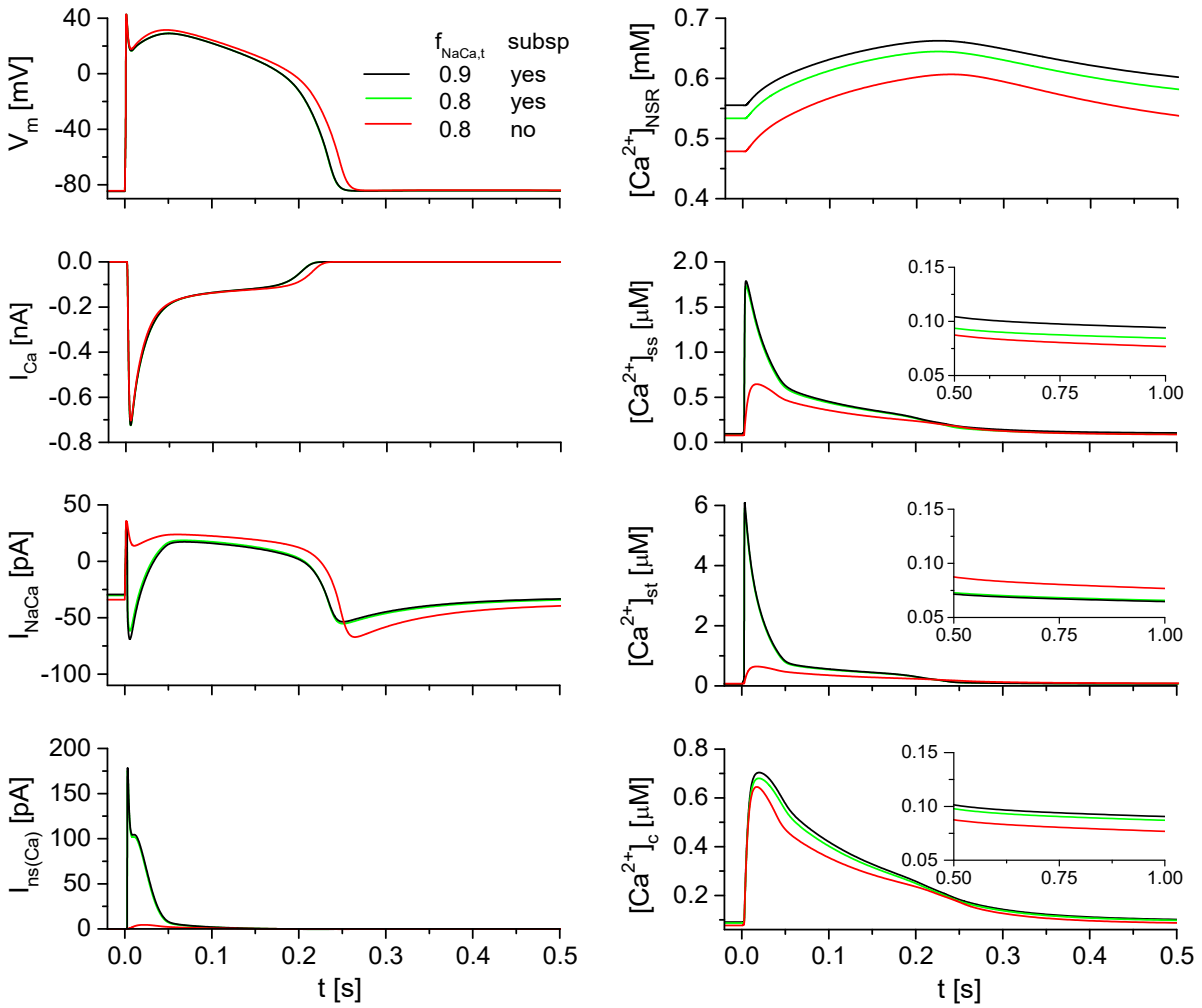

Fig. 2: Simulations of the action potential, I_{Ca}, I_{NaCa}, $I_{ns(Ca)}$, and of Ca^{2+} concentration changes in the network compartment of SR ($[Ca^{2+}]_{NSR}$), submembrane spaces (surface: $[Ca^{2+}]_{ss}$, t-tubular: $[Ca^{2+}]_{st}$), and in the cytosol ($[Ca^{2+}]_c$) during 0.5 s of 1 Hz steady-state stimulation cycle at $f_{NaCa,t}$ of 0.8 (green line) and 0.9 (black line) and at disabled function of the t-tubular and surface submembrane spaces (red line). The disablement of the function of both submembrane spaces was done by multiplying the corresponding time constants controlling the Ca^{2+} fluxes between them and cytosol, τ_{ssc} and τ_{stc}, by 10^{-6}. The insets represent the intracellular Ca^{2+} concentrations $[Ca^{2+}]_{ss}$, $[Ca^{2+}]_{st}$, and $[Ca^{2+}]_c$ at the end of the stimulation cycle.

(see the inset to $[Ca^{2+}]_{st}$ in Fig. 2) and, thus, the Ca^{2+} extrusion via $I_{NaCa,t}$. As the reduction of Ca^{2+} extrusion during the diastolic phase prevailed over its increase at the beginning of AP, the final effect of the changes in $[Ca^{2+}]_{st}$, as predicted by the model, was the increase of SR Ca^{2+} load and of the peak value of CaT_c (by 5–9 %) and, thus, the increase of cellular inotropy. Unlike for $[Ca^{2+}]$, the differences between submembrane and cytosolic $[Na^+]$ and $[K^+]$ during the whole cycle were small (< 2 % and 0.1 %, respectively, not shown) and appeared to have a negligible effect on cellular electrophysiology.

4. Discussion

The results of this study indicate that the ion concentration changes in the limited submembrane spaces of human ventricular cardiomyocytes induce a shortening of AP and an increase of CaT_c. While the shortening of AP was mainly caused by the activation of $I_{ns(Ca)}$ due to the higher submembrane Ca^{2+} transients, the mechanism of the increase of CaT_c was more complex. First, an increased Ca^{2+} extrusion via the Na^+-Ca^{2+} exchanger was apparent in our model in agreement with the published data from rabbit cardiomyocytes (Weber et al., 2002, Shannon et al., 2004). This was due to strong submembrane Ca^{2+} concentration gradients induced by Ca^{2+} induced Ca^{2+} release from the junctional SR at the beginning of the simulated AP. Second, after the termination of AP, the lower concentration of Ca^{2+} in the t-tubular submembrane space caused a reduction of Ca^{2+} extrusion via the Na^+-Ca^{2+} exchanger. This opposite effect during the diastolic phase of the stimulation cycle ultimately led to an increase of SR Ca^{2+} load and CaT_c. Thus, according to the model, the combination of limited Ca^{2+} diffusion between the t-tubular submembrane space and cytosol with predominant localisation of the Na^+-Ca^{2+} exchanger at the t-tubules underlies the formation of submembrane Ca^{2+} concentration gradient that increase the inotropic state of human ventricular cardiomyocytes.

Acknowledgement

This study was realized with the institutional support RVO: 61388998 and with the support of the grant project NU22-02-00348 from the Ministry of Health of the Czech Republic.

References

Hong, T. T., Smyth, J. W., Chu, K. Y., Vogan, J. M., Fong, T. S., Jensen, B. C., Fang, K., Halushka, M. K., Russell, S. D., Colecraft, H., Hoopes, C. W., Ocorr, K., Chi, N. C. and Shaw, R. M. (2012) BIN1 is reduced and Cav1.2 trafficking is impaired in human failing cardiomyocytes. *Heart Rhythm*, 9, pp. 812–820.

Hrabcová, D., Pásek, M., Šimurda, J. and Christé, G. (2013) Effect of ion concentration changes in the limited extracellular spaces on sarcolemmal ion transport and Ca^{2+} turnover in a model of human ventricular cardiomyocyte. *International Journal of Molecular Sciences*, 14, pp. 24271–24292.

Pásek, M., Christé, G. and Šimurda, J. (2003) A quantitative model of the cardiac ventricular cell incorporating the transverse-axial tubular system. *General Physiology and Biophysics*, 22, pp. 355–356.

Pásek, M., Šimurda, J. and Christé, G. (2006) The functional role of cardiac T-tubules explored in a model of rat ventricular myocytes. *Philosophical Transactions of The Royal Society A*, 364, pp. 1187–206.

Pásek, M., Šimurda, J. and Orchard, C. H. and Christé, G. (2008) A model of the guinea-pig ventricular cardiac myocyte incorporating a transverse-axial tubular system. *Progress in Biophysics and Molecular Biology*, 96, pp. 258–280.

Pásek, M., Šimurda, J. and Orchard, C. H. (2012) Role of t-tubules in the control of trans-sarcolemmal ion flux and intracellular Ca^{2+} in a model of the rat cardiac ventricular myocyte. *European Biophysics Journal*, 41, pp. 491–503.

Shannon, T. R, Wang, F., Puglisi, J., Weber, C. and Bers, D. M. (2004) A mathematical treatment of integrated Ca dynamics within the ventricular myocyte. *Biophysical Journal*, 87, pp. 3351–3371.

Synková, I., Bébarová, M., Andršová, I., Chmelikova, L., Švecová, O., Hošek, J., Pásek, M., Vít, P., Valášková, I., Gaillyová, R., Navrátil, R. and Novotný, T. (2021) Long-QT founder variant T309I-Kv7.1 with dominant negative pattern may predispose delayed afterdepolarizations under β-adrenergic stimulation. *Scientific Reports*, 11, 3573.

Weber, C. R., Piacentino, V., Ginsburg, K. S., Houser, S. R. and Bers, D. M. (2002) Na^+-Ca^{2+} exchange current and submembrane $[Ca^{2+}]$ during the cardiac action potential. *Circulation Research*, 90, pp. 182–189.

30th International Conference
ENGINEERING MECHANICS 2024
Milovy, Czech Republic, May 14 – 16, 2024

DEGEREE OF SUSCEPTIBILITY OF THE GAS-BEARING COAL MASSIF TO CHANGES UNDER VIBRATION AND TECHNICAL SOLUTIONS FOR INCREASING METHANE EXTRACTION FROM THE RESERVOIR

Pavlenko M. V.*

Abstract: *Application of the vibration effects for effective preparation of a low-permeability coal seam is a promising process, which requires to be continuously improved. The main difficulty of the theoretical research in this area is that the coal seams are very diverse in their properties and represent complex environment. During the vibration action, their volume and filtration characteristics change, which leads to the change of the massif structure and amount of the pore-crack space in the coal. This effect can be controlled.*

Keywords: Coal mass, vibration impact, permeability, methane, impact array, microcracks.

1. Introduction

Destabilization of a coal massif caused by vibration of the formation is highly sensitive to changes of external factors (Asomov, 1960). Control of the process parameters is crucial for increasing methane recovery from the reservoir. The discussed method estimates spatial variability of the vibration and identification of the directional variability of the coal massif properties. A great interest in technologies for increasing fracturing in the coal massif has formed the research direction.

Considering this effect, it is possible to choose a proper frequency and amplitude of the vibration process acting on the formation, which leads to the growth of cracks in low-permeability coal (Jia et al., 2012). Despite a large amount of experimental information, the degree of susceptibility of the coal massif to changes of the vibration parameters and the wave propagation in the coal seam remains poorly understood (Pavlenko, 2022). The phenomena occurring both in pores and in micropores of a low-permeable coal massif have not been sufficiently studied by experimental methods, yet. At the same time, it is necessary to pay a special attention to the problematic areas of the coal deposits in promising fields considering the technical possibilities.

2. Technological solution

The research focuses on the mechanism of vibration action at frequencies that induce resonance in the coal seam and ensure creation of the most favorable conditions for emerging new crack systems, which makes the stable methane recovery from the coal massif possible. Accomplishing the process requires to build up the proper organizational procedures.

The procedure concerning increase of methane recovery from a low-permeability coal massif consists in a sequence of technological solutions and means with the goal to ensure maximum purposefulness and effectiveness of the process. The key factor, which follows preparation of the coal seam for safe and effective exploitation, is the type of management activity reflecting a set of priorities playing the role in formation of the impact on a low-permeable gas-saturated coal massif. Next, using vibration of the low

* Prof. Mikhail Pavlenko, PhD.: NUST (MISiS), National research technological University, Moscow Institute of Steel and Alloys (Mining Institute). Moscow Russia, mihail_mggy@mail.ru

doi: 10.21495/em2024-234

frequency range is investigated. Organization of the management decisions is determined primarily depending on geological conditions of the underlying reservoir and on the vibration parameters, which are also important.

Initially, the experimental studies of the vibration effect on the K-2 gas-bearing coal seam of the Victoria mine in Donbass were carried out using the underground vibration wells in the frequency range from 1 to 100 Hz. The resonant frequencies, at which the maximum cracking and gas release from the coal massif was observed, were determined to 7–14 Hz.

Fracturing and gas permeability of a coal massif are characterized by two different states. It was found that the response of the coal massif on the vibration action is appearance of new cracks and their branching in the form of the blocks (Fig. 1).

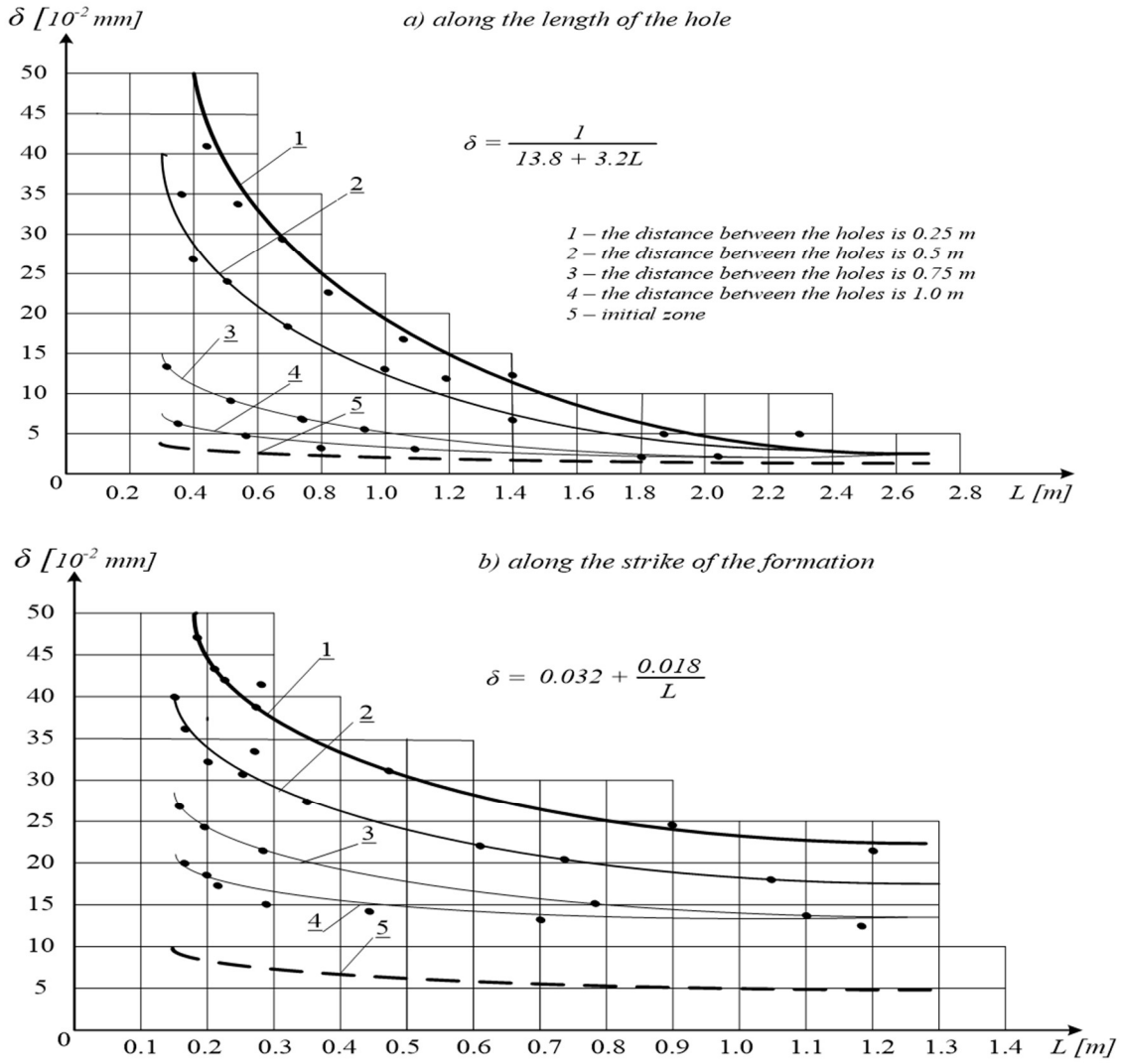

Fig. 1: Nature of changes in the gaping of microcracks of the K-2 formation of the Victoria mine in Donbass from the length of the hole during vibration.

The conducted studies in the field of the Victoria mine in Donbass were aimed at investigation of the nature and rate of the gas recovery during the transition from the zones without and with the vibration treatment.

The results show a clear difference in the process rate if the new system of cracks appears. The study shows that the vibration effect increases diffusion and filtration permeability of the formation by 3–5 times and the degree of permeability and softening of the array rises as well as the gas-releasing capacity. It leads to the conclusion that the new crack systems in the impact zone allow methane to be more intensively drained from the coal bed and ensure successful degassing of the treatment site (Fig. 2). The study also confirms

the assumption that it is possible to achieve a directional change of the coal seam properties (e.g. the massif permeability) leading to increase of the gas recovery.

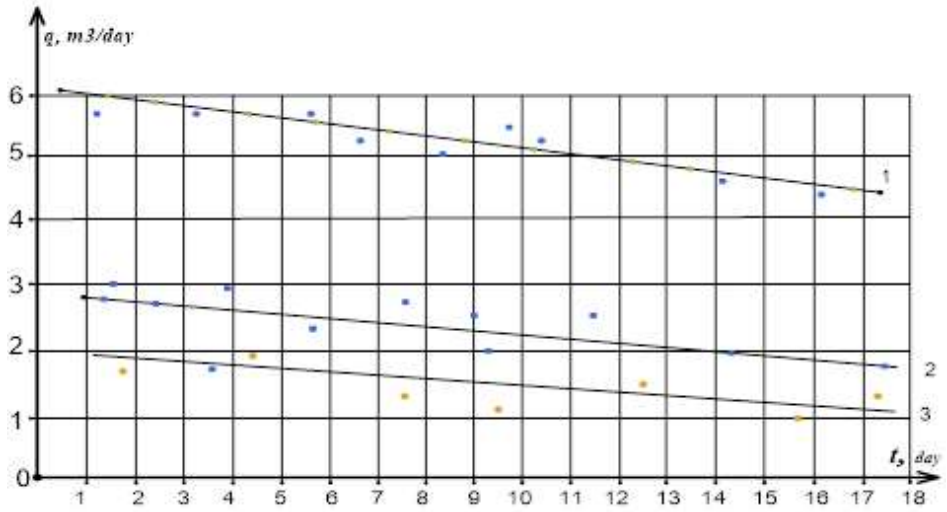

Fig. 2: The rate of gas recovery of the K-2 formation into the holes in the vibration area.

Further research is required in the field of the vibration technology. The study will focus on application of hydraulic vibrators (Fig. 3) whose principle of work is based on generation of pressure fluctuations that propagate in porous medium filled with liquid and lead to occurrence of new systems of cracks and microcracks in the coal massif and to destruction of its spatial structure. The working fluid makes the vibrator barrel to rotate providing the pulse frequency from 10 to 150 Hz and the pressure amplitude from 1 to 10 MPa. The cone reflector focuses the generated pulse, which increases impact of the transmitted energy on the formation.

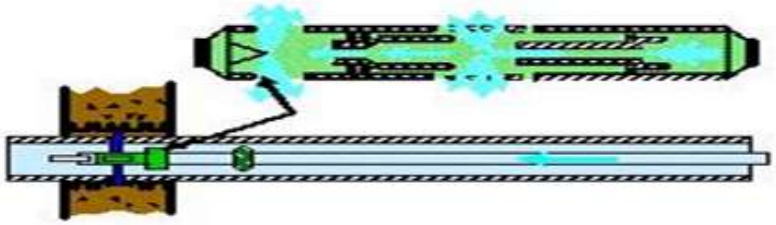

Fig. 3: Hydraulic vibrator in a coal seam.

The fluctuations of the pressure generated by vibrators spreading in the porous medium and fluid reservoirs give rise to new systems of cracks and microcracks in the coal massif and to destruction of its the spatial structure. The mobility of the water-methane interface increases, the surface tension of the liquid at the boundary with the solid surface decreases, and the rate of capillary impregnation of water in the coal structure rises. The pressure fluctuations in the flooded reservoir contribute to intensification of the coal impregnation processes, which leads to increase of the absorption capacity of the hydraulic injection wells and to appearance of a new crack system.

The technological scheme of the vibration device in a coal massif intended for experiments corresponding to the technological solutions for preparing a gas-bearing coal massif for intensive mining is shown in Fig. 4.

On one hand, the vibration, which is a part of the destabilization process of the coal massif, is affected by external conditions and factors. On the other hand, the methane release from the coal seam has its own dynamics, which provides different possibilities for maintaining stability of the process.

The scientific concept of destabilization in the coal-methane system consists in action of external active factors, namely vibration.

At the same time, the vibration effect of the coal massif is induced both through the surface and underground wells, which influences the process of intensification of the methane recovery. These vibration effects are going to be considered in the next stage of the study related to increasing permeability under the influence of the vibration sources.

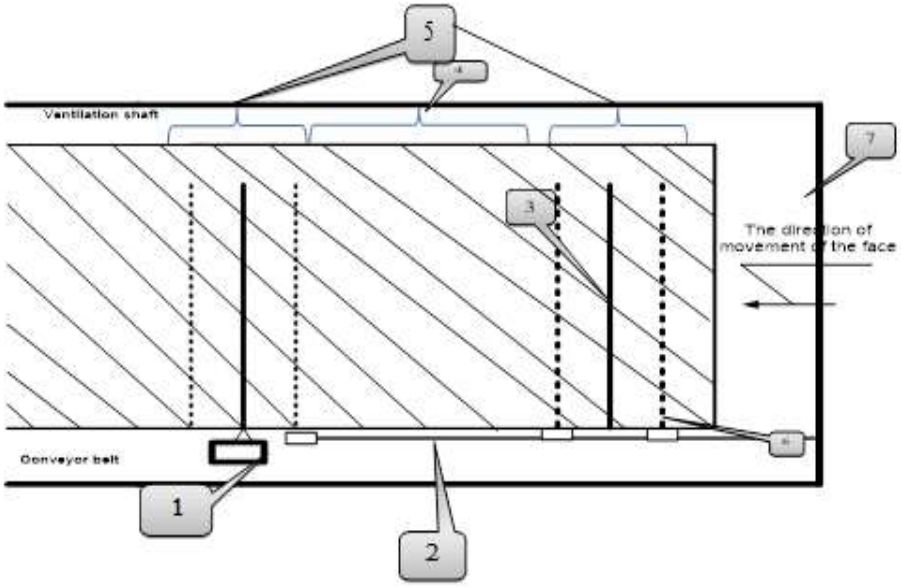

Fig. 4: Scheme of vibration action on the coal seam through underground wells: 1 - vibration oscillator; 2 - degassing pipeline from degassing wells; 3 - vibration wells; 4 - comparison zones (length 300–400 m); 5 - vibration treatment zones of coal seam; 6 - formation degassing wells; 7 - mounting chamber 10–20 m long.

According to the results of the field studies conducted in the mine field, the vibration method is an effective one of exposure. It leads to increase of the methane recovery in the zone of fractured coal forming a block of massif of low-permeability coal seam. The excavation is done at certain frequencies close to the formation resonant ones. If the natural frequency of the coal-liquid system coincides with the frequency of the field vibration, then the resonance occurs, and the energy of vibration is transformed to kinetic energy of the liquid in the formation, which leads to development of cracks.

3. Conclusions and discussion

The paper examines patterns of fracturing under vibro-wave action in conditions of heterogeneous state of stress of a coal seam before formation of the additional crack systems during in advanced prepared coal massif. From a scientific point of view, it is important to understand why the penetration of the pressure waves into the coal seam leads to increase and intensification of the methane recovery from the coal mass. A vibration method is proposed to ensure structural disruption and formation of additional systems of gas-conducting cracks in a coal seam. Its efficiency depends on the vibration frequency, considering the resonant ones of the array of fractured blocks. This predicts intensity of methane extraction from coal.

The specified method increases impact on the formation, which depends on the power of the used vibration source. The further development of the vibration method leads to increase of its efficiency in the field of degassing. The process does not depend only on the intensification factors, but also on meeting the requirements of the correct choice of active exposure technology. The process of increasing magnitude and number of the crack openings during the vibration is achieved not only by the frequency of exposure, but also by the time of action on the coal massif. This is utilized in the pore space.

It should be noted that in this case the wave pulse completely produced by the vibratory device causes changes in the coal massif. Consequently, the vibration in the coal seam causes changes in the stress-strain state of the array, which has additional effect on the permeability and porosity of the array.

References

Amosov, I. I. and Eremin I. V. (1960) *Fracturing of coals*. Iyd. Akad. Nauk SSSR, 100 p. (in Russian).

Jia, P., Tang, C. A., Zhang, Y. B. (2012) Numerical study on zonal disintegration of rock mass around deep underground openings, In: *Proc. of the 12th ISRM International Congress on Rock Mechanics*, CRC Press, pp. 179–180.

Pavlenko, M. V., Bazarov, B. A., Konakbayeva, A. N., Mezentseva, A. V. (2022) The effect of mechanical vibrations on a gas-saturated coal massif as a deformable system. *Ugol Magazine*, 4, pp. 46–49.

30th International Conference
ENGINEERING MECHANICS 2024
Milovy, Czech Republic, May 14 – 16, 2024

ENHANCING MEDICAL INSIGHTS THROUGH COMPUTATIONAL FLUID DYNAMICS: VALIDATING SIMULATION MODEL FOR BLOOD FLOW IN VASCULAR SYSTEM

Ples M.*, Wolański W., Sobkowiak M.*****

Abstract: *Understanding blood flow dynamics within the intricate network of blood vessels is crucial for advancing medical diagnostics and interventions. Computational methods, particularly Computational Fluid Dynamics (CFD), have emerged as powerful tools for studying blood flow behavior, offering invaluable insights into hemodynamic parameters and various physiological conditions. However, the utility of computational simulations in clinical decision-making relies on their accuracy and reliability, necessitating rigorous validation. In this paper, we describe a method of validating shear stress simulation on blood vessel walls by comparing it with a physical erosive model. The parametric arterial model was created in ANSYS, using morphometric parameters obtained from Murray's law. The model was simulated with non-Newtonian blood properties and a constant velocity. A physical model was created using 3D printing and tested under similar flow conditions. Results show agreement between simulated and physical models, confirming the efficacy of computational simulations in understanding vascular physiology and pathology. This underscores the need for continued validation and refinement to maximize their clinical utility.*

Keywords: Computational Fluid Dynamics (CFD), wall Shear Stress (WSS), validation, artery, blood flow.

1. Introduction

Understanding blood flow dynamics within the intricate network of blood vessels is crucial for advancing medical diagnostics and interventions (Nichols et al., 2012). Over the years, computational methods, particularly Computational Fluid Dynamics (CFD), have emerged as powerful tools for studying blood flow behavior. These methods offer invaluable insights into the hemodynamic parameters governing blood flow, providing a deeper understanding of various physiological and pathological conditions. By virtually replicating the complex fluid dynamics within blood vessels, CFD facilitates the exploration of flow patterns, shear stresses, and pressure distributions, offering predictive capabilities for assessing vascular pathologies such as atherosclerosis, aneurysms, and thrombosis. However, while computational simulations hold immense promise, their utility in clinical decision-making hinges upon their accuracy and reliability. As such, the validation of these simulations becomes paramount. Validating CFD models involves comparing simulated results with empirical data obtained from *in vivo* or *in vitro* experiments, ensuring that the computational predictions align with real-world observations. Furthermore, the development of physiologically accurate models is essential for bolstering the credibility of CFD simulations. Incorporating realistic anatomical geometries, tissue properties, and boundary conditions into these models is imperative to mimic physiological conditions faithfully. Additionally, refining computational algorithms to accurately capture fluid-structure interactions and biological phenomena further enhances the fidelity of simulations.

* Marek Ples MSc: Department of Biomechatronics of Silesian University of Technology, PL, marek.ples@polsl.pl

** Wolanski Wojciech BEng, PhD., DSc.: Department of Biomechatronics of Silesian University of Technology, PL, wojciech.wolanski@polsl.pl

*** Marta Sobkowiak PhD., Eng: PL, marta.sobkowiak.pilorz@gmail.com

doi: 10.21495/em2024-238

In this paper, we will describe a simple method of validating the simulation of shear stress acting on the walls of blood vessels by comparing it with a simple physical erosive model developed by us. Through this discussion, we aim to underscore the key role of computational simulations in deepening our understanding of vascular physiology and pathology, while simultaneously emphasizing the critical need for rigorous validation and refinement of simulation models to maximize their utility in clinical practice.

2. Methods

The analysis was performed on parametric arterial model created in ANSYS environment. Morphometric parameters were obtained using the Murray's law (1), which tells about maintaining the lowest possible energy during flow. This law refers to both the division of angles and the radii of individual inlet r_0 and outlets r_1, r_2.

$$r_0^n = r_1^n + r_2^n \quad (1)$$

The flow is most energy-efficient when given exponent n is 3 (Murray, 1926).

Having the arterial morphometric data, the parametric model was modelled in ANSYS Design Modeler software. Boundary conditions, as well as parameters of the inflationary layer was setted. The inflationary layer consists of six layers (0.0075 mm high). Properties of the artificial blood to be simulated as non-newtonian liquid (Bird-Carreau Model, Bird et al., 1987), with molar mass: 18.02 kg/kmol, density: 1 050 kg/m^3, thermal capacity: 4 181.7 J/kg.K and viscosity: 0.0035 Pa.s. In the simulations the constant blood velocity Vs = 0.45 m/s was used. The model prepared in this way was simulated. The optimal bifurcation angle calculated in the previous simulations was used (Wolański et al., 2018).

The physical model of the vessel was created using the 3D printing technique FDM with the Czech company Prusa's i3 MK3 printer. ABS material was used for the inner mold with standard printing parameters (0.4 mm nozzle, hotend temperature – 225 °C, hotbed temperature – 90 °C). The printed mold was then coated externally with transparent chemically-cured epoxy resin. After the resin cured, the inner mold was dissolved using acetone. The next step involved applying a thin layer (0.1−0.2 mm) of water-soluble poly(vinyl alcohol) plastic on the inner walls of the vessel model with bifurcation. The vessel was then subjected to a circulation loop simulating flow conditions similar to those in the aforementioned simulation in the ANSYS environment.

3. Results

The simulation result of Wall Shear Stress (WSS) values is illustrated in Fig. 1, while the simulation result using the physical method is shown in Fig. 2.

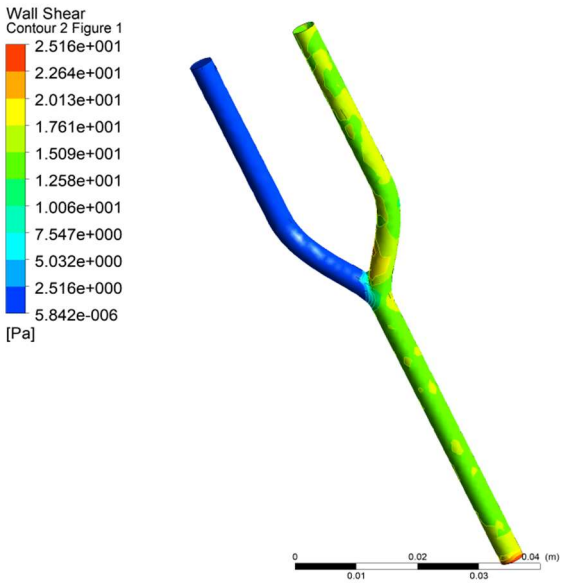

Fig. 1: WSS simulated in silico.

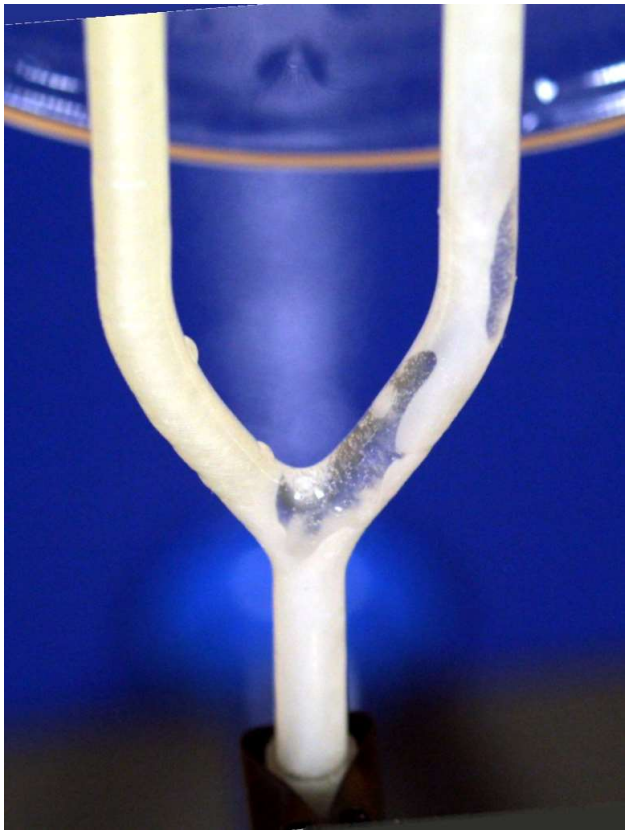

Fig. 2: Effect of physical simulation.

It can be clearly observed that in the areas where the numerical method predicts the highest WSS values, the water-soluble material in the physical model undergoes the fastest dissolution, indirectly confirming the actual highest WSS values at those points (Fig. 3).

The experiment's outcome appears to confirm the convergence of the effects of computer-based simulations (*in silico*) with simulations utilizing real physical effects in the real world.

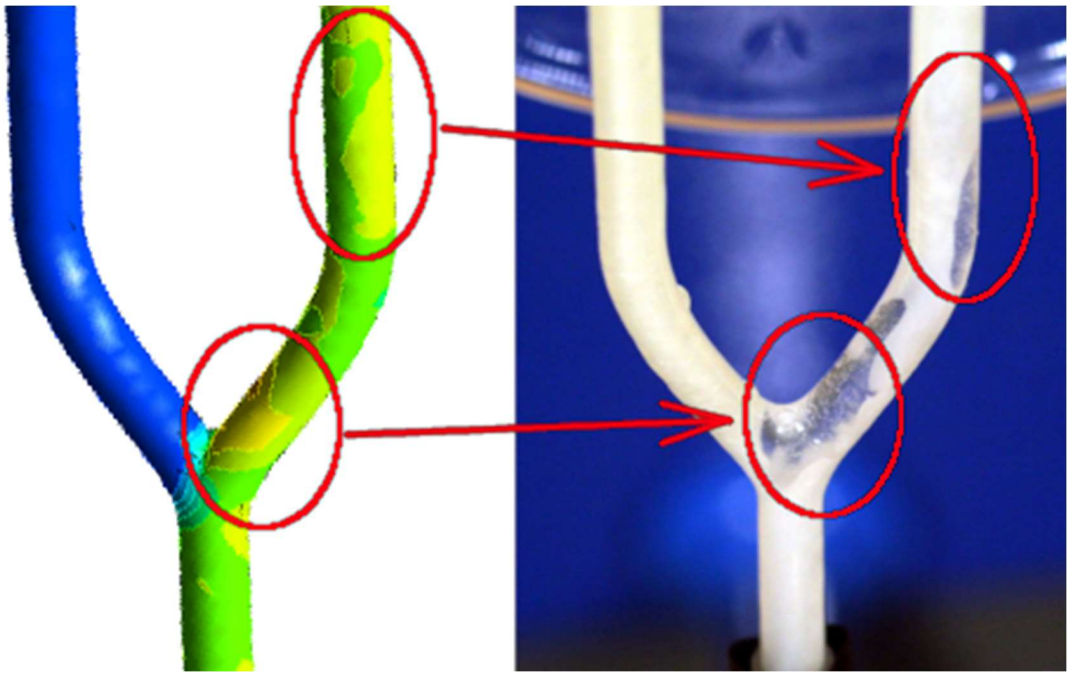

Fig. 3: Comparison effect of in silico and physical simulation results.

4. Conclusions

The presented physical method has demonstrated its efficacy in facilitating rapid validation of computer simulations of blood flow through bifurcated blood vessels. This approach ensures a robust comparison between simulated and observed phenomena, enhancing the accuracy and reliability of computational models in biomedical research and clinical applications. The ability to validate computational simulations with experimental data strengthens confidence in their predictive capabilities and fosters advancements in understanding complex physiological processes, ultimately benefiting medical diagnostics and treatment strategies.

References

Bird, R. B., Armstrong, R. C. and Hassager, O. (1987) *Dynamics of polymeric liquids*. vol. 1. Fluid mechanics, 2nd ed. John Wiley & Sons, New York

Murray, C. D. (1926) The Physiological Principle of Minimum Work: I. The Vascular System and the Cost of Blood Volume. *Proc. of the National Academy of Sciences of the United States of America*. 12 (3) pp. 207–214

Nichols, M. et al. (2012) European Cardiovascular Disease Statistics 2012. *European Heart Network*, Brussels, European Society of Cardiology, Sophia Antipolis.

Wolański, W., Gzik-Zroska, B., Joszko, K., Kawlewska, E., Sobkowiak, M., Gzik, M. and Kaspera, W. (2018) Impact of Vessel Mechanical Properties on Hemodynamic Parameters of Blood Flow. In: *Innovations in Biomedical Engineering, Proceedings IiBE 2017*, Cham: Springer, 271–278.

30th International Conference
ENGINEERING MECHANICS 2024
Milovy, Czech Republic, May 14 – 16, 2024

INVESTIGATION OF THE EFFECT OF SURFACE TEXTURING IN HYDRODYNAMIC SLIDING CONTACTS

Polach P.[*], Smolík L.[**], Byrtus M.[***], Hajžman M.[†]

Abstract: *Hydrodynamic lubrication is an effective method for connecting various relatively moving structural components in engines, rotors, manipulators, and other systems. Surface texturing can enhance the performance of such contacts. Initially, a theoretical framework for modeling textured surfaces of journal bearings is introduced, which is then employed to analyze the dynamic behavior of rotors. Additionally, a pin-on-disc approach for determining the properties of a lubricated textured surface is presented. The objective of utilizing the pin-on-disc method is to enhance computational models of lubricated textured pins by comparing experimental measurements with numerical simulation results. The knowledge gained can be applied to optimize parameters in computational models of hydrodynamic contact for textured surfaces in various applications, such as the model presented for journal bearings.*

Keywords: Hydrodynamic lubrication, textured surface, journal bearing, pin-on-disc method.

1. Introduction

Hydrodynamic sliding contacts are often found in various mechanical components. These are, for example, journal and thrust bearings, piston rings, and thrust washers and seals. Low friction, high load-carrying capacity, and long service life are the main goals in developing these contacts. One of the most important directions of development is surface texturing.

A large number of studies have been written and have reported a positive contribution of surface texturing since the 1960s when the first evidence of positive effect was found by Hamilton et al. (1966). There are various positive contributions of targeted surface modifications. Generally speaking, it is believed that surface dimples can help to supply the contact with lubricant, entrap wear particles, and reduce the direct contact area and level of adhesion. In a hydrodynamic regime, dimples can increase load-carrying capacity thanks to local cavitation with asymmetric pressure distribution or inertia-related effects (Gropper et al., 2012; Lu and Wood, 2020).

As indicated, surface texturing is one important approach to improving the tribological performance of hydrodynamic contacts. A certain problem is that the effect of the texture strongly depends on a large number of contacts and operating parameters concerning the mode in which the lubricated contact works. There is also texture coupling to wall slip, cavitation, thermal effects, etc. It should be noted that a positive effect under certain conditions can therefore become detrimental under other conditions.

Based on the comparison of experimental and simulation results in the field of textured journal bearings (which we mainly focus on), despite the careful construction of computational models, discrepancies appear

[*] Assoc. Prof. Dr. Ing. Pavel Polach: New Technologies for the Information Society, European Centre of Excellence, University of West Bohemia, Univerzitní 8; 306 14, Plzeň; CZ, ppolach@ntis.zcu.cz

[**] Ing. Luboš Smolík, PhD.: New Technologies for the Information Society, European Centre of Excellence, University of West Bohemia, Univerzitní 8; 306 14, Plzeň; CZ, carlist@ntis.zcu.cz

[***] Assoc. Prof. Ing. Miroslav Byrtus, PhD.: Department of Mechanics, Faculty of Applied Sciences, University of West Bohemia, Univerzitní 8; 306 14, Plzeň; CZ, mbyrtus@kme.zcu.cz

[†] Assoc. Prof. Ing. Michal Hajžman, PhD.: Department of Mechanics, Faculty of Applied Sciences, University of West Bohemia, Univerzitní 8; 306 14, Plzeň; CZ, mhajzman@kme.zcu.cz

doi: 10.21495/em2024-242

in the results achieved. The differences arise from the complex interplay of the above-mentioned influences on the behavior of the hydrodynamic contact. Legitimate doubts may arise regarding the quantitative experimental reproducibility of published theoretical work on fluid-induced instability, indicating the need for further research in this field. Some of the mentioned effects can be experimentally measured and computationally modeled on a simpler system than a journal bearing. The experimental laboratory pin-in-disc method offers a means to explore the tribological properties of textured hydrodynamic contact under diverse conditions. The knowledge gained from the modeling of this simpler system can subsequently be applied to the modeling of real textured journal bearings.

A theoretical approach to modeling textured surfaces for the journal bearings case is presented in Chapt. 2 of this paper. A pin-on-disc method used to determine the effect of different texture configurations on the tribological properties of the contact is presented in Chapt. 3.

2. A theoretical approach to the modeling textured surfaces for the case of journal bearings

This section presents a model appropriate for simulating the dynamics of a rotor that is supported by a textured journal bearing (see Fig. 1).

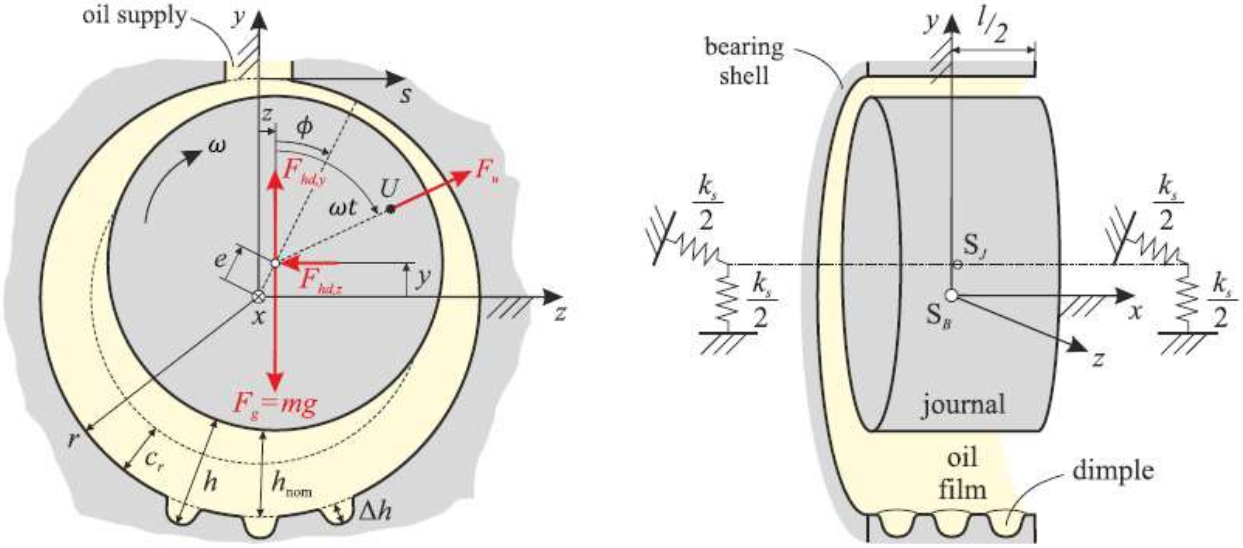

Fig. 1: The geometry of a journal bearing with a textured shell (taken from Smolík et al., 2023).

2.1. Equations of motion

It will be assumed that the mass m of the rotor is supported by a journal bearing rotating at an angular speed ω. The rotor is subjected to hydrodynamic forces, out-of-balance forces, and gravitational force. The motion of the rotor can be expressed, for instance, as shown by Smolík et al. (2023), by the equations

$$\begin{bmatrix} m & 0 \\ 0 & m \end{bmatrix} \begin{bmatrix} \ddot{y}(t) \\ \ddot{z}(t) \end{bmatrix} + \begin{bmatrix} k_s & 0 \\ 0 & k_s \end{bmatrix} \begin{bmatrix} y(t) \\ z(t) \end{bmatrix} = \begin{bmatrix} U\cos(\omega t) \\ U\sin(\omega t) \end{bmatrix} + \begin{bmatrix} F_{\mathrm{hd},y}(\dot{y},\dot{z},y,z) \\ F_{\mathrm{hd},z}(\dot{y},\dot{z},y,z) \end{bmatrix} + \begin{bmatrix} -mg \\ 0 \end{bmatrix} \tag{1}$$

where k_s is the artificial stiffness of the system, which includes the stiffness of auxiliary bearings, shaft, and shaft coupling to the drive, U is the static unbalance of the rotor, g is the gravitational acceleration, $\ddot{y}(t)$, $\ddot{z}(t)$ are the accelerations in the direction of the respective axes and $F_{\mathrm{hd},y}(\dot{y},\dot{z},y,z)$, $F_{\mathrm{hd},z}(\dot{y},\dot{z},y,z)$ are components of the hydrodynamic forces (see Sect. 2.2).

Equations of motion (1) are the same for rotors with textured and non-textured bearings. The influence of the texture is reflected only when hydrodynamic forces are determined (see Sect. 2.2).

Equations of motion are usually solved by one of the numerical integration methods.

2.2. Hydrodynamic forces

The hydrodynamic force acting in the journal bearing is determined by the hydrodynamic pressure $p = p(s,x,t)$ developed within the oil film. The lateral hydrodynamic force acting on the rotor is obtained by integrating p over the bearing surface

$$\begin{bmatrix} F_{\mathrm{hd},y}(\dot{y},\dot{z},y,z) \\ F_{\mathrm{hd},z}(\dot{y},\dot{z},y,z) \end{bmatrix} = -\int_{-l/2}^{l/2}\int_{0}^{2\pi} p(s,x,t) \begin{bmatrix} \cos\left(\frac{s}{r}\right) \\ \sin\left(\frac{s}{r}\right) \end{bmatrix} \mathrm{d}s\mathrm{d}x, \tag{2}$$

where s and x are circumferential and axial coordinates relative to the bearing shell, r is the radius of the bearing shell and l is the length of the bearing (see Fig. 1).

The most common approaches to simulate hydrodynamic lubrication in textured journal bearings depend on a numerical solution of the Reynolds equation (Gropper et al., 2012) which governs the pressure distribution $p = p(s,x,t)$ in a thin two-dimensional fluid film. The precise formulation of the equation that governs the pressure distribution in the oil film relies on simplifying assumptions. In this context, it is assumed that the oil film comprises an incompressible Newtonian fluid, laminar flow occurs within the film, and only the bearing shell is textured (see Fig. 1). Consequently, the pressure distribution is described by the Reynolds equation as outlined by Stachowiak and Batchelor (2013)

$$\frac{\partial}{\partial s}\left(\frac{h^3}{\mu}\frac{\partial p}{\partial s}\right) + \frac{\partial}{\partial x}\left(\frac{h^3}{\mu}\frac{\partial p}{\partial x}\right) = 6\omega r\frac{\partial h}{\partial s} + 12\frac{\partial h}{\partial t}, \tag{3}$$

where $\mu = \mu(s,x,t)$ is the dynamic viscosity of the oil and $h = h(s,x,t)$ is a gap between the journal and the shell, comprising the combination of nominal gap $h_{\mathrm{nom}} = h_{\mathrm{nom}}(s,t)$, and local deviation $\Delta h = \Delta h(s,t)$ caused by surface texture. It is presumed that all dimples are relatively smooth, meaning there are no abrupt variations in the bearing gap. If both the journal and the shell are circular, nominal gap h_{nom} is defined as

$$h_{\mathrm{nom}} = c_r - e\cos\left(\frac{s}{r} - \phi\right), \tag{4}$$

where c_r is the radial clearance of the bearing, $e = e(t) = \sqrt{y(t)^2 + z(t)^2}$ is the eccentricity and $\phi = \phi(t) = \mathrm{atan2}\left(\frac{z(t)}{y(t)}\right)$ is the attitude angle.

The Reynolds equation is usually solved by the finite difference method, but the finite element and volume methods are also common (Gropper et al., 2012).

3. Pin-on-disc method

To understand the local effects of texture on tribological properties, direct experimental observation of the contact is invaluable. In recent years, researchers have utilized high-speed cameras to observe cavitation phenomena in various surface textures, including a parallel thrust bearing (Cross et al., 2012; Bai et al., 2016), and in a pin-on-disc setup (Hsu et al., 2014). Optical techniques are also suitable for accurately measuring lubricant film thickness. Although these are widely established for lubricant film thickness mapping in point contacts (e.g. Křupka and Hartl, 2007), the number of studies applying these methods to hydrodynamic contacts is very limited (Vladescu et al., 2015).

The pin-on-disc experimental arrangement, involving a small pin interfacing with a rotating disc, is a prevalent technique employed in tribological investigations. Through this approach, crucial tribological parameters such as transmitted forces, oil film height, temperature, etc., can be examined and documented. Initially, it is imperative to establish the experiment's configuration accurately to ensure proper measurement of all essential variables. Subsequently, the creation, solution, and analysis of an appropriate mathematical model constitute the second step.

An experimental approach developed at the Department of Tribology Brno University of Technology, which uses optical methods, was used to study the film thickness, the load-carrying capacity of the contacts, and the influence of the various shapes, locations and geometry of texture (in this case the dimples). The experimental test rig is presented by Hajžman et al. (2023).

The mathematical model used for modeling and simulating measurements on the experimental test rig is based on the Navier-Stokes equation, and the numerical solution using the finite element method is implemented in the COMSOL software. The computational models are refined based on the validation of simulation results with the results of experimental measurements. Typical numerical results in the form of temperature and pressure fields for one of the textured pins are shown in Fig. 2.

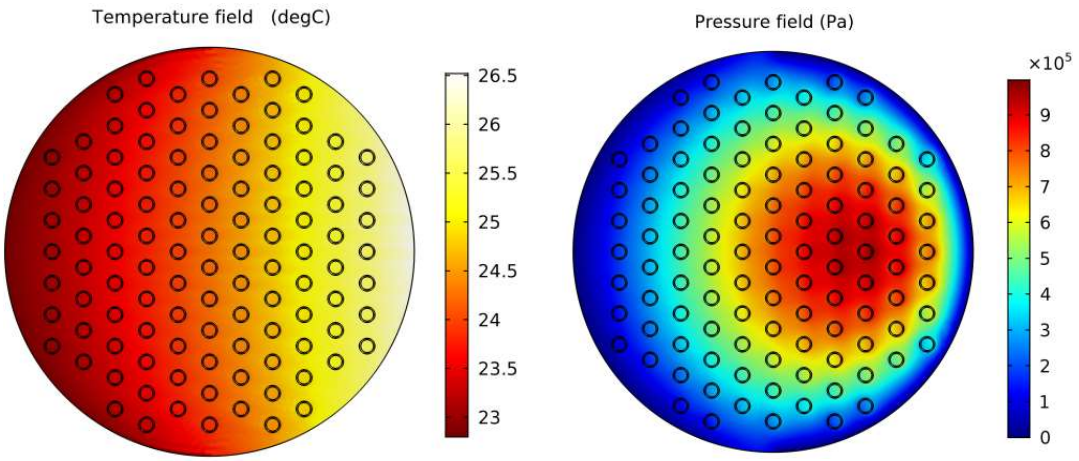

Fig. 2: Example of calculated temperature field (left) and pressure distribution (right) for the full textured pin with dimples.

4. Conclusions

The paper deals with hydrodynamic sliding contact in textured surfaces. Initially, a theoretical framework for modeling textured surfaces of journal bearings is introduced, which is then applied to analyze the dynamic behavior of rotors. Additionally, a pin-on-disc methodology for assessing the characteristics of a lubricated textured surface is presented. By comparing experimental measurements with numerical simulation results obtained from the pin-on-disc method, computational models of lubricated textured pins are refined. The knowledge gained can be used to enhance parameters in computational models of hydrodynamic contact across diverse applications.

Acknowledgment

This research work was supported by the Czech Science Foundation project 22-29874S "Thermohydrodynamic effects of boundary slip and surface texturing in sliding contacts". Chosen simulations were performed in the AVL Excite software which is available in the framework of the University Partnership Program of AVL List GmbH, and whose usage is greatly acknowledged.

References

Bai, L., Meng, Y. and Zhang, V. (2016) Experimental Study on Transient Behavior of Cavitation Phenomenon in Textured Thrust Bearings. *Tribology Letters*, 63, 2, pp. 1–15.

Cross, A. T., Sadeghi, F., Cao, L., Rateick, R. G. and Rowan, S. (2012) Flow Visualization in a Pocketed Thrust Washer. *Tribology Transactions*, 55, 5, pp. 571–581.

Gropper, D., Wang, L. and Harvey, T. J. (2016) Hydrodynamic lubrication of textured surfaces: A review of modeling techniques and key findings. *Tribology International*, 94, pp. 509–529.

Hajžman, M., Rendl, J., Smolík, L., Omasta, M. and Šperka, P. (2023) Methodology for the computational analysis of hydrodynamic lubrication in pin-on-disc experiments. In: *Proc. of the Int. Colloquium DYMAMESI 2023*, Cracow University of Technology, Cracow (Poland), pp. 31–34.

Hamilton, D. B., Walowit, J. A. and Allen, C. M. (1966) A Theory of Lubrication by Microirregularities. *Journal of Basic Engineering*, 88, 1, pp. 177–185.

Hsu, S. M., Jing, Y., Hua, D. and Zhang, H. (2014) Friction reduction using discrete surface textures: principle and design. *Journal of Physics D: Applied Physics*, 47, 33, paper 33/335307.

Křupka, I. and Hartl, M. (2007) The effect of surface texturing on thin EHD lubrication films. *Tribology International*, 40, 7, pp. 1100–1110.

Lu, P. and Wood, R. J. K. (2020) Tribological performance of surface texturing in mechanical applications—a review. *Surface Topography: Metrology and Properties*, 8, 4, paper 043001.

Smolík, L., Rendl, J., Omasta, M., Byrtus, M., Šperka, P., Polach, P., Hartl, M. and Hajžman, M. (2023) Comprehensive analysis of fluid-film instability in journal bearings with mechanically indented textures. *Journal of Sound and Vibration*, 546, paper 117454.

Stachowiak, G. W. and Batchelor, A. W. (2013) *Engineering Tribology*. Butterworth-Heinemann, St. Louis.

Vladescu, S.-C., Olver, A. V., Pegg, I. G. and Reddyhoff, T. (2015) The effects of surface texture in reciprocating contacts – An experimental study. *Tribology International*, 82, pp. 28–42.

30th International Conference
ENGINEERING MECHANICS 2024
Milovy, Czech Republic, May 14 – 16, 2024

INFLUENCE OF SINE-SHAPED PROFILE DEVIATIONS ON STATIC TRANSMISSION ERROR

Rackovský D. M.*, Czakó A.**

Abstract: *Transmission error (TE), a parameter influencing gears vibration and subsequent noise, is a subject addressed in many papers. However, most researchers consider ideal or modified involute while neglecting machining errors. This case study extends the author's previous work (Czakó et al., 2020) by incorporating tooth profile errors and investigating their impact on static transmission error (STE). Parametric geometry of 2D spur gears, including sine-shaped involute profiles, was generated directly within the Ansys Mechanical environment using APDL (Ansys Parametric Design Language), where all finite element analyses (FEA) were conducted. Various amplitudes corresponding to ISO 1328-1 accuracy grades 1–8, and wavelengths of sine functions modulated onto involutes, were simulated and compared in terms of resulting STE. The results underscore the importance of including profile deviations in models, mainly those common in industry, as they significantly influence transmission error.*

Keywords: Static transmission error, machining errors, gears, accuracy grades, finite element analysis.

1. Introduction

Demands on transmission systems, especially in the automotive industry, continue to grow in terms of vibration and noise. Transmission error is a well-known parameter closely related to the vibration and noise of transmission systems (Smith, 2003). Its values and waveforms, depending on the rotation of meshing gears, are influenced by many factors, such as time-varying mesh stiffness (TVMS), stiffness of adjacent components (bearings, shafts, housing), micro-geometric modifications, damages, and lubrication conditions of gear teeth, as well as the presence of assembly and machining errors. Notably, deviations from the theoretical shape of the tooth profile/flank have a significant impact on resulting TE as they may reach similar values, depending on the machining accuracy grade, as the transmission error itself.

Kiekbusch et al. (2011) developed 2D and 3D finite element (FE) models of meshing gear pairs using APDL scripts. Their model included an adaptive meshing algorithm to refine mesh in contacts zones. However, only ideal involute profiles were considered. Lin and He (2017) presented a parametric program for creating helical gears with machining errors in Matlab. Both profile and helix errors were generated by a model of a cutter tool with error represented by sine functions. They concluded that, compared to ideal teeth, both average and peak-to-peak (PTP) TE increased significantly. Liang et al. (2023), who created a FE model of a hypoid gear pair to investigate the impact of measured tooth surface errors on TE and contact pattern, reached a similar conclusion. Liu et al. (2022) developed a mathematical model for TVMS of helical gears with various types of machining errors considering three accuracy grades (4–6) according to ISO standard. Similarly, Guo and Fang (2020) analyzed random tooth profile and pitch errors (grades 5–7) and their influence on vibrational response of meshing helical gears. Hjelm et al. (2021) examined at spur gears the relationship between static transmission error (STE), contact pressure, and manufacturing tolerances commonly used in the automotive industry (grades 5–8) for spur gears. The results were transmission error curves for various combinations of pitch and tooth profile slope errors.

* Bc. Daniel Milan Rackovský: Institute of Automotive Engineering, Brno University of Technology, Technicka 2896/2; 61669, Brno; CZ, 217568@vutbr.cz

** Ing. Alexander Czakó: Institute of Automotive Engineering, Brno University of Technology, Technicka 2896/2; 61669, Brno; CZ, alexander.czako@vutbr.cz

doi: 10.21495/em2024-246

2. Methods

2.1. Parametric geometry

The geometry of the 2D spur gear pair was created using APDL in Ansys Mechanical. The script developed for this purpose consisted of input parameters for the gears, equations for macro-geometry, and profile errors represented by sine functions. These sine functions were modulated onto the involutes by adding them in the normal direction of the involute. Additionally, the root fillet curve was defined by the trochoid equation (Mohammed, 2023). The model also allows for the addition of tip chamfer. To ensure transitions between curves, the minimum and maximum values of parameters for construction of each curve were computed. Other teeth were created by rotating the curves about the gear center. An arbitrary number of teeth can be chosen; in this study, it was five on each gear. Using these equations of the curves, coordinates of keypoints were determined enabling the creation of closed areas for the gears. Moreover, the gears were rotated until the teeth just touched.

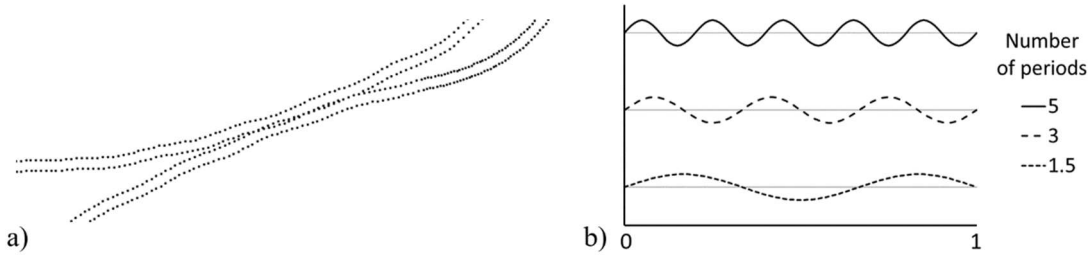

Fig. 1: Profile deviations: a) created by keypoints, b) schematic (0 – start, 1 – end of the involute).

In this study, one set of macro-geometry parameters was considered for further analysis. Specifically, normal module of 2.5 mm, number of teeth of 21 and 32, pressure angle of 20 °, addendum coefficient of 1, tip clearance coefficient of 0.25, working center distance of 66.3 mm, and tip chamfer of 0.3 mm × 45 °. The gear pair differed only in micro-geometry – sine wavelength (see Fig. 1b) and PTP amplitude which was determined by total profile tolerance in the given grade (see Tab. 1). All teeth of a single gear pair were modeled with identical profile deviations.

Grade	1st	2nd	3rd	4th	5th	6th	7th	8th
Profile tolerance (total) [µm]	2	2.9	4.1	6	8	12	16	23

Tab. 1: Profile tolerances (total) for different accuracy grades according to ISO 1328-1.

2.2. Finite element analysis

Numerical simulations of the gear engagement were carried out in the same environment as the generation of geometry, which is advantageous in terms of shorter preprocessing time. Firstly, the finite element mesh was generated based on the keypoints, where the keypoints defined positions of the nodes. The keypoints along the involutes and trochoids were offset into the gear to create a layer, which was then meshed by square elements PLANE183 (see Fig. 2) considering plane strain. The element size, the distance between corresponding keypoints, of these layers was set to be relatively small to capture the curvature precisely. Based on the sensitivity study, the element size of 0.05 mm, and layer width of two elements were chosen.

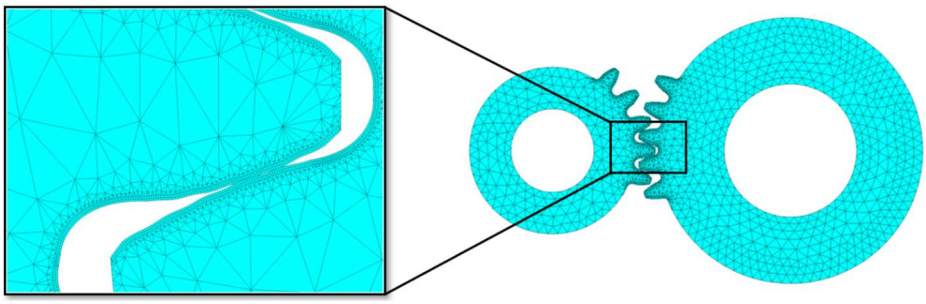

Fig. 2: Finite element mesh of the gears.

The gears were constrained at their centers, allowing only one rotational degree of freedom about their axes. The driven gear was loaded with a moment of 20 N.m, while the driving one was defined to rotate by 30 °, with an increment of 0.1 °, to capture more than one period of the TE. Surface-to-surface contact

between the meshing teeth was ensured by contact elements CONTA172 and TARGE169. The contact settings remained consistent throughout all simulations, with the friction coefficient of 0.1, the normal contact stiffness factor and penetration tolerance factor of 1. The Augmented Lagrange method was used.

Based on the results of stress-strain contact analysis (see Fig. 3), the static transmission error was subsequently calculated from the definition as follows (Smith, 2003):

$$STE = r_1\theta_1 - r_2\theta_2 \tag{1}$$

where r is pitch circle radius, θ is angular displacement (in radians) of the gear center, and indexes 1 and 2 refer to the driving and driven gear, respectively.

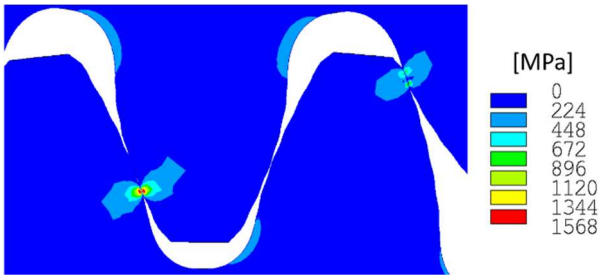

Fig. 3: Equivalent stress von-Mises in loaded teeth of meshing gears.

3. Results and discussion – static transmission error

The resulting graphs of the static transmission error are shown in Fig. 4, where the accuracy grades are compared for each number of periods of the sine function. Since spur gears with contact ratio between 1 and 2 were considered, one and two tooth pairs alternated in the mesh. Observing the graph for the ideal involute, higher STE values correspond to the single-pair engagement. Notably, the higher the grade, the more pronounced deviations from the ideal involute graph. However, the way the deviations transform the ideal involute graphs strongly depends on the sine wavelength.

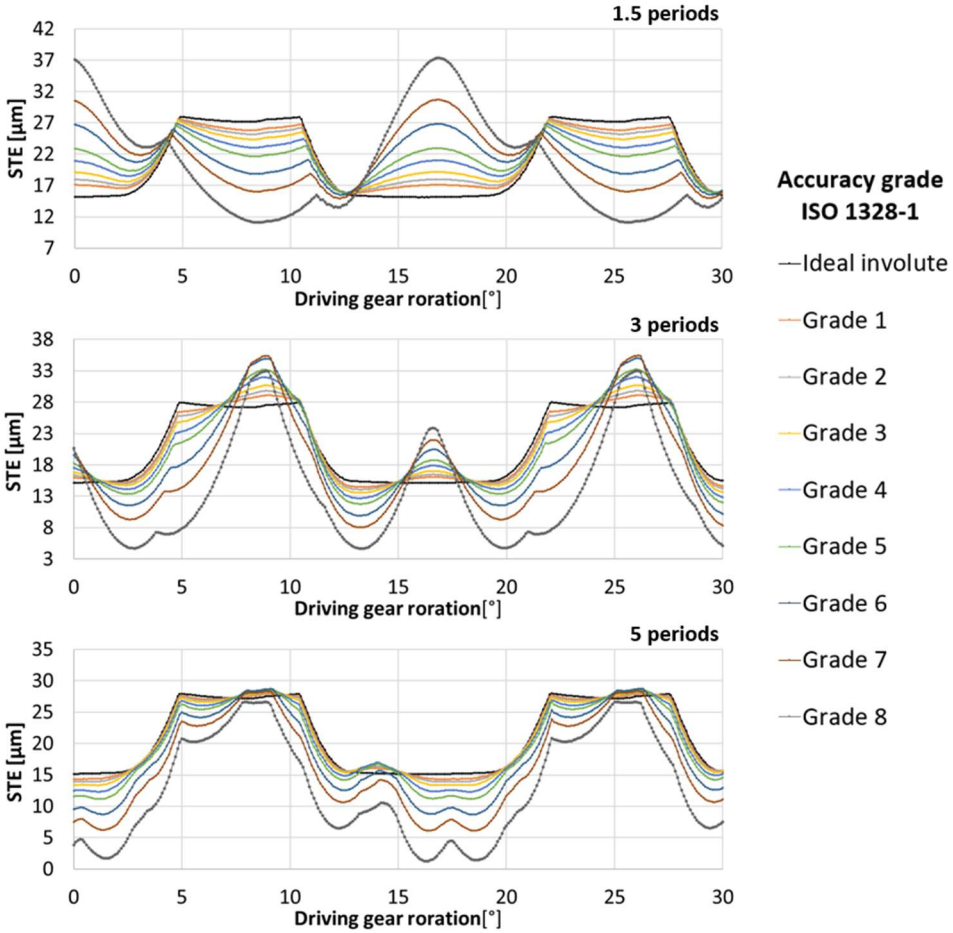

Fig. 4: STE graphs for various numbers of sine periods and ISO accuracy grades.

For the case of 1.5 periods, with the increasing grade, the STE of single-pair engagement decreases while that of two-pair engagement increases. This leads in a slight decrease in the PTP-STE up to the grade 6. However, beyond this point, the values start to increase rapidly (see Fig. 5 – note that the value of zero indicates the ideal involute). As the number of sine periods increases, the waveforms tend to resemble the trend of the ideal involute graph. Furthermore, PTP-STE values grow more gradually with higher grades in the case of 3 and 5 periods reaching similar values to those of 1.5 periods for the grade 8. Specifically, each of them is approximately two times higher than that of the ideal involute. It can be concluded that not only do the grades influence transmission error, but also the way they are distributed along the involutes.

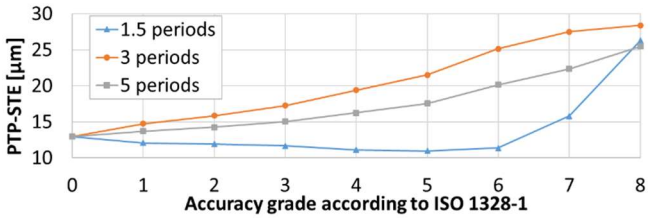

Fig. 5: Comparison of different tooth profiles through accuracy grades in terms of PTP-STE.

4. Conclusions

The case study presented in this paper focuses solely on 2D tooth profiles. While this approach offers the advantage of shorter computational times, it also means that flank line deviations and modifications, and helical gears cannot be incorporated. Therefore, future plans involve extending the FEM model to include 3D representations. Additionally, there is potential to enhance fidelity of the simulation by considering more complex curves beyond simple sine shapes and defining different deviations across the teeth to better reflect real-world conditions. This may also help to improve dynamic models (Otipka et al., 2019) and (Prokop and Řehák, 2017) of geared transmission systems by providing more realistic transmission error waveforms, considering inevitable machining errors, as the input.

Acknowledgement

The research leading to these results has received funding from the project Specific research on BUT FSI-S-20-6267. The authors gratefully acknowledge this support.

References

Czakó, A., Řehák K. and Prokop A. (2020) Determination of transmission error at helical gear. In: *Proc. of 26th Engineering Mechanics*, Brno, pp. 118–121.

Guo, F. and Fang, Z. (2020) The statistical analysis of the dynamic performance of a gear system considering random manufacturing errors under different levels of machining precision. *Proc. of the Institution of Mechanical Engineers*, Part K: Journal of Multi-body Dynamics, 234, 1, pp. 3–18.

Hjelm, R., Ahadi, A. and Wahlström, J. (2021) Gear tolerancing for simultaneous optimization of transmission error and contact pressure. *Results in Engineering*, 9, pp. 1–8.

Kiekbusch, T., Sappok, D., Sauer, B. and Howard, I. (2011) Calculation of the Combined Torsional Mesh Stiffness of Spur Gears with Two- and Three-Dimensional Parametrical FE Models. Strojniški vestnik - *Journal of Mechanical Engineering*, 57, 11, pp. 810–818.

Liang, Ch., Song, Ch., Zhu, C. and Liu, S. (2023) Modelling method, simulation and experimental verification of hypoid gear involved tooth surface deviation under manufacturing process. *Mechanism and Machine Theory*, 182, pp. 1–19.

Lin, T. and He, Z. (2017) Analytical method for coupled transmission error of helical gear system with machining errors, assembly errors and tooth modifications. *Mechanical Systems and Signal Processing*, 91, pp. 167–182.

Liu, Ch., Shi, W. and Liu, K. (2022) Calculation method of mesh stiffness for helical gear pair with manufacturing errors, assembly errors and tooth modifications. *Meccanica*, 57, 3, pp. 541–565.

Mohammed, O. D. (2023) An analytical approach for the determination of helical gear tooth geometry. *Journal of Engineering, Design and Technology*, pp. 1–23.

Otipka, V., Zajac, R., Řehák, K. and Prokop, A. (2019) Numerical dynamic analysis of gearbox behaviour. *Acoustics and Vibration of Mechanical Structures*, 25, pp. 433–441.

Prokop, A. and Řehák, K. (2017) Virtual prototype application to heavy-duty vehicle gearbox concept. In: *Proc. of 23rd Engineering Mechanics*, Svratka, pp. 810–813.

Smith, J. D. (2003) *Gear noise and vibration*. 2nd edition. New York: Marcel Dekker.

30th International Conference
ENGINEERING MECHANICS 2024
Milovy, Czech Republic, May 14 – 16, 2024

EXPERIMENTAL INVESTIGATION OF FLUID-STRUCTURE-ACOUSTIC COUPLINGS BY STUDYING THE RESONANCE PROPERTIES OF VOCAL TRACT MODELS WITH YIELDING WALLS

Radolf V.[*], Horáček J.[**], Košina J.[***]

Abstract: *The novel experimental setup has been designed to study fluid-structure-acoustic interaction of the self-oscillating vocal folds model with vocal tract cavities and with a dynamical system originating in vibration of the soft tissue. The compliance of the vocal tract walls changes the phonation threshold so that a very small airflow is sufficient to vibrate the vocal folds. Comparing the same flow rates, the subglottal and radiated sound pressures are higher in the yielding-walled model. The shift of acoustic resonances towards higher frequencies due to the yielding wall corresponds to earlier experimental and numerical simulations.*

Keywords: Biomechanics of voice, vocal tract acoustics, artificial vocal folds, fluid-structure-acoustic interaction.

1. Introduction

Generation of voice is a complex process involving couplings between airflow coming from the lungs, self-oscillating vocal folds and acoustic resonances of the vocal tract. A primary sound, generated in the vocal folds (VFs), is modified in the acoustic cavities of the vocal tract (VT) above the VFs. The resulting sound thus includes acoustic resonances of the VT cavities, which occur as peaks in the envelope of the voice spectrum, referred to as formants, see e.g. Sundberg (1987). Formant frequencies define vowels and the voice timbre. The VT walls are not in reality acoustically hard but so-called yielding walls. This brings damping effects on the acoustic waves influencing the resulting sound radiated from the mouth. These effects were studied on an artificial laboratory model of voice production comprising the sound excitation by a silicone replica of self-oscillating VFs and a plexiglass VT model, where part of the VT wall was elastic.

2. Methods

First, the simplified vocal tract model was made of plexiglass. The base of its main geometric configuration was taken from a 3D volume model obtained from magnetic resonance images for the Czech vowel [u:], see Vampola et al. (2008). Cross-sectional rectangular areas of the model with hard walls corresponded to the areas of the human vocal tract. Second, the upper wall of the VT model, from the laryngeal part to the lips, was replaced with a soft membrane made of silicone rubber Ecoflex™ 00-50, see Radolf et al. (2020). The membrane of thickness 1 mm was slightly stretched during attachment to the VT model.

The developed simplified model of the human lungs, which includes splitting of the airways up to the fourth order branching, was built in the subglottic part of the experimental facility; see e.g. Horáček et al. (2017).

[*] Ing. Vojtěch Radolf, PhD.: Institute of Thermomechanics of the Czech Academy of Sciences, Dolejškova 1402/5, 182 00 Prague, CZ, radolf@it.cas.cz

[**] Ing. Jaromír Horáček, DSc.: Institute of Thermomechanics of the Czech Academy of Sciences, Dolejškova 1402/5, 182 00 Prague, CZ, jaromirh@it.cas.cz

[***] Ing. Jan Košina: Institute of Thermomechanics of the Czech Academy of Sciences, Dolejškova 1402/5, 182 00 Prague, CZ, kosina@it.cas.cz

doi: 10.21495/em2024-250

The air was flowing through the model of the lungs to the trachea. Total trachea length was 23 cm and inner diameter 18 mm.

The measurements were performed with a 1:1 scaled three-layer vocal folds model (Horáček et al., 2017). The vocal folds were excited by airflow coming from the trachea. The airflow rate was increased step by step from the phonation onset up to the airflow rate and the subglottic pressure, which are in the range of physiologically relevant values for a normal human voice production. The sound level meter B&K 2239 was installed at a distance of 20 cm from the mouth of the vocal tract model. The pressure below the vocal folds (subglottal pressure) was measured by a special dynamic semiconductor pressure transducer developed in IT CAS. A Polytec OFV-505 laser vibrometer with an OFV-5000 controller was used for measuring vibration of the silicone membrane at the mouth cavity level, i.e. in the position of the cheek in the human vocal tract.

3. Results

The existence of a compliant wall caused the vocal folds start to oscillate at lower airflow rate $Q = 0.024$ l/s compared to 0.06 l/s for the hard-walled VT. The mean subglottal pressure and sound pressure level radiated from the mouth of the VT model increased for the compliant VT wall, see graphs in Fig. 1.

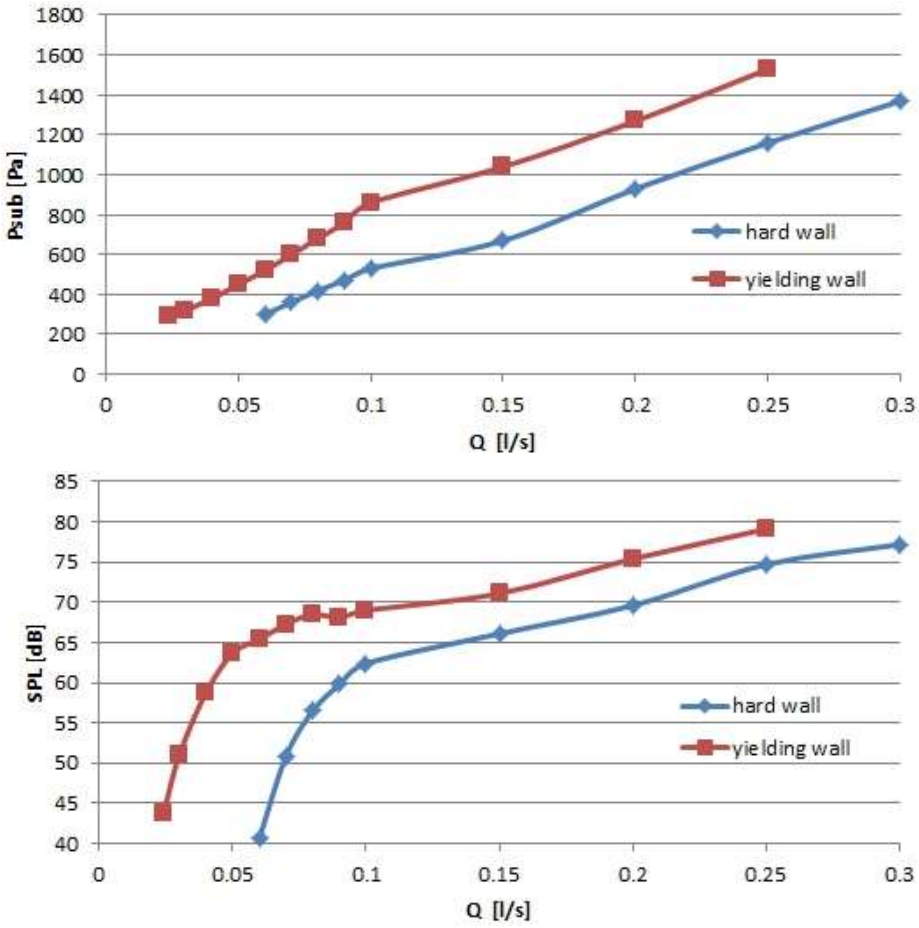

Fig. 1: Mean subglottal pressure (top) and sound pressure level radiated from the mouth (bottom) measured for hard-walled VT and yielding-walled VT.

Spectra of subglottal pressures for the mean airflow rate $Q = 0.1$ l/s are shown in Fig. 2. Harmonics in the spectra were filtered out (see e.g., Radolf et al., 2016) to better recognize their character and peaks. Interaction of the pressure oscillations with the compliant VT wall caused higher pressure levels, compared to hard-walled VT, in the frequency range from 200 Hz to 2 000 Hz and especially at the first subglottal resonance frequency at ca 700 Hz. Fundamental frequency of VFs oscillation was 82 Hz and 85 Hz for the hard-walled and yielding-walled model, respectively.

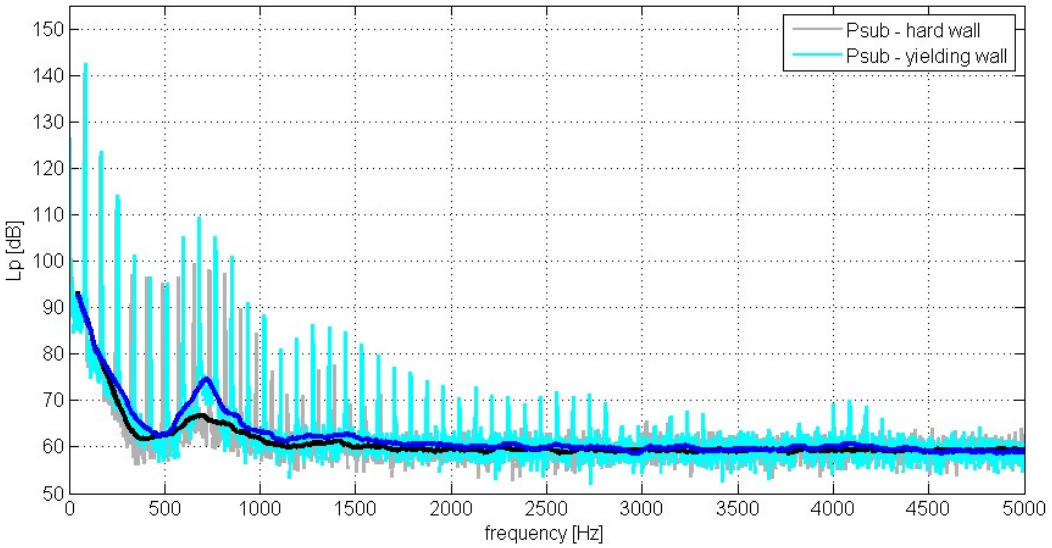

Fig. 2: Spectra of the subglottal pressure for hard-walled VT and yielding-walled VT, Q = 0.1 l/s.

Sound pressure levels measured outside the VT models show an even greater influence of the yielding wall. The energy of the sound waves increased significantly across almost the entire frequency band, see Fig. 3. All acoustic resonance frequencies increased in the case of the compliant-walled VT model compared to the model with the hard walls. The first and second acoustic resonances shifted significantly towards higher frequencies (F_1 from 440 Hz to 580 Hz and F_2 from 720 Hz to 780 Hz). The higher three resonance frequencies increased only negligibly. A new low resonance frequency at ca 230 Hz appeared for yielding walls in VT. This may have its origin in the weak resonance of the yielding wall in the epilaryngeal region, see the green curve in Fig. 4.

Spectra of the velocity of vibrating VT yielding wall show a sharp peak at about 40–50 Hz, which is the first mechanical resonance identified in the former study (Radolf et al., 2020), see the red curve in Fig. 3. Second peak at 780 Hz corresponds to the second acoustical resonance frequency.

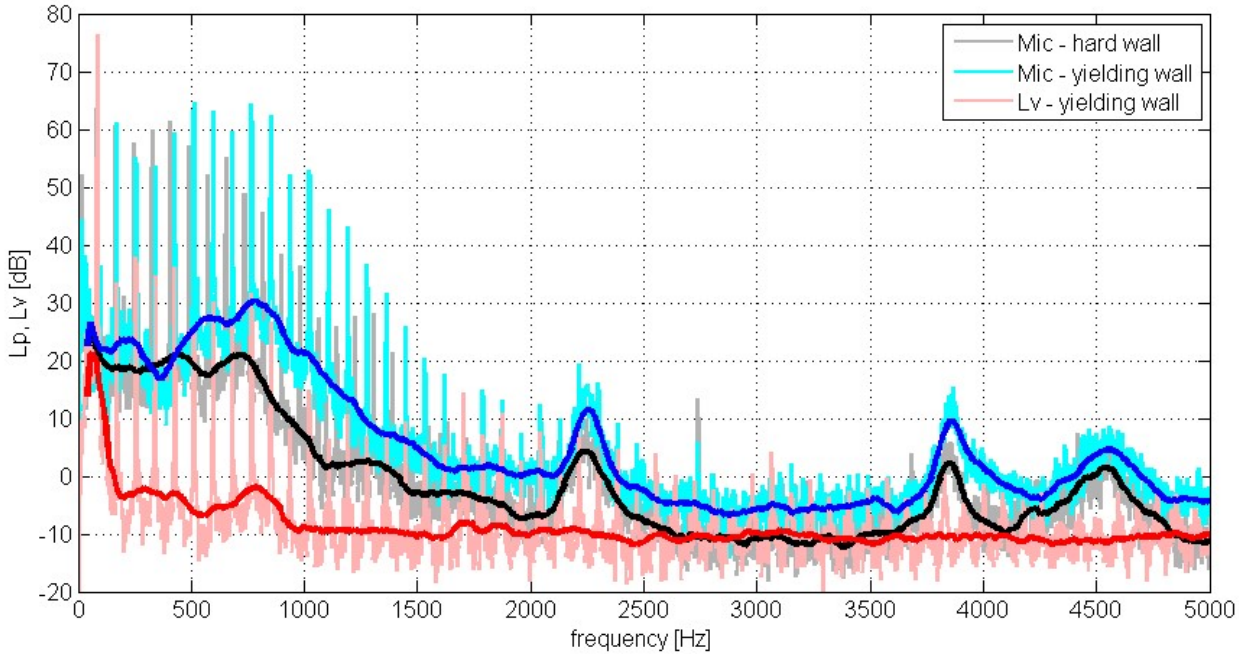

Fig. 3: Sound pressure spectra measured 20 cm from the mouth:
1/ for hard-walled VT (grey and black curves), 2/ for yielding-walled VT (blue curves)
and 3/ spectra of the velocity of vibrating yielding wall measured at the cheek
of the VT model (red curves), Q = 0.1 l/s.

The effect of the yielding wall shifting the acoustical resonances towards higher frequencies is qualitatively similar to the results of earlier measurements (Radolf et al., 2020), where the excitation of acoustic cavities

of the VT model was realized by a small speaker placed instead of the vocal folds, see Fig. 4.

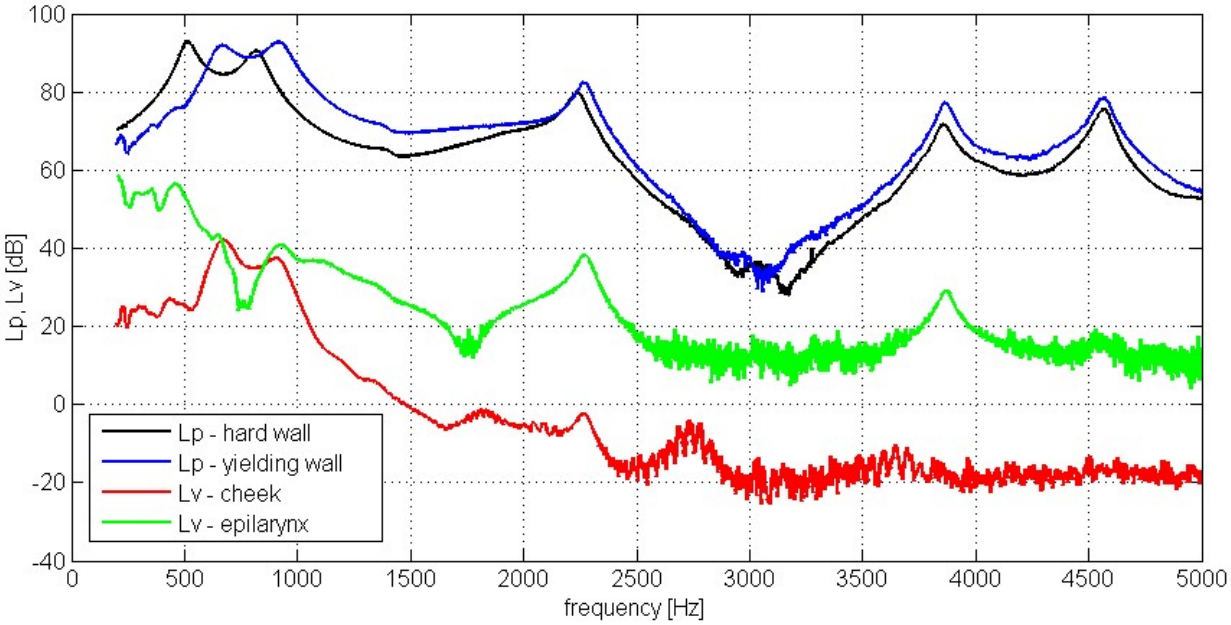

Fig. 4: a) Sound pressure spectra measured with microphone probe at the lips for hard-walled VT (black curve) and yielding-walled VT (blue curve), b) spectra of the velocity of vibrating yielding wall measured at the cheek of the VT model (red curve) and c) spectra of the vibrating yielding wall at the epilarynx position (green curve).

4. Conclusion

The compliance of the vocal tract walls significantly shifts the phonation threshold so that a very small airflow is sufficient to vibrate the vocal folds. Comparing the same flow rates, the subglottic pressures and SPL radiated from the mouth are noticeably higher in the model with a compliant wall. However, the phonation threshold subglottal pressure remains approximately the same for both models. The shift of acoustic resonances towards higher frequencies due to the compliant wall is consistent with previous experimental and numerical simulations (Radolf et al., 2016).

Acknowledgment

The study was supported by a grant from the Czech Science Foundation: No. 24-11121S "Redistribution of acoustic energy output in human voice and its effect on vocal folds loading using computer and physical modeling".

References

Horáček, J., Radolf, V., Bula, V. and Košina, J. (2017) Experimental modelling of phonation using artificial models of human vocal folds and vocal tracts, In: *Proc. 23rd Conference Engineering*, Svratka, pp. 382–385.

Radolf, V., Horáček, J., Dlask, P., Otčenášek, Z., Geneid, A. and Laukkanen, A. M. (2016) Measurement and mathematical simulation of acoustic characteristics of an artificially lengthened vocal tract. *Journal of Sound and Vibration*, 366, pp. 556–570.

Radolf, V., Horáček, J. and Košina, J. (2020) Experimental modelling of vibroacoustics of the human vocal tract with compliant walls, In: *Proc. 26th Conference Engineering mechanics*, Brno, pp. 424–427.

Sundberg, J. (1987) *The science of the singing voice*. DeKalb, Illinois: N. Illinois Univ. Press.

Vampola, T., Horáček, J. and Švec J. G. (2008) FE modeling of human vocal tract acoustics. Part I: Production of Czech vowels. *Acta Acustica united with Acustica*, 94, pp. 433–447.

30th International Conference
ENGINEERING MECHANICS 2024
Milovy, Czech Republic, May 14 – 16, 2024

ENHANCING SENSITIVITY IN PIEZOELECTRIC MICRO CANTILEVER DESIGNS USING STRESS CONCENTRATION REGIONS FOR LABEL FREE DETECTION

Raziyan M. S.*, Janusas G.**

Abstract: *The focus of this research project is to enhance cantilever beam designs for biosensing applications by including Stress Concentration Regions (SCRs). The stress distribution across several cantilever beam designs was determined by simulating them using COMSOL Multiphysics. The earliest designs were developed utilizing Polyvinylidene fluoride (PVDF) to showcase improved sensitivity for mechanical detection without the need for labels in biosensor applications. The analysis of cantilever beams involves the examination of their eigenfrequency and stationary behavior in the context of piezoelectric effect physics. An analysis is conducted on several cantilever beam structures to determine the most appropriate one. In this analysis, the various beams are exposed to an identical mechanical force, and their respective displacements, potential voltage, von Mises stress, and eigenfrequencies are examined.*

Keywords: Cantilever, stress concentration region, biosensor, COMSOL.

1. Introduction

Cantilever sensors, which utilize surface stress, are becoming increasingly popular for biochemical detection due to their compact dimensions and accurate detection of induced deflection. These sensors can detect biomolecule absorption by detecting changes in surface properties due to the binding or hybridization of analytes to receptor molecules. These self-powered biochips can be used for disease identification and chemical and biological warfare weapon detection. However, they require external equipment for deflection measurements and have high size and power requirements (Kumar, 2023). Micromachined cantilevers are increasingly used as biochemical sensors due to their ability to identify chemical species by altering their mechanical characteristics. Static detection involves stress gradients across the cantilever's thickness, while dynamic analysis involves specific species adhering to the surface, resulting in a change in vibration frequency (Norouzi, 2009). PVDF (polyvinylidene fluoride) and PZT (lead zirconate titanate) are the two most used piezoelectric materials. Scientists demonstrated the ability of PVDF to generate higher voltage output than PZT by conducting experiments with different beam sizes. Both PZT and PVDF piezoelectric beams were tested, and it was discovered that the PVDF beam produced the highest output power (Guo, 2021). Compared to PZT's brittle nature, which can cause fatigue failure under high-frequency cyclic load, particularly in outdoor applications, PVDF performs better due to its high flexibility, lightweight, and low acoustic, and mechanical impedance (Wong, 2017). As a result, PVDF is becoming more popular, and many commercial PVDF sensors make it easier to conduct impact tests. Only a prototype of a PVDF beam (energy harvester) bimorph cantilever was designed and tested (Chu Duc, 2018).

* Motahareh Sadat Raziyan, PhD. student: Faculty of Mechanical Engineering and Design, Kaunas University of Technology, Studentu Street 56, LT 51373 Kaunas, Lithuania, motahareh.raziyan@ktu.edu

** Prof. Giedrius Janusas, PhD.: Faculty of Mechanical Engineering and Design, Kaunas University of Technology, Studentu Street 56, LT 51373 Kaunas, Lithuania, giedrius.janusas@ktu.lt

doi: 10.21495/em2024-254

2. Theory and modeling

A piezoresistive microcantilever beam uses one end fixed and the other free. When a substance is under pressure, its electrical resistivity changes. Microcantilevers resonate at their most conspicuous oscillation frequency. For self-sensing biosensors, semiconductor microcantilevers with piezo resistivity are ideal. Analyte-receptor responses on its active surface stress their piezo resistor, causing it to change electrical resistance. The maximum deflection, maximum stress, and resistance change are critical parameter for analyzing a beam stationary at one end. These crucial insights disclose the beam's structural integrity, mechanical performance, and material properties (Brugger, 1999). Two strategies to increase resistance change are to increase differential surface stress or decrease microcantilever thickness. Material qualities affect resistance change. Lower beam stiffness or deformation resistance may cause increased deflection. This may indicate structural integrity or stability difficulties. Low deflection indicates a stiffer, more deform-resistant beam (Selvan, 2020).

3. Design and simulation

A design is a mechanical structure with one rigid end and a free end that moves when acted upon by a force. The cantilever acts as a sensor, detecting both cantilever bending and changes in vibration frequency. The structure and material used in the design play an important role in determining beam stiffness. Applied force and geometry information are shown in the table below. The features of the PVDF material, such as its elasticity and density, were allocated to correctly mimic the conditions that exist in the real world. The use of boundary conditions was done to simulate a fixed-free cantilever configuration. For modeling the dynamic behavior of the cantilever while it is being loaded, the appropriate physics modules in COMSOL Multiphysics were chosen. The geometry information is shown in Tab. 1.

Beam length	Beam width	Beam height	Holes radius	Applied force
200 μm	100 μm	1.5 μm	5 μm	2.10^{-7} N

Tab. 1: Beam details.

To conduct precise numerical analysis, the solver settings were adjusted. To investigate the distribution of stress under the conditions of loading that were stated, a von Mises stress analysis was carried out. First step was to design 2 different microcantilever to test PVDF piezoelectricity properties for sensor application and evaluate result of applying SCR.

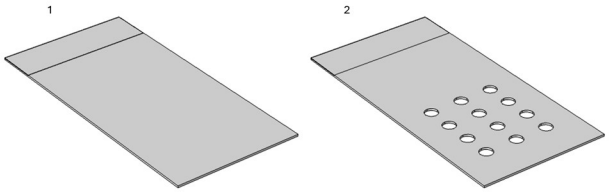

Fig. 1: Geometry before and after SCR.

As the simulation process progressed, iterative optimization was carried out whenever it was deemed necessary. This involved the modification of virtual models and simulation parameters to improve accuracy. This study highlights the comprehensive technique of simulating cantilever behavior in COMSOL Multiphysics. This approach mirrors situations that occur in the real world and provides insights into the performance of structures under various scenarios.

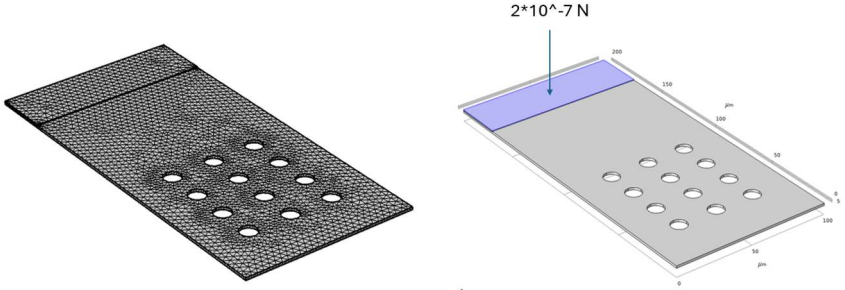

Fig. 2: Boundary load and meshing.

4. Results and discussion

This study examines the performance of two microcantilever samples made from PVDF, specifically designed for early detection purposes. Sample 1 is a basic cantilever beam, whereas Sample 2 is the same as Sample 1 but has holes, which create areas of stress concentration. The primary parameters examined comprise displacement, Von Mises stress, eigenfrequency, and electric potential as shown in Fig. 2. The analyzed parameters encompass displacement, Von Mises stress, eigenfrequency, and electric potential. Sample 2 demonstrates a marginally greater displacement in comparison to Sample 1. The heightened displacement observed in Sample 2 could potentially be attributed to the incorporation of holes, indicating potential modifications in structural flexibility. Sample 2 exhibits an elevated level of Von Mises stress. The existence of voids in Sample 2 can result in localized stress concentrations, thereby contributing to an overall elevated stress level. Sample 1 has a greater eigenfrequency.

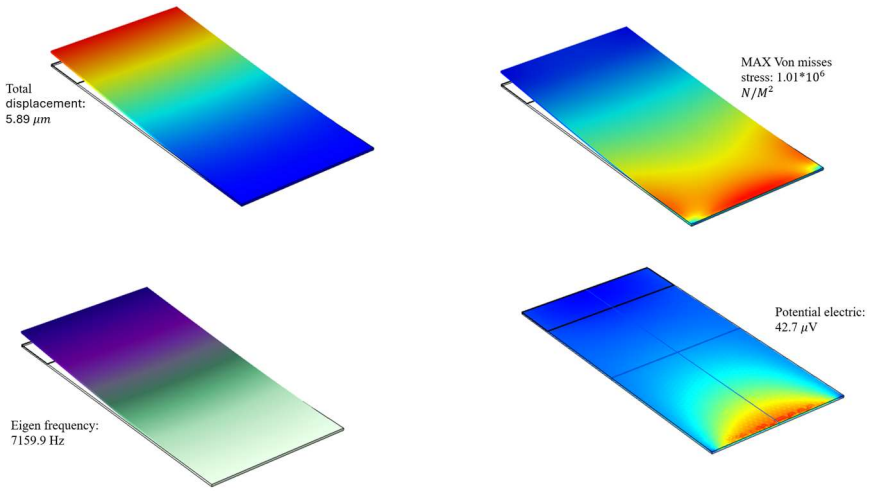

Fig. 3: Simulation results without applying SCR, as shown in Tab. 2. Four important parameters were measured.

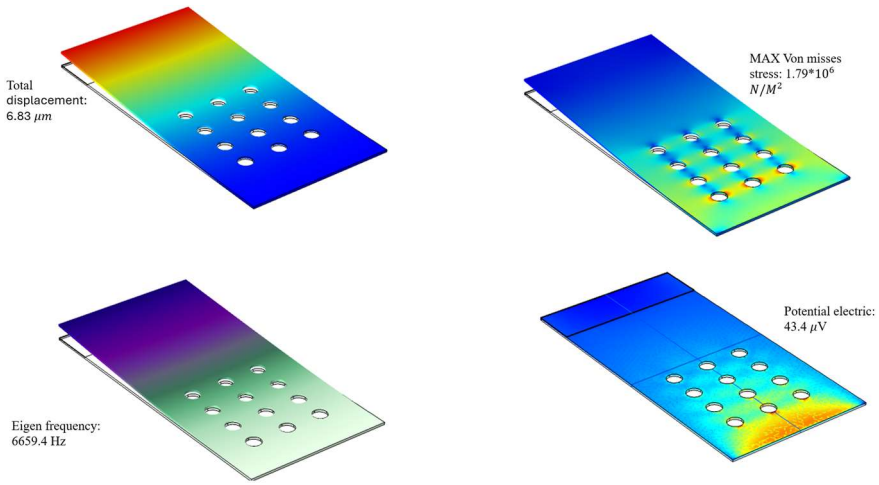

Fig. 4: Simulation results after applying SCR. Parameters are shown in Tab. 2.

The incorporation of voids in Sample 2 may have modified the structural rigidity, leading to a decreased natural frequency. The alteration in eigenfrequency is essential for applications that involve detection mechanisms based on resonance. The electric potential is nearly identical. Microcantilevers are specifically engineered for the purpose of early detection, wherein even slight variations in physical parameters can indicate the existence of conditions or substances. The greater displacement observed in Sample 2 indicates a potentially heightened responsiveness to external stimuli. Nevertheless, it is crucial to thoroughly evaluate the elevated levels of stress and reduced eigenfrequency, as they have the potential to impact both the structural soundness and the speed of response of the cantilever.

The graph shows in sample after applying SCR we are facing three picks which explain the presents of holes. The maximum amount for each parameter was chose for comparison which is in Tab. 2.

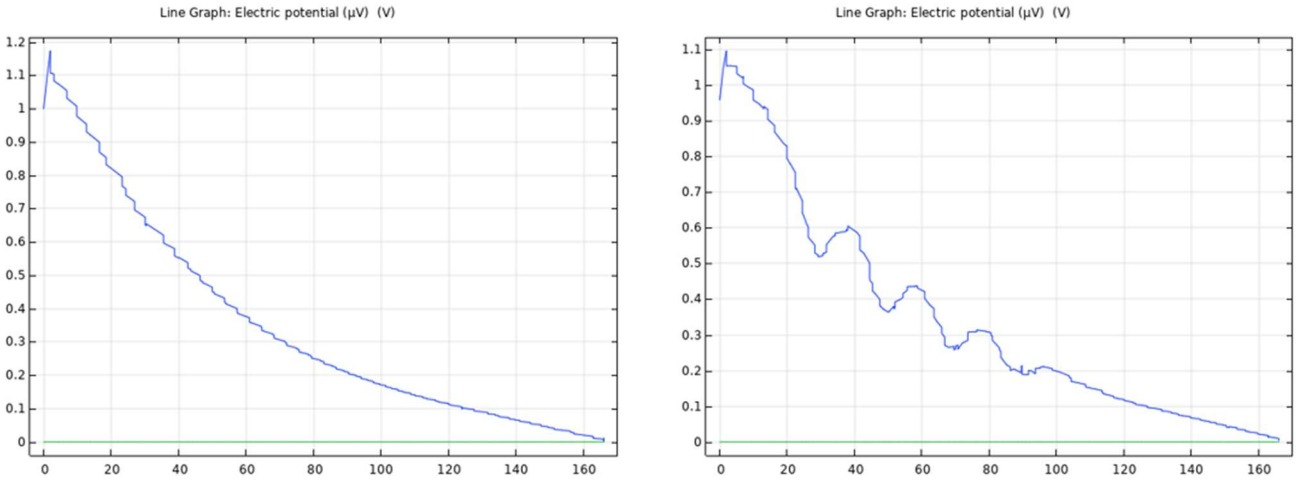

Fig. 4: Electric potential - Arc length graphs for both samples. This graph shows Electrical distribution through the length of the beam.

Parameters	1	2
Von Mises stress $[N/M^2]$	$1.01 \cdot 10^6$	$1.79 \cdot 10^6$
Total displacement $[\mu m]$	5.89	6.83
Potential electric $[\mu V]$	42.7	43.4
Eigen frequency [Hz]	7 159.8	6 659.4

Tab. 2: Results from simulation.

5. Conclusion

This study thoroughly analyzed the performance of two PVDF microcantilever samples created for early detection. The addition of holes in Sample 2 resulted in a slight increase in displacement, indicating possible adjustments in structural flexibility. The almost identical electric potential suggests a uniform characteristic present in both samples. The results show us how utilizing stress concentration regions can be useful in increasing the sensitivity of the cantilever, which is helpful for the early detection of microcantilevers. The addition of holes creates these areas. More tests, experiments, and tweaking should be done to confirm and improve these results. This will make sure that microcantilevers can be used reliably and effectively in early detection systems.

References

Kumar, L., Bagha, A. K., Singh, K., Kumar, S. and Kumar, S. (2023) Sensing and control of the static deflection of a cantilever beam using piezoelectric patches. *Physica Scripta*, 98(9), 095244.

Norouzi, M. and Alireza, A. (2009) Design of Piezoelectric micro cantilever Chemical Sensor in Comsol Multiphysics Area. *Electrical and Electronics*, 2(1), 184.

Guo, K., Jiang, B., Liu, B., Li, X., Wu, Y., Tian, S., Gao, Z., Zong, L., Yao, S., Zhao, M., Mi, C. and Zhu, G. (2021) Study on the progress of piezoelectric microcantilever beam micromass sensor. *IOP Conf. Ser. Earth Environ Sci*, 651, 022091.

Wong, C. H. and Dahari, Z. (2017) Development of Vibration-Based Piezoelectric Raindrop Energy Harvesting System. *J. Electron. Mater.*, 46, 1869–1882.

Chu Duc, T., Creemer, J. F. and Sarro Pasqualina, M. (2017) Piezoresistive cantilever beam for force sensing in two dimensions. *IEEE Sensors J.*, 1, 96–104.

Brugger, J., Despont, M., Rossel, C., Rothuizen, H., Vettiger, P. and Willemin, M. (1999) Microfabricated ultrasensitive piezoresistive cantilevers for torque magnetometry, *Sensors and Actuators A*, 73, 3, pp. 235–242.

Selvan, R. T. et al. (2020) Modelling and Analysis of Elliptical Cantilever Device Using Flexure Method and Fabrication of Electrospun PVDF/BaTiO3 Nanocomposites. *Nano*, 15.

30th International Conference
ENGINEERING MECHANICS 2024
Milovy, Czech Republic, May 14 – 16, 2024

ELASTODYNAMICS IN PERIODIC MEDIA – APPROXIMATION BY HIGHER ORDER HOMOGENIZATION AND METAMATERIALS WITH RESONATORS

Rohan E.[*], **Naili S.**[**]

Abstract: *We consider elastodynamics in periodically heterogeneous solids described by 1D continua. The homogenization based on the higher order asymptotic expansions is applied to derive effective (macroscopic) models. Relevance of these models is extended beyond the assumption of the perfect scale separation to respect finite size of the heterogeneities. These models involve higher order gradients enabling to interpret models of the generalized continua introduced using phenomenological approaches. Particular examples of bi- and triple-layered periodic composites are explored in the context of the wave dispersion analysis. It appears that a variety of models which approximate the response up to the 2nd order of accuracy with respect to the scale parameter can be used, leading to different dispersion properties. Due to the volume forces involved in the asymptotic analysis, structures with resonators can be represented to enhance band gap effects.*

Keywords: Higher order homogenization, wave dispersion, elastodynamics, composite materials, metamaterials.

1. Introduction

Wave propagation in periodically heterogeneous elastic media belongs to one of the most studied topics in the field of composite materials. However, a unified satisfactory description of this phenomena in the framework of the continuum mechanics remains cumbersome and ambiguities remains to interpret correctly different modelling approaches. Phenomenological extended continuum based theories involving higher order gradients provide micromechanically based models incorporating size effects and internal length scales, though not straightforwardly related to a specific microstructure under consideration. The homogenization based methods provide a promising alternative enabling to introduce internal length scales in a natural way. The asymptotic based homogenization of the 1st order provides the limit model of the Cauchy medium, where the microstructure size ℓ is infinitely small compared to a macroscopic size L, so that such models do not capture the dispersion properties emerging when wave lengths $L \not\gg \ell$. As the remedy, higher order homogenization leads to models with effective material coefficients computed directly for a given microstructure, whereby the internal length scale is retained. This issue has been discussed in several important works, namely comprising papers by Andrianov et al. (2008); Dontsov et al. (2013); Wautier and Guzina (2015); Cornaggia and Guzina (2020); Schwan et al. (2021). The present short paper contributes to these works by considering scale-dependent heterogeneity of the type reported in Rohan et al. (2009), such that the dispersion due to the finite scale ℓ/L interferes with the resonance features of the "metamaterial" with soft elastic components.

2. Elastodynamics in a periodic 1D continuum

We consider domain $\Omega =]0, L[\subset \mathbb{R}$ occupied by an elastic solid whose properties are given by an elasticity E^ε and the density ρ^ε, where $\varepsilon = \ell/L$ is the scale parameter, the ratio of the characteristic length featuring

[*] Prof. Dr. Ing. Eduard Rohan, DSc.: Department of Mechanics, Faculty of Applied Sciences, University of West Bohemia, Univerzitní 2732/8; 301 00, Plzeň; CZ, rohan@kme.zcu.cz

[**] Prof. Salah Naili, PhD.: Univ Paris Est Creteil, Univ Gustave Eiffel, CNRS, UMR 8208, MSME, F-94010 Créteil, France; naili@u-pec.fr

doi: 10.21495/em2024-258

the micro- and macroscopic scales, respectively. The solid is represented by the 1D periodically heterogeneous continuum generated by copies of the (zoomed) representative periodic cell, $Y =]0, \bar{y}[$, such that $\Omega^\varepsilon = \bigcup_{k\in\mathbb{Z}}(\varepsilon Y + \varepsilon k\bar{y})$, where $\varepsilon\bar{y} = \ell$ is the real sized period length. The heterogeneity can be introduced via n subdomains $Y_i \subset Y$, such that $Y = Y_1 \cup \cdots \cup Y_n$, $Y_i \cap Y_j = \emptyset$ for $i \neq j$.

Material parameters can be introduced due to the coordinated unfolding, $x = \xi + \varepsilon y$ with $y \in Y$ and $\xi = \varepsilon[x/\varepsilon]_Y$ being the "lattice coordinate".In this context, the material properties, *i.e.* the elasticity $E^\varepsilon(x) = E(y)$ and the density $\rho^\varepsilon(x) = \rho(y)$ are assumed to be piecewise continuous (even piecewise constant) in $Y_i \subset Y$, being functions $y = \{x/\varepsilon\}_Y = (x - \xi)/\varepsilon$. The unfolded spatial derivatives $\tilde{\partial}_x := \partial_x + \varepsilon^{-1}\partial_y$ of the displacements are used to derive the usual cascade of equations correspondingly to the employed asymptotic expansions.

Elastodynamic equation governing the displacement field u^ε is defined in any layer characterized by properties (E_i, ρ_i),

$$-\tilde{\partial}_x(E_i\tilde{\partial}_x u^\varepsilon) + \rho_i(\partial_{tt}^2 u^\varepsilon - f^\varepsilon) = 0 \ , \quad \text{in any } \Omega \times Y_i \ , \tag{1}$$

where f^ε is a given generalized volume force.

3. Effective model with characteristic scales

3.1. Asymptotic analysis – higher order homogenization

In what follows, the time-dependence of displacement u^ε on t is considered, though t is not in the list of its arguments. The asymptotic expansion of the displacement is considered in its unfolded form,

$$u^\varepsilon(x) = \sum_{k=0,1,2,\ldots} \varepsilon^k u^k(x,y) \ , \quad u^k(x,y) = U^k(x) + \tilde{u}^k(x,y) \ , \quad U^k(x) = \left\langle u^k(x,\cdot)\right\rangle_Y \ , \tag{2}$$

where $\langle\ \rangle_Y$ is the average in Y. These expansions are substituted in (1), where the differential oprerator is unfolded

$$\begin{aligned} -\mathbb{L}^\varepsilon u^\varepsilon + \rho(\ddot{u}^\varepsilon - f^\varepsilon) = 0 \ , \quad x \in \Omega, \quad y \in Y_i \ , \\ \text{with } \mathbb{L}^\varepsilon(v) \equiv \mathbb{L}_{xx}(v) + \varepsilon^{-1}[\mathbb{L}_{xy}(v) + \mathbb{L}_{yx}(v)] + \varepsilon^{-2}\mathbb{L}_{yy}(v) \ , \end{aligned} \tag{3}$$

involving the differential operators $\mathbb{L}_{yy}\circ = \partial_y(E(y)\partial_y\circ)$, $\mathbb{L}_{xy} = \partial_x(E(y)\partial_y\circ)$, etc. Due to the linearity, for $k = 1, 2, 3$, $\tilde{u}^k$ can be expressed using the characteristic responses w^k, $k = 1, 2, 3$ (the so-called correctors of order ε^k), which are Y-periodic, *i.e.* $w^k(y) = w^k(y + \bar{y})$, satisfy in all subdomains Y_i, $i = 1, \ldots, n$ the following cascade of equations (complemented by interface conditions $[w^k] = 0$ and $[E\partial_y w^k + w^{k-1}] = 0$, where $[\ ]$ is the jump on any interface between Y_i and Y_{i+1})

$$\begin{aligned} -\mathbb{L}_{yy}w^1 &= \partial_y E w^0 \ , w^0 \equiv 1 \ , \\ -\mathbb{L}_{yy}w^{k+1} &= \partial_y(Ew^k) + E(\partial_y w^k + w^{k-1}) - \rho w^{k-1}D^0/\rho_0 \ , \text{ for } k = 1, 2 \ , \\ -\mathbb{L}_{yy}\varphi^3 &= \rho(M^1/\langle\rho\rangle_Y - w^1) \ , \end{aligned} \tag{4}$$

involving $\rho_0 = \langle\rho\rangle_Y$ and D^0, the standard effective elasticity, as defined below. Then the effective medium material properties can be computed

$$\begin{aligned} D^0 &= \left\langle E(1 + \partial_y w^1)\right\rangle_Y \ , \\ D^2 &= \left\langle E(w^2 + \partial_y w^3)\right\rangle_Y \ , \\ M^k &= \left\langle \rho w^k \right\rangle_Y \ , \quad k = 1, 2 \ , \\ M^3 &= \left\langle E\partial_y\varphi^3\right\rangle_Y \ . \end{aligned} \tag{5}$$

Based on (2), one can define the truncated averaged expansions of displacements $U^{(2)}(x,t) = U^0 + \varepsilon U^1 + \varepsilon^2 U^2$ and external forces $F^{(2)}(x,t) = F^0 + \varepsilon F^1 + \varepsilon^2 F^2$, such that the homogenized elastodynamic equation providing an approximation of (1) up to $o(\varepsilon^2)$ accuracy attains the following form

$$\mathcal{W}_{tx} \circ U^{(2)}(t,x) = \mathcal{F}_{tx} \circ F^{(2)}(t,x) \ , \tag{6}$$

where the operators $\mathcal{W}_{tx}$ and $\mathcal{F}_{tx}$, being parameterized by α and β are given,

$$\begin{aligned}\mathcal{W}_{tx} \circ U(t,x) := &\left(1 + \varepsilon^2 r_2(1-\alpha-\beta)\partial_{xx}^2 + \varepsilon^2 r_2 \frac{\beta}{c_0^2}\partial_{tt}^2\right)\partial_{tt}^2 U(t,x) \\ &-c_0^2\left[1-\varepsilon^2\left(r_2\alpha - D^2/D^0\right)\partial_{xx}^2\right]\partial_{xx}^2 U(t,x)\ , \\ \mathcal{F}_{tx} \circ F(t,x) := &\left[1 - \varepsilon\frac{M^1}{\rho_0}\partial_x - \varepsilon^2 r_2\left(\left(\alpha - \frac{\bar{M}^3}{M^2}\right)\partial_{xx}^2 + \frac{\beta}{c_0^2}\partial_{tt}^2\right)\right]F(t,x)\ ,\end{aligned} \tag{7}$$

involving the sound speed $c_0^2 = D^0/\rho_0$, and further coefficients $r_2 = M^2/\rho_0$, and $\bar{M}^3 = M^3 + \frac{(M^1)^2}{\langle\rho\rangle_Y}$. In, principle, parameters α, β can be chosen, whereby constraints are to be considered to ensure the hyperbolic character of (6), *cf.* Schwan et al. (2021). The external force $F^{(2)}$ can also be interpreted as the interaction force imposed by "resonators", as introduced below.

3.2. Periodic structures with resonators

The periodic structures like heterogeneous rods (rather than layered media) can be fitted with "ball-spring" couples which can be tuned to induce the acoustic band gaps. In the context of the asymptotic homogenization, these couples are characterized by the mass and the stiffness related proportionally to ε, see Rohan et al. (2009), which leads to the negative effective mass in the 1st order homogenized model, *i.e.* for $\varepsilon = 0$. Further we shall consider $M^1 = 0$ (which holds for any 2-component material), $\beta = 0$ and $\alpha = M^3/M^2$. For such a special case, denoting by $u_m^{(2)}$ the displacement of the resonator characterized by λ_m and Λ_m,

$$\begin{aligned}&\mathcal{W}_{tx} \circ U^{(2)} = \mathcal{F}_{tx} \circ F^{(2)}(t,x) = 0\ , \quad \text{with } F^{(2)} = \Lambda_m(u_m^{(2)} - U^{(2)})\ , \\ &\partial_{tt}^2 u_m^{(2)} + \lambda_m(u_m^{(2)} - U^{(2)}) = 0\ ,\end{aligned} \tag{8}$$

whereby also the operator $\mathcal{W}_{tx}$ is reduced due to $\beta = 0$, yielding the following equation,

$$\begin{aligned}&\Lambda_m\partial_{tt}^2 U^{(2)} + (\lambda_m + \partial_{tt}^2)\left(1 + \varepsilon^2 r_2(1-\alpha)\partial_{xx}^2\right)\partial_{tt}^2 U^{(2)} \\ &-c_0^2(\lambda_m + \partial_{tt}^2)\left[1-\varepsilon^2\left(r_2\alpha - D^2/D^0\right)\partial_{xx}^2\right]\partial_{xx}^2 U^{(2)} = 0\ .\end{aligned} \tag{9}$$

3.3. Dispersion analysis

The influence of the higher order terms on the modelling of wave propagation can be studied using the classical dispersion analysis. For this, using the plane wave ansatz involving the wave number $\varkappa$ and the circular frequency ω is substituted in (6) which, in general, yields a bi-quadratic equation involving both $\varkappa^{2k}$ and ω^{2k}, $k = 1, 2$. The dispersion can be analyzed using the mappings $\varkappa^2 \mapsto \omega^2$, or $\omega^2 \mapsto \varkappa^2 =: \gamma$. For the latter alternative, the following quadratic equation is obtained for the model involving the resonators,

$$\begin{aligned}&A\gamma^2 + B\gamma + C = 0\ , \quad \text{where} \\ &A = \varepsilon^2 c_0^2(\alpha r_2 - D^2/D^0)(\lambda_m - \omega^2)\ , \\ &B = (\lambda_m - \omega^2)[c_0^2 + \varepsilon^2\omega^2 r_2(1-\alpha)]\ , \\ &C = \omega^2[\omega^2 - (\Lambda_m + \lambda_m)]\ .\end{aligned} \tag{10}$$

Propagating wave modes exist for positive roots $\gamma = \varkappa^2 > 0$, while negative roots $\gamma = \varkappa^2$ indicate band gaps. When $\varepsilon = 0$, (10) reduces to one obtained for the 1st order homogenization result, $\omega = c_0\varkappa$. For the model without resonators, (10) still holds with $\Lambda_m = \lambda_m = 0$, which consequently enables to divide by ω^2. To illustrate the wave dispersion, we consider a simplified model extended only by $\partial_{xxxx}^4 U$ w.r.t. the 1st order homogenized model, so that the microscopic length is involves in coefficient A through r_2 and D^2. In particular, for a bi-laminate structure represented by E_j and ρ_j in layers Y_j, $j = 1, 2$, we consider $\rho_1 = \rho_2$, whereas $E_2 \gg E_1$, and put $\alpha = 1$, $\beta = 0$, which yields (the case without resonators)

$$\omega^2 = K^\varepsilon(\varkappa^2) := \varkappa^2 c_0^2\left(1 - \varepsilon^2\frac{D^2}{D^0}\varkappa^2\right)\ , \tag{11}$$

which clearly yields two real frequencies for any $\varepsilon < (D^0/(D^2\bar{\varkappa}))^{1/4}$, noting that $\varkappa = \varepsilon\bar{\varkappa}$, where $\bar{\varkappa} = 2\pi/\bar{y}$ is expressed in terms of the period length $\bar{y}$. It is of interest to explore the influence of the resonators; in this case, (10) leads to

$$\omega^4 - \left(K^\varepsilon(\varkappa^2) + \Lambda_m + \lambda_m\right)\omega^2 - \lambda_m K^\varepsilon(\varkappa^2) = 0\,. \tag{12}$$

For $\varepsilon = 0$, (11) verifies the standard model, $\omega = c_0\varkappa = \sqrt{K^0(\varkappa)}$,however, due to the added resonators characterized by Λ_m and λ_m, the band gap effect appears for $\omega \in]\sqrt{\lambda_m}, \sqrt{\lambda_m + \Lambda_m}[$. For $\varepsilon > 0$, also the inner length $\ell^\varepsilon = \varepsilon\bar{y}$ is pronounced through the term $\varkappa^4$ in K^ε, see Fig. 1. Of the 2 roots of the bi-quadratic equation for $\gamma = \varkappa^2$, only one mode can propagate, if $\gamma > 0$, the stop bands are indicated for $\gamma < 0$.

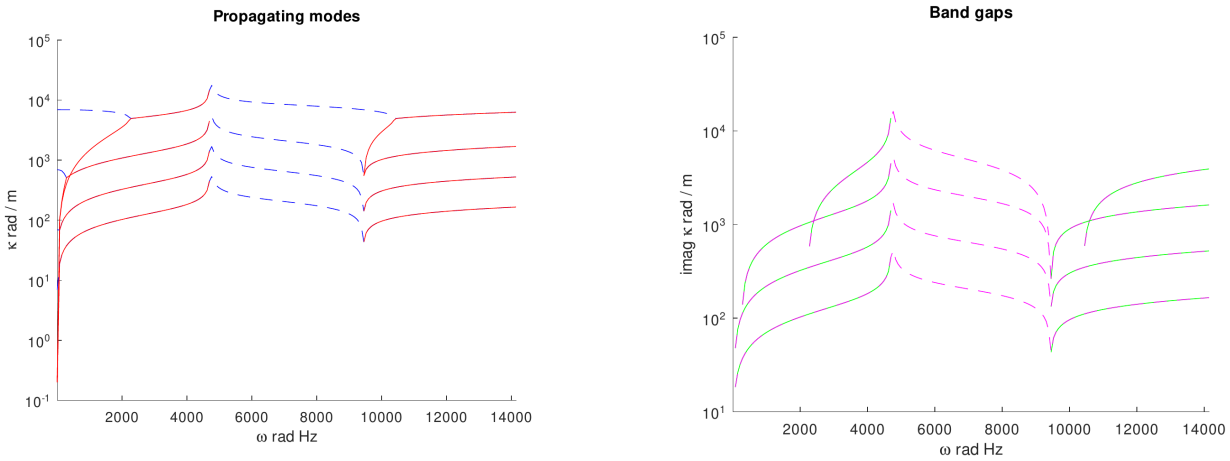

Fig. 1: Dispersion analysis $\omega \mapsto \varkappa$ for the model with resonators, Eq. (10), attaining the form (12). Clear band gaps between 4714 Hz and 9428 Hz. Four scales considered: $\varepsilon \in \{0.001, 01, 0.1, 1\}$.

4. Conclusion

The paper presents the higher order homogenization base modelling approach which provides the effective elastodynamics models involving higher orders temporal and spatial derivatives, namely $\partial^4_{xxxx}U$, $\partial^4_{tttt}U$ and $\partial^2_{xx}\partial^2_{tt}U$. Such models are comparable with the ones proposed on the purely phenomenological basis. Moreover, specific metamaterial features can be introduced, providing many further perspectives in the context of electro-mechanical devices with vast applications.

Acknowledgment

The research has been supported by the project GACR 23-06220S of the Czech Science Foundation.

References

Andrianov, I., Bolshakov, V., Danishevs'kyy, V., and Weichert, D. (2008) Higher order asymptotic homogenization and wave propagation in periodic composite materials. *Proceedings of the Royal Society A: Mathematical, Physical and Engineering Sciences*, 464, 2093, pp. 1181–1201.

Cornaggia, R. and Guzina, B. (2020) Second-order homogenization of boundary and transmission conditions for one-dimensional waves in periodic media. *International Journal of Solids and Structures*, 188-189, pp. 88–102.

Dontsov, E., Tokmashev, R., and Guzina, B. (2013) A physical perspective of the length scales in gradient elasticity through the prism of wave dispersion. *International Journal of Solids and Structures*, 50, 22, pp. 3674–3684.

Rohan, E., Miara, B., and Seifrt, F. (2009) Numerical simulation of acoustic band gaps in homogenized elastic composites. *International Journal of Engineering Science*, 47, 4, pp. 573–594.

Schwan, L., Favrie, N., Cottereau, R., and Lombard, B. (2021) Extended stress gradient elastodynamics: Wave dispersion and micro-macro identification of parameters. *International Journal of Solids and Structures*, 219–220, pp. 34–50.

Wautier, A. and Guzina, B. (2015) On the second-order homogenization of wave motion in periodic media and the sound of a chessboard. *Journal of the Mechanics and Physics of Solids*, 78, pp. 382–414.

30th International Conference
ENGINEERING MECHANICS 2024
Milovy, Czech Republic, May 14 – 16, 2024

QCONCEPT OF SMART CYMBAL STRUCTURE FOR STRUCTURAL HEALTH MONITORING APPLICATIONS

Slabý V.[*], Bajer J.[**], Hadaš Z.[***]

Abstract: *The area of embedded sensors, adaptronics, smart material and smart structures has a key role in Structural Health Monitoring. The aim of embedding smart materials into engineering structures is to monitor a wide variety of material's properties and enabling continuous or permanent measurements of their structural integrity. The integration of sensors into the structure is limited to processing technology used for embedding sensors and the possibility to damage the structure during insertion. This study focuses on developing sensory structure with force to voltage amplifying capabilities. The base unit and periodic concept of such structure is developed, and FEM model of base unit is done to observe basic behavior under load. Experiments with base unit for its voltage response were carried out on a prototype. Furthermore, a three base unit sample is created and a concept of a planar three-layer structure is developed.*

Keywords: Adaptronics, cymbal structure, metamaterial, MFC, smart structure, sensing.

1. Introduction

Integration of embedded sensors and smart material sensors to form a smart structure that can be used for standard design practices, fabrication, construction, and general industrial use belongs to one of the greatest engineering research challenges (Varshney et al., 2021). When studying engineering structure's behavior, a set of approaches can be taken from the field of Structural Health Monitoring (SHM). Destructive techniques use methods of permanently damage structures such as drilling out samples or mechanically exciting testing structures. Non-destructive techniques (NDT) can be on-site with the presence of educated personnel or off-site where remote monitoring and/or testing takes place. The standard approach of NDT is to glue sensors on the surface or using devices with thermometers, ultrasonic sensors, or acoustic sensors. The lack of real-time monitoring during the lifetime of the engineering structure leads to unpredictable behavior and failures. This opens up the need of continuous monitoring and predictive maintenance of engineering structures (Askari et al., 2019; Gharehbaghi et al., 2022).

In the field of smart structures several studies focused on the use of optic fiber sensors, piezoelectric materials, and strain gauges. Ramly et al. (2012) deployed fiber bragg grating sensor in a composite honeycomb structure for monitoring strains in a composite structure (Ramly et al., 2012). To sense external stimuli and react to external stimuli a piezoelectric transducer can be used. Silva et al. focused on a research for nonlinear energy sink with the use of piezoelectric elements and achieve the vibration attenuation for wide range of frequencies (Silva et al., 2018). Yesner et al. (2019) deployed an energy harvesting smart structure for engineering civil structures as a monitoring and harvesting unit. They also evaluated the limitations of the adhesive layer thickness and uniformity (Yesner et al., 2019). Gurung et al. focused on using a shape memory alloy (SMA) for its self-sensing properties to exploit its self-actuation potential.

[*] Vojtěch Slabý: Faculty of Mechanical Engineering, Brno University of Technology, Technicka 2896/2; 616 69, Brno; CZ, vojtech.slaby@vutbr.cz

[**] Jan Bajer: Faculty of Mechanical Engineering, Brno University of Technology, Technicka 2896/2; 616 69, Brno; CZ, jan.bajer@vutbr.cz

[***] Assoc. Prof. Zdenek Hadas, PhD.: Faculty of Mechanical Engineering, Brno University of Technology, Technicka 2896/2; 616 69, Brno; CZ, hadas@fme.vutbr.cz

doi: 10.21495/em2024-262

They used extended Kallman filter for displacement prediction. Huang et al. used auxetic mechanical metamaterial foams with strain gauges to enhance sensitivity and an operation range of strain smart material sensors for bionic hand grip sensing. They also implemented a statistical correlation algorithm to run in real-time on a budget controller, and they achieved 100 ms response time (Huang et al., 2022).

We propose a concept of a periodic cymbal structure for a pressure to voltage converter with high sensitivity and scalability properties. The proposed structure converts compression forces in one axis into tensile forces in the second axis. The compression force is amplified and converted into a larger tensile force that creates a high sensitivity range.

2. Methods

The base unit in 0 consists of a top and bottom cymbal structure that converts compression into a higher tension. Between top and bottom lamellas is a smart macro fiber composite (MFC) in a d33 operation mode. For larger planar vibration monitoring a periodic cymbal structure with piezoelectric macro fiber composites is considered. The idea comprises of determining the mechanic vibration wave characteristics and direction. The prototype testing unit has a dimension of 28 x 7.5 x 5.5 mm.

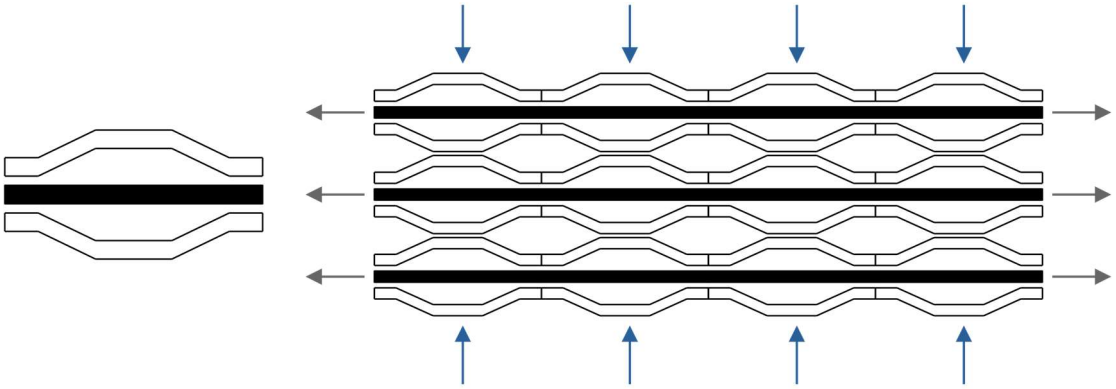

Fig. 1: A concept of smart sensory structure a) base unit with MFC, b) planar metamaterial; structure with MFC patches.

3. Results

3.1. Finite element analysis of the cymbal transducer

FE analysis (0) was performed to investigate the behaviour of a single transducer under static loading. The cymbal (bridge) transducer was fixed in the base and a compressive force of 10 N was applied to the top cap. The converted tensile force applied to the MFC film between the caps of the transducer was 30.4 N. The ratio of these values gives the transducer gain, which is approximately 3.

At this load, the stress in the MFC in the constant region between the caps is about 11.5 MPa. This region is responsible for generating the electrical charge in the pizoelectric material and is also the most critical point of the entire transducer in terms of stress.

3.2. Compression to stretching base unit capabilities

The integrated piezoelectric material serving as a sensing element is a macro fiber composite (MFC). The chosen smart material is suitable for sensing applications because of its lower power densities and more robust to cracks compared to fragility of lead zirconium titanate (PZT), however the Young's modulus of MFC is five times less than PZT (Shen et al., 2007).

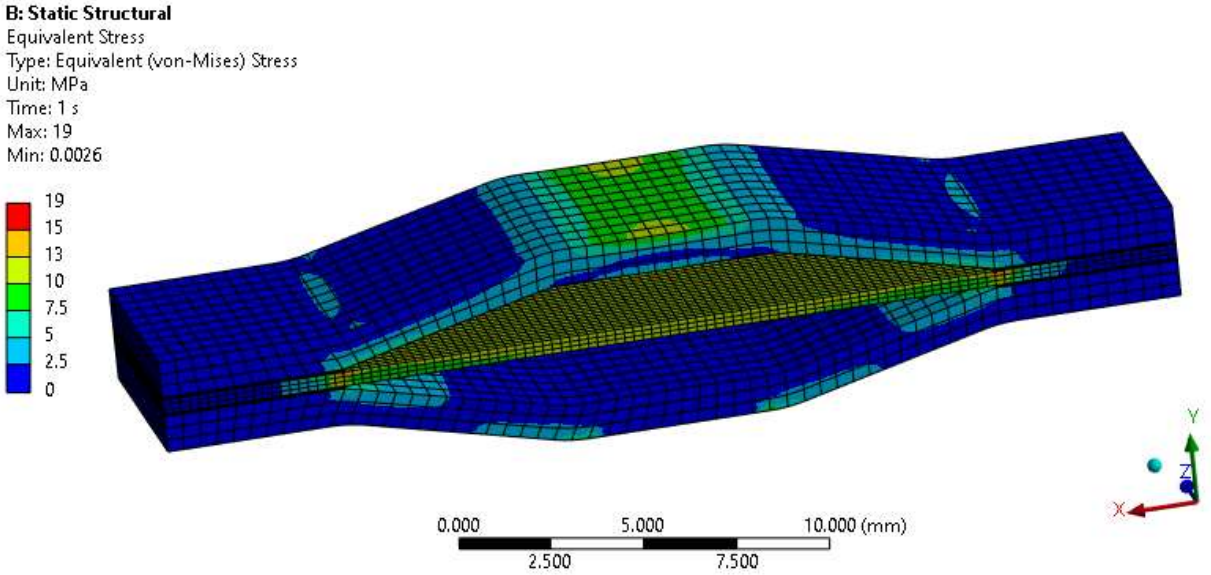

Fig. 2: FEA results for equivalent stress in cymbal transducer.

The measurement was conducted with an impact hammer and an oscilloscope probe with a 1 MΩ input impedance. The impact hammer and the probe were connected to the National Instruments measurement card. The base unit was connected to a voltage divider to lower the output voltage and prevent damaging the measurement card. While measuring the voltage response with the NI card a voltage divider was used to lower the output voltage of a base unit. The periodic oscillation character of the system will be analyzed further for sensing applications.

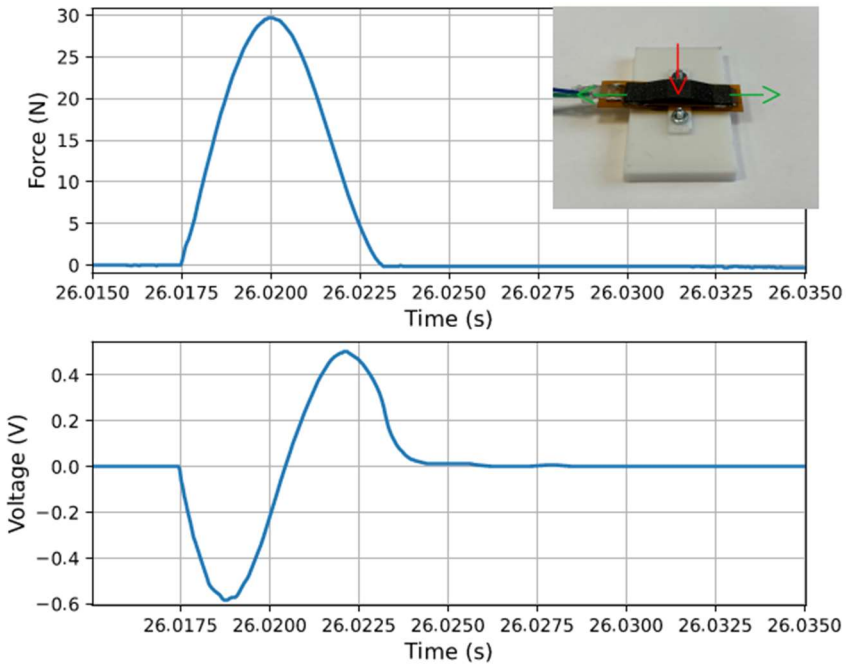

Fig, 3: Experimental response measurement of a smart structure's base unit.

4. Conclusion

The smart material structure's base unit with integrated MFC was tested to evaluate voltage response. Firstly, a concept was developed based on composite smart structure with integrated piezoelectrics as is illustrated in 0. Secondly, FEM analysis for static response of proposed geometry was performed. A base unit of proposed smart structure was manufactured and its voltage response to external impact force was measured. Lastly, a concept for three base units and three-layer planar structure was constructed

as shown in 0. From the measurements of the base unit, further investigation of its planar and spatial capabilities will be performed.

Fig. 4: Three base unit testing sample and a planar three-layer concept smart structure.

Future research will be aimed at the embedding smart materials in a structure in 0, and on the design of a sensory platform for sensing and identification of external stimuli, characterization, identification of a mechanical wave propagation in the structure, and identifying the load characteristics across the spatial geometry.

Acknowledgement

The presented research was supported by the project GACR 22-14387J "Design and manufacturing of 4D metamaterials based on printed structures with embedded elements of smart materials".

References

Askari, H., Amir, K., Mir, B. K. and Zhong, L. W. (2019) Embedded Self-Powered Sensing Systems for Smart Vehicles and Intelligent Transportation. *Nano Energy,* 66, 104103.

Gharehbaghi, V. R., Farsangi, E. N., Noori, M., Yang, T. Y., Li, S., Nguyen, A., Málaga-Chuquitaype, Ch., Gardoni, P. and Mirjalili, S. (2022) A Critical Review on Structural Health Monitoring: Definitions, Methods, and Perspectives. *Archives of Computational Methods in Engineering,* 29 (4), 2209–2235.

Xin, H., Guo, W., Liu, S., Li, Y., Qiu, Y., Fang, H., Yang, G., Zhu, K., Yin, Z., Li, Z. and Wu, H. (2022) Flexible Mechanical Metamaterials Enabled Electronic Skin for Real-Time Detection of Unstable Grasping in Robotic Manipulation. *Advanced Functional Materials,* 32 (23): 2109109.

Ramly, R., Wahyu, K. and Rahman, M. K. A. (2012) Using Embedded Fiber Bragg Grating (FBG) Sensors in Smart Aircraft Structure Materials. *Procedia Engineering*, International Symposium on Robotics and Intelligent Sensors (IRIS 2012), 41: 600–606.

Shen, D., Choe, S.-Y. and Kim, D.-J. (2007) Analysis of Piezoelectric Materials for Energy Harvesting Devices under High-g Vibrations. *Japanese Journal of Applied Physics,* 46 (10R): 6755.

Silva, T. M. P., Clementino, M. A., De Marqui, C. and Erturk, A. (2018) An Experimentally Validated Piezoelectric Nonlinear Energy Sink for Wideband Vibration Attenuation. *Journal of Sound and Vibration,* 437, 68–78.

Varshney, A., Garg, N., Nagla, K. S., Nair, T. S., Jaiswal, S. K., Yadav, S. and Aswal, D. K. (2021) Challenges in Sensors Technology for Industry 4.0 for Futuristic Metrological Applications. *MAPAN* 36 (2): 215–26.

Yesner, G., Jasim, A., Wang, H., Basily, B., Maher, A. and Safari, A. (2019) Energy Harvesting and Evaluation of a Novel Piezoelectric Bridge Transducer. *Sensors and Actuators A: Physical,* 285: 348–54.

30th International Conference
ENGINEERING MECHANICS 2024
Milovy, Czech Republic, May 14 – 16, 2024

NON-LINEAR PROBABILISTIC ASSESSMENT OF EXISTING BRIDGE CONSIDERING DETERIORATION

Slowik O.*, Šomodíková M., Novák D.*****

Abstract: *The integration of the non-linear finite element method with deterioration-based analysis represents a powerful approach for accurately simulating structural behaviors. However, conducting fully probabilistic analyses on large-scale models that incorporate numerous stochastic variables remains a significantly time-intensive task. As a result, structural designers and engineers frequently prefer semi-probabilistic methods, which significantly reduce the need for extensive non-linear computations. This paper concentrates on evaluating the reliability of an existing railway bridge constructed with cast-in steel beams. It employs an advanced numerical analysis through a non-linear finite element model, combined with established semi-probabilistic approaches, including the ECoV method and the newer eigen ECoV method. To accurately reflect the current state of the bridge's superstructure, the analysis models the carbonation of concrete and the ensuing corrosion of steel beams using analytical models that consider both the fundamental material properties and environmental factors.*

Keywords: Non-linear finite element analysis, stochastic analysis, deterioration-based analysis, reliability analysis, semi-probabilistic methods.

1. Introduction

Assessing the residual carrying capacity of bridges is crucial for civil engineers to ensure the safety of road and railway infrastructure. Utilizing reliability assessment methods alongside finite element method (FEM) analysis, which accounts for material and geometric non-linearities, allows for a more realistic simulation of structural behavior. This approach offers a precise evaluation of existing structures. According to EN 1994-2 (2005), non-linear analysis can be employed to evaluate the global resistance of bridges, though specific application rules are not provided. Despite the high accuracy of non-linear FEM, incorporating uncertainty in material parameters is vital for accurate real-world modeling, making complex stochastic analysis necessary over deterministic approaches. The structural condition and degradation processes, like concrete carbonation or corrosion of metal components, significantly affect the load capacity assessment, underscoring the importance of advanced stochastic non-linear numerical analysis in evaluating bridge deterioration. This comprehensive assessment is crucial for allocating maintenance budgets efficiently. The methodology for this advanced deterioration-based probabilistic assessment, applicable to both reinforced and prestressed concrete as well as steel-concrete structures, is detailed in research by Červenka (2008) and Šomodíková et al. (2016). The paper presents an analysis of a standard railway bridge in the Czech Republic, determining its load-carrying capacity through probabilistic and semi-probabilistic methods combined with a FEM model, and considers the current state and degradation of concrete, reinforcement, and steel elements, modeling the effects of concrete carbonation and steel corrosion.

* Ing. Ondřej Slowik, PhD.: Faculty of Civil Engineering, Brno University of Technology; Veveří 331/95; 602 00, Brno; CZ, slowik.o@fce.vutbr.cz

** Ing. Martina Sadílková Šomodíková, PhD.: Faculty of Civil Engineering, Brno University of Technology; Veveří 331/95; 602 00, Brno; CZ, martina.sadilkova.somodikova@vut.cz

*** Prof. Ing. Drahomír Novák, DSc.: Faculty of Civil Engineering, Brno University of Technology; Veveří 331/95; 602 00, Brno; CZ, Drahomir.Novak@vut.cz

doi: 10.21495/em2024-266

2. Methods

In case of reliability assessment of existing structures based on the non-linear FEM analysis semi-probabilistic methods are being increasingly used due to the time-consuming nature of FEM simulation. In general, a structure is reliable if the structural resistance, R, is greater that the action effect, E. Failure of the structure is represented by the condition $R - E < 0$ with $Z = R - E$ being the so-called safety margin. In the semi-probabilistic approach, the resistance of structure, R, is separated and the design value, R_d, that satisfies safety requirements is evaluated. For this purpose, the ECoV method (Červenka, 2008) and the eigen ECoV method (Novák & Novák, 2021) are used in this paper.

2.1. ECoV method

The ECoV method by Červenka (2008) works with the estimation of the coefficient of variation (CoV) of the resistance, v_R, defined based on the estimation of the mean and characteristic values of the resistance (R_m and R_k). Assuming a log-normal distribution of the resistance, the coefficient of variation is defined as:

$$v_R = \frac{1}{1.645} \ln\left(\frac{R_m}{R_k}\right) \tag{1}$$

When using v_R, the global safety factor is calculated according to the formula:

$$\gamma_R = \exp(\alpha_R \beta v_R) \tag{2}$$

where α_R is the sensitivity factor defined by the value of $\alpha_R = 0.8$ according to EN 1990 (2002) and β is the reliability index defined for a given design situation. The design value of the resistance is calculated as:

$$R_d = \frac{R_m}{\gamma_R} \tag{3}$$

2.2. Eigen ECoV method

A proposed eigen ECoV method by Novák and Novák (2021) is derived directly from Taylor series expansion, a classical method for a statistical analysis of function of random input vector. However, there is an assumption of fully correlated input random variables similarly to ECoV according to the fib Model Code 2010 (2013). The eigen ECoV formula for the estimation of v_R is defined in the following form:

$$v_R \approx \frac{3R_m - 4R_{\Theta\frac{\Delta}{2}} + R_{\Theta\Delta}}{\Delta_\Theta} \cdot \frac{\sqrt{\lambda_1}}{R_m} \tag{4}$$

With utilization of mean and characteristic values of the resistance, the value of $R_{\Theta\Delta} = R_k$ corresponds to the value of resistance calculated with the characteristic values of input random variables, $X_{i,k}$, and $R_{\Theta\frac{\Delta}{2}} = R_{\frac{\Delta}{2}}$ value is assessed based on the simulation with intermediate values of random variables according to:

$$X_{i,\frac{\Delta}{2}} = \frac{\mu_{X_i} + X_{i,\Delta}}{2} \tag{5}$$

Finally, the Δ_Θ represents the distance between the mean value, μ_Θ, and desired quantile $F_\Theta^{-1}(\Phi(-c))$ where c is a step size parameter ($c = 1.645$ in this case), F_Θ^{-1} is an inverse cumulative distribution function and Φ is the cumulative distribution function of the standardized Gaussian distribution. The following approximation can be used:

$$\Delta_\Theta = \mu_\Theta - \mu_\Theta \cdot \exp\left(-c \cdot \frac{\sqrt{\lambda_1}}{\mu_\Theta}\right) \tag{6}$$

The global safety factor, γ_R, and the design value of the resistance, R_d, are assessed based on Eqs. (2–3).

3. Case study

A single span railway bridge located in the Czech Republic was analyzed as a case study using semi-probabilistic methods described above. The bridge was put into service 135 years ago with the last major reconstruction before 85 years. A double-track railway line slab bridge spans a local road, supported by two concrete abutments and reinforced concrete bearing seats. Its superstructure comprises 28 cast-in steel I-beams, measuring 11.00 m in width and 8.10 m in length. Inspections of similar structures in the Czech Republic indicate concrete degradation up to 40 mm deep across the beam shell, attributed to deterioration and mechanical damage on the superstructure's bottom. Additionally, the beams' flanges show localized exposure with metal plates suffering from pitting corrosion, reaching depths of up to 3.0 mm.

Non-linear deterministic model of the bridge superstructure was created in the ATENA Science programming shell. The "3D Nonlinear Cementitious 2" material model used to represent the behavior of concrete. For steel, a bilinear stress-strain law without hardening was considered. Rolled I45 steel beams are the main carrying elements of the bridge deck superstructure. The beams are placed in the concrete slab deck. Beams placement was considered on linear supports. The axial distance of the beams in the deck is 390 mm. A typical segment of the bridge deck is shown in Fig. 1 (left). The use of steel beams made of S235 steel and C8/10 concrete class was assumed. The values of the material parameters used for the deterministic analysis correspond to the mean values, μ, of these parameters according to the stochastic model of input random variables used for the subsequently performed stochastic analysis; see Tab. 1. The imposed load by rail traffic was considered in accordance with EN 1991-2 (2003), simplified as uniformly distributed over the length of the deck.

3.1. Stochastic analysis

Due to the lack of information on the material parameters of concrete and steel used, the values derived from the assumed nominal values typical for the defined strength classes of materials were considered. The stochastic model (Tab. 1) in the form of mean values, μ, and coefficients of variation (CoV) of material parameters for concrete was defined based on the value of concrete compressive strength, f_c, from which other parameters of the concrete were derived according to EN 1992-1-1 (2004) and the fib Model Code 2010 (2013). The probability distribution function (PDF) and material parameters of steel were determined according to Joint Committee on Structural Safety (JCSS, 2001). For the basic stochastic analysis of carrying capacity, 30 random simulations were generated using Latine Hypercube Sampling method and simulated annealing approach to introduce correlations. The mid-span measured load–deflection curves corresponding to simulated realizations of stochastic model are captured in the Fig. 1 (right).

Parameter* **[Unit]**	$\boldsymbol{\mu}$	**CoV**	$\boldsymbol{k}^{**}$	$\frac{\Delta}{2}=\frac{\boldsymbol{\mu}+\boldsymbol{k}}{2}$
E_c [GPa]	25.331	0.15	19.601	22.466
f_t [MPa]	1.905	0.30	1.126	1.515
f_c [MPa]	16.0	0.06	8.0	12.0
G_f [$\times 10^{-5}$ N/m]	12.02	0.128	9.67	10.85
E_{st} [GPa]	210.0	0.03	199.8	204.9
$f_{y,st}$ [MPa]	265.0	0.07	235.0	250.0

* All the parameters have log-normal (2-par.) PDF

** Characteristic value corresponds to 5 % or 95 % percentile of PDF

Tab. 1: Stochastic model of input random variables.

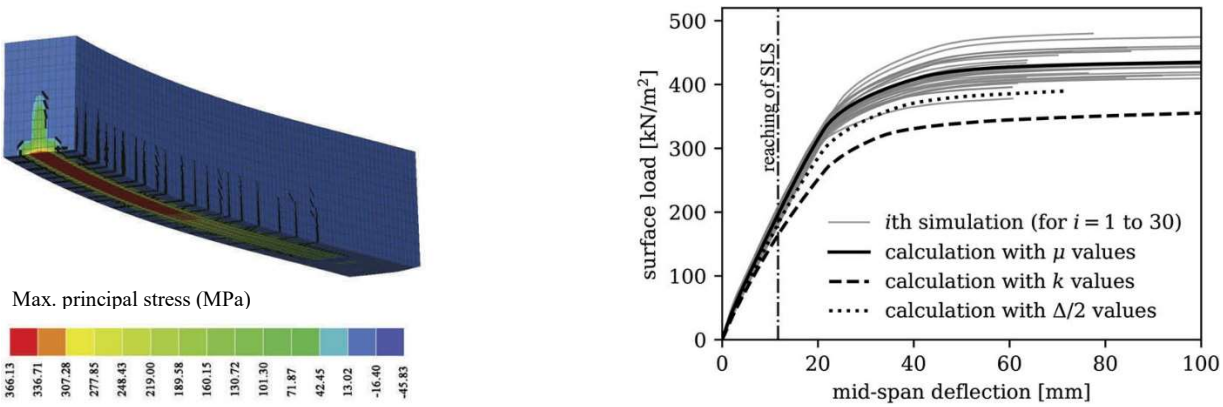

Fig. 1: A typical segment of the bridge deck at ultimate limit state (left), and the load–deflection curves corresponding to simulated realizations of stochastic model (right).

The serviceability limit state (SLS, $l/600 = 11$ mm) and ultimate limit state (ULS, reaching the yield strength with partial plasticization of the steel beams) were analyzed. The estimation of the design

resistance value at ULS was performed for a reliability index $\beta = 3.8$ multiplied by a sensitivity coefficient $\alpha_R = 0.8$ in accordance with EN 1990 (2002) as a quantile corresponding to a failure probability $p_f = 0.001183$. When reaching the SLS, i.e. the limit value of the vertical deflection of the typical segment, the design value of the resistance was determined for the reliability index value $\beta = 0.0$.

3.2. Modelling of degradation processes

In order to take the actual condition of the bridge superstructure into account, modelling of degradation processes was performed. Processes of concrete carbonation due to CO_2 and consequent following corrosion of cast-in I45 steel beams were modelled using analytical models recommended by the fib Model Code for Service life design (2006). The models take the material parameters as well as the environmental characteristics into account. For detailed description of degradation analysis, see Šomodíková et al. (2022). The stochastic evaluation of analytical degradation was performed on the model. The design values of load carrying capacity for SLS and ULS where than calculated on models with different state of degradation over time using ECoV a eigen ECoV methods (see Chap. 2). The results are summarized in Tab. 2. The results confirmed a gradual decrease in design carrying capacity due to deterioration. Both semi-probabilistic methods give similar results, the ECoV method is slightly more conservative.

	R_m	R_k	$R_{\frac{\Delta}{2}}$	ECoV design value	Eigen ECoV design value
Load at SLS (0 years)	196.8	164.3	182.1	196.8	196.8
Load at SLS (85 years)	181.8	152.9	168.6	181.8	181.8
Load at SLS (100 years)	178.0	150.8	165.9	178.0	178.0
Load at ULS (0 years)	425.2	342.3	383.6	284.8	292.7
Load at ULS (85 years)	402.4	328.3	365.0	276.3	281.7
Load at ULS (100 years)	395.7	322.1	358.1	270.5	273.6

Tab. 2: Resulting carrying capacity values in kN/m^2.

4. Conclusions

To accurately simulate structural behavior and current load carrying capacity of existing bridge structure, the study utilized advanced stochastic methods, detailed FEM analysis considering material and geometric non-linearities, and analytical models for deterioration processes. It outlined steps for a numerical deterioration-based probabilistic assessment of structural design resistance.

Acknowledgement

The financial support from the European Union within the framework of program Interreg Austria-Czechia 2021-2027, project No. ATCZ00068 / IREC, is gratefully acknowledged. Some theoretical achievements developed under the Czech Science Foundation (GAČR) project No. 22-00774S have been utilized here.

References

Červenka, V. (2008) Global safety format for nonlinear calculation of reinforced concrete. *Beton- Stahlbetonbau*, 103, S1, pp. 37–42.

Novák, L. and Novák, D. (2021) Estimation of coefficient of variation for structural analysis: The correlation interval approach. *Structural Safety*, 92, p. 102101.

Šomodíková, M., Lehký, D., Doležel, J. and Novák, D. (2016) Modeling of degradation processes in concrete: Probabilistic lifetime and load-bearing capacity assessment of existing reinforced concrete bridges. *Engineering Structures*, 119, pp. 49–60.

Šomodíková, M., Slowik, O., Lehký, D. and Doležel, J. (2022) Deterioration-based probabilistic assessment of design resistance of railway bridge. Bridge Safety, Maintenance, Management, Life-Cycle, Resilience and Sustainability. In: *Proc. 11th Int. Conf. on Bridge Maintenance, Safety and Management (IABMAS 2022)*, CRC Press, pp. 339–347.

30th International Conference
ENGINEERING MECHANICS 2024
Milovy, Czech Republic, May 14 – 16, 2024

INVESTIGATION OF 3D FLOW STRUCTURES IN A LINEAR BLADE CASCADE WITH STEREO PARTICLE IMAGE VELOCIMETRY

Šnábl P.*, Procházka P., Uruba V.***, Pešek L.†**

Abstract: *In most experiments and numerical calculations of flow through blade cascades, there is a tendency to reduce the problem to 2D. This is understandable due to the design of the experimental rigs and measurement methods, as well as the very long computation times of 3D numerical flow simulations. In reality, however, 3D flow structures such as streamwise vortices begin to appear in wakes behind profiles even for 2D geometry even at low Reynolds nubers. They can create force variations acting along the blade span, which can be represented on average by the 2D measurement and simulation and give a correct result, e.g. for the total lift and drag of the profile. However, when investigating dynamic aeroelastic instabilities such as flutter, local variations in aerodynamic forces can greatly influence the overall behaviour, e.g. by inducing stall flutter.*

Keywords: Experimental flow dynamics, blade cascade, 3D flow structures, stereo PIV.

1. Introduction

The aeroelastic stability of blade cascades is a very complex fluid-structure interaction phenomenon. In real turbomachinery there is a very complex 3D geometry with non-homogenous flow under rotation where gravity, centrifugal forces, Coriolis effect, etc. play their role, and so far it is impossible to numerically calculate the non-stacionary fluid-structure interaction on a full scale model. In the Institute of Thermomechanics of the CAS we have used reduced order structure models with Van der Pol model to describe the instabilities (Pešek et al., 2023a,b) and also the reduced order flow models (Prasad and Pešek, 2019; Prasad et al., 2023).

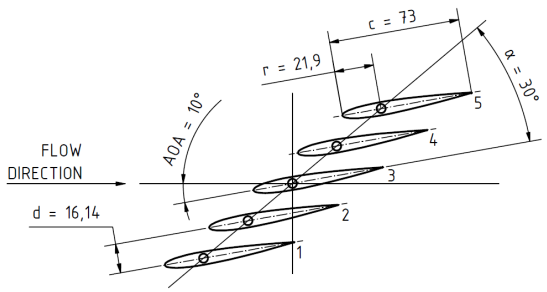

Fig. 1: The geometry of the blade cascade.

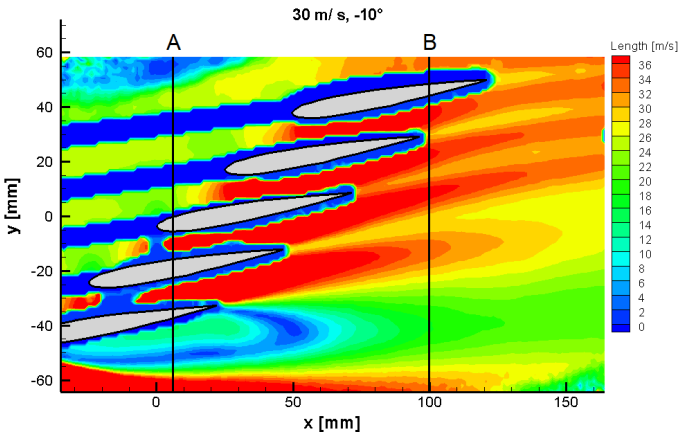

Fig. 2: 2D PIV measurement of the blade cascade.

* Ing. Pavel Šnábl: Institute of Thermomechanics of the CAS, Dolejškova 5; 182 00, Prague; CZ, snabl@it.cas.cz
** Ing. Pavel Procházka, PhD.: Institute of Thermomechanics of the CAS, Dolejškova 5; 182 00, Prague; CZ, prochap@it.cas.cz
*** Prof. Ing. Václav Uruba, CSc.: Institute of Thermomechanics of the CAS, Dolejškova 5; 182 00, Prague; CZ, uruba@it.cas.cz
† Ing. Luděk Pešek, CSc.: Institute of Thermomechanics of the CAS, Dolejškova 5; 182 00, Prague; CZ, pesek@it.cas.cz

doi: 10.21495/em2024-270

In order to study the aeroelasticity in a blade cascade experimentally, simplifications have to be made in order to make any measurements possible. Most researchers therefore use linear cascades: parallel blades with constant cross-sections. Although linear cascades lack some key features such as rotational periodicity and variation of parameters in the radial direction, it is still possible to obtain and study aeroelastic couplings. However, even though all the perpendicular cross sections along the blade span are the same and thus the geometry can be considered as 2D, the flow field does not necessarily have a 2D structure. In particular, corner vortices can emerge at the corners where the sidewalls and blade ends meet (Moon and Koh, 2001; Liu et al., 2016) and streamwise vortices in wakes start to appear appear at low Reynolds numbers (Procházka and Uruba, 2019).

To assess the significance of such 3D vortex structures on a linear blade cascade, which has been used in the past to study aeroelastic phenomena such as flutter (Šnábl et al., 2021, 2022), an experimental setup with the same geometry, shown in Fig. 1, was prepared. The prismatic NACA 0010 blades with a span of 100 mm fill the entire width of the test section channel with a cross-sectional dimension of 250×100 mm.

2. Methods

The experimental investigation of 3D flow structures within the cascade geometry was performed by using 3D Particle Image Velocimetry (PIV). Unlike standard 2D PIV, where a single fast camera is positioned perpendicular to an laser-illuminated plane, the 3D PIV measurement method incorporates two PIV cameras that are pointed at the illuminated plane under an angle from both sides. This enables to capture motion of the illuminated particles not only in the illuminated plane, but also through the plane. When the captured data from both cameras are handled by the post-processing software, all three velocity components of the flow in the plane of measurement (PoM) are calculated.

Our measurement system consists of a NewWave Pegasus laser to create the laser sheet and consequently illuminate the seeding particles. Two NanoSense MKIII cameras (1280×1024 px, 1024 Hz) are mounted on Scheinpflug adapters to correct for distortion as the camera lens plane is not parallel to the image plane. A special calibration procedure is also desirable to dewarp the images and evaluate the correct values of the velocity signal.

The cascade was exposed to a wind speed of 30 m/s that gives $Re = 140\ 000$ with respect to the blade cord; the angle of attack of all fixed blades was set to -10°. Two independent PoM A and B, perpendicular to the free stream and located 6 mm and 99 mm respectively downstream of the origin of the coordinate system, were selected and are shown in Fig. 2, where the flow field through the central plane of the cascade measured by 2D PIV is shown. The PoM A targets the large separation area under blade 1 and the channel between blades 1 and 2. The PoM B targets the wake region behind blades 1 and 2 further downstream.

3. Results

There is a distribution of time-averaged streamwise velocity component (W) in PoM A shown in Fig. 3a). The channel region between blade 1 and 2 is characterised by the occurrence of high velocity region (up to 60 m/s). The area describing the flow separation is more important - there is a black line marking the region of backflow (in terms of the W-component). Note that this region does not extend over the whole width of the channel, but fills about 80 % of the width. This is due to the presence of secondary (corner) vortices. These vortices were not fully captured; however, their presence is evident from the streamlines in Fig. 3b) – marked by red circles. Fig. 4a) reveals two individual time instants of the flow below the blade 1. Based on the vector lines, we can observe fully 3D and dynamic nature of the flow with a large amount of coherent structures; pseudo-periodic corner vortices are still visible.

The PoM B mainly covers the wake behind blade 1 and partly 2. The wake extension is large (green moderate velocity in Fig. 5a)), but it is in good agreement with the previous 2D PIV measurement shown in Fig. 2. The wake width is more than 30 mm. Fig. 5a) and Fig. 5b) are supplemented by dashed lines indicating the projection of the trailing edges well in front of the measurement plane. Just behind the trailing edge of the second blade there is a location of higher velocity (close to 30 m/s) - however this is not a contradiction as the actual wake region of the second blade is a little higher (as can be seen in Fig. 2). The flow rises in the whole area (Fig. 5b)) because it is deflected by the inclined blades. As in the previous case, there are two snapshots in time (0.15 s step) in Fig. 6, proving that the flow field behind the blade cascade is not only composed of spanwise oriented vortex structure, but mainly of streamwise oriented vortices, which

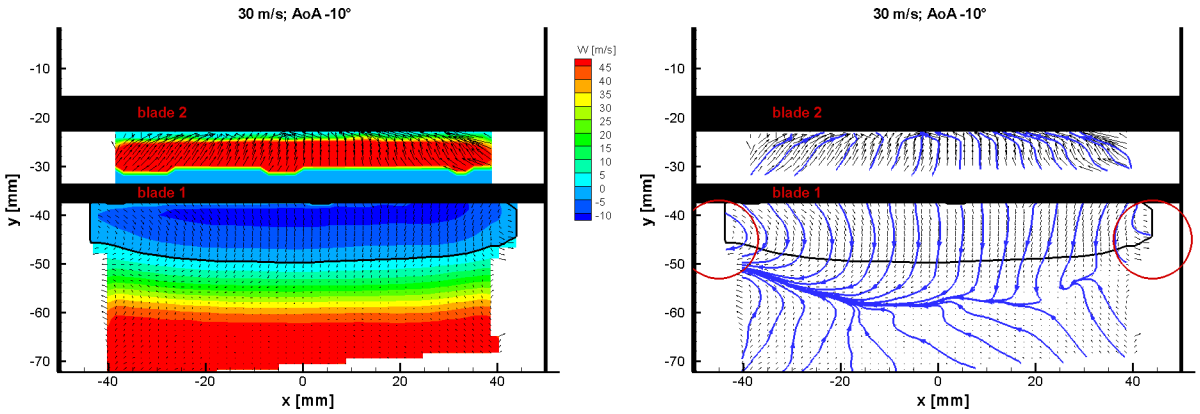

a) With contours of streamwise velocity component. *b) With streamlines in the PoM.*

Fig. 3: Time-averaged velocity in PoM A located 6 mm downstream the origin.

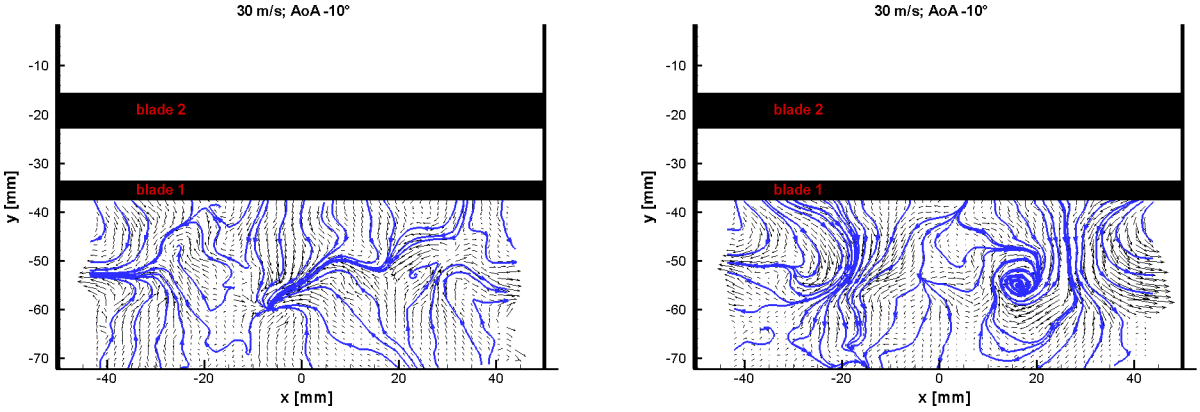

a) Time 0.04 s *b) Time 0.36 s*

Fig. 4: Two snapshots; streamlines mapping the structures in PoM A 6 mm downstream the origin.

play a crucial role in influencing the following blades. These streamwise vortices have a vortex axis parallel to the blade chord and occur mainly for larger values of AoA, when their vortex strength is significant compared to the case without flow separation.

4. Conclusions

The aim of this work was to measure 3D flow structures using 3D stereo PIV in order to map the vortex structures that could play an important role in the aeroelastic stability of the blade cascade. Two measurement planes were chosen; PoM A intersecting the inter-blade channel between blades 1 and 2, and PoM B located in the wake region far downstream of the blades.

The time averaged results show a fairly uniform velocity distribution which would correspond to the 2D case. The separation spanwise vortex fills about 80 % of the channel width and the corners are filled with streamwise corner vortices. However, the streamwise vortices emerge randomly in instantaneous flow field snapshots in the large separation bubble under blade 1 and then spread downstream. These vortices do not appear in a time-averaged image, nor could they even be shown in the 2D representation (in the streamwise plane).

In the research of aeroelastic stability of blade cascade, such local 3D flow structures can have impact on blade cascade stability and their importance will be further studied.

Acknowledgment

This research is supported by the research project of Czech science foundation No. 24-12144S “Investigation of 3D flow structures and their effects on aeroelastic stability of turbine-blade cascades using experiment and deep learning approach”.

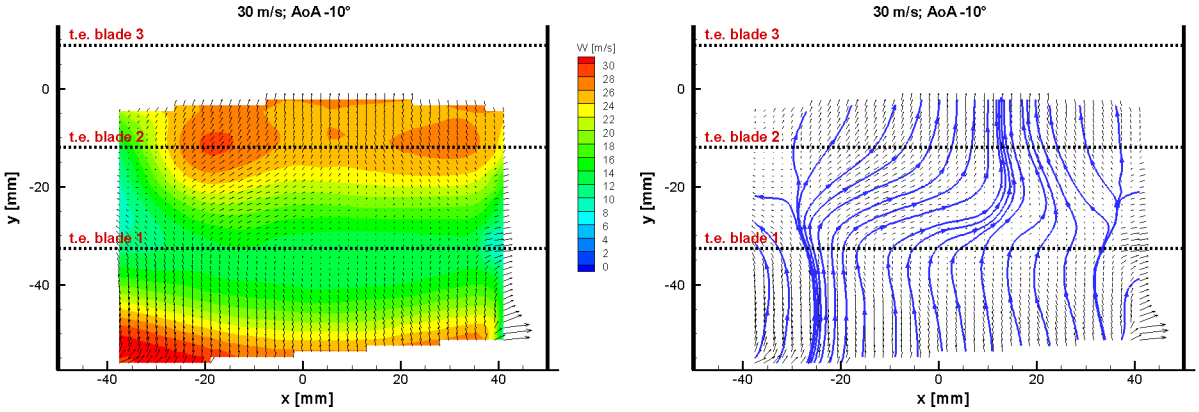

a) With contours of streamwise velocity component. *b) With streamlines in the PoM.*

Fig. 5: Time-averaged velocity in PoM B located 99 mm downstream the origin.

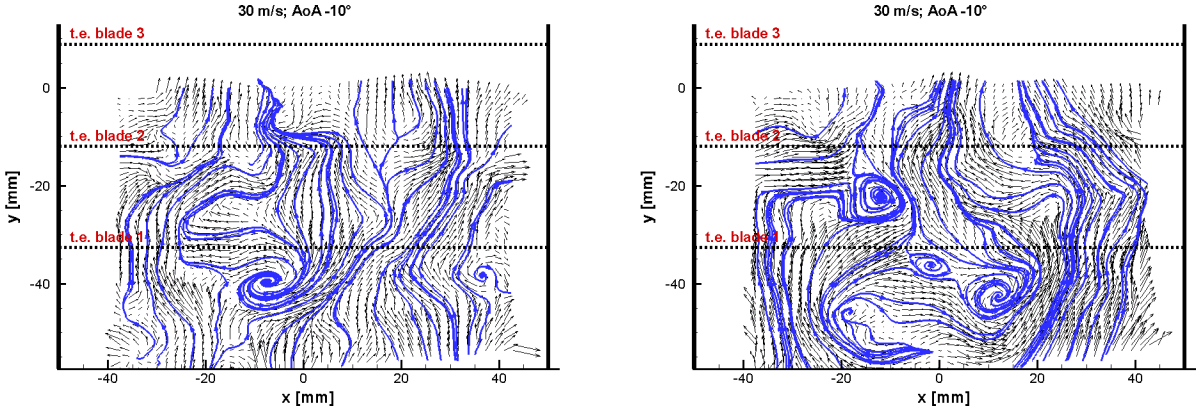

a) Time 0.02 s. *b) Time 0.17 s.*

Fig. 6: Two snapshots; streamlines mapping the structures in PoM B 99 mm downstream the origin.

References

Liu, Y., Yan, H. and Lu, L. (2016) Numerical Study of the Effect of Secondary Vortex on Three-Dimensional Corner Separation in a Compressor Cascade, *International Journal of Turbo & Jet-Engines, 33(1)*, pp. 9–18.

Moon, Y. J. and Koh, S. R. (2001) Counter-rotating streamwise vortex formation in the turbine cascade with endwall fence, *Computers & fluids, 30(4)*, pp. 473–490.

Pešek, L., Šnábl, P. and Prasad, C. S. (2023a) Turbine wheel reduced modal model for self-excited vibration suppression by inter-blade dry-friction damping, *Bulletin of the Polish Academy of Sciences. Technical Sciences, 71(6)*.

Pešek, L., Šnábl, P., Prasad, C. S. and Delanney, Y. (2023b) Numerical simulations of aeroelastic instabilities in a turbine-blade cascade by a modified Van der Pol model at running excitation, *Applied and Computational Mechanics, 17(1)*.

Prasad, C. S. and Pešek, L. (2019) Classical flutter study in turbomachinery cascade using boundary element method for incompressible flows, In: *Advances in Mechanism and Machine Science: Proceedings of the 15th IFToMM World Congress on Mechanism and Machine Science 15*, pp. 4055–4064.

Prasad, C. S., Šnábl, P. and Pešek, L. (2021) A meshless method for subsonic stall flutter analysis of turbomachinery 3D blade cascade, *Bulletin of the Polish Academy of Sciences. Technical Sciences, 69(6)*.

Procházka, P. and Uruba, V. (2019) Streamwise and spanwise vortical structure merging inside the wake of an inclined flat plate, *Mechanics & Industry 20(7)*, pp. 705.

Šnábl, P., Pešek, L., Prasad, C.S., Bula, V. and Cibulka, J. (2021) Experimental Setup and Measurement for Evaluation of Blade Cascade Stall Flutter Instability, In: *27th International Congress on Sound and Vibration*, Praha.

Šnábl, P., Pešek, L., Prasad, C.S. and Procházka, P. (2022) Experimental Investigation of Classical Flutter in Blade Cascade, In: *International Forum on Aeroelasticity and Structural Dynamics 2022*, Madrid.

30th International Conference
ENGINEERING MECHANICS 2024
Milovy, Czech Republic, May 14 – 16, 2024

INFLUENCE OF ARTERY UNFOLDMENT ON ITS MECHANICAL RESPONSE

Sochor O.*, Hrubanová A., Joukal M.***, Burša J.‡**

Abstract: *This study investigates the influence of artery unfoldment on its mechanical response in planar tension test. Inflation test was chosen for comparison because, with the axial stretch $\lambda_z = 1$, it also keeps plane strain condition. Both tests were simulated in silico using finite element method. The geometry models correspond to aorta and common carotid artery with distinguished two layers within the arterial wall; a homogenous wall model was also used for comparison. Material models were acquired by fitting the uniaxial tension tests of human carotid arteries dissected into media and adventitia layers with 3rd order Yeoh hyperelastic model. The results showed that the artery segment straightening leads to a non-uniform stress distribution throughout the specimen thickness with the maximum stress located at the inner surface of the artery. By comparing stresses (averaged throughout the thickness) at specified strain levels up to 30 %, the influence of specimen unfoldment was estimated with inflation test taken as a basis. For the carotid artery, stresses in the planar tension test were higher by 27−61 % while for the aorta the difference was between 8 and 17 %. The difference between individual arteries occurs due to the varying thickness-to-radius ratio.*

Keywords: Tension test, inflation test, finite element simulation, unfoldment, arterial wall.

1. Introduction

For 2019 the World Health Organization reported that one-third of all deaths were caused by diseases associated with the cardiovascular system (WHO, 2020). The leading causes were heart attack and stroke, both resulting dominantly from atherosclerotic plaque rupture and consequent thrombus formation. Thrombus can embolize and plug smaller blood vessel, resulting in the previously mentioned diseases. The main course in recent years leads to evaluation of the risk of plaque rupture using biomechanical modelling (Gholipour et al., 2018). Here the knowledge of geometry, loading conditions and material characteristics is crucial. Various mechanical tests such as uniaxial (Lisický et al., 2021) or equibiaxial (Polzer et al., 2015).

	Parameters	Carotid model	Aorta model
Inner radius [mm]	R_i	2.9	7.9
Media thickness [mm]	T_M	0.72	0.88
Adventitia thickness [mm]	T_A	0.37	0.41
Artery length [mm]	L	10	10

Tab. 1: Geometry parameters.

* Ing. Ondřej Sochor: Inst. Solid Mechanics, Mechatronics and Biomechanics, Brno University of Technology, Technická 2896/2; 616 69, Brno; CZ, 209128@vutbr.cz

** Ing. Anna Hrubanová: Inst. Solid Mechanics, Mechatronics and Biomechanics, Brno University of Technology, Technická 2896/2; 616 69, Brno; CZ

*** Assoc. Prof. MUDr. Marek Joukal, PhD.: Department of Anatomy, Faculty of Medicine, Masaryk University, Kamenice 126/3; 625 00, Brno; CZ

‡ Prof. Ing. Jiří Burša, PhD.: Inst. Solid Mechanics, Mechatronics and Biomechanics, Brno University of Technology, Technická 2896/2; 616 69, Brno; CZ

doi: 10.21495/em2024-274

tension tests, planar tension test (Cunnane et al., 2016), or inflation tests (Sommer et al., 2010) are used to obtain artery wall response. Except for the last one, the specimens must be axially cut and unfolded to obtain response in the circumferential direction. However, this unfoldment leads to a certain pre-strain before testing, which might influence the mechanical response of artery tissue. The aim of this study is to analyze the influence of artery segment straightening on its mechanical response in the planar tension tests, using finite element simulations.

2. Material and methods

2.1. Geometry models

To analyze the effect of unfoldment on mechanical testing, simulations of a planar tension test and an inflation test were performed. These tests evoke the same stress/strain states if the axial stretch of the cylinder specimen is kept at $\lambda_z = 1$. For both simulations, a bilayer model and a homogeneous model were used. To simulate the planar tension test, a 2D plane strain model of a closed (unloaded) artery was employed (Fig. 1 left), with one end fixed and the other end rotated and shifted to obtain an unfolded (planar) configuration. In the second loadstep, its stretch was simulated by displacement condition in the x-axis. Regarding simulation of the inflation test, a 2D axisymmetric model of a cylindrical artery was used (see Fig. 1 right). To prevent axial (y-axis) deformation, a zero-displacement condition in axial direction on both ends was used. A 0.20 MPa pressure was applied on the inner surface of the model. Geometry characteristics of both models are summarized in Tab. 1; those of thoracic aorta were taken from (Holzapfel et al., 2007); those of carotid were measured during specimen preparation. Mesh sensitivity analysis was done, resulting in 4 400 quadratic elements for each model. Each loadstep was divided into 100 substeps to obtain a dense response curve.

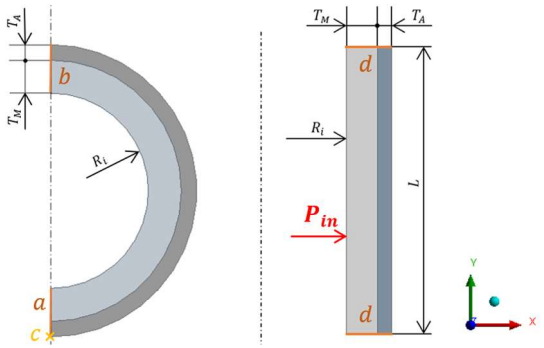

Fig. 1: Geometry models and boundary conditions for each test:
Left: planar tension test – model before unfoldment. Loads: a: UX = 0 mm; c: fixed support; b: remote rigid displacement, rotZ = -180 (in the first loadstep), UX = 16 mm (in the second loadstep),
Right: inflation test – cylindrical model, loads: d: UY = 0, p_{in} = 0.20 MPa.

2.2. Mechanical testing

Three samples of non-pathological carotid artery from human cadavers (age 88, 77, 83) were excised during autopsy at Masaryk University, Department of Pathology. Fresh samples were immersed in 0.9 % saline solution and kept frozen at -20 °C. Before testing the samples were thawed and the artery was carefully separated into adventitia and media layers. In total, 10 rings with average width of 3 mm were obtained for each layer. Each ring was cut axially and the created specimen was clamped in a tensile tester (Camea s.r.o., Czech Republic). A pre-load of 0.01 N was applied to straighten the specimen (in saline bath at 37 °C) and then load was increased till rupture (Lisický et al., 2021).

2.2. Constitutive models

For each layer the obtained stress-strain curves were averaged at specified stress levels and then fitted with hyperelastic incompressible 3rd order Yeoh model (Yeoh, 1993) using Hyperfit software (www.hyperfit.wz.cz). The resulting material parameters are summarized in Tab. 2.

To acquire material parameters for the homogeneous wall, which was not tested, a simulation of uniaxial tension test of the bilayer wall was performed in Ansys Workbench 2023 R2 with the mean thickness

0.78 mm (media) and 0.34 mm (adventitia) measured during the tension tests. The response of each material model is shown in Fig. 2.

Material constants	Media	Adventitia	Homogeneous
C_{10} [kPa]	44.9	67.9	53.0
C_{20} [kPa]	1 102.7	2 155.6	1 469.2
C_{30} [kPa]	0	0	29.1

Tab. 2: Material constants for Yeoh model.

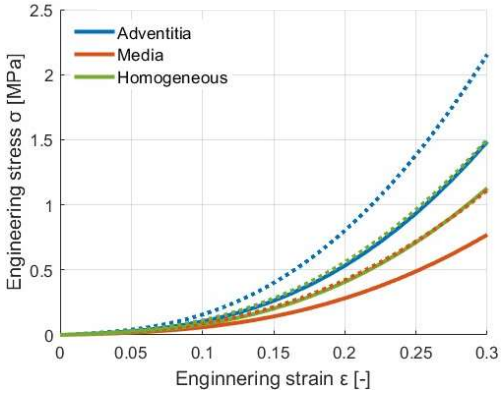

Fig. 2: Uniaxial tension curves of the models: solid lines - uniaxial tension, dotted - planar tension.

3. Results

First, the x-axis stresses/strains of the unfolded models were evaluated. The transmural stress distribution of unfolded bilayer model after the second load step, i.e. end of plane tension (Fig. 3a) was obtained.

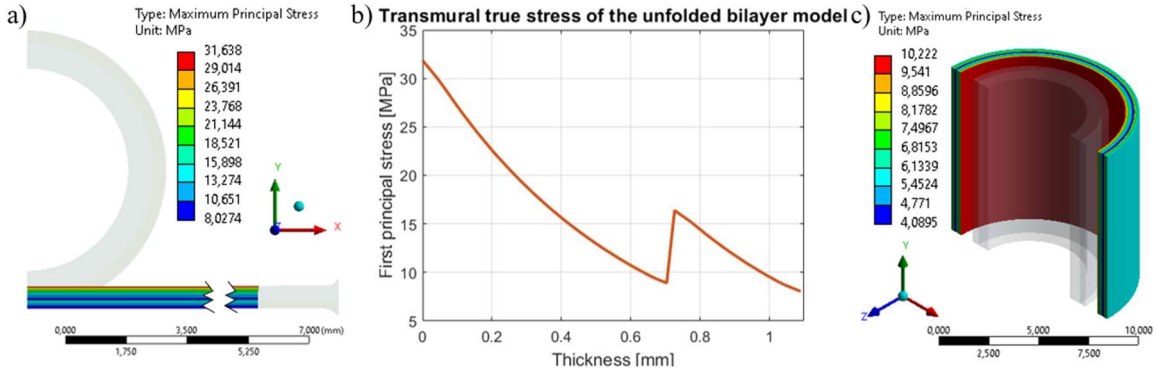

Fig. 3: a–b) Unfolded bilayer model, a) stress at the end of the simulated test, b) transmural stress; 0 mm - inner edge of media, c) cylindrical model after inflation.

As a stress singularity occurred at the free end of the unfolded model (due to the remote displacement condition with rigid behavior), this area was excluded from evaluation. The unfolded (originally half cylindrical) model was bended after the first load-step, thus a linear distribution of stress throughout the wall thickness occurred, with maximum and minimum stresses situated at the inner and outer edges of the model, respectively. At the end of test, the stress distribution decreases from the inner edge of media (global maximum) to the media's outer edge (Fig. 3b). A second local maximum occurs at the inner edge of adventitia. For the homogeneous wall, the stress decreases monotonously with distance from the inner edge. For the cylindrical models under inflation, the first principal stresses were evaluated (see Fig. 3c); their

	Carotid	Aorta
$\varepsilon_{0.10}$	61.4 %	16.9 %
$\varepsilon_{0.20}$	36.8 %	8.3 %
$\varepsilon_{0.30}$	27.5 %	8.3 %

Tab. 3: Percentual stress differences between the unfolded and cylindrical bilayer models for both arteries at strain levels of 10, 20 and 30 %.

transmural trends were the same as for the unfolded model. For each model, the average values of engineering stresses/strains throughout the specimen thickness were calculated. For plotted stress-strain curves see Fig. 4.

To estimate the influence of unfoldment on stress-strain curves of each artery, differences between the bilayer unfolded and cylinder models were calculated at three strain levels (in percentage, with the cylindrical model considered as a basis, see Tab. 3).

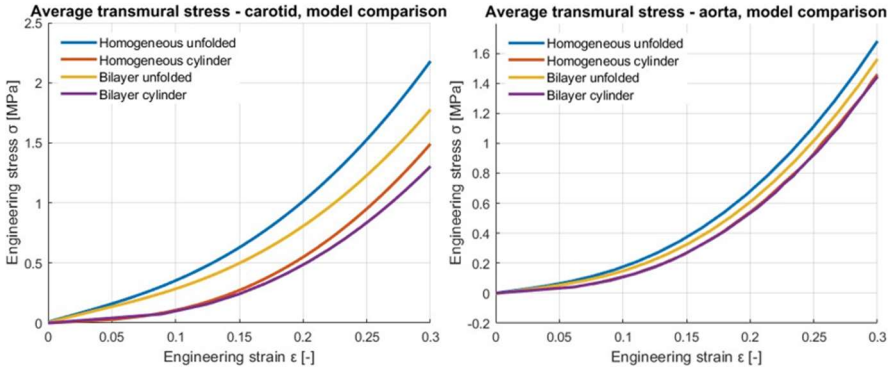

Fig. 4: Averaged stress/strain characteristics for different models.

4. Discussion and conclusion

The obtained results indicate that the specimen unfoldment significantly influences the plane strain tension tests of carotid arteries (Fig. 4), with differences reaching more than 60 % (Tab. 3). The unfoldment leads to non-uniform transmural distribution of stress, resulting in maximum stress occurring at the inner edge of the carotid artery. Due to the pronounced stiffening response of the artery tissues, the maximum stresses at the inner surface of the artery dominate the response, resulting in a more than 60 % increase of the initial stiffness. Similarly, the initial stiffness of the aorta is also increased, but by 17 % only. This difference between both arteries is given by their very different thickness-to-radius ratio (0.38 for carotid artery and 0.16 for aorta) and decreases with increasing strains. These numerical results, however, relate not only to the specific geometric parameters but also to the material properties of the investigated arteries and do not consider residual stresses. While the axial pre-stress is negligible due to the high age of donors, the circumferential component may be significant. For a positive opening angle being a typical representation of these residual stresses, they are negative on the inner surface and thus could reduce the presented effect. Due to lack of experimental data, however, this is out of scope of this paper. Thus, the impact of unfoldment on the stress-strain responses should be assessed individually for each investigated artery and ideally with exploitation of its specific material properties and opening angles.

Acknowledgements

This work was supported by Czech Science Foundation, project No. 21-21935S.

References

Cunnane, E. M. et al. (2016) Mechanical properties and composition of carotid and femoral atherosclerotic plaques: A comparative study. *J Biomech*, 49 (15), 3697–3704.

Gholipour, A. et al. (2018) Three-dimensional biomechanics of coronary arteries. *Int J Engin Sci*, 130, 93–114.

Holzapfel, G. A. et al. (2007) Layer-specific 3D residual deformations of human aortas with non-atherosclerotic intimal thickening. *Annals of biomedical engineering*, 35(4), 530–545.

Lisický, O., Hrubanová, A., Staffa, R., Vlachovský, R. and Burša, J. (2021) Constitutive models and failure properties of fibrous tissues of carotid artery atheroma based on their uniaxial testing. *J Biomech.*, 129, 110861–110861.

Polzer, S., Gasser T. C., Novák K., Man V., Tichy M., Skacel P. and Bursa J (2015) Structure-based constitutive model can accurately predict planar biaxial properties of aortic wall tissue. *Acta Biomaterialia*, 14, 133–145.

Sommer, G. et al. (2010) Biaxial mechanical properties of intact and layer-dissected human carotid arteries at physiological and supraphysiological loadings. *Am J Physio Heart Circ Physiol*, 298(3), H898–H912.

Yeoh, O. H. (1993) Some forms of the strain energy function for rubber. *Rubber Chemistry and Technology*, 754–771.

World Health Organization (2020) The top 10 causes of death. from https://www.who.int/news-room/fact-sheets/detail/the-top-10-causes-of-death.

30th International Conference
ENGINEERING MECHANICS 2024
Milovy, Czech Republic, May 14 – 16, 2024

DAMAGE IDENTIFICATION OF SMALL HOUSES IN DIFFERENT SEISMIC REGIONS

Sokol M.[*], Crespo-Sanchez S.[**], Rodríguez-Paz M.[***], Mazáčková K.[*], Gogová Z.[*]

Abstract: *Comparison of seismic resistance capacity of masonry structures with site dependent seismic demand is presented. Five building types are selected and subjected to the analysis. Push-over analyses have been performed assuming non-linear behaviour of individual walls. Five different damage grades have been identified starting with first crack on a wall up to the total collapse of the structure.*

Keywords: Seismic risk assessment, damage identification, push-over analysis, non-linear analysis.

1. Introduction

Although design analyzes can be linear in seismic codes, such as response spectrum (RS) methods, while in practice the situation is in many cases much more complicated to be described only by RS analysis. The RS method does not provide accurate information about critical cross-sections or the type and extent of damage a structure may suffer after an earthquake. The degrees of damage are described quite clearly in (Lang, 2002; Lang, 2004; Okada, 2000). Many studies have been carried out (Corsanego, 1994; Okada, 2000; Giovinazzi, 2004; Kegyes-Brassai, 2007), etc. focusing on the vulnerability of existing buildings. Vulnerability is expressed by functions or parameters that can be obtained either by statistical studies of damaged buildings in earthquake-affected areas or by simulations using numerical or analytical methods. This paper uses simulations using a combination of numerical and analytical methods according to (Lang, 2002) and (Lang, 2004). Computer code was prepared to perform these simplified push-over analyzes on small masonry (or concrete) buildings. Conditions and results in different regions of Central Europe and Central America were compared.

2. Seismic vulnerability

The seismic vulnerability of selected small houses is expressed in such a way that for the relevant buildings located in a specific area, the degree of their damage after an earthquake is calculated, and accordingly, the house buildings are classified into five categories of damage, starting with the lightly damaged building. (DG1) to the level (DG5) representing the complete destruction of the building (Fig. 4).

2.1. Central Europe

Typical family houses in Central Europe region are assumed, where the seismic risk map is taken, e.g. for Slovakia (Fig. 1a) according to (NA STN EN1998-1, 2005) or (Madarás, 2008). The PGA in selected region close to the city Trnava reaches values up to 1.1 ms^{-2}. Structural types were selected according to catalogue projects (Euroline, 2012).

[*] Milan Sokol, Karolína Mazáčková, Zuzana Gogová: Slovenská University of Technology in Bratislava, Radlinského 11, 810 05 Bratislava, SK, milan.sokol@stuba.sk, xmazackova@stuba.sk

[**] Saul Crespo-Sanchez, Tecnológico de Monterrey, Campus Qurétaro, Mexico, secrespo@tec.mx

[***] Miguel X. Rodríguez-Paz, Tecnológico de Monterrey, Campus Puebla, Mexico, rodriguez.miguel@tec.mx

doi: 10.21495/em2024-278

The most ordinary types of buildings in the region are unreinforced masonry buildings. Evaluating objects with significant building populations for the selected area is more interesting than the assessment of individual buildings. Vulnerability functions of existing buildings are established with regard to its earthquake response.

2.2. Central America

One of the countries most affected by seismicity is Mexico (Fig. 1b). Maximum peak ground acceleration in Mexico reaches the value of 5.6 ms^{-2}. This value is five times larger than in Central Europe. The seismic risk is much higher; much higher consequences are expected.

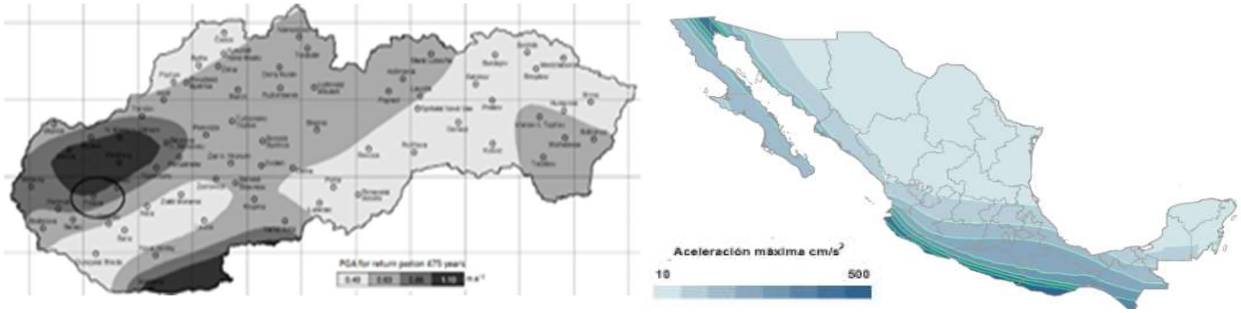

a) *b)*

Fig. 1: Seismic risk maps: a) Slovakia (STN EN 1998-1, 2012), b) Mexico.

2.3. Typical small houses

Five typical family houses often built in Central Europe (Fig. 2) and Mexico (Fig. 3b) were selected. Constructions from Fig. 2 have the same wall systems (Fig. 3b) as the houses assumed according to Fig. 3a. Family houses are built mainly in villages in the region of Central Europe, and in America this type of house is common everywhere in cities, but also in villages. In Central Europe, the region in Slovakia near the city of Trnava was selected, in Central America - the state of Mexico, it is the most important area of the southern coast of the Pacific Ocean. There is constant seismic activity on the coast of Guerrero and Oaxaca, several seismic events in this area have led to earthquakes with significant acceleration in the center of the country. The 1985 and 2017 earthquakes in this region saw the collapse of many buildings and significant damage to buildings and houses.

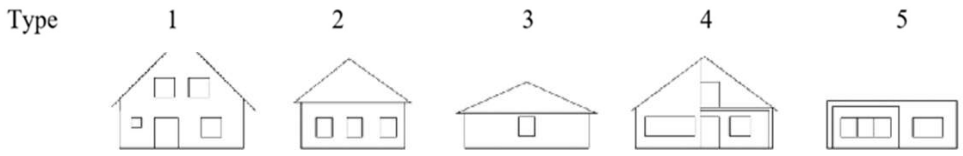

Fig. 2: Five selected types of houses in Europe - Slovakia with plan view according to Fig. 3b.

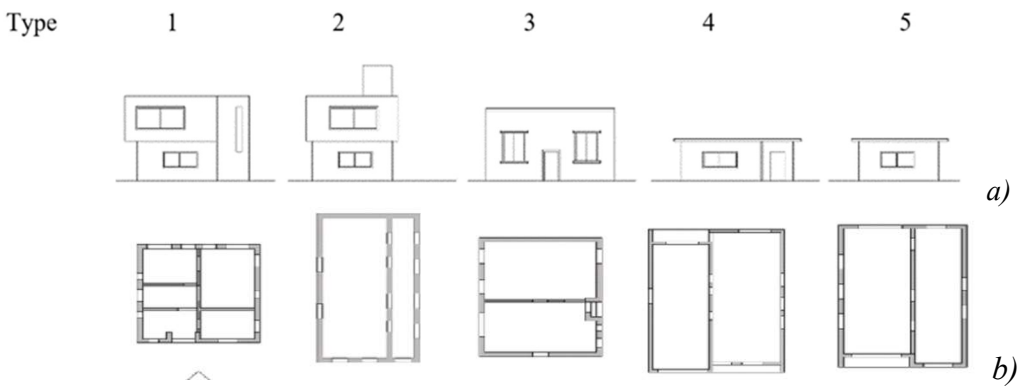

Fig. 3: Typical houses constructed in region Mexico a) and b) wall system in plan view.

2.4. Damage description

Five damage categories (Fig. 4) have been introduced according to (Okada, 2000).

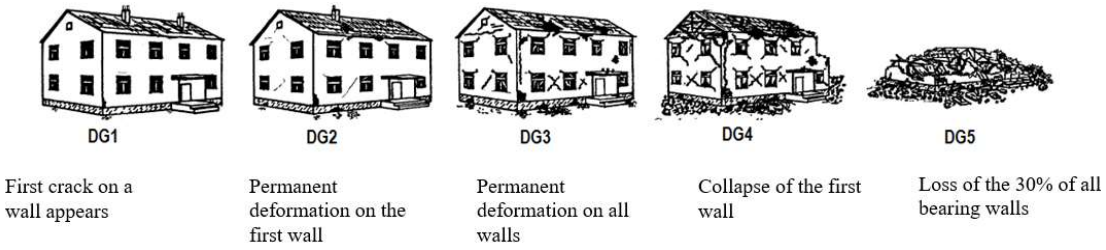

Fig. 4: Damage grades according to Macroseismic Intensity Scale 1998 (Okada, 2000).

3. Analysis

Simplified non-linear push-over analyses have been used. Details of the quasi non-linear solution based on seismic demand and capacity comparison are described in (Lang, 2002) and (Sokol, 2013). The entire process is automated using a prepared computer code. First, it is necessary to identify all structural walls. It is essential is to assess the behavior of the structural system (if the wall acts like a frame or wall system). The capacity curves of individual walls and their bilinear approximations are summing up to get the relationship between total shear forces V_s vs. top displacement Δ, so that is possible to obtain the capacity curve of the structure (Fig. 5), where the damage grades (DG1 to DG5) can be easily identified.

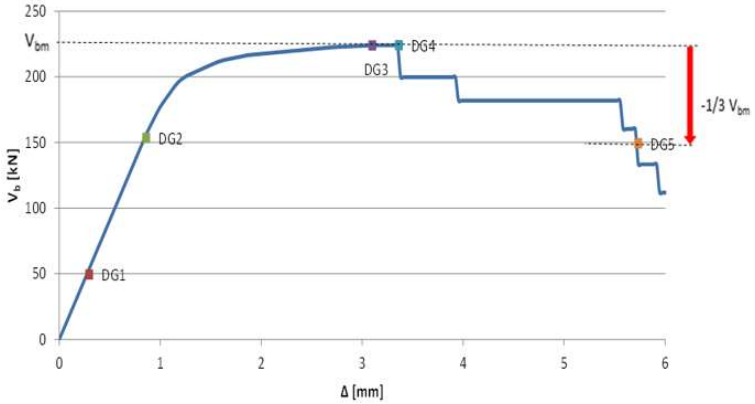

Fig. 5: Capacity curve of structure (Sokol, 2013).

4. Seismic risk assessment

Using analysis automation, we can create simple risk scenarios assessment for a region (Fig. 6).

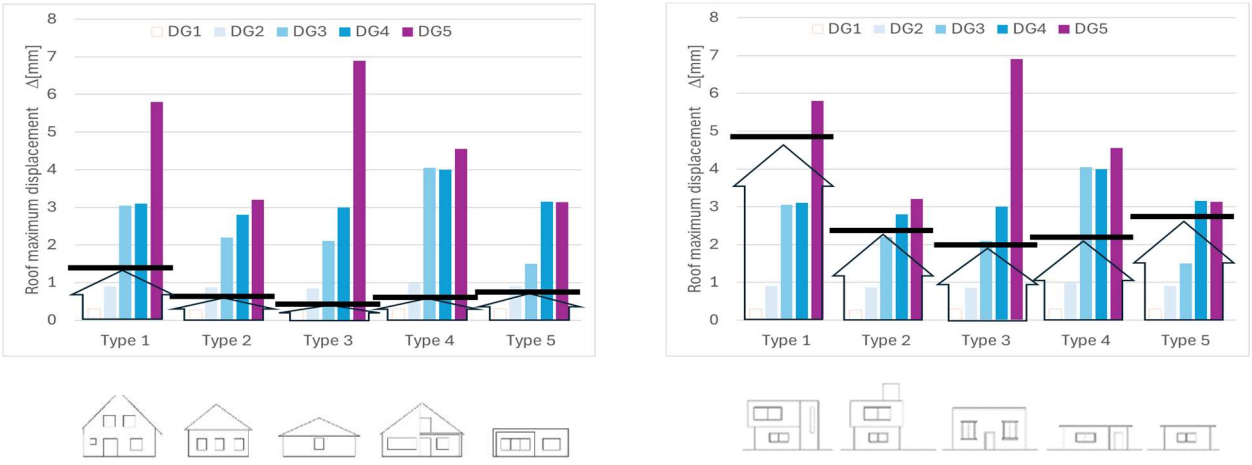

a) Slovakia (PGA = 1.1 m.s^{-2}, soil category C)

b) Mexico (PGA = 5.6 m.s^{-2}, soil category C)

Fig. 6: Seismic performance of typical small houses.

Horizontal bold line (in Fig. 6 drawn in black at the top of a house scheme) represents the seismic displacement demand expressed in mm. If one of the five blue columns representing structural capacity ends under this line it means the corresponding damage grade has already been reached, e.g. for the house (Type 1) in Slovakia the damage grade DG2 Fig. 6a has been reached while the same type in Mexico can offer by damage grade DG4 Fig. 6b. In Slovakia an earthquake can affect such amount of buildings where 20 % of population live (Fig. 6a). In the rest of Slovakia even smaller damages are expected, because of the smaller value of design ground acceleration. From all selected types only masonry multi storey building (Type 1) can suffer from damage grade DG2 which is the permanent deformation of first structural wall. No collapse is threatened.

The damage scenarios for different structural types of buildings in Mexico are shown in Fig. 6b. Earthquake can affect 90 % of Mexican population. In Mexico all types of assumed buildings can suffer from severe damages, starting with DG 3 (Permanent deformation on all walls) up to DG 5 (Loss of the 30 % of all bearing walls).

5. Conclusions

The most common types of simple masonry constructions were selected according to available statistical data. The quasi-nonlinear response of these buildings was analyzed. The most vulnerable regions of Slovakia and Mexico according to seismic risk maps were taken into account. Earthquake demand was compared with structural capacity. The vulnerability of five selected building types was presented, including a description of the damage scenario. Family houses in Slovakia will not be greatly affected by the earthquake, expect small cracks on the walls. On the other hand, most Mexican single-family homes are at risk of more serious damage, possibly ending in collapse.

Acknowledgment

Author thank to the Slovak Research and Development Agency (SRDA) for supporting and providing grant from research program APVV-22-0431 and project VEGA 1/0230/22.

References

Corsanego, A. and Petrini, V. (1994) Evaluation criteria of seismic vulnerability of the existing building patrimony on the national territory. *Seismic Engineering*, vol. 1, pp. 16–24.

Okada, S. and Takai, N, (2000) Classifications of Structural Types and Damage Patterns of Buildings for Earthquake Field Investigation. In: *12th World Conference on Earthquake Engineering*, Auckland, New Zealand, Balkema, paper 0705.

Lang, K. (2002) *Seismic vulnerability of existing buildings*. Zurich: Swiss federal institute of technology.

Giovinazzi, S. and Lagomarsino, S. (2004) A Macroseismic Method for the Vulnerability Assessment of Buildings. In: *13th World Conference on Earthquake Engineering*, Vancouver, B.C., Canada, paper 896.

Lang, K. and Bachmann, H. (2004) On the Seismic Vulnerability of Existing Buildings, A Case of the City of Basel. *Earthquake Spectra*, 43–66.

Kegyes-Brassai, O. (2007) Risk analysis and building vulnerability. In: *Conference on earthquake safety in Hungary*, Györ, pp. 181–200.

Madarás, J. et al. (2008) Earthquake in Slovakia. http://www.enviromagazin.sk/enviro2008/enviro5/03_zemetrasenia.pdf, (in Slovak).

NA STN EN 1998-1 (2012) Design of Structures for earthquake resistance – Part 1: General rules, seismic actions and rules for buildings. National Annex. SUTN, Bratislava, (in Slovak).

Euroline (2012) Overview of constructed buildings in Slovakia. http://www.eurolineslovakia.sk/sk/mapa-realizovanych-stavieb.html

Sokol, M., Ároch, R. and Gogová, Z. (2013) Seismic Performance of Typical New Family Houses in Slovakia. In: *Vienna Congress on Recent Advances in Earthquake Engineering and Structural Dynamics* (VEESD 2013). Vienna, Austria, paper 429.

30th International Conference
ENGINEERING MECHANICS 2024
Milovy, Czech Republic, May 14 – 16, 2024

ACOUSTIC EMISSION METHODS IN STEEL BRIDGE DEGRADATION IDENTIFICATION AND MONITORING

Šorm F.*

Abstract: *Acoustic emission methods proved to be an effective diagnostic tool in many industrial sectors. The potential of this method in the field of steel bridge diagnostics is explored in this article. The goal is to find the most effective use of this method.*

Keywords: Steel bridges, diagnostics, acoustic emission.

1. Introduction

Many cases of steel bridge degradation (cracks, corrosion) are sources of acoustic emission signals. This gives an opportunity to use acoustic emission based methods for structure diagnostics. However, there is a problem with identification of the nature of acoustic emission source. There may be many sources of acoustic emission present in steel bridges, not all of them originating in degraded parts (like e.g. friction in joints). It is the goal of this research to define the conditions of acoustic emission use, which would make the interpretation of measured results more certain.

Analysis of real structure data was considered necessary. Degraded part of steel bridge deck has been therefore tested in ITAM laboratory as a first step of the research. Results and some initial conclusions derived from the experiment are discussed in this article.

2. Test method

The tested element (see Fig. 1) was a degraded steel orthotropic deck element from the bridge over the Labe river in Opatovice. The element consisted of a 1050 x 3040 mm upper plate with a non-slip profiled driven surface. Soffit of the plate was reinforced with 4 longitudinal U profiles, closed by vertical front plates at both ends. Lower edges of the front plates formed bearing surface of the element, which spanned simply supported between cross girders of the bridge.

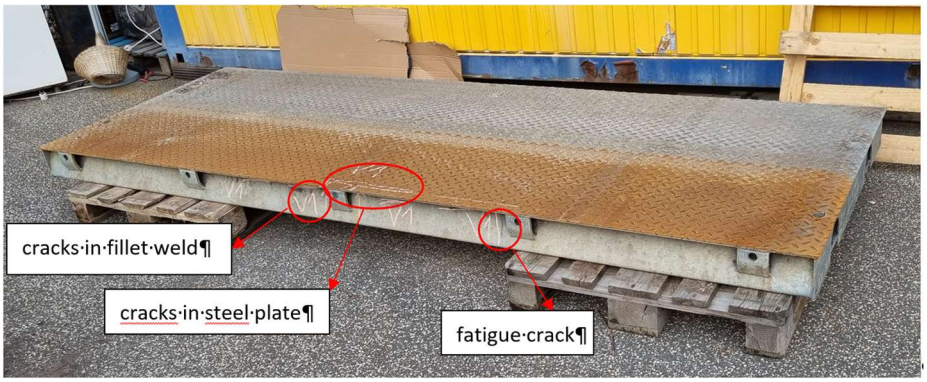

Fig. 1: Tested steel bridge deck element.

* Ing. Filip Šorm: Institute of Theoretical and Applied Mechanics, Prosecká 809/76; 140 00, Prague; CZ, sorm@itam.cas.cz

doi: 10.21495/em2024-282

The examination was carried out in the Institute of Theoretical and Applied Mechanics laboratory in Prague. Test method was designed in such a way, so that the laboratory action was analogous to the actual load on the element in the bridge deck.

The element oriented with the upper (driven) surface downwards was placed between two special test frames modeling the bearing of the element on the cross girders of the bridge (see Fig. 2). Pair of hydraulic jacks was placed under the worst degraded longitudinal stiffener in the least favorable position to represent critical action of rear axle wheels of a truck. The effect of tire elasticity was simulated by elastomeric profiles placed between the element and the hydraulic jacks. Magnitudes of applied forces were controlled by force sensors placed under the loading jacks. Acoustic emission measurement was focused on the area of the wall of the outermost longitudinal U-profile, where fatigue crack was formed (see Fig. 3).

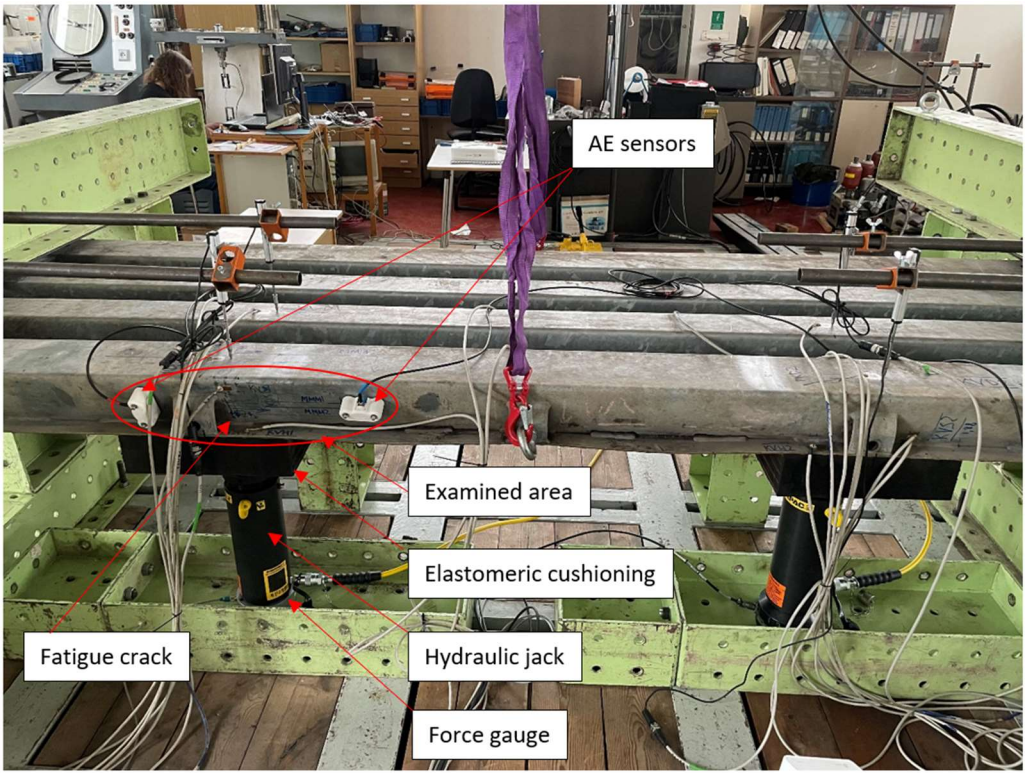

Fig. 2: Arrangement of tested element.

Load on the element was increased gradually. The forces in jacks reached in successive steps 0 - 40 - 50 - 60 - 70 - 75 kN. The final load level (75 kN) exceeded the most onerous load that could occur on the bridge (max. 67 kN per truck wheel). Such overloading was designed to force propagation of existing fatigue crack (Fig. 3). Acoustic emission signals emitted at the tip of propagating crack would then be recorded and analysed.

Acoustic emission signals were recorded by 2 piezoelectric sensors PK15I, attached to the element using magnetic holders. Location of the sensors can be seen in Fig. 2.

Recorded acoustic emission signals were analysed using Micro-SHM station controlled by the AEwin program supplied by the Physical Acoustics Company (USA).

Fig. 3: Fatigue crack.

3. Results

3.1. Identification of sources of acoustic emission (AE events)

Acoustic emission signals (AE signal) have a form of mechanical waves propagating through material from its source. They originate in continuum if energy is suddenly released during so called AE events (e.g. crack propagation, corrosion processes, etc.). These waves cause voltage signals in piezoelectric sensors which can be recorded and then processed (see Fig. 4 for an example of typical AE signal record).

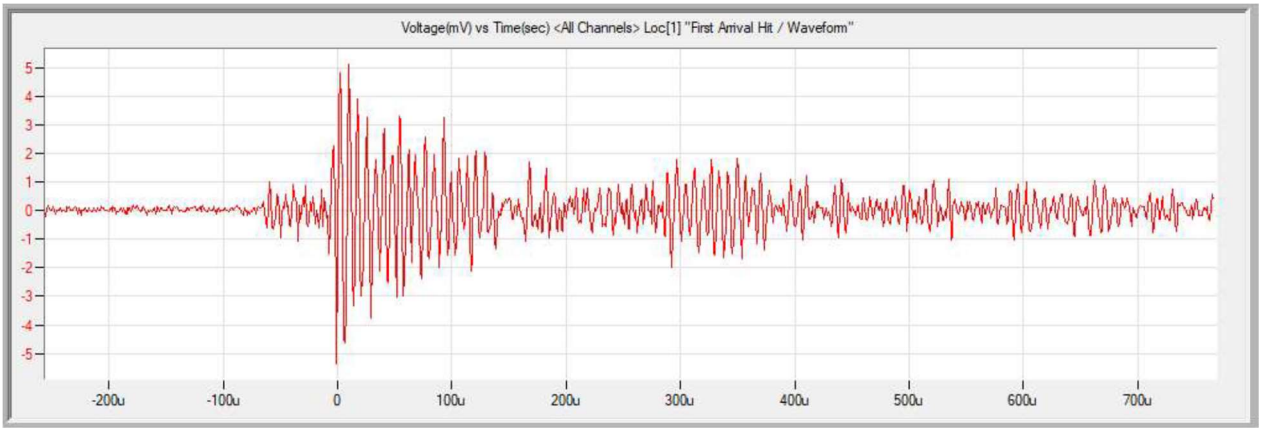

Fig. 4: Typical record of acoustic emission signal.

A large number of signals was recorded during the experiment. The first step of the analysis was therefore identification and removal of unwanted signals (noises).

In particular, all too short signals (EMI) were excluded, as well as signals that were not recorded approximately simultaneously on both sensors and thus could not originate inside the examined area.

Every pair of signals recorded (nearly) simultaneously indicated release of energy (AE event) inside the monitored area. These events could indicate energy release from strained material at the tip of progressing fatigue crack.

If pair of signals was recorded simultaneously on both sensors, only the first recorded signal (first arrival hit) was selected for further evaluation. The sensor which recorded this hit was obviously closer to the source of the acoustic emission (event) than the other one. The first arrival hit was thus less affected by attenuation and was therefore taken as the representative of the recorded AE event.

The numbers of recorded AE events (first arrival hits) are given in Tab. 1.

AE Event	**Individual loading levels [kN]**					**Load increase total**	**Load relieve total**
Load interval	(0-40)	(40-50)	(50-60)	(60-70)	(70-75)	(0-75 kN)	(75-0 kN)
AE Events #	**160**	**5**	**29**	**35**	**13**	**242**	**110**

Tab. 1: Number of identified AE Events.

Tab. 1 shows, the sources of acoustic emission (AE events) emerged in the examined area during all phases of the experiment. The crack clearly does not propagate at low levels of load or during load relieve. It means, there have to be also other sources of acoustic emission in addition to the sought-after AE events originating in propagating crack. Most likely, these were sources of acoustic emission signals arising as a result of friction between the elastomer profile and the strained element.

The next task was therefore to identify AE signals (first arrival hits) which could possibly come from the propagating crack. Parameters of the individual AE signals were analyses and characteristics identifying them as the right signals coming from the crack were searched for.

3.2. Analysis of AE signals

Analyses was based on an assumption that different signal parameters could signal different origins of the signal. The amplitude and the energy of recorded AE signals were examined.

Results of the AE signal amplitude analysis are summarized in Tab. 2.

Amplitude [μV]	**Individual loading levels [kN]**					**Load increase total**	**Load relieve total**
Load interval	(0-40)	(40-50)	(50-60)	(60-70)	(70-75)	(0-75 kN)	(75-0 kN)
Average value	50	47	50	50	52	**50**	**51**
Average deviation	7	3	7	6	10	**7**	**6**
Max. value	74	54	64	62	72	**74**	**74**
Min. value	35	42	36	37	35	**35**	**35**

Tab. 2: Amplitude analysis results.

The comparison of maxima and minima shows that signals with a significantly different amplitude were not recorded at the highest levels of loading. It is clear from the last two columns in Tab. 2., that the amplitudes of signals recorded during both loading and unloading are similar and therefore probably originate from the same source. This source cannot be a progressing crack as the crack does not progress during load relieve.

This result was interpreted in a following way: no fatigue crack developed during the experiment, all recorded AE signals have their origin in friction between the tested element and the elastomer profile.

The energy analysis of the measured signals led to the similar conclusions.

4. Conclusions

Although the experiment took place in laboratory conditions, the interpretation of results had to be based on an assumptions and carried some uncertainty about the AE source origin (the AE signals from progressing crack were assumed to be different from signals originating in friction which may or may not be true). Such uncertainty only increases if the measurements are carried out on real world structures, where many sources of acoustic emission could be present.

The acoustic emission methods need to be combined with other diagnostic methods to make reliable identification of detected sources of acoustic emission possible. In our case the conclusion of crack stability should have been confirmed by e.g. simple crack-gauge monitor.

The experiment rather disappointingly demonstrated fact, that the degradation of the element may not be discovered by acoustic emission based methods. Only progressing degradation produces AE signals which could be registered.

As the progressing degradation should be avoided on operated bridges, rather than for defects identification, these methods seem to be suitable for long-term monitoring of already identified defects that cannot be removed operatively and whose further development could threaten the safety of the structure.

If applied in such a way, the methods have an ability to monitor entire areas of the structure, detecting and locating activity of AE sources in real time.

Acknowledgement

Research was carried out within the Doprava 2020+ CK04000042 project supported by TAČR.

References

Beattie, A. (2013) *Acoustic Emission Non-Destructive Testing of Structures using Source Location Techniques*. Sandia Report, California USA.

30th International Conference
ENGINEERING MECHANICS 2024
Milovy, Czech Republic, May 14 – 16, 2024

DEVELOPMENT AND VERIFICATION OF NOVEL DUAL PLUNGER HYBRID KINETIC ENERGY HARVESTER

Sosna P.*, Hadaš Z.**

Abstract: *This paper presents the development and verification of a novel dual plunger hybrid kinetic energy harvester, which combines piezoelectric and electromagnetic conversion principles to effectively generate electricity from ambient mechanical motion and vibrations. This device utilizes two cantilevered steel plungers forming a parallel mechanism which makes non-arc oscillations, therefore maximizing energy harvesting efficiency. A single degree of freedom model is initially proposed for description, which is later extended to incorporate nonlinear effects with magnets. The paper discusses the optimization of resistance parameters, preliminary experimental measurements on the adhesive type and thickness for piezoelectric patches, as well as the measurement of the damping factor. Additionally, the verification and validation of the model through frequency sweeps for different input acceleration levels are detailed, along with the refinement of the model based on manufactured samples.*

Keywords: Energy harvesting, resonator, piezoelectrics, electromagnetics, dual plunger design.

1. Introduction

Energy harvesting from ambient vibrations and motion of structures is a rapidly developing subject in recent years due to the possibility to power low-consumption electronic devices and wireless sensor networks in IoT applications. There have been many techniques and methods developed to effectively convert mechanical energy of vibrations into useful electricity. This paper focuses on the development and verification of a novel dual plunger hybrid vibration energy harvester, which combines two common conversion principles: piezoelectric and electromagnetic. Piezoelectric (Yang et al., 2018), electromagnetic (Bradai et al., 2018; Zhu and Beeby, 2013), and electrostatic (Edwards and Gould, 2016) conversion principles have been extensively studied. However, each approach has its limitations and challenges, such as narrow bandwidth, low efficiency, and sensitivity to environmental conditions. The integration of multiple conversion principles offers the potential to overcome these limitations (Ryu et al., 2019) and improve overall energy harvesting performance (Margielewicz et al., 2023).

2. Design of novel dual plunger hybrid energy harvester

Building upon previous designs and techniques, our research aims to enhance energy harvesting efficiency by integrating piezoelectric and electromagnetic conversion principles in a novel dual plunger hybrid energy harvester. By leveraging the advantages of both technologies, we seek to develop a robust and versatile device capable of harvesting energy from a wide range of mechanical sources. Fig. 1 shows the schematic of the developed energy harvester, which consists of an adjustable piezoelectric parallel beam system, electro-magnetic circuit with coil and electrical load for both converters. The two-plunger design also allows for use in printed structures with integrated piezoelectric elements and such harvesting system could be fully integrated for a complex printable energy harvester.

* Ing. Petr Sosna: Institute of Solid Mechanics, Mechatronics and Biomechanics, Brno University of Technology, Technická 2896/2; 616 69, Brno; CZ, petr.sosna@vut.cz

** Assoc. Prof. Ing. Zdeněk Hadaš, PhD.: Institute of Automation and Computer Science, Brno University of Technology, Technická 2896/2; 616 69, Brno; CZ, hadas@fme.vutbr.cz

doi: 10.21495/em2024-286

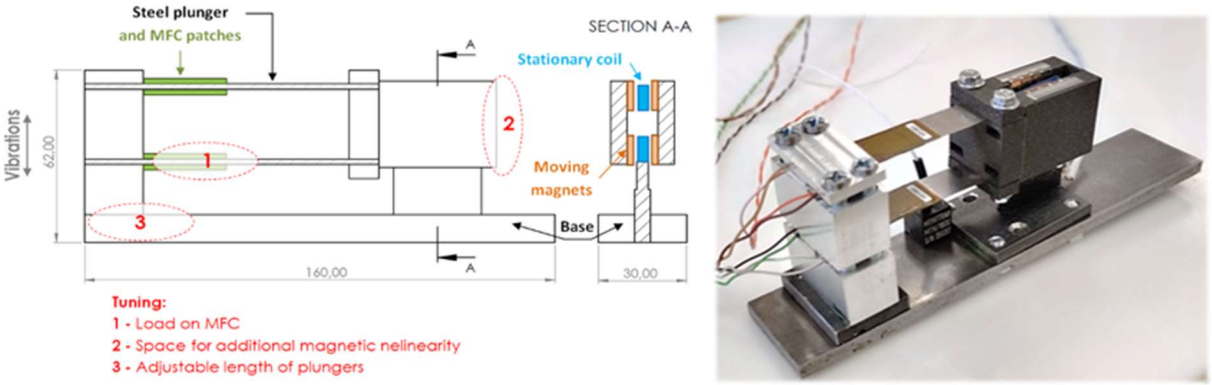

Fig. 1: Schematic of the developed energy harvester and manufactured sample.

The new hybrid tunable vibration energy harvester is approximately 30 mm wide, 160 mm long and has a height of 60 mm. The dual plunger hybrid energy harvester utilizes a parallel mechanism with two steel plungers to ensure non-arc oscillations, thereby maximizing energy harvesting efficiency.

As a piezoelectric converter we chose *macro-fiber composite* (MFC) layers of the company with dimensions of $28 \times 14 \times 0.3\ mm$. The MFC patch consists of rectangular piezo ceramic (PZT) rods sandwiched between layers of adhesive, electrodes and polyimide film. Stretching and compressing the fibers during oscillations creates voltage between the electrodes. The MFC patch is attached from both sides in a bimorph configuration to a steel plunger with dimensions $50 \times 14 \times\ 0.3\ mm$.

The design of the electromagnetic part features a stationary coil and the magnetic circuit, which is a part of the moving mass. This design of the electromagnetic part alone has proven to be efficient in real-world applications, so the idea is to use it as a part of the new hybrid harvester.

3. 1-DOF model of hybrid energy harvesting system

The 1-DOF model for description of the system is based on a discretization procedure described e.g., in (Erturk and Inman, 2011) or (Stanton et al., 2010) which utilizes energy formulation of a continuum system and Hamilton's principle and outputs the basic equations of motion with only four discretized parameters, discretized mass m, beam stiffness k, piezoelectric coupling Θ and piezoelectric capacitance C_p. This simple model is extended to also include viscous damping d_m, base excitation F_{EV}, electromechanical coupling C_{EM}, coil resistance R_c and nonlinear stiffness force F_{NL}. Applying these additions could extend the basic model and it describes the motion of the tip mass of the hybrid vibration energy harvester.

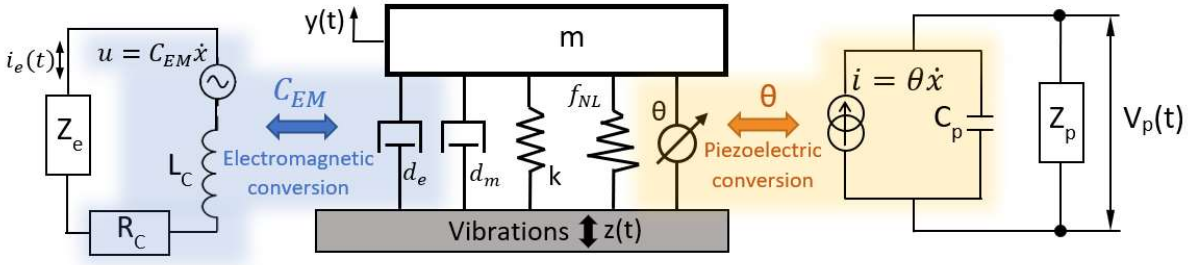

Fig. 2: The 1-DOF model of the proposed hybrid harvester. Mechanical oscillator is coupled to two other subsystems by piezoelectric and electromagnetic couplings.

$$m\ddot{y} + d_m\dot{y} + ky + f_{NL}(y, \dot{y}, t) + C_{EM}i_e + \theta V_p = F_{EV} \tag{1}$$

$$\theta\dot{y} = \dot{V}_p C_p + \frac{V_p}{Z_p} \tag{2}$$

$$C_{EM}\dot{y} = i_e R_C + i_e Z_e, \tag{3}$$

We only consider the simplest form of energy harvesting which is through resistive load Z_e and Z_p, the harvested power can be estimated as$P_e = i_e^2 Z_e$ and $P_p = 2\dot{V}_p^2/Z_p$. Such that V_p is the total voltage on one bimorph beam considering the upper and lower patches connected in series. The factor of two signifies two bimorphs on the same harvester. Fig. 2 shows the schematic of the model. Such a model was transferred into MATLAB Simulink environment and can be time integrated.

Parameter	m	d_m	k	f_{NL}	C_{EM}	Θ	C_p	Z_e	Z_p	R_c
Value	92	0.326	1 586	0	13.15	0.73	52	1 200	1 450	145
Unit	g	Ns/m	N/m	-	N/A	mN/V	nF	Ω	$k\Omega$	Ω

Tab. 1: Discretized parameters of the energy harvester used for simulations.

4. Experimental verification

4.1. Preliminary experimental investigation on adhesive types

Two methods of fixing the MFC patch to the steel base are CA glue and epoxy resin ("5-minute epoxy") we tested for their effects on mechanical damping. We tested the glues by attaching together two steel plungers with dimensions $L_s \times w_s \times t_s = 80\ mm \times 15\ mm \times 0.2\ mm$. The schematic is in Fig. 3. Two samples are manufactured, their total and plunger thicknesses are measured, and the respective thickness of the adhesive layer is recalculated. The CA glue has average thickness of $t_g = 0.04\ mm$ and epoxy resin $t_e = 0.13\ mm$.

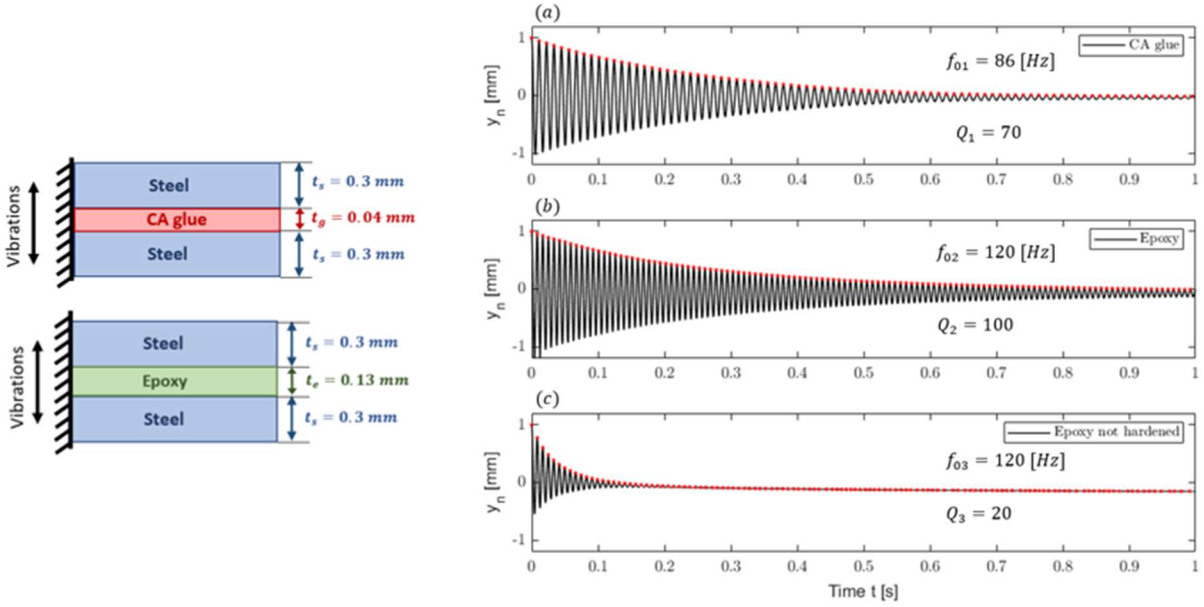

Fig. 3: Schematic of manufactured samples (left) to test the effect of adhesive type on the composite beam's first natural frequency and stiffness and the resulting free oscillations (right).

The quality factor is calculated from free vibrations and natural frequency and quality factor are determined. CA glue creates thinner layers but is quite brittle and breaks for higher strains. The epoxy creates a bond that can withstand higher amplitudes before cracking and that has better damping properties. Although the stiffness of the glue layer is negligible compared to the steel, it pushes the steel layer further away from the neutral axis of oscillations and therefore could affect the overall stiffness. For manufacturing, we decided to use epoxy resin, bearing in mind that Fig. 3c strongly suggests that the epoxy must be fully cured to ensure a stiff bond, in order to not lower the damping.

4.2. Frequency sweeps

The developed model is verified and validated through frequency sweeps for two different input acceleration levels. The manufactured sample was subjected to harmonic base excitation of vibration

amplitudes $\ddot{z} = 50\ mg$ and $\ddot{z} = 100\ mg$. National instruments DAQ cards were used to record the voltages on the piezoelectric patches and the induced electromagnetic voltage. A series of harmonic tests were done for a range of frequencies, where the accelerometer was used to correct the input vibration voltage.

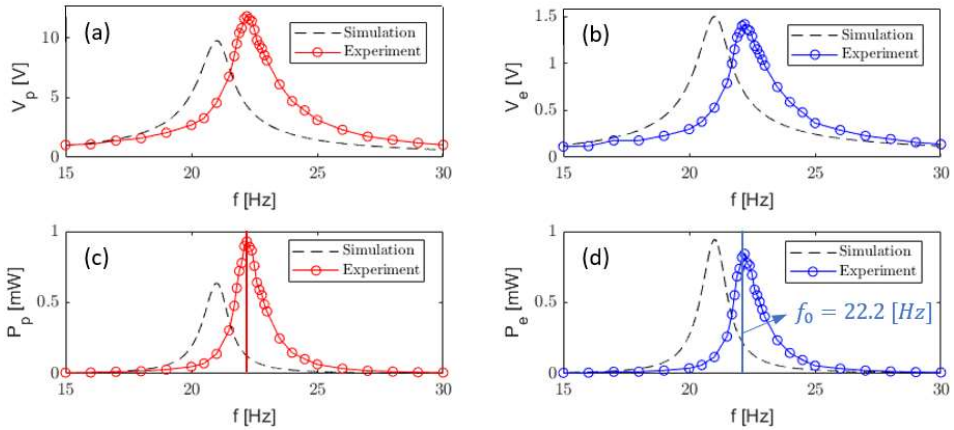

Fig. 4: Comparison of SDOF simulation results and experimental measurement. Subplot (a) is summed measured piezoelectric voltage, (b) is measured electromagnetic voltage. Plots (c) and (d) are recalculated harvested power on respective resistive loads Z_p and Z_e.

The biggest conclusion we can deduce is that the resonant frequency doesn't match, it differs by approx. $1\ Hz$. We assume that the reason behind that is the discretized stiffness k determined from can never be exact because of manufacturing variances in dimensions of the steel plunger, type of clamping and uncertainties in general. The glue thickness also affects the resonant frequency. We can see that the model of electromagnetic conversion fits correctly. Piezoelectric coupling, on the other hand, is pessimistic, only approximately 70 % of the generated power is predicted.

5. Conclusions

In conclusion, our paper presents a novel dual plunger hybrid energy harvester that effectively combines piezoelectric and electromagnetic conversion principles to generate electricity from ambient mechanical motion and vibrations. Through experimentation and modeling, we have demonstrated the efficiency and reliability of our device. Moving forward, further optimization and refinement will enhance its potential for practical applications in various fields, contributing to the advancement of renewable energy technologies.

Acknowledgement

The presented research was supported by the project GACR 22-14387J Design and manufacturing of 4D metamaterials based on printed structures with embedded elements of smart materials.

References

Bradai, S., Naifar, S., Viehweger, C. and Kanoun, O. (2018) Electromagnetic Vibration Energy Harvesting for Railway Applications. In: *International Conference on Engineering Vibration (ICoEV 2017)*.

Edwards, R. and Gould, C. (2016) Review on micro-energy harvesting technologies. In: *Proc. 51st International Universities Power Engineering Conference*, UPEC.

Erturk, A., Inman, D. J. (2011) Broadband piezoelectric power generation on high-energy orbits of the bistable Duffing oscillator with electromechanical coupling. *J Sound Vib.,* 330, 2339–2353.

Margielewicz, J., Gąska, D., Litak, G., Wolszczak, P. and Yurchenko, D. (2023) Influence of impulse characteristics on realizing high-energy orbits in hybrid energy harvester. *Energy Convers Manag.,* 277, 116672.

Ryu, H., Yoon, H. J. and Kim, S. W. (2019) Hybrid Energy Harvesters: Toward Sustainable Energy Harvesting. *Advanced Materials,* 31, 1802898.

Stanton, S. C., McGehee, C. C. and Mann, B. P. (2010) Nonlinear dynamics for broadband energy harvesting: Investigation of a bistable piezoelectric inertial generator. *Physica D,* 239, 640–653.

Yang, Z., Zhou, S., Zu, J. and Inman, D. (2018) High-Performance Piezoelectric Energy Harvesters and Their Applications. *Joule,* 2, 642–697.

Zhu, D. and Beeby, S. P. (2013) A broadband electromagnetic energy harvester with a coupled bistable structure, *Journal of Physics: Conference Series*, vol. 476.

30th International Conference
ENGINEERING MECHANICS 2024
Milovy, Czech Republic, May 14 – 16, 2024

PARALLELIZATION OF DEM SOLVER FOR NON-SPHERICAL SOLIDS: A PATHWAY TO SCALABLE CFD-DEM SIMULATIONS

Studeník O.*, Kotouč Šourek M., Isoz M.***, Kočí P.†**

Abstract: *Granular matter formed from non-spherical solids appears in both natural and industrial settings. These include, among others, landslides, mixing, and fluidization. The commonly used predictive method for granular matter is the discrete element method (DEM). However, DEM was initially designed for spherical particles and faces many challenges in modeling the non-spherical ones , which are prevalent. Therefore, various approaches, including multi-sphere clusters, super-quadrics and polyhedral models, were developed to approximate the irregular shapes. The polyhedral approach offers the highest level of fidelity, but comes with the biggest computational costs, particularly for non-convex particles. Hence, optimization and parallelization of codes with polyhedron-based DEM solvers are of great interest. In this work, we present recent advances in the development of our custom polyhedron-based DEM solver, focusing on parallel computing. With improvements in the solver architecture and boosted computational efficiency, the DEM code scales well at least up to 32 cores and allows for efficient coupling with computational fluid dynamics (CFD) to simulate complex particle-laden flows.*

Keywords: Discrete element method, non-spherical particles, MPI, CFD-DEM, OpenFOAM.

1. Introduction

The omnipresence of granular matters in nature and, consequently, industry requires ways to predict their behavior according to a given situation, e.g. prediction of landslides, mixing, or separation. One possible way is to use the discrete element method (DEM), which is capable of describing the movement of individual particles while considering collisions either reciprocal or with system boundaries (Cleary, 2010). DEM was initially proposed for spherical particles due to their simple definition and the existence of an analytic solution for collisions (Antypov and Elliott, 2010). However, irregular particle shapes are prevalent in nature and particle morphology tends to play a crucial role in the granular matter behavior. This fact poses a number of challenges in modeling systems with non-spherical particles, starting from shape approximation, including applied contact model, and ending with computational efficiency. Furthermore, when solids are transported by and densely dispersed in a fluid, the shape of the particles also plays a key role in the resulting flow properties (Xiong et al., 2021). Therefore, coupling a non-spherical DEM solver with computational fluid dynamics (CFD) might provide a deeper insight into such systems.

Today, the DEM treatment of arbitrarily shaped solids might be divided into three main approaches: (i) multi-sphere model, (ii) super-quadrics model and (iii) polyhedral model (Zhong et al., 2016). Each approach varies in level of fidelity of the shape approximation. At the same time, models (i) and (ii) are more suited to approximate smoothly curved surfaces, while benefiting from the sphere contact model with minor adjustments. The polyhedral model is the most general approach and is best suited for solids with sharp

* Ing. Ondřej Studeník: Institute of Thermomechanics, Czech Academy of Sciences (CAS), Dolejškova 1402/5; 182 00, Prague; CZ and Department of Chemical Engineering, University of Chemistry and Technology (UCT), Technická 5; 166 28, Prague; CZ

** Ing. Martin Kotouč Šourek: Department of Chemical Engineering, UCT, Technická 5; 166 28, Prague; CZ

*** Ing. Martin Isoz, PhD.: Institute of Thermomechanics, CAS, Dolejškova 1402/5; 182 00, Prague; CZ and Department of Mathematics, Informatics, and Cybernetics,UCT, Technická 5; 166 28, Prague; CZ,e-mail: isozm@it.cas.cz

† Prof. Ing. Petr Kočí, PhD.: Department of Chemical Engineering, UCT, Technická 5; 166 28, Prague; CZ

doi: 10.21495/em2024-290

edges or corners (Chen, 2012). Nevertheless, its non-trivial shape definition demands estimation of geometric properties. Furthermore, significant modifications to the contact model with respect to the particle overlap characterization are required. Thus, overall computational efficiency of the polyhedral model is low compared to other approaches.

In this work, we present recent improvements in parallel computing of a polyhedron-based in-house developed DEM solver that is primarily designed for particle-resolved direct numerical simulation in CFD-DEM applications (Isoz et al., 2022). As such, it was implemented in the OpenFOAM C++ library, which uses message-passing interface (MPI) parallelization. In particular, the framework architecture was improved with a focus on computational time scaling. Scaling results of the DEM solver are presented in detail and conclusions regarding CFD-DEM applications are hinted at.

2. Framework fundamentals

Movement of the particles The presented DEM solver is being developed primarily for polyhedron-based solids, described with stereolithographic templates (STL files). Each solid $\mathcal{B}_i$ is added to the computational domain Ω and prescribed with standard material properties such as Young's modulus Y, Poisson's ratio ν and density ρ. The particles are considered to be rigid and homogeneous. Geometrical properties, such as the mass or the moment of inertia, are estimated from the body projection $\mathcal{B}_i^{\mathrm{h}}$ onto finite volume mesh $\Omega^h \approx \Omega$.

The movement of individual solids is governed by Newton's second law of motion,

$$m_i \frac{\mathrm{d}^2 \boldsymbol{x}_i}{\mathrm{d}t^2} = \boldsymbol{f}_{\mathrm{g}} + \boldsymbol{f}_{\mathrm{c}}, \quad I_i \frac{\mathrm{d}\boldsymbol{\omega}_i}{\mathrm{d}t} = \boldsymbol{t}_{\mathrm{c}}\,, \tag{1}$$

here m_i is the mass of $\mathcal{B}_i$ and $\boldsymbol{x}_i$, $\boldsymbol{\omega}_i$, I_i are its centroid position, angular velocity and the matrix of its inertial moments at time t, respectively. The solver considers $\mathcal{B}_i$ to be affected by gravity (g) and by contact (c) with other bodies or boundaries of Ω. Thus, $\boldsymbol{f}$ and $\boldsymbol{t}$ in (1) represent the forces and torques acting on $\mathcal{B}_i$, respectively. The equations are solved using the finite difference method, assuming that the forces and torques are constant during each time step.

Contact The contact treatment affects the overall efficiency of any DEM solver, and there are many approaches to its solution. The presented solver utilizes the *soft*-DEM approach, which estimates contact force according to the magnitude of particle's overlap during contact. The resulting force defined by the Hertz-Mindlin model (Soltanbeigi et al., 2021) was originally proposed for spheres, for which the overlap can be characterized by the overlap length. However, such a treatment is not suitable for arbitrarily shaped solids. Thus, we reformulated the contact model to use the overlap volume introduced in (Chen, 2012). For collision of bodies $\mathcal{B}_i$ and $\mathcal{B}_j$ the normal contact force is implemented as

$$\boldsymbol{f}_{\mathrm{c}}^{\mathrm{n}} = \left(\frac{Y^{\mathrm{red}} V_{ij}^{\mathrm{o}}}{\ell_{\mathrm{c}}} + \gamma^{\mathrm{red}} \sqrt{\frac{Y^{\mathrm{red}} M^{\mathrm{red}}}{(\ell_{\mathrm{c}})^3}} \frac{\mathrm{d}V_{ij}^{\mathrm{o}}}{\mathrm{d}t} \right) \boldsymbol{n}_{\mathbf{c}}\,, \quad \ell_{\mathrm{c}} = 4 \frac{\|\boldsymbol{\ell}_i\|\ \|\boldsymbol{\ell}_j\|}{\|\boldsymbol{\ell}_i\| + \|\boldsymbol{\ell}_j\|}\,, \tag{2}$$

where γ represents the damping coefficient, M represents the mass of the colliding pair, $\boldsymbol{n}_{\mathrm{c}}$ stands for the contact normal, ℓ_{c} represents the characteristic length of the contact, with $\boldsymbol{\ell}$ representing the distance between particle's centroids and the contact centre and V_{ij}^{o} represents the overlap volume shared by the two solids $\mathcal{B}_i$ and $\mathcal{B}_j$. At last, the material properties with superscript red denote the harmonic average of the material properties of individual solids.

The tangential contact force is evaluated as

$$\begin{gathered} \Delta \boldsymbol{f}_{\mathrm{c}}^{\mathrm{t}} = k^{\mathrm{t}}\, \Delta \boldsymbol{\xi}^{\mathrm{t}} - 2\gamma^{\mathrm{n}} \sqrt{k^t M^{\mathrm{red}}}\, \boldsymbol{u}_{\mathrm{r}}^{\mathrm{t}}, \quad k^{\mathrm{t}} = 8\, G^{\mathrm{red}} \frac{\bar{A}_{\mathrm{c}}}{\ell_{\mathrm{c}}}\,, \quad \Delta \boldsymbol{\xi}^{\mathrm{t}} = \boldsymbol{u}_{\mathrm{r}}^{\mathrm{t}}\, \Delta t, \\ \boldsymbol{u}_{\mathrm{r}} = \boldsymbol{u}_i - \boldsymbol{u}_j + (\boldsymbol{\omega}_i \times \boldsymbol{\ell}_i - \boldsymbol{\omega}_j \times \boldsymbol{\ell}_j)\,, \quad \boldsymbol{u}_{\mathrm{r}}^{\mathrm{t}} = \boldsymbol{u}_{\mathrm{r}} - (\boldsymbol{u}_{\mathrm{r}} \cdot \boldsymbol{n}_{\mathbf{c}})\, \boldsymbol{n}_{\mathbf{c}}\,, \end{gathered} \tag{3}$$

where G is shear module, $\bar{A}_{\mathrm{c}}$ is cross-section area of the overlap volume, $\Delta\xi^{\mathrm{t}}$ the tangential overlap, k^{t} is tangential stiffness and $\boldsymbol{u}_{\mathrm{r}}$ is relative velocity and $\boldsymbol{u}_{\mathrm{r}}^{\mathrm{t}}$ its tangential component. The contact defining parameters such as $V_{,}^{\mathrm{o}}\, \ell_{\mathrm{c}}$, $\bar{A}_{\mathrm{c}}$, $\boldsymbol{n}_{\mathrm{c}}$ are evaluated using a virtual mesh algorithm, first presented in (Studeník et al., 2022). An increment of tangential force is added to the tangential contact force from the previous time step. Furthermore, tangential force magnitude is compared to the magnitude of the normal contact force scaled by the static friction coefficient μ. If the value is smaller, it's not modified and added to the normal component $\boldsymbol{f}_{\mathrm{c}} = \boldsymbol{f}_{\mathrm{c}}^{\mathrm{n}} + \boldsymbol{f}_{\mathrm{c}}^{\mathrm{t}}$; otherwise the value is scaled to $\mu\, \|\boldsymbol{f}_{\mathrm{c}}^{\mathrm{n}}\|$.

Solver parallelization The presented approach to contact treatment of polyhedral solids poses high demands on computational efficiency, even though the applied algorithm is highly optimized. The established approach to increasing computational efficiency is to divide solved tasks among available computational resources and solve them in parallel. The OpenFOAM library provides MPI-based parallelization (Bruck et al., 1997) and is designed for general CFD applications. Therefore, it is built to decompose finite-volume domains into subdomains, where each CPU is assigned one. During the simulation, CPUs work independently to limit information exchange to only boundary data. This is the first level (L_1) of our solver parallelization, which we employ to evaluate particle properties. Nevertheless, this approach has proven ineffective for DEM. To illustrate the situation, let us consider pouring of particles and let each CPU treat only particles within its bounds and share information with neighbors about the shared ones. Eventually, the particles start piling up on the bottom CPUs, which will be overloaded with their contact treatment, while the CPUs at the top will wait idly for the next iteration, as depicted in Fig. 1.

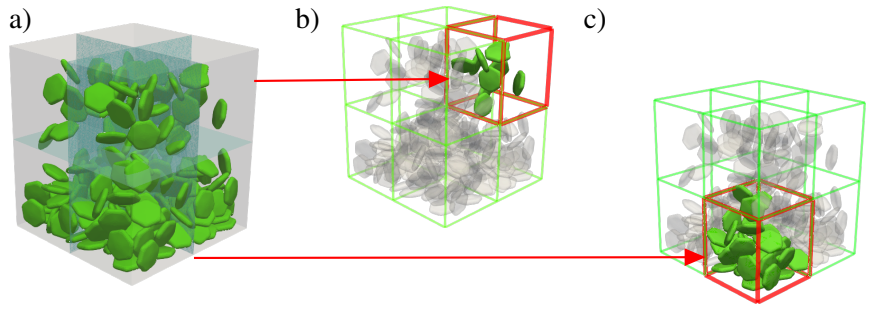

Fig. 1: Particle pouring, task distribution with standard MPI approach, outline of hexahedron domain decomposition with particles a). Illustration of uneven task distribution with b) showing an idle CPU and c) CPU overloaded with collision treatment.

Nevertheless, the L_1 MPI-imposed limitations can be mitigated by a construction of a second parallelization level (L_2). To employ all available computational resources and improve load balancing between overloaded and idle CPUs the contact solution must be distributed equally among all CPUs. However, without further treatment, the interprocessor communication tends to stall simulation speed. To avoid this, we created synchronized memory of the positions and orientations of all STL files, and each CPU can access all particle positions and each possible contact pair.

Although this approach has proved to increase computational efficiency, MPI parallelization is not designed to work with synchronized memory. This leads to significant RAM memory requirements, as each CPU must allocate space for all particles, scaling the memory requirements according to the number of CPUs. Moreover, with synchronized memory, every interprocessor communication instance must happen among all CPUs. This limited effective use to bellow 16 CPUs, when synchronization costs start outweighing the time spared. Nevertheless, this communication-related drawback was overcome with a new memory structure arranging the overall particle information to n-dimensional arrays, with a unique range for each CPU when working in parallel. Thus, shifting processor communication from individual particles to large data structures, and leading to well-scalable simulations, as demonstrated in the results.

3. Results

To illustrate the solver properties, we designed a particle pouring test containing 1, 3 and 5 thousand of particles; 1K, 3K, and 5K, respectively. The particles are monodisperse 20-sided polyhedra with characteristic dimension $d_\mathrm{c} = 4\,\mathrm{mm}$, while the auxiliary finite volume mesh has the resolition of $d_\mathrm{c}/4$. Particles are poured into a rectangular domain with dimensions $200\,d_\mathrm{c} \times 250\,d_\mathrm{c} \times 200\,d_\mathrm{c}$. Material properties for particles are $Y = 0.5\,\mathrm{GPa}$, $\nu = 0.3$, $\rho = 4\,000\,\mathrm{kg\,m^{-3}}$, $\mu = 1$, dissipation coefficient is set to correspond to the restitution coefficient being 0.25, system boundaries have similar properties with exception of $Y = 0.1\,\mathrm{GPa}$. Particles have no initial velocity and are pulled downward by gravity set to $g = 9.81\,\mathrm{m\,s^{-2}}$. The system is studied in terms of computational time scaling with respect to the used number of CPUs or the amount of particles. Results are displayed in Fig. 2.

4. Conclusions

In this contribution, we present recent advances in parallelization of our in-house developed DEM solver. The work led to a significant increase in computational efficiency, achieving approximately 75 % of the ideal

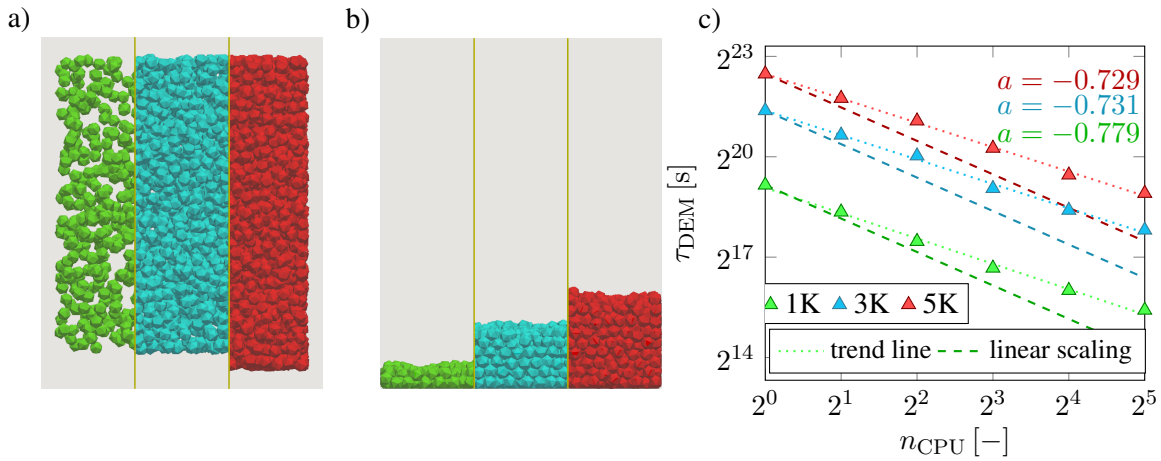

Fig. 2: Scaling of computational time for pouring polyhedral particles of different quantities; green – 1 thousand particles (1K), cyan – 3K particles and red – 5K particles. Qualitative results are shown in a) for simulation start and in b) for the end. Scaling of the current DEM implementation for given tests is compared to the linear scaling in c) with the measured trend line slope at the top right corner.

linear scaling in computational time. Significantly extended capabilities of the presented solver towards large-scale applications are demonstrated. Furthermore, with the improved parallelization of the DEM part of our CFD-DEM solver, a pathway to scalable CFD-DEM simulations is paved as the OpenFOAM, i.e. the solver CFD part, is known to scale well even on thousands of cores.

Both the DEM and CFD-DEM variants of our solvers are presently available from github.com/techMathGroup/openHFDIB-DEM

Acknowledgments

The work was financially supported by the Czech Science Foundation (GA22-12227S). Ondřej Studeník and Martin Isoz acknowledge the financial support provided by the Ministry of Education, Youth, and Sports of the Czech Republic via the project No. CZ.02.01.01/00/22_008/0004591 (Ferroic Multifunctionalities), co-funded by the European Union, by the grant project with No. TN02000069/001N of the Technology Agency of the Czech Republic, and the institutional support RVO:6138899. Ondřej Studeník acknowledges support from the grant of Specific university research – grant No. A2_FCHI_2024_022.

References

Antypov, D. and Elliott, J. A. (2010) On an analytical solution for the damped hertzian spring. *Europhysics Letters*, 94.

Bruck, J., Dolev, D., Ho, C., Roşu, M., and Strong, R. (1997) Efficient message passing interface (mpi) for parallel computing on clusters of workstations. *Journal of Parallel and Distributed Computing*, 40, 1, pp. 19–34.

Chen, J. (2012) *Understanding the Discrete Element Method: Simulation of Non-Spherical Particles for Granular and Multi-Body Systems*. PhD thesis.

Cleary, W. (2010) Dem prediction of industrial and geophysical particle flows. *Particuology*, 8, 2, pp. 106–118.

Isoz, M., Šourek, M. K., Studeník, O., and Kočí, P. (2022) Hybrid fictitious domain-immersed boundary solver coupled with discrete element method for simulations of flows laden with arbitrarily-shaped particles. *Computers and Fluids*, 244, pp. 105538.

Soltanbeigi, B., Podlozhnyuk, A., Kloss, C., S. Pirker, J. Y. O., and Papanicolopulos, S. (2021) Influence of various dem shape representation methods on packing and shearing of granular assemblies. *Granular Matter*, 26.

Studeník, O., Kotouč Šourek, M., and Isoz, M. (2022) Octree-generated virtual mesh for improved contact resolution in CFD-DEM coupling. *Topical Problems of Fluid Mechanics 2022*, pp. 151–158.

Xiong, H., Wu, H., Bao, X., and Fei, J. (2021) Investigating effect of particle shape on suffusion by cfd-dem modeling. *Construction and Building Materials*, 289, pp. 123043.

Zhong, W., Yu, A., Liu, X., Tong, Z., and Zhang, H. (2016) Dem/cfd-dem modelling of non-spherical particulate systems: Theoretical developments and applications. *Powder Technology*, 302, pp. 108–152.

30th International Conference
ENGINEERING MECHANICS 2024
Milovy, Czech Republic, May 14 – 16, 2024

NON-STATIONARY WAVES IN THICK ELASTIC AND VISCOELASTIC PLATES

Šulda J.[*], **Adámek V.**[**]

Abstract: *This study deals with the dynamics of non-stationary wave propagation in thick, homogeneous, isotropic, elastic and viscoelastic plates, employing a combination of analytical and numerical approaches. The first aim of this work is to efficiently enumerate the previously derived solution for transient wave propagation in a thick elastic plate. For this purpose, a numerical inverse Laplace transform (NILT) algorithm is used, which significantly improves computational efficiency. The results from this semi-analytical approach were compared to those results obtained using a Finite Element (FE) model to ensure the accuracy and validity of both methods. Additionally, the effect of viscoelasticity on wave propagation characteristics is discussed in this work.*

Keywords: Wave propagation, thick elastic plate, thick viscoelastic plate, analytical solution, numerical solution.

1. Introduction

In this work, non-stationary waves in a thick elastic and viscoelastic plate are investigated using a numerical and analytical approach. In contrast to the numerical solution, the knowledge of the analytical one can be advantageously used in solving many inverse problems, especially due to its computational speed. This is used, for example, to identify material properties, the source of excitation and to detect defects and factors that could lead to a limited life and reliability of machines. One could find the application of this approach in civil, aeronautical, mechanical and many other engineering fields.

The problem of wave propagation in an elastic thick plate was solved in the work of Valeš (1983), where the solution for basic mechanical quantities in the Laplace domain was derived. The evaluation of the derived formulas was then carried out in Pátek (1996) using the exact inverse Laplace transform based on the dispersion curves calculation and on the use of the residue theorem. This approach is exact, but with respect to high demands on CPU time, it is unsuitable for effective solving of inverse problems.

In view of this fact, the exact analytical inversion procedure will be replaced by the numerical inverse Laplace transform (NILT), specifically using the algorithm presented in Brančík (1999), which is based on the combination of FFT and Wynn's algorithm (Cohen , 2007). The same algorithm proved to be suitable for solving similar problems of transient waves as shown, e.g. in Šulda (2024). As known, every real material shows some degree of damping, i.e. energy dissipation, and therefore this work will also focus on the attenuation effects of the viscoelastic material on waves propagated in the plate. The discussion of this effect will be based on a comparison with the elastic case.

2. Analytical solution for a thick elastic plate

An infinite thick plate of thickness $2d$ is considered. The plate is assumed to be in a cylindrical coordinate system with $r \in \langle 0; \infty \rangle$ as the radial coordinate, $\vartheta \in \langle 0; 2\pi \rangle$ as the angular coordinate, and $z \in \langle -d; d \rangle$

[*] Ing. Jakub Šulda: Faculty of Applied Sciences, University of West Bohemia, Univerzitní 8; 301 00, Plzeň; CZ, jsulda@kme.zcu.cz

[**] Ing. Vítězslav Adámek, PhD.: Faculty of Applied Sciences, University of West Bohemia, Univerzitní 8; 301 00, Plzeň; CZ, vadamek@kme.zcu.cz

doi: 10.21495/em2024-294

as the coordinate in the plate thickness direction. On the upper surface, i.e. $z = -d$, the plate is excited by a constant transverse pressure of magnitude σ_0 on a circular region of radius R. The remaining parts of both plate surfaces are considered free of load. In such a case, the boundary conditions can be formulated as follows

$$\begin{aligned} \sigma_z(r,-d,t) &= \begin{cases} -\sigma_0 & \text{for } r < R \\ 0 & \text{otherwise} \end{cases}, \qquad \tau_{rz}(r,-d,t) = 0, \\ \sigma_z(r,d,t) &= 0, \qquad\qquad\qquad\qquad \tau_{rz}(r,d,t) = 0, \end{aligned} \tag{1}$$

where the functions σ_z and τ_{rz} represent the normal stress in the z direction and the shear stress in the rz plane, respectively. The equations of motion for such a plate can be derived using the Cauchy equations formulated in the cylindrical coordinate system (Graff , 1991). Due to the rotational symmetry of the problem, these equations will be independent of the coordinate ϑ. Substituting the kinematic equations for small strains into the constitutive relations and then into the Cauchy equations, the following equations for dilatation Δ and rotation ω_ϑ can be obtained (Valeš, 1983)

$$\begin{aligned} \frac{\partial^2 \Delta}{\partial t^2} &= c_1^2 \left(\frac{\partial^2 \Delta}{\partial r^2} + \frac{\partial^2 \Delta}{\partial z^2} + \frac{1}{r}\frac{\partial \Delta}{\partial r} \right), \\ \frac{\partial^2 \omega_\vartheta}{\partial t^2} &= c_2^2 \left(\frac{\partial^2 \omega_\vartheta}{\partial r^2} + \frac{\partial^2 \omega_\vartheta}{\partial z^2} + \frac{1}{r}\frac{\partial \omega_\vartheta}{\partial r} - \frac{\omega_\vartheta}{r^2} \right), \end{aligned} \tag{2}$$

where

$$\Delta = \frac{u_r}{r} + \frac{\partial u_r}{\partial r} + \frac{\partial u_z}{\partial z}, \;\; \omega_\vartheta = \frac{1}{2}\left(\frac{\partial u_r}{\partial z} - \frac{\partial u_z}{\partial r} \right). \tag{3}$$

As clear, the system of partial differential equations (2) for Δ and ω_ϑ is uncoupled in this case, which significantly simplifies the solving procedure. The constants $c_1 = \sqrt{(\lambda + 2G)/\rho}$ and $c_2 = \sqrt{G/\rho}$ denote the phase velocity of dilatation and shear waves in an elastic continuum of the density ρ, the shear modulus G and the Lame's constant λ. The solution of the system (2) can be advantageously found using the Laplace transform in time t and the Hankel transform in the spacial coordinate r. The resulting relations for the Laplace transforms of displacements $\overline{u}_r$ and $\overline{u}_z$ can be written as (Valeš, 1983)

$$\begin{aligned} \overline{u}_r &= \frac{\sigma_0 R}{2G} \int_0^\infty \left(\frac{F_3}{pL} - \frac{G_3}{pT} \right) \frac{1}{\gamma} J_1(\gamma R) J_1(\gamma r)\, d\gamma, \\ \overline{u}_z &= \frac{\sigma_0 R}{2G} \int_0^\infty \left(\frac{G_4}{pT} - \frac{F_4}{pL} \right) \frac{K_1}{\gamma} J_1(\gamma R) J_0(\gamma r)\, d\gamma, \end{aligned} \tag{4}$$

where the real parameter γ is the variable of the Hankel transform, and p represents the complex variable of the Laplace transform. The functions J_0 and J_1 are the Bessel functions of the first kind and of the zero and first order. The remaining complex functions F_3, F_4, G_3, G_4, L, T, K_1 introduced in (4) are mostly defined as a combination of hyperbolic sines and cosines and can be found in Valeš (1983).

Considering the relations for the Laplace transforms of time derivatives and with respect to the zero initial condition of the solved problem, one can write $\overline{v}_r = p\overline{u}_r$, $\overline{v}_z = p\overline{u}_z$ for the transforms of velocities. The formulas for displacement and velocity components were evaluated using a Matlab code. A plate with the thickness of $2d = 40$ mm was considered and excited with the constant pressure $\sigma_0 = 1$ MPa at a circular area with the radius $R = 2$ mm. The material parameters of the plate corresponded to steel, i.e. $\rho = 7\,800$ kg/m^3, $E = 2.11 \cdot 10^{11}$ Pa and $\nu = 0.3$. The resulting visualisation of wavefronts in one half of the plate cross-section at times of 5, 10 and 20 μs is depicted using the velocity component v_z in Fig. 1. The vertical axis corresponds to the radial direction r and the horizontal one to the vertical coordinate z. Different types of waves propagated in the plate by their characteristic velocities can be simply identified from Fig. 1. The fastest is the dilatational wave (P-wave), which propagates at speed $c_1 \doteq 6\,020$ m/s and which is followed by a shear wave (S-wave) propagated with $c_2 \doteq 3\,218$ m/s. The largest amplitude gains the Rayleigh wave (R-wave), which travels on the free surface of the plate, and its speed can be estimated as $c_R \approx 0.92 c_2 \doteq 2\,960$ m/s.

3. Comparison of semi-analytical results with results obtained by FEM

Regarding the fact that the analytical formulas are complex, it is advisable to use another method to verify the evaluation procedure. For this purpose, an axisymmetric problem of a thick elastic plate of thickness

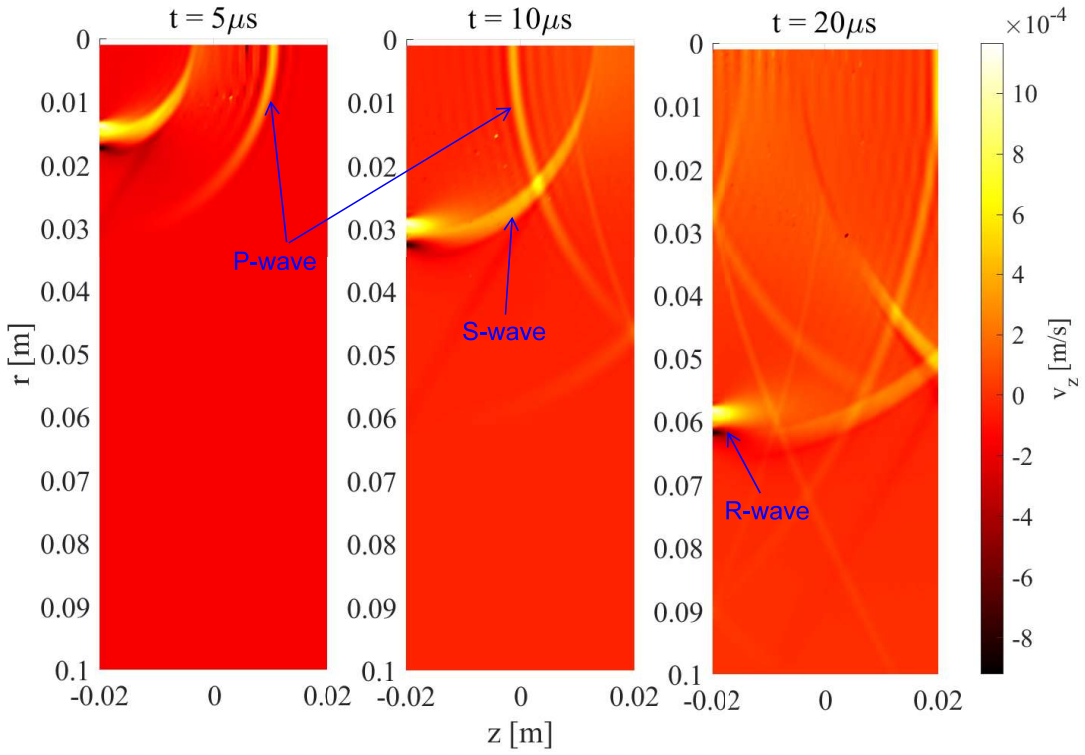

Fig. 1: Velocity v_z distribution in a thick steel plate.

40 mm and radius 100 mm was solved in the software MSC.Marc. The linear axisymmetric elements (type 10) with the size 0.4×0.4 mm were used. To study the effect of energy dissipation, the viscoelastic plate was also considered. The Young moduli of both plates correspond to polypropylene (PP) and were chosen as $E = 2.8090 \cdot 10^9$ Pa (see Šulda (2024)). The viscoelastic properties of the second plate was modelled using the standard viscoelastic solid in Zener configuration, the parameters of which were identified for a thin PP rod in Šulda (2024). These parameters are summarised in Tab. 1. With respect to the maximal wave speed in these materials ($c_1 = 2\,203$ m/s) and to the mentioned size of elements, the integration time step of the Newmark integration method was chosen as $1.82 \cdot 10^{-7}$ s.

ρ [kg/m^3]	ν [-]	E_E [Pa]	E_1 [Pa]	λ_1 [Pa·s]
928.6	0.35	$2.2608 \cdot 10^9$	$5.4821 \cdot 10^8$	$1.9099 \cdot 10^4$

Tab. 1: Material parameters of PP modelled by the standard viscoelastic solid (Zener model).

Fig. 2a) shows a comparison of the displacement u_z for the $z = -20$ mm and $r = 4$ mm from both approaches and for elastic and viscoelastic material up to time $t_{max} = 100$ μs. The compared results for the elastic case have a maximum relative error of 1.1 %. Approximately from $t = 88$ μs, the numerical results are influenced by the P-waves reflected from the plate boundary at $r = 100$ mm. On the other hand, the effect of the finite dimension of the plate in the transverse direction z has a more significant impact in both cases after the time of 35 μs (approx. $4d/c_1$) when the P-wave reflected from the bottom surface of the plate arrived at the monitored point. After the R-wave passes this point (approx. 6.5 μs) and before the arrival of the mentioned reflected P-wave, it can be seen that the excitation does not cause any change in u_z in the elastic case. In the viscoelastic case, a rising trend of u_z occurs when constant stress is applied, and thus, there is a remarkable deviation from the results for the elastic plate. Another change-point in the results is at 75 μs. This time corresponds to the arrival of the reflected S-wave. These same changes in solutions can be observed in Fig. 2b), where the displacement u_r is shown at the same monitored location. The results of the numerical and the semi-analytical elastic model deviate by the maximal relative error 3 % up to t_{max}, except the initial arrival of the wave. In this region, the maximal relative error is 14 % in peaks. Within this time interval, we can also observe the effect of energy dissipation resulting in a small decrease in amplitudes. The viscoelastic case differs relatively from the elastic one in the mentioned peaks by 3 %.

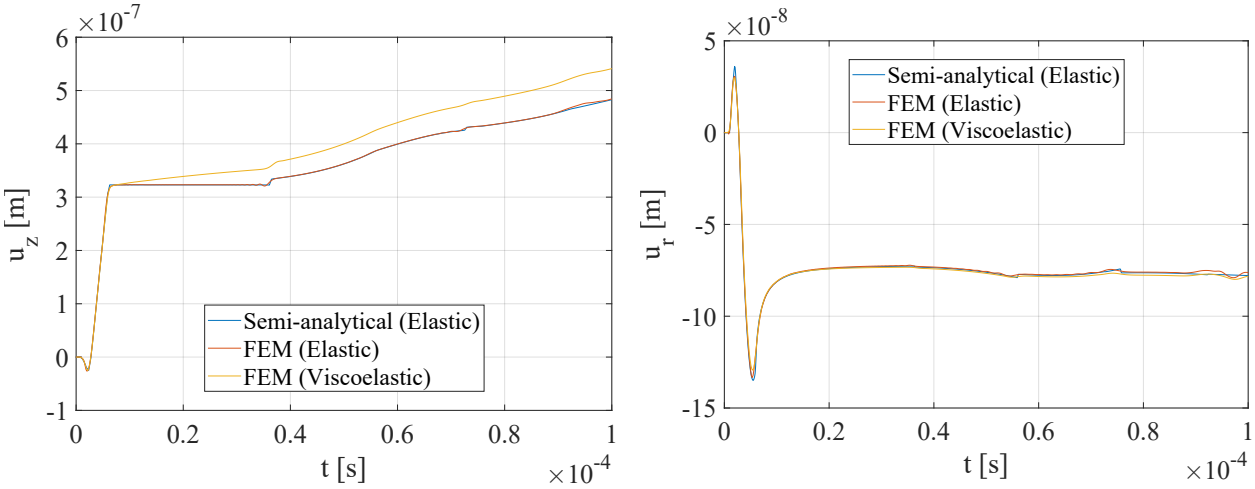

a) displacement u_z *b) displacement u_r*

Fig. 2: Comparison of semi-analytical and numerical results obtained for elastic and viscoelastic plate.

4. Conclusions

The analytical solution for the non-stationary state of stress in a thick elastic plate under transverse pressure loading previously derived in Valeš (1983) was evaluated using a numerical inverse Laplace transform algorithm. Contrary to the traditional and exact evaluation procedure based on dispersion curves and residual theorem, this approach enables the effective calculation of plate response in the 2D domain. These semi-analytical results agreed well with the results obtained by FE simulation performed in the software MSC.Marc. The FE model was also used to study the effect of energy dissipation in short times.

This work is a starting point for the derivation of the analytical solution for (i) a similar problem of a thick viscoelastic plate and (ii) a problem of a thick layered viscoelastic plate. The latter one could then be used as an approximation of the response of a viscoelastic plate made of functionally graded material.

Acknowledgment

The publication was supported by the project SGS-2022-008 and by the grant GA 22-00863K.

References

Brančík, L. (1999) Programs for fast numerical inversion of Laplace transforms in Matlab language environment. In: *Proc. of 7th MATLAB Conference*, Prague, pp. 27–39.

Cohen, A. M. (2007) Numerical methods for Laplace transform inversion, Springer, New York.

Graff, K. F. (1991) Wave motion in elastic solids. Dover Publications, Inc., New York.

Pátek, J. (1996) Use of non-stationary stress calculations of transversely excited thin and thick plates in diagnostic methods. *Technical report 143 VP*, University of West Bohemia, Pilsen (in Czech).

Šulda, J., Adámek, V. and Kroft, R. (2024) Transient response of non-prismatic heterogeneous viscoelastic rods and identification of their material properties. *European Journal of Mechanics - A/Solids*, 105, 105241.

Valeš, F. (1983) State of stress in a thick elastic plate under non-stationary transverse loading. Part I - Derivation of Laplace transforms for displacement and stress components. *Technical report Z 847/83*, Institute of Thermomechanics of the CAS, Prague (in Czech).

30th International Conference
ENGINEERING MECHANICS 2024
Milovy, Czech Republic, May 14 – 16, 2024

EXPERIMENTAL ASSESMENT OF THE MECHANICAL BEHAVIOR OF IMPRESSION MATERIAL FOR ANAESTHESIOLOGY USE: A PRELIMINARY STUDY

Thomková B.[*], Hrubanová A.[**], Košková O.[***], Richtrová M.[†], Skácel P.[††], Štourač P.[†††], Marcián P.[‡]

Abstract: *This study examines a silicone material designed for a high precision impressions. We explore the possibility of using this material for creation of patient specific obturator for soft tissue protection of upper jaw while intubating neonatal patients with cleft palate. The biaxial tensile tests were performed to examine the material properties of the selected silicon material. Specimen were compressed in 2-part mold made by 3D printing technology. The preliminary results suggest isotropic properties (p-value 0.198), showing no statistically significant differences between measured directions. The study also suggests potential viscoelastic behavior since the slowest deformation speed showed slightly different behavior compared to the higher strain rate. However, this is just a preliminary study thus, to strengthen the study's reliability, further validation on larger datasets is recommended.*

Keywords: Cleft, silicone material, biaxial tensile test, stiffness.

1. Introduction

Neonatal patients with a cleft palate are operated on as soon as possible after birth to ensure not only an airway but also a better intake of food. However, performing intubation in such young patients is often challenging due to the danger of damaging the patients soft tissue of upper jaw. A protective obturator made of silicone material can be used for these intubations (Richtrová et al., 2023). The aim of this study is to examine the mechanical behavior of the selected silicone material. To do so, series of biaxial tensile tests were performed to explore the isotropic and viscoelastic nature of this material.

[*] Ing. Barbora Thomková: Institute of Solid Mechanics, Mechatronics and Biomechanics, Faculty of Mechanical Engineering, Brno University of Technology, Technická 2896/2, 616 69 Brno, Czech Republic; CZ, barbora.thomkova@vutbr.cz

[**] Ing. Anna Hrubanová: Institute of Solid Mechanics, Mechatronics and Biomechanics, Faculty of Mechanical Engineering, Brno University of Technology, Technická 2896/2, 616 69 Brno, Czech Republic; CZ, anna.hrubanova@vutbr.cz

[***] MUDr. Olga Košková, PhD.: Department of Burns and Plastic Surgery, Faculty of Medicine, Masaryk University, Jihlavská 340/20, 625 00 Brno, Czech Republic; CZ, koskova.olga@fnbrno.cz

[†] MUDr. Michaela Richtrová: Department of Paediatric Anaesthesiology and Intensive Care Medicine, Masaryk University, Černopolní 212/9, 662 63 Brno, Czech Republic; CZ, 60032@mail.muni.cz

[††] Ing. Pavel Skácel, PhD: Institute of Solid Mechanics, Mechatronics and Biomechanics, Faculty of Mechanical Engineering, Brno University of Technology, Technická 2896/2, 616 69 Brno, Czech Republic; CZ, skacel@fme.vutbr.cz

[†††] Prof. MUDr. Petr Štourač, PhD., MBA, FESAIC: Department of Paediatric Anaesthesiology and Intensive Care Medicine, Masaryk University, Černopolní 212/9, 662 63 Brno, Czech Republic; CZ, stourac@med.muni.cz

[‡] Ing. Petr Marcián, PhD.: Institute of Solid Mechanics, Mechatronics and Biomechanics, Faculty of Mechanical Engineering, Brno University of Technology, Technická 2896/2, 616 69 Brno, Czech Republic; CZ, marcian@fme.vutbr.cz

doi: 10.21495/em2024-298

2. Methods

2.1. Specimen preparation

The study tested Zhermack Elite HD+ putty, a two-component silicone material used for orthodontic purposes. The mixed material (ratio 1:1), was inserted into a mold and cured for 3.5 minutes.

The mold (Fig. 1a) for sample preparation was created using additive 3D printing technology (Prusa i3 MK3S+) with polylactic acid (PLA). The mold, featuring an outlet channel for excess material removal, maintained its stiffness during sample production without deformation. Each specimen, sliced to 18 × 18 mm after molding (Fig. 1b), was labeled with black markers for deformation tracking (Fischer et al., 2023). Eight marks on each specimen's sides ensured consistent clamp spacing across all tests (Fig. 1c). In total, 24 specimens were prepared for the study. Note that 4 specimens had to be excluded from the analysis because a pre-existing defect in the specimen prior to testing or because the initial damage during the clamping process.

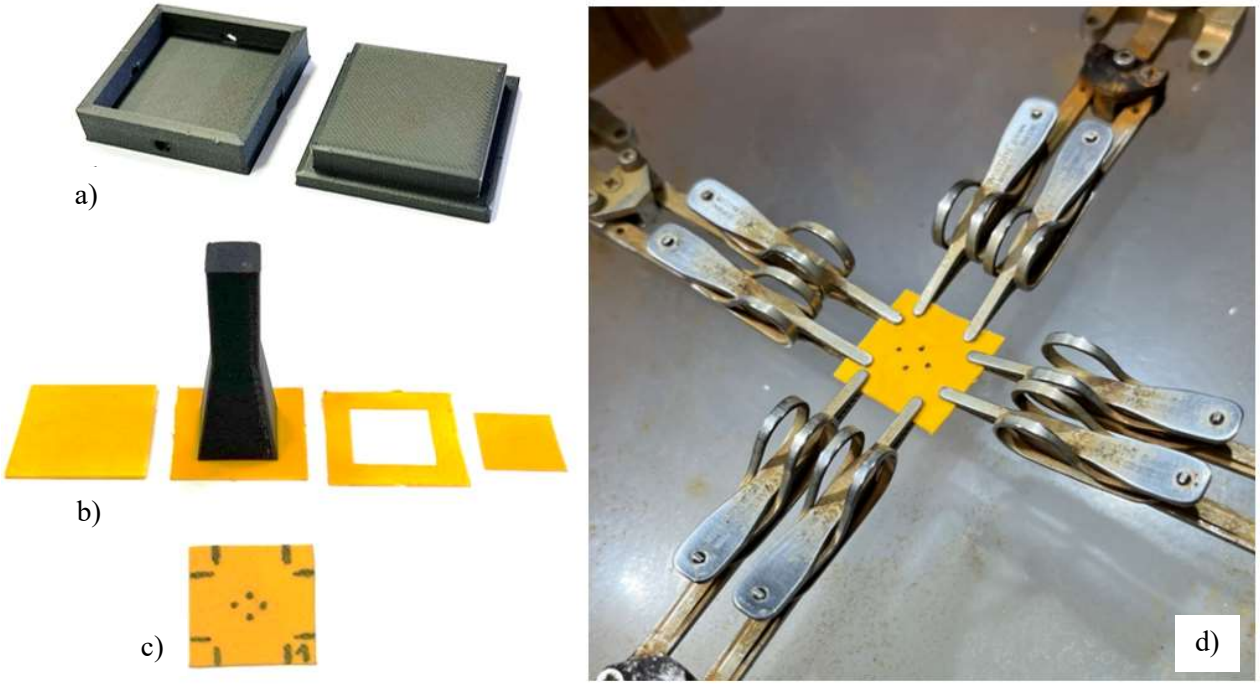

Fig. 1: a) 3D printed mold; b) the process of cutting the final 18 x 18 mm specimen; c) final specimen used for testing with markers for deformation evaluation (center) and markers for clamp spacing (outer boundary); d) the specimen mounted in the biaxial tensile device ready for the testing.

2.2. Testing and evaluation

All mechanical tests were performed on a testing device (Camea, s.r.o., CZ). The device consists of 2 perpendicular axes with linear-stepped motors realizing the mechanical displacement of clamps. In case of biaxial testing, two motors are used, and the specimen is attached by eight spring clamps (Fig. 1d) with serrations preventing the slipping of specimen during testing. The forces are measured by load cells with nominal capacity of 20 N mounted on both actuator axes providing the controlled displacement. The area of the specimen is captured by CCD camera (sampling frequency of 8–33 Hz) with 0.02 mm/pixel resolution mounted perpendicularly to the testing area. To ensure high contrast images, the measured area is illuminated by two external lights. The sample clamped in the testing device is shown in Fig. 1d. The sample thickness was measured by dial indicator (MarCator 1075, produced by Mahr, Germany, accuracy 0.01 mm, pin diameter 4.1 mm) at 5 locations of each specimen; the mean value is used for further analysis. After clamping a pre-tension of 0.1 N was applied to each specimen to ensure its flatness (Lisický, 2021). The testing is displacement controlled; three different displacement speeds

of 0.167; 0.33 and 0.667 mm/s (8 specimen per speed) were employed to explore the potential viscoelastic behavior of the material.

The evaluations of the testing area are done in software Tibixus (Turčanová et al., 2023) from the images captured by CCD camera. The first captured image is taken as a reference and the deformation is determined by digital image correlation (DIC) techniques, tracking the relative position of the contrast markers on specimen marked on it prior to testing, and calculating the corresponding strain values. The first Piola-Kirchhoff stress is calculated as follows:

$$\sigma = \frac{F_{exp}}{b\,T}, \tag{1}$$

where F_{exp} is the force measured by the load cell, b and T are the measured initial (undeformed) dimensions of the specimen (width and mean thickness, respectively).

The initial parts of the obtained stress-strain curves were cut off - due to experimental errors at extremely low stresses/strains (caused by 3D effects from clamping, specimen planarity imperfections, parasitic effects of gravity, etc.) Thus, only the rest of the stress-strain curves with stabilized progression are considered and fitted by first order polynomial function; the slope represents the given initial stiffness.

3. Results

The resulting stiffnesses of 20 specimens in x and y direction are summarized in Tab. 1:

Def. speed [mm/s]	**S_x [MPa]**	**S_y [MPa]**	**Def. speed [mm/s]**	**S_x [MPa]**	**S_y [MPa]**	**Def. speed [mm/s]**	**S_x [MPa]**	**S_y [MPa]**
0.167	11.249	10.690	0.333	19.427	10.604	0.667	15.653	15.441
0.167	11.395	12.285	0.333	15.674	8.5102	0.667	10.748	10.434
0.167	11.944	9.822	0.333	10.301	13.616	0.667	11.176	19.383
0.167	12.538	10.086	0.333	17.680	14.635	0.667	17.560	14.614
0.167	9.343	10.065	0.333	22.703	11.990	0.667	11.330	9.5393
0.167	21.285	10.133	0.333	16.648	14.837	0.667	13.304	18.771
Median (Q1;Q3)	11.67 (10.77;14.72)	10.11 (10.00;11.09)	0.333	19.536	19.390	0.667	7.380	11.541
			Mean ± SD	17.42 ± 3.89	13.37 ± 3.49	**Mean ± SD**	12.45 ± 3.38	14.25 ± 3.92

Tab. 1: The stiffness in both measured direction with given deformation speed used during equibiaxial testing.

The subsequent statistical analysis was performed using software Minitab 15; statistical significance assumed if $p < 0.05$. The stiffnesses were compared for x and y direction for entirety of 20 specimens by Wilcoxon signed rank test since the normality of distribution was not confirmed for all datasets (Anderson Darling test). Then, the same comparison was made for distinctive deformation speeds to eliminate the potential influence of viscoelastic effects. The resulting p-values are summarized in Tab. 2.

Statistical test	**All**	**0.167 mm/s**	**0.333 mm/s**	**0.667 mm/s**
Wilcoxon signed rank test	0.198	0.295	0.108	0.554

Tab. 2: The p-values for statistical analysis comparing the stiffness in X and Y direction for all specimens and for the three distinctive deformation speeds.

Based on the statistical significance levels, as indicated by the p-values presented, an evidenced deduction affirming the isotropic nature of the material can be drawn. Subsequently, the stiffnesses for three

deformation speeds can be compared to determine the possible viscoelastic behavior. Analogously, Anderson-Darling test was performed, the normality of data was not confirmed for all datasets thus the Mann-Whitney test was used. The p-values are displayed in Tab. 3.

Statistical test	0.167 vs 0.333 mm/s	0.167 vs 0.667 mm/s	0.333 vs 0.667 mm/s
Mann-Whitney	0.019	0.190	0.161

Tab. 3: The stiffness in both measured direction with given deformation speed used during equibiaxial testing.

These results show that there is a significant difference between the 0.167 and 0.333 mm/s deformation speeds indicating possible viscoelastic behavior.

4. Discussion

The study results reveal no statistically significant differences between the two measured directions, confirming material isotropy. However, limitations must be acknowledged. The thinness of specimens (approximately 0.25 mm) ensured biaxial strain conditions but led to premature fractures during clamping, restricting maximal strain to no more than approx. 6 % for most specimens. Consequently, the dataset primarily captures the initial stress-strain curve, presenting challenges in strain evaluation due to reference zero strain determination and clamp micro adjustments.

Moreover, the dataset size is insufficient for robust statistical analysis, particularly for nonparametric tests. Data at 0.167 mm/s deformation rate did not meet normal distribution criteria, possibly influenced by clamp-induced damage during the longer test duration. Further statistical analysis indicated significant differences in low deformation, suggesting potential viscoelastic behavior. All conclusions drawn should be validated on larger datasets.

Despite being a preliminary study, it supports the assumption of isotropic behavior and highlights potential viscoelastic effects.

Acknowledgement

The research was supported by the AZV - Czech Health Research Council (NU23-06-00301).

References

Richtrova, M., Koskova, O., Marcian, P., Joukal, M., Musilova, T., Janku, M., Fabian, D., Matyskova, D. and Stourac, P. (2023) Use of computer-aided design and 3D printing for airway management in paediatric patients with a cleft facial defect: a pilot study. *British Journal of Anaesthesia*, 130, 65, e469–e471.

Fischer, J., Turcanová, M., Man, V., Hermanova, M., Bednarik, Z. and Bursa, J. (2023) Importance of experimental evaluation of structural parameters for *constitutive modelling of aorta. Journal of the Mechanical Behavior of Biomedical*, 138, 105615.

Turcanová, M., Fischer, J., Hermanova, M., Bednarik, Z., Skácel, P. and Bursa, J. (2023) Biaxial stretch can overcome discrepancy between global and local orientations of wavy collagen fibres. *Journal of Biomechanics*, 161, 111868.

Lisický, O., Hrubanová A., Staffa R., Vlachovský R. and Burša J. (2021) Constitutive models and failure properties of fibrous tissues of carotid artery atheroma based on their uniaxial testing. *Journal of Biomechanics,* 129.

30th International Conference
ENGINEERING MECHANICS 2024
Milovy, Czech Republic, May 14 – 16, 2024

INFLUENCE OF DENTAL IMPLANT INSERTION DEPTH ON STRAIN IN PERIIMPLANT BONE TISSUE

Thomková B.[*], Borák L.[**], Podešva P.[***], Podešva M.[‡], Joukal M.[‡‡], Marcián P.[‡‡‡]

Abstract: *This study investigates the influence of dental implant insertion depth on strain states within the peri-implant bone tissue. Using a finite element model based on a human mandible CT data, variations in insertion depth were simulated, ranging from 0 mm to 2 mm in 0.5 mm increments. The analysis focused on a defined volume around the implant, evaluating strain intensities categorized according to the Mechanostat hypothesis. Results revealed notable differences in strain distribution within cancellous bone with increasing insertion depth, highlighting potential implications for bone response. While cortical bone showed consistent strain patterns, variations in cancellous bone suggest a nuanced relationship between insertion depth and peri-implant bone strain.*

Keywords: Dental implant, strain states, computational modelling.

1. Introduction

The discovery of the phenomenon of osseointegration has led to significant advancements in the field of dental implantology. Modern implantology introduces new possibilities in terms of sizes, materials, and designs for dental implants. These possibilities extend beyond visual differences to also encompass techniques used for dental implant insertion. Among others, 3D imaging techniques are becoming widely employed not only for pre-insertion preparation but also during the actual implant insertion.

The effort expended during insertion is crucial not only for ensuring the problem-free function of the dental implant but also for aesthetic considerations. One widely used protocol for implant placement involves subcrestal placement, where the implant is positioned beneath the alveolar crest. The depth of insertion can vary between 0.5 mm and 3 mm below the crest (Poovarodom et al., 2023).

Mechanical strains in the bone tissue around the dental implant are influenced by the quality of the bone tissue itself, but the method and depth of insertion also play their significant roles (Chou et al., 2010; Rito-Macedo et al., 2021). From the perspective of determining strain states, the peri-implant area around the dental implant is crucial. The aim of this study is to investigate the impact of dental implant insertion depth on strain states in peri-implant bone tissue.

[*] Ing. Barbora Thomková: Institute of Solid Mechanics, Mechatronics and Biomechanics, Faculty of Mechanical Engineering, Brno University of Technology, Technická 2896/2, 616 69 Brno, Czech Republic; CZ, barbora.thomkova@vutbr.cz

[**] Ing. Libor Borák, PhD.: Institute of Solid Mechanics, Mechatronics and Biomechanics, Faculty of Mechanical Engineering, Brno University of Technology, Technická 2896/2, 616 69 Brno, Czech Republic; CZ, xmborak01@vutbr.cz

[***] Ing. Pavel Podešva: IPPON s.r.o., Dolní Jasenka 770, 755 01 Vsetín, Czech Republic; CZ, pavel.podesva@euroimplant.com

[‡] Ing. Martin Podešva: Nyrtonn s.r.o., Srbská 2741/53, Královo Pole, 612 00 Brno, Czech Republic; CZ, martin.podesva@nyrtonn.com

[‡‡] Assoc. Prof. MUDr. Marek Joukal, PhD.: Department of Anatomy, Faculty of Medicine, Masaryk University, Kamenice 126/3, 625 00 Brno, Czech Republic; CZ, mjoukal@med.muni.cz

[‡‡‡] Ing. Petr Marcián, PhD.: Institute of Solid Mechanics, Mechatronics and Biomechanics, Faculty of Mechanical Engineering, Brno University of Technology, Technická 2896/2, 616 69 Brno, Czech Republic; CZ, marcian@fme.vutbr.cz

doi: 10.21495/em2024-302

2. Methods

To assess mechanical strains in the peri-implant bone tissue resulting from dental implant loading, computational modelling using the finite element method was utilized. Specifically, Ansys software (ANSYS Academic Research Mechanical, Release 2022 R2; Swanson Analysis Systems Inc) was employed for the solution. Details regarding the development of the computational model are provided in the following subsections.

2.1. Geometry model

One human mandible was acquired from the Department of Anatomy, Faculty of Medicine, Masaryk University Brno, Czech Republic in full compliance with relevant institutional and legislative requirements. The mandible was then scanned using CT (Philips) with voxel size 0.49 mm x 0.49 mm x 0.45 mm. In total, 231 anonymized CT images were obtained. These images were processed using automatic and manual segmentation to create a model of the geometry of the typical human mandible. It should be noted that the cortical and cancellous bone tissues were segmented and modelled separately. Both bone tissue geometry models are available at 10.5281/zenodo.10636072.

The dental implant was positioned in the premolar region. Specifically, the Brånemark dental implant including the abutment (Brånemark® System Mk III Groovy (NP Ø 3.3 mm, 11.5 mm)) was utilized in all variants. The variants differed in the depth of dental implant insertion, ranging from 0 mm to 2 mm in increments by 0.5 mm (see Fig. 1). It is assumed that there is no direct contact between the abutment and the bone; hence, no abutment osseointegration was modelled. Instead, a conical gap between the abutment and the cortical bone was modelled as illustrated in Fig. 2a.

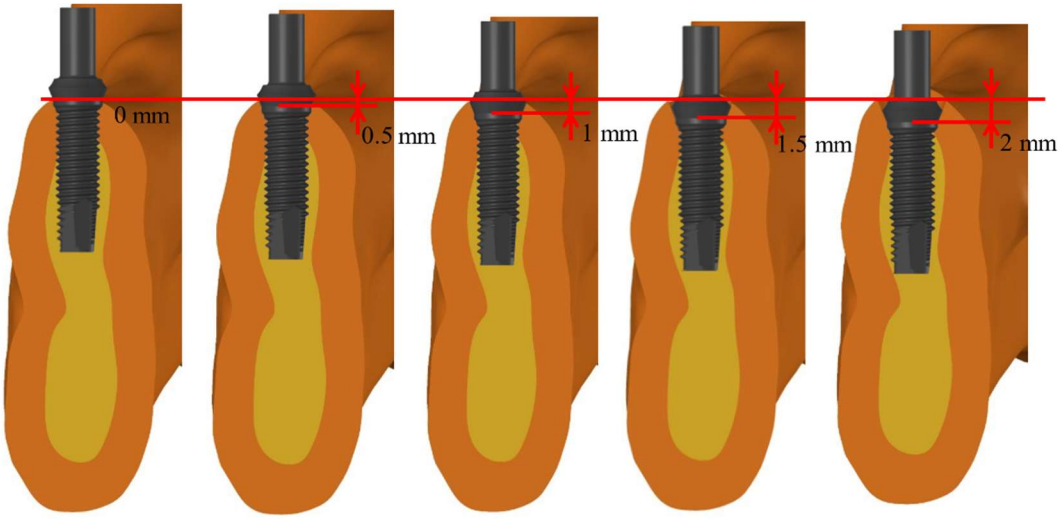

Fig. 1: Model variants with different insertion depths.

2.2. Material model

Cortical bone tissue, a portion of cancellous bone tissue and the dental implant (made of a titanium alloy) were modeled assuming a linear-elastic, homogenous, and isotropic material defined by two material characteristics, Young's modulus (E) and Poisson's ratio (μ). Specifically, E = 13 700 MPa and μ = 0.3 for cortical bone (Menicucci et al., 2002), E = 1 370 MPa and μ = 0.3 for cancellous bone, E = 110 000 MPa and μ = 0.34 for the implant (Park et al., 2022).

A portion of cancellous bone assuming a linear-elastic and isotropic material that is inhomogeneously distributed. This material model was created based on CT images data; specifically, utilizing the relationship between Hounsfield units (HU), bone density (ρ) and Young's modulus (E) (Eqs. (1) and (2)), an APDL macro was generated using the CTPixelMapper_v1-7 software application (Borák and Marcián, 2017). This macro assigns material characteristics to the nodes of the FE model (see Fig. 2b).

$$\rho = 0.114 + 0.000916 \cdot HU \; [g/cm^3] \tag{1}$$

$$E = 2349 \cdot \rho^{2.15} \; [MPa] \tag{2}$$

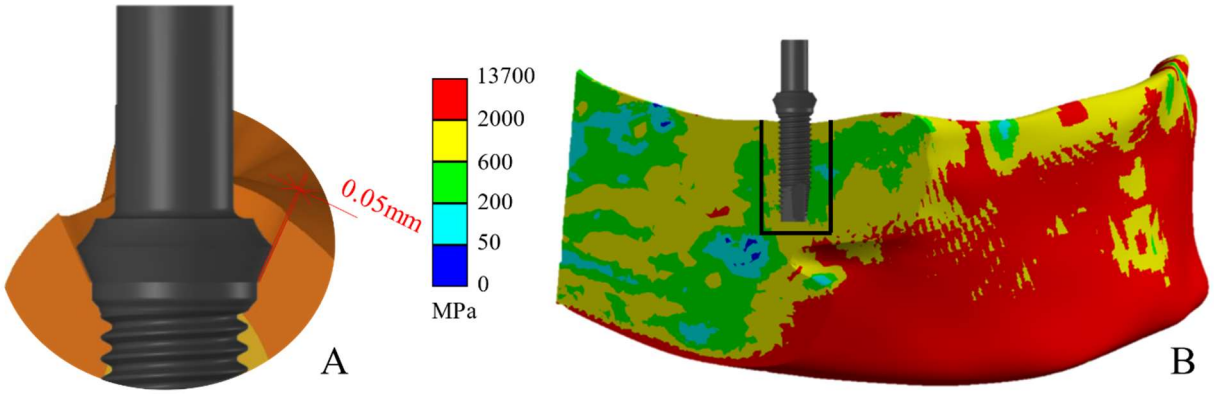

Fig. 2: a) Gap between abutment and cortical bone tissue, b) Distribution of material properties of segment of cancellous bone tissue (black lines represent VOI).

2.3. Load and boundary conditions

For the purpose of this analysis, masticatory muscle static forces were taken into account to simulate chewing. Forces and their directional vectors, as per authors Korioth and Hannam (Korioth, 1996), were incorporated into the FE model. The function of the temporomandibular joint was simulated by applying a spherical constraint to the surfaces associated with the mandibular condyles. To simulate the biting, the top of the abutment was restricted from moving in the direction of implant axis by using a remote displacement function in the FE software.

2.4. FE mesh

The geometry was meshed in Ansys using quadratic tetrahedral SOLID 187 elements, with a global element size of 0.45 mm and 0.04 mm for dental implant and areas of contact between dental implant and bone tissue, respectively. The mechanical interaction between the bone tissue and the implant was modelled using contact elements CONTA174 and TARGE170. The implant was assumed to be fully osseointegrated (i.e., a bonded contact option was used in the FE model).

3.Results and discussion

The analysis focused on strains in a limited volume of the peri-implant region of the bone. The volume of interest (VOI) was defined as a cylinder with a diameter of 6 mm around the implant and height of 18 mm from top of the abutment. Specifically, the VOIs in all variants were evaluated for strain intensity, defined as the difference between the maximum and minimum principal strains. Isolines of strain intensity for all variants can be seen in Fig. 3.

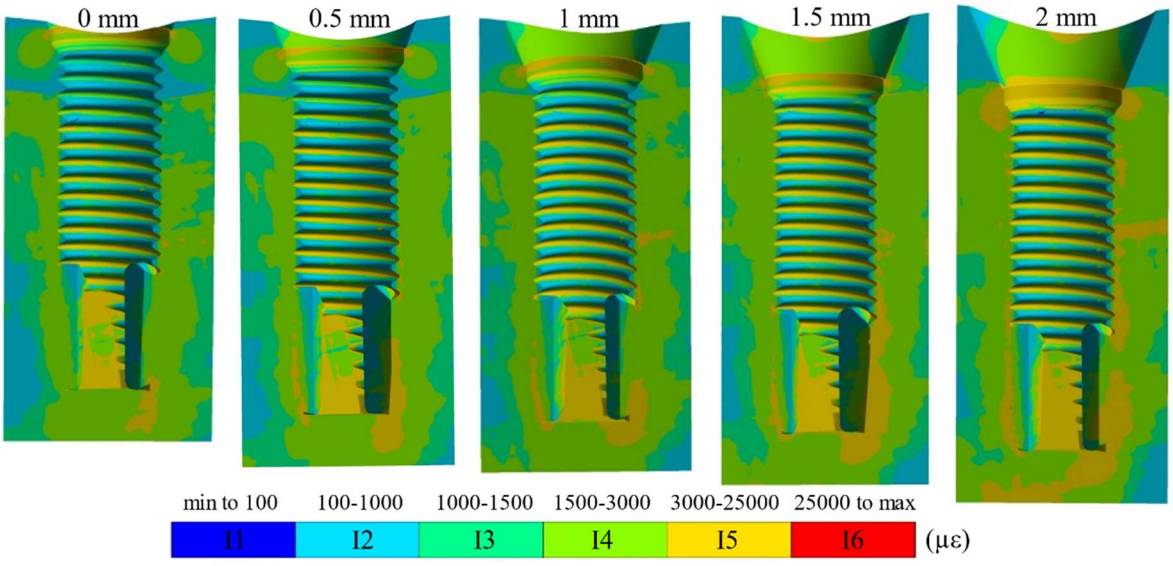

Fig. 3: Isolines of strain intensity in VOI.

Subsequently, the strain intensities in the FE nodes of the VOI were categorized using strain intervals defined by the Mechanostat hypothesis (Frost, 2004). Percentage shares of these intervals within the VOI were evaluated and compared among the variants (see Fig. 4). In particular, the intervals are defined as follows: (I1) 0–100 με, indicating no bone response; (I2) 100–1 000 με for bone resorption; (I3) 1000–1500 με and (I4) 1 500–3 000 με for bone modelling; (I5) 3 000–25 000 με for pathological overload; and the last one (I6), >25 000 με, representing the threshold for bone fracture.

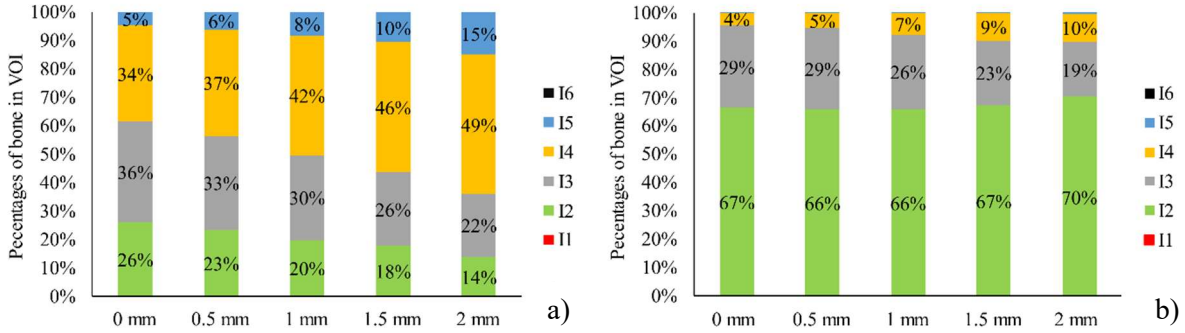

Fig. 4: Percentage of bone tissue in VOI: a) cancellous bone tissue, b) cortical bone tissue.

The difference in percentages within cortical bone tissue is not significant across all variants. Regardless of the insertion depth, the majority of strains within the VOI fall within interval I2 (67–70 %). As the insertion depth increases, the proportion of cortical bone tissue in direct contact with the dental implant decreases, leading to a slight increase of overload in the areas of contact (share of I4 in the VOI increased from 4 % to 10 %) while other tissues remain underutilized.

However, in cancellous bone, a noticeable shift in the percentages within individual intervals is observed with an increase of the insertion depth. As the depth increases, there is a noticeable increase in the shares of intervals I4 and I5, indicating a greater portion of the VOI is subjected to increased strains. Specifically, for a dental implant inserted crestally (with a 0 mm insertion depth), most of the bone tissue is distributed across intervals I3 and I4. With a 2 mm insertion depth, the predominant amount of bone tissue is found within interval I4.

Acknowledgement

This publication was supported by the project "Mechanical Engineering of Biological and Bio-inspired Systems", funded as project No. CZ.02.01.01/00/22_008/0004634 by Programme Johannes Amos Commenius, call Excellent Research. The research was supported by the specific research FSI-S-23-8240.

References

Borák, L. and Marcián, P. (2017) Inhomogeneous Material Properties Assignment to Finite Element Models of Bone: A Sensitivity Study. In: *Proc. 23rd Conference Engineering Mechanics*, Svratka, pp. 190–193.

Frost, H. M. (2004) A 2003 Update of Bone Physiology and Wolff's Law for Clinicians. *The Angle Orthodontist*, 74(1), pp. 3–15.

Chou, H., Müftü, S. and Bozkaya, D. (2010) Combined effects of implant insertion depth and alveolar bone quality on periimplant bone strain induced by a wide-diameter, short implant and a narrow-diameter, long implant. *The Journal of Prosthetic Dentistry,* 104(5), pp. 293–300.

Park, J., Park, S., Kang, I. and Noh, G. (2022) Biomechanical effects of bone quality and design features in dental implants in long-term bone stability. *Journal of Computational Design and Engineering,* 9(5), pp.1538–1548.

Korioth, T. W. P. and Hannam, A. G. (1996) Deformation of the Human Mandible During Simulated Tooth Clenching. *Journal of Dental Research,* 73(1), pp. 56–66.

Menicucci, G., Mossolov, A., Mozzati, M., Lorenzetti, M. and Preti, G. (2002) Tooth-implant connection: some biomechanical aspects based on finite element analyses. *Clinical Oral Implants Research,* 13(3), pp. 334–341.

Poovarodom, P. et al. (2023) Effect of implant placement depth on bone remodeling on implant-supported single zirconia abutment crown: A 3D finite element study. *Journal of Prosthodontic Research*, 67(2), pp. 278–287.

Rito-Macedoet, F. et al. (2021) Implant insertion angle and depth: Peri-implant bone stress analysis by the finite element method. *Journal of Clinical and Experimental Dentistry*, 13(12), pp. 1167–1173.

30th International Conference
ENGINEERING MECHANICS 2024
Milovy, Czech Republic, May 14 – 16, 2024

DESIGN STUDY OF COOLING FOR FORWARD-TYPE DETECTORS UNDER INCREASED LUMINOSITY EXPECTED AT THE FUTURE LHC OPERATING CONDITIONS

Vacek V.[*], Petrášek Š.[**], Horvath J.[***]

Abstract: *The team members of the Faculty of Mechanical Engineering of the Czech Technical University in Prague have been working together on projects at CERN for more than 22 years. Some work is related to cooling systems for the inner detector of the ATLAS experiment and to forward types of detectors. Such as TOTEM experiment, today incorporated under CMS as PPS2 and AFP ATLAS. Based on our prototypes, two cooling systems in the LHC tunnel have been implemented so far, namely a compressor cooling circuit with C3F8 refrigerant for TOTEM and the second system for the AFP project using AIRCOOLER-Split type units It was designed by us and worked for the last 5 years without failure and free of maintenance for needs of AFP forward detectors. We are starting work on systems for forward-type detectors to withstand increased luminosity conditions in the LHC tunnel to be expected after 2027. A substantial part of our paper is related to this ongoing research work and to the possibilities of variable 3D metal printed heat exchangers. These could be used for cooling forward detectors and their electronics under demanding operating conditions and limits given by their dimensions soon.*

Keywords: Particle detectors, CERN LHC experiments, cooling systems, forward type detectors, 3D metal type heat exchangers.

1. Introduction

Our research group has been working for more than 25 years on developing and applying cooling systems for detector technology in the field of elementary particle physics research. These activities include carrying out studies of the thermophysical properties of fluids, designing, constructing, and testing various types of cooling equipment, optimizing the heat transfer for high-tech electronics, and developing adequate DAQ systems, including sensors that can be used for these special applications.

Our paper will present examples of vortex-tube cooling applications around the two largest detectors of the LHC (**L**arge **H**ydron **C**ollider - project (see Fig. 1) at CERN, i.e. the ATLAS (**A T**oroidal **L**HC **A**pparatu**S**) and CMS (**C**ompact **M**uon **S**olenoid) detectors. In both projects, we are a part of a broad international cooperation network.

Many traditional elements known from classical refrigeration technology cannot be simply applied due to the minimal available space for installation inside the detector, and due to issues with radiation, the strong magnetic field, and dialectical and cleanliness requirements. Due to environmental restrictions, fluoroinerts will no longer be used for future types of inner detectors and cooling systems, and many next systems will use CO_2 as a refrigerant for the future runs. We will limit our presentation here only to activities related to the forward type detectors located both around main detectors ATLAS and CMS. In these installations, the range of cooling power is usually between 500 W and 1.5 kW. We will mainly concentrate to problems of cooling systems AIRCOOLER Split type unit using an air as the coolant (Vacek et al., 2016; Seabra et al., 2017 and Vacek and Doubek, 2021).

[*] Assoc. Prof. Václav Vacek, CSc.: CTU Prague, F. of Mech. Eng., Technická 4; 166 07, Prague; CZ, vaclav.vacek @cern.ch

[**] Ing. Šimon Petrášek: CTU Prague, F. of Mech. Eng., Technická 4; 166 07, Prague; CZ, simon.petrasek@fs.cvut.cz

[***] Ing. Jakub Horváth, PhD.: CTU Prague, F. of Mech. Eng., Karlovo náměstí 13; 120 00, Prague; CZ, jakub.horvath@fs.cvut.cz

doi: 10.21495/em2024-306

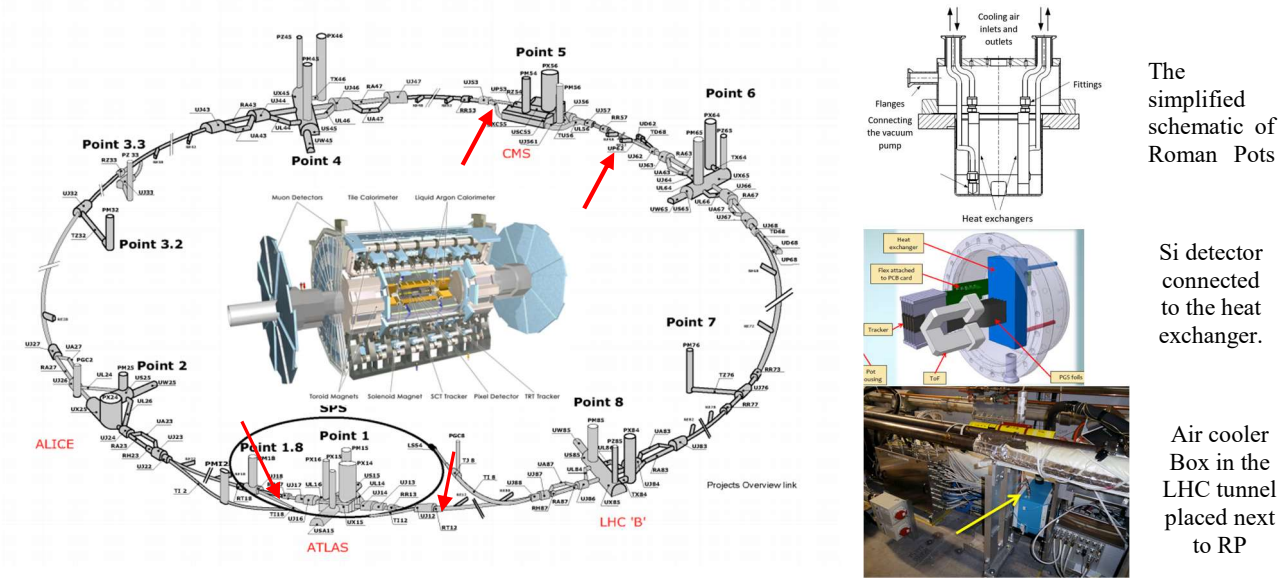

Fig. 1: The large hadron collider project map (adopted from https://cds.cern.ch). Red darts indicate approximate locations of forward type detectors.

Limiting elements are small and efficient heat exchangers that must be placed as close as possible to the silicon detectors and their electronics. All these sub-components are located inside the highly vacuumed space of the detector body referred to as the Roman Pot.

2.1. Heat exchanger development

There were developed several types of heat exchangers over the last 15 years starting from the fully machining units up to the multi-component variations and we must cope with the "ever-shrinking" space that was available for its placement. However, this is in direct contradiction to the gradual increase in cooling performance. The problem was solved using foam metal inserts. Our latest installation of AIRCOOLER-Splits units with the use of metal heat exchangers (Al or Cu) plus foam inserts. Such exchangers fulfill requests for cooling AFP detectors and has been in maintenance-free operation for the past 5 years without a single defect.

A brief overview of the development of exchangers and their improved functionality is shown in Fig. 2.

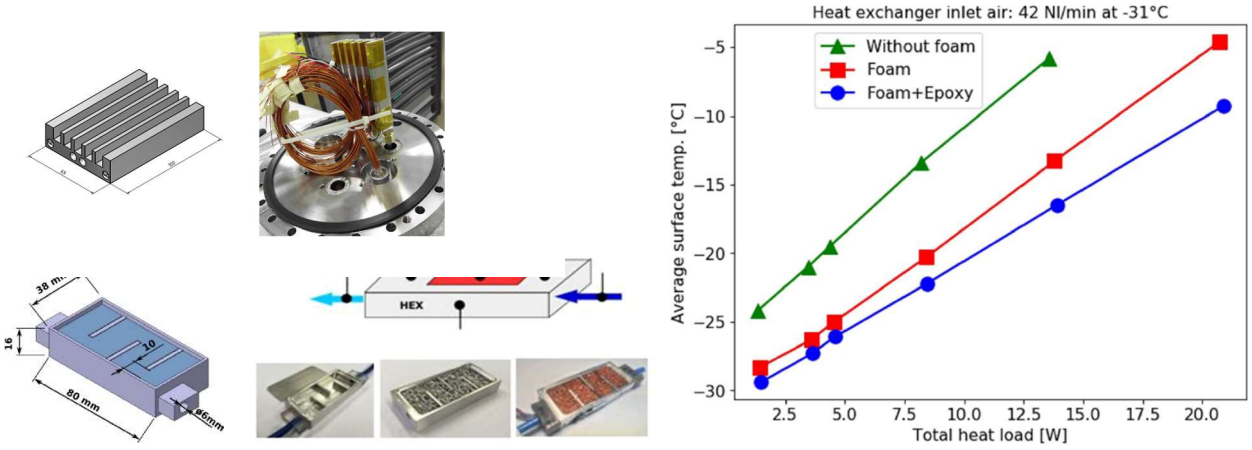

Fig. 2: The summary of the development of exchangers and improvement their functionality.

$$Q = h.A.(T_w - T_f) \quad (1)$$

From Eq. (1), it is obvious that the transferred heat depends on the heat transfer coefficient h [W/(m^2·K)], the heat transfer contact surface A [m^2] and the temperature difference $(T_w - T_f)$ [K]. So it is necessary increase the heat transfer coefficient, the surface area or the temperature difference. In order to keep the cold plate surface temperature T_w within the requirements for the AIRCOOLER outlet air temperature T_f has to be maximally lowered for a large transferred heat flux. The heat transfer coefficient is small for gas

flows (in comparison with liquids or two-phase flows), depending mainly on the air flow velocity, which is itself limited by the working pressure achievable at the AIRCOOLER output unit. Since the available air pressures are also imposed by the safety regulations for compressed air installations (usually 7–9 bars). It can be concluded that the surface area is the most important parameter to be optimized in order to achieve the desired performance in our applications. An enhanced inner surface of the cold plate exchangers was therefore investigated in several studies and configurations. Fig. 3 shows typical values recorded during the test, where the value of dissipated energy reaches 20 W.

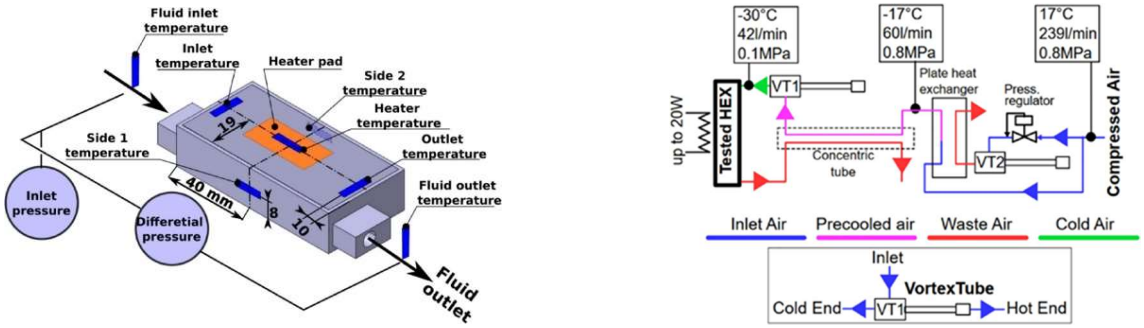

Fig. 3: The parameters during one of the many tests are illustrated in here.

2.2. 3D printed metal heat exchangers development

In the last few years, 3D printing experienced an enormous rise, since technology improves and processes are refined, metal 3D printing has grown increasingly popular and accessible. But even as price points for 3D printers come down and new applications for additive manufacturing are discovered, problems and challenges remain that still prevent many companies from utilizing this innovative technology to its full potential (Andronov, 2021). The R&D project of forward detectors for operating conditions with significantly increased luminosity after 2027 begins at CERN this year. That's why we decided to focus more on 3D printing of metallic materials. This will allow for easy adaptation to frequently changing specifications. This technology brings several advantages, among which flexibility in terms of shape and dimensions dominates. Such changes of the specifications will undoubtedly occur within development cycle. Considering our experience with many types of exchangers for these demanding applications, we were particularly concerned on studies of commonly known problems with metal 3D printing. The most important ones for us were the porosity of the products obtained and its impact on required tightness and the necessary cleaning of micro particles after 3D printing (Vafadar, 2021).

2.3. 3D printed heat exchangers tests

To print functional heat exchanger its design needs to be adjusted. For this purpose, original model was scanned with the CT (computed tomography) and data were transferred to surface model format STL. Surface model worked as reference geometry for new heat exchanger design. Some geometrical changes were made in the design to improve cooling properties or to secure flawless printing result. The main changes were following inner radiuses were added to lower tension in corners, partitions to increase cooling channel length, holes for threaded pneumatic connectors were added.

A model was used to get printing data for LPBF machine GE Concept Laser M2 in Materials MAGICS. Aluminum alloy AlSi10Mg was selected among available range of materials to ensure good heat transfer properties. Next step was a post processing of printed part. Printed heat exchanger was then cleaned, outer surfaces were machined, and preprinted inlet and outlet holes were drilled and tapped. Printed heat exchangers are going to be installed inside the Roman Pots with the high level of vacuum. No leaks are acceptable. Because of expected use of heat exchangers in particles detector surrounding, leak tests were carried out. Test setup was prepared for this purpose as shown in Fig. 4.

The first five 3D printed samples of the exchangers showed varying degrees of leaks. The load pressure test was slowly decreasing despite the series of setup modifications. We have observed small leaks in the screw connections, but the main leakage was probably formed during machining due to high deformations and insufficient machining thickness allowance. Then machining allowances were increased for the second set of heat exchangers. The heat exchanger ver. 2 was printed with the same post processing techniques and heat exchanger inlets and outlets were sealed with silicon high temperature gasket and tested. The standard operational pressure of cooling air on the site will be up to 2 bars.

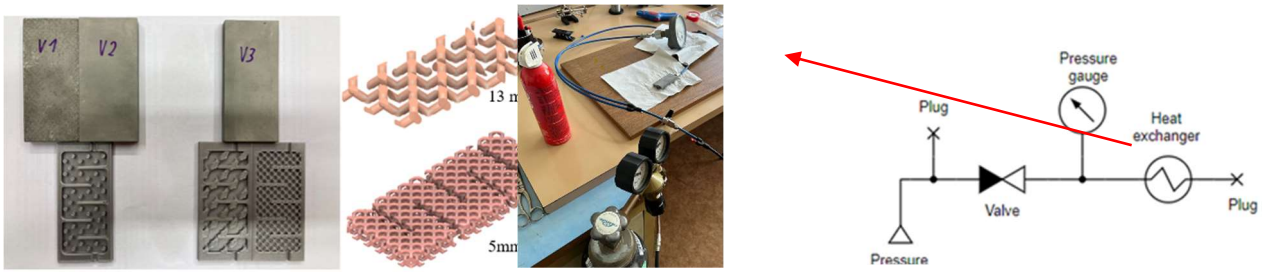

Fig. 4: Overview of heat exchanger prototypes with inner structures details and leak test setup.

Following experiment, even with higher pressure of 7 bars, was finally successful with no noticeable pressure loss in three days. Then testing under extreme conditions of 10 bars was carried out to verified reliability of printed part. Even under high pressure no leakage occurred for nearly one month. Density of the structure was chosen according to previous test with copper foam porosity to 30 %. Inner structures of the tested heat exchangers diamond like shapes we prepared with two diameters of 5 and 13 mm. It may show us its impact on cooling performance. We plan to investigate the operating parameters of the 3D printed exchangers to compare with the most efficient and used original exchangers nowadays. We will study and compare mainly differences in temperature profiles, pressure losses and flow, i.e. consumption of cooling medium-air. For this purpose, third version of heat exchanger with complex diamond shape structure was designed.

2. Conclusions

In our article, we mainly dealt with the issue of cooling the forward-type elementary particle detectors used at the CERN LHC accelerator. Special attention was paid to the optimization of the small heat exchangers used for cooling both the detectors themselves and their electronics. R&D projects are starting this year aimed at the operation of the LHC accelerator after 2027, when a significant increase in its luminosity is expected. We chose the path of developing the necessary metal heat exchangers by 3D printing. At the end of last year 2023 and the beginning of this year, we produced the first prototypes of such exchangers and carried out successful tests for their required tightness and their necessary cleaning from micro particles after 3D printing. A test set up is being prepared, including the DAQ system and the necessary sensors for conducting measurements on the Roman Pots mock-up with a new type of heat exchangers. By the end of the year, experiments aimed at proving the suitability of using exchangers produced by 3D printing will be carried out in comparison to heat exchangers with foam metal inserts used so far. We will focus on comparing relevant temperature profiles, pressure losses and consumption of cooling medium-air of all types of heat exchangers.

Acknowledgement

The research has been supported by the following grants: LM2015058, LTT17018 and CAAS, No.: CZ.02.1.01/0.0/0.0/ 16_019/0000778 and project SGS22/158/OHK2/3T/12 F. of Mech. Eng, of the CTU in Prague

References

Andronov, V., Šimon, J., Pelikán, L., Beránek, L. and Novák, P. (2021) Analysis of strength properties of 3D printed lightweight structures made of AlSi10Mg material: A Review of Common Processes, *IOP Conference Series: Materials Science and Engineering*.

Seabra, L., Banaś, E., Caforio, D. et al. (2017) The AFP detector control system. In: *Proc. 16th International Conference on Accelerator and Large Experimental Physics Control Systems (ICALEPCS)*.

Vacek, V. and Doubek, M. (2016) Air-driven cooling device for high tech electronics. In: *Proc. 12th IIR-Gustav Lorentzen Natural Working Fluids Conference (GL 2016)*, Edinburgh, United Kingdom.

Vacek, V. and Doubek, M. (2021) Universal heat exchanger for air and evaporative cooling of electronics, *Thermal Science and Engineering Progress*, Elsevier, vol. 32, pp. 11.

Vafadar, A., Guzzomi, F., Rassau, A. and Hayward, K. (2021) Advances in Metal Additive Manufacturing: A Review of Common Processes, Industrial Applications, and Current Challenges, *Applied Sciences*, vol. 11, iss. 3.

30th International Conference
ENGINEERING MECHANICS 2024
Milovy, Czech Republic, May 14 – 16, 2024

AI BASED ASSISTIVE MAINTENANCE OF MACHINES VIA QUERIX EXPERT-SYSTEM

Vechet S.*, Krejsa J., Chen K. S.*****

Abstract: *In the context of the expanding domain of Industry 4.0 and the integration of smart factories, there has been increasing interest in advanced diagnostics for industrial machines. This paper introduces an evolution of state-of-the-art expert system designed to aid in diagnosing issues encountered during the operation of industrial machines. Advanced diagnostic and maintenance systems serve as crucial components in the digital era of smart factories, so as the use-case scenario a mobile robotic platforms was used.*

Keywords: Assistive maintenance, decision making, advanced diagnostic.

1. Introduction

Expert systems have been a subject of interest for utilization of expert knowledge in various control systems over the past two decades. However, their prominence has been put aside in recent years in favour of artificial neural networks, largely due to the abundance of data available for training and the extensive usage of frameworks for rapid solutions deployment.

Despite the dominance of neural networks, there remains space for alternative AI methods such as expert systems, particularly due to their inherent capability to clarify decision-making processes. This paper addresses the need for advanced diagnostics in the industry, focusing on the development of an expert system to assist in diagnosing issues with mobile robotic platforms, represented by the BREACH platform.

While neural networks may seem as the only solution due to their popularity and accessible tool-chains, alternative AI methods like expert systems offer the advantage of backtracking the decision processes, an inherent feature of their design (Zhang, 2019; Bloecher and Alt, 2021; Valerio de Moraes et al., 2022). This capability is even more suited in industrial contexts where the hidden process behind each decisions is as crucial as the decisions themselves. (Korb and Nicholson, 2004; Thrun et al., 2005).

This research is motivated by industry demands, particularly in utilizing the advanced diagnostic capabilities for platforms like BREACH (Krejsa and Vechet, 2018; Vechet, 2011). The development of an advanced diagnostic assistant is based on the necessity to involve maintenance workers, enabling them to address all possible issues efficiently, thereby preventing costly down-times and the need for professional services.

2. Materials and methods

Our experimentation utilizes various autonomous mobile robots, primarily centered around the BREACH platform, developed in collaboration with Bender Robotics. Additionally, the ZALEELA project, aimed

* Assoc. Prof. Stanislav Vechet, PhD.: Institute of Thermomechanics AS CR, v.v.i., Technicka 2, 616 69, Brno; CZ, vechet@it.cas.cz

** Assoc. Prof. Jiri Krejsa, PhD.: Institute of Thermomechanics AS CR, v.v.i., Technicka 2896/2, 616 69, Brno; CZ, krejsa@it.cas.cz

*** Prof. Kuo-Shen Chen, PhD.: National Cheng Kung University, Department of Mechanical Engineering, No. 1, Ta-Hsueh Road, Tainan 701; Taiwan, kschen@ncku.edu.tw

doi: 10.21495/em2024-310

at indoor plant watering, and the LEELA robot, a lighter version of BREACH, are employed (Vechet et al., 2020). These platforms share common components such as laser range finders, ultrasonic distance sensors, encoders, and motor controllers, all operated using the Robot Operating System (ROS) (Vechet et al., 2020).

Hypothesis \ Evidence	A - RViz running	B - Map of environment is visible	C2 - Lidar data NOT visible in the map	D - Robot is well localized	D2 - Robot is NOT localized	E - Robots goal properly defined	F2 - Robot is NOT moving	S - Robot rotates in place
D - Lidar (Hokuyo) not connected	✓	✓	✓					
E - Battery low	✓			✓		✓	✓	
G - Robot doesn't boot properly	✓				✓			
A - Encoder not connected								✓
F - Problem with RoboClaw					✓			
B - RoboClaw not connected							✓	

Tab. 1: Attention table which represents the probabilistic model of the machine via the relation between possible hypothesis (problem description) and evidences which can be observed by user.

The mobile robots mentioned above are equipped with standard components such as laser range finders (Hokuyo Lidars), ultrasonic distance sensors (SRFxx), encoders, and motor controllers (RoboClaw), with control software based on the Robot Operating System (ROS) (Vechet et al., 2020).

3. Assistive maintenance

The primary objective of our expert system, named Querix (Vechet and Chen, 2023), is to aid in highlevel maintenance decisions, distinguishing between issues that can be resolved locally and those requiring professional intervention. The further improved solution uses this expert system to identify most probable sources of malfunctions and uses this information to quickly address the possible problem.

Querix operates based on a set of hypotheses and corresponding evidence, utilizing a Bayesian network to model its behavior (Murphy, 2001; Murphy et al., 2001; McGuffin, 2012; Vechet et al., 2016). A limited set of hypothesis and issues was presented in previous work (Vechet and Chen, 2023) and for the reason of limited space we present smaller set of rules condensed into Tab. 1.

Using the hypothesis and evidences outlined in Tab. 1, inference rules are formulated, aiding decisionmaking processes. These rules can be expressed in natural language or in the form of IF-THEN statements (Vechet and Chen, 2023). Tab. 2. provides corresponding conditional probabilities used for decisionmaking.

To compute the probability of possible hypothesis and continue with problem solving the standard Bayes theorem (1) is utilized.

$$P(Hypothesis|Evidences) = \frac{P(Evidences|Hypothesis)P(Hypothesis)}{P(Evidences)} \quad (1)$$

While the conditional probability is common practice in various systems, to naturally get information about the state of the system from knowing some of the evidences about the actual machine status, there is also possibility to use inverse procedure to help the users to identify the possible cause of the system failure from given set of question provided by the system itself. This so called assistive maintenance removes

	$P(Evidence\|Hypothesis)$							
Hypothesis	A - RViz running	B - Map of environment is visible	C2 - Lidar data NOT visible in the map	D - Robot is well localized	D2 - Robot is NOT localized	E - Robots goal properly defined	F2 - Robot is NOT moving	S - Robot rotates in place
D - Lidar (Hokuyo) not connected	0.18	0.18	0.18	0.09	0.09	0.09	0.09	0.09
E - Battery low	0.17	0.08	0.08	0.17	0.17	0.17	0.08	0.08
G - Robot doesn't boot properly	0.20	0.10	0.10	0.10	0.10	0.10	0.20	0.10
A - Encoder not connected	0.11	0.11	0.11	0.11	0.11	0.11	0.11	0.22
F - Problem with RoboClaw	0.11	0.11	0.11	0.11	0.11	0.11	0.22	0.11
B - RoboClaw not connected	0.11	0.11	0.11	0.11	0.11	0.22	0.11	0.11

Tab. 2: Attention table which represents the probabilistic model of the machine via the relation between possible hypothesis (problem description) and evidences which can be observed by user.

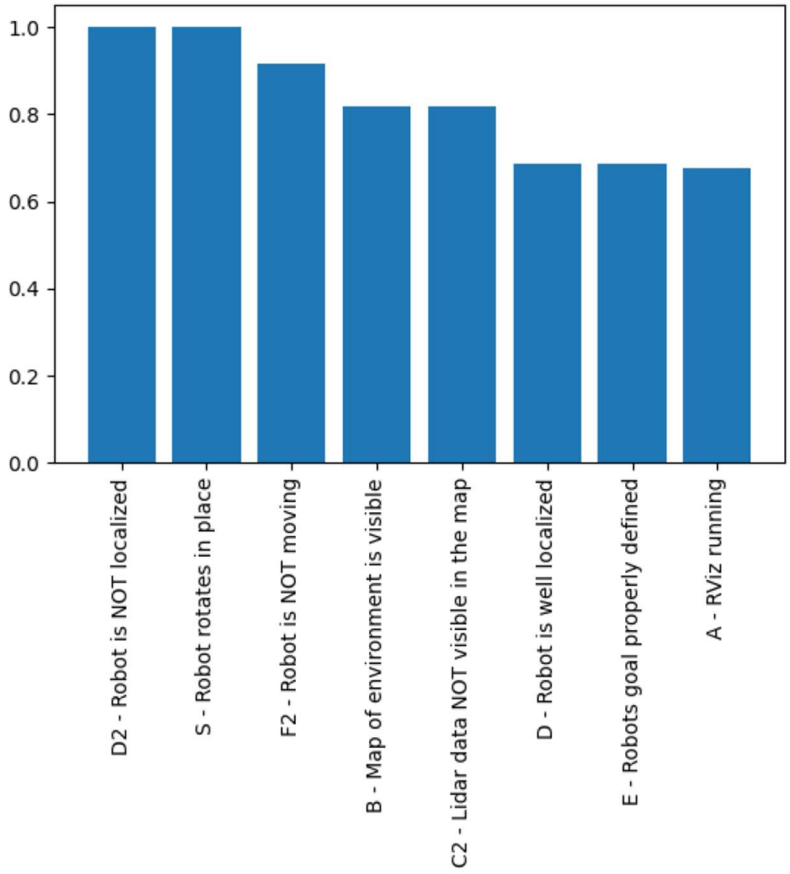

Fig. 1: Most informative evidences calculated for given system of probabilistic rules.

the necessity to call a trained maintenance every-time some problem occurs. To quickly get the right root cause of the systems malfunction the most informative evidences are calculated via Eq. (2). This is the guidance for the expert system what evidence's knowledge leads to the fastest problem identification.

$$mostInformativeFeature = max_{\{i = 1 : m\}} \left[\frac{max_{\{j = 1 : n\}} P(Evidences(j)|Hypothesi\ (i))}{min_{\{j = 1 : n\}} P(Evidences(j)|Hypothesis(i))} \right] \quad (2)$$

The list of most informative evidences is shown in Fig. 1 where the results are normalized to have the value for maximum relevance is 1 and it decreases with the relevance for evidence is less informative. This means that when the user provides answer to the most informative evidences the expert system can quickly find the right solution for given problem.

4. Conclusions

The presented expert system, Querix, addresses the need for advanced diagnostics in industrial machinery within the framework of smart factories under Industry 4.0. By developing an inference engine capable of online monitoring, we offer continuous maintenance support to promptly address failures or provide early warnings. The newly added feature of provide the information about most probable causes of failure wider the potential practical usage.

Acknowledgement

This study was realized with the institutional support RVO: 61388998.

References

Bloecher, K. and Alt, R. (2021) AI and robotics in the European restaurant sector: Assessing potentials for process innovation in a high-contact service industry. *Electronic Markets,* 31(3), pp. 529–551.

Korb, K. B. and Nicholson, A. E. (2004) *Bayesian artificial intelligence*. vol. 1. CRC Press.

Krejsa, J. and Vechet, S. (2018) Fusion of local and global sensory information in mobile robot outdoor localization task. In: *18th International Conference on Mechatronics - Mechatronika (ME)*, pp. 296–300.

McGuffin, M. J. (2012) Simple algorithms for network visualization: A tutorial. *Tsinghua Science and Technology,* 17(4), pp. 383–398.

Murphy, K. (2001) An introduction to graphical models. *Rap. tech,* 96, pp. 1–19.

Murphy, K. et al. (2001) The bayes net toolbox for matlab. *Computing Science and Statistics,* 33(2), pp. 1024–1034.

Thrun, S., Burgard, W. and Fox, D. (2005). *Probabilistic robotics.* MIT Press.

Valerio de Moraes, C. H., Scolimoski, J., Lambert-Torres, G., Santini, M., Alves Dias, A. L., Guerra, F. A., Pedretti, A. and Ramos, M. P. (2022) Robotic process automation and machine learning: a systematic review. *Brazilian Archives of Biology and Technology,* 65.

Vechet, S. and Chen, K. S. (2023) The design of bayesian diagnostic expert system querix and it's engineering application. In: *29th International Conference on Engineering Mechanics*, Milovy, Czech Republic, pp. 259–262.

Vechet, S. (2011) The rule based path planner for autonomous mobile robot. In: *17th International Conference on Soft Computing – MENDEL 2011*, pp. 546–551. B&R Automat CZ Ltd; Humusoft Ltd; AutoCont CZ Ltd.

Vechet, S., Hrbacek, J. and Krejsa, J. (2016) Environmental data analysis for learning behavioral patterns in smart homes. *In: 17th International Conference on Mechatronics - Mechatronika (ME)*, pp. 386–391.

Vechet, S., Krejsa, J. and Chen, K. S. (2020) AGVs mission control support in smart factories by decision networks. In: *19th International Conference on Mechatronics - Mechatronika (ME)*, pp. 1–4.

Zhang, C. A. (2019) Intelligent process automation in audit. *Journal of Emerging Technologies in Accounting,* 16(2), pp. 69–88.

30th International Conference
ENGINEERING MECHANICS 2024
Milovy, Czech Republic, May 14 – 16, 2024

APPARENT YOUNG'S MODULUS OF HUMAN CRANIAL CANCELLOUS BONE

Votava T.[*], Marcián P.[**], Borák L.[***], Fuis V.[†], Zikmund T.[††], Kaiser J.[†††], Wolff J.[‡]

Abstract: *This study investigates the biomechanical behavior of cancellous bone in the os occipitale through finite element modeling. Utilizing micro-computed tomography scans, 47 bone segments were analyzed, and their apparent Young's moduli of each segment were determined in three orthogonal directions. The results revealed strong directional dependencies of Young's modulus on bone volume fractions. In contrast, non-directional dependency exhibited a weaker correlation, indicating an orthotropic elasticity. The derived correlation equations offer an efficient means to describe cancellous bone in cranial biomechanical simulations, especially when a detailed trabecular representation is impractical.*

Keywords: Mechanical properties, skull, cancellous bone tissue, FEM.

1. Introduction

In cases of head injury or disease, irreversible damage to bone tissue can occur. In such circumstances, it becomes necessary to replace the missing bone tissue with a reconstruction plate, which is then secured to the surrounding bone using fixation screws. Biomechanical assessment of the reconstruction plate and fixation screws can be accomplished through computational modelling, often employing the finite element method (FEM) (Marcián et al., 2019). For FEM solutions, understanding the mechanical properties of cranial bone tissue is essential. Currently, when considering the mechanical interaction of a reconstruction plate or fixation screw with cranial bone tissue, cancellous bone tissue is typically modeled as a homogeneous continuum. While it's feasible to create computational models with a more precise representation of cancellous bone trabeculae at the micro level using micro-computed tomography (μCT) imaging, this approach is time-consuming. Utilizing a homogeneous model with a constant apparent Young's modulus serves as a practical compromise, providing satisfactory results. The objective of this study is to establish the correlation between the apparent Young's modulus of the skull's cancellous bone tissue and the bone volume fraction (referred to as BV/TV) through computational modelling.

[*] Ing. Tomáš Votava, Dis.: Institute of Solid Mechanics, Mechatronics and Biomechanics, Brno University of Technology, Technická 2896/2; 616 69, Brno; CZ, 200956@vutbr.cz

[**] Ing. Petr Marcián, PhD.: Institute of Solid Mechanics, Mechatronics and Biomechanics, Brno University of Technology, Technická 2896/2; 616 69, Brno; CZ, macian@fme.vutbr.cz

[***] Ing. Libor Borák, PhD.: Institute of Solid Mechanics, Mechatronics and Biomechanics, Brno University of Technology, Technická 2896/2; 616 69, Brno; CZ, xmborak01@vutbr.cz

[†] Assoc. Prof. Vladimír Fuis, PhD.: Centre of Mechatronics – Institute of Thermomechanics of the Czech Academy of Sciences – branch Brno and Faculty of Mechanical Engineering, Brno University of Technology, Technická 2896/2; 616 69, Brno; CZ, fuis@fme.vutbr.cz

[††] Assoc. prof. Tomáš Zikmund, PhD.: Central European Institute of Technology, Brno University of Technology, Kolejní 2906/4; 61 200, Brno; CZ, tomas.zikmund@ceitec.vutbr.cz

[†††] Prof. Jozef Kaiser, PhD.: Central European Institute of Technology, Brno University of Technology, Kolejní 2906/4; 61 200, Brno; CZ, jozef.kaiser@ceitec.vutbr.cz

[‡] Prof. Jan Wolff, PhD.: Department of Dentistry and Oral Health, Aarhus University, Aarhus, Denmark, Vennelyst Boulevard 9; DK-8000 Aarhus C, DK, jan.wolff@dent.au.dk

doi: 10.21495/em2024-314

2. Methods

The correlation between the Young's modulus of cancellous bone tissue in the skull and the bone volume fraction (BV/TV) can be established by conducting computational tension/compression tests on a series of bone segments. Through these tests, the apparent moduli for each segment are calculated and then correlated with the corresponding BV/TV value (Fleps et al., 2020). Models created for this purpose utilize trabecular structure data acquired from micro-CT scans.

2.1. Model of Geometry

In this study the *os occipitale* of a human skull was cut into 5 block segments (Fig. 1) using surgical saw. Initially, these segments were measured using a micro-computed tomography scanner (GE phoenix v|tome|x L240, GE Sensing & Inspection Technologies GmbH, Wunstorf, Germany) with a voxel size of 25 µm × 25 µm × 25 µm. Subsequently, image processing and thresholding methods were applied to digitize data, capturing the detailed geometry of each segment, including trabecular structures. For the image processing, the STL Model Creator application proposed by Marcián et al. (2011) and scripted in Matlab software (Matlab 2012, MathWorks, USA) was employed. Five block segments were discretized into 47 segments with dimensions of 7.2 mm x 6.75 mm x 3.6 mm (Fig. 1), geometry of each segment was then discretized to generate computational models in Ansys software (ANSYS Academic Research Mechanical, Release 17.2; Swanson Analysis Systems Inc). Based on the digitized data, the BV/TV value was calculated for each segment.

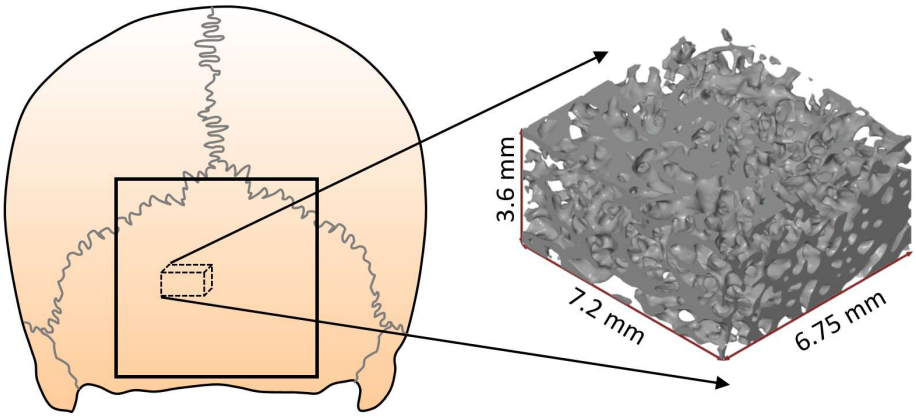

Fig. 1: a) Solved area on the cranial bone - os occipitale; b) micro structure of cancellous bone tissue.

Each segment consisted exclusively of cancellous bone tissue (i.e. no cortical bone was included). Due to limitations in image processing, certain trabeculae within the modeled segments appeared disconnected from the remaining cancellous bone tissue. These small isolated parts were removed and not considered in subsequent calculations or in the measurements of bone volume fraction. For discretization tetrahedron quadratic element was used, each segment was discretized into approximately 1 200 000 elements. The approximate number of nodes was 2 500 000 for each segment.

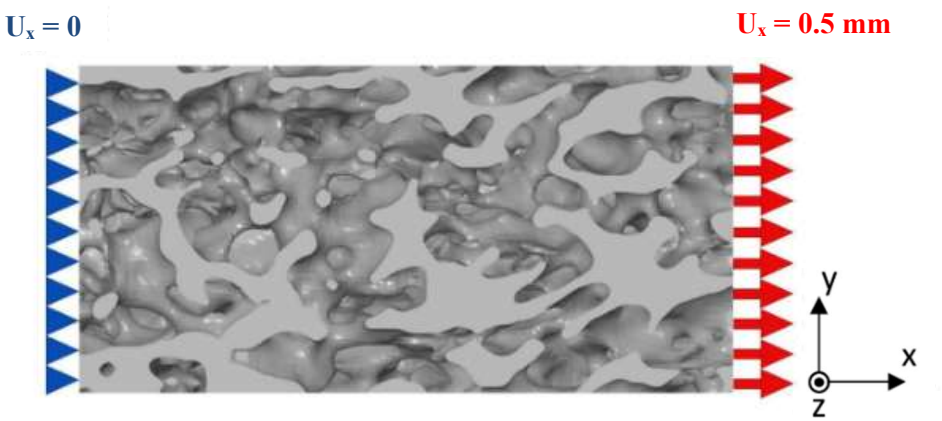

Fig. 2: Boundary and load conditions (Note: Conditions only for the tensile test in X-direction is shown. Conditions for the tests in Y- and Z-directions are analogous.).

2.2. Boundary conditions

To simulate a tensile test, each segment was subjected to loading in three directions parallel to the coordinate axes shown in Fig. 2 (Ševeček et al., 2019). The load was displacement-driven; specifically, one side of the segment was elongated in a particular direction by 0.5 mm while the other side was fixed in the same direction (u = 0 mm) as shown in Fig. 2.

2.3. Material model

In this study, trabeculae in the cancellous bone tissue were modeled as a homogeneous, isotropic, linear-elastic material represented by two material parameters: Young modulus (E) and Poisson ratio (μ). The applied values are $E = 15\ GPa$ (Rho, 1993) and $\mu = 0.3\ [-]$.

2.4. Determination of apparent Young's modulus

The apparent Young's modulus of cancellous bone represents its effective stiffness. It is determined by applying Hooke's law, considering a homogeneous distribution of the bone tissue within the bone volume:

$$\sigma = E \cdot \epsilon \Rightarrow E = \frac{F \cdot l}{S \cdot u}, \tag{1}$$

where F is the normal force acting in the volume in the loaded direction (calculated as a resultant reaction force in constraints in the FE model), l is the length of the segment in the loaded direction, S is the area of the cross section parallel to the loaded direction and u is the given displacement.

Apparent Young's moduli for all segments in all three directions are presented in Fig. 3 (blue symbols). Using the least square method, four relationships in a commonly-used power form $E = b + c \cdot (BV/TV)^d$ were determined; specifically, three sets of constants b, c and d were calculated to derive three direction-dependent equations (Eqs. (2) through (4)), along with one set of constants for a non-directional dependency (5). For each relationship, coefficient of determination R^2 was calculated. The relationships are visualized in Fig. 3 as well. Data are available at the link: 10.5281/zenodo.10635546.

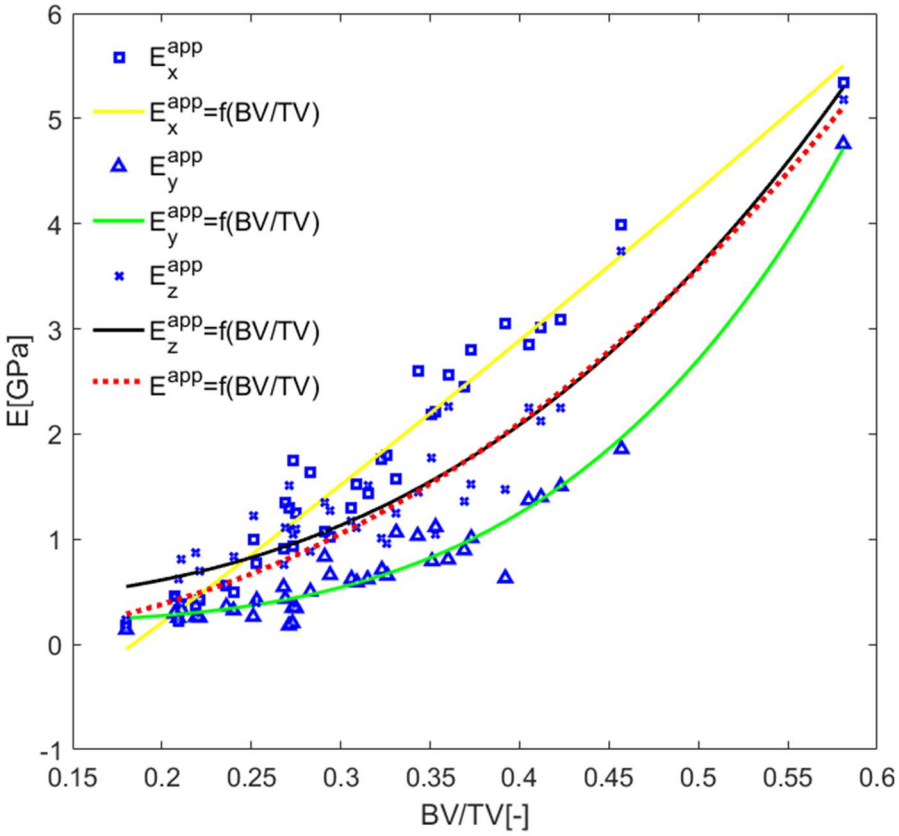

Fig. 3: Relationship between apparent Young's modulus and BV/TV.

$$\mathrm{E}_{\mathrm{x}}^{\mathrm{app}} = 13.98 \cdot \left(\frac{\mathrm{BV}}{\mathrm{TV}}\right)^{1.14} - 2.02\,[\mathrm{GPa}];\ R^2 = 0.95 \quad (2)$$

$$E_y^{app} = 37.86 \cdot \left(\frac{BV}{TV}\right)^{3.92} - 0.20\,[GPa];\ R^2 = 0.96 \quad (3)$$

$$E_z^{app} = 22.81 \cdot \left(\frac{BV}{TV}\right)^{2.82} - 0.37\,[GPa];\ R^2 = 0.87 \quad (4)$$

$$E^{app} = 18.41 \cdot \left(\frac{BV}{TV}\right)^{2.35} - 0.04[GPa];R^2 = 0.68 \quad (5)$$

While substituting BV/TV values near zero into Eqs. (2) through (5) would produce negative Young's moduli, practical calculations necessitate constraining the validity of these equations. Thus, realistic values of Young's modulus can be obtained by applying the equations only within the BV/TV range of *(0.18; 0.58)*.

3. Conclusions

Strong correlations ($R^2 > 0.85$) were observed between the apparent moduli in each direction and BV/TV. When Eqs. (2) through (5) are compared to the similar study published by van Ruijven et al. (2003), a similar slope can be observed. If same Young's modulus is substituted into dependencies published by van Ruijven, comparable values of apparent Young's modulus will be returned. On the contrary, non-directional dependency showed a much weaker correlation, indicating an orthotropic elasticity of cancellous bone in the *os occipitale*. The derived equations can effectively describe trabecular structure in biomechanical simulations of cranial bone using the FEM, especially when a more detailed trabecular finite element representation is impractical due to its time-consuming nature.

The derived equations hold significant clinical implications. They can steer optimal implant design and placement in the cranial region, underscore the importance of considering orthotropic elasticity in surgical planning, and present a time-efficient approach for biomechanical simulations in clinical research. In emergency cases, these equations offer a practical and prompt means of assessing cancellous bone properties, assisting clinicians in making informed decisions swiftly.

Acknowledgement

This publication was supported by the project "Mechanical Engineering of Biological and Bio-inspired Systems", funded as project No. CZ.02.01.01/00/22_008/0004634 by Programme Johannes Amos Commenius, call Excellent Research. The research was supported by the specific research FSI-S-23-8240 and institutional support RVO: 61388998.

References

Marcián, P., Konečný, O., Borák, L., Valášek, J., Řehák, K., Krpalek, D. and Florian, Z. (2011) On the Level of Computational Models in Biomechanics Depending on Gained Data from Ct/Mri and Micro-Ct. In: *MENDEL 2011 - 17th Int. Conf. on Soft Computing*, Brno University of Technology, Brno, pp. 255–267.

Marcián, P., Narra, N., Borák, L., Chamrad, J. and Wolff, J. (2019) Biomechanical performance of cranial implants with different thicknesses and material properties: A finite element study. *Computers in Biology and Medicine*, 109, pp. 43–52.

Ingmar, F., Hassan B., Philippe K. Z., Stephen J. F., Halldór P. and Benedikt H. (2020) Empirical relationships between bone density and ultimate strength: A literature review. *Journal of the Mechanical Behavior of Biomedical Materials*, 110.

van Ruijven, L. J., Giesen, E. B. W., Farella, M. and van Eijden T. G. M. J. (2003) Prediction of Mechanical Properties of the Cancellous Bone of the Mandibular Condyle. *Journal of Dental Research*, 82, 10, pp. 819–823.

Ševeček, O., Bertolla, L., Chlup, Z., Řehořek, L., Majer, Z., Marcián, P. and Kotoul, M. (2019) Modelling of cracking of the ceramic foam specimen with a central notch under the tensile load, *Theoretical and Applied Fracture Mechanics*, vol. 100, pp. 242–250.

Rho, J. Y., Ashman, R. B. and Turner, C. H. (1993) Young's modulus of trabecular and cortical bone material: Ultrasonic and microtensile measurements. *Journal of Biomechanics*, 26, 2, pp. 111–119.

30th International Conference
ENGINEERING MECHANICS 2024
Milovy, Czech Republic, May 14 – 16, 2024

PREFABRICATED SYSTEM FOR STRENGTHENING FULL-SIZE WOODEN GIRDERS USING PRE-STRESSED FIBER-REINFORCED POLYMERS AND STEEL – BENDING SHEAR TESTS

Wdowiak-Postulak A.*, Świt G., Krampikowska A.*****

Abstract: *This paper describes a study of four-point bending with shear of full-size KG and KS grade glulam beams using glued-in pre-stressed basalt BFRP, glass GFRP and steel rods. From the tests, it was found that the composite bars as well as the glass bars perfectly compensated for the heterogeneous structure of the timber, showing significant ductility in contrast to the brittle fracture of unreinforced beams, the same applies to the shear area in the support zones and on the supports. Using pre-stressed composite bars and pre-stressed steel bars in tension and compression, the following results were obtained: an increase in load capacity and stiffness, respectively steel bars - 39.2 %, 20.2 %; basalt bars - 35.4 %, 19.4 %; glass bars - 32.7 %, 17.2 % compared to unreinforced beams, also influenced by the distance from the neutral axis. The use of composite and steel bars is an effective, economical, environmentally friendly, ecological and natural technology for the repair of elements, as well as the possibility of increasing the span of the girders and reducing their cross-sections, which gives an increase in the possibility of using wood-based products with other materials, including natural materials - fibre-reinforced polymers - for structural elements.*

Keywords: Glued Laminated Timber, FRP and steel bars, pre-stressed, bending with shear test, load capacity, local and global stiffness.

1. Introduction

Wood is the few natural renewable raw materials that can be used as structural elements in construction. And, in addition, wood provides an attractive natural appearance and a high strength-to-weight ratio compared to traditional building materials such as concrete or structural steel (Corradi et al., 2021; Jian et al., 2022). Thus, by enhancing the natural limitations of wood, engineered timber products offer a sustainable alternative to traditional building materials. These products include: solid beams, I-beams, Glued Laminated Timber or Cross Laminated Timber (CLT) - e.g. beams, slabs, and Laminated Veener Lumber (LVL), as well as other materials made of glued veneers or other wood-based materials, e.g. plywood, Parallel Strand Lumber, Laminated Strand Lumber, construction beech wood (BauBuche) - experimental, theoretical and numerical research carried out by the author on these products under static, dynamic, ad hoc, repeatedly variable, cyclic, long-term loads reinforced by various artificial and natural fibers, fiber composites, Fiber Reinforced Polymer, polyester, hybrid, steel, in various shapes and forms, under pressure and pre-stressed, in addition fire, temperature and humidity resistance, among others bars, pipes, different profiles, angles, C-sections, I-sections, T-sections, T-bars, fasteners, shapes, sheets, fabrics, tapes, mats, sandwich structures - bending, shear, bending with shear, tension, compression. Therefore, the recent growth of mass timber construction is mainly due to the popularity of CLT applications or advanced manufacturing technologies for large-scale glulam structural elements. In contrast, the use of timber

* Agnieszka Wdowiak-Postulak, PhD.: Faculty of Civil Engineering and Architecture, Kielce University of Technology, al. Tysiąclecia Państwa Polskiego 7, 25-314 Kielce; Poland, awdowiak@tu.kielce.pl; awdowiak@tu.kielce.pl

** Prof. Grzegorz Świt, PhD.: Faculty of Civil Engineering and Architecture, Kielce University of Technology, al. Tysiąclecia Państwa Polskiego 7, 25-314 Kielce; Poland, gswit@tu.kielce.pl

*** Aleksandra Krampikowska, DSc.: Faculty of Civil Engineering and Architecture, Kielce University of Technology, al. Tysiąclecia Państwa Polskiego 7, 25-314 Kielce; Poland, akramp@tu.kielce.pl

doi: 10.21495/em2024-318

reinforcement is often used to increase the structural strength of major elements, e.g. beams, columns. The use of FRP reinforcement is a convenient, economical method of improving the static performance of a structure (Jian et al., 2022; Bi et al., 2021 and Sun, 2022). This application can improve the load-bearing capacity, just as it improves the operational safety of the structure and meets higher performance requirements. Considering fibre-reinforced polymers is a component formed by mixing a fibre material and a matrix material (resin) in a specific proportion. The benefits of such materials include lightness, non-conductivity, high mechanical strength, recyclability and improved corrosion resistance. Therefore, over time FRP can partially replace steel bars for the reinforcement of timber beams. Using FRP reinforcement can increase the ultimate load-bearing capacity and flexural stiffness of timber beams. There are different types of FRP on the market, such as CFRP (carbon fibre reinforced polymer), GFRP (glass fibre reinforced polymer), AFRP (aramid fibre reinforced polymer), BFRP (basalt fibre reinforced polymer), etc. The use of FRP reinforcing bars prevents the risk of possible corrosion, as with steel bars. In the same way, they can improve the stiffness, load-bearing capacity and ductility of timber beams. Based on studies (Wdowiak-Postulak, 2019; Wdowiak-Postulak, 2021; Wdowiak-Postulak, 2023; Wdowiak-Postulak et al., 2023a; Wdowiak-Postulak et al., 2023b; Wdowiak-Postulak et al., 2023c and Wdowiak-Postulak et al., 2024), it was found that the decisive factors affecting the effectiveness of FRP-reinforced timber beams are the degree of reinforcement, the type of FRP, the length of the beams, the grain direction or the bonding surface (Jian et al., 2022). Liu et al. (Liu et al., 2020) performed an experimental study of BFRP-reinforced poplar beams with different lengths. Based on the study, they found that timber beams reinforced with BFRP bars of 1900 × 50 mm showed the highest load capacity and maximum deflection, which increased by 77.8 % and 110.1 %, respectively, compared to unreinforced beams. Kramár et al. (2020) investigated the effect of using corrugated surfaces on improving adhesion between FRP and wood. Based on the experimental study, they found that beams with CFRP corrugated surfaces had the highest flexural strength, here the adhesion between FRP and the corrugated wood surface helped.

2. Methods

Wood of pine, spruce and fir was used in the study. Specifically, the timber used in the study was from the same sawmill, with the designation of origin coming from the Małopolska Region Nature and Forest of Poland and from the beginning and end of the growing season, at the full moon, thus reducing variability. The glued laminated beams had a GL20c grade, tensile strength of 15 MPa, modulus of elasticity of 10 400 MPa (outer laths T13 and inner laths T8) according to PN-EN 14080:2013-07. The structural lumber was previously dried artificially in a drying kiln, then classified according to PN-D-94021:2013-10 into KG grades - inferior quality grade and KS grades - medium quality grade. In the laboratory, the resulting glued laminated beams, pieces of 20 with dimensions 82 x 162 x 3650 mm, were stored with a relative humidity of 65 ± 5 % and a temperature of 20 ± 2 °C. The moisture content was tested in accordance with EN 13183-1:2004 and an average moisture content of 10.7 % with a standard deviation of 0.89 % was obtained, the average density was 359.5 kg/m^3 with a standard deviation of 25.4 kg/m^3. The influence of humidity and temperature was constantly determined and their parameters were determined. An epoxy resin-based adhesive layer was obtained by mixing LG 815 epoxy resin with HG 353 hardener. After mixing the resin and hardener, the adhesive achieved a flexural strength of 110–120 MPa and an elastic modulus of 2 700 ÷ 3 300 MPa. For the reinforcement, first 14 mm by 14 mm holes were cut in the beams, then the wood and bars were cleaned. Similarly, to obtain the straightness of the rod in the cut holes and milling cutters, thin steel nails and steel wires were inserted every 40 centimeters. And at the ends of the beam to properly anchor and fasten the bars, pre-stressed, by threading the rods at the ends, then applied appropriate anchoring plates, nuts, steel and aluminum profiles, steel sheets, plexiglass, pads, connectors were introduced, the nuts were screwed in, obtaining the reverse arrow, to obtain an initial stress of 15 MPa - measured by extensometer. Moreover to prevent shearing occurring along the beam at supports and in support zones – applied appropriate vertical FRP and steel rods for the entire height of the beam, anchors. Then pre-stressed basalt BFRP, glass GFRP, and steel rods with a diameter of 10 mm were used for reinforcement. Material data were obtained from in-house, experimental studies: BFRP - elastic modulus 79.2 MPa, GFRP - elastic modulus 60.1 MPa, steel - ribbed, B500SP. The experimental investigations included the effects of reinforcement on the load-carrying capacity and static working stiffness of reinforced glued beams compared to unreinforced beams. The beam configurations are shown in Fig. 1 and the test scheme is shown in Fig. 2. Five repetitions were tested for each configuration for better statistics of the results. Reinforcement included a tensile zone as well as a compressive zone with identical degrees of reinforcement. Experimental tests of glued beams were carried out in four-point

bending with shear according to EN 408+A1:2012. First, all unreinforced beams were tested by determining the global and local stiffness, using two actuators with a piston area of 50 cm^2 and a maximum exerted pressure of 10 MPa from VEB Werkstoffprufmaschinen Leipzig. The local stiffness measurement is suspended from the neutral axis over a length of five times the beam height. Local indentations were minimised by placing 80 mm × 80 mm × 5 mm steel plates at the support and actuator locations. Load did not exceed the elastic limit or exceed 40 % of the ultimate load - only to local rigidity. The modulus of formability was also determined. On the basis of the shear zone - strains, shear stresses, the modulus of shear deformation was also determined.

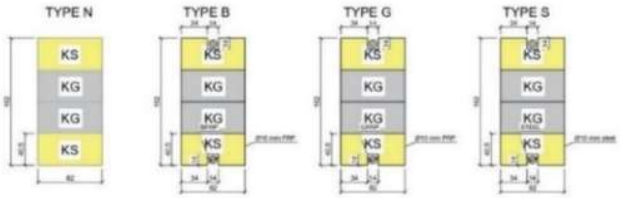

Fig. 1: Beam reinforcement diagrams.

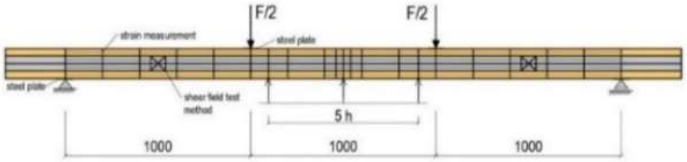

Fig. 2: Four-point bending with shear test stand.

3. Results

The load-deflection ratio as noted in the figure for the failure of unreinforced beams showed in a linearly elastic manner up to the point of failure (Fig. 3). The beams mostly failed in the lower layers in the tension zone due to timber defects. The compression and tension reinforcement resulted in the neutral axis being placed approximately mid-height due to the balanced reinforcement layout adopted. Longitudinal shear cracks of the fibers often appeared in the zones adjacent to the actuator and on the supports. Pre-stressed basalt, glass, steel bars placed in the tensile and compression zones reduced the knot area ratio in the top and bottom layers and thus reduces the likelihood of ductility. Therefore, it can be seen that the ultimate tensile strength of the wood is usually reached in the lower layer, as long as the ultimate compressive strength occurs in the upper layer. A mean global stiffness of 3.95×10^{11} $N.mm^2$ with a standard deviation of 0.23×10^{11} $N.mm^2$ and a mean local stiffness of 4.34×10^{11} $N.mm^2$ with a standard deviation of 0.35×10^{11} $N.mm^2$ were obtained.

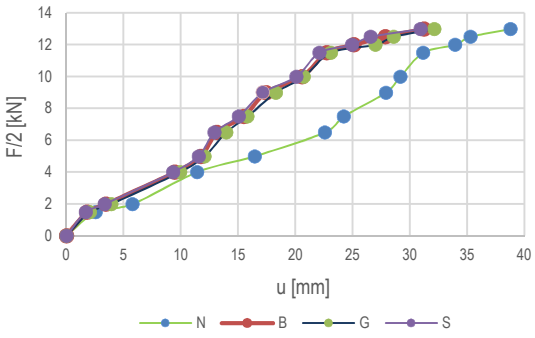

Fig. 3: Load-deflection diagram for all beams at mid-span.

4. Conclusions

On the basis of experimental investigations of the bending reinforcement of low-quality laminated glulam using pre-stressed basalt, glass and steel glued-in rods, the following conclusions were obtained:

- Unreinforced glued laminated beams tended to fail in the tension zone and worked in the linear-elastic range, brittle fracture occurred. Compared to reinforced beams, where in the tension and compression zones, the neutral axis was usually at mid-height of the height of the beams and

shear also occurred. Shear was most common along the beam, shear in the support zones outside the loads and at the supports, especially with pre-stressed steel reinforcement, pre-stressed basalt reinforcement, less so in pre-stressed glass reinforcement. Pre-stressed bars increased shear strength through compressive stresses developed in the beam.

- Noticeable non-linear work is exhibited by beams consisting of lamellas of lower quality classes of structural lumber.
- The use of reinforcement equally distributed in the tension and compression zones resulted in an increase in load capacity and stiffness, respectively: pre-stressed steel bars - 39.2 %, 20.2 %; pre-stressed basalt bars - 35.4 %, 19.4 %; pre-stressed glass bars - 32.7 %, 17.2 % compared to unreinforced beams.

Funding: Fee for conference materials from - Kielce University of Technology 02.0.18.00/1.02.001 SUBB.BKWK.24.002.

Acknowledgement

Many thanks for the research materials: TATRAN 3R Sp. z o. o., Orlitech Composite systems, Trokotex Polymer Group Sp. zoo., Epstal, CENTROSTAL S.A., POLPREK Sp. z o.o., GRM Systems sp. z o.o., New Composite Solutions Sp. z o.o., TECH SOLUTIONS, FIBER-PLAST Manufacturer of pultrusion profiles, Tartak „Olczyk" Sp. z o. o., Kronospan Polska Sp. z o.o., Konsbud KONSTRUKCYJNE DREWNO KLEJONE.

References

Bi, W., Li, H., Hui, D., Gaff, M. and Lorenzo, R. (2021) Effects of chemical modification and nanotechnology on wood properties. *Nanotechnology Reviews*, 10(1), 978–1008.

Corradi, M., Mouli, V. C., Edmondson, V., Poologanathan, K. and Nagaratnam, B. (2021) Local FRP reinforcement of existing timber beams. *Composite Structures*, 258, 113363.

Jian, B., Cheng, K., Li, H., Ashraf, M., Zheng, X., Dauletbek, A., Hosseini, M., Lorenzo, R., Corbi, I., Corbi, O. and Zhou, K. (2022) A Review on Strengthening of Timber Beams Using Fiber Reinforced Polymers. *Journal of Renewable Materials*, 10(8), pp. 1–26.

Kramár, S., Brabec, M., Pařil, P., Rousek, R. and Král, P. (2020) Constraining delamination of CFRP by beam corrugation. *Engineering Structures*, 207.

Liu, Q., Ma, S. and Han, X. (2020) Study on the flexural behavior of poplar beams externally strengthened by BFRP strips. *Journal of Wood Science*, 66(1).

Sun, H. et al. (2022) Nanotechnology application on bamboo material: A review. *Nanotechnology Reviews*, 11, 1670–1698.

Wdowiak-Postulak, A., Bahleda, F. and Prokop, J. (2023a) An Experimental and Numerical Analysis of Glued Laminated Beams Strengthened by Pre-Stressed Basalt Fibre-Reinforced Polymer Bars. *Materials*, 16(7), 2776.

Wdowiak-Postulak, A., Gocál, J., Bahleda, F. and Prokop, J. (2023b) Load and Deformation Analysis in Experimental and Numerical Studies of Full-Size Wooden Beams Reinforced with Prestressed FRP and Steel Bars. *Appl. Sci.,* 13(24), 13178.

Wdowiak-Postulak, A., Świt, G. and Dziedzic-Jagocka, I. (2024) Application of Composite Bars in Wooden, Full-Scale, Innovative Engineering Products – Experimental and Numerical Study. *Materials*, 17(3), 730.

Wdowiak-Postulak, A., Wieruszewski, M., Bahleda, F., Prokop, J. and Brol, J. (2023c) Fibre-Reinforced Polymers and Steel for the Reinforcement of Wooden Elements – Experimental and Numerical Analysis. *Polymers*, 15(9), 2062, 1–13.

Wdowiak, A. (2019) *Structural and strength properties of bended wooden beams reinforced with fiber composites.* PhD. Thesis, Kielce University of Technology, Kielce, Poland.

Wdowiak-Postulak, A. (2021) Basalt Fibre Reinforcement of Bent Heterogeneous Glued Laminated Beams. *Materials*, 14, 51.

Wdowiak-Postulak, A. (2023) Numerical, theoretical and experimental models of the static performance of timber beams reinforced with steel, basalt and glass pre-stressed bars. *Composite Structures* 305 (2023), 116479.

PN-D-94021:2013-10 (2013) Coniferous construction timber sorted by strength methods; Polish Committee for Standardization: Warsaw. Poland (in Polish).

PN-EN 13183-1:2004 Moisture content of lumber. Part 1: moisture determination using the dryer-weighing method.

PN-EN 14080:2013-07 Wooden structures – Glued laminated wood and structural glued solid wood - Requirements.

PN-EN 408+A1:2012 Timber Structures – Structural Timber and Glued Laminated Timber – Determination of Some Physical and Mechanical Properties. Polish Committee for Standardization: Warsaw. Poland.

30th International Conference
ENGINEERING MECHANICS 2024
Milovy, Czech Republic, May 14 – 16, 2024

CONSTRUCTION OF A MODULAR DEVICE FOR TESTING HIGH-TEMPERATURE FLUE-GAS FOULING IN WASTE-HEAT SOURCES

Zabloudil J.[*], Jegla Z.[**], Daxner J.[**], Babička Fialová D.[**], Freisleben V.[*], Reppich M.[***]

Abstract: *The article discusses the construction aspects of a developed modular device for testing the influence of high-temperature flue-gas fouling on chosen heat exchanger tube-bundle geometries and the effectiveness of various methods of online tube-bundle cleaning, which is currently being developed by the Institute of Process Engineering (IPE) at Brno University of Technology (BUT), in cooperation with the company Eveco Brno. The device will ease designing new heat exchangers, withstanding longer operation in severe fouling conditions.*

Keywords: Fouling, flue gas, testing device, high-temperature application.

1. Introduction

Combustion of various liquid and, in particular, solid fuels entails the problems of entrainment of inert ash, which is introduced into the combustion process as an integral part of the fuel. Part of the fine fraction of this ash, often enriched with solid products of incomplete combustion, is carried off by the flue-gas stream from the combustion space of the boiler onto the convective heat-exchange surfaces. Here, depending on the flow conditions, temperature, chemical composition of the ash, and other factors, a coating can form on the heat-exchange surfaces (Kakac, 1991).

The effect of the flow is mainly manifested by ash setting in areas with a sharply reduced flue-gas flow rate, especially in the areas of inlets and sudden expansions in the casing of tube boilers and on the downstream side of the tube bundles in water-tube boilers.

The effect of temperature is closely related to chemical composition. Different combinations of inert salts and minerals, which are contained in the burned fuel, lead to the somewhat different behaviour of the ash entrained by the flue gas (Niessen, 2010). Each mineral component exhibits a different melting temperature. Therefore, the empirically determined (average) softening and melting temperatures of the ash, or other recognizable intermediate temperatures according to a relevant local standard, depend on the proportional amounts of these individual components in the ash. If the so-called ash-softening temperature is reached, the cohesion of the ash mass increases considerably. At the melting temperature, fly ash passes into a glassy viscous phase. After resolidification, the heat-exchange surface of the exchanger remains covered with a solid crust, increasing the thermal resistance and significantly reducing the device's efficiency (Spalding and Taborek 1983). The ashes of certain fuels exhibit a softening temperature so low that considerable fouling must be expected even at temperatures necessary for the economical operation of the boiler. In particular, during combustion or co-combustion of grass biomass, ash with an ash-softening temperature lower than 700 °C is often found (Niessen, 2010).

[*] Ing. Jan Zabloudil, Ing. Vít Freisleben, PhD.: Eveco Brno, s.r.o.; Hudcova 321/76d; 612 00, Brno; CZ, {zabloudil, freisleben}@evecobrno.cz

[**] Assoc. Prof. Ing. Zdeněk Jegla, PhD., Ing. Ján Daxner, Ing. Dominika Babička Fialová, PhD.: Institute of Process Engineering, Faculty of Mechanical Engineering, Brno University of Technology; Technická 2; 616 69, Brno; CZ, {Zdenek.Jegla, Jan.Daxner, Dominika.Fialova}@vutbr.cz

[***] Prof. Dr.-Ing. Marcus Reppich: Faculty of Mechanical and Process Engineering, Augsburg University of Applied Sciences; An der Hochschule 1; 86161 Augsburg; DE, marcus.reppich@hs-augsburg.de

doi: 10.21495/em2024-322

However, fouling layers can also be created by other processes. In the case of flue-gas heat exchangers, it is possible to encounter ash fractions that tend to form deposits by mainly mechanical binding. Therefore, the variable nature of fouling requires a device that allows engineers to determine the fouling properties of a given flue-gas stream in advance and as precisely as possible so that suitable heat-exchange surfaces can be designed in order to utilize the heat produced. Universal testing devices enabling the determination of the necessary parameters of real flue-gas fouling effects before the final design of an industrial heat exchanger are not currently available. An essential step in designing the heat exchanger is the correct choice of its basic geometric parameters. In the case of applications operated in fouling conditions, however, it is usually unknown which specific geometry will be resistant to fouling and which will perform rather badly. And eventually, what choice of online cleaning technology would offer sufficiently prolonged operation time without necessitating downtime.

The developed modular mobile device (see Fig. 1) aims to prevent operational problems of the newly designed heat exchangers through a better design with higher resistance to fouling and, hence, higher reliability. Thanks to its mobility and modularity, laboratory and industrial experiments can be performed. Consequently, its high potential also lies in the ongoing research at BUT in the field of industrial fouling.

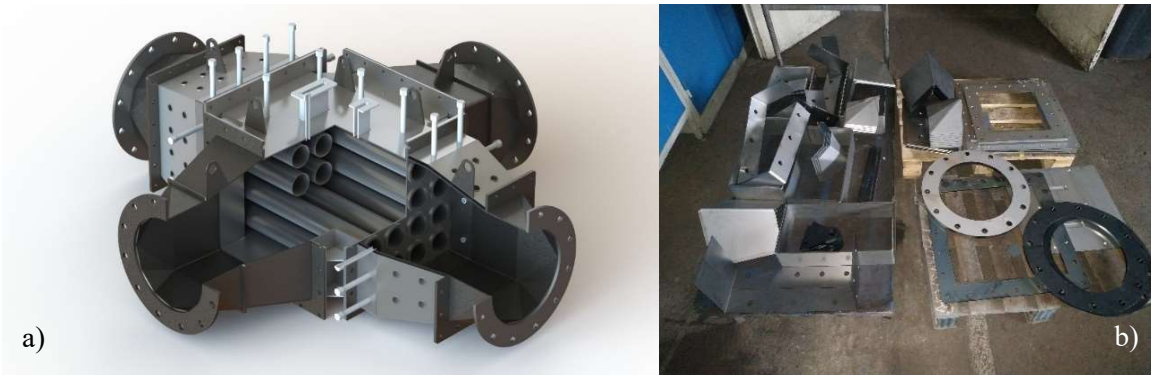

Fig. 1: a) Partial section of the final design of the developed device, b) cut and folded metal sheets of the device prepared for welding.

2. Construction of the high-temperature modular device

The developed construction of the mobile testing system, presented in Fig. 1, is conceptually designed as a modular crossflow flue-gas/air tube exchanger. During its design, the following was emphasized:

1. The closest possible approximation of the geometry parameters of the device's tube bundle to a typical geometry of an industrial flue-gas heat exchanger.
2. Capacity enabling both laboratory tests and tests under industrial conditions.
3. Temperature resistance to withstand high temperatures on the flue gas side up to 800 °C.
4. Modular variability of the tube-bundle geometry and the ability to operate with flue gas both on the tube and shell sides.
5. The device is equipped with welded sockets enabling tests of different tube-bundle cleaning methods, endoscope access for deposit analyses and measurement devices' access for data acquisition.
6. Possibility of easy transport of equipment between laboratory and industrial plants and easy assembly/disassembly

Fulfilment of the above requirements is ensured in the following way:

The device's basic, primarily tested tube bundle contains 16 smooth pipes DN65 (ø 76.1 mm) in a 4 × 4 inline configuration set within a tube sheet with an axial spacing of 98 mm. The tubes' nominal size and spacing correspond to the design of an industrial device rather than a laboratory model. This leads to better approximation of real conditions and eliminates errors introduced by simplifying assumptions (e.g., using characteristic numbers when extrapolating the obtained data to real operation). At the same time, it is thus possible to insert the apparatus into a flue-gas bypass of a real industrial application (for measurements 'in the field') in addition to the laboratory testing.

The 4×4 configuration also determines the size of the device, which can still be supplied with flue gases during laboratory tests, using burners already available in the IPE burner testing facility, but also by sampling from any existing industrial flue pipe with the help of a specially designed ejector (jet pump). Such configuration grants 4 tubes in the bundle that are 'central', i.e., the flow around their perimeter is affected only by the surrounding tubes, not the edge effects of the heat-exchanger shell. It will be possible to observe the formation of the deposit layers and the influence of their removal methods with the greatest possible informative value.

The device is designed as modular; therefore, it can be equipped with staggered configurations, smaller nominal diameters, and other tube-bundle modifications, which expands the usability and applicability in various testing scenarios. Although most industrial applications operate at flue-gas temperatures lower than 800 °C, such a high temperature is considered mainly due to the possibility of using equipment for fouling testing even under such extreme conditions. Operability at high temperatures is mainly ensured by the combination of factors listed in Tab. 1.

Concept as a heat exchanger	The fouling tester itself is designed as a flue-gas/air heat exchanger, which enables the cooling of the device by the airflow. An air fan increases the volumetric flow rate and sufficient turbulence of air for intensive heat transfer. The fan can be removed during tests on low-potential flue gases or tests on 'polluted air' (ash carried by the air current), and the device thus can be operated as a non-cooled static obstacle to the flow. In the case of air cooling, the air-stream temperature will be measured at the inlet and outlet.
Materials	All parts of the device, which can be exposed to high temperatures on the flue-gas side, are made of heat-resistant steels of grades 1.4841 and 1.4845. This solution aims to prevent the formation of scalings and other oxidative damage at elevated temperatures. The selection of materials is based on the criteria of a design temperature of 800 °C.
Additional water-cooling	Flue-gas inlet modules are designed as an analogue to a water-cooled jacketed vessel. In the case of operation at temperatures close to the maximum design temperature, cooling water will be introduced into the empty volume between the inner and outer shell. This water will then be diverted into a cooler or a waste sump.
Thermal insulation	This measure is not intended to protect the device but the operators. When operating at high temperatures, the device is coated with an insulating layer designed to maintain the external temperature at the maximum admitted by EN ISO 13732-1 for touchable surfaces.

Tab. 1: High-temperature heat protection concept.

As for the additional water cooling, the flow will be distributed into several inlet sockets on the lower side of each jacketed flue-gas intake/outlet and collected again by hoses connected to several ports on the opposite side. This technical solution leads to a better fluid-flow distribution within the inter-shell space. Each of the distribution sockets in the jacketed inlets is equipped with a ball valve for rough flow regulation, and each module is equipped with a safety valve, preventing an increase of pressure in the inter-shell space in the event of local overheating and boiling of the cooling water. Cooling water temperature and pressure will be monitored. Both the inter-shell space clearance and the dimensions of welded sockets enabling cooling water feed are designed to accommodate the heat output without raising the cooling water temperature by more than 20 K.

The device consists of 6 main modules that might be removed and reattached at any convenience:

- 1× central cross module – the tube-bundle casing and the device's main part;
- 1× tube bundle with two tube sheets – may be replaced with a bundle of any required geometry;
- 2× cooled inlet with double shell (jacketed) – for the hot side of the heat exchanger;
- 2× non-cooled inlet – for the cold side of the heat exchanger.

The central cross module and individual inlets are equipped with identical square flanges with M12 bolt connections. The flange joints are additionally secured with a sealing cord that is resistant to high temperatures.

The tube sheets carrying the tube bundle are designed as intermediate flanges. They can be placed between the central cross module and the cooled jacketed inlet, as well as between the central cross module and the air-cooling inlet. This solution makes it possible to achieve flue-gas flow inside the tubes and on the shell side simply by changing the assembly configuration.

The connection of the device with an existing flue-gas pipe and additional cooling and driving streams is

depicted in Fig. 2 below. In the case of laboratory experiments, the assembly may be equipped with a particulate source (as a substitute for fouling flue gas) and a fabric filter.

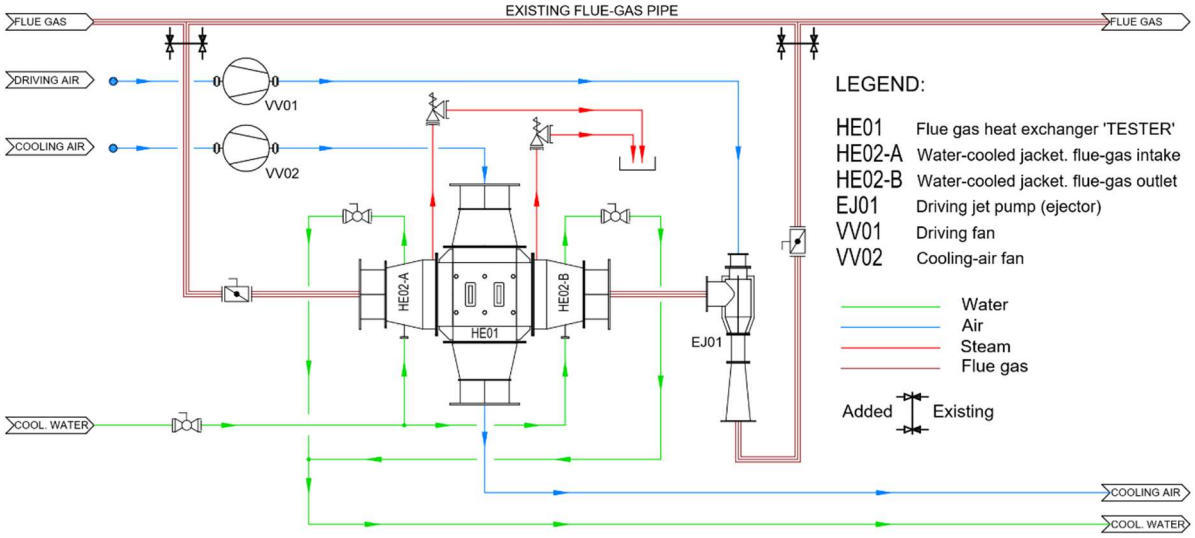

Fig. 2: Simplified operational diagram of the device when connected to an existing flue-gas pipe.

The device has a sufficient number of welded sockets with a plug, distributed on the device in such a way that it is possible to place nozzles for spraying the inner space of the tubes, as well as the space between the tubes, with a stream of compressed air, steam, or water – simulating common on-line fouling-deposit removal methods.

The modules need to be easily transported between the place of industrial application, laboratory, and storage room in the time between individual tests. The size of the assembled device is thus, to some extent, derived from the need for repeated assembly and transport. The body of the apparatus will be placed on a folding frame, which can be secured onto the bed of a truck. The individual modules of the device are equipped with load-bearing eyes, so in addition to manual assembly, it is possible to use a lifting device that will be placed upon the structure of the load-bearing frame.

3. Conclusion

The currently developed construction of the high-temperature flue-gas testing device discussed in this article is supposed to allow the BUT researchers and the private-sector engineers of the company Eveco Brno to determine the real fouling effects of a given flue-gas stream on a chosen heat-exchanger geometry, without the necessity of building a whole new heat exchanger for the initial test or depending overly on the tabular values of the fouling factors with limited accuracy. Compared with commonly used methods, it should offer a wider and more reliable data set to design more economical solutions, withstanding longer maintenance-free operation periods in severe fouling conditions. No comparable testing device is currently available, nor the authors are aware of any other such device being developed.

Acknowledgement

The authors gratefully acknowledge the financial support provided by the Technology Agency of the Czech Republic within the research project No. TK05020076 'Development of a mobile tester for safe and reliable heat recovery from fouling flue gases and an ammonia generator for their cleaning', GA BUT within the research project No. FSI-S-23-8173, and the EU project 'Strategic Partnership for Environmental Technologies and Energy Production', funded as project No. CZ.02.1.01/0.0/0.0/16_026/0008413 by Czech Republic Operational Programme Research, Development and Education.

References

Kakac, S. (1991) *Boilers, evaporators and condensers*. Wiley.

Niessen, W. R. (2010) *Combustion and Incineration Processes – Applications in Environmental Engineering*. Taylor and Francis Group.

Spalding, D. B. and Taborek, J. (1983) *Heat exchanger design handbook*. Hemisphere Publishing Corp.

30th International Conference
ENGINEERING MECHANICS 2024
Milovy, Czech Republic, May 14 – 16, 2024

OPTIMIZING VENTURI NOZZLE DESIGN FOR ENHANCED CAVITATION AND PRESSURE DYNAMICS: A COMPARATIVE ANALYSIS OF TURBULENCE MODELS FOR CAVITATING FLOW CHARACTERIZATION

Zeman R.*, Rudolf P.**

Abstract: *This article compares three Venturi nozzle geometries using CFD to determine the best geometry variant for enhanced cavitation and pressure pulsations. Simulations were performed using two different turbulence models, a hybrid SBES and a RANS model SST k-ω. Comparisons were made from the time recording of the vapor volume and pressure monitors. Changing the turbulence model led to different results, and therefore the outputs of the more complex SBES model were considered as valid. Venturi nozzle with zero throat length was found to be the best choice at the selected boundary conditions for vapor phase formation while increasing amplitudes of pressure pulsations.*

Keywords: Cavitation, CFD, Venturi, pulsations.

1. Introduction

Cavitation has long been known for its negative effects especially during the operation of hydraulic machines. Vibrations, noise or cavitation erosion accompanying the formation and violent collapse of cavitation bubbles have therefore become a subject of numerous studies. Efforts have been made to fully or at least partially mitigate these negative effects. One of the ways for cavitation suppression is shape optimization of those machine parts which are susceptible to cavitation and cavitation erosion. (Epps, 2015 and Sun, 2022).

Recently, cavitation has been studied so that its destructive effects can in turn be used for the benefit of the cause. If cavitation is to be generated on purpose, it is desirable that the most intense cavitation possible occurs in the device, using as little energy as possible. This fact opens the door to shape optimization, which in turn will enhance cavitation and thus allow cavitation generators to become more efficient. Water purification using hydrodynamic cavitation is one of the areas of research (Dular, 2016), where venturi nozzles of different shapes are widely used for this purpose (Jančula, 2014). Improving the efficiency of these simple devices would promote their eventual deployment in industry.

2. Methods

All three nozzle geometries were designed with a circular cross-section, 0.5 mm wide throat, 5 mm wide upstream section, 3 mm wide downstream section and confuser section with 60 ° angle. Geometry variant A, Fig. 1, had a 2 mm long neck and a diffuser angle of 12 °, while variant B had a wider diffuser angle of 14 °. Variant C, while maintaining a diffuser angle of 12 °, lacked the full length of the throat and the converging part was therefore directly connected to the diffuser.

* Ing. Radek Zeman: Faculty of Mechanical Engineering, Brno University of Technology, Technická 2896/2; 616 69, Brno; CZ, 192038@vutbr.cz

** Assoc. Prof. Ing. Pavel Rudolf, PhD.: Faculty of Mechanical Engineering, Brno University of Technology, Technická 2896/2; 616 69, Brno; CZ, rudolf@fme.vutbr.cz

doi: 10.21495/em2024-326

Fluid domains were created for all three 3D geometries with appropriate decomposition. Structured conformal hexagonal meshes were then generated with respect to y+ not exceeding value of 5 in the regions of interest (nozzle throat and diffuser) during the simulation. The final meshes consisted of A) 4 050 000, B) 4 050 000 and C) 3 690 000 elements.

Y+ values for mesh sizing and boundary conditions were determined from preliminary simulation. The boundary conditions were chosen to enable testing of the manufactured nozzles in an available hydraulic laboratory if necessary. Prior to running the simulation, pressure monitors were set at 21 points located in the nozzle diffuser. The pressure at the inlet and the volume of the vapor phase in the fluid domain were also monitored. Simulations were performed with all three geometries in Ansys Fluent software using the hybrid turbulence model SBES and the two-equation RANS turbulence model SST k-ω. The boundary conditions correspond to the values of the Reynolds number $Re = 19\,904$ (1) and the cavitation number $\sigma = 0.124$ (2).

$$Re = \frac{D_H \cdot v_T}{\nu}\ [-], \tag{1}$$

$$\sigma = \frac{p_2 - p_V}{\rho \cdot \frac{v_T^2}{2}}\ [-], \tag{2}$$

where $D_H\ [m]$ denotes the hydraulic diameter of nozzle throat, $v_T\ [m \cdot s^{-1}]$ the mean velocity in nozzle throat, $\nu\ [m^2 \cdot s^{-1}]$ the kinematic viscosity of water, $p_2\ [Pa]$ the absolute pressure at the outlet, $p_V\ [Pa]$ the saturated water vapor pressure, $\rho\ [kg \cdot m^{-3}]$ the density of water.

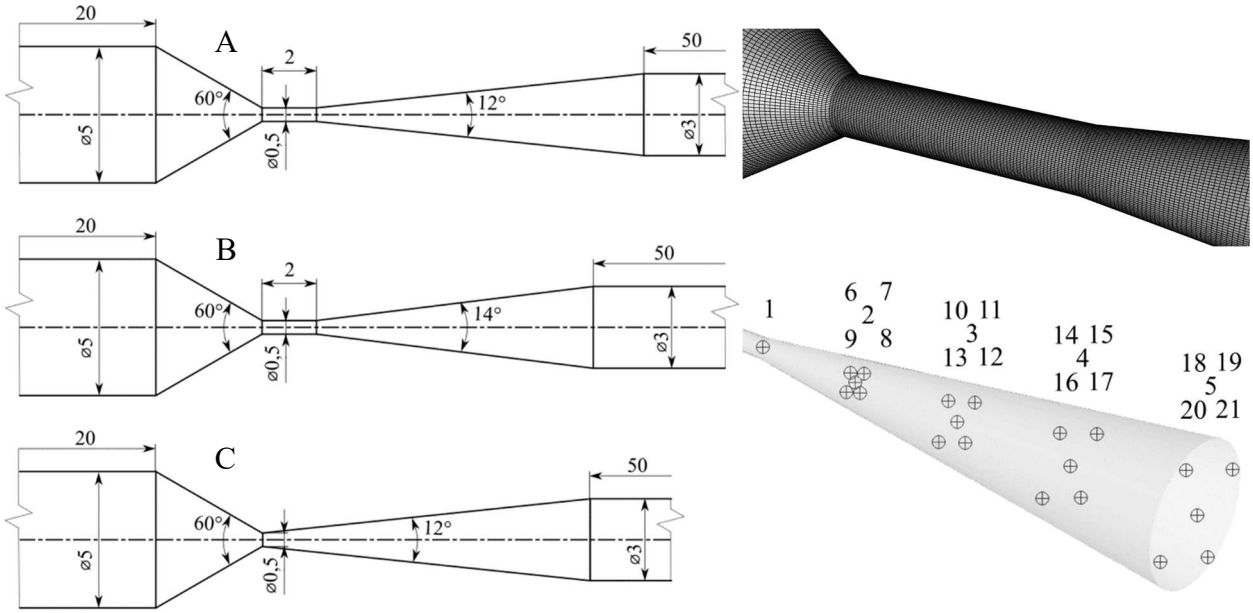

Fig. 1: Fluid domain geometry variants (on letf), mesh (upper right), pressure monitors (bottom right).

Although SBES has been called a hybrid turbulence model previously, it is more of a new way to combine existing RANS and LES models through the so-called shielding (blending) function (3):

$$\mu_T = \mu_T^{RANS} f_S + \mu_T^{LES}(1 - f_S) \tag{3}$$

The combination of RANS and LES is designed to model certain flow cases where conventional RANS would not produce accurate results (strong mixing, separation, etc.), while reducing the computational demands in comparison with LES simulations (Menter, 2018).

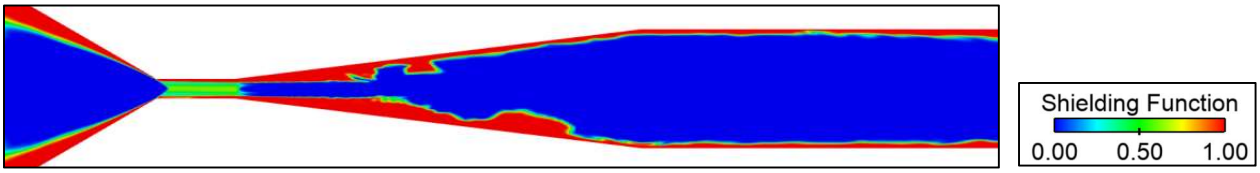

Fig. 2: Contour of shielding function for var B at maximum cavity length.

3. Results

The graphical representation of the vapour volume monitor (Figs. 3 and 4) showed a sinusoidal pattern for all three geometries, and for both the SBES and SST k-ω turbulence models. However the amplitudes of the sinusoids for the two selected turbulence models differed significantly for each nozzle design, sometimes by an order of magnitude (nozzle A and B). SBES predicted the highest amplitudes of the vapour phase change for geometry variant C, and smaller amplitudes for A and B, while the descending order of A, B ,C was determined by using the SST k-ω turbulence model.

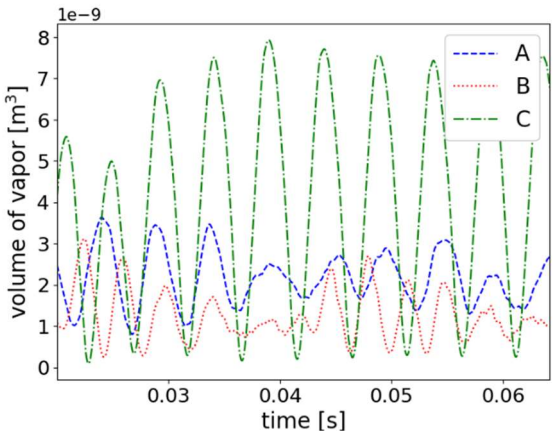

Fig. 3: SBES volume fraction monitor.

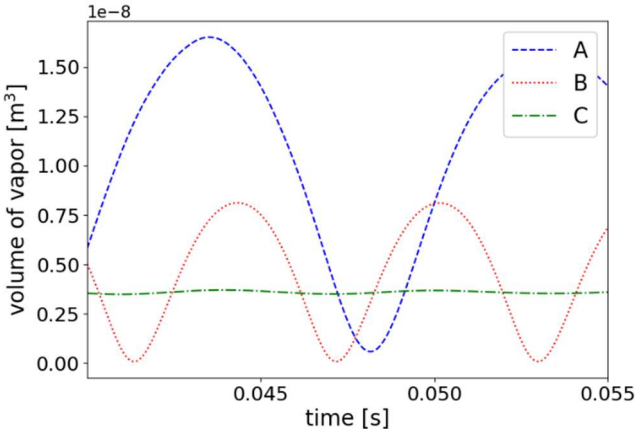

Fig. 4: SST k-ω volume fraction monitor.

The periodic change in the volume of the vapour phase corresponded with the typical behaviour of developed cavitation, where periodic shrinkage and growth of the cavity from the nozzle throat to the diffuser is usually observed. Except for variant A for SBES and variant C for SST k-ω, almost complete shrinkage of the cavity up to the nozzle neck always occurred during the simulation.

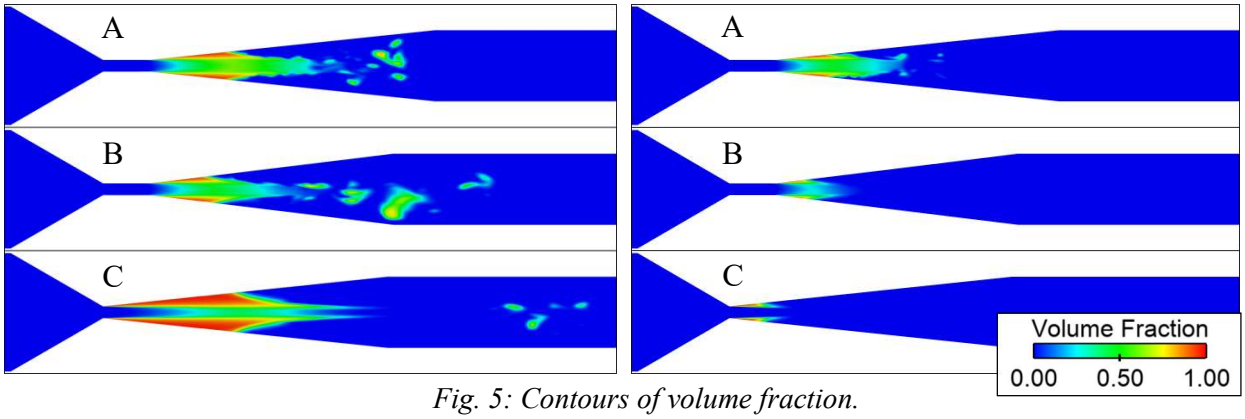

Fig. 5: Contours of volume fraction.

Fig. 5 shows the contours of the volume fraction for SBES simulation in a longitudinal section of each nozzle at the moment of cavity shrinkage and full expansion. The presence of separated parts of the vapor phase could also be observed on the contours. Pressure monitors showed that cavity shrinkage was accompanied by pressure pulsations as shown in Figs. 6 and 7. The amplitude of the pressure pulsations increased with increasing distance from the nozzle throat, while the amplitudes of a group of pressure monitors at the same distance from the throat (e.g. 2, 6, 7, 8, 9) did not differ significantly. SBES predicts a more credible pressure record compared to the smoother pattern coming from the RANS simulation. Secondary pulsations were probably caused by the collapse of the separated vapor fractions, which were present in the flow field only when using the hybrid turbulence model. The peaks of pressure pulsations were highest for SBES variant C, less so for B and A, while SST k-ω predicted a decreasing order of B, A and C.

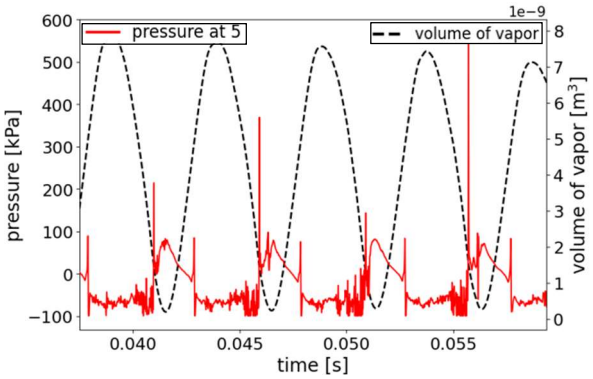

Fig. 6: SBES-monitor 5, C var.

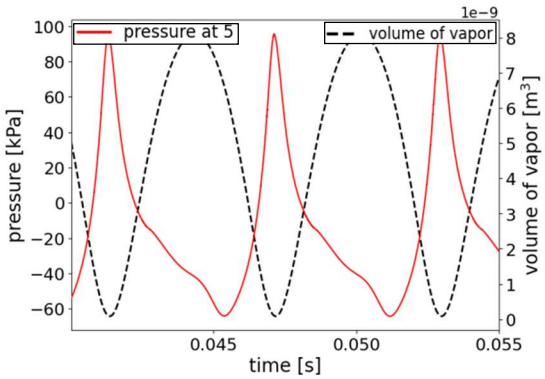

Fig. 7: SST k-ω-monitor 5, B var.

4. Conclusion

The CFD simulations showed different results when using different turbulence models. This could lead to the conclusion that the choice of turbulence model has a great influence on the results obtained from the simulations if cavitation is focus of interest. To confirm this, further CFD simulations would be needed to rule out the influence of the mesh on the results obtained, and even so, it would be necessary to perform experiments for final confirmation.

With the increase in computational complexity, SBES simulations should lead to more physical results, and therefore these results were considered as more reliable. SBES simulations showed that nozzle design C, i.e. without a throat, should be the best choice, whether the goal was to hold the highest possible volume of vapor phase in the nozzle or to create the highest pressure pulsations under the chosen boundary conditions.

Acknowledgement

Czech Science Foundation is acknowledged for support of the research under project 22-11456S „Exploring fundamental interactions of hydrodynamic cavitation and low-temperature plasma to enhance the disinfection effects“, conference attendance was supported by specific research project FSI-S-23-8183.

References

Dular, M. et al. (2016) Use of hydrodynamic cavitation in (waste)water treatment. *Ultrasonics Sonochemistry*, 29, pp. 577–588.

Epps, B., Víquez, O. and Chryssostomidis, C. (2015) A Method for Propeller Blade Optimization and Cavitation Inception Mitigation. *Journal of ship production and design*. 31, 2, pp. 88–98.

Jančula, D., Mikula, P., Maršálek, B., Rudolf, P. and Pochylý, F. (2014) Selective method for cyanobacterial bloom removal: hydraulic jet cavitation experience. *Aquaculture International*, 2 (22), pp. 509–521.

Menter, F. (2018) Stress-Blended Eddy Simulation (SBES) – A New Paradigm in Hybrid RANS-LES Modeling. In: *HRLM 2016: Progress in Hybrid RANS-LES Modelling*, pp. 27–37.

Sun, Z., Li, D., Mao, Y., Feng, L., Zhang, Y. and Liu, C. (2022) Anti-cavitation optimal design and experimental research on tidal turbines based on improved inverse BEM. *Energy* (Oxford), 239.

Author Index

I

J

K

L

M

N

O

P

R

S

T

U

V

W

Y

Z